# TWO DIMENSIONAL CHARACTERIZATION OF TOPOGRAPHIES OF GEOMATERIAL PARTICLES AND SURFACES

A Dissertation
Presented To
The Academic Faculty

By

Zeynep Bade Sozer

In Partial Fulfillment
Of the Requirements for the Degree
Doctor of Philosophy in Civil and Environmental Engineering

Georgia Institute of Technology

March, 2005

# TWO-DIMENSIONAL CHARACTERIZAZTION OF TOPOGRAPHIES OF GEOMATERIAL PARTICLES AND SURFACES

Approved By:


Dr. J. David Frost, Advisor
School of Civil and Environmental Engineering
*Georgia Institute of Technology*

Dr. Yi-Chang Tsai
School of Civil and Environmental Engineering
*Georgia Institute of Technology*

Dr. Leonid N. Germanovich
School of Civil and Environmental Engineering
*Georgia Institute of Technology*

Dr. Alexander Shapiro
School of Industrial & Systems Engineering
*Georgia Institute of Technology*

Dr. Glenn J. Rix
School of Civil and Environmental Engineering
*Georgia Institute of Technology*


Date Approved: March 10, 2005

To the Warrior, the hero and the cure of my Life. To my Dad. My love for you never had a beginning and never ended but grew even when you were gone. The sun still shines through your eyes, wind blows with your words, rain drops fall like the tears through my face on the day you had to leave.

I love you Dad.

# ACKNOWLEDGEMENT

Writing this dissertation has been a life-long journey for me. Throughout a lot has happened; loosing my lovely dad, health struggles, births, even an earthquake at home. If it was not for the great people that I had around me I could never have reached this point writing acknowledgements .

Dr. Frost; I am so fortunate to have had the opportunity to think and explore with you. Although your official title was “advisor” you were really much more to me than that. Thank you for your trust in me. Thank you for supporting me through my tough journey. Thank you for showing me how to be a good and considerate advisor and companion along the Ph.D. journey. I do not have enough space here to tell you how much you mean to me.

To my wonderful family:

Dad; I couldn’t have done this without your ever smiling face and shining heart. You were by my side in this world patting me on the back and now you come to me in my dreams. Thank you for still being around. This big place in my heart is still burning for you. My selfish ego desires you never left this world. My lovely mom and beautiful sister; thank you for giving me courage, boundless patience, even more boundless love, and support and all those feelings that made me feel home when I was six thousand miles away. I am so fortunate to have this beautiful and loving family. A family protected by the endless love for each other.

And of course my Uncle Moiz; you are not my real dad and I am not your daughter but

we are almost there. Thank you for “who you are” and for “who you have become for me”.

Edison; thank you for insightful discussions, patience with my persistent questions and sharing your brilliant mind. I feel fortunate to have met you. John; there are no words for your endless support all through this time in so many ways. Cemre; for the most precious friendship, most beautiful laughter, and purest heart. I do not understand how you keep up with me after 18 years. But, just so you know I will never leave you alone. Rome…Thank you for listening and guiding all through my GT life. I owe you too much. John Lynch; for reminding me to keep my perspective and my real self and helping me to do so. Erkin; for helping me tackle any formatting problems as well as personal ones. Berkin; for reminding me that all is going to be well and all is already great. Ali, I have become a better person with you. Firat, Serra, and Lara; for their support. Xuan; you are an expert in image analysis as good as Gaurav is in the computer world. I thank you both for listening, helping, and being part of my journey. Ines; you are a lovely yogi and my soul mate. I would also like to thank Dr. Frost’s research group for always being nice to me although I failed to be part of everything that I wished I could be. John Merideth; thank you for making me come to the moment only to breathe when I was either crying about the past or dreading the future. Thank you for the “present”, and thank you for your yogi heart. Scott; you are one of those people who never give up. Dr. Santamarina; for your comforting chats and words of courage. I would also like to thank my committee members for their time, efforts, and for encouraging me for my future.

# TABLE OF CONTENTS


ACKNOWLEDGMENTS iv

LIST OF TABLES ix

LIST OF FIGURES xiii

SUMMARY xx

CHAPTER 1 INTRODUCTION 1

1.1 Motivation for Study 1
1.2 Scope of Thesis 7

CHAPTER 2 LITERATURE REVIEW 9

2.1 Engineering Behavior of Surfaces 9
2.1.1 Interface Mechanisms 9
2.1.2 Properties Affecting Particulate-Continuum Interfaces 14
2.2 Effect of Relative Particle Dimensions on Interface Behavior 22
2.3 Effect of Relative Material Roughness on Interface Behavior 28
2.3.1 Particle Shape and Particle Surface Roughness Analysis 28
2.3.2 Continuum Surface Roughness Analysis 104
2.4 Concluding Commentary 129

CHAPTER 3 STUDY MATERIALS AND ANALYSIS METHODS 131

3.1 Overview of Study Particles and Surfaces 131
3.1.1 Real Particles and Surfaces 131
3.1.2 Derived Particles 138
3.1.3 Derived Surfaces 154
3.2 Validation of Particle Unrolling and Surface Wrapping Algorithms 155
3.2.1 SURF-DPART Conversion with Three Offset Surfaces 157
3.2.2 PART-DSURF Conversion with Three Proportionate Particles 158
3.2.3 PART-DSURF-DDPART Conversion 161
3.2.4 SURF-DPART-DDSURF Conversion 163
3.3 Analysis of Particle Shape Characterization Methods 175
3.3.1 Image to Particle Outline Procedure – Outline Extraction Algorithm 178
3.3.2 Selection of Particle Shape Parameters 183
3.3.3 Sukumaran and Ashmawy Form Factor 184
3.3.4 Minimum Zone Circles using Voronoi Diagrams 189
3.3.5 Particle Angularity 196
3.3.6 Boyce and Clark Shape Index 207
3.3.7 Wadell's Roundness 209
3.4 Analysis of Surface Roughness Characterization Methods 226
3.4.1 Selection of Surface Roughness Parameters 226
3.4.2 Conventional Surface Roughness Parameters 226
3.4.3 Normalized Roughness Parameter 233
3.4.4 Spike Parameter Quadratic on Surface Profiles 233

3.4.5 Centroid Trace on Surface Profiles 238
3.5 Concluding Commentary 238

CHAPTER 4 ANALYSIS RESULTS AND DISCUSSION 240

4.1 Results of Analysis of Particle Shape Parameter Values 240
4.1.1 Sukumaran and Ashmawy Form Factor 240
4.1.2 Minimum Zone Circles using Voronoi Diagrams 243
4.1.3 Particle Angularity 248
4.1.4 Boyce and Clark Shape Index 257
4.1.5 Property Differences between Real and Derived Particles 262
4.2 Results of Analysis of Surface Roughness Parameter Values 264
4.2.1 Conventional Roughness Parameters 264
4.2.2 Normalized Roughness Parameter 265
4.2.3 Spike Parameter Quadratic on Surface Profiles 268
4.2.4 Centroid Trace on Surface Profiles 270
4.2.5 Property Differences between Real and Derived Surfaces 280
4.3 Resolution Analysis 285
4.3.1 Particle Shape Parameters 285
4.3.2 Surface Roughness Parameters 308
4.4 Concluding Commentary 312

CHAPTER 5 DEVELOPMENT OF NEW SURFACE ROUGHNESS AND PARTICLE SHAPE PARAMETERS 314

5.1 Development of Equivalent Surface Roughness Parameters based on Particle Shape Analysis 314
5.1.1 Selected Parameters and Surface Profiles 315
5.1.2 Surface Roughness Characterization by Characteristic Radius Ratio 316
5.1.3 Surface Roughness Characterization by Spike Parameter 322
5.1.4 Surface Roughness Characterization by Spike Parameter Quadratic 325
5.1.5 Surface Roughness Characterization by Shape Index 338
5.2 Development of Equivalent Particle Shape Parameters based on Surface Roughness Analysis 343
5.2.1 Selected Parameters and Particle Outlines 343
5.2.2 Particle Shape Characterization by Conventional Surface Roughness Parameters 344
5.3 Comparison between Particle Shape and Surface Roughness Parameters 346
5.4 Concluding Commentary on Particle Shape Parameters 360
5.5 Concluding Commentary on Surface Roughness Parameters 372
5.6 Implications of Study Findings for 3D Characterization Studies 377

CHAPTER 6 SUMMARY, CONCLUSIONS, AND RECOMMENDATIONS 384

6.1 Summary 384
6.2 Conclusions 387
6.2.1 Particulate-Continuum Interfaces 388
6.2.2 Particle Shape and Surface Roughness Parameters 389
6.2.3 Proposed techniques for A Unified Particle-Continuum Interface Analysis 391
6.3 Recommendations 394

APPENDIX A Table of Mathgrams 399

APPENDIX B The Square Wheel 412

REFERENCES 422

# LIST OF TABLES


| | | |
|---|---|---|
| 2.1 | Properties affecting particle – continuum interfaces (after DeJong, 2001). | 20 |
| 2.2 | The shear mechanisms at geomembrane-sand interfaces (after Frost et al., 1999). | 21 |
| 2.3 | Particle size parameters. | 23 |
| 2.4 | Brief remarks on the particle shape analysis methods. | 31 |
| 2.5 | Particle macro- & meso- & micro- shape parameters. | 36 |
| 2.6 | Particle macro- & meso- shape parameters. | 38 |
| 2.7 | Particle meso– shape parameters. | 40 |
| 2.8 | Particle micro– shape parameters. | 43 |
| 2.9 | Angularity parameters (literature review). | 81 |
| 2.10 | Five shape parameters used by Podczeck (1997) for NS. | 100 |
| 2.11 | Review of commonly used surface roughness parameters (adapted from Thomas, 1981). | 108 |
| 3.1 | The names and the mineralogy of the selected study materials. | 134 |
| 3.2 | Initial and sequential formats of the study materials | 135 |
| 3.3 | Resolution properties of the selected real particles. | 140 |
| 3.4 | The profile lengths and the corresponding circle diameter ranges for the CT analysis. | 142 |
| 3.5 | The maximum CT surface parameter values for the concrete profile. | 149 |
| 3.6 | The correlation values for maximum CT surface parameters (concrete). | 150 |
| 3.7 | Height and radius averages for SO, S1, and S2 and P0, P1, and P2, respectively. | 159 |
| 3.8 | Procedure for PART-DSURF-DDPART conversion. | 161 |
| 3.9 | Procedure for SURF-DPART-DDSURF conversion. | 167 |
| 3.10 | Surfaces selected for SURF-DPART-DDSURF conversion. | 167 |
| 3.11 | Numerical values in relation to the four study cases. | 173 |
| 3.12 | Calculated and the reported SF and AF values for 10 grains (Ashmawy, 2004). | 186 |

| | | |
|---|---|---|
| 3.13 | Table of FF values from the reported and calculated SF and AF for 10 grains (Ashmawy, 2004). | 189 |
| 3.14 | Table of calculated and reported SP values. | 199 |
| 3.15 | The values of SP reported and SP calculated with the First Alternative Method. | 201 |
| 3.16 | The values of SP reported and SP calculated with the Second Alternative Method. | 203 |
| 3.17 | Table of calculated and reported SPQ values. | 207 |
| 3.18 | Table of calculated and reported SI values. | 209 |
| 3.19 | Computed and reported roundness values for varying minimum radius thresholds. | 219 |
| 3.20 | Computed Wadell's roundness values of four particles by different methods. | 220 |
| 3.21 | Computed Wadell's roundness values of twelve particles by different methods. | 222 |
| 3.22 | Computed Wadell's roundness values of *Wadell2* using handdom approach. | 224 |
| 3.23 | Computed Wadell's roundness values of *Wadell2* using Teh and Chin (1989) dominant point method. | 225 |
| 3.24 | Table of calculated and reported conventional surface roughness values. | 228 |
| 3.25 | Table of calculated normalized roughness values for four surface profiles. | 233 |
| 3.26 | Table of calculated and reported SPQ-surf values for seven abrasive surface profiles. | 237 |
| 4.1 | SF, AF, and FF values for the study parts and dparts. | 241 |
| 4.2 | CRR values for the study parts and dparts. | 248 |
| 4.3 | SP values for the study parts and dparts. | 250 |
| 4.4 | SPQ values for the study parts and dparts. | 252 |
| 4.5 | SP and SPQ values for the study parts and dparts. | 254 |
| 4.6 | SP and SPQ values calculated for Hamblin and Stachowiak (1996) study particles. | 255 |
| 4.7 | SI and radial distribution standard deviation values for the study *parts* and *dparts* | 258 |
| 4.8 | Selected conventional surface roughness parameters for study *surfs* and *dsurfs*. | 264 |
| 4.9 | Normalized Roughness Parameter values for the study *surfs* and *dsurfs*. | 265 |

| | | |
|---|---|---|
| 4.10 | SPQ-surf values for the study *surfs* and *dsurfs*. | 268 |
| 4.11 | Average Surface Roughness ($R_a$) values for selected geomaterials (after DeJong, 2001). | 280 |
| 4.12 | Additional surface roughness parameters' abbreviations and equations. | 282 |
| 4.13 | Additional surface roughness parameters values for the study *surfs* and *dsurfs*. | 283 |
| 4.14 | Particle data points and the corresponding CRR, SP, and SPQ particle shape parameters. | 287 |
| 4.15 | SF and AF resolution study results for *p4* and *p2* defined by 45, 360, 720, 1440, and 2880 data points. | 294 |
| 4.16 | SF and AF resolution study results for *concrete-par* defined by 180, 250, 360, 720, 2000, and 3750 data points | 296 |
| 4.17 | Number of *p4* outline data points versus AF values | 301 |
| 4.18 | Number of *p2* outline data points versus SF values. | 303 |
| 4.19 | *p4* outline data points with corresponding sqrtAF stabilized values. | 306 |
| 4.20 | Shape index (SI) resolution study results for *p4*. | 307 |
| 4.21 | Surface roughness parameter values for varying resolutions (15-mm long, concrete profile). | 309 |
| 5.1 | Procedure for attaining study surfaces. | 316 |
| 5.2 | CRR-surf values for the study *surfs* and *dsurfs.* | 319 |
| 5.3 | CRR values for the *parts* and *dparts*. | 319 |
| 5.4 | Spike Parameter values for the *surfs* and *dsurfs*. | 323 |
| 5.5 | SPQ and SPQ-surf values for *parts* and *surfs*, respectively. | 325 |
| 5.6 | SPQ-surf values for *p4-surf* with different # of decimal places. | 327 |
| 5.7 | The matrix output for *p4* SPQ calculation. | 330 |
| 5.8 | The matrix output for *p4-surf* SPQ-surf calculation. | 331 |
| 5.9 | Final step for *p4* SPQ and *p4-surf* SPQ-surf computation. | 333 |
| 5.10 | SPQ and SPQtr-surf values for *parts* and *surfs*, respectively. | 335 |
| 5.11 | The matrix output for *p4-360* SPQ calculation. | 336 |
| 5.12 | The matrix output for *p4surf-360* SPQtr-surf calculation. | 338 |
| 5.13 | Shape Index-surf values for the *surfs* and *dsurfs.* | 339 |

| | | |
|---|---|---|
| 5.14 | Shape Index-surf values for *p1-surf* and *concrete* profiles for varying number of intervals. | 342 |
| 5.15 | Output of New Particle Shape Parameters with *part* and *dpart* inputs. | 346 |
| 5.16 | Output of Conventional Surface Roughness Parameters with *surf* and *dsurf* inputs. | 346 |
| 5.17 | Observation numbers corresponding to the particle shape parameters. | 355 |
| 5.18 | The MINITAB output for the particle shape parameters dendrogram. | 355 |
| 5.19 | The amalgamation steps and observed cluster groups. | 356 |
| 5.20 | Correlation Analysis within micro-shape cluster. | 358 |
| 5.21 | Observation numbers corresponding to the surface shape parameters. | 358 |
| 5.22 | The MINITAB output for the particle shape parameters dendrogram. | 359 |
| 5.23 | The amalgamation steps and observed cluster groups. | 360 |
| 5.24 | Particle Shape Parameters analyzed by Podczeck et al. (1999). | 364 |
| 5.25 | Various equivalent diameters for several different geometrical shapes (after Matsuyama and Yamamoto, 2004). | 367 |
| 5.26 | Particle outline data points and the corresponding $R_a$-part, $R_q$-part, $R_p$-part, $R_{max}$-part, and $R_n$-part values. | 377 |
| A.1 | Table of mathgrams and abbreviations used in this study. | 400 |

# LIST OF FIGURES


| | | |
|---|---|---|
| 2.1 | Single point and multiple point contact showing adhesion and plowing (after Briscoe, 1992). | 12 |
| 2.2 | Normal stress (kPa) versus peak secant friction coefficient (after Dove and Frost, 1999). | 15 |
| 2.3 | Normalized surface roughness ( $R_n$ ) versus coefficient of friction ( $\mu$ ) for sand-steel interfaces (after Uesugi and Kishida, 1986b). | 17 |
| 2.4 | Normalized Roughness ( $R_n$ ) versus average interfacial friction angle ( $\mu$ ) (after Paikowsky, 1995). | 18 |
| 2.5 | Wadell's definition of sphericity and roundness (after Hawkins, 1993). | 34 |
| 2.6 | A simplified representation of form, roundness, and surface texture by three linear dimensions to illustrate their independence (after Barrett, 1980). | 35 |
| 2.7 | The nearest (N(A)) and farthest (F(A)) regions for point A (after Huang,1999). | 51 |
| 2.8 | The Nearest and Farthest Voronoi Diagrams for the points A, B, C, and D (after Huang, 1999). | 51 |
| 2.9 | Four different particle arrangements for local scale analysis (after Estrin et al., 1999). | 52 |
| 2.10 | An example of polygon extraction procedure (after Ye, 1995). | 56 |
| 2.11 | The data points labeled as $P_i$, where $i = \{1,2,\ldots\ldots,12\}$ and the convex outerhull (the dotted line) with vertices labeled as $V_i$ (after Samuel and Shunmugam, 2000). | 58 |
| 2.12 | The initial farthest edges for the construction of the farthest ED diagram (after Samuel and Shunmugam, 2000). | 58 |
| 2.13 | The Farthest Voronoi Diagram and the Minimum Circumscribed Circle (MCC) (after Samuel and Shunmugam, 2000). | 61 |
| 2.14 | The transformed data and the convex inner hull (after Samuel and Shunmugam, 2000). | 61 |
| 2.15 | The Nearest Voronoi Diagram and the Maximum Inscribed Circle (MIC) (after Samuel and Shunmugam, 2000). | 64 |
| 2.16 | Superimposed Farthest and Nearest Voronoi Diagrams along with MZC (after Samuel and Shunmugam, 2000). | 64 |
| 2.17 | Freeman chain code | 75 |
| 2.18 | Fitting of a circular arc to a set of points. | 79 |

| | | |
|---|---|---|
| 2.19 | Illustration of boundary features that participate in abrasive wear (after Leavers, 2000). | 85 |
| 2.20 | Schematic drawing for Shape and Angularity Factor Calculation (adapted from Sukumaran and Ashmawy, 2001) | 88 |
| 2.21 | Triangle construction along particle boundary (after Hamblin and Stachowiak, 1995). | 91 |
| 2.22 | Comparison of triangle A and B for a particular triangle base (after Hamblin & Stachowiak, 1995). | 92 |
| 2.23 | Six artificial shapes (after Hamblin & Stachowiak, 1995). | 93 |
| 2.24 | A plot of the artificial shapes vs. selected shape parameters (after Hamblin and Stachowiak, 1995). | 94 |
| 2.25 | Method of SPQ (spike parameter – quadratic) calculation (after Hamblin & Stachowiak, 1996) | 96 |
| 2.26 | Surface texture at different scales (Anonymous, 1985). | 105 |
| 2.27 | Surfaces with identical Average Roughness ( $R_a$ ) values (after Hamrock, 1994). | 112 |
| 2.28 | Method of evaluating the SPQ from a surface profile (after Stachowiak, 1998). | 115 |
| 2.29 | Terminology of the Envelope System (after von Weingraber, 1972). | 120 |
| 2.30 | The definition of a Motif (after Fahl, 1982). | 123 |
| 2.31 | Theoretical profile and Centroid Traces for 1.0 and 20.0 mm diameter particles (after DeJong, 2001). | 127 |
| 3.1 | The general algorithm for the analysis methodology. | 132 |
| 3.2 | Images and identifications of the abrasives studied; **(a)** Particle 1, **(b)** Particle 2, **(c)** Particle 3, **(d)** Particle 4. | 133 |
| 3.3 | Modified surface profiles; **(a)** Rough Finished Concrete, **(b)** HDPE Medium Textured Geomembrane, and **(c)** Tooled Steel (after DeJong, 2001). | 137 |
| 3.4 | Figure showing the derived particle process. | 139 |
| 3.5 | CT surface parameter plots versus the circle diameter for the selected profile lengths. | 143 |
| 3.6 | The maximum CT surface parameter values for the corresponding profile lengths. | 149 |
| 3.7 | Derived particle outlines; **(a)** concrete-par, **(b)** HDPE-par, and **(c)** steel-par. | 153 |
| 3.8 | Derived surface profiles; **(a)** p1-surf, **(b)** p2-surf, **(c)** p3-surf, and **(d)** p4-surf | 156 |
| 3.9 | Schematic drawing of the reversibility of **(a)** PART-DSURF-DDPART | |

conversion, **(b)** SURF-DPART-DDSURF conversion 157

3.10 Three identical but offset surfaces of two 60° ridge surface. 158

3.11 The outputs *P0, P1,* and *P2.* 159

3.12 Three different size but same shape particles. 160

3.13 The outputs S*0, S1,* and S2. 161

3.14 Four selected PART outlines for validation of PART-DSURF-DDPART conversion. 162

3.15 Output of *particle unrolling* for the selected particles during PART-DSURF-DDPART conversion. 164

3.16 Output of *surface wrapping* for the DSURFS of the selected particles during PART-DSURF-DDPART conversion. 165

3.17 Comparison of PART & DDPART for PART-DSURF-DDPART validation. 166

3.18 Input surface profiles for SURF-DPART-DDSURF conversion. 168

3.19 Output of *surface wrapping* for the selected surface profiles during SURF-DPART-DDSURF conversion. 169

3.20 Output of *particle unrolling* for the DPARTS of the selected surface profiles during SURF-DPART-DDSURF conversion. 170

3.21 SURF, RSURF, and DDSURF for the SURF-DPAR-DDSURF conversion. 172

3.22 Comparison of RSURF & DDSUF2 for validation. 174

3.23 Real and derived study particles outlines. 176

3.24 Real and derived study surface profiles. 177

3.25 Real particle outlines; **(a)** p1, **(b)** p2, **(c)** p3, and **(d)** p4. 182

3.26 **(a)** Graph showing the trend of SF (calculated) and SF (reported) for the 10 grains used for validation, **(b)** Plot of regression analysis between the calculated and reported SF for the 10 grains used for validation. 187

3.27 **(a)** Graph showing the trend of AF (calculated) and AF (reported) for the 10 grains used for validation, **(b)** Plot of regression analysis between the calculated and reported AF parameters for the 10 grains used for validation. 188

3.28 **(a)** Graph showing the trend of FF (calculated) and FF (reported) for the 10 grains used for validation, **(b)** Plot of regression analysis between the calculated and reported FF parameters for the 10 grains used for validation. 190

3.29 Theoretical profile and Centroid Traces for a range of particles; **(a)** 0.075 – 2.0 mm, **(b)** 3.0 – 20.0 mm (after DeJong, 2001). 194

3.30 Abrasive grit images used for SP & SPQ Analysis (after Hamblin and Stachowiak, 1996); **(a)** glass beads, **(b)** garnet, **(c)** silicon carbide, **(d)** crushed

sintered alumina, **(e)** silica sand, **(f)** diamond, **(g)** quartz. 198

3.31 **(a)** Graph showing the trend of SP (calculated) and SP (reported) by Stachowiak (1995), **(b)** Plot of regression analysis between the calculated and reported SP parameters. 200

3.32 **(a)** Graph showing the trend of SP (calculated – First Method) and SP (reported) by Stachowiak (1995), **(b)** Plot of regression analysis between the calculated and reported SP parameters. 202

3.33 **(a)** Graph showing the trend of SP (calculated – Second Method) and SP (reported) by Stachowiak (1995), **(b)** Plot of regression analysis between the calculated and reported SP parameters. 204

3.34 **(a)** Graph showing the trend of SPQ (calculated) and SPQ (reported), **(b)** Plot of regression analysis between the calculated and reported SPQ parameters 208

3.35 **(a)** Grain projections referenced by Hawkins (1993), **(b)** Selected roundness values for grain projections (after Hawkins, 1993). 211

3.36 Dominant points of the selected shapes by Teh and Chin (1989); **(a)** chromosome shape, **(b)** semicircle curve, and **(c)** leaf curve; original outline points, Teh and Chin (1989) dominant points (after Wu, 2003). 215

3.37 Comparison of Teh and Chin (1989) dominant points and *handdoms* for selected grain projections; **(a)** *w8* first trial, **(b)** *w8* second trial, **(c)** *w19,* and **(d)** *w24* 217

3.38 Sketch of curves executed by the roundness algorithm using *handdoms*; **(a)**, **(b)**, **(c)** *w8* first trial, **(d)** *w8* second trial, **(e)** *w19,* and **(f)** *w24.* 218

3.39 Sand grain images termed as *Wadell2* (after Wadell, 1933). 223

3.40 Sand grain images grouped under heading *Wadell2* – upon editing (adapted from Wadell, 1933). 224

3.41 Real surface study profiles with 0.004mm resolution and 15-mm length. 227

3.42 **(a)** Graph showing the trend of $R_a$ (calculated) and $R_a$ (reported), **(b)** Plot of regression analysis between the calculated and reported $R_a$ values. 229

3.43 **(a)** Graph showing the trend of $R_q$ (calculated) and $R_q$ (reported), **(b)** Plot of regression analysis between the calculated and reported $R_q$ values 230

3.44 **(a)** Graph showing the trend of $R_p$ (calculated) and $R_p$ (reported), **(b)** Plot of regression analysis between the calculated and reported $R_p$ values 231

3.45 **(a)** Graph showing the trend of $R_{max}$ (calculated) and $R_{max}$ (reported), **(b)** Plot of regression analysis between the calculated and reported $R_{max}$ values 232

3.46 Comparison of the original profiles scanned from Stachowiak (1998) shown in black and digitized profiles for processing using *Enguage Digitizer* shown in red (aspect ratio = z/x = 1). 235

3.47 Plot of regression analysis between the calculated and reported SPQ-surf

parameters. 237

4.1 Plot of SF versus AF for the study particles; **(a)** with data points, **(b)** with particle outlines (the real particle outlines are enlarged for visualization). 242

4.2 Plot of FF for the study particles; **(a)** with data points, **(b)** with particle outlines (the real particle outlines are enlarged for visualization). 244

4.3 Plot of the particle outlines with MIC and MCC circles and the MZC centroid (the real particle outlines are enlarged for visualization). 246

4.4 Plot of CRR for the study particles; **(a)** with data points, **(b)** with particle outlines (the real particle outlines are enlarged for visualization). 249

4.5 Plot of NSP for the study particles; **(a)** with data points, **(b)** with particle outlines (the real particle outlines are enlarged for visualization). 251

4.6 Plot of NSPQ for the study particles; **(a)** with data points, **(b)** with particle outlines (the real particle outlines are enlarged for visualization). 253

4.7 Plot of SP vs. SPQ for the study particles; **(a)** with data points, **(b)** with particle outlines (the real particle outlines are enlarged for visualization). 256

4.8 Plot of SI for the study particles; **(a)** with data points, **(b)** with particle outlines. 259

4.9 Plot of radial number vs. % of radial distribution plots for the study materials. 260

4.10 Plot of surface names vs. average surface roughness parameter ($R_a$). 266

4.11 Plot of surface names vs. root mean square surface roughness parameter ($R_q$). 266

4.12 Plot of surface names vs. depth of surface smoothness ($R_p$). 267

4.13 Plot of surface names vs. maximum peak to valley roughness parameter ($R_{max}$). 267

4.14 Plot of surface names vs. normalized roughness parameter ($R_n$). 269

4.15 Plot of surface names vs. SPQ-surf parameter values. 269

4.16 CT surface parameters' plots for real and derived surfaces. 271

4.17 Particle *p4* outline at varying number of data points. 286

4.18 Figure showing CRR, SP, and SPQ with the number of data points/intervals. 288

4.19 *p2*, *p4*, and *concrete-par* sampled at different particle samplings; **(a)** p2, **(b)** p4, and **(c)** concrete-par. 293

4.20 *p2* SF and AF variation for different particle outline data points vs. the number of sampling intervals; **(a)** *p2* SF, **(b)** *p2* AF. 297

4.21 *p4* SF and AF variation for different particle outline data points vs. the number of sampling intervals; **(a)** *p4* SF, **(b)** *p4* AF. 298

4.22 *concrete-par* SF and AF variation for different particle outline data points vs. the number of sampling intervals; **(a)** *concrete-par* SF, **(b)** *concrete-par* AF. 299

4.23 AF value versus number of AF sampling intervals for *p2* 302

4.24 Sumangularity versus sampling interval plot for varying *p4* outline data points. 305

4.25 SQRTSumangularity versus sampling interval plot for varying *p4* outline data points. 305

4.26 sqrtAF versus sampling interval plot for varying *p4* outline data points. 306

4.27 *p4* Shape Index (SI) variation with the number of sampling intervals; **(a)** Number of sampling intervals from 0 to 1500, **(b)** Magnified section from 0 to 150 numbers of sampling intervals. 308

4.28 15 mm long *concrete* elevated profiles at different resolutions. 309

4.29 Surface roughness parameters versus profile resolution (for 15-mm long concrete profile). 311

5.1 **(a)** Plot of regression for CRR versus CRR -surf values, **(b)** Plot of CRR & CRR-surf versus particle and surface labels. 320

5.2 **(a)** Plot of regression for SP versus SP-surf values, **(b)** Plot of SP & SP-surf versus particle and surface labels 324

5.3 **(a)** Plot of regression for SPQ versus SPQ-surf values, **(b)** Plot of SPQ & SPQ-surf versus particle and surface labels. 326

5.4 The starting, apex, and end points of the spikes located for the 3-decimal places and 5-decimal places p4-surf profile inputs (The "**+**"s denote the apex, and the "**x**"s denote the starting and end points of spikes). 328

5.5 *p4* outline with the least squares circle (LSC) and the spike locations (The "**x**" symbols show the spikes' middle points and "**+**" symbols show the start and end points for the spikes). 331

5.6 *p4-surf* outline with the average mean line and the spike locations (The "**x**" symbols show the spikes' middle points and "**+**"symbols show the start and end points for the spikes). 332

5.7 **(a)** Plot of regression analysis between the SPQ for particle outlines and SPQtr-surf for surface profiles, **(b)** Plot of SPQ & SPQtr-surf vs. particle and surface labels. 337

5.8 **(a)** Plot of regression analysis between the SI for particle outlines and SI-surf for surface profiles, **(b)** Plot of SI & SI-surf vs. particle and surface labels. 340

5.9 Figure showing SI-surf values for selected surface profiles with the number of intervals; **(a)** *p1-*surf, **(b)** *p1-surf* magnified, **(c)** *concrete*, and **(d)** *concrete-*magnified. 343

5.10 **(a)** Plot of regression analysis between the $R_a$ for surface outlines and $R_a$-part for particle outlines, **(b)** Plot of $R_a$-part & $R_a$ versus particle and surface labels. 347

5.11 **(a)** Plot of regression analysis between the $R_q$ for surface outlines and $R_q$-part

for particle outlines, **(b)** Plot of $R_q$-part & $R_q$ versus particle and surface labels. 348

5.12 **(a)** Plot of regression analysis between the $R_p$ for surface outlines and $R_p$-part for particle outlines, **(b)** Plot of $R_p$-part & $R_p$ versus particle and surface labels. 349

5.13 **(a)** Plot of regression analysis between the $R_{max}$ for surface outlines and $R_{max}$-part for particle outlines, **(b)** Plot of $R_{max}$-part & $R_{max}$ versus particle and surface labels. 350

5.14 **a)** Plot of regression analysis between the $R_n$ for surface outlines and $R_n$-part for particle outlines, **(b)** Plot of $R_n$-part & $R_n$ versus particle and surface labels. 351

5.15 Particle shape parameters dendrogram using Hierarchical Cluster Observations with Centroid Euclidean distance measures. 356

5.16 Surface shape parameters dendrogram using Hierarchical Cluster Observations with Centroid Euclidean distance measures. 359

5.17 Dimensions of particle characterization (after Scott, 2003). 361

B.1 Particle *p1* rolling over its perfect road with a straight line centroid trace. 415

B.2 Particle *p2* rolling over its perfect road with a straight line centroid trace. 416

B.3 Particle *p3* rolling over its perfect road with a straight line centroid trace. 417

B.4 Particle *p4* rolling over its perfect road with a straight line centroid trace. 418

B.5 Particle *concrete-par* rolling over its perfect road with a straight line centroid trace. 419

B.6 Particle *HDPE-par* rolling over its perfect road with a straight line centroid trace. 420

B.7 Particle *steel-par* rolling over its perfect road with a straight line centroid trace. 421

# SUMMARY

The soil-structure interface is fundamental to the performance of many geotechnical engineering systems including penetration test devices, deep foundations, and retaining structures. The counterface to the soil may range from being a relatively soft polymer with a rough surface in the case of a geosynthetically reinforced earth retaining structure to a relatively hard steel with a smooth surface in the case of a cone penetrometer or a pile foundation. Irrespective of the properties of the soil or counterface, the interface is optimally analyzed as a “particulate-continuum” interface.

Two of the principal parameters responsible for the observed interface mechanisms are the particle shape and the continuum surface roughness. To date common practice has been to characterize counterface surface roughness by a roughness parameter based on only its spatial properties and particle shape by various incoherent means resulting in two values unrelated to each other. The vast number of analysis methods and associated parameters in both disciplines reveal the general confusion regarding this concept.

Besides these deficiencies in particle shape and surface roughness characterization, no analysis is currently employed in practice to capture the kinematic nature of the contact between a particulate and continuum medium. A relative measure of a particulate material (e.g. particle shape) compared to the contacting continuum surface (e.g. surface roughness) is more fundamental to the particulate-continuum analysis than

individually determined properties of the particle and surface components of the interface. Rather than analyzing the particulate and continuum media separately, it is appropriate to coalesce the analysis and quantify the relative nature of interface behavior. This can be facilitated by examining the particulate and continuum media using analytical tools that have the same conceptual origins.

The motive for this study is to identify means of investigating the particulate and continuum medium forming an interface with a unified approach. This is accomplished by examining several particle shape and surface roughness parameters in terms of their ability to uniquely describe and distinguish particulate medium and continuum roughness, respectively. Algorithms were developed for each of the chosen particle shape and surface roughness parameters. Upon validating the algorithms with the original study materials and results, the same algorithms are utilized with the particle outlines and surface profiles obtained for this study. The main hypothesis of the study is that particle and surface components of the interface can be analyzed by transforming them to derived surfaces and derived particles, respectively. Accordingly, a large section of this thesis involves the analysis of shape parameters with both real particles as well as particles *derived* from the continuum surface profiles. Similarly, surface roughness parameter algorithms were used to analyze real surface profiles and surfaces *derived* from the real particle outlines. The transformation of real particles into *derived* surfaces was accomplished by unrolling the particle outlines into a surface profile, and similarly *derived* particles were obtained by wrapping the real surface profiles. The hypothesis was tested using the particle shape and surface roughness parameter results.

An alternative approach to move towards a unified analysis system for particulate-continuum interface materials examined in this thesis includes transforming the analysis methods rather than the input particles or surfaces. Parameters developed originally for particle shape characterization were modified to capture surface roughness based on the same concepts and similarly, surface roughness characterization parameters were modified to allow particle shape characterization. An example is that a widely known surface roughness parameter, average roughness, $R_a$, was modified for a particle outline input and termed as $R_a$-part. The input for the original $R_a$ algorithm is real (or derived) surfaces, whereas for $R_a$-part, the input is real (or derived) particles. Since both analysis methods are based on the same concepts, this provides a coherent analysis framework for characterization of both materials at particulate-continuum interfaces.

A robust unified approach for particulate shape and continuum roughness characterization will ultimately lead to a better understanding of micro-scale interaction mechanism and better quantification of macro-scale mobilized resistance for soil and engineering surface interaction. Both approaches investigated in this thesis aim to combine particle shape and surface roughness analyses in terms of either similar format inputs or similar analysis algorithms. For both cases, the results are investigated and discussed.

# CHAPTER ONE

# INTRODUCTION

## 1.1 Motivation for Study

A wide range of geotechnical systems require the insertion of a man-made material into the subsurface in order to augment the overall system performance by introducing a soil to man-made material friction and/or adhesion interface. The purpose of the introduction of a man-made material into the subsoil can be to improve stability and bearing capacity, or reduce vertical (settlement) and lateral deformations. Examples include anchored, soil-nailed, or reinforced retaining structures, deep foundations utilizing piles, bridge abutments, and liner systems for landfills. For all of the above systems, the soil mass to man-made material interface is the common and critical feature that is the focus of this study. The performance of soil at the interface with many man-made materials, including steel, polymers, concrete, aluminium, and timber has been investigated and shown to depend on the behavior of the soil mass in proximity to the man-made material, which in turn is affected by the properties of the man-made material. It is generally accepted that the shear deformations concentrate within a thin zone of soil, adjacent to the man-made material after shearing is initiated. This interface zone is

characterized by strong local dilatancy, high displacement gradients, and significantly high grain rotations. At the micro-scale, the soil in shear consists of individual soil particles, which can be analyzed as a particulate medium. In contrast to the soil particle size and magnitude of relative displacement between the soil and man-made material, the man-made material is relatively long and typically behaves as a “continuum”. Thus, the soil to man-made material interface is best explored as a “particulate-continuum” zone.

The behavior of a granular soil mass to man-made material interface is complex and requires careful consideration when designing a system. As summarized by Lee (1998), two of the principal parameters responsible for the interface mechanisms are the particle shape and continuum surface roughness. Interfacial behavior at a particulate-continuum interface is also governed by other particle and surface properties as well as by boundary conditions. Other significant individual particle and particle mass properties mentioned include particle angularity and soil density, whereas initial soil structure, particle surface roughness, and the uniformity coefficient have negligible influence. Another dominant continuum surface property besides surface roughness is surface hardness. The boundary conditions such as the strain rate (for dry conditions) have a minor influence on interfacial behavior; whereas the influence of normal stress can be significant.

Accepted data suggests that sharp angular particles produce more erosion of the continuum surface than rounded particles with all other properties being equal. As early

as 1973, Brumund and Leonards performed static and dynamic testing with sand and typical construction materials and concluded that the coefficient of friction increased with the material surface roughness, sand angularity, and the relative roughness of the continuum surface with respect to the particle size. Another influential study by Uesugi et al. (1986) confirmed these conclusions with simple shear apparatus tests. Uesugi et al. (1986) developed correlations for interface friction with modified roundness of sand particles and normalized roughness of sand-steel interfaces.

Particle shape analysis is essential in many disciplines including ceramic, hydraulic, geological, geotechnical, petroleum, chemical, and metallurgical engineering. At least 50 particle shape parameters have been reported in literature. A source of confusion for particle shape analysis however is the diverse spectrum of definitions used; such as roundness, form, angularity, and particle roughness. Particle shape literature includes analyses based on verbal descriptions, visual comparisons with established particle outlines or classification charts, single-number classification methods, as well as representations of the particle outline as a mathematical series.

Surface roughness has also been the subject of abundant research. Surface roughness parameters are generally categorized into three groups; amplitude parameters, spacing parameters, and hybrid parameters. At least 60 surface roughness parameters have been reported in the literature, however no individual surface roughness parameter has been identified as being adequate to capture the complicated multi-scale nature of surface profiles.

Besides the deficiencies in particle shape and surface roughness analyses, no analysis is currently employed in practice to capture the kinematic nature of the contact between a particle and a continuum. The general procedure for a combined analysis is to analyze the particle shape and surface roughness separately with unrelated particle shape and surface roughness parameters. The divergence of techniques for the two components of the interface results in values with no mutual implication. The relative value of a property of a particulate material (e.g. particle shape) compared to that of the contacting continuum surface (e.g. surface roughness) is fundamental to the particulate-continuum analysis. The interaction between two media is a function of many factors including the relative shape and roughness characteristics.

The aim of this work is to make a contribution towards the development of new techniques to replace or supplement existing analysis methods by establishing an integrated fundamental understanding of the particle shape and surface roughness features. A unique topographical analysis system is desirable for both components of the interface. The potential for this is investigated through a systematic approach in this thesis. Following an extensive literature search on both particulate and continuum shape features at different scales (macro-, meso-, and micro-), promising and widely used particle shape and surface roughness analysis techniques were selected for further study based on their robustness and their ability to capture the complex nature of particle shape and surface roughness. First, mathgrams (i.e. Mathcad algorithms) were developed for the chosen particle shape and surface roughness parameters and executed with the study materials used in the original development in order to validate the mathgrams.

After the mathgrams for each of the study parameters were validated, they were utilized for a series of selected study particles and surfaces. These study particles and surfaces covered the range of particles and surfaces typically encountered in geotechnical engineering practice. Next, in an attempt to move towards a unique analysis system for both components of a particulate-continuum interface, the hypothesis of transforming particle outlines to surface profiles and surfaces to particle outlines was investigated. A particulate-continuum system, where the particle component is transformed to an equivalent surface profile, can be analyzed using only surface roughness analysis methods. Similarly, if the surface component is transformed to an equivalent particle outline, particle shape analysis can provide a common basis for both interface components. For this purpose, particle to surface profile (termed as *dsurf*) and surface to particle outline (termed as *dpart*) conversion mathgrams were developed in this study. The conversion mathgrams were validated by ensuring that the same surface profile (*dsurf*) at the same elevation was obtained when particles of proportionate sizes were converted and similarly, the same particle outline (*dpart)* was derived when similar surface profiles with different baseline elevations were converted. This validation was required to assure that the mathgrams (particle to surface conversion and surface to particle conversion) did not depend on particle size magnification or surface profile baseline location.

Using the *dparts* and *dsurfs,* the study utilized different particle shape analysis methods on real particles and *dparts* and surface roughness analysis methods on real surface profiles and *dsurfs.* In this manner, particles and surfaces were analyzed with the same technique.

An alternative approach towards developing a unified analysis system for particulate-continuum interface components involved converting analysis methods rather than the interacting components as explained above. This was achieved by performing modifications to particle shape analysis algorithms so that they could be used to determine the roughness of surface profiles. Similarly, surface roughness analysis algorithms were modified to characterize particle outlines. Thus, for a particle-surface interface, the particulate component was analyzed with the original particle shape parameter and the surface component with a modified algorithm based on the particle shape parameter. Since both analysis methods were based on the same concepts, this was intended to provide a coherent analysis framework for particulate-continuum interfaces.

Both approaches mentioned above aim to combine particle shape and surface roughness analyses in terms of either same format inputs or same concept algorithms. For both cases, the results were investigated and discussed in the thesis. Resolution analyses on the selected particle shape and surface roughness parameters are performed to illustrate the effect of particle outline and surface profile resolution discrepancies.

The analysis methods included in this thesis are generally non-dimensional. They are derived for particulate-continuum interface analysis for geotechnical applications in mm scale, however, they may also be valid for large-scale processes including fault gauges and thrust faults, which could be in the range of several hundred km's.

## 1.2 Scope of Thesis

This thesis is organized into six chapters including this introduction. Chapter 2 is a comprehensive review of previous research on interface mechanisms and parameters affecting the interface behavior, with an emphasis on the role of particle shape and continuum surface roughness.

Based on the literature review on particle shape and surface roughness, several analysis methods are selected for further investigation. The selection is based on the robustness of the analysis techniques. Chapter 3 involves detailed analyses of the selected particle shape and surface roughness analysis methods. The analysis methods (for particle shape or surface roughness characterization) are also scrutinized for their ability to distinguish between different inputs (particles or surface profiles). For all of the selected study analysis methods, Mathcad 2001 Professional algorithms are generated. In Chapter 3, the mathgrams are verified by comparing the mathgram output values with the reported values for that specific study analysis method. Thus, Chapter 3 utilizes the same inputs as the original parameter studies did.

In addition to the selected study analysis methods, the study materials (particle outlines and surface profiles) are also presented in Chapter 3. The study materials include four particle shape outlines and three surface profiles; where the full ranges of frequently encountered cases are accounted for. Besides the real particle shape outlines and

surface profiles, novel methods of defining and obtaining derived particles through surface profile wrapping and derived surfaces by particle outline unrolling are presented.

The validation of the real surfaces conversion to derived particles (surface wrapping) and real particles conversion to derived surfaces (particle unrolling) is presented in Chapter 4. The accepted study analysis methods from Chapter 3 are further explored using the selected study particles (real & derived) and surface profiles (real & derived) and results are interpreted.

Chapter 5 investigates the coherence of particle shape parameters applied to surface profiles and of surface roughness parameters applied to particle outlines. This is followed by a comparison between the fundamental properties of particle and surface shape parameters.

Chapter 6 presents the conclusions of this study and recommendations for future research in order to continue progress towards the desired coherent analysis method for characterization of materials particulate-continuum interfaces.

# CHAPTER 2

# LITERATURE REVIEW

## 2.1 Engineering Behavior of Interfaces

### *2.1.1 Interface Mechanisms*

Tribology is the branch of mechanical engineering that studies contact, friction, and wear of materials. Most of the analysis in tribology is concerned with metals; however, the governing laws are also valid for geotechnical materials. Friction is an energy dissipation mechanism and it amounts to the resistance to motion during sliding or rolling when one solid body moves tangentially over another with which it contacts.

Having loaded two bodies together, the tangential force required to initiate movement is the static friction force. On the other hand, the kinetic friction force is the tangential force required to maintain the movement. The static friction force is either higher than or equal to the kinetic friction force. Stick-slip load-deformation behavior results when the coefficient of static friction is markedly greater than the coefficient of kinetic friction. Amonton's laws state that the friction force is proportional to the normal force and independent of the apparent area of contact between two bodies, formulated as:

$$F = \mu N \quad \textbf{(2.1)}$$

where $\mu$ is a constant known as the coefficient of static friction ($\mu_s$) or kinetic friction ($\mu_k$), F and N are the shear (friction) and normal force, respectively.

Different mechanisms occur at the interface, such as rolling, sliding, shearing, and plowing. The coefficient of friction determines whether sliding or rolling will occur. As the pushing force initiates relative motion, the friction force starts increasing to resist the motion. If the coefficient of friction is too low, sliding will begin. However, if it is large enough the body will roll. Rolling ceases when the friction force reaches its maximum value and at that point sliding begins. Rolling is a much-preferred motion than sliding. For comparison, with hard materials the coefficient of rolling friction between a cylindrical or spherical body against itself or a flat surface is approximately $5 \times 10^{-3}$ to $10^{-5}$; whereas the sliding friction coefficient between dry bodies ranges from 0.1 to 1 (Bhushan, 1999). Hence the power required for sliding increases with increasing interface friction factor, $\mu$, however, $\mu$ has no effect on the power required for rolling (Avitzur et al., 1991).

Rolling motion can be considered as a combination of rolling, sliding, and spin (Johnson, 1985). Free rolling refers to rolling motion in which no tangential force or sliding can occur; whereas during tractive rolling the friction force is nonzero. For tractive rolling to take place, the friction force must be smaller or equal to $\mu$N in the contact region. As the magnitude of the friction force approaches $\mu$N, local (microslip) or gross sliding (in the entire contact) occurs.

Sliding friction has a dual nature comprising of adhesion and plowing (plastic deformation), which are schematically shown in Figure 2.1. If little interaction between

adhesion and deformation is assumed, the total intrinsic frictional force ( $F_i$ ) can be represented as the sum of the force required to shear adhered junctions ( $F_a$ ) and the force needed to supply the energy of deformation ( $F_p$ ) (Bowden and Tabor, 1964):

$$F_i = F_a + F_p \tag{2.2}$$

Adhesion is a consequence of material yielding at the real contact areas (which is only $10^{-4}$ to $10^{-2}$ of the nominal contact area) due to the high stresses developed at these peak points (asperities). Thus, the work required to overcome adhesion is proportional to the real contact area (Bowden and Tabor, 1950):

$$F_a = \tau_a \cdot A \tag{2.3}$$

where $A$ is the real contact area and $\tau_a$ is the material shear strength at points of contact. Adhesion can occur either at elastic or plastic contacts. For elastic contacts, the coefficient strongly depends on the surface roughness. For plastic contacts, it is inversely proportional to the hardness of the softer material and independent of the surface roughness.

Plowing of the harder material into its softer component resulting in abrasion and removal of the softer material constitutes the second part of friction. The additional force required for plowing of the contacting surfaces during relative motion is given as:

$$F_p = \tau_p \cdot A_p \tag{2.4}$$

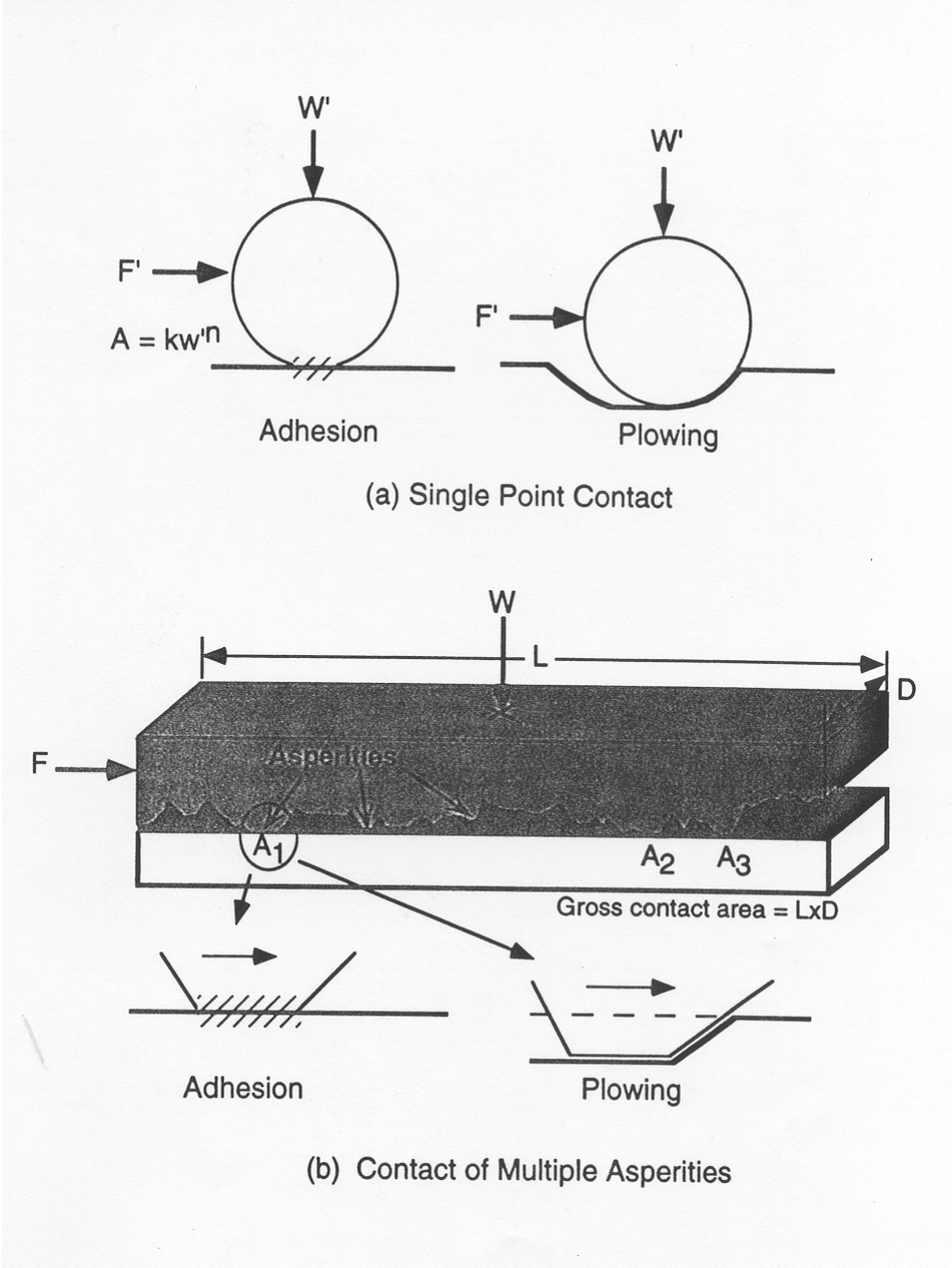


**Figure 2.1 –** Single point and multiple point contact showing adhesion and plowing (after Briscoe, 1992).

where $\tau_p$ is the bulk strength of the softer material and $A_p$ is the cross-sectional area of the plowed track (Adamson, 1982). The relative contribution of the plowing component to friction is a function of surface roughness, relative hardness of the two surfaces, and the characteristics of the wear debris between them.

There are various means to quantify interface shear in laboratory testing. Paikowsky et al. (1995) provide a comprehensive review of these devices. The direct and simple shear devices are most commonly used. The ring torsion device is preferable if large displacements are desired.

Soil displacement behavior and the dominant mechanisms at the interface have been investigated by many researchers in order to develop a better understanding of interface phenomena. Direct shear tests revealed that sand exhibited uniform shear deformation until slip or local shear developed along the interface at about 80% of the peak strength (Yoshimi and Kishida, 1981). Similarly, Uesugi and Kishida (1986a, 1990) observed shear deformation and sliding along the interface as the main displacement mechanisms prior to and after yielding of the contact surface, respectively. Smooth ($R_n$ = 15 x $10^{-3}$) steel surfaces resulted in mainly sliding of the sand particles along the surface; whereas sliding accompanied by rolling with a shear zone formation was observed for rough ($R_n$ = 68 x $10^{-3}$) surfaces (Uesugi et al., 1988). O'Rourke et al. (1990) investigated the mechanisms at the sand-polymer interfaces by performing direct shear tests and capturing scanning electron microscope (SEM) photographs of the polymer before and after the test. The interface strength decreased with the Shore D Hardness ($H_D$) of the polymer due to the lack of dilatancy. Hard polymer surfaces ($H_D$ > 60) promoted sliding of the particles along the surface, which was evident from the parallel, several

millimeters long scratches of approximately 0.01–mm deep subsequent to the test. For softer polymer surfaces particle rolling with no permanent indentation was the main displacement mechanism. Similarly, Dove and Frost (1999) examined the influence of normal stress and material hardness by shearing smooth geomembranes against dense Ottawa 20/30 sand. The results show that, for a given hardness, as the normal stress increased, the number and area of particles contacting the surface increased, thereby decreasing the particle-surface contact force per particle. After the number and area of particles contacting the surface reached their maximum at a certain normal stress level, any increase in normal stress was transferred to the particle/surface contact. At this point, if the contact stress became high enough to damage the surface, then the main shearing mechanism changed from only sliding to sliding plus plowing. During plowing, the particles penetrate the surface and remove or displace material from the surface. Figure 2.2 shows that below the critical normal stress, interface friction decreases due to the reduction of the contact force per particle. After the maximum number and area of contacting particles is reached and plowing is initiated, interface friction increases with normal stress. Further studies revealed that plowing is a function of the relative hardness of the interface materials and the grain shape such that angular particles result in more plowing.

### *2.1.2 Properties Affecting Particulate-Continuum Interfaces*

To date several studies have been performed on interface shear to identify the factors affecting the interface strength. Potyondy (1961) pioneered work in this area and evaluated interface friction between various soil types and construction materials, including steel, wood, and concrete. He identified four major influential parameters;

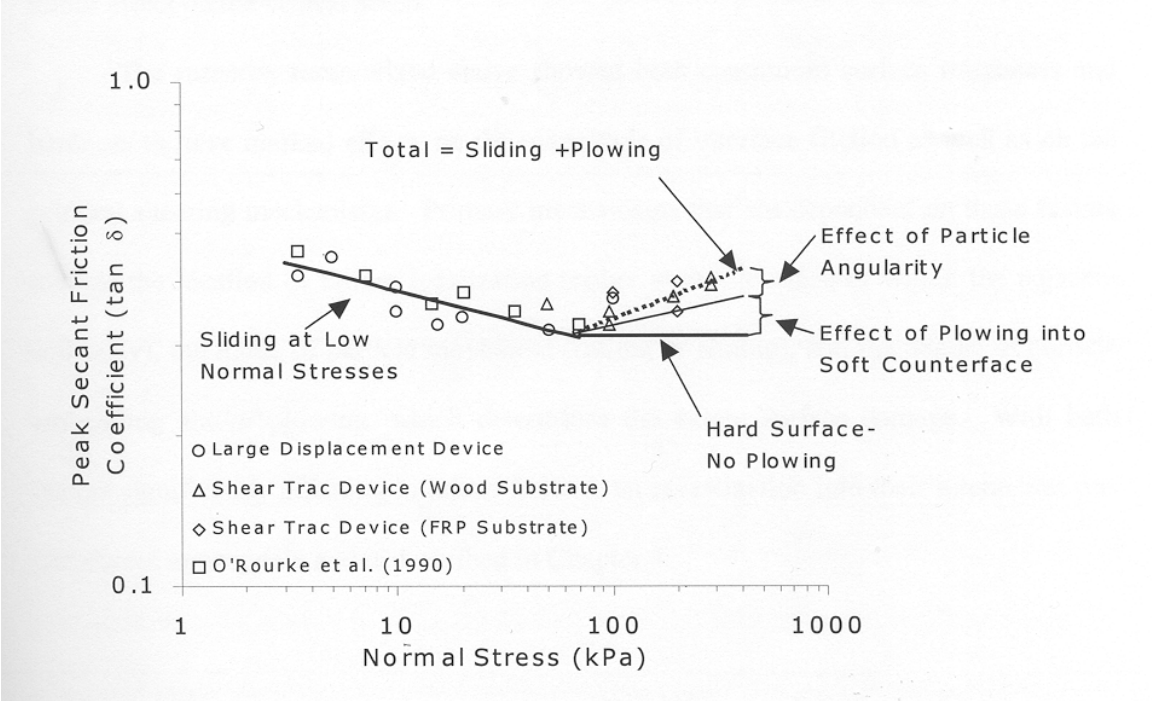


**Figure 2.2 –** Normal stress (kPa) versus peak secant friction coefficient (after Dove and Frost, 1999).

moisture content of the soil, surface roughness, soil composition, and intensity of the normal load.

Brumund and Leonards (1973) studied sand interfaces with steel, cement mortar, graphite, and teflon surfaces. Their results exhibited an increase in friction values with surface roughness and angularity of the sand grains. They recognized the importance of surface roughness with respect to sand particle size and showed that the coefficient of friction increases as the surface roughness increases with respect to the sand particle size.

Yoshimi and Kishida (1981) utilized the ring torsion apparatus to examine the friction between sand and metal surfaces. They stated an interface friction angle as low as $\phi_u / 2$, where $\phi_u$ is the particle-to-particle friction angle, could be obtained for a very smooth surface and that the upper limit to the interface friction was always lower than the internal angle of friction of the sand used. An equation based on the ultimate internal friction angle ($\phi_{ult}$) and $\phi_u$ was proposed to estimate the upper limit to the interface friction.

Uesugi and Kishida (1986a, 1986b) were also interested in interface friction between dry sand and steel surfaces. Simple shear test results proved that sand type (mineralogy) and steel surface roughness significantly affected the interface friction; whereas the effect of normal stress (98 – 980 kPa) and sand mean grain size (0.15-0.62 mm) could be neglected. Contrary to the Yoshimi and Kishida (1981) finding, the upper bound for the interface strength was identified as the shear strength of the granular material. When the applied interface shear stress reached the shear strength of the soil, the failure occurred within the soil mass rather than along the contact surface if the steel surface was above a critical roughness. The authors explained the discrepancy in their results with Yoshimi and Kishida (1981) findings by different sample preparation techniques used in two experiments. In ring torsion tests performed by Yoshimi and Kishida (1981), the steel surface was pressed against the already prepared specimen; whereas in simple shear tests sand was pluviated onto the steel surface. In their subsequent paper, Uesugi and Kishida (1986b) investigated a wider grain size range and acknowledged the mean grain size (0.16-1.82 mm) as a significant factor. Test type (simple vs. direct shear test) and the uniformity coefficient of sand (1.1 – 5.1) were observed to be inconsequential for interface strength. A major finding from this study

was the development of the normalized roughness parameter, $R_n$, which is calculated by measuring the vertical relief between the highest peak and the lowest valley over a lateral distance equal to the average particle size ($D_{50}$) and dividing the value by $D_{50}$. As shown in Figure 2.3, the relationship between the interface strength and $R_n$ is bilinear and is linearly increasing up to the "critical" surface roughness ($R_n$ = 75 * $10^{-3}$) beyond which the increase in surface roughness does not affect the interface strength. This behavior has been observed by several researchers after Uesugi and Kishida (1986b).

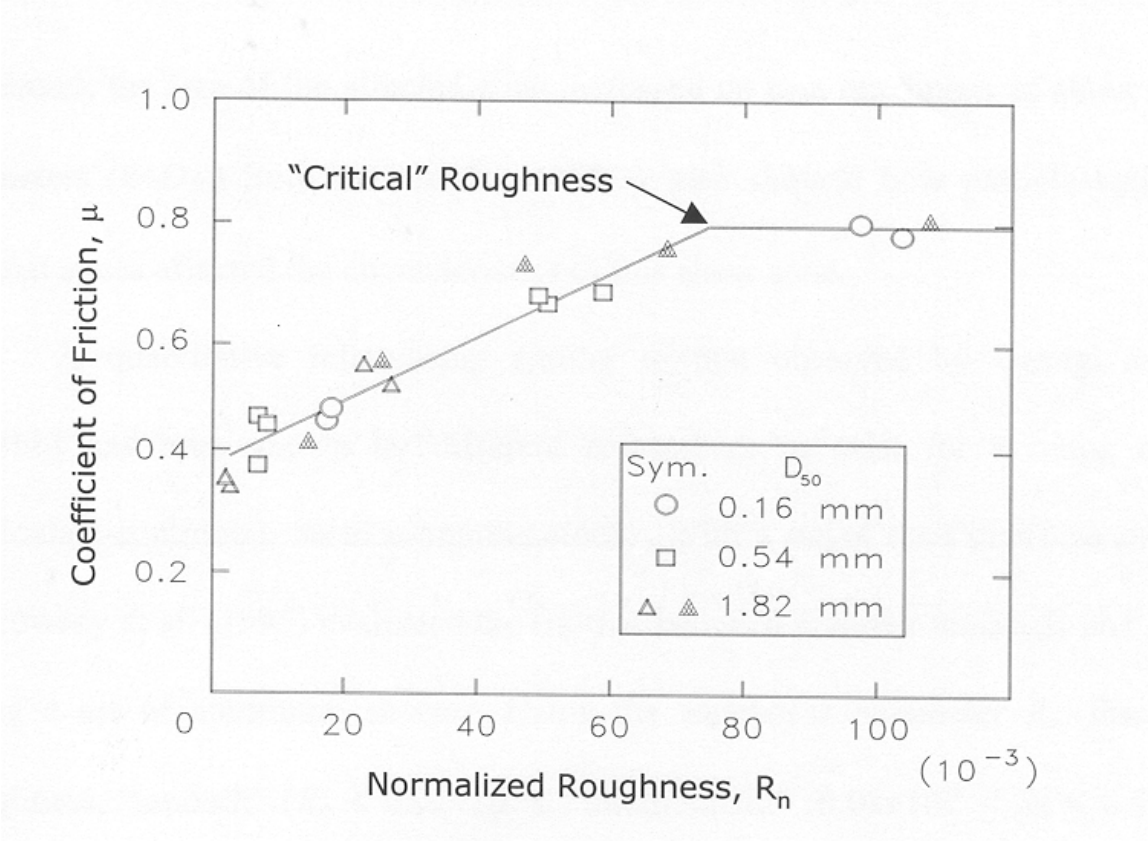


**Figure 2.3 –** Normalized surface roughness ($R_n$) versus coefficient of friction ($\mu$) for sand-steel interfaces (after Uesugi and Kishida, 1986b).

Paikowsky et al. (1995) tested several different size glass beads and Ottawa sand against controlled and random solid surfaces utilizing a dual interface apparatus. As shown in Figure 2.4, three zones of roughness were identified based on the failure type (interfacial versus internal): (1) "smooth" ( $R_n$ < 0.02 * $10^{-3}$), (2) "intermediate" (0.02 * $10^{-3}$ $\leq$ $R_n \leq$ 0.5 * $10^{-3}$), and (3) "rough" ( $R_n$ > 0.5 * $10^{-3}$). Within the "smooth" zone, the coefficient of friction was constant for all particle sizes for a given particle shape; whereas interface friction increased with $R_n$ in the "intermediate" zone. In both zones, failure occurred along the grain/solid contact with no observed dilation. Within the "rough" zone, the shear strength of the granular media was fully mobilized resulting in failure within the sand mass following dilation.

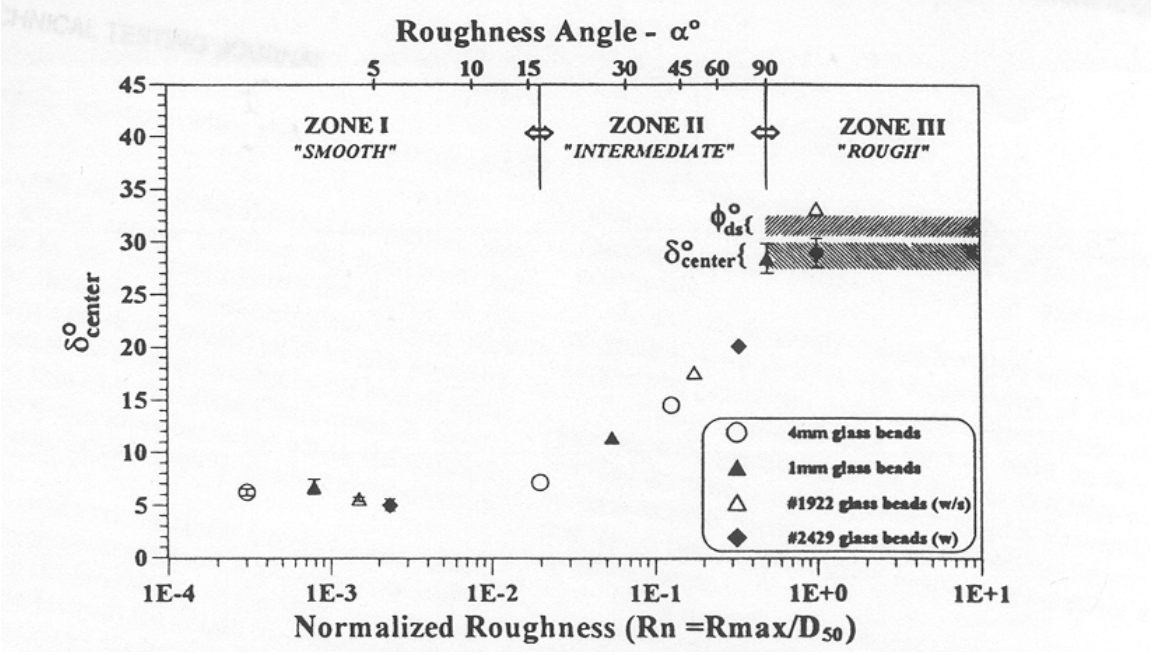


**Figure 2.4 –** Normalized Roughness ( $R_n$ ) versus average interfacial friction angle ( $\mu$ ) (after Paikowsky, 1995).

The concept of adding tensile strength to a soil mass by inserting reinforcement within the soil mass has been around for many years in numerous forms. Although natural materials were used initially, with advance in technology man-made reinforcing materials have been introduced. Geosynthetics is the family of widely used polymeric reinforcement materials that consist of geotextiles, geomembranes, geogrids, geonets, and geocomposites. Soil-geosynthetic interfaces have been the focus of many interface studies.

Direct shear tests of sand-polymer interfaces performed by O'Rourke et al. (1990) showed that the interface strength increased with soil density. Vaid and Rinne (1995) performed ring shear tests with two geomembrane types (smooth/rough) and two sand particle shapes (angular/rounded). Smooth HDPE interfaces mobilized 65 to 90% of the friction angle of the contacting sand, whereas with rough HDPE and PVC interfaces as high as 100% of the friction angle of the contacting sand could be attained. In relation to the particle shape, the peak friction angle observed was 55 to 65% of the constant volume friction angle for the rounded Ottawa sand, and 65 to 90% for the angular Target sand. Thus, a rough HDPE with the angular Target sand was identified as the best combination for an efficient interface.

The behavior at soil/geomembrane interfaces was further studied by Dove et al. (1997) in terms of the surface roughness parameter, $R_S$ (see Table 2.11 for definition). Test results revealed a linear increase of the peak and residual interface friction with surface roughness up to a critical $R_S$ value ( $R_{S,critical}$ =1.4 for granular soils). Further increase in $R_S$ did not affect the interface friction. The same relationship of friction and surface

roughness was reported by Uesugi and Kishida (1986b) in terms of relative roughness parameter $R_n$.

Lee (1998) identified the factors affecting interface behavior and their relative significance to the overall behavior as shown in Table 2.1.

**Table 2.1** - Properties affecting particle - continuum interfaces (after DeJong, 2001).

| Type | Factor | Significance |
|---|---|---|
| **Particulate Material (Soil)** | Angularity | High |
| | Density | High |
| | Initial Soil Structure | Low |
| | Mean Grain Size (D50) | Medium |
| | Shape | High |
| | Surface Roughness | Low |
| | Uniformity Coefficient (Cu) | Low |
| **Continuum Surface** | Surface Hardness | High |
| | Surface Roughness | High |
| **Testing Conditions** | Normal Stress | High |
| | Test Method | Low |
| | Strain Rate | Low |

Frost and Han (1999) presented direct shear test results performed on sand/fiber-reinforced polymer interfaces. The interface friction decreased with normal stress and increased linearly with relative roughness, $R_n$ (surface roughness/particle mean size).

For a given counterface, as the particle size decreased (i.e. relative roughness increased) the effect of particle angularity on peak interface friction coefficient (peak interface friction angle/internal friction angle of soil) was less prominent. The failure

plane moved away from the sand/fiber interface to within the soil mass with an increase in peak interface friction coefficient, and the upper bound for the interface friction was noted as the internal friction angle of sand. On the other hand, particle angularity dominantly affected the lower bound, which is termed as the “true interface friction”.

The mechanisms involved at geomembrane-sand interfaces during direct shear tests were investigated in terms of surface roughness and particle angularity (Frost et al., 1999). Their results are tabulated in Table 2.2 for 100kPa normal stress.

**Table 2.2 –** The shear mechanisms at geomembrane-sand interfaces (after Frost et al., 1999).

| Geomembrane Surface Roughness | Shear Mechanisms | Shear Zone Thickness |
|---|---|---|
| Smooth ($R_s$ = 1.09) | Sliding and slight plowing | $2 \cdot D_{50}$ |
| Slightly Textured ($R_s$ = 1.25) | Interlocking between sand and geomembrane results in dilation of sand particles | $4 \cdot D_{50}$ |
| Moderately/heavily textured ($R_s$ = 1.71) | Interlocking and dilation develops more fully | $6 \cdot D_{50}$ |

Table 2.2 shows the significant influence of surface roughness on shear mechanisms and shear zone thickness. Further plowing was observed as particle angularity increased for smooth geomembrane surfaces; however, the effect of angularity on plowing was not as significant for moderately/heavily-textured geomembranes.

## 2.2 Effect of Relative Particle Dimensions on Interface Behavior

Size, shape, roundness, and roughness are four independent characteristic features of particles (Pahl et al., 1973). Although it is easy to define particle size in the case of a sphere, as the particle shape becomes more complex, it is challenging to independently define the size and shape of a particle. The definition of size may appear as straightforward, however, as conveyed in Table 2.3, numerous studies on this concept yield several unrelated definitions.

Wadell (1932) is one of the major contributors to particle shape analysis. He has also studied particle size. He argued that arithmetic or geometric means of the diameters are not accurate size parameters since they depend on the particle shape. To illustrate, consider a cube with a side length of 2 mm (i.e. with a diagonal of 3.46mm) and a sphere with the *same volume*. The sphere has a diameter of 2.48mm, which is different from the same volume cube particle and this is due to its shape. He recommended particle volume or the diameter of a sphere having the same particle volume, i.e. *the true nominal diameter*¸ as a size indicator.

In tribology, the effect of particle size on wear rate has been investigated extensively (Kramer & Demer, 1961;Misra & Finnie, 1981; Gahlin & Jacobson, 1999; Clark & Hartwich, 2001; Xie & Bhushan, 1996; Pintaude et al., 2001, etc.). However, no consensus has yet been obtained on the “size effect”. The *size-shape hypothesis* (Xie & Bhushan, 1996) suggests increasing particle roundness with decreasing size; whereas the *size-strength hypothesis* (Clark & Hartwich, 2001) implies strength increase with smaller scales.

**Table 2.3 –** Particle size parameters.

| Size Parameter | Description | Remarks | References |
|---|---|---|---|
| Feret's diameter | $\frac{P}{\pi}$, for convex particles<br>$\frac{P_H}{\pi}$, for re-entrant particles;<br>$P_H$ is the perimeter of the convex hull | • It is the mean distance of tangents of a constant direction drawn at opposite sides of the grain contour with a sufficient number of grains approximately the same size<br>• Large (10%) positive error was recorded for elongated particles.<br>• It is not a measure of the area of the particle but of the perimeter of the convex hull of the profile. | Bodziony and Kraj, 1983 |
| Convex Body – Minkowski's inequality | $F^2 - 3MV \geq 0$<br>$M^3 - 48\pi^2 V \geq 0$ | • [V,F,M] constitute natural characteristics of a natural grain; however the relationship is not one-to-one. Therefore, these limits for a convex body are utilized. | Bodziony and Kraj, 1983 |
| Martin's Diameter | Length of chord through the particle which also bisects the particle | • Measurement direction needs to be specified.<br>• Note that the difference between Martin's diameter and the centroid diameter reflects the shape. | Beddow, 1980 |
| Stokes Diameter | $d_{st}$<br>$d_{st} = \sqrt{d_v^3 / d_s^2}$ | Free-falling diameter in the laminar flow regime | Allen, 1997 |
| Sieve Diameter | $d_A$ | Width of the minimum square aperture through which the particle passes. | Allen, 1997 |
| Weight Mean Diameter (also known as DeBroucker mean) | $d_w$<br>$d_w = \sum d^4 / \sum d^3$ | The average size based on the unit weight of particles. | Stockham, 1977 |
| Arithmetic Mean | $d_{av}$<br>$d_{av} = \sum d / n$ | The sum of all diameters divided by the total number of particles. | Stockham, 1977 |
| Volume | $d_v$<br>$V = \left(\pi \cdot d_v^3\right) / 6$ | Diameter of a sphere having the same volume as the particle. | Allen, 1997 |
| Surface | $d_s$<br>$S = \pi \cdot d_s^2$ | Diameter of a sphere having the same surface as the particle. | Allen, 1997 |
| Surface-volume diameter | $d_{sv}$<br>$d_{sv} = d_v^3 / d_s^2$ | Diameter of a sphere having the same external surface to volume ratio as the particle. | Allen, 1997 |
| Projected Area | $d_p$ | Diameter of a circle having the same projected area as the particle in random orientation. | Allen, 1997 |

Misra and Finnie (1981) compiled previous studies and disputed prior arguments on the "size effect" by revealing opposing experiment results. Principally, Misra and Finnie (1981) argued that since the "size effect" is observed in all wear processes; e.g. erosion, two-body, three-body abrasion, grinding, and metal-cutting, a sound explanation should be valid for all wear cases. They supported the hard ("debris") layer model proposed by Kramer and Demer (1961). The model suggests that a surface layer of thickness about 50-100 μm hardens, so that as fine particles traverse the surface they can only penetrate to the hard layer; whereas larger particles can penetrate the bulk softer material through the "debris" and thus result in larger wear rate. The influence of the debris layer diminishes and thus particle size effect is negligible beyond a critical particle size around 100 μm. Mechanically, this can be explained by smaller portion of applied load sustained by the particles as the particle size gets smaller, which in return decreases the wear rate. However, on the conflicting side, the study by Pintaude et al. (2001) showed that for abrasive wear of high-chromium white cast iron balls under dry - and wet - grinding, the largest wear rate was observed with fine portion (<3.36 mm) of the granite mass; whereas the coarser portion (>3.36 mm) exhibited the lowest wear rates. Gahlin & Jacobson (1999) have performed controlled experiments to observe and understand the size and sharpness/ dullness effect on wear. They have simulated particle size by manufacturing micro mechanically etched surfaces with different packing density. The concept of this simulation is that the packing density affects the number of particles in contact with the abrasive surface and thus the load per particle, which further influences the scratch size. Performed experiments revealed that the relative bluntness of abrasive particles produce a size effect, i.e. blunt particles exhibit size effect; whereas sharp particles do not. This is attributed to at least two mechanisms; i.e. the low attack angle

of round tips compared to sharp tips and the larger ratio of ploughing cross-section area, $A_p$ to load bearing area, $A_{lb}$ as the penetration depth of round particles increases.

Contrary to Misra and Finnie (1981), who claim that the "size effect" should be valid for all wear processes, Xie and Bhushan (1996) discuss the quandary related to using two-body abrasion theory to elucidate three-body abrasion even though the particle removal processes are the same. One of the differences is the effect of particle (or protuberance) size on wear rate. To simulate two-body abrasion, a surface comprised of hard asperities with spherical top (with constant radius of curvature R and a Gaussian peak height distribution with standard deviation of $\sigma$) has been used against a flat work piece in a two-body abrasion test. On the other hand, for the three-body abrasion test, hard particles of constant radius of R were placed between the flat work piece and the surface with the same peak height distribution and standard deviation. For two-body abrasion, when $NR\sigma$ ($N$ as the density of the hard asperities per unit area) is constant, wear rate decreases with increase in the radius R due to the smaller attack angle. Smaller attack angles result in less material removal from the surface. However, when the particle density per unit volume (proportional to $NR^3$) is considered constant, particle size increase is associated with wear increase similar to Misra and Finnie (1981). This effect is explained by increasing stress at each contact resulting in increasing fraction of contacts exhibiting plastic deformation. Three-body abrasion, on the other hand, shows wear increase with particle size increase for all cases.

Several studies were performed in relation to the effect of the particle size on the friction coefficient for commonly utilized geotechnical interfaces. (Brumund & Leonards, 1973, Uesugi & Kishida, 1986b, Yoshimi & Kishida, 1982; Kishida & Uesugi, 1987; Bauer &

Mowafy ,1990; Juran et al., 1988; Athanasopoulos, 1993; Dove & Harpring, 1999; Hryciw & Irsyam, 1993). In shear testing literature, the importance of relative size was recognized by the introduction of the normalized roughness parameter, $R_n$, as the ratio of the vertical relief between the highest peak and lowest valley over the lateral distance equal to the average particle size (Uesugi & Kishida, 1986b).

Brumund and Leonards (1973) studied sand interfaces with steel, cement mortar, graphite, and teflon surfaces. Their results exhibited the increase of friction values with surface roughness and angularity of the sand grains. They recognized the importance of the surface roughness with respect to sand particle size and showed that coefficient of friction increases as the surface roughness increases with respect to the sand particle size.

Some studies were involved with the *geometrical and spatial properties of the continuum with respect to soil particle size*; however, these studies did not produce coherent results. Analysis by Yoshimi and Kishida (1982) and Kishida and Uesugi (1987) showed that as the particle size to surface asperity spacing ratio decreases, more interface shear strength is mobilized. Juran et al. (1988) observed maximum interface friction angle for sand-geosythetic interface (equal to the internal friction of sand) when sand particles of were tested on geosynthetic with the opening ( $A$ ) equal to the mean particle size ($D_{50}$). Bauer and Mowafy (1990) performed pull-out tests of steel meshes to observe that maximum pull-out resistance is obtained for $A \approx 3.1 * D_{50}$ and Athanasopoulos (1993) reported $A \approx 1.6 * D_{50}$ for maximum sand/woven geotextile interface friction efficiency. Dove and Harpring (1999) suggested that a soil with a median grain diameter of the

same order of magnitude as the surface asperity height and spacing was required to obtain full interface efficiency.

Hryciw and Irsyam (1993) used a direct shear box to test two types of sands against rigid plane ribbed inclusions. The inclusions were carefully designed by varying the rib geometry and spacing. As far as rib design, closely spaced trapezoidal ribs performed as a rougher surface compared to rectangular ribs. A shear zone within the sand was only observed in the former case. The study concluded that the rib spacing is a crucial parameter and it affects the presence of the passive soil zone ahead of the advancing rib.

The significance of "relative size" is also evident in the Centroid Trace (CT) experiments performed by DeJong et al. (2000). CT experiments reveal that a 1.0-mm and a 20.0-mm diameter particle experience the same surface profile in different ways. The relative dimensions of the particle and the surface profile comprising of peaks and valleys is captured by the Centroid Trace method. Thus, further understanding of interface shear in terms of "relative size" can be achieved via an analysis based on the Centroid trace concept.

The research summarized above represents only a part of the studies performed on "size effect" in relation to friction and wear. As evident from the above discussion, although the effect is accepted by many, conflicting findings exist in the literature to explain and quantify the effect. The importance of the "relative size" is also not agreed on yet.

## 2.3 Effect of Relative Material Roughness on Interface Behavior

In this research, the effect of relative material roughness has been studied at different scales employing different approaches wherein both particle and continuum characteristics are considered. Particles are investigated based on their shape and surface roughness; whereas continua are represented in terms of their surface roughness.

### *2.3.1 Particle Shape and Particle Surface Roughness Analysis*

Particle shape analysis has been the focus of many research studies. As the numerous different approaches show, shape is a difficult concept to define and to date there still is not a single established parameter developed to define shape.

Several definitions exist for shape. Beddow (1980) defines shape as "…the recognized pattern of relationships among all of the points, which constitute the external surface.". He further identifies shape as an *intrinsic characteristic of a material system*, such that shape 1 and shape 2 cannot be added to get shape 3. Shape is *informative* regarding the pattern the overall quantity is fitted together and is concerned merely with the material outline, such that it does not provide any information related to the internal pore characteristics of the particle.

Despite the ongoing confusion around the topic, shape analysis is not a new topic of interest. As cited in Hawkins (1993), shape has been discussed since Sorby (1880), who classified sands into five shape groups. Markwick (1937) references studies by

Rittinger (1867) and Free (1911), who studied soil movement as a function of shape and drag in wind and water.

Clark (1981), in his shape review, states the desired properties of a well-founded shape descriptor as uniqueness, parsimony, rotation, scale, and reflection invariance. He also notes a descriptor related to a physical property would be beneficial and it is desirable that a shape parameter allows the reconstructing of the image from its description. While the vast majority in the particle science field define shape as dimensionless, some researchers argue otherwise. In his critical analysis, Winkelmolen (1982) states that "size" should be omitted as a variable in Sedimentology and particles can be defined by three independent variables: mass, volume, and shape. He defines shape as (volume / surface ratio) with the physical dimension of length and allocates vectorial properties to shape.

There are several approaches to define particle shape and even more schemes to classify these methods. Clark (1981) classifies the methods according to whether they are based on the outline only or the grain area. He further categorizes outline methods based on whether they use the information related to vertices or the chords that join the vertices. All outline methods can be either storing or discarding the data sequence. Another particle shape assessment scheme classification was proposed by Beddow (1980).

Frequently used techniques include dimensional measurements (the ratios of certain measurements on the particle outline), projection methods (a 2D image of the particle is obtained and utilized for categorizing), standard shape comparison methods (words are used to describe categories), functional methods (e.g. Fourier, Walsh method,

polynomial methods that aim to regenerate the particle shape), distributional approaches (the radial information is used mostly with statistical methods), and fractal methods. Table 2.4 illustrates some of the basic properties related to each method. For a more thorough discussion, the reader is referred to Beddow (1980) and Clark (1981).

In powder technology, separation of particles based on shape is a field with ongoing research. Four common shape separation techniques are based on (1) the particle velocity on a tilted solid wall, (2) the time it takes for the particles to pass through a mesh aperture, (3) cohesive force to a solid wall, and (4) settling velocity in liquid. As discussed by Furuuchi and Gotoh (1992), these methods rely on certain dynamic properties of particles that are affected in part by shape. For example, as particle elongation increases, the time required for the particle to pass through a sieve opening increases since it takes longer for the elongated particle to change its orientation. In relation to the third method, as the sphericity of the particle increases, the adhesion force increases at constant humidity. In the fourth method, the drag coefficient and the Reynolds number both depend on particle shape. However, Furuuchi and Gotoh (1992) also argue that since dynamic properties are affected by parameters other than shape (e.g. size, density), a shape separation technique that relies on another principle should be developed.

There has been a large amount of discussion regarding the definitions of sphericity and roundness initiated between Wadell (1932) and Wentworth (1933). Hawkins (1993) reviews the history of this confusion. Wadell (1932) was the first to differentiate between the two concepts of sphericity and roundness. He categorized sphericity and roundness as descriptors for form and angularity, respectively.

**Table 2.4 –** Brief remarks on the particle shape analysis methods.

| METHOD | REMARKS |
|---|---|
| Fourier Methods (general) | ▪ Reflect particle shape but don't render specific shape parameters, which can be correlated with physical behavior.<br>▪ None of the Fourier series can cope with holes within an object.<br>▪ Computationally extensive.<br>▪ Invariance to translation, scale, and rotation.<br>▪ Orthonormality is an advantage. |
| Fourier Methods - Radius Expansion | ▪ Need to select center of gravity, requires interpolation, it is not accurate.<br>▪ Cannot represent multivalued function, problem with reentrants.<br>▪ Parameters: ($a_0$ ) is rotation invariant but origin variant, ($a_m$ & $b_m$) are rotation and origin variant.<br>▪ Large magnitude & small frequency components relate to shape, small magnitude & high frequency components relate to surface roughness. |
| Fourier Methods - Angular Bend | ▪ Deals with the outline in terms of chord that changes with angular direction.<br>▪ No problem of multivalued functions.<br>▪ No problem of origin.<br>▪ In reconstruction the outline may not be continuous.<br>▪ Reparameterizes the profile in terms of the change of slope of the tangent with distance moved around the profile. |
| Distributional Shape Approaches | ▪ Star and a kidney shapes have the same radius distribution.<br>▪ It throws away all the information on the relationship between adjacent points on the perimeter, i.e. the sequence information is discarded.<br>▪ Data obtained can be used in Fourier description. |
| Planar Surface Analysis | ▪ The outline analysis cannot deal with holes within the particle.<br>▪ Examples: Equivalent ellipse having the same mechanical moment as the particle, binary representation of the outline as a grid made up of presence and absence information, functional approaches, e.g. Walsh again to calculate the presence or absence information. |
| Planar Surface – Functional Approaches | ▪ 2D Walsh function.<br>▪ "0" designates empty, "1" designates full.<br>▪ Advantages: similar to Fourier, converges well, orthonormal.<br>▪ Disadvantages: empty cells become important. |
| Indirect Methods – Bulk Properties | ▪ Based on behavior the material as a bulk.<br>▪ Can lead to problems in interpretation for other applications.<br>▪ Hard to eliminate all other affects during measurement.<br>▪ Some (e.g. dynamic shape factor) is advantageous since they take into account all points.<br>▪ Very insufficient literature. |
| Single Number Classification Systems (General) | ▪ Mathematically convenient, quick (large number of particles can be analyzed), easy to relate to other numbers, can be used as a shape sorter<br>▪ Two very different shapes can have the same number.<br>▪ The particle outline cannot be regenerated from a single number. |
| Dimensional Measurements | ▪ Fail to describe the shape.<br>▪ Confusion identifying L, T, and B.<br>▪ Dimensions may not be orthogonal.<br>▪ Do not take into account the number of sides, i.e. they cannot distinguish between triangular, rectangular, and pentagonal sections. |

**Table 2.4 (continued).**

| | |
|---|---|
| Projection Methods | ▪ Significant error with very flat grains. A circular disk and sphere could have the same shape value.<br>▪ Description of roundness (based on the sharpest corner).<br>▪ Origin definition, mean radius problem<br>▪ Convex hull methods, i.e. fitting convex figure of definite shape around the particle, are unduly subject to the effect of protuberances or other minor variations in shape. |
| Standard Shape Comparison Methods – Word Descriptors | ▪ Wentworth (1936) was the first to compare grains to standard geometrical shapes, such as prismoidal, bipyramidal, pyramidal, wedge-shaped, etc.<br>▪ In 2D, the outline is described with words, such as hexagonal, pentagonal, trapezoidal, oval, rhombic, etc.<br>▪ Disadvantages: No two systems will have the same boundary between classifications. Thus, one cannot envisage the "rounded", "well-rounded", or "angular" particle. |
| Fractals | ▪ Does not give any information regarding the shape.<br>▪ Same angularity for smooth circle and smooth rhombus.<br>▪ Small change in D (value) for a big change in roughness.<br>▪ No real discrimination between circle and an ellipse.<br>▪ Works good with reentrants whereas decomposition techniques work best with particles that are basically regular in macro-sense.<br>▪ Parallel-line (divider) and area-perimeter method to quantify roughness.<br>▪ Level of scrutiny is important to differentiate between textural and structural (Hyslip and Vallejo, 1997). |

According to Wadell (1932), true sphericity is equal to *[(surface area of a sphere of the same volume as the particle) / (actual surface area of the particle)]*. Wadell (1934) later modified the definition due to the difficulty of measuring surface area as *[(diameter of sphere of the same volume as the particle) / (diameter of circumscribing sphere)]*. In 2D, the sphericity can be stated as *[(diameter of circle equal in area to that of the particle outline) / (diameter of the smallest circle circumscribing the particle outline)].*

Roundness was defined by Wentworth (1933) as *[(radius of curvature of the most convex part) / ½ (longest diameter through the most convex part)].*

Alternatively, Wadell's concept of roundness is based on the sharpness of the corners. It is the average radii r of the N corners of the grain image divided by the radius of the maximum inscribed circle, R (Wadell, 1935):

$$roundness = \frac{\Sigma r}{N} \cdot \frac{1}{R} \quad \textbf{(2.5)}$$

Wadell's differentiation of sphericity and roundness is shown schematically in Figure 2.5. This definition has been used widely among American geologists. French geologists mostly followed Cailleux (1947)'s roundness concept based on the sharpest corner; *[(radius of curvature of the most convex part) / (L/2)].*

One of the most widely acknowledged definitions of shape was proposed by Barrett (1980). As illustrated in Figure 2.6, it is based on three independent scales: (a) form (macroscale): first order quantity related to the gross shape of the particle, (b) roundness (mesoscale): second order related to number and sharpness of corners, and (c) surface texture (microscale): third order related to number, size and sharpness of asperities on corners. As Figure 2.6 shows, shape encompasses all three definitions and it involves all aspects of external morphology. Form is the gross shape of a particle and is independent of roundness and roughness. It signifies the degree at which a particle approaches a definite geometrical form.

Some have utilized the term "angularity" in preference to "roundness", i.e. large-scale smoothness. Roundness has been defined in three different ways based on (i) on the sharpest corner, (ii) sharpness of all corners (or average roundness of all corners), and

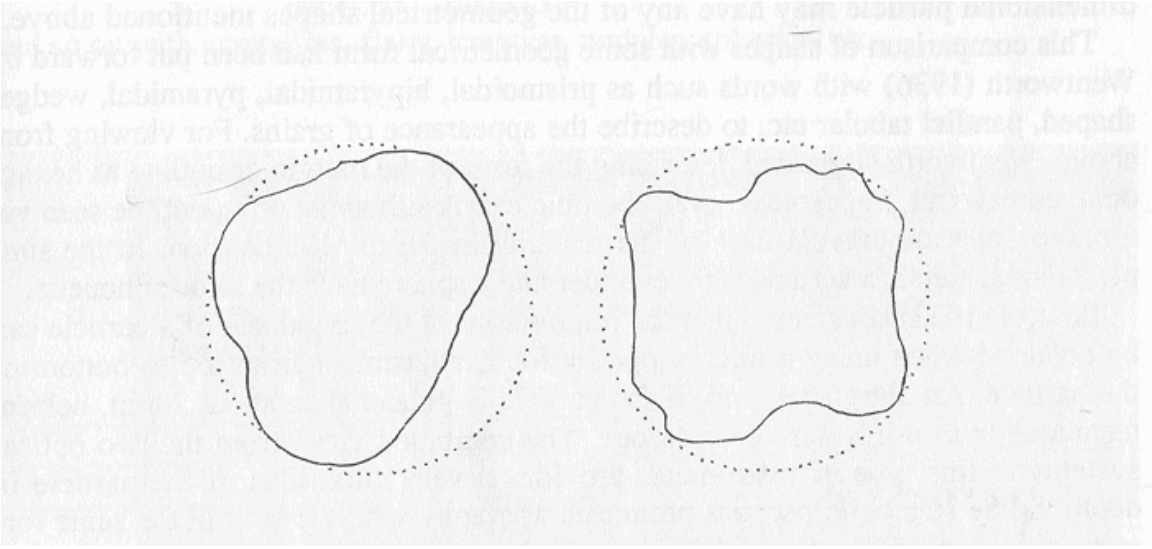

Two outlines with the same sphericity, but different roundness.

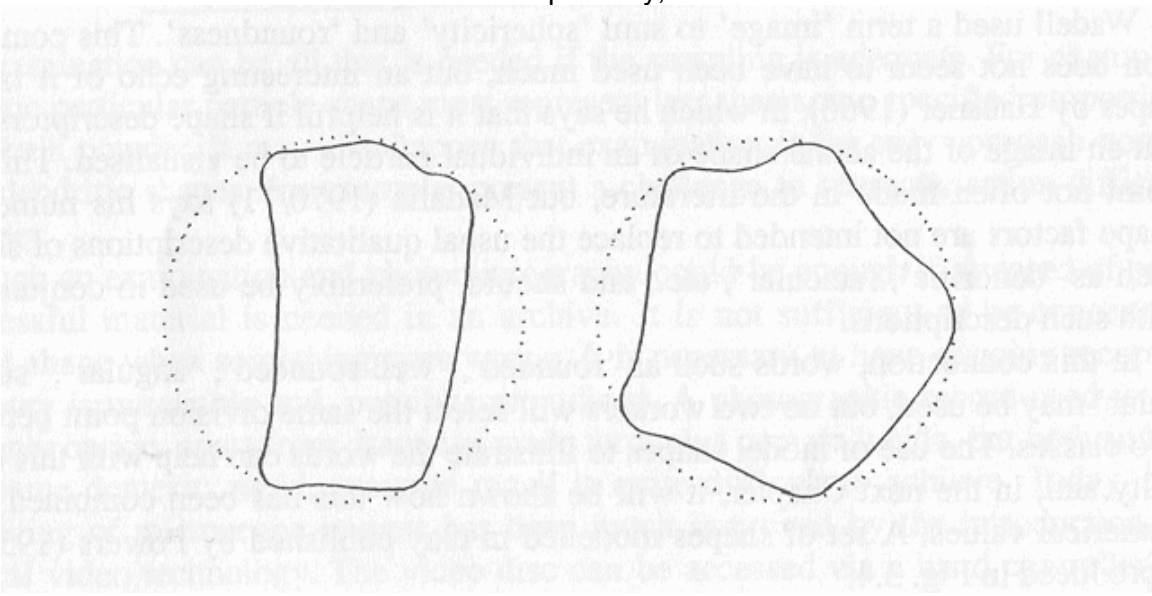

Two outlines with the same roundness, but different sphericity.

**Figure 2.5 –** Wadell's definition of sphericity and roundness (after Hawkins, 1993).

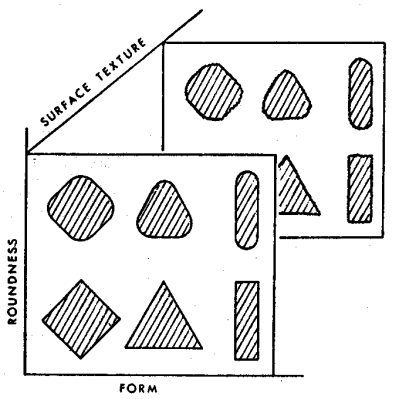


**Figure 2.6 -** A simplified representation of form, roundness, and surface texture by three linear dimensions to illustrate their independence (after Barrett, 1980).

(iii) the convexity in the particle outline. Note that cube and tetrahedron have different forms but the same angularity (their corners are equally sharp). Finally, texture is what roundness is at the microscale and it is superimposed on the corners. Figure 2.6 shows the three scales superimposed on particle outlines.

Based on Barrett's definition, the existing shape parameters in the literature are categorized in Tables 2.5 – 2.8 for this study. Note that terms as macro-, meso-, or micro- parameter correspond to form, roundness, and surface texture. Tables 2.5 and 2.6 display parameters that capture macro- & meso- & micro- scales and macro- & meso-, respectively based on the author's opinion. Tables 2.7 and 2.8 display particle shape parameters that represent only meso- and micro- scales, respectively

**Table 2.5–** Particle macro- & meso- & micro- shape parameters.

| Macro- & Meso- & Micro – Scale Parameters | Description | Remarks | Reference |
|---|---|---|---|
| Slope Density | | ▪ For any given angle, calculate the proportional outline length<br>▪ Advantage: outline segment at n° is distinguished from one at 180°+n°.<br>▪ Origin dependent.<br>▪ Can end up with negative frequencies if series is truncated. | In Clark, 1980 |
| Chord to Perimeter (Asphericity Spectrum) | $F(l_p / L) = \frac{15}{16 l_c} \int_0^L \left\{1 - l_c^2 / l_p^2\right\} dL$<br>$Q(l_p/L) = F(l_p/L)_{particle} - F(l_p/L)_{circle}$ | ▪ Compare length of chord to the perimeter length between those points in counterclockwise direction.<br>▪ Compares the shape to a circle. | Davis and Dexter, 1972 in Clark, 1980 |
| Morphic Descriptors | $L_0, L_2(n), L_3(m,n), \mu_2, \mu_3$ | ▪ (x,y) : (R,θ) : ($A_n$,$B_n$): $R_0$ and shape parameters<br>▪ Not clear physical meaning for the coefficients.<br>▪ Σ $L_2$ = radiance, Σ $L_3$ = skewness<br>▪ Can be used to regenerate the shape.<br>▪ Rotationally invariant. | Outline – Fourier<br><br>Beddow et al., 1984 |
| Total Roughness, T - Fourier | $P_n = \left[\frac{1}{2}\sum_{k=1}^{n}(A_k^2 + B_k^2)\right]^{1/2}$<br>$T = \frac{C \times L}{P_n}$<br>$T = P_c + T_c$<br>$P_c = 10 \times P_n$ | ▪ L depends on the length of the periphery; C is to eliminate the effect of elongation.<br>▪ Decreasing total roughness with size, i.e. size-dependent.<br>▪ Particles become less elongated and less textured when smaller.<br>▪ Total roughness represented by one value, which consists of two factors representing the contributions of gross shape and surface texture. | Czarnecka and Gillott, 1980 |
| Lumpiness, Roughness and Texture | $L_k = \sum_{n=1}^{n=n_1} A_n$ ,<br>$R_k = \sum_{n=n_1}^{n=n_2} A_n$ , $T_k = \sum_{n=n_2}^{n=n_3} A_n$ | ▪ No definite way to determine the threshold parameters, $n_1$, $n_2$ and $n_3$.<br>▪ Low frequency terms show the global effect.<br>▪ High frequency terms represent the local effect; e.g. friction, shear resistance. | Luerkens et al., 1982 |
| Particle signature parameter, α | $\alpha = \left(\frac{R_0}{a_0}\right)^2$ , $a_0$ = av radius of profile, $R_0$ =eq radius of a circle with the same x-sectional area enclosed by the outline<br>$\alpha = 1 + \alpha_s + \alpha_r + \alpha_t$<br>$\alpha_s = \sum_{m=1}^{n_1} \sqrt{(a_m^2 + b_m^2)}$ | ▪ Signature is scale invariant; signature vs. m relationship is rotation invariant.<br>▪ Determination of $n_1$, $n_2$ and $n_3$ is subjective, not a well developed procedure. | Fourier and Image Analysis<br><br>Wang, Lai, and Frost, 1997 |

**Table 2.5 (continued).**

| | | | |
|---|---|---|---|
| Particle signature | Plot of natural log of spectral coefficients versus the frequency (amplitude of coefficients decrease rapidly as a function of n) | ▪ Unroll particle (all particles are considered isotropic deviant spheres with no re-entrants).<br>▪ Uses discrete Fast Fourier, Walsh (allows superposition) or HAAR functions.<br>▪ Assumes: (i) particle information is in the amplitude coefficients, not in phase relationships; (ii) particles with similar genesis, chemical composition and history should have similar signature<br>▪ Using the coefficients, physical properties are calculated. For example, ($A_0$+$A_2$) = measure of aspect ratio, ($A_0$+$A_3$) = measure of triangularity component | Meloy, 1977 |
| Specific rugosity index, $S_{TV}$ | $100\frac{V_{ST}}{V_p} = 100\left[1 - \frac{G_{px}}{G_{ap}}\right]$, $V_{st}$: = Volume between packing volume membrane and volume of macro and micro surface voids, $V_p$ = packing volume, $G_{px}$ = packing specific gravity, $G_{ap}$ = apparent specific gravity (ASTM) | ▪ Accounts for interparticle voids and particle surface voids (macro & micro).<br>▪ Based on the approach that any difference between the porosity of smooth spherical particles and aggregate is due to the irregularities.<br>▪ "Different types of one-size aggregates, smooth or irregular, will be compacted to the same volume in bulk when they possess identical total packing volume of the particles under identical compaction procedure." | Indirect Method<br><br>Ishai and Tons, 1977 |
| Dynamic Shape Coefficient | $\left(\frac{v_s}{v_n}\right)^2$, $V_s$: fall velocity, $V_n$: velocity of a nominal sphere | ▪ Shape is measured by means of its effect on the hydraulic properties of the particle compared to a smooth sphere of equal mass density and volume<br>▪ Plot of Reynolds Number vs. Drag Coefficient showed that shape is as important as specific gravity in sorting heavy minerals. | Indirect Method<br><br>Briggs et al., 1962 |
| Fractals, $D_T$, $D_1$, $D_2$ | $\log P \propto (D_T - 1)\log S$ | ▪ P = perimeter, S = step lengths<br>▪ Range: 1.0-2.0<br>▪ A plot of log P vs. log S can have two linear plots. Small step lengths having a fractal dimension of $D_1$ (micro-scale edge textural effects) and larger steps with $D_2$ (macro-scale particle structural effects generated by reentrants).<br>▪ The particle shows two separate "self-similar" scales of surface morphology.<br>▪ The method identifies 3 types of fractal assemblages: <u>One</u>: single fractal population (with only $D_T$) associated with relatively regular outlines with only $D_T$, <u>Two</u>: convex, more irregular, no real observable edge texture, slope increasing (i.e. $D_2 > D_1$) , <u>Three</u>: very marked irregular, edge texture, slope decreasing. | Orford and Whalley, 1983 |

**Table 2.6 –** Particle macro-& meso- shape parameters.

| Macro and Meso – Scale Parameter | Description | Remarks | Reference |
|---|---|---|---|
| Planar surface – binary representation | $M_{i,j} = \sum x^i y^i$ | ▪ Grid representation as present or absent. Grids can be square, rectangular, hexagonal, etc<br>▪ Calculate moment with present cells.<br>▪ It is scale invariant (divide moments by total grain area).<br>▪ Origin dependence can be handled by defining coordinates in relation to center of gravity.<br>▪ Orientation independence can be achieved.<br>▪ Interior information is redundant. Takes into account only the outline but problematic in case there are holes within the particle (Sebestyn, 1959). | In Clark, 1980 |
| Form Factor – Image Analysis | $FF = \sqrt{(Shape\ \ Factor)^2 + (Angularity\ \ Factor)^2}$ | ▪ Relates to engineering behavior of granular materials. | Sukumaran and Ashmawy, 2001 |
| Triangular Plot | $\frac{T}{L}, \frac{L-B}{L-T}, \Psi_m$ ; $\Psi_M$: maximum projected sphericity | ▪ Used a cube to show elongation and flattening<br>▪ Cannot distinguish between a cube and a sphere. | Sneed & Folk, 1958 |
| Form – Roundness Feature Space Representation | $\frac{T}{L}, \frac{L-B}{L-T}, \Psi_m$ , and Wadell's roundness in vertical scale | ▪ A feature-space representation accounting for both form and roundness is suggested. Roundness is plotted in the vertical scale.<br>▪ Added triaxial contour plots of shape distribution in each horizontal plane makes it a feature-space representation<br>▪ Hard to plot. | Davies, 1975 |
| Degree of Angularity, A | $A_i = (180^\circ - a)\frac{x}{r}$, a = measured angle, r = maximum inscribed circle radius, x = distance of corner to the center | ▪ Total angularity is the sum of all the values for all corners measured in three mutually perpendicular planes.<br>▪ Accounts for both roundness of corners and how far they are (their location).<br>▪ Angularity increases when acuteness of corners and number of corners increase. | Lees, 1964 |
| (Martin's Diameter / Feret's Diameter) | $\frac{E[d_M]}{E[d_F]} = \frac{b}{a}\frac{K(b/a)}{E(b/a)}$ | ▪ High standard variation, i.e. many measurements needed.<br>▪ Orientation of the particle is an issue. | Individual Dimensional Church, 1968 |
| Statistical Shape Indices | $(\frac{E(d_R)}{d_H}, \frac{d_H}{d_L}, \frac{E(d_R)}{d_L})$ or $(\frac{E(d_F)}{d_L}, \frac{d_H}{d_L}, \frac{d_H}{E(d_F)})$ | ▪ $D_H$: eq area circle, heywood diameter<br>▪ $D_L$: eq perimeter circle diameter<br>▪ $D_R$: length through the center of gravity | Jimbo et al., 1980 |

**Table 2.6 (continued).**

| | | | |
|---|---|---|---|
| Roundness | % of concave C, convex V, and plane P are used on a triangular plot | ▪ Mechanically traced profile.<br>▪ Distinguishes between roundness due to rock structure and mode of origin of deposit<br>▪ The only roundness parameter that takes into account parts other than convex<br>▪ Curvatures of complete outline are evaluated, semi-quantitative, no single roundness value, very laborious | Szadeczky – Kardoss, 1933 in Krumbein and Pettijohn, 1902 |
| Rollability Shape Factor | Time it takes for half the tested weight to emerge from the cylinder | ▪ Related to the angle of slope on which grain rolls down in air with a uniform motion at a given velocity on a smooth but anti-skid surface when it is pulled by gravity forces alone.<br>▪ Measured on the inside of slightly inclined revolving cylinder mantle.<br>▪ The plot of size vs. rollability factor show special types and the character of these curves is called Shape Distribution Character. The types include; rising, down sloping, bridge, valley type curves. | Indirect Method<br><br>Winkelmolen, 1971 |
| Angularity Number, AN | $67-\frac{100M}{cG_a}$, c = water mass to fill the same volume, M = aggregate mass of standard volume | ▪ Range: 0 –12.<br>▪ Recommended by British Standards (BS 812 1975) for calculating the angularity of concrete aggregates.<br>▪ Based on packing.<br>▪ The formula is based on (% of voids – 33%).<br>▪ The method calculates higher Angularity Number for a sphere than for a cube. | Indirect Method<br><br>Shergold, 1953 in Janoo, 1998 |
| Modified AN | $\eta = Cd^n$, C = shape factor (specific to a material), d = volume mean aggregate diameter (mm), n = -0.032 | ▪ Modification of AN to account for shape.<br>▪ Same procedure as AN, calculated percentage voids differently.<br>▪ When using AN, compare with a material of same size. | Indirect Method<br><br>Gupta, 1985 in Janoo, 1998 |
| Particle Index, $I_a$ | $I_a = 1.25V_{10} - 0.25V_{50} - 32$<br>$V_n = \left[1-\frac{W_n}{S\,v}\right]100$, S = bulk density, V =volume of mold, $W_n$ = net weight of aggregate in the mold at n strokes per layer | ▪ Shape, angularity, texture of a grain affects "e" as well as the rate at which "e" changes when the aggregate is compacted in a standard mold.<br>▪ Capable of distinguishing between smooth, rounded and rough<br>▪ Problem defining volume of voids, $V_n$ | Indirect Method<br><br>Huang, 1962 in Janoo, 1998 |
| Uncompacted voids in aggregate, UVC | $\frac{V_{cyl}-\left(\frac{M}{G_{sb}}\right)}{V_{cyl}}x100$, $V_{cyl}$ = Volume of cylinder ($cm^3$), M = mass of aggregate in cylinder (g), $G_{sb}$ = bulk specific gravity of aggregates | ▪ UCV increases with angularity and roughness of the aggregate.<br>▪ Apparatus similar to specific rugosity index. | Indirect Method<br><br>Aldrich, 1996 in Janoo, 1998 |
| Relative Angularity | 25.95 / (porosity of compacted sample) | ▪ Indirect method based on the minimum porosity of sand obtained by compacting compared to the theoretical minimum for spherical sand grains<br>▪ The value gets closer to 1.0 as the sand gets angular in shape. | Indirect Method<br><br>Lamar, 1927 in Krumbein and Pettijohn, 1902 |

**Table 2.7 –** Particle meso – shape parameters.

| Meso Parameter | Description | Remarks | Area and Reference |
|---|---|---|---|
| Roundness | $r_1 / R$ , $r_1$: radius of curvature of the sharpest developed edge (most convex part); R: mean radius | ▪ R: difficult to define, e.g. arithmetic vs. geometric | Sharpest Corner Wentworth, 1919 |
| Shape Index | $\frac{D_s}{D_x}$ | ▪ Range: 0 –1<br>▪ $D_s$: diameter of circle fitting sharpest corner<br>▪ $D_x$ : diameter of pebble particle through $D_s$ (measured corner)<br>▪ Assumed all particles develop into spheres during transport and that optimal roundness can be attributed to spheres.<br>▪ Regards sphericity and roundness implicitly.<br>▪ Regards position of measured corner on the particle, definite ultimate shape (sphere) (Diepenbroek, 1992).<br>▪ Only one corner is analyzed, influence of sphericity. | Sharpest Corner<br><br>Wentworth, 1919 |
| Shape Index | $\frac{D_s}{\frac{(L + S_m)}{2}}$ | ▪ Range: 0 – 1<br>▪ $S_m$: shortest axis in maximum projection line.<br>▪ Reduction to maximum projection plane measurement (Diepenbroek, 1992).<br>▪ Only one corner is analyzed, influence of sphericity<br>▪ Laborious. | Sharpest Corner<br><br>Wentworth, 1922 |
| Angularity | (Sum of angles subtended by the straight parts / 360°) | ▪ No instructions for the selection of the central point, (inscribed or circumscribed circle center?) | Fischer, 1933 in Krumbein and Pettijohn, 1902 |
| Cailleux Roundness Index | $\frac{D_s x 1000}{L}$ | ▪ Range: 0 –1000<br>▪ Strong influence of sphericity, only one corner and laborious (Diepenbroek, 1992)<br>▪ Based on Wentworth (sphere is the ultimate shape) | Sharpest Corner<br><br>Cailleux, 1947 in Barrett, 1980 |
| Kuenen Roundness Index | $\frac{D_s}{I}$ | ▪ Range: 0 –1<br>▪ Based on Wentworth, i.e.sphere is the ultimate shape.<br>▪ Influence of sphericity reduced, only one corner, laborious (Diepenbroek, 1992). | Sharpest Corner<br><br>Kuenen, 1956 in Diepenbroek, 1992 |
| Modified Wentworth Roundness | $\frac{D_s}{D_i}$ | ▪ Range: 0 –1<br>▪ $D_I$ : diameter of the inscribed circle<br>▪ Based on both Wadell and Wentworth procedure (Diepenbroek, 1992)<br>▪ Only one corner, laborious. | Sharpest Corner<br><br>Dobkins and Folk, 1970 |
| Modified Wentworth Roundness | $\frac{\frac{(D_{s1} + D_{s2})}{2}}{D_i}$ | ▪ Range: 0 –1<br>▪ Only two corners, laborious (Diepenbroek, 1992).<br>▪ Based on Wadell and Wentworth (Diepenbroek, 1992). | Sharpest Corner<br><br>Swan, 1974 in Diepenbroek, 1992 |

**Table 2.7 (continued).**

| | | | |
|---|---|---|---|
| Degree of Roundness | $\frac{\Sigma r}{N} \cdot \frac{1}{R}$ | ▪ Range: Low = 0-0.4, Medium = 0.4-0.6, High = 0.6-1.0.<br>▪ Fitting of arcs to the corners is very subjective (400% scatter).<br>▪ Sharpness only measured at corners, neglects the entire surface of the grain<br>▪ Use a standard size (7 cm) for comparable results.<br>▪ Curvatures of all corners averaged, influence of sphericity reduced.<br>▪ Only convex parts, no ultimate shape, laborious. | Wadell, 1932 |
| Russel and Taylor Scale | Angular (0.00-0.15), subangular (0.15-0.30), subrounded (0.30-0.50), rounded (0.50-0.70), well rounded (0.70-1.00) | ▪ Range: 0 –1<br>▪ Used photographs of grain types to develop 5 grade terms based on visual comparison.<br>▪ Used Wadell's concept.<br>▪ Quick, no discrimination of higher roundness grades. | Visual<br><br>Russel and Taylor, 1937 in Yudhbir and Abedinzadech, 1991 |
| Krumbein Chart | Visual chart, nine classes at equal intervals | ▪ Based on Wadell's roundness concept.<br>▪ Subjective method. | Krumbein, 1941 |
| Pettijohn Scale | Angular (0.00-0.15),Subangular (0.15-0.25), Subrounded (0.25-0.40), Rounded (0.40-0.60), Well rounded (0.60-1.00) | ▪ Range: 0 –1.<br>▪ Modified Russel and Taylor using "geometric scale" and rounding off the class limits.<br>▪ Used silhouettes rather than photographs. | Visual<br><br>Pettijohn, 1949 in Yudhbir and Abedinzadech, 1991 |
| Power's Roundness Scale | Very angular (0.12-0.17), Angular (0.17-0.25), Subangular (0.25-0.35), Subrounded (0.35-0.49), Rounded (0.49-0.70), well Rounded (0.70-1.00) | ▪ Range: 0.12 - 1.00.<br>▪ Added another descriptive term to the two above.<br>▪ Ratio of upper limit to the lower limit is 0.7 for every group. | Visual<br><br>Powers, 1953 |
| Roundness Index – image Analysis | $R = 0.14\exp(2.7 - 0.22T)$ | ▪ Distribution of average tangent counts can be used to classify soils based on angularity.<br>▪ T (tangent counts) is used to calculate R in Power's Roundness.<br>▪ Eliminates subjective visual classification.<br>▪ T = 4 represents a well-rounded grain. | Image Analysis<br><br>Yudhbir and Abedinzadeh, 1991 |
| Coefficient of Angularity, E | E = Specific surface of particle/specific surface of equivalent spheres<br><br>$R = 0.14\exp(3.35 - 1.38E)$ | ▪ Range: 1.24 (R=1.0) – 2.54 (R=0.12).<br>▪ E increases with angularity, varies directly with T and inversely with R.<br>▪ Equal to one for perfectly spherical grain but is in practice less than 1.24. | Image Analysis<br><br>Yudhbir and Wood, 1989 in Yudhbir and Abedinzadeh, 1991 |
| Angularity – ASTM | | ▪ Angular: sharp edges, relatively plane sides with unpolished surfaces, Subangular: similar to angular with rounded edges. Subrounded:nearly plane sides but well-rounded corners and edges, Rounded: smooth curved sides and no edges. | Visual<br><br>ASTM D 2488-90, 1996 |

**Table 2.7 (continued).**

| | | | |
|---|---|---|---|
| Roundness | $RMS^f = \frac{1}{r}\left[\frac{1}{2\pi}\int_0^{2\pi}\{r(\phi\}-r'(\phi)\}^2\,d\phi\right]^{1/2}$ | ▪ Roundness: relative magnitude of the contribution to the total Fourier expression made by the higher order terms.<br>▪ Polygons not same roundness with this procedure, whereas conventional roundness analysis would classify together as "angular", R=0.<br>▪ Rapid procedure, objective, influence of sphericity is compensated, regards position of curvatures (Diepenbroek, 1992)<br>▪ No ultimate shape, insufficient discrimination of higher roundness grades (Diepenbroek, 1992) | Fourier<br><br>Schwarcz and Shane, 1969 |
| Angularity Factor | AF | ▪ Range: 0 (sphere) –1 (most angular particle)<br>▪ Based on number and sharpness of corners.<br>▪ As it goes from ellipse to square to rectangle to rhombus to triangle, AF increases.<br>▪ Angularity of rectangle stays the same irrespective of the aspect ratio (because angles do not change). | Sukumaran and Ashmawy, 2001 |
| Angularity Index | $AI = \sum_{\theta=0}^{355} \frac{\lvert R_\theta - R_{EE\theta}\rvert}{R_{EE\theta}}$<br>where $R_{EE\theta}$ is the radius of an equivalent ellipse with the same aspect ratio | ▪ Normalizing the measurements with the aspect ratio in order to minimize the effect of form on angularity.<br>▪ No correlation between AI and aspect ratio. | Masad et al., 2001 |
| Roundness | $P = \mathbf{exp}(-1.25P_{pre})$<br>$P_{pre} = \sum_{k=3}^{n} c_k(R_k - R_{ek} - R_{npts})$<br>$C_k = 0.56\,\mathbf{exp}(0.2k)$ | ▪ $R_k$: amplitude of kth frequency, $R_{ek}$: amplitude of the best fitting ellipse derived from b/a , $R_{npts}$ is to avoid pixel noise<br>▪ $C_k$: weighting coefficient<br>▪ For perfect ellipsoid, $P_{pre}$ = 0 | Diepenbroek et al., 1992 |

**Table 2.8 –** Particle micro – shape parameters.

| Micro-Scale Parameter | Description | Remarks | References |
|---|---|---|---|
| Roughness Coefficient | $P = \sqrt{\frac{1}{2}\sum_{n=1}^{\infty}(A_n^2 + B_n^2)}$ | ▪ Average squared deviation of the grain perimeter from a circle of equal area (zeroth harmonic).<br>▪ At least twice the number of points must be known as the number of the highest desired harmonic.<br>▪ Ten harmonics represent a degree of "overkill" with regard to solution of many geological problems, although higher orders carry additional info.<br>▪ Coefficient magnitude decreases with increasing harmonics. The first few coefficients account for the bulk of the roughness coefficient but occupy only a small space on the axis. | Fourier Method<br><br>Ehrlich and Weinberg, 1970 |
| Roughness, R | Perimeter / Convex Perimeter | ▪ R = 1.0 for smooth | Image Analysis<br>Janoo, 1998 |
| Texture Index | Number of dominant peaks in FFT after reducing the lower 5% of the peaks to zero | ▪ Texture was measured on gray-scale images.<br>▪ Highly textured aggregates displayed a greater number of dominant frequencies than aggregates with a smooth-textured surface. | Masad et al., 2001 |
| Fractals, $D_T$, $D_1$, $D_2$ | $\log P \propto (D_T - 1)\log S$ | ▪ P = perimeter, S = step lengths<br>▪ Range: 1.0-2.0<br>▪ A plot of log P vs log S can have two linear plots. Small step lengths having a fractal dimension of D1 ( micro-scale edge textural effects) and larger steps with D2 (macro-scale particle structural effects generated by reentrants).<br>▪ The particle shows two separate "self-similar" scales of surface morphology.<br>▪ The method identifies 3 types of fractal assemblages: <u>One</u>: single fractal population (with only $D_T$ ) associated with relatively regular outlines with only $D_T$, <u>Two</u>: convex, more irregular, no real observable edge texture, slope increasing (i.e. $D_2 > D_1$) , <u>Three</u>: very marked irregular, edge texture, slope decreasing. | Fractals<br><br>Orford and Whalley, 1983 |
| Fractal Dimension, D | $N_n = C(r_n)^{-D}$, $N_n$ = Number of segments, $r_n$ = segment length, C = constant, D = fractal dimension | ▪ D increases with roughness.<br>▪ Glass beads: 1.1190, Ottowa sand: 1.1193, Pittsburg sand: 1.1313<br>▪ 4-digit precision is required.<br>▪ The parallel-line and area-perimeter fractal dimensioning techniques can be used to determine D (Hyslip and Vallejo, 1997). | Fractals<br><br>Vallejo, 1995 |
| Ruggedness Index | Plot measurement stick scaled to maximum Feret's diameter vs. perimeter to estimate the fractal dimension, D. | ▪ Error level is within 7%.<br>▪ It is classified as a grid method to determine D.<br>▪ Notice discontinuity when measurement approaches the radius of sphere from which the agglomerates are built. | Fractals<br><br>Kaye, 1978 |

#### 2.3.1.1 Particle Roundness

Based on the foregoing discussion regarding particle shape, different methods were selected for use in this study. A general review on the selected topics is presented herein and further details of the analysis method will be provided in Chapter 3 and Chapter 4.

In the subsequent subsections, the method implemented for roundness calculation and computational geometry tools utilized for automated computation will be presented.

##### 2.3.1.1.1 Wadell's Roundness

Wadell's concept of roundness as previously defined in Eq. 2.7 is implemented in this study. Wadell has separately defined sphericity and roundness. His definition implies the same roundness but different sphericity for a sphere and cylinder with hemispherical ends. In one of his early arguments with Wentworth, Wadell has investigated into the literal meaning of the word "roundness". He supported his argument of the discrepancy of sphericity and roundness by (Wadell, 1933): "The *Oxford* dictionary says that *roundness* is the quality of being round and that the meaning of *round* as a spherical or granular body is "somewhat rare" "

He continues his argument by stating that a projection of a sphere may be round due to its round circumference. However, this does not conclude the 3D shape is a sphere by just its round projection, e.g. round moon may have any shape, e.g. cylinder, cone with one circular outlined section.

Initially, he defined roundness as $\frac{\sum_{i=1}^{N}(\frac{r_i}{R})}{N}$, but later modified the equation to $\frac{N}{\sum_{i=1}^{N}(\frac{r_i}{R})}$,

where *N* is the number of corners, *r* is the radii of individual corners located, and *R* is the radius of the maximum inscribing circle. The modification resulted in less standard deviation. The maximum roundness value attainable by this formula is 1.000. Wadell's definition of a corner is (Wadell, 1932): "every such part of the outline of an area (projection area) which has a radius of curvature equal to or less than the radius of curvature of the maximum inscribed circle of the same area".

In an attempt to overcome the effect of size on roundness, roundness measurements were performed on a *standard size*. To obtain a sand roundness value comparable to a boulder roundness value, he magnified or shrank every particle to a *standard size* of 70 mm average diameter.

The curvature measurement was performed manually with a circle scale. A manually created scale consisted of several circles drawn 2 mm radius apart from each other; starting from 1mm, 2mm, up to 70 mm. Corners with radius less than 1 mm were ignored and included in the analysis with 0.5 mm radius.

The present study is focused on multiscale representation of particle shape. Thus, Wadell's roundness concept was chosen as appropriate for meso-scale shape representation. However, manual measurements are prone to user-dependent results. To overcome user-dependency, the procedure is automated in this study applying Voronoi diagrams and pattern recognition; specifically with respect to dominant point

selection. The radius of the maximum inscribing circle was calculated using Voronoi Diagrams. The literature review and procedure for developing Voronoi Diagrams are explained in the next section.

#### 2.3.1.1.2 The Minimum Zone Circles-Voronoi Diagrams

Roundness is also investigated thoroughly in computational geometry, precision engineering, industrial engineering, or mechanical engineering, mainly using geometrical tools. For this study, a method used in precision engineering was adapted for soil particle shape analysis.

Roundness is one of the most important geometric measures for circular objects in the process of mechanical assembly. It is the amount of permitted variation in a circular size. The specifications for roundness are provided by ISO (International Organization for Standardization). According to the ANSI Dimensioning and Tolerance Standard Y14.5, form tolerances need to be specified with reference to an ideal geometric feature. On the other hand, the ISO standards guide the engineer to specify the reference/ideal features based on the actual measurement data in a way that the discrepancy between the object and the reference feature is minimized. However, methods for establishing the ideal feature or to calculate the form of errors are not included in either of these standards.

Several previous studies have been as part of the background review for the present study (Shunmuga, 1986, Yeralan and Ventura, 1988, Chetwynd and Phillipson, 1980, Le and Lee, 1991, Murthy and Abdin, 1980, Chetwynd, 1985, Kaiser and Morin, 1994,

Murthy, 1986, Ventura and Yeralan, 1989). These methods differ from each other by the geometric/arithmetic tools and/or the algorithms utilized.

Commonly used methods for establishing the reference feature and evaluating the circularity error are least-squares method (LSM), normal least-squares fit, medial axis techniques and Voronoi diagrams. The LSM aims to minimize the sum of squared deviations of the measured points from the fitted features (Shunmugam, 1986). It is widely used in many other applications; however, the least-squares circle does not necessarily coincide with the minimum radial separation center (Huang, 1999). Normal least-squares fit equations require tedious mathematical calculations, and Monte Carlo method, spiral search, and simplex linear programming are among the few that have been used (Murthy and Abdin, 1980). Search techniques, e.g. 2D simplex search were also proposed (Murthy, 1986 , Shunmugam, 1987). Although the method is easy to program and efficient, the search does not guarantee a global minimum. Minimum zone values were obtained by Danish and Shunmugam (1991) using discrete Chebyshev approximations. Ventura and Yeralan (1989) utilized minimax approximation method for the evaluation of roundness. Computational geometry based techniques, such as medial axis and Voroni diagrams have been utilized (Roy and Zhang, 1992, 1994). The first application was first by Lai and Wang (1988). They used medial axis and farthest Voronoi diagram concepts, which was further implemented by Le and Lee (1991).

Voronoi diagrams were chosen to assess roundness in this study. Subsequent remarks will concentrate mainly on this powerful computational geometry tool. Voronoi diagrams can be implemented for any dimensions; however, in this study only 2D applications are considered.

The origin of Voroni diagrams dates back to the 17th century. The mathematicians Dirichlet in 1850 and Voronoi in 1908 were first to introduce and formulate this concept (Aurenhammer and Klein, 2000). They have been utilized in various fields of science. The Voroni diagrams have been termed differently in different sciences; *medial axis transform* in biology and physiology, *Wigner-Seitz zones* in chemistry and physics, *domains of action* in crystallography, and *Thiessen polygons* in meteorology and geography.

The *Minimum Zone Circles (MZC)* is described as (Roy and Zhang, 1992):

"For a set S of *n* points $(P_1, P_2, \cdots\cdots, P_n)$ in a plane of $n \geq 4$, find a pair of concentric circles $C_1$ and $C_2$ with the minimum radial separation, such that no point is exterior to the space bounded by these two circles."

The two concentric circles - $C_1$ and $C_2$ - are the ***Minimum Zone Circles*** *(MZC).*

In mathematical terms; Voronoi region, edge, and vertex are defined as (Preparata and Shamos, 1985):

S denotes a set of $n \geq 3$ point sites *p,q,r,…….* in the plane. For point sets $p = (p_1, p_2)$ and $x = (x_1, x_2)$, the Euclidean distance is denoted by $d(p,x) = \sqrt{(p_1 - x_1)^2 + (p_2 - x_2)^2}$. Throughout this section $\overline{pq}$ denotes the line segment from *p* to *q,* and $\overline{A}$ denotes the closure of a set *A.*

For $p,q \in S$, let $B(p,q) = \{x \mid d(p,x) = d(q,x)\}$ denote the *bisector* of *p* and *q.* It separates the half plane $D(p,q) = \{x \mid d(p,x) < d(q,x)\}$ containing *p,* from the other halfplane, $D(q,p)$, which contains *q*.

$VR(p,S) = \bigcap_{q \in S, q \neq p} D(p,q)$ is called the *Voronoi region* of *p* with respect to S, and the *Voronoi diagram* of *S* is defined by $V(S) = \bigcup_{p,q \in S, p \neq q} \overline{VR(p,S)} \cap \overline{VR(q,S)}$. A *Voronoi edge* is the common boundary of two Voronoi regions belonging to $V(S)$, the endpoints of the Voronoi edge are called *Voronoi vertices*, and they belong to the common boundary of three or more Voronoi regions. The analysis is based on the assumption that no four points of the original set S are cocircular.

The *nearest Voronoi diagram* can be defined as follows (Novaski and Barczak, 1997): "Given a set of $S$ of $n$ sites in the Euclidean plane, the *nearest Voronoi polygon* associated with a site $p_i$ of the set is the locus of points nearest to $p_i$ than to any other element. The $n$ regions defined similarly for all sites, divide the plane into a convex net called the *nearest Voronoi diagram* of *S.*" For example, for *point A* in the region, any point in the nearest region of point A, denoted by *N (A)* has a shorter distance to measured *point A* than any other point in the plane. Similarly, in *the farthest Voronoi diagram* the locus of points is the farthest than any other point.

A schematic figure is presented in Figure 2.7, where *V (x,y)* represent the perpendicular bisector between two measured points, and *N(A)* and *F(A)* the nearest and farthest Voronoi regions of *point A*. Figure 2.7 displays Voronoi regions only for point A,

whereas Figure 2.8 shows the nearest and farthest regions of all measured points in the plane.

Voronoi diagrams are used to solve many geometrical problems. Some common geometrical applications involve *distance problems*; such as the post office (From a given set of post office sites evaluate for any query point x, the closest post office), nearest neighbors and closest pair (Given a point site of S, for every point determine the nearest neighbor in S), and largest empty and smallest enclosing circle (A location problem in which a point farthest from *n* sources of disturbance is required. If the area is confined by a convex polygon *A* over *m* vertices, the solution becomes the largest circle with center located in *A* that excludes a point in *S*). Voronoi diagrams are utilized in ecology when investigating, for example, the number of neighbors an organism needs to struggle for food and light, in archeology to study the effect of rival centers of commerce on the ancient culture (Aurenhammer and Klein, 2000).

Voronoi diagrams are also implemented to account for local differences in a material behavior. Using this technique, a certain region with different mechanical, chemical, or dynamical properties can be assigned to each particle. One such example is the study by Estrin et al. (1999), in which four different particle arrangements were accounted for by subdividing the material into a mesh of Voronoi cells each containing a single particle. This allowed an analysis based on a local scale. They considered different particle arrangements and developed Voronoi diagrams for each as shown in Figure 2.9.

In determining roundness, Voronoi diagrams were implemented in various techniques. Ebara et al. (1992) have introduced an exact polynomial-time algorithm to compute the

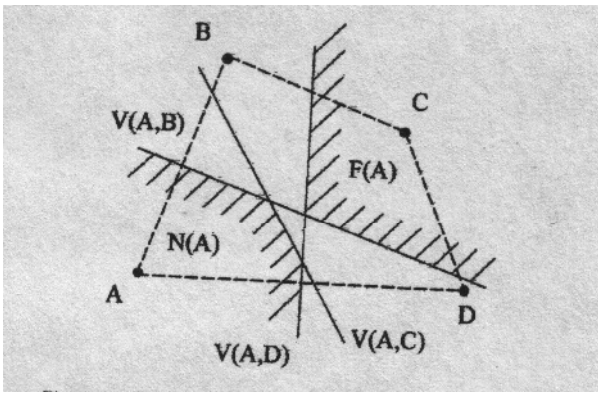


**Figure 2.7 -** The nearest (N(A)) and farthest (F(A)) regions for point A (after from Huang,1999).

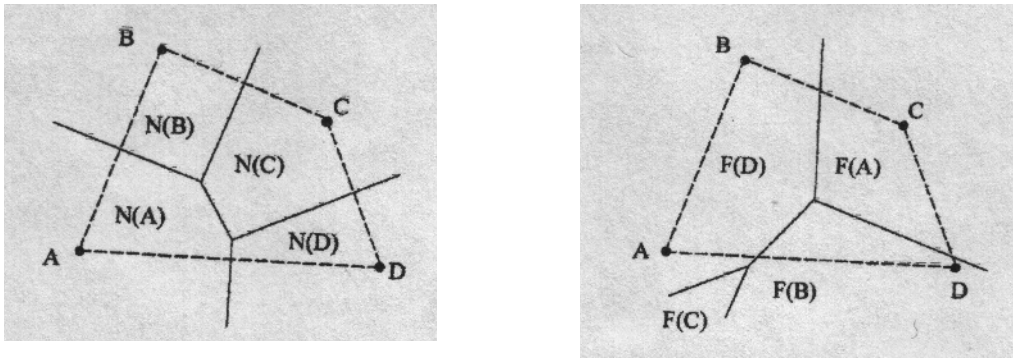


**Figure 2.8** - The Nearest and Farthest Voronoi Diagrams for the points A, B, C, and D (after from Huang, 1999)**.**

roundness. The algorithm progressed by deleting unnecessary points. The proposed technique involved the union of the nearest- and the farthest-point Voronoi diagrams. Upon locating the intersection points between the nearest- and the farthest-point Voronoi, they computed the difference of the distances from these intersection points to the nearest and farthest points. The point with the minimum distance is taken as the center of the concentric circles determining the roundness and the value of the difference as the roundness.

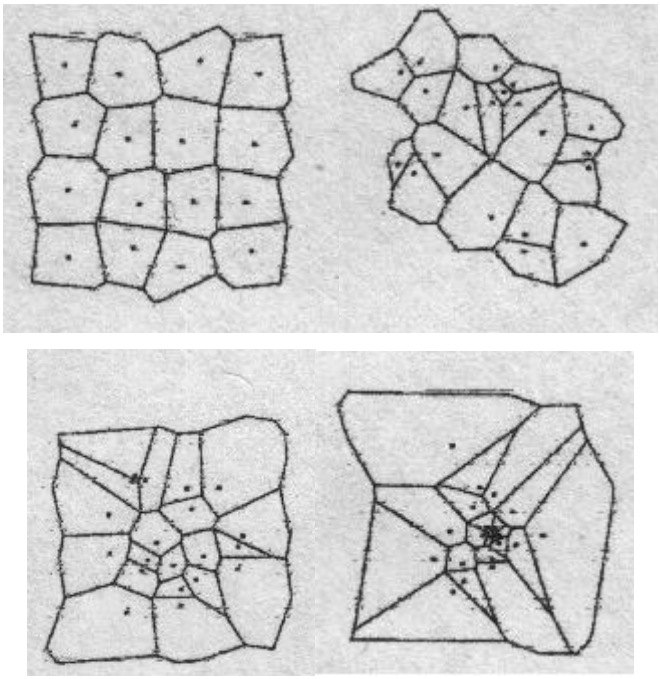

**Figure 2.9 -** Four different particle arrangements for local scale analysis (after Estrin et al., 1999).

Huang (1999) introduced another exact solution to evaluate roundness. He defined *max region* as an intersection between the corresponding farthest and nearest regions, e.g. the intersection of farthest region of A, F(A), and the nearest region of C, N(C), creates a region *max (A, C)*. Huang (1999) proves that the minimum roundness can be obtained only at the vertex of the max region between one farthest and one nearest region, rather than at the intersection of two farthest or two nearest regions. Thus, the vertices belonging to the *max regions* of one farthest and one nearest Voronoi diagrams are evaluated as possible candidates for the MZC center.

Another commonly referenced work is by Roy and Zhang (1992). They compare three cases for the minimum zone circles. In case one, the intersection of the nearest and

farthest Voronoi is computed and two concentric circles centered at the vertices with each of them passing through at least two data points are evaluated. In case two, concentric circles are centered at every vertex of the nearest Voronoi, in which case the inner circle passes through at least three data points and the outer one at least one point. Case three is similar to case two except that farthest Voronoi vertices are used. The roundness is given by the minimum separation distance of the three cases.

The method proposed by Samuel and Shunmugam (2000) is used in this study. The method works for both uniform and nonuniform spacing datasets with a guaranteed minimum value. The calculation time is short with a time complexity of O(*NlogN*) and the algorithm provides a unique solution. The remainder of this section explains the technique for Voronoi Diagrams and Samuel and Shunmugam's (2000) method for MZC.

For Voronoi Diagram construction, first a convex hull is computed. A convex hull of any set $S$ is the smallest convex set that encloses $S$ and is denoted by $conv(S)$. A domain is convex iff (if and only if) for any two points in the domain the segment joining the two points is within the domain itself. Unlike the definition, computation of the convex hull is not straightforward.

Several algorithms exist for the convex hull. Some procedures are provided in Preparata and Shamos (1985). The "Divide and Conquer" and "Merge" technique was implemented by Samuel and Shunmugam (2000). However, for this study the algorithm proposed by Ye was employed (1995).

*In convex hull construction*, first the extreme points should be identified. As given by Preparata and Shamos (1985), a point $p$ of a convex set $S$ is an extreme point when no two points $a, b \in S$ exist such that the point $p$ is on the open line segment of $\overline{ab}$. Any point that does not qualify as an extreme point would lie inside a triangle with vertices other than the extreme point. As the subsequent step, the extreme points are sorted in angular order to form the convex polygon.

The existing convex hull algorithms are classified into two categories based on the input data of the given set *S*. The set S could be input either as an arbitrary connected object, or as a set of distinct points. Several references of both cases are provided in Ye (1995). This algorithm calculates the convex hull for several kinds of input data (e.g. set of distinct points, arbitrary connected objects, or a set containing both distinct points and connected objects) provided that the data is stored as a 2D image. This algorithm is based on the assumption that the polygon is non-self intersecting since the convexity test cannot detect self – intersecting polygon.

The two steps involved in the computation are: (1) *polygon extraction*, and (2) *convex hull extraction*. During polygon extraction, the image is scanned clockwise to obtain the set of candidate extreme points, and at the second step, the attained polygon is checked for convexity and updated by deleting concave parts if necessary. Convexity can be verified by various rules. A *vector cross-product rule* is used by Ye (1995). The procedure detects whether a right or a left turn is made, as three adjacent vertices of the polygon set, *P,* $(P_1, P_2, P_3)$ are swept counterclockwise. For a unit normal vector, $n$, of the plane containing $(P_1, P_2, P_3)$, and the edge vectors, $a = OP_2 - OP_1$ and

$b = OP_3 - OP_2$ originating from the origin of the image to points $P_i$ for $i = 1,2,$ and $3$, the turn is *a right turn* if $n \cdot (a \times b) > 0$. Otherwise, it is a *left turn* or the points are *collinear*.

(1) *Polygon Extraction Procedure*: The process is schematically shown in Figure 2.10. Note that in all four scanning directions, a row/column search ceases if a column/row number of the last point is reached. For the purpose of convex hull, there is no need to scan further than extreme points located at the previous step, i.e. no information regarding the interior of the object is needed. The systematic scanning starts from the right top end of the image and initially goes downward searching every row from right to left. A scan of a row is ceased after either locating a point in the existing row or when the left edge of the image is reached. The next search (as shown in 4b) starts from the column number of the last point extracted and ends at the left edge of the image, and every column is searched from bottom to top. At the third stage, scanning starts from the row number of the last point extracted and ends at the row of $P_0$, which was already established as the topmost point. Finally, scanning from the column number of the last point extracted to the column number of the first point extracted, $P_0$.

(2) *Convex Hull Extraction*: The input is the $n+1$ extreme points from the previous procedure, where $(x_0, y_0) = (x_n, y_n)$. Starting with $j = 0$, the following steps are carried.

1. Calculate $P = (x_{j+1} - x_j)(y_{j+2} - y_{i+1}) - (y_{j+1} - y_j)(x_{j+2} - x_{j+1})$.
2. Stop if $P > 0$ and point $j+2$ is the last point of the set.
3. Go to the next point and continue from Step 1 if $P > 0$

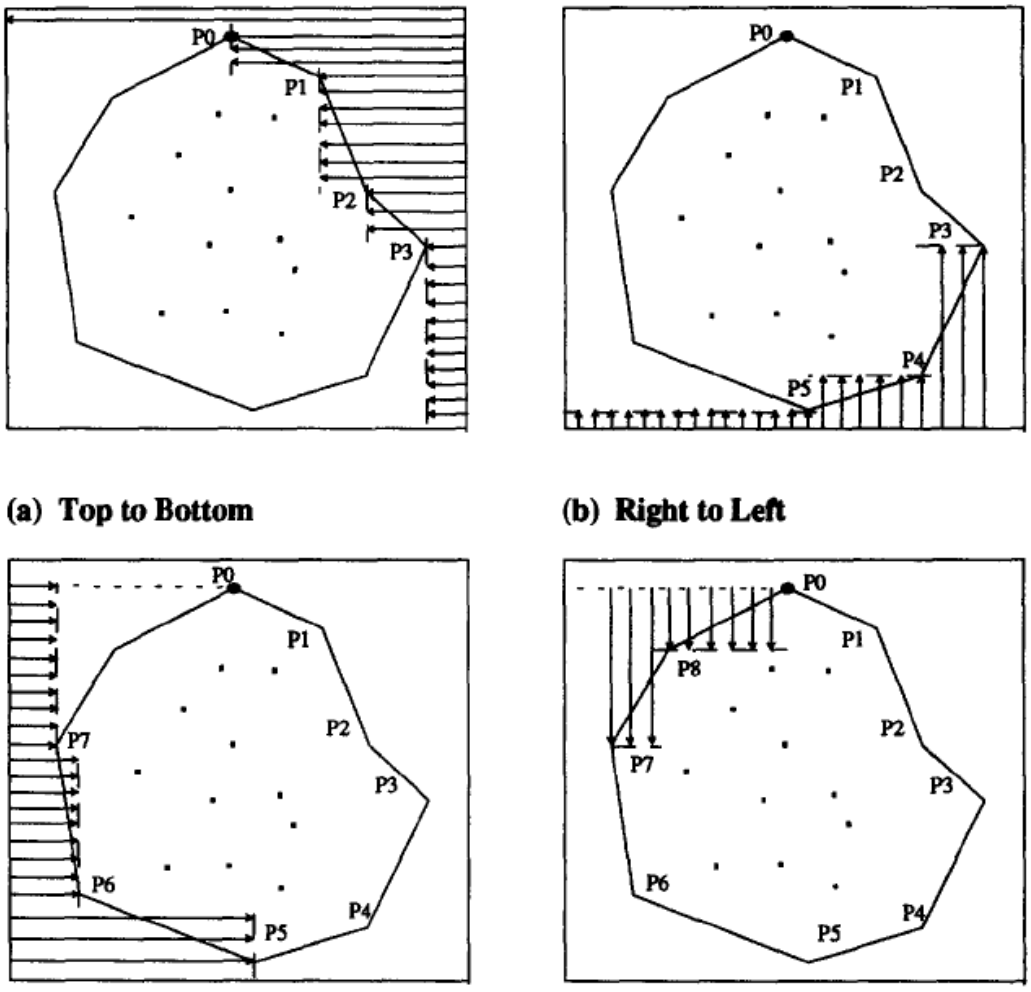


**Figure 2.10 -** An example of polygon extraction procedure (after Ye, 1995).

4. Discard point $j+1$. If $j>0$, move one point backward, otherwise move one point forward.
5. Go to Step 1.

Note that in Step 4, the polygon is checked again for convexity when a concave point is deleted to prevent another concave point occurring when a concave corner is deleted.

The polygon extraction and the convex hull extraction procedures have complexities of $O(N^2)$ and $O(N)$, respectively (Ye, 1995).

Once the convex hull is extracted, the method proceeds as the one proposed by Samuel and Shunmugam (2000). In the following sections, a description of the computation method for the Minimum Circumscribing Circle (MCC) will be followed by a description of the procedure for the Maximum Inscribing Circle (MIC) computation.

**THE MINIMUM CIRCUMSCRIBING CIRCLE AND THE FARTHEST VORONOI DIAGRAM.**

- *Construct the convex outer hull of the given datapoints:* This is performed as explained above. In Figure 2.11, the object of interest is shown by the solid line and the corresponding convex outer hull for the 12 points by the dotted line.
- *Form equidistant (ED) lines for each edge:* For example, for the edge $V_1V_2$, ED line $L_{12}$ is constructed, which is the locus of the points that are at equal distance from both $V_1$ and $V_2$. Similarly, $L_{23}$ and $L_{34}$ are constructed corresponding to edges $V_2V_3$ and $V_3V_4$, respectively (see Figure 2.12).

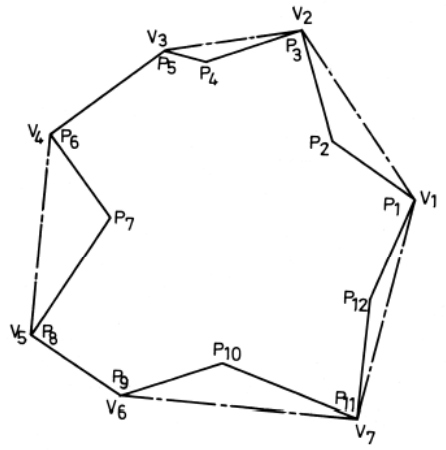


**Figure 2.11 -** The data points labeled as $P_i$, where $i = \{1,2,\ldots\ldots,12\}$ and the convex outerhull (the dotted line) with vertices labeled as $V_i$ (after Samuel and Shunmugam, 2000).

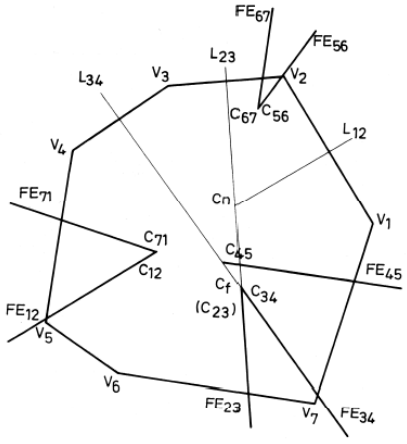


**Figure 2.12 -** The initial farthest edges for the construction of the farthest ED diagram (after Samuel and Shunmugam, 2000).

- *Find the farthest centers for each edge:* For edge $V_2V_3$, equidistant line $L_{23}$ intersects with both the ED line from the previous edge $L_{12}$ and the ED line for the next edge $L_{34}$, at $C_n$ and $C_f$, respectively. $C_f$ is further from $V_2V_3$ than $C_n$, which implies that the former is the farthest center, $C_{23}$. A circle passing through $V_2$ and $V_3$ can be drawn with $C_{23}$ as the center (see Figure 2.12).
- *Construct the farthest edges for each edge:* The farthest edge corresponding to, for example edge $V_2V_3$ is the portion of the ED line $L_{23}$ beyond $C_f$ and it is denoted by $FE_{23}$. Record the farthest centers located.
- *Update the convex hull:* This is done by locating common farthest centers for the edges. For example, as shown in Figure 2.12, edges $V_2V_3$ and $V_3V_4$ have common centers as $C_{23}$ and $C_{34}$. For any point in the region enclosed by these edges, edge $V_3$ will be farthest vertex, thus, it can be dropped. $V_1$ and $V_6$ are also dropped in this first iteration, since both ($C_{12}$ & $C_{71}$) and ($C_{67}$ & $C_{56}$) are common centers. The convex is updated with only the remaining vertices.
- Start the iteration over with the remaining vertices and continue this loop until three or less vertices are left.

As the final step, the circle with the least radius circumscribing the dataset with one of the computed farthest centers as the center of the circle is established. This circle is the **Minimum Circumscribed or Crest Circle (MCC)**. The diagram with all farthest edges constructed is the **Farthest Voronoi Diagram**. Figure 2.13 shows the constructed Farthest Voronoi Diagram for the example given by Samuel and Shunmugam (2000).

**THE MAXIMUM INSCRIBING CIRCLE AND THE NEAREST VORONOI DIAGRAM.**

Figure 2.14 shows the construction of the nearest Voronoi diagram. Note that the original profile is shown as $P_i$, where $i = \{1,2,\cdots\cdots,12\}$ and the vertices of the obtained inner convex hull as $P_i'$ for $i = \{1,2,\cdots\cdots,12\}$.

- *Construct the inner hull of the given datapoints:* The inner hull is the boundary of the largest empty subset of given points. The method used is provided below.
    - *Locate a suitable center*: One choice is the Minimum Circumscribing Center (center O in Figure 2.14).
    - *Determine a suitable diameter and construct a circle*: The diameter should be large enough to ensure that all points on the profile are within this circle and the center is the suitable center from the previous step.
    - *Transform the profile:* This is accomplished by performing the method below *for each vertex* on the original profile:
        - Find the radial deviations (from the center's circle) between the original profile and the estimated circle (in Figure 2.14 this deviation is shown as "a" as the distance between $S_3$ and $P_3$ for vertex 3).
        - Move radially distance "a" from the circle's center to locate the new vertex corresponding to the original vertex (move "a" for vertex 3 from the circle's center in the direction of $OP_3$ and locate $P_3$' corresponding to $P_3$ on the original profile).
        - Perform this process for every vertex.

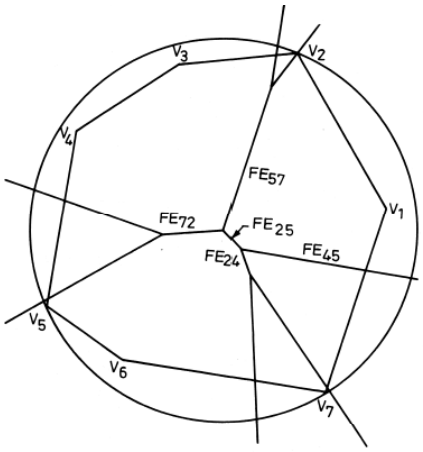


**Figure 2.13 -** The Farthest Voronoi Diagram and the Minimum Circumscribed Circle (MCC) (after Samuel and Shunmugam, 2000).

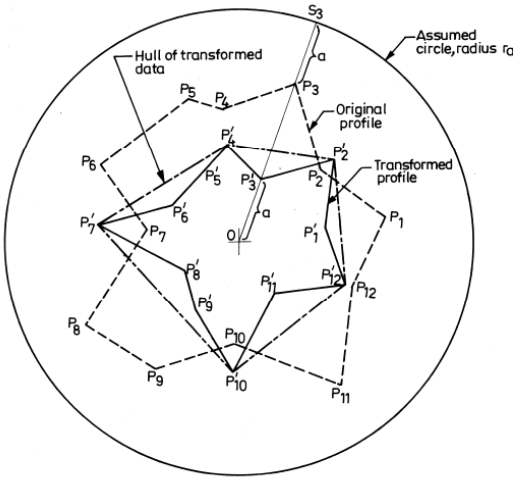


**Figure 2.14 -** The transformed data and the convex inner hull (after Samuel and Shunmugam, 2000).

- *Determine the convex hull for the transformed profile*: After obtaining the transformed inner hull (shown by the solid line), the convex hull extraction procedure is executed to generate the inner convex hull. The subsequent operations are performed on the inner convex hull.
- *Form the ED lines for each edge*: This is performed as explained in the previous section for MCC.
- *Find the nearest centers for each edge:* For the nearest Voronoi diagram, the nearest intersection points are considered rather than the farthest points. The nearest centers are mentioned as $C_n$ in the previous section.
- *Construct the nearest edges for each edge:* These are denoted as NE in Figure 2.15.
- *Update the convex hull*.
- Iterate the whole procedure with the remaining vertices until three or less vertices are left

As the final step, circle with the least radius circumscribing the dataset with one of the nearest centers as the center of the circle is constructed. This circle is the **Maximum Inscribing or Crest Circle (MIC)**. The diagram with all nearest edges constructed is the **Nearest Voronoi Diagram**. The Nearest Voronoi Diagram for the example given in Samuel and Shunmugam (2000) is shown as the dotted diagram in Figure 2.16.

**THE MINIMUM ZONE CIRCLES.**

As mentioned above, the minimum zone circles are two concentric circles that encompass all the data points and have minimal radial distance between. Note that, the minimum zone circles should pass through at least four data points. This can be

accomplished by either one circle passing through three points and the other one or by both of them passing through two datapoints.

To construct the minimum zone circles, the farthest and nearest ED diagrams are superimposed. The smallest circumscribing and the largest inscribing circles centered at one of the intersection points of the farthest and nearest Voronoi diagrams are found. The pair with the minimum radial distance between is taken as Minimum Zone Circles (MZC). Figure 2.16 shows the constructed Minimum Zone Circles for the example given by Samuel and Shunmugam (2000).

#### 2.3.1.1.3 Pattern Recognition – Edge and Corner Detection

For Wadell's roundness, the Minimum Circumscribing Circle (MCC) and the Maximum Inscribing Circle (MIC) are determined as explained in the previous section. Wadell's roundness calculation requires the radii of curvature for selected corners along the grain shape. Originally, the method was implemented manually and every data point was considered. However, in this study, the significance of each data point is investigated and only those with important shape information are considered for further curvature measurements.

In a similar approach, computer vision is involved in extracting meaningful features from images by pattern recognition. Pattern recognition is based on the concept that dominant points along a curve are sufficient to describe the shape of a particle. Dominant point detection in digital contours allows efficient representation to apply

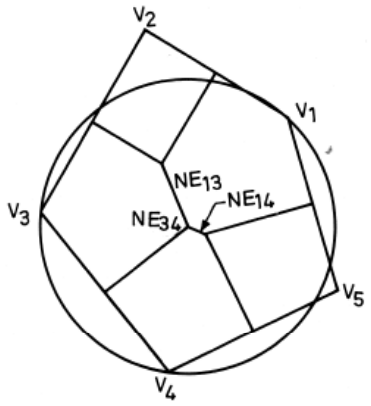


**Figure 2.15 -** The Nearest Voronoi Diagram and the Maximum Inscribed Circle (MIC) (after Samuel and Shunmugam, 2000).

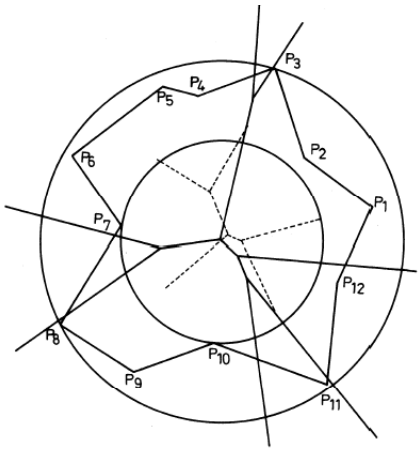


**Figure 2.16 -** Superimposed Farthest and Nearest Voronoi Diagrams along with MZC (after Samuel and Shunmugam, 2000).

feature extraction or shape matching algorithms. The purpose of pattern recognition is to capture the essential feature points along a digital curve with the fewest possible polygonal segments and/or curves, so that the amount of data that needs to be processed for future computations is reduced.

The research on pattern recognition has been initiated by the interest in the study of the Human Visual System (HVS). The aspects of visual perception has been studied by several researchers with the noteworthy contribution from Gestalt school of psychology (Wertheimer, 1923), Hebb (1949) by his book *The Organization of Behavior,* and Gibson (1950) by his book *The Perception of the Visual World*.

In his classical work, Attneave (1954) has demonstrated that by extracting points with high curvature and connecting them with straight lines, a recognizable sketch of the object could be obtained implying high curvature points contain rich information about the contour of an object (Attneave, 1954). Conflicting with this concept, Hoffman and Richards (1984,1985) argued that high negative curvature points, where are natural breakpoints for the visual system to decompose the objects. Leyton (1989), on the other hand, based his theorem on the idea that all shapes are basically circles that have gone through various deformations, and thus change of forms. Among these ideas, Attneave's work has gained most recognition.

Several shape analysis methods and almost as many classification schemes exist in literature. A noteworthy classification has been proposed by Pavlidis (1978) as;

(i) *Boundary vs. Global Techniques:* Boundary class involves those algorithms that use shape boundary points; whereas global class

algorithms use the points interior to the boundary. Examples of the former include the methods based on outline and Fourier transforms of the boundary. Medial axis transform (MAT) and moment based approaches are examples for the global shape analysis methods.

(ii) *Numeric vs. Non-Numeric Result Techniques:* The class names are self-explanatory. MAT, Fourier, and moment-based techniques can be used as an example for the latter technique.

(iii) *Information Preserving vs. Information Non-Preserving Methods*: The former techniques enable the reconstruction of the shape; whereas the latter do not.

Generally, two approaches have been utilized in dominant point detection algorithms: (a) *dominant point selection via angle or corner detection*, (b) *linear polygonal approximation* (Wu and Wang, 1993; Cornic, 1997). Angle/corner detection requires the determination of curvature for each point on the curve and then selecting the points that are local maximums or the ones with sharp angles as dominant points (Rosenfeld and Johnston, 1973; Rosenfeld and Wezska, 1975; Freeman and Davis, 1977; Teh and Chin, 1989). Angle/corner detection can be classified in three different categories: (a) direct curvature estimation, (b) curvature estimation followed by Gaussian filtering, and (c) scale space procedures. Gaussian filtering has been utilized in order to overcome the difficulties with the digital representation of the curve. However, as pointed out by many it suffers from scale issues such that too small width selection will result in an output of several redundant dominant points; whereas a too large width will miss details of the curve. Cornic (1997) points out that the maxima defined by Gaussian filter are ill defined. Pei and Horng (1995) propose using an adaptive Gaussian filtering method, where each point is treated based on its individual properties. However, the authors

themselves abandon this method and concentrate on dynamic programming algorithms for further studies.

A simpler approach, polygonal approximation, fits digital segment with straight-line segments (Horng and Li, 2001). Polygonal approximation can be performed either sequentially or iteratively. The three approaches are: (i) *Split,* (ii) *Merge*, and (iii) *Split-and-Merge* algorithms. The Split method suffers from sensitivity to scale, orientation, and starting point. Merge algorithms start by a segment, and data points are added to the segment while a certain criteria is met. In case a point does not satisfy the criteria, it is regarded as the starting point of a new segment. As the name applies, Split-and-Merge combines both techniques (Cornic, 1997).

As expected, fitting higher-order curves rather than straight-line segments between data points provides a higher level of accuracy. In that respect, some studies have utilized both straight lines and circular arcs (Ichoku et al., 1996, Horng & Li, 2001, Wu & Wang, 1993). The method implemented by Wu and Wang (1993) is termed as *curvature based polygonal approximation.* Their methodology involved deleting points on a straight line (since they can not be dominant points), applying corner detection to obtain dominant points, and further partitioning the curve between successive dominant points by iterative polygonal approximation.

Pei and Horng (1996) propose a method where dynamic programming is used to find M vertex points along a digital curve of N ordered points and circular arcs are fitted between adjacent vertices. Although promising, this algorithm requires the number of vertices as input. Studies were conducted where line segments along with circular arcs were used for segment representation (Ichoku et al., 1996, Horng & Li, 2001). Ichoku et

al. (1996) proposed a dynamic focusing algorithm-defined as the inverse of region growing algorithm based on two rules: (i) straight line segments are chosen over circular arcs, and (ii) longer lines/curves are preferred over short lines/curves. Horng and Li (2001) formulate the perceptual significance introducing an objective measure. In another study in order to improve on the dynamic approach for polygonal approximation of digital curves proposed by Pei and Horng (1996), Horng and Li (2002) utilize a termination mechanism to determine the number of vertices. Although dynamic programming results in the global optimum solution, it suffers from two main important disadvantages. As mentioned above, it requires the assumed number of vertices prior to the calculation. However, this prediction is complicated due to the multiscale nature of features along the curves and the geometric size. In addition, dynamic programming has extensive processing time, especially with closed curves. Although several methods are proposed to decrease the processing time (Horng & Li, 2001; Salotti, 2001, 2002, etc.), dynamic programming was not selected for this study.

Among the studies mentioned, the polygonal approximation method proposed by Teh and Chin (1989) is utilized in this study to select dominant points along a digital curve by angle detection, in particular by direct curvature estimation. The analysis procedure is described in detail below.

Curvature definition in the real Euclidean plane is simply the rate of change of slope as a function of arc length. Thus, curvature for a curve $y = f(x)$ is defined as

$\frac{\partial^2 y / \partial x^2}{(1+(\partial y / \partial x)^2)^{3/2}}$. However, for digital curves the definition is not straightforward. In case the derivatives are replaced by 1- differences (i.e. $k = 1$, where $k$ is the smoothing factor) the small changes in curvature cannot be detected, since angles can only differ

by 45°. In that respect, several methods to obtain a smoothing factor, e.g. $k\,(k>1)$ have been proposed, most of which are parallel procedures, i.e. the results at one point do not depend on previously obtained results at other points.

Teh and Chin (1989) based their study on the claim that the accuracy of dominant point selection depend not only on the determination of discrete curvature, but mainly on the precise determination of the smoothing factor of each point based on the local properties of that region. The main problem with most algorithms, which require input smoothing parameters, is the scale issue. A single parameter to compute the region of support (i.e. smoothing factor) for every point on a curve causes a problem since curves consist of multiple size features. When the region of support is too large, the fine details are smoothened; on the other hand, when the parameter is small redundant dominant points will be selected similar to the problems associated with Gaussian filtering width. The study performed by Teh and Chin (1989) proves that the region of support determination is more critical in dominant point detection than the measure of significance of a point. Thus, they compare and argue no differences between three measures of significance, i.e. different degrees of accuracy of discrete curvature estimates (note that in all definitions $k$ stands for the *smoothing factor* mentioned above): (a) ***k-cosine*** as defined in Rosenfeld-Johnston algorithm, which is at a point $p_i$:

$$\cos_{ik} = \frac{a_{ik} \cdot b_{ik}}{|a_{ik}||b_{ik}|} \qquad \textbf{(2.6)}$$

where,

$a_{ik} = (x_i - x_{i+k}, y_i - y_{i+k})$ $\qquad\qquad$ $b_{ik} = (x_i - x_{i-k}, y_i - y_{i-k})$

are the k-vectors at $p_i$. Obviously $-1 \le \cos_{ik} \le 1$, where the upper limit is for the sharper angles and the lower limit for the straight lines; (b) ***k-curvature***, which is the difference in mean angular direction of k vectors on the leading and trailing curve segment of the point $p_i$. It is calculated as:

$$CUR_{ik} = \frac{1}{k}\sum_{j=-k}^{-1} f_{i-j} - \frac{1}{k}\sum_{j=0}^{k-1} f_{i-j} \qquad \textbf{(2.7)}$$

where $f_i$ is an integer between 0 and 7 (module 8) in Freeman chain code (see Figure 2.17); (c) ***1-curvature***, which is given when *k=1* for the above measurement. The results show that the three significance values produce very similar results, supporting the initial claim by Teh and Chin (1989) that the region of support is more crucial in the analysis.

The main advantage of the Teh and Chin algorithm is that it is parameter-free, i.e. the algorithm adjusts itself to the multiscale nature of the objects. Some related opposing and supporting arguments succeeding the work by Teh and Chin (1989) are given below.

Note that the algorithm proposed by Teh and Chin (1989) and the one used herein determines a region of support that is symmetrical with respect to the point of interest. Ray and Ray (1992) discuss that there is no need that the region of support should be symmetrical and thus propose a parameter-free method with non-symmetrical region of support. They define dominant points as those that have local maximum *k-l cosine*

value (similar to *k cosine* except that one side of point *i* have a region of support of length *k* and the other side of length *l*) compared to its neighbors. Although the method proposed by Ray and Ray (1992) resulted in less error (in terms of integral square and maximum errors) and more dominant points for the outlines compared, asymmetric region of support is not essential in Wadell's roundness calculation, and thus is not considered in this analysis.

Ansari and Huang (1991) concentrate on the effect of noisy contours in dominant point selection and they favor a nonparametric approach, i.e. which requires no input parameters. They propose a Gaussian filter to smooth the curve before applying a dominant point detection algorithm proposed by Teh and Chin (1989). The filtering is adjustable to local conditions of the contour and provides an improved shape in the presence of noise. However, the Teh and Chin algorithm works better in terms of the total error, computation time, and number of points. Additionally, it is been argued that Ansari and Huang algorithm suffers from discretization effects when real objects rather than artificial shapes are used (Inesta et al., 1998).

The performance of an algorithm can be evaluated in various ways. The efficiency of the yielded representation is quantified by the number of dominant points ( $M$ ) evaluated; the accuracy is measured by the distance between the original shape and approximated polygon. For $N$ total data points along a curve, if $M$ *and* $e_i$ represent the number of dominant points and the distance from each contour point to the closest segment of the polygonal approximation, respectively, then the most commonly used criteria for algorithm performance evaluation are:

(1) Compression Percentage (CP) $$\tau\% = 100\frac{N}{M} \quad \textbf{(2.8)}$$

(2) Integral Square Error (ISE) $$ISE = \sum_{i=1}^{N} e_i^2 \quad \textbf{(2.9)}$$

(3) Maximum Error $$E_\infty = \max_{1 \le i \le N} e_i \quad \textbf{(2.10)}$$

(4) Computation Time $$t \quad \textbf{(2.11)}$$

Unfortunately, comparing the polygonal approximations based $CP$ or $ISE$ only does not necessarily show how good the approximation is, since a high $CP$ leads to high distortion of the polygon, i.e. high $ISE$ ; on the other hand, a low $ISE$ results in a low $CP$ . In that respect, Sarkar (1993) has combined the two measures as a ratio in figure of merit as:

(5) Figure Of Merit (FOM) $$FOM = \frac{CP}{ISE} = \frac{N}{M \times ISE} \quad \textbf{(2.12)}$$

Rosin (1997) points out that, although Sarkar's $FOM$ is promising, it cannot be used to compare algorithms with different number of lines. He argues that when equally good representations of a curve with different number of lines are compared, the criteria should give them the same rate, however, that is not the case.

Inesta et al. (1998) have proposed another criteria as the ratio of the committed error (accuracy) versus number of points (compression), termed as the optimization error:

(6) Optimization Error (OE) $$OE = ISE\frac{M}{N^2} \quad \textbf{(2.13)}$$

For a lower optimization error, the approximation is efficient and precise. However, to prevent the case $M = N$ as the possible best solution, the definition also includes the statement that if $ISE = 0$ , then $OE = \frac{N}{M}$ .

In comparing different criteria, Rosin (1997) argue the importance of the natural scales of the curve related to the curve's shape as well as the number of dominant points. The proposed performance evaluation criterion is $Merit = \sqrt{Fidelity \times Efficiency}$ . The related definitions are:

$$Fidelity = \frac{E_{opt}}{E_{approx}} \times 100 \quad \textbf{(2.14)}$$

$$Efficiency = \frac{M_{opt}}{M_{approx}} \times 100 \quad \textbf{(2.15)}$$

where, the subscripts $opt$ and $approx$ stand for the optimal and approximated solutions, respectively. In other words, *fidelity* is a measure of how well the polygon fits the curve relative to the optimal solution and *efficiency* signifies how compact the polygon representation of the curve is relative to the optimal solution. Rosin (1997) has used the dynamic programming by Perez and Vidal to find the optimal solution and defined the error in terms of the *ISE*. They have ranked 23 algorithms based on $Merit$ . The Teh and Chin (1989) algorithm ranked 17$^{th}$ among the tested. The assessment performed by Rosin (1989) is not necessarily pertinent to the application of the Teh and Chin (1989) algorithm in this study. The assessment technique used by Rosin (1989) is a function of how well the polygon fits the curve, however, this study utilizes the set of dominant

points selected by the algorithm and uses other techniques to merge the dominant points.

In addition to the above performance evaluation methods; the minimal polygon perimeter, the maximal internal polygon area, and the minimal external polygon area have also been reported as evaluation methods (Loncaric, 1998).

The relevance of an error measure or a compaction percentage is poor for the presented technique. Even though it is rarely specified, some algorithms are goal-oriented and thus it is significant to assess the algorithms performance depending on its purpose. For example, in case the approximated polygon will be the input of a classifier, then the performance can be assessed based on how satisfactory the classification rates are and how informative the polygon is regarding the vertices with rich information. On the other hand, if the purpose is to obtain a polygon for feature extraction, then the least amount of dominant points is desirable (Inesta et al., 1998). Having reviewed the work mentioned above, the Teh and Chin Algorithm was implemented as explained below.

The Teh and Chin Algorithm

**Step 1.** *Perform break point detection by checking the chain codes*. Freeman chain code is made up of integers $[0,1,2,3,4,5,6,7]$ each of which represents a vector $p_{i-k}p_{i+k}$ as shown below:

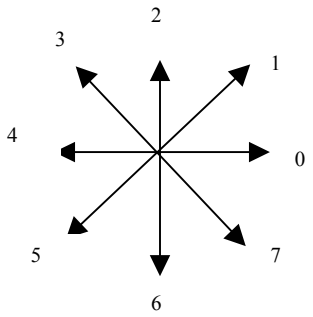


**Figure 2.17 -** Freeman chain code.

Several studies on Freeman chain codes proved the following as general rules (Wu, 1982):

- If two consecutive sections have identical Freeman codes, they form a straight segment.
- Within the same segment, at the most two different codes can appear from one another in 1 modulo 8.
- If there exists two codes within a segment, the length of one of the codes is one, i.e. whenever one of the codes appears it is only once and the codes before and after are from the other code. The length of the second code is either $n$ or $n+1$, where $n$ depends on the coefficients of the straight line.

**Step 2.** *Determine the region of support using the criteria by Teh and Chin*. Two parameters are required; $l_{ik}$ and $d_{ik}$, where the former is the length of the chord joining the points $p_{i-k}$ and $p_{i+k}$, and the latter is the perpendicular distance of the point $p_i$ to the chord $\overline{p_{i-k}p_{i+k}}$. Starting with $k=1$, compute $l_{ik}$ and $d_{ik}$ until *condition a* or *b* as stated below is satisfied:

*Condition (a)* $l_{ik} \geq l_{i,k+1}$ for $d_{ik} \equiv 0$

*Condition (b)* $\frac{d_{ik}}{l_{ik}} \geq \frac{d_{i,k+1}}{l_{i,k+1}}$ for $d_{ik} > 0$ $\frac{d_{ik}}{l_{ik}} \leq \frac{d_{i,k+1}}{l_{i,k+1}}$ for $d_{ik} < 0$

Subsequently the region of support for that particular point can be defined as:

$$D(p_i) = \{(p_{i-k}, \ldots, p_{i-1}, p_i, p_{i+1}, \ldots, p_{i+k} \mid condition\ (a)\ or\ condition\ (b)\}$$

**Step 3.** *Calculate the measure of significance for every point and record its absolute value* as $|S(p_i)|$. Of the three measures of significance suggested, *k-cosine* is used. Subsequently, the point is tested based on the following set of laws and the dominant points are determined thereafter.

***First Pass****:* Record points $p_i$ where:

$|S(p_i)| \geq |S(p_j)|$ for all $j$ such that: $|i - j| \leq k_i / 2$

***Second Pass:*** Out of the recorded values following the first pass, discard those with *zero 1- curvature* and perform the third pass with the remaining.

***Third Pass:*** If $([k_i\ of\ D(p_i)] = 1)$ and $p_{i-k}$ or $p_{i+k}$ still survived, then discard $p_i$ if $|S(p_i)| \leq |S(p_{i-1})|$ or $|S(p_i)| \leq |S(p_{i+1})|$.

The points survived from the third pass are the *dominant points*, termed as $B_i$.

Upon the retrieval of dominant points, Wadell's roundness equation requires the radii of curvature for the curves between those points. However, the two dominant points are not sufficient to fit a curve in between, i.e. when the two endpoints are fixed there

remains one more degree of freedom for a circular arc fitting. No closed form solution exists for this problem. The arc parameters are obtained in this study by the estimation technique proposed by Pei and Horng (1996). The method is explained below.

For a set of $N$ given points:

$$A = \{a_1, a_2, \cdots\cdots, a_N\}$$
$$= \{(x_1, y_1), (x_2, y_2), \cdots\cdots, (x_N, y_N)\}$$

Let the set of $M$ dominant points be denoted by:

$$B = \{b_1, b_2, \cdots\cdots, b_M\}$$
$$= \{(x_1, y_1), (x_2, y_2), \cdots\cdots, (x_M, y_M)\}$$

and the set of $M-1$ curve segments to be computed as:

$$F = \{f_1, f_2, \cdots\cdots, f_{M-1}\}$$

where $f_m$ is the curve between the dominant points $b_m$ and $b_{m+1}$. Then the Pei and Horng (1996) method is implemented to obtain the radius $R$ and the center $(x_c, y_c)$ of each $f_m$ arc, where $m = \{1,2,\cdots\cdots, M-1\}$. Note that the following derivations fit a curve between the endpoints $\{(x_i, y_i), (x_j, y_j)\}$. Considering $(x_i, y_i)$ and $(x_j, y_j)$ are two consecutive dominant points from the set $B$, the derivations are based on minimizing the $ISE$ between the fitted curve and all the data points that lie between the two

consecutive dominant points. The initial data points for the object for this section are $\{(x_{n-1}, y_{n-1})\}$ and $\{(x_n, y_n)\}$. The formula for the center and radius calculation are:

$$(x_c, y_c) = \left( -\frac{\sum_{n=i}^{j} K_1 K_2}{\sum_{n=i}^{j} K_1 K_3}, a\,x_c + b \right) \qquad R = \sqrt{(x_i - x_c)^2 + (y_i - y_c)^2} \qquad \textbf{(2.16)}$$

**(2.16-a)** **(2.16-b)**

where,

$$a = -\frac{x_j - x_i}{y_j - y_i}, \qquad b = \frac{y_i + y_j}{2} - a\frac{x_i + x_j}{2},$$

$$K_1 = -x_i - a\,y_i + x_n + a\,y_n,$$
$$K_2 = x_i^2 + (y_i - b)^2 - x_n^2 - (y_n - b)^2$$
$$K_3 = -2x_i - 2a\,(y_i - b) + 2x_n + 2a\,(y_n - b)$$

As mentioned above, this solution is achieved by minimizing the integral square error of the incremental area between the digital sub-segment and the circular arc. In Figure 2.18, the coordinates $\{(cx_{n-1}, cy_{n-1})\}$ and $\{(cx_n, cy_n)\}$ stand for the approximated position of $\{(x_{n-1}, y_{n-1})\}$ and $\{(x_n, y_n)\}$, respectively. Then the equation to minimize $ISE$ becomes:

$$ISE = \sum_{a_n = a_i}^{a_j} \left\{ \pi R^2 - \pi[(x_n - x_c)^2 + (y_n - y_c)^2] \right\}^2 \qquad \textbf{(2.17)}$$

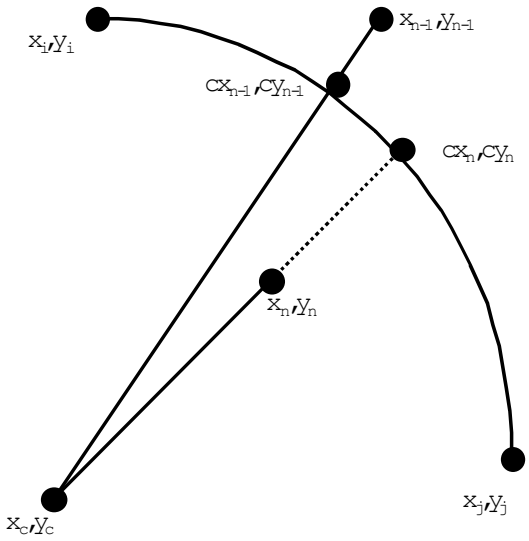


**Figure 2.18 –** Fitting of a circular arc to a set of points.

The radii calculation completes the required information to calculate Wadell's roundness for an object. Chapter 3 involves any modifications or constraints added to this procedure for particle shape roundness analysis.

#### 2.3.1.2 Particle Angularity

Particle angularity is a morphological property, i.e. it should be determined based on the geometrical shape of the particles. Despite much effort to develop a universal definition of particle angularity, no precise definition exists to date.

In this study, particle angularity is recognized as a separate shape parameter rather than the absence of roundness. Angularity is significant when a particle is in contact with a surface.

The shape parameters developed to measure particle angularity are compiled in Table 2.9. As the literature review in Table 2.9 clearly shows, very different definitions of angularity exist and yield parameters mostly unrelated to each other. The angularity has been expressed by several means; e.g. angle of corners, radii of curvature and corner tips, corner height and convexity/concavity of the corners (Mora and Kwan, 2000).

The motivation of the particle shape and morphology studies in tribology was mainly to study abrasive wear. As a hard mineral travels along a surface, due to the induced localized stresses and strains, surface removal occurs. Abrasion becomes significant especially when the number of interacting particles and loading conditions are increased. Although abrasive wear has been defined mathematically in terms of parameters; such as load, speed, particle size, particle and counterface hardness, etc., the influence of particle shape still has a limited definition. Particle shape has been quantified using e.g. roundness factor, aspect ratio, and kurtosis. Although they have proven to be good indicators of particle irregularity, they have failed to relate well to particle abrasivity and wear. Several studies have confirmed that the particle angularity is strongly related to abrasive wear rates through two- and three-body abrasive wear and erosive wear laboratory experiments. A particle shape analysis can be conducted by the visual inspection of a particle microscopy image; however, this technique is time-consuming, expensive and the results are operator-dependent. Thus, the qualitative methods, where mostly a scale based on visual observation is used as shown in Table 2.9, suffer from these disadvantages. Fractal methods have also been utilized in tribology (Kaye et

**Table 2.9 -** Angularity parameters (literature review).

| Angularity Parameter | DEFINITION | REMARKS | Reference |
|---|---|---|---|
| Angularity | (sum of angles subtended by the straight parts / 360°) | ▪ No instructions for the selection of the central point (inscribed or circumscribed circle center) | Fischer in Krumbein and Pettijohn, 1902 |
| Relative Angularity | 25.95 / (porosity of compacted sample) | ▪ Indirect method based on the minimum porosity of sand obtained by compacting compared to the theoretical minimum for spherical sand grains<br>▪ As the sand becomes less angular, the ratio gets closer to 1.0. | Indirect Method<br><br>Lamar, 1927 in Krumbein and Pettijohn, 1902 |
| Russel and Taylor Scale | Angular (0.00-0.15), subangular (0.15-0.30), subrounded (0.30-0.50), rounded (0.50-0.70), well rounded (0.70-1.00) | ▪ Range: 0 –1<br>▪ Used photographs of grain types to develop 5 grade terms based on visual comparison.<br>▪ Used Wadell's concept.<br>▪ Quick, no discrimination of higher roundness grades. | Visual<br><br>Russel and Taylor, 1937 in Yudhbir and Abedinzadech, 1991 |
| Pettijohn Scale | Angular (0.00-0.15),Subangular (0.15-0.25), Subrounded (0.25-0.40), Rounded (0.40-0.60), Well rounded (0.60-1.00) | ▪ Range: 0 –1.<br>▪ Modified Russel and Taylor using "geometric scale" and rounding off the class limits.<br>▪ Used silhouettes rather than photographs. | Visual<br><br>Pettijohn, 1949 in Yudhbir and Abedinzadech, 1991 |
| Power's Roundness Scale | Very angular (0.12-0.17), Angular (0.17-0.25), Subangular (0.25-0.35), Subrounded (0.35-0.49), Rounded (0.49-0.70), well Rounded (0.70-1.00) | ▪ Range: 0.12 - 1.00.<br>▪ Added another descriptive term to the two above.<br>▪ Ratio of upper limit to the lower limit is 0.7 for every group. | Visual<br><br>Powers, 1953 |
| Angularity Number, AN | $67-\frac{100M}{cG_a}$, c = water mass to fill the same volume, M = aggregate mass of standard volume | ▪ Range: 0 –12.<br>▪ Recommended by British Standards (BS 812 1975) for calculating the angularity of concrete aggregates.<br>▪ Based on packing.<br>▪ The formula is based on (% of voids – 33).<br>▪ The method calculates higher Angularity Number for a sphere than for a cube. | Indirect Method<br><br>Shergold, 1953 in Janoo, 1998 |
| Angularity Number, AN | $67-\frac{100M}{cG_a}$, c = water mass to fill the same volume, M = aggregate mass of standard volume | ▪ Same as above.<br>▪ Digital Image Processing was used.<br>▪ The AN obtained correlated well with the form and convexity factors that are related to packing, however, the argument is that this parameters are naturally related to packing density.<br>▪ Conclude that AN is not a sufficient parameter to convey the sharpness of the corners. | Mora and Kwan, 2001 |
| Degree of Angularity, A | $A_i = (180^\circ - a)\frac{x}{r}$, a = measured corner angle, r = maximum inscribed circle radius, x = distance of corner to the center | ▪ Total angularity is the sum of all the values for all corners measured in three mutually perpendicular planes.<br>▪ Accounts for both roundness of corners and how far they are (their location).<br>▪ Angularity increases when acuteness of corners and number of corners increase.<br>▪ Defines not only form because x/r increases with roundness of corners, so use x': dist to the corner where angle is measured (Barrett ,1980). | Lees, 1964 |

**Table 2.9 (continued).**

| | | | |
|---|---|---|---|
| Degree of Angularity, A (continued) | | ▪ This definition implies that angularity is not the absence of roundness, but rather a distinct concept (Verspui, 1996). | |
| Modified AN | $\eta = Cd^n$, C = shape factor (specific to a material), d = volume mean aggregate diameter (mm), n = -0.032 | ▪ Modification of AN to account for shape.<br>▪ Same procedure as AN, calculated % voids differently.<br>▪ When using AN, compare with a material of same size. | Indirect Method<br><br>Gupta, 1985 in Janoo, 1998 |
| Particle Angularity | $\frac{W}{L}$ and $\frac{P^2}{A}$<br>W = width, L = length, P = perimeter, A = area | ▪ Correlated the angularity parameters with erosion rates.<br>▪ Derived an exponent $m$ and $n$ for the first expression and second, respectively.<br>▪ $m$ and $n$ are functions of particle material<br>▪ However, these parameters reflect more irregularity than angularity (Palasamudram and Bahadur, 1997). | Bahadur and Badruddin 1990 in Palasamudram and Bahadur, 1997 |
| Roundness Index – image Analysis | $R = 0.14\exp(2.7 - 0.22T)$ | ▪ Distribution of average tangent counts can be used to classify soils based on angularity.<br>▪ T (tangent counts) is used to calculate R in Power's Roundness.<br>▪ Eliminates subjective visual classification.<br>▪ T = 4 represents a well-rounded grain.<br>▪ They do not take into account the actual shape of the protrusions | Image Analysis<br><br>Yudhbir and Abedinzadeh, 1991 |
| Coefficient of Angularity, E | E = Specific surface of particle/specific surface of equivalent spheres<br>$R = 0.14\exp(3.35 - 1.38E)$ | ▪ Range: 1.24 (R=1.0) – 2.54 (R=0.12).<br>▪ E increases with angularity, varies directly with T and inversely with R.<br>▪ Equal to one for perfectly spherical grain but is in practice less than 1.24. | Image Analysis<br><br>Yudhbir and Wood, 1989 in Yudhbir and Abedinzadeh, 1991 |
| Angularity – ASTM | | ▪ Angular: sharp edges, relatively plane sides with unpolished surfaces, Subangular: similar to angular with rounded edges. Subrounded:nearly plane sides but well-rounded corners and edges, Rounded: smooth curved sides and no edges. | Visual<br><br>ASTM D 2488-90, 1996 |
| Angularity | $S_i = 2\arcsin\left(\frac{\lambda_{ui} - \lambda_{xi}}{d_{uxi}}\right)$<br>$\lambda_{xi}$ = radius of inscribing circle at the end of bump "i" of stone "x"<br>$\lambda_{ui}$ = radius of the circumscribing circle a the base of the bump<br>$d_{uxi}$ = distance between the center of the base circle and the center of the end circle | ▪ Purpose: To correlate the form of penetrators used in geotextile perforation testing with those of coarse grains, so that the perforation tests can be valuable when a geomembrane perforation is prevented by a geotextile.<br>▪ Beta Law has been used to characterize "dangerous" and "average" stones | Antoine and Courard, 1996 |
| Angularity | $r(s) = (A_x s^2 + B_x s + C_x)i +$<br>$(A_y s^2 + B_y s + C_y)j$<br>$\kappa = \sqrt{(2A_x)^2 + (2A_y)^2}$ | ▪ Defined corner as a part of the contour with high curvature ($\kappa > level\ 1$)<br>▪ Applied Least Squares Fitting to filter pixel noise.<br>▪ Further improvements on reducing the pixel noise is suggested. | Verspui et al., 1996 |

**Table 2.9 (continued).**

| | | | |
|---|---|---|---|
| Angularity, $A_n$ | $A_n = K\sum_{i=1}^{n} a_i \cdot p_i$<br>$a_i = K / \alpha_i$<br>$p_i = (\pi - \alpha_i)/(2\pi)$<br>$\sum_{i=1}^{n} p_i = 1$<br>n = # of corners<br>$\alpha_i$ = angle of a corner<br>$K$ = constant | ▪ Simple analysis.<br>▪ Defined particle angularity as inversely proportional to the corner angle.<br>▪ Takes into account the probability of a corner contacting a target surface.<br>▪ Takes into account concave corners by using a modified formula.<br>▪ The $A_n$ values differed for different starting points. The highest value was considered as the angularity number.<br>▪ For constant size, the erosion rate increases with the obtained $A_n$. | Palasamudram and Bahadur, 1997 |
| Angularity Factor | AF | ▪ Range: 0 (sphere) –1 (most angular particle)<br>▪ Based on number and sharpness of corners.<br>▪ As it goes from ellipse to square to rectangle to rhombus to triangle, AF increases.<br>▪ Angularity of rectangle stays the same irrespective of the aspect ratio (because angles do not change). | Sukumaran and Ashmawy, 2001 |
| Angularity Index | $AI = \sum_{\theta=0}^{355} \frac{\lvert R_\theta - R_{EE\theta} \rvert}{R_{EE\theta}}$<br>where $R_{EE\theta}$ is the radius of an equivalent ellipse with the same aspect ratio | ▪ Normalizing the measurements with the aspect ratio in order to minimize the effect of form on angularity.<br>▪ No correlation between AI and aspect ratio. | Masad et al., 2001 |
| Angularity Ratio | $\theta = \tan^{-1}(\pi\lambda)$<br>$\lambda$ : slope of actual groove area vs. projected penetration area curve<br>$\theta$ :the angle of attack | ▪ Cone Fit Analysis is used; i.e. cones were fitted to the projected profiles.<br>▪ The actual and real particle study showed deviation from the cone analogy.<br>▪ Used linear regression to correlate the actual groove area and the projected penetration area. The slope (angularity ratio) was converted to the angle of attack, which was used as a measure of angularity.<br>▪ The angularity ratio correlated linearly with the wear rate for the tested real particles. | Pellegrin and Stachowiak, 2001 |
| Active Angularity Factor, AAF | Radon Transform | ▪ Parametric transformation of the boundary to develop the bounding curve of the image.<br>▪ Based on the concept that the bounding curve gives information regarding the convex hull of the shape and the abrasion participating corners along the boundary are those that generate associated maximum on the bounding curve in transform space.<br>▪ The sharpness of the corners is derived from as the average of the accumulated values around the maximum.<br>▪ The average value of all angularity factors developed for each protrusion individually give the overall AAF | Leavers, 2000 |

al., 1992; Vallejo, 1995; Orford & Whalley, 1983; Moore & Donaldson, 1995). One of the main problems with fractal methods is that a range of fractal dimensions can be obtained for a single Euclidean particle image when different starting points are used for the "structured-walk" (Kaye, 1989; Hamblin and Stachowiak, 1993). As discussed by Hamblin and Stachowiak (1993, 1995, 1997 and 1998) this problem is overcome by using all possible starting points for perimeter estimates and then averaging the results. This procedure is repeated for every step size. Stachowiak (1998) also suggests an exponential step size increase rather than arithmetic since the latter has been proven biased at larges steps. Although the fractal dimensions provide information regarding the complexity of the shape, they fail to convey the spatial arrangement of the boundary in space. For example, two corners may geometrically be similar in an image; however, one may contribute more to the abrasive wear process. This can be observed in Figure 2.19 for boundary points A and B. Obviously, point B does not participate in abrasive wear until the protrusions on both sides have worn out (Leavers, 2000). This should be accounted for in developing an angularity factor to relate to abrasive wear. This aspect is also overlooked in methods utilizing mathematical functions; such as Fourier Transform (e.g. by Swanson & Vetter, 1984; Ehrlich & Weinberg, 1970; Anstey & Delmet, 1973; Ehrlich et al., 1980; Piper, 1971).

It is vital in this analysis to locate protrusions that contribute to abrasion and parameterize the angularity of those protrusions. Also of equal importance is the fact that the particle outline should be analyzed in multi-scale, since no single-scale analysis can capture the multi-scale nature of the outline. Two such methods are those proposed by Leavers (2000) and Hamblin & Stachowiak (1995). The Active Angularity Factor (AAF) developed by Leavers (2000) is based on the Radon transform. A convex hull is

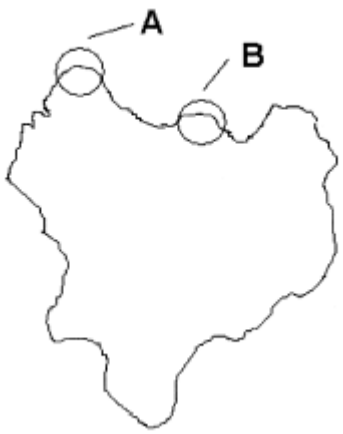


**Figure 2.19 -** Illustration of boundary features that participate in abrasive wear (after Leavers, 2000).

generated and only the boundary protrusions that support the convex hull are included in the measurement. The convex hull radius of curvature at those locations is combined to calculate the AAF. However, the method suffers from disregarding penetration during abrasive wear; i.e. a polygon and a star-shape with same number of sides will yield the same AAF, whereas the physical wear process for the two of them are noticeably different (Pellegrin and Stachowiak, 2002).

Shape and Angularity Factors by Sukumaran and Ashmawy (2001) were also selected for further analysis in this study. The parameters are further explained in the following sections. For particle angularity analysis, also Spike Parameter (SP) and Spike Parameter Quadratic (SPQ) are chosen and explored in detail. SP and SPQ parameters are developed by Hamblin and Stachowiak in 1995 and 1996, respectively. SP and SPQ represent particle angularity at the meso and macro scales, respectively.

#### 2.3.1.2.1 Sukumaran and Ashmawy Shape and Angularity Factors

A new technique to quantify particle shape and angularity was introduced by Sukumaran and Ashmawy (2001). The method utilizes 512x512 pixel 2D projection of the image magnified to a standard size by covering the whole image field. The obtained outline is processed as discussed below to obtain the Shape Factor (SF) and Angularity Factor (AF).

Shape factor quantifies the deviation of a particle outline from a circular outline. The calculation is performed as explained below:

1. The particle is divided into equal sampling intervals and the intersection points of these sampling radials with the particle outline are connected to form a polygon. In relation to Figure 2.20, point E is connected with point F and point F with point G, etc.
2. A larger circle centered at the polygon center is divided into sections using the same number of intervals and the intersection points of the circle outline with the sampling radials are connected with chords to form a second polygon. In relation to Figure 2.20, this refers to Point B connecting with Point C, C with D, etc.
3. The distortion angle for a sampling interval, $i$, is denoted as $\alpha_i$. For any sampling interval, the distortion angle is measured as the angle between the corresponding chords forming the polygons for the circle and particle. As a function of the particle chord vector relative to that of the circle, the distortion angle $\alpha_i$, may take positive or negative values.

4. The SF for the particle is obtained by the summation of the absolute value of the distortion angles for every interval. To normalize the parameter, the SF for a flat particle is used as a denominator. Sukumaran and Ashmawy (2001) quantify the SF for a flat particle as $N \times 45°$, where $N$ is the number of the sampling points.

Thus, the normalized SF is calculated as:

$$SF = \frac{\sum_{i=1}^{N} \left| \alpha_{i\ particle} \right|}{\sum_{i=1}^{N} \left| \alpha_{i\ flat\ particle} \right|} \times 100\% \qquad \textbf{(2.18)}$$

$$SF = \frac{\sum_{i=1}^{N} \left| \alpha_{i\ particle} \right|}{N \times 45^{\circ}} \times 100\% \qquad \textbf{(2.19)}$$

The upper and lower limit for the SF is zero and one, respectively. Evidently, a circular and a flat particle stand for the lower and upper limits, respectively.

The angularity factor (AF) calculation is based on the same methodology as the SF. AF is based on the number and sharpness of the corners. It requires the square of the summation of the differences between 180° and the internal angles of the particle, i.e. $\beta_i$ (angle EFG) in Figure 2.20. The difference is squared to amplify sharper corners. This summation is further processed by subtracting the same formulation for a circle. A cross-shaped particle with twelve 90° corners is used in the denominator to normalize the angularity factor as:

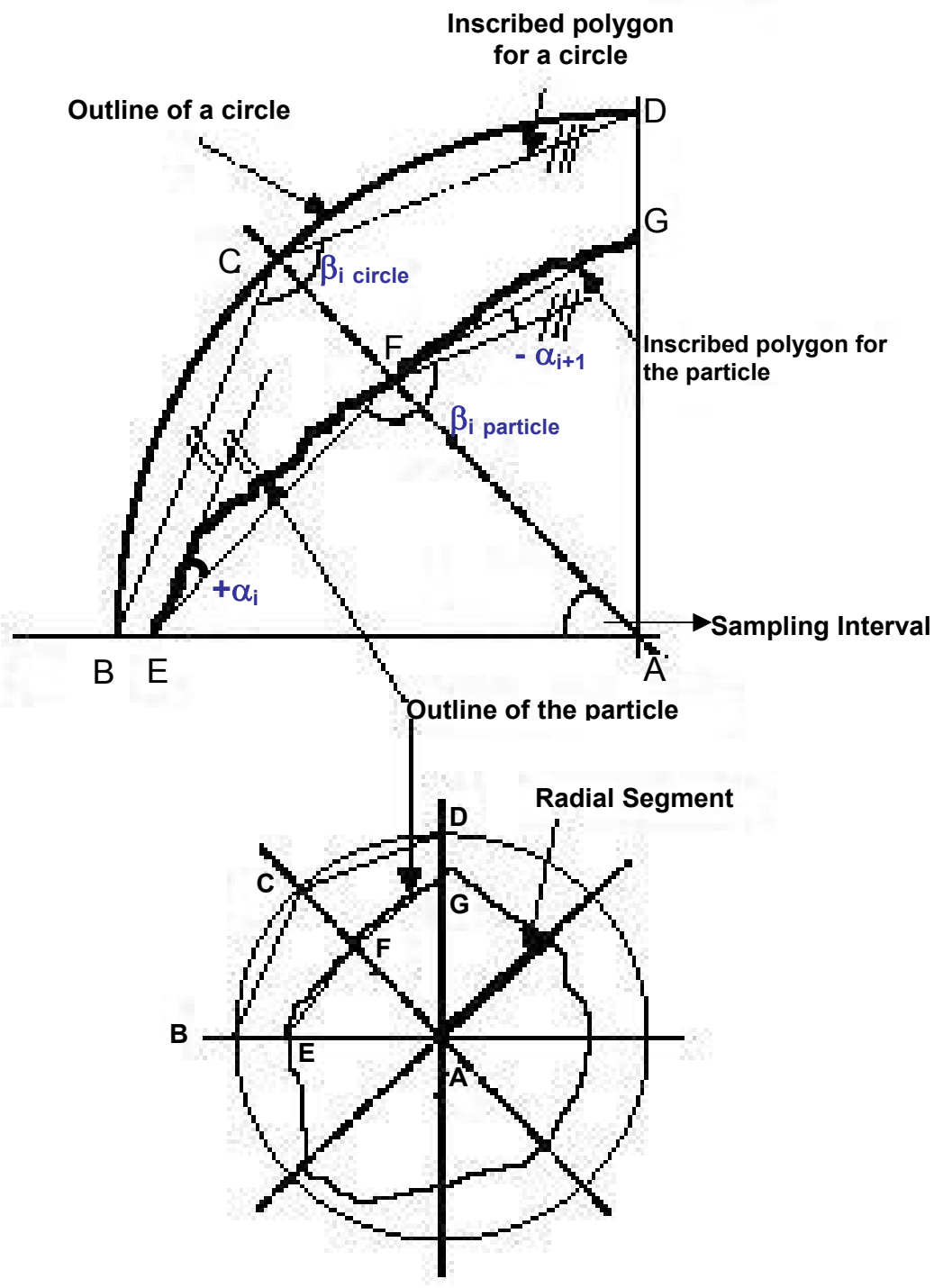


**Figure 2.20 –** Schematic drawing for Shape and Angularity Factor Calculation (adapted from Sukumaran and Ashmawy, 2001)

$$AF = \frac{\sum_{i=1}^{N}(\beta_{iparticle} - 180^{\circ})^2 - \sum_{i=1}^{N}(\beta_{i\,circle} - 180^{\circ})^2}{3\times(180^{\circ})^2 - \sum_{i=1}^{N}(\beta_{i\,circle} - 180^{\circ})^2}\times 100\% \qquad \textbf{(2.20)}$$

Correspondingly, since $\sum_{i=1}^{N}(\beta_{i\,circle} - 180^{\circ})^2$ is always equal to $(360^2 / N)$ (Sukumaran and Ashmawy, 2001), the normalized AF can be calculated as:

$$AF = \frac{\sum_{i=1}^{N}(\beta_{iparticle} - 180^{\circ})^2 - (360^2 / N)}{3\times(180^{\circ})^2 - (360^2 / N)}\times 100\% \qquad \textbf{(2.21)}$$

The lower limit for AF obviously represents a sphere. For the upper limit, the highest value of 100% was obtained for a four-point star shape (Sukumaran and Ashmawy, 2001).

In the proposed particle geometry analysis, Sukumaran and Ashmawy (2001) utilized $9^{\circ}$ intervals between sampling lines corresponding to $N = 40$. Based on pure judgment, this value was considered as a cut-off between angularity and particle roughness (Sukumaran and Ashmawy, 2001).

Several ideal, i.e. geometric, as well as real particles images were evaluated in the Sukumaran and Ashmawy (2001) study. Additionally, for the real particles, measurements of the large-strain angle of friction, pluviated, maximum, and minimum void ratios were performed. Detailed analysis is available in Sukumaran and Ashmawy (2001).

#### 2.3.1.2.2 Spike Parameter and Spike Parameter Quadratic

In Spike Parameter (SP) analysis, particle boundary, represented by 90° pixels, is "walked" similar to fractal analysis; however, a triangle is used as the step tool rather than a straight line. The step size is the number of pixels between the start and end points (pixels) of the triangle base, i.e. the start and end points are the two corners of the triangle. The third corner is chosen among the pixels between the start and end pixels. The triangle's sharpness and size is calculated for every pixel candidate between the start and the end points and the most appropriate one is chosen. The criterion for the third corner selection analysis is based on the assumption that particle abrasivity is directly related to the sharpness (measured by the apex angle) and the size (measured by the perpendicular height) of the triangle (Stachowiak, 1998).

The spike parameter calculation is as follows (Hamblin and Stachowiak, 1995):

1. Each step forms a triangle, the start point is arbitrarily chosen for a particular walk and each step's end point is determined by the step size (see Figure 2.21 and 2.22).
2. The midpoint (apex) is selected such that the product of the perpendicular height of the triangle and the $\cos(\frac{\theta}{2})$ term is maximum, where $\theta$ is the apex angle. This ensures the selection of the triangle based on both its sharpness and size. At every step, a triangle is selected and the corresponding spikiness value (sv), as $sv_{\max} = \max(\cos[\theta/2]h)$ is recorded. As the particle boundary is walked, these values are summed.

3. After the boundary is walked for one step size, the starting point is changed and the procedure is repeated for all possible starting points.
4. All of the above procedure is repeated for different step sizes.

The spike value is calculated as:

$$SP = \frac{\sum\left(\sum\left[\frac{sv_{\max}}{h_{\max}}\right]/m\right)}{n} \qquad \textbf{(2.22)}$$

where $sv_{\max} = \max(\cos[\theta/2]h)$ for a given step size, $h_{\max}$ = height at $sv_{\max}$; $m$ = number of valid sv's for a given step size; $n$ = number of different step sizes used.

As noted above the calculation of SP assumes that particle abrasivity is related to both the apex angle and the height of the triangle. Figure 2.22 shows an example of a calculation. For example if only triangles A and B were compared for a particular base,

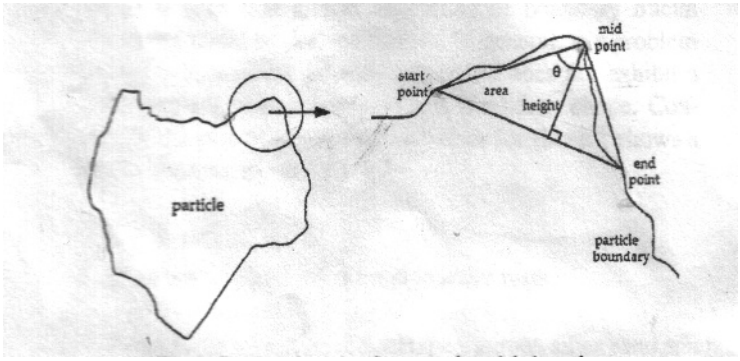


**Figure 2.21 -**Triangle construction along particle boundary (after Hamblin and Stachowiak, 1995).

although triangle B is higher than triangle A, the apex angle of triangle A is smaller. Triangle B would be chosen for that base due to its higher *sv* value compared to Triangle A.

The Spike Parameter (SP) has been calculated for a circle and five other artificial shapes generated by adding spikes to the base circle (Hamblin and Stachowiak, 1995). The shapes are shown in Figure 2.23 and the numbering starts from the upper left corner with the circle and ends at the lower right corner with the star shape. Shape one is the base circle, shape two has a small blunt spike added to it. Shape three has a bigger proportional triangle as shape two, shape four has the same base length as shape two but a smaller base angle, shape five has an enlarged version of the triangle on shape four and shape six has four of the same triangles in shape five. Along with the spike parameter, fractal dimension, the reciprocal of the shape factor and the aspect ratio have also been calculated. The normalized parameters are shown in Figure 2.24.

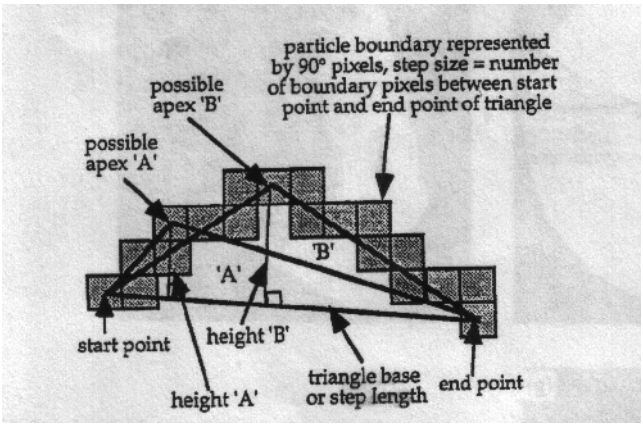


**Figure 2.22-** Comparison of triangle A and B for a particular triangle base (after Hamblin & Stachowiak, 1995).

The boundary fractal dimension has an inconsistent jump at shape four and the aspect ratios sensitivity to asymmetric shapes is apparent with the jump at shape five. On the other hand, the reciprocated shape factor is the same value for shape two and four as a sign of its inadequacy. Among the parameters, only the spike parameter has shown to be consistently increasing with intuitively increasing angularity/spikiness. Instinctively, one would expect shape six to have four times angularity than shape five. Based on the calculation, the spike parameter prior to normalization for shape six is four times the shape five.

One argument critical of the spike parameter may be that it is concentrated on the spikes (i.e. peaks) ignoring the valleys on the particle. However, this is realistic since the contact between the particle and any solid surface occurs through the spikes. Spike parameter can quantify Euclidean, non-ideal fractal and ideal fractal objects. It is relatively insensitive to image focus, while other parameters such as the boundary fractal dimension and shape factor have been found to change abruptly with image focus (Hamblin and Stachowiak, 1995).

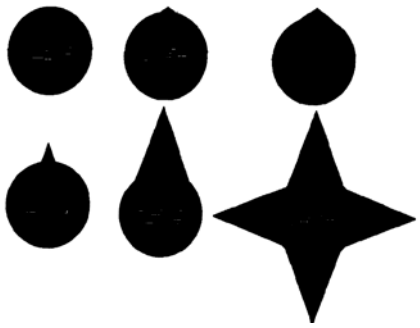

**Figure 2.23 -** Six artificial shapes (after Hamblin & Stachowiak, 1995).

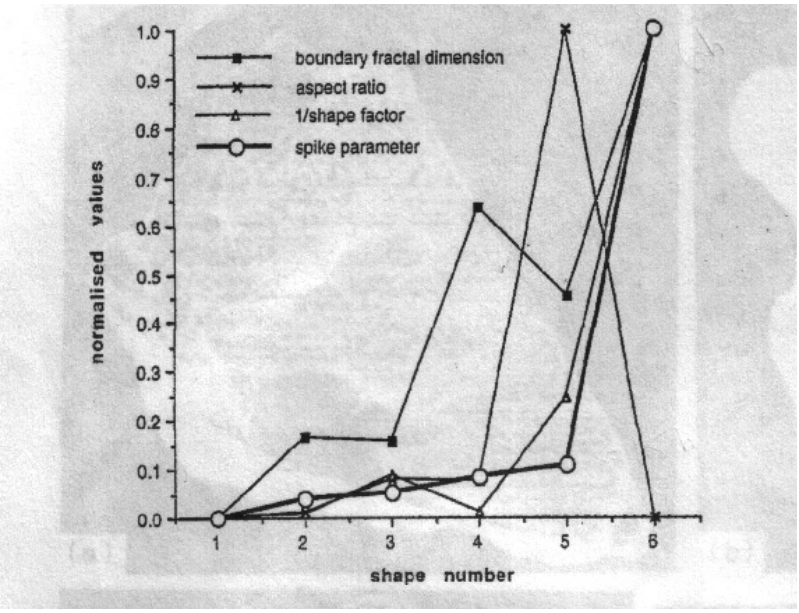


**Figure 2.24-** A plot of the artificial shapes vs. selected shape parameters (after Hamblin and Stachowiak, 1995).

Hamblin and Stachowiak (1995) showed that a small change in focus affected the shape factor by 20%, while the spike parameter decrease was only 5%. Boundary fractal dimension is also sensitive to image focus.

For small step sizes, the spike parameter can be sensitive to digitization errors resulting in high spike values for smooth shapes. This is accounted for within the analysis by ignoring triangles with an apex angle larger than 2.9 radians. This rule also deals with flat or concave regions by assigning no spike value. The spike parameter has also been observed to potentially account for some insignificant boundary features that may not have a big impact on particle wear in the calculations.

Studies to overcome these deficiencies have led to the development of a slightly better particle angularity parameter, *SPQ (*spike parameter, Q-quadratic fit) (Hamblin & Stachowiak, 1996). As noted earlier, this study will utilize SP as a particle angularity parameter for the meso scale, and the SPQ for the macro scale. The SPQ is different in concept that it only considers the parts of the boundary that are outside the least squares circle, termed as “spikes”. The portion inside the circle does not contribute to particle wear process. The particle boundary is represented by a quadratic fit rather than triangles (see Figure 2.25).

The calculation of the SPQ is given as (Hamblin and Stachowiak, 1996):

1. For each spike (particle regions outside the least square radius circle), the local maximum radius is found and this point determines the *spike apex* or the middle point of the spike.
2. The spike is represented by a start point (sp), a middle point (mp), and an end point (ep). The “sp” is where the particle boundary crosses the circle, the “mp” is located at the spike apex with the local maximum radius, and the “ep” is the other end to the particle boundary (see Figure 2.25).
3. The apex angle is calculated by fitting quadratic polynomials to the particle boundary between sp-mp and mp-ep and then differentiating both curves at the “mp” point. The polynomial fitting requires the rotation of axis so that lines sp-mp and mp-ep are collinear with the x-axis (see Figure 2.25).

The analysis performed with the SPQ has shown satisfying results. When compared

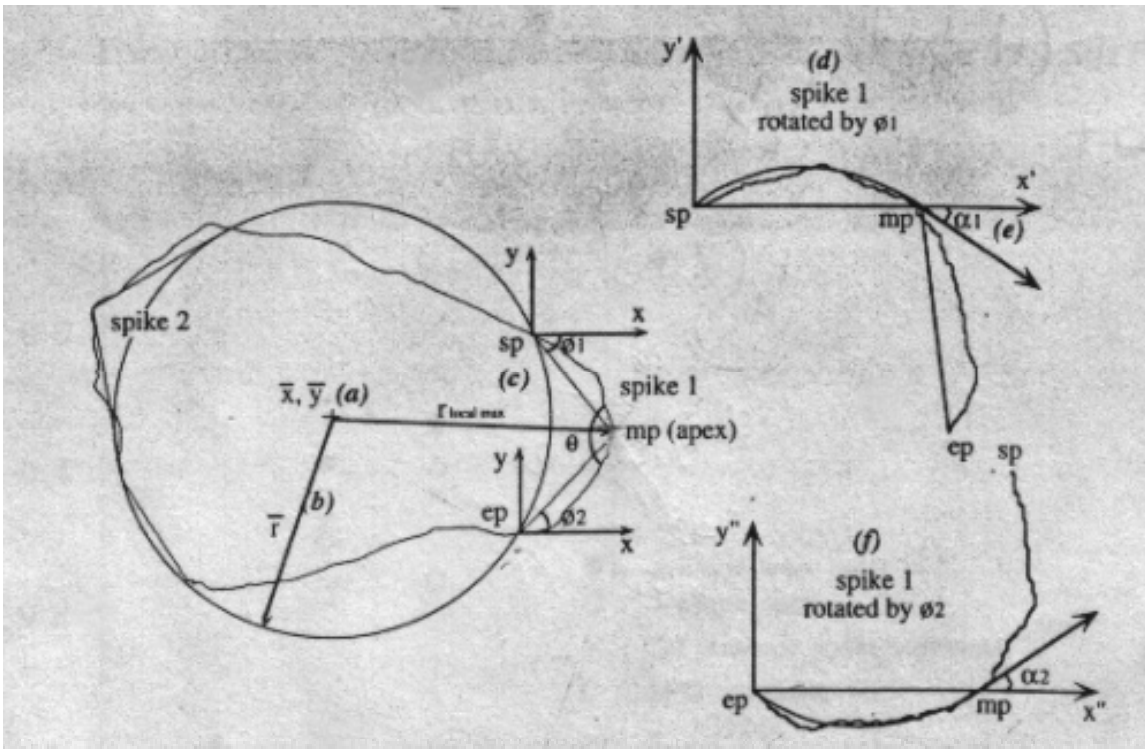


**Figure 2.25 -** Method of SPQ (spike parameter – quadratic) calculation (after Hamblin & Stachowiak, 1996)

with the original spike parameter (SP), SPQ is less sensitive to particle image flaws and the calculation only takes into account the boundary features that are likely to come to contact with the opposing surface. It does not take into account every triangle as in SP, thus the process time is considerably shorter. It is noted by Stachowiak (2000) that the SPQ can be used to model and predict abrasive and erosion rates, however, it may show some fluctuations when other processes, such as adhesion or pure erosion are involved.

In Stachowiak (2000), two- and three-body abrasive wear rates were performed with the same grits for SPQ. Randomly selected twenty particles were used from each group

after being sieved to achieve uniform size distribution. Further details of the analysis are provided in Stachowiak (2000). The only changing variable in the tests was particle angularity, and the results confirm that SPQ demonstrate almost a linear relationship with the abrasive wear rates.

It can be argued that the concept of average radius is not reliable to estimate the depth beyond which particle interior information for wear becomes negligible. In other words, the radius of the least square circle may or may not accurately predict the depth from where outwards spikes can be constructed. However, for the purposes of this research, the spike parameter is applied for an ideal system with a single particle traveling along a counterface, i.e. the complete system of particles, the physical properties (e.g. relative density, confinement, particle size distributions, etc.), the transferred loads, and the corresponding strains are neglected.

#### 2.3.1.3 Boyce and Clark Shape Index

In a completely different discipline, Boyce and Clark (1964) performed shape analysis on towns and cities in urban geography. The aim of the study was to be able to rank the cities based on their shape properties. The purpose for urban geography analysis by Boyce and Clark (1964) was to infer particular characteristics about cities; such as comparing the cities with specific geometric forms, hypothesizing that a circular-shape allows improvement of a central business district more than an elongated shape city, or that a hexagonal shape is best suited for a trading city, etc. For this purpose, Boyce and Clark (1964) developed the Shape *Index (SI),* where the distance from the shape's center of gravity to the outline is measured along equally spaced radials and each radial

percentage is subtracted from the percentages that each radial would have if shape were circular. The *SI* is calculated using:

$$SI = \sum_{1}^{N} \left| \left\{ \frac{r_i}{\sum_1^n r_i} * 100 - \frac{100}{n} \right\} \right| \qquad \textbf{(2.23)}$$

where $r$ stands for the radials extending from the center of gravity, and $n$ for the number of radials used. Observably, the *SI* for a circle is zero. Boyce and Clark (1964) in their analysis for geometrical shapes and selected metropolises used 16 radials, thus the $\frac{100}{n}$ term in the equation is used as *6.25.*

This parameter is different from the previously mentioned parameters for the reason that radial measurements along the outline have been considered. In addition to calculating the *SI,* Boyce and Clark (1964) suggest developing a *shape curve* for a solid shape, where the radial percentage numbers from *1* to *n* versus the percentage distance for each radial. For a circle, the *shape curve* plots a straight line, whereas for a square a sine curve with four nodes above and below the line is observed.

Boyce and Clark (1964) suggest using *16* radial intervals, corresponding to an angular spacing of *22.5°.*

#### 2.3.1.4 Particle Surface Roughness

Table 2.8 listed the shape parameters developed to represent the particle at the micro scale. The particle surface contains microrelief features, such as scratches and pits that contribute to surface roughness (also called surface texture). Although the relative contribution of surface texture on the overall particle shape may seem negligible, the effect depends on the process considered. Roughness has frequently been analyzed via Fourier or fractal analysis. The general methods utilized and brief remarks are included in Table 2.4. The advantages and disadvantages for both methods have been extensively reviewed.

#### 2.3.1.5 Additional Particle Shape Characterization Parameters

As mentioned throughout this chapter, there are abundant particle shape descriptors that have been introduced in the literature. Most of the shape parameters introduced in literature involve a measure of the particle size at some stage in the calculation process. Thus, since shape is a dimensionless property, the size measurements are combined to produce a dimensionless parameter. The need for shape parameter search rises due to the inadequacy of the already introduced ones. In most of the cases, a single shape parameter is not enough to uniquely define the outline since different outline shapes may have the same parameter values providing an unsatisfactory classification tool. Based on this approach, some authors have attempted to combine some shape parameter. Podczeck (1997) have introduced a shape factor, termed as *NS*, combining five shape parameters as shown in Table 2.10 with the corresponding descriptions. The size measures included in the shape parameters are:

$s$ …… Shortest Feret diameter.
$sp$ …….. Feret diameter perpendicular to $s$.
$P$ ……... Perimeter of the particle outline.
$l$ ……. Longest Feret diameter.

where Feret's diameter is defined as the distance between two tangents drawn on any opposite sides of the particle outline.

**Table 2.10 –** Five shape parameters used by Podczeck (1997) for *NS*.

| Parameter | Description |
|---|---|
| $H_1 = \frac{Area}{s\ x\ sp}$ | The deviation of the particle outline from a perfect *square* outline in terms of area. |
| $H_2 = \frac{Area}{(\pi/4)\ x\ sp^2}$ | The deviation of the particle outline from a *circular* outline in terms of area. |
| $H_3 = \frac{Area}{(s\ x\ sp)/2}$ | The deviation of the particle outline from a *triangle* outline in terms of area. |
| $H_4 = \frac{P}{l}$ | The *elongation* of the particle outline. |
| $Co$ | The number of *characteristic corners* attributed to the particle image. |

Based on the parameters shown in Table 2.10, *NS* is given by:

$$NS = Co + \det\begin{bmatrix} H_4 & H_1 \\ H_2 & H_3 \end{bmatrix} \quad \textbf{(2.24)}$$

Initially, Podczeck (1997) defined guidelines for classifying real particle images based on $NS$ based on geometrical outlines. Although *NS* is an improvement compared to conventionally used shape parameters, as Hentschel and Page (2003) later discuss, it

has some disadvantages. In the derivation of *NS*, six independent size measures are used increasing the possibility of obtaining same NS value for different shape outlines due to high degrees of freedom. The other disadvantage mentioned in Hentschel and Page (2003) is already discussed above. The new shape parameter *NS* is highly dependent on the number of outline corners since it is introduced as an additive term in the final Eq. 2.26. Characteristic corner determination is subjective and it results in user-dependency. Although Podczeck (1997) has suggested determining $Co$ either by visual inspection or by the number of turning points in the particle outline's waveform, no clear definition exists for the magnitude of deviation or the "sharpness" associated with the "corner" definition. It is important to note that NS is a measure of the macro-shape and does not contain any meso- or micro-scale feature information. In addition to the disadvantages noted by Hentschel and Page (2003), it is important to realize that $NS$ is dependent on single measurements of length, i.e. it does not introduce multiple estimations of length or width.

Another combination shape parameter is also introduced by Podczeck and Newton (1994,1995) in two- and three-dimensions for use in pharmaceutical studies. The two-dimensional definition is:

$$e_R = \frac{2\pi}{P}\frac{r_e}{f} - \sqrt{1-\left(\frac{b}{l}\right)^2} \qquad \textbf{(2.25)}$$

where $r_e$ is defined as the mean radius from 72 equal-angle (every 5°) radius measurements taken between the centroid and outline of the particle, $b$ and $l$ are the particle breadth and length, respectively and $f$ is a correction factor defined as:

$$f = 1.008 - 0.231\left(1 - \frac{b}{l}\right) \quad \textbf{(2.26)}$$

Based on Eq. 2.27, $e_R$ takes into account both the eccentricity and surface texture of the outline. Podczeck and Newton (1994) have performed analysis of the new shape parameter based on geometrical shapes. The results showed that, although a very commonly used parameter aspect ratio fails to distinguish between a circle and a square, $e_R$ values for circles of different dimensions (radii of 10mm, 7.5mm, 5mm, and 3mm) were in the range of (0.926-0.937) and for different size squares (side dimensions of 10mm, 7.5mm, 5mm, and 3mm) were in the range of (0.854-0.832). Note that an $e_R$ value less than 1 is observed for circles due to minor shape alterations occurred in image analysis. The limiting lower value for a circular image is selected as 0.9. Another example of the $e_R$ superiority over aspect ratio was proved by circle to different sized ellipse comparisons. For an ellipse with an almost negligible aspect ratio of 1.02, $e_R$ value is 0.797 far less than the accepted circle $e_R$ value. On the other hand, surface roughness simulations showed that $e_R$ is not as sensitive at surface roughness scale. For a 16% difference between the measured and calculated perimeters, $e_R$ reduced to 0.861 from 0.999.

Almeida-Prieto et al. (2004) have investigated the performance of $e_R$ with other parameters. For a study of geometrical shapes, the combined parameter $e_R$ failed to distinguish between different outline shapes with the same aspect ratio (length-to-breadth ratio) such as a perfect circular and a square outline. In addition, $e_R$ is highly dependent on the aspect ratio (Almeida-Prieto et al., 2004). An aspect ratio difference <0.2% resulted in the $e_R$ value change from 0.94 to 0.88.

Another recent study of parameter study is performed by Hentschel and Page (2003) in an effort to perceive number and type of particle shape parameters required to uniquely describe the particle outline using statistical methods. Combining 17 size measures, 136 dimensionless conventional shape parameters were identified in the form of:

$$S_{ij} = \frac{x_i}{x_j} \tag{2.27}$$

where $x_i$ and $x_j$ are two measures of particle size. The size parameters were initially standardized in order to prevent larger valued parameters dominating the smaller valued parameters. Using agglomerative hierarchical cluster analysis upon standardizing, 136 size parameters were reduced to five groups, from which five most important size measures were identified as the most correlated parameter within each group. Five size measures can be combined to ten dimensionless shape parameters. Authors have preferred to scale the shape parameters to yield a value of unity for a circular image. The shape parameters were calculated for six individual particle outlines (produced by commercial manufacturing methods) and the results were processed through a cluster analysis to obtain the redundant shape parameters. Finally, Hentschel and Page (2003) conclude that at least two shape parameters are required to distinguish the particles produced by commercial manufacturing methods. The two statistically important shape parameters were:

$$S_1 = \frac{b}{l} \qquad S_2 = \frac{2\sqrt{\pi A}}{P} \tag{2.28}$$

where as previously defined $b$ and $l$ are the minimum and maximum Feret diameters for all possible particle orientations, $A$ is the area and $P$ is the perimeter of the particle outline.

The more important outcome of this study is that a measure of particle elongation ( $S_1$ ) in addition to a measure of particle ruggedness ( $S_2$ ) is necessary to uniquely define a particle outline. The authors have proposed using both parameters separately rather than combining them to a single parameter.

### *2.3.2 Continuum Surface Roughness Analysis*

Any solid surface contains irregularities that range from shape deviations to irregularities in the order of interatomic distances. Surface texture refers to the locally limited deviations of a surface from the smooth ideal surface and is comprised of roughness (nano and micro), waviness, lay and flaws. Figure 2.26 shows the terminology used in describing surface topography (Bhushan, 1999). Waviness can also be identified as macroroughness and results from material variations. Roughness is the finer irregularities of surface texture that are intrinsic to the production process characterized by asperities (local maxima) and valleys (local minima). Lay is the principal direction of surface pattern and flaws are unintentional defects in the texture.

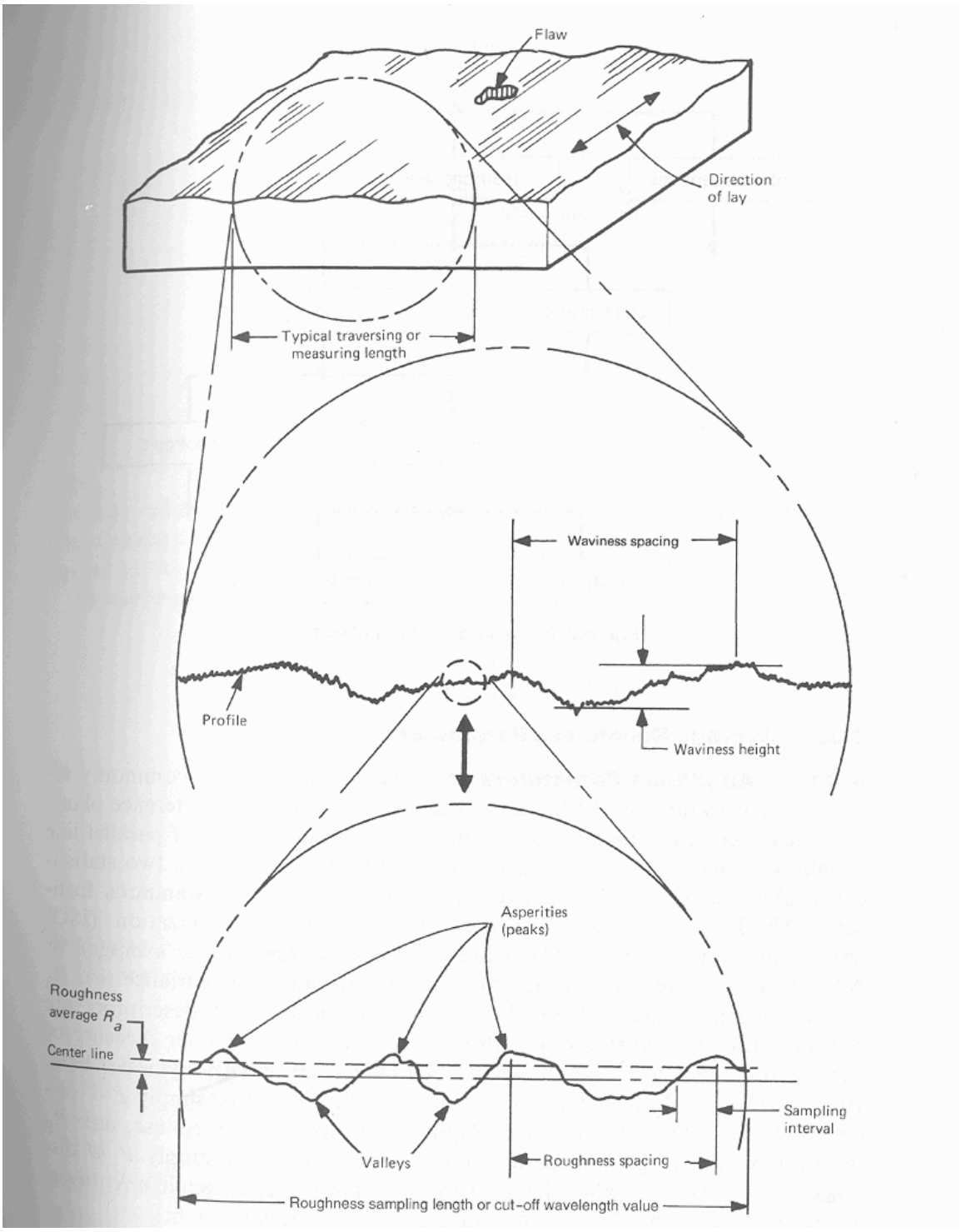


**Figure 2.26 –** Surface texture at different scales (Anonymous, 1985).

#### 2.3.2.1 Surface Roughness Parameters

Due to the complexity of surfaces, a single or a few parameters are not enough to provide ample information about the surface, which has led to the "parameter rash" as defined by Whitehouse (1982). In ISO 4287 – *Surface Roughness – Terminology – Part I: Surface and Its Parameters* standards, 27 amplitude parameters, 3 spacing, and 12 hybrid parameters are provided for the description of the unfiltered primary profile, the waviness profile, and the filtered roughness profile.

Generally used surface roughness parameters are given in Table 2.11. The statistical height descriptors define the average value of the behavior of a profile in a plane normal to the surface. Extreme-value height descriptors are functions of isolated events, and the texture descriptors describe the variation of the profile in the horizontal plane. Other categories include normalized and functional parameters.

The need for a better surface roughness parameter is evident by the number available in the literature and reported parameter variations as much as 50% for machined surfaces (Thomas and Charlton, 1981). Several factors are responsible for these variations depending on the definition of the parameter. All height descriptor parameters depend on the high-pass cut-off and generally increase with the square root of the cut-off value (Thomas, 1981). Although $R_a$, $R_q$, and the texture parameters are quite insensitive to range, the extreme-value parameters vary with range by a factor of three or more as the signal-to-noise ratio decreases (Thomas and Charlton, 1981). As the sampling interval decreases, the texture parameters are greatly affected and the mean of the extreme-value parameters is likely to increase. Among the texture parameters, the correlation

length is the most popular, however it is very sensitive to filtering and tedious to calculate (Thomas, 1981).

#### 2.3.2.1.1 Average Surface Roughness ($R_a$)

The average roughness, $R_a$, is the most widely used parameter and it is easy to calculate. It is also referred to as centerline average (CLA). It is defined as the average absolute deviation from the mean line over the surface length and its mathematical definition is as shown in Eq.2.29.

$$R_a = \frac{1}{L} \cdot \int_0^L |z| dx \tag{2.29}$$

It is a good indicator of height variation, however, it does not provide any information regarding the wavelength and it is insensitive to irregularities in the profile. As noted in Table 2.11, it is not a fundamental property, since it increases with the square root of the sampling length. Its lack of functional significance is obvious from the six obviously different profiles in Figure 2.27, all of which have the same $R_a$ value (Hamrock, 1994).

#### 2.3.2.1.2 Root Mean Square Roughness Parameter ($R_q$)

The $R_q$ parameter (also referred to as RMS) shows the standard deviation of the height distribution. It is the second most universally used parameter after $R_a$. Since it involves a square term, it is more sensitive to outliers in the surface profile than $R_a$. Its mathematical definition is given as:

**Table 2.11 –** Review of commonly used surface roughness parameters (adapted from Thomas, 1981).

| Surface Roughness Parameter | Definition | Remarks | Area and Reference |
|---|---|---|---|
| **STATISTICAL HEIGHT DESCRIPTORS** | | | |
| Average Roughness | $R_a = \frac{1}{L} \cdot \int_0^L \lvert z \rvert dx$ | ▪ Mostly used parameter<br>▪ Good description of height variation using vertical distribution<br>▪ Does not reveal irregularities<br>▪ Insensitive to wavelength, to small changes in profile geometry, and to occasional high peaks and deep valleys<br>▪ Not an intrinsic property (increases as the square root of the sampling length)<br>▪ Can vary from place to place on a calibration standard by several percent (usually <10%)<br>▪ The total area of the material-filled profile above the mean line should be equal to the total are of voids below the mean line | Stachowiak and Batchelor, 1993<br><br>ASME, 1995 |
| Root Mean Square (RMS) Roughness | $R_q = \left( \frac{1}{L} \cdot \int_0^L z(x)^2 \, dx \right)^{1/2}$ | ▪ Vertical distribution<br>▪ Shows the standard deviation of the height distribution<br>▪ Easy to use, widely used after $R_a$<br>▪ Similar disadvantages to $R_a$ | Stachowiak and Batchelor, 1993<br><br>ASME, 1995 |
| Skewness | $R_{sk} = \frac{1}{R_q^3} \cdot \frac{1}{L} \cdot \int_0^L \left( z(x) \right)^3 dx$ | ▪ Vertical distribution<br>▪ Third central moment of profile amplitude probability density function<br>▪ Easy to define<br>▪ Represents the degree of symmetry of a distribution<br>▪ A symmetrical height distribution has a value zero<br>▪ Profiles with peaks removed or deep scratches have negative skewness<br>▪ Used to characterize running-in[15-17] and to correlate drag coefficients of rough surfaces[18]<br>▪ Large scatter due to random sampling[8] | ASME, 1995 |
| Kurtosis | $R_{ku} = \frac{1}{R_q^4} \cdot \frac{1}{L} \cdot \int_0^L \left( z(x) \right)^4 dx$ | ▪ Vertical distribution<br>▪ Fourth central moment of profile amplitude density function<br>▪ Represents the peakedness of the distribution<br>▪ Used to characterize running in[15,17] and to correlate drag coefficients of rough surfaces[8]<br>▪ A Gaussian height distribution has a kurtosis of 3.<br>▪ If K<3, few high peaks and low valleys | ASME, 1995 |

**Table 2.11 (continued).**

| | | | |
|---|---|---|---|
| Kurtosis (continued) | | ▪ If K>3, relatively many high peaks and low valleys<br>▪ Large scatter due to random sampling[8] | |
| Depth of Surface Smoothness | $R_p = \frac{1}{L} \cdot \int_0^L (z_{\max} - z) dx$ | ▪ Vertical distribution | DIN 4762/1 |
| ***EXTREME VALUE HEIGHT DESCRIPTORS*** | | | |
| Ten-point height | $R_z = \left( \sum_{i=1}^{5} P_i - \sum_{i=1}^{5} V_i \right) / 5$ | ▪ Defines the mean separation of 5 highest peaks and 5 lowest valleys<br>▪ More sensitive to occasional high peaks or deep valleys than $R_a$<br>▪ Large scatter due to random sampling<br>▪ Depends on sampling interval[8]<br>▪ Lengthy to compute | Thomas, 1981<br><br>ISO 4287, 1984 |
| Maximum Peak to Valley Roughness – Unfiltered Profile | $P_t$ | ▪ Defines the vertical distance between two parallel straight lines enveloping the unfiltered profile within the evaluation length<br>▪ Same as what $R_{max}$ (for a filtered profile) is to an unfiltered profile | Sander, 1991 |
| Average peak-to-valley height | $R_z = \sum_{i=1}^{5} (P_i - V_i) / 5$ | ▪ Defines the separation of highest and lowest peak in a single sampling length, averaged over 5 sampling lengths<br>▪ Has similar advantages and disadvantages to ten-point height with less scatter and less dependence on sampling length | Thomas, 1981<br><br>DIN 4762, 1989 |
| Average roughness depth | $R_{3z} = \sum_{i=1}^{5} ({}_3P_i - {}_3V_i) / 5$ | ▪ Defines the separation of the 3rd highest peak and 3rd lowest valley in a single sampling length averaged over 5 lengths<br>▪ Has similar properties to ten-point height | Thomas, 1981 |
| Ten-point mean roughness | $R_z = P_3 - V_3$ | ▪ Defines the separation of the 3rd highest peak and 3rd lowest valley in a single sampling length<br>▪ Has similar properties to ten-point height | Thomas, 1981 |
| Maximum Peak to Valley Roughness - Filtered Profile | $R_{\max}$ | ▪ Defines the separation of the highest and lowest peaks in a single sampling length<br>▪ Sensitive indicator of high peaks or deep scratches<br>▪ Large scatter due to random sampling<br>▪ Vertical distribution | Stachowiak and Batchelor, 1993<br><br>ASME, 1995 |
| Allison System | GST | ▪ Step 1. Truncate the 10% highest peaks and lowest valleys<br>▪ Step 2. Position the peak and valley GST lines<br>▪ Step 3. Define the difference between them as roughness | (Hydell, 1967/8) in Thomas, 1999 |

**Table 2.11 (continued).**

| *TEXTURE DESCRIPTORS* | | | |
|---|---|---|---|
| High-spot count | $HSC$ | ▪ Defines the number of excursions above profile mean line per unit length<br>▪ Insensitive to short wavelengths<br>▪ Describes the number of high regions in a length of profile which is related to the number of high spots in a given area of a bearing surface | Thomas, 1981 |
| Mean high-spot spacing | $S_m$ | ▪ Defines the mean separation of excursions above profile mean line<br>▪ Has similar properties to HSC | Thomas, 1981 |
| Average Slope | $\Delta_a = \frac{1}{L} \cdot \int_0^L \left\| \frac{dz}{dx} \right\| dx$ | ▪ Vertical and horizontal distribution<br>▪ Applications: friction, elastic contact, plastic contact, reflectance, fatigue crack initiation, hydrodynamic drag, spalling and hydrodynamic spalling<br>▪ Depends on sampling interval[3] | ASME, 1995<br>Thomas, 1981 |
| Root Mean Square Slope | $\Delta_q = \left[ \frac{1}{L} \cdot \int_0^L \left( \frac{dz}{dx} \right)^2 dx \right]^{1/2}$ | ▪ Vertical and horizontal distribution | ASME, 1995 |
| Average Wavelength | $\lambda_a = 2 \cdot \pi \cdot \frac{R_a}{\tan(\Delta_a)}$ | ▪ Vertical and horizontal distribution<br>▪ Depends on sampling interval<br>▪ Has been suggested for quality control[27] | Thomas, 1982 |
| Root Mean Square Wavelength | $\lambda_q = 2 \cdot \pi \cdot \frac{R_q}{\tan(\Delta_q)}$ | ▪ Vertical and horizontal distribution | Thomas, 1982 |
| Mean peak radius of curvature | $C_p = \frac{d^2 z}{dx^2}$ | ▪ Defines the mean reciprocal curvature of all peaks in sampling length<br>▪ Strongly dependent on sampling interval[13]<br>▪ Applications: elastic contact[28], to characterize wear[29,30], an lip seal performance[31] | Thomas, 1981 |
| Correlation length | $\beta^* = 2.3\, a$ where $\rho(\tau) = \exp(-a\tau)$ | ▪ Defines the distance over which an exponential autocorrelation function decays to 10% of its initial value<br>▪ Highly sensitive to long wavelengths[9]<br>▪ Applications: to characterize anisotropy[32], and wear[33] | Thomas, 1981 |
| Density of extrema | $D_e$ | ▪ Defines the number of local maxima and minima per unit length of the profile | Thomas, 1981 |

**Table 2.11 (continued).**

| | | | |
|---|---|---|---|
| Density of extrema (continued) | | ▪ Together with high spot count it completely characterizes statistical surface topography[4]<br>▪ Dependent on sampling interval | |
| Bandwidth parameter | $\alpha = m_0 m_4 / m_2^2$ | ▪ A measure of the range of wavelengths present in a surface profile<br>▪ Used to characterize hydrodynamic drag[34]<br>▪ For certain spectra $\alpha$ is independent of bandwidth | Thomas, 1981 |
| Topothesy | $k = R_q^2 / \lambda_0$ where $R_q$ is measured at cut-off $\lambda_0$ | ▪ Characterizes completely the statistical topography of surfaces with this form of power spectrum independent of cut-off or sampling interval[7] | Thomas, 1981 |
| Average Spacing | S | ▪ Defines the mean local peak-to-peak spacing between asperities<br>▪ Horizontal distribution | Dove and Harpring, 1999 |
| ***NORMALIZED PARAMETERS*** | | | |
| Normalized Roughness Parameter | $R_n = \frac{R_{\max}(L = D_{50})}{D_{50}}$ | ▪ Vertical distribution<br>▪ Relative parameter<br>▪ See the text | Uesugi and Kishida, 1986b |
| Profile Roughness Parameter | $R = \exp\left[2.3(\varepsilon / \varepsilon_c)^{-\alpha}\right]$ where $\varepsilon$ is the length of the measuring yardstick, $\varepsilon_c$ is a parameter specific to a given surface, $\alpha$ is a parameter with a value of 2. | ▪ R is the contoured length between two surfaces normalized by the straight – line distance<br>▪ The nature of the equation is not explainable.<br>▪ In the upper limit, as $\varepsilon$ goes to infinity, R approaches 1.<br>▪ Valid for $\varepsilon$ ranging from 1 mm to 230 nm. | Ling, 1989 |
| Surface Roughness Parameter | $R_s = \frac{Actual\ surface\ area}{\Pr jected\ surface\ area}$ | ▪ Based on 3D characteristics of the profile<br>▪ Hard to measure | Underwood and Banerji, 1987a |
| Surface Roughness Parameter | $R_s = \overline{R_L \cdot \psi}$<br>$R_L = \frac{Actual\ \Pr ofile\ Length(L_0)}{\Pr ojected\ \Pr ofile\ Length(L)}$<br>$\psi(\phi_p) = \int_0^{\pi} [\sin\alpha + (\pi/2 - \alpha)\cos\alpha] f(\alpha, \phi_p) \cdot d\alpha$ | ▪ Based on the 3D characteristics of the profile<br>▪ Developed assumption free and statistically exact<br>▪ Accounts for surface asymmetry<br>▪ Is not affected by the direction of profiling | Gokhale and Underwood, 1990 |
| Fractal Dimension | | ▪ See the text | |
| ***FUNCTIONAL PARAMETERS*** | | | |
| Bearing ratio at the level of the mean line | $t_m$ | ▪ It is the sum of lengths of individual plateaux at the mean line normalized by the total assessment length<br>▪ May be useful in characterizing multiprocess surfaces<br>▪ $t_m$ when used along with the ratio, $R_a/R_q$ the law of surface roughness ordinate distribution | Gorlenko, 1981 |

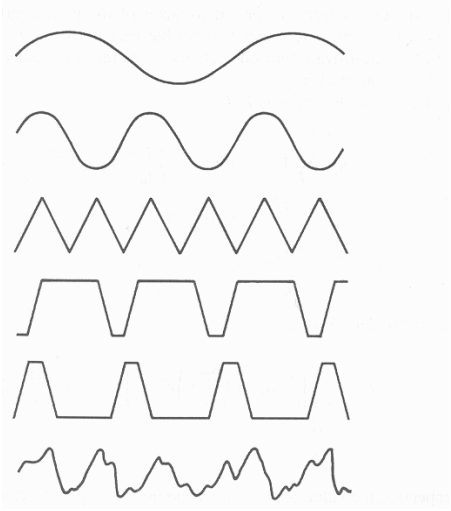

**Figure 2.27 –** Surfaces with identical Average Roughness ( $R_a$ ) values (after Hamrock, 1994).

$$R_q = \left( \frac{1}{L} \cdot \int_0^L z(x)^2 \, dx \right)^{1/2} \qquad \textbf{(2.30)}$$

The $R_q$ mean line divides the profile so that the sum of deviations of the profile heights above and below the mean line are equal to each other.

#### 2.3.2.1.3 Depth of Surface Smoothness ($R_p$)

$R_p$ is defined as the deviation of the height from the maximum height within the profile over the sampling length as shown in Eq. 2.31.

$$R_p = \frac{1}{L} \cdot \int_0^L (z_{\max} - z) dx \tag{2.31}$$

#### 2.3.2.1.4 Maximum Peak to Valley Roughness Parameter ($R_{max}$)

This parameter defines the vertical distance between the highest peak and lowest valley along the profile length. It is very sensitive to outliers in the data, e.g. high peaks or deep scratches. It is related to the vertical distribution of the profile, and again provides no information regarding the horizontal distribution.

$$R_{\max} = (R_{peak} - R_{valley}) \tag{2.32}$$

#### 2.3.2.1.5 Normalized Roughness Parameter ($R_n$)

A notable roughness parameter, normalized roughness parameter, $R_n$, was proposed by Uesugi and Kishida (1986b):

$$R_n = \frac{R_{\max}(L = D_{50})}{D_{50}} \tag{2.33}$$

where $R_{\max}$ is the absolute vertical distance between the highest peak and lowest valley over a length of the profile equal to the average particle size, $D_{50}$. This is one of the few relative parameters utilized in surface roughness analysis. However, although $R_n$ captures the relativity of the surface to particle, it is limited to sampling length of $D_{50}$.

#### 2.3.2.1.6 Spike Parameter Quadratic on Surface Profiles (SPQ-surf)

Similar to particle surface characterization, numerical characterization of continuum surface is also complex and remains mostly unresolved to date.

Problems with surface topography characterization include accurate representation of the anisotropy and directionality, the dependence of the height distribution on the sampling length. In order to characterize surface topography, scale-independent parameters are required.

An angularity measurement, similar to particle surface analysis, was developed by Hamblin & Stachowiak (1997). In abrasivity, the main interaction of the surface with the abrasive particle occurs at its peaks, i.e. at above–surface features; similar to particles contacting through their protrusions. In surface angularity analysis, the spikes above the mean line measured by, e.g. Talysurf, are deemed of interest. A quadratic function is fit from the left point (lf) to the right point (rp) of every spike, which is further differentiated at the spike apex yielding the apex angle, "$\theta$" (refer to Figure 2.28). Then, the SPQ fit is calculated using:

$$SPQ = \frac{1}{n}\sum_{n}\cos\left(\frac{\theta_t}{2}\right) \qquad \textbf{(2.34)}$$

where:

$n$ = # of spikes

$\theta_t$ = the apex angle of an individual spike

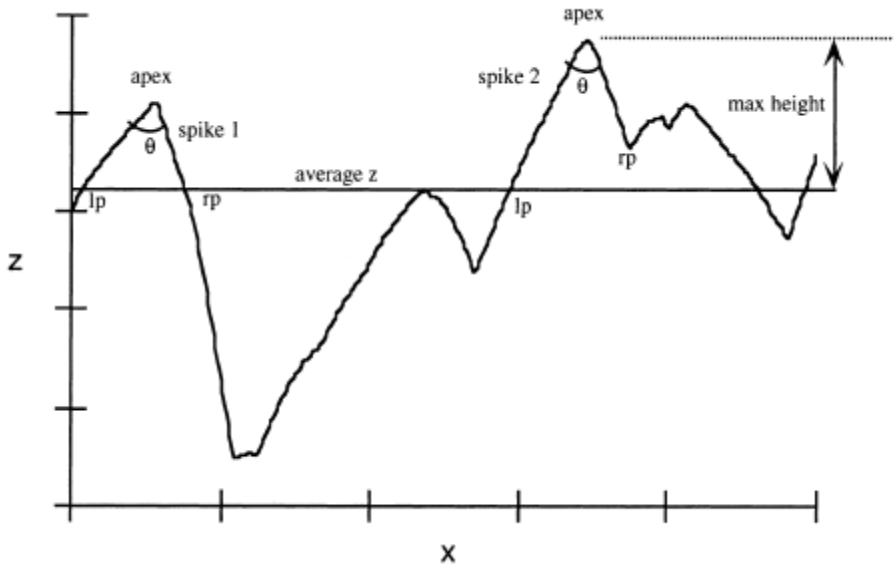


**Figure 2.28 -** Method of evaluating the SPQ from a surface profile (after Stachowiak, 1998).

Further analysis is required for the “little spikes”, i.e. turning points, on the apex. The turning points around the apex are considered as spikes only when the vertical amplitude of the turning point pair is greater than 10% of the apex height from the mean centerline. Otherwise, they are neglected. In addition, for purposes of fine-tuning, the spikes apex height less than 25% of the maximum spike height are not included in the final measurement.

#### 2.3.2.1.7 Additional Surface Roughness Calculation Schemes

*Fractal methods* have been widely used in surface roughness characterization (Majumdar & Bhushan, 1990; Ling, 1989; Vallejo & Zhou,1995; Hamblin & Stachowiak, 1995; Russ, 1994, Vandenberg & Osborne, 1992; Dubuc et al., 1989; Russ, 1992;

Majumdar & Tien, 1990). Fractal analysis captures the multiscale and random nature of the surface roughness profile and is scale-independent. Majumdar and Bhushan (1990) argue that given the surface processing technique is random and directionally unbiased within a range of length scales, the surface roughness can be characterized using fractal methods. Otherwise, the surface is non-fractal. Note that the spectra of surfaces (fractal or non-fractal) follow power laws. Based on this, Ling (1989) argued that the contour length is describable by an exponential law in the macro scale ( $R$ as shown in Table 2.11), while fractal law can be utilized at the micro scale.

The basic difference between particle boundary and surface profile is that the former attains a self-similar structure; whereas the latter is self-affine, i.e. the profile possesses different scales in horizontal (x) and vertical (y) directions.

Due to these structural differences, 1D Richardson plot is modified for surface profiles (Stachowiak, 1998). The details of the process are provided in Stachowiak (1998). One of the problems with fractal dimensional analysis is the noticeable effect of noise on the calculation. As the noise rises up to 10%, most of these techniques yield erroneous results (Stachowiak, 1998).

In relation to geotechnical engineering practice, Vallejo and Zhou (1995) quantified geomembrane surface roughness by fractal dimension and concluded that at least four-digit precision past the decimal point is required to differentiate between different geomembranes. They also proved that, the fractal dimension, $D$, is not a function of the profile direction.

With advances in technology and developments in digital techniques, there has been growing interest toward *3D analysis* and characterization of surfaces. In 2D analysis, a parameter derived from a single 2D analysis, implicitly agrees that the surface is isotropic and homogenous. Surfaces interact three-dimensionally and the information, in 3D is more robust and reliable. The time and cost associated with 3D analysis are obstacles for the present-day.

In general, to characterize three-dimensional surfaces, 2D surface roughness parameters (see Table 2.11) are extended to 3D; such as $R_a$, $R_q$, $R_z$, $R_t$, skewness, kurtosis, average, and RMS slopes. The "Birmingham set" of 14 parameters is generally acknowledged as a standard for 3D surface roughness parameter analysis. A three-dimensional surface roughness parameter, $R_S$, which is calculated as the ratio of the actual three-dimensional surface area to the projected surface area was proposed (Gokhale & Underwood,1990; Gokhale & Drury,1990). By implementing stereology theory, a relationship between $R_S$ and its two-dimensional equivalent $R_L$ (i.e. the ratio of the true length of the fracture profile to the apparent profile projected length) is derived. Although this relationship is assumption-free and $R_S$ sufficiently describes the 3D nature of the profile, computation is time-consuming and lacks dimensional and directional surface information.

#### 2.3.2.2 Kinematic Measures of Surface Roughness

So far, only static measures have been considered for roughness. Surface roughness has also been evaluated by means of kinematic measures, which are believed to be of

greater value for this study. Rather than quantifying the surface roughness by analyzing its 2D profile, kinematic measures consider a particle rolling over the profile taking into account the interaction between the particle and surface profile.

#### 2.3.2.2.1 E – System

The profile output from the stylus profilometer comprises errors of form, waviness, and roughness. The roughness is characterized by the shorter wavelengths superimposed on the longer wavelengths, which comprise the waviness. Thus, in order to obtain the roughness profile the longer wavelengths should be eliminated. A way of achieving this is by filtering, where the output profile can be expressed in reference to the longer wavelength profile.

There are two methods of obtaining a reference line by filtering; the mean line (M) system and the envelope (E) system.

In the more popular M-system, the mean line is defined such that the sum of squares of the deviation of the profile from the mean line is a minimum. The exact determination of this line is difficult, thus, it has become common practice to use filters instead; such as 2RC or Gaussian. Gaussian filters are preferred because; (i) the original profile can be reconstructed by adding the roughness and waviness components arithmetically, and (ii) the standard 2RC filter results in a profile phase distortion (ASME, 1995). Both are filtering techniques adapted from electrical engineering, where the surface profile is considered as sinusoidal, continuous, and stationary. None of these properties is necessarily valid for the geotechnical surfaces of interest; however, these filtering techniques are still widely used (Thomas, 1999). In Gaussian filters, the high-pass cutoff

wavelength is of importance and it represents the boundary when roughness is regarded as waviness.

E-system is based on rolling a circle of certain radius along the profile (von Weingraber, 1957). By taking into account every surface profile ordinate, the locus of the center of the circle approximates the shape of the profile and the envelope curve is obtained by shifting down the locus of the center of the circle by a distance equal to its radius. However, this procedure is quite lengthy. Simplifications have been proposed by Shunmugam and Radhakrishnan (1976) based on two approaches: (i) for a rolling circle of radius larger than 2.5 mm - only the prominent peaks of the profile are considered, and (ii) for a smaller radius - all peaks as well as flanks of the profile are taken into account. In the former approach, the profile is divided into a number of sections and a scanning method is used to find the prominent peaks in each section since the rolling circle touches the profile only at these points. Selected prominent peaks differ by using of a different scanning section width, which is best characterized by the predominant wavelength of the profile.

The terminology used for the E – system is given in Figure 2.29. The curve of form (Formprofil) is obtained from the locus of the larger circle, whereas the contacting envelope (Hüllprofil) is the trace of the smaller circle locus. The geometrical profile represents the design surface, excluding errors of form and surface roughness and the effective profile is the nearest instrumental approximation to the real profile, i.e. the measured profile. In scaling down from macro to micro; the errors of form, waviness and the primary texture (roughness) can be represented by the areas between these curves: (i) *errors of form* - by the area between the geometrical profile and the curve of form, (ii) *waviness* - by the area between curve of form and the contacting profile; and (iii)

*roughness* - by the area between the contacting and effective profiles. Mean line is defined by displacing the contacting profile downwards where it cuts the effective profile in such a way that the areas enclosed between that line and the effective profile are equal on both sides. After locating the E - mean line, the roughness parameters are calculated based on this mean line and the effective profile.

The selection of radius size is critical in the E-system. In acquiring roughness, it is important to have small enough radius, so that shorter wavelengths representing roughness are not skipped. In decreasing the radius size, the contact stress at the tip sets the lower limit. The circle diameters have been standardized to 25 mm and 250 mm for the curve of form and contacting profile, respectively (Radhakrishnan, 1972).

Obviously, the E-system is physically sound. However, it exhibits some disadvantages. On a visual display when the magnifications in the vertical and horizontal directions for

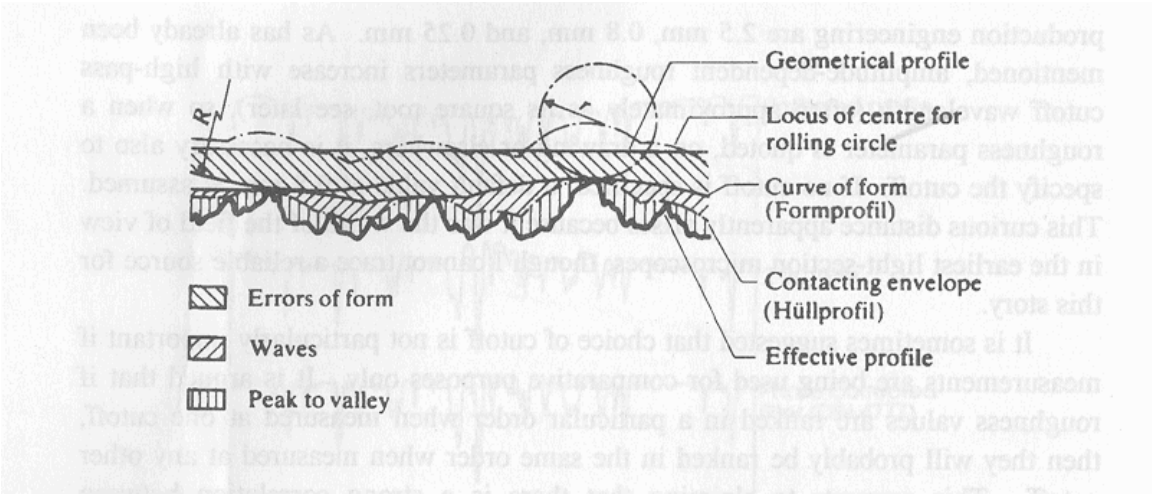


**Figure 2.29 –** Terminology of the Envelope System (after von Weingraber, 1972).

the surface profile are different, the rolling circle becomes a rolling ellipse. In order to adjust this distortion, arcs of circle needs to be replaced by arcs of ellipses or with circles of radius, $R_a$:

$$R_a = r_e \cdot V_x^2 / V_y \quad \textbf{(2.35)}$$

where $r_e$ is the initial radius, $V_x$ and $V_y$ are magnifications in –x and –y, respectively (von Weingraber, 1957). Another disadvantage of the E-mean line is that the line is mathematically discontinuous, and continuous mean lines can be obtained by the M – system.

Shunmugam and Radhakrishnan (1976) analyzed the reference lines for the surface profile itself and its true replica using both M- and E-systems, where the replica surface is defined as the mirror image of the actual surface. For highly random surfaces or surfaces with deep scratches rather than high peaks and different valley and peak spacings, E-system reference lines are different for the actual and replica surfaces. Thus, for replica work, the mean line obtained using the M-system is preferred.

The E-system was employed in order to analyze the effect of stylus radius on the surface profile (Radhakrishnan, 1980). In his study, as the stylus radius is increased the minute irregularities in the profile became less pronounced in the measured profile and when the radius was large enough to touch only the peaks the measured profile consisted only of circular arcs. The study also included variations in some roughness values as a function of the stylus radius. The variations depended on the specific parameter and the nature of the profile. For example; for high, narrow peaks and flat

valleys, $R_a$ increased for minor changes in the radius size. This is expected since peaks get wider although the valleys do not change as much with increasing radius and also the absolute mean slope of the profile decreases.

With more advanced computer systems available today, attempts have been made to bring back the envelope system approach. Studies have been conducted to develop a computational method for three-dimensional characterization of surface roughness using the E-system (Tholath & Radhakrishnan, 1999).

#### 2.3.2.2.2 Motif System

Motif system – an alternative envelope system - has evolved from the French automotive industry based on purely graphical methods. It is a pattern recognition scheme and can be utilized as a sampling method as well as for surface filtering. The scheme is based on expertise of French automotive industry and it has been at the French norm since 1972. In relation to engineering surfaces, it was first proposed by Fahl (1982).

A "motif" is the part of a profile between two peaks and is characterized by two depths, $H_1$ and $H_2$ (see Figure 2.30). $R_i$ is the mean depth, and $AR_i$ is the width of the motif. The smaller of $H_1$ and $H_2$ is the characteristic depth, $T_i$. The Motif analysis involves checking whether two adjacent motifs are both significant for the application so that they should be treated individually or whether one is insignificant with respect to the other such that they should be combined. In performing this analysis, the following procedure is defined (Fahl, 1982):

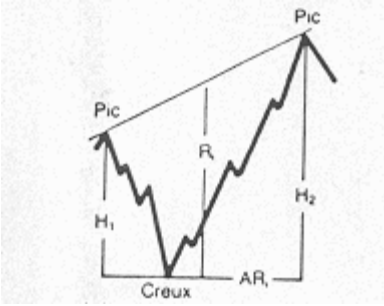


**Figure 2.30 –** The definition of a Motif (after Fahl, 1982).

1. Identify all the peaks.
2. Identify motifs (two adjacent peaks with the lowest valley in between).
3. Combine motifs if all of the following rules are satisfied:
    a. *Envelope Condition*: The common peak must be shorter than any of the adjacent peaks. This condition prevents eliminating any peaks that may span over an envelope line.
    b. *Width Condition*: Width of the combined motif should be less than or equal to 500 μm. For waviness profile calculation 2500 μm width is used.
    c. *Magnification Condition*: Characteristic depth of the combined motif should be equal to or greater than the larger of the characteristic depth of the two motifs. This condition serves to the elimination of small local peaks (Dietzsch et al., 1998).
    d. *Relationship Condition*: Smaller of the characteristic depths should be less than 60% of the local reference depth in order to prevent combination of adjacent motifs that are similar in size. The local reference depths is defined in two ways: (i) largest depth found in any

section that is 500 μm wide, termed also as local depth reference, (ii) characteristic depth of the combined motif.

4. Check every new motif formed with its neighboring ones until no further combinations in any section is possible. The final profile is the roughness profile.
5. Join the peaks to determine the upper envelope.
6. Use the same procedure starting from the beginning for the waviness profile but work on the upper envelope rather than the actual surface profile. When no further combination is possible, the waviness parameters are calculated.
7. Combine the peaks of the waviness profile to obtain the form profile.
8. The roughness, $R$ is calculated as the mean value of depths and $AR$ is as the mean value of widths from the roughness profile. Similarly, the mean value of depths in waviness profile is $W$, and the average width is $AW$.

As mentioned above, the Motif system can be used as both a filter and a sampling method. In filtering systems, confusion remains as to when waviness becomes roughness. The advantage of the Motif system as a filter is that it uses the actual block widths as sampling lengths, where each block starts at a peak and ends at the next peak, thereby capturing the local roughness (Fahl, 1982). Furthermore, there is no phase distortion and the direction of the analysis does not alter the result.

A triangular pattern can be obtained if the peak and valley ordinates identified during motif combination are combined with straight lines. This profile may be used as a substitute profile for the original profile for some applications and also the difference between the two profiles can be quantified for analysis by means of the mean number of valleys per motif and the amplitude distribution curve (Fahl, 1982).

Motif analysis only suggests two amplitude and one spacing parameter for roughness and three amplitude parameters and one spacing parameter for waviness; whereas 42 parameters are defined in ISO 4287 (1996) for the M-system. It is possible to reconstruct the typical surface profile with the parameters calculated and the additional information of the standard deviation for the mean values of R, AR, W, and AW (Dietzsch et al., 1998). The Motif analysis gives more importance to peaks and this is an advantage in most applications, e.g. rolling, sealing, electrical contact, etc. where the functional behavior is dependent on the contact with the peak features of the profile. Furthermore, unlike the M-system, where most parameters are related to the vertical distribution of the profile, the Motif system accounts for both vertical and horizontal features.

In Motif analysis, although a small indentation at the peak is taken into account, a large indentation at the bottom of a valley may be missed. This may present a problem depending on the dominant process being considered. The width condition mentioned above sets an arbitrary limit to the analysis. Fahl (1982) recommends adjusting the width condition by taking the characteristic horizontal length of the roughness instead.

Scott (1992) has worked on developing mathematical theory of Motif and motif combination and presented the properties required to have a unique and stable solution.

#### 2.3.2.2.3 Centroid Trace Method

The Envelope system has been discussed above. A similar concept has been adopted by DeJong (2001), which led to the development of the *Centroid Trace Method*.

As discussed above, the shearing behavior at particulate-continuum interfaces depend strongly on continuum surface roughness. However, in interpreting and quantifying interface strength, the roughness the particle experiences as it traverses the surface is a more relevant and accurate quantity for the interface strength than the roughness of the surface alone (DeJong et al., 2000). This phenomenon has been established by comparing the centroid traces of two spherical particles with diameters of 1.0 mm and 20.0 m going over a theoretical surface as shown in Figure 2.31. The surface contains a peak and a valley having slopes of +/- 45º, a plateau 1.0-mm wide at a height +/- 1.0 mm from the mean line. The centroid trace profile for the 1.0-mm diameter particle is slightly different from the actual profile of the surface particularly at the corners of the peak and valley. However, for the 20.0-mm diameter particle profile the valley has almost diminished; whereas the width of the peak has increased and it is still at a height of 1.0 mm from the horizontal portion of the profile. Thus, regardless of the actual surface roughness the 1.0-mm and the 20.0-mm particles experienced the surface in a different way. By performing the same analysis for several particles within this range, it was clearly shown that as the particle diameter increases the valley feature diminishes to only a minor deviation in the Centroid trace; whereas the peak base width significantly increases (3.0 mm for the theoretical profile to 9.7 mm for the 20.0 mm contacting particle) maintaining a constant peak height. This clearly shows that particles experience valley and peak features differently and the particle acts as a low pass filter removing features that are insignificant with respect to its size. The recognition that whether features extend above or below the mean line is important has led to the development of the Centroid Trace Method in an attempt to capture the relative nature of interface shear.

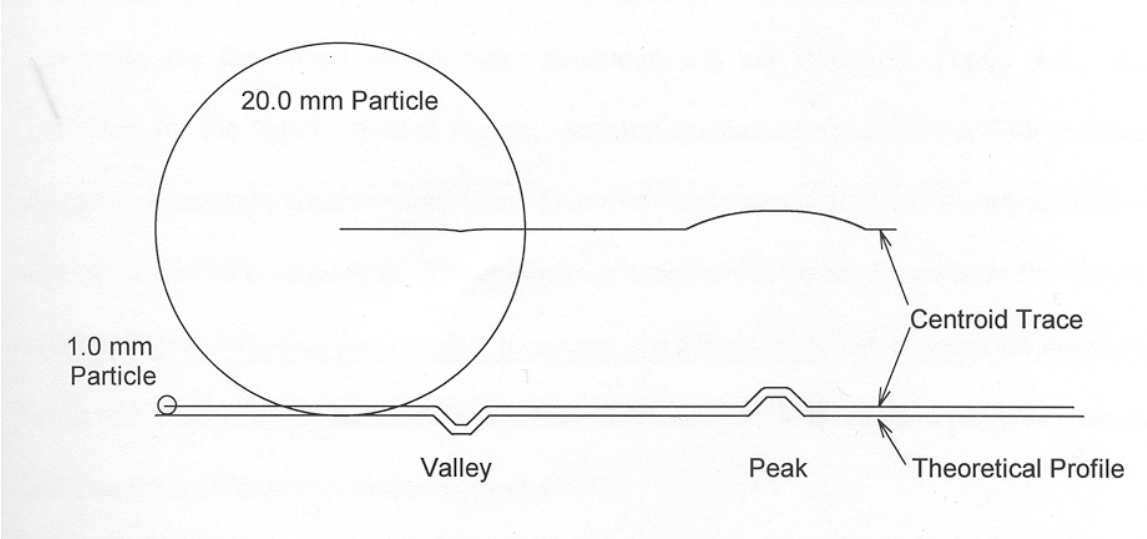


**Figure 2.31 –** Theoretical profile and Centroid Traces for 1.0 and 20.0 mm diameter particles (after DeJong, 2001).

Conventionally, high and low pass filters have been used in practice to achieve a degree of relativeness (by removing components of a surface that are of secondary importance to the mechanism governing the magnitude of interface friction). As part of the analysis, the study also included Gaussian low pass filter profiles (with the threshold wavelength corresponding to fifty percent passing) and simple low pass filter profiles (by removing the wavelengths smaller than the threshold wavelength via fast Fourier transform) for different particle sizes (DeJong, 2001).

Various roughness parameters were calculated for three different profiles (centroid trace profile, Gaussian profile, and low-pass filter profile), including average roughness, $R_a$, root mean square roughness, $R_q$, skewness, $R_{sk}$, normalized roughness parameter, $R_n$, etc. In the M-system, only one of the many parameters, $R_n$, accounts for the property of the contacting particulate media while the rest are related to mostly vertical

topographic surface properties. For additional detail, the reader is referred to the original study (DeJong, 2001). A clear conclusion drawn by comparing the variation of the parameters with particle size is that conventional roughness parameters do not realistically account for the relative aspect of surface roughness. For example, the average roughness, $R_a$, increased by 140% for the 20.0-mm diameter Centroid trace; while a decrease in relative roughness is expected with an increase in particle size.

The Gaussian and simple low pass filter profiles had similar roughness parameters and trends with respect to particle size. This trend was remarkably different from the trend observed for the Centroid trace since the Centroid trace method differentiates between peaks and valleys; whereas filters accounts for the features equally regardless of whether they are above or below the mean line. Considering that a larger particle will magnify the size of a peak but diminish the size of a valley on the surface, the filters' inadequacy in quantifying the relative roughness is easily perceived.

Besides the ideal surface the same analysis was performed for HDPE medium textured geomembrane, tooled steel and rough finished concrete with similar conclusions.
As explained above the Centroid Trace Method is basically the same concept as the E-system. Note that conclusions from the E-system were similar to the findings of the Centroid Trace Method. However, the E-system is developed to locate the mean reference line for the calculation of the conventionally used roughness parameters derived for the M-system. Thus, having determined the E-mean line the procedure for the calculation of the roughness parameters is the same as the conventional methods. On the other hand, with the Centroid Trace Method the traces of the Centroid are used as the roughness profile itself.

## 2.4 Concluding Commentary

For particulate-continuum interfaces, rather than analyzing the particulate and continuum media separately, it is important to coalesce the analysis and realize the relative nature of interface behavior. As outlined within Chapter 2, the interface behavior can be better comprehended if analyzed in terms of the effect of relative material hardness, dimensions, and roughness parameters. Several examples from the literature have been included above.

Chapter 2 emphasized more on the significance of the effect of relative material roughness. However, it is argued that the relative nature of material hardness and dimensions should also be investigated further. For particle surface roughness analysis, it is important to recognize the different effects of the macro-, meso-, and micro- scale shape characteristics. For this purpose, different measuring techniques from diverse fields of study have been integrated into this study. For continuum surface roughness analysis, kinematic measures of roughness have been highlighted due to their emphasis on the relative nature of interfaces.

The findings of DeJong (2001) initiated the urge to further research the measurement of relative roughness at particulate-solid interfaces. Clearly, relative roughness is a key property in evaluating performance of soil to engineering surface interaction. Its proper identification would lead to a better understanding of micro-scale interaction mechanism and better quantification of macro-scale mobilized resistance for soil and engineering surface interaction. It is obvious that conventional parameters and filtering procedures are not sufficient for this purpose. There is a need for a dimensionless roughness

parameter that accounts for several independent factors that affect interface strength. The analysis consisted of a simple theoretical surface and a 2D perfectly circular particle. The influence of particle shape, angularity, grain size distribution, and particle clogging are among the factors that should be further investigated (DeJong, 2001).

Diverse techniques have been used for particle and surface roughness analysis; however, if relative nature is to be quantified it is necessary to examine the particulate and continuum media by means of the same powerful tools. This is the motivation for the rest of this study and succeeding chapters will concentrate more on the qualitative analysis of this value.

# CHAPTER 3

# STUDY MATERIALS AND ANALYSIS METHODS

This chapter provides an overview of the particles and surfaces used in this study along with the details of the selected particle shape and surface roughness parameters. A broad algorithm for the analysis methodology is provided in Figure 3.1 and all the steps for the algorithm are explained in the subsequent sections. An extensive table of all the mathgrams developed and utilized is provided in Appendix A.

## 3.1 Overview of Study Particles and Surfaces

### *3.1.1 Real Particles and Surfaces*

A thorough analysis on particle shape requires processing and evaluation of real particles as well as the idealized particles. The same is valid for surface profile analysis. Although the idealized particle analysis may give insight for the bounds of the analysis, they do not necessarily provide relevant information for practical cases.

The *real particles* used for the analysis are as shown in Figure 3.2. In this analysis, four different particles are evaluated. The mineralogical and relevant geotechnical properties for each particle are shown in Table 3.1. Table 3.2 demonstrates the initial

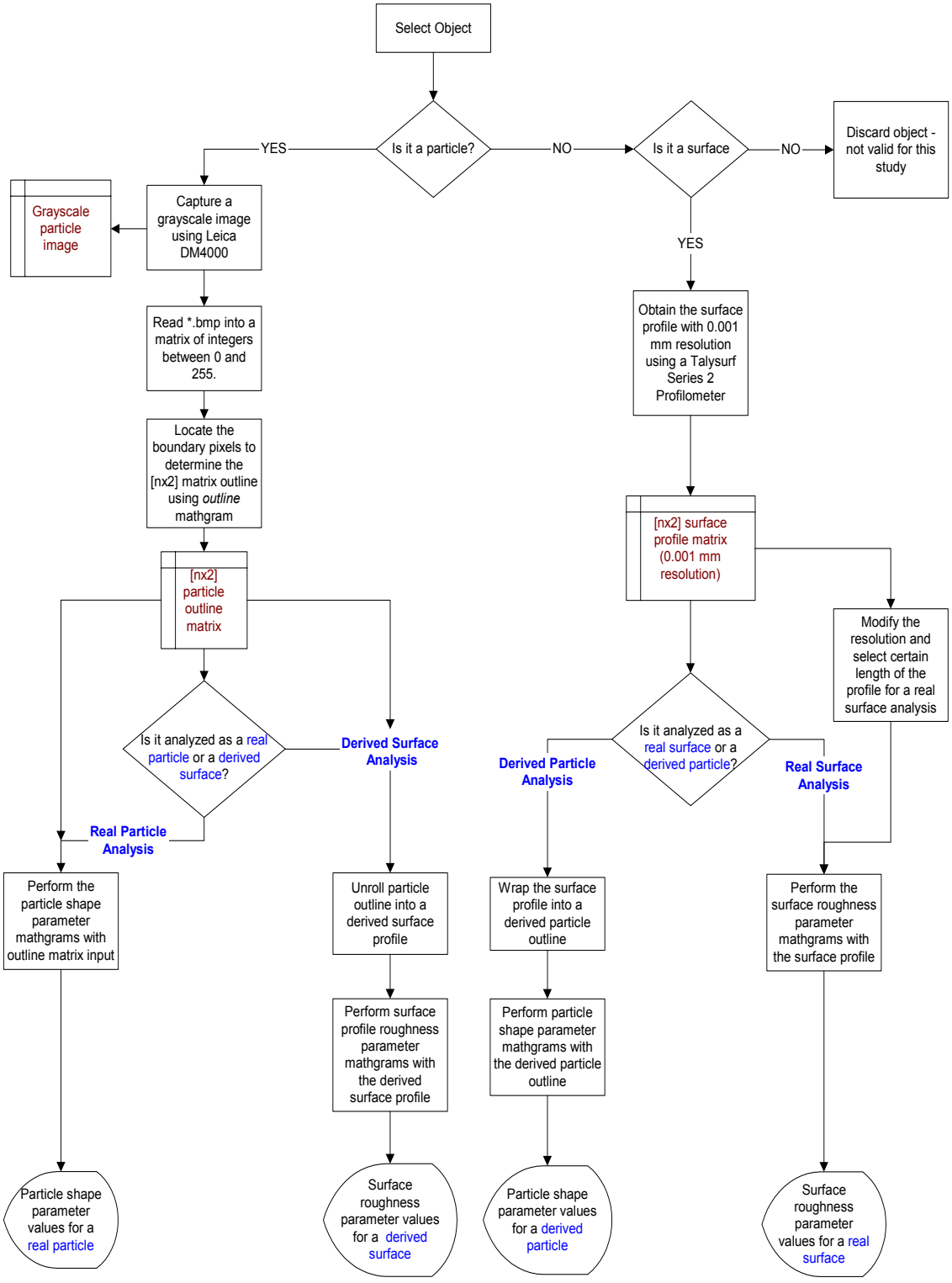


**Figure 3.1 –** The general algorithm for the analysis methodology.

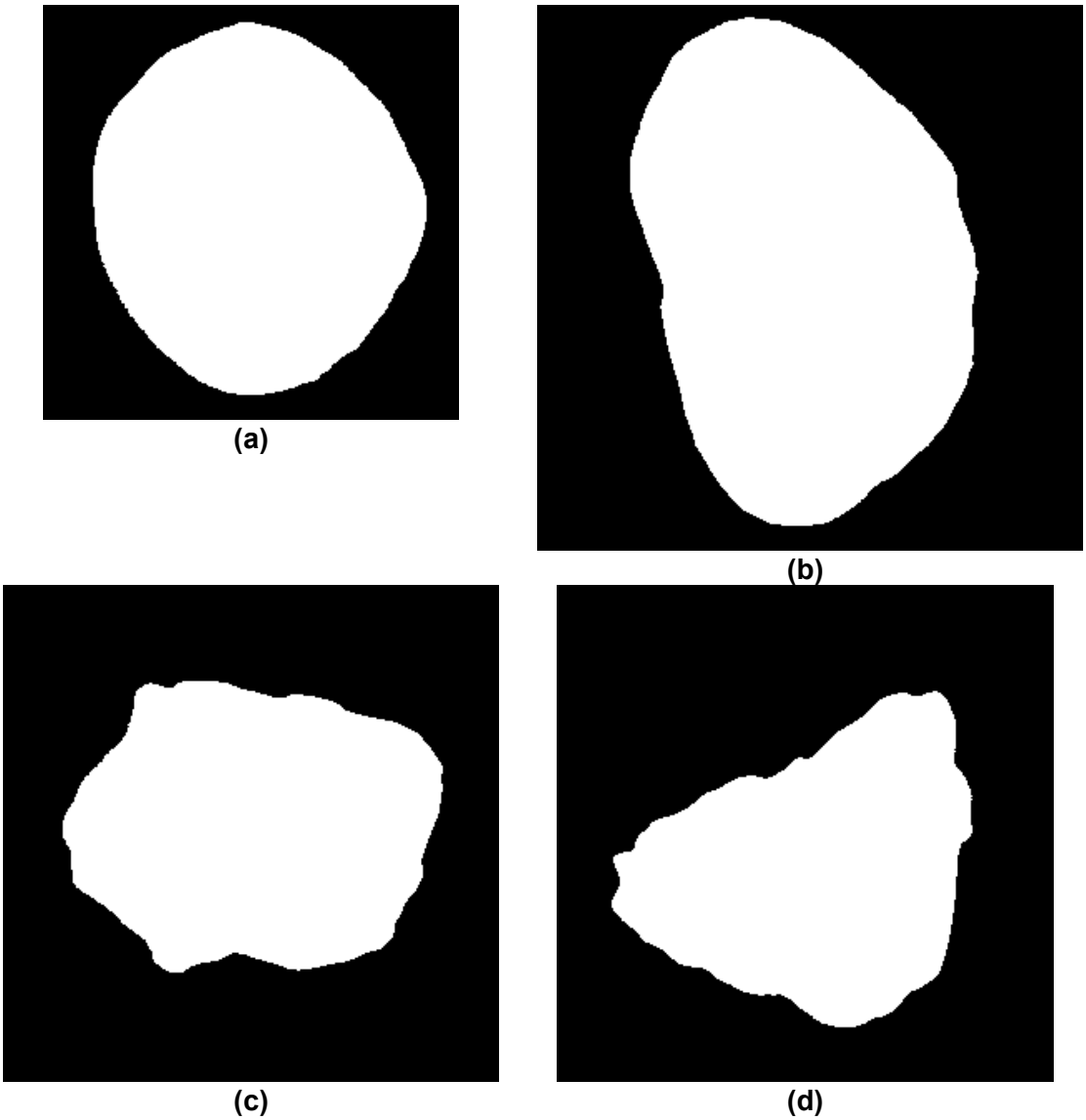


**Figure 3.2 –** Images and identifications of the particles studied; **(a)** Particle 1, **(b)** Particle 2, **(c)** Particle 3, **(d)** Particle 4.

**Table 3.1 –** The names and the mineralogy of the selected study materials.

| Name | Description | $D_{50}$(mm) | $C_u$[1] | $C_c$[2] |
|---|---|---|---|---|
| Particle 1 *(p1)* | Ottawa 20/30 sand | 0.64 | 1.46 | 0.96 |
| Particle 2 *(p2)* | Ottawa 20/30 sand | 0.64 | 1.46 | 0.96 |
| Particle 3 *(p3)* | Ottawa 20/30 sand | 0.64 | 1.46 | 0.96 |
| Particle 4 *(p4)* | Atlanta 20/30 blasting sand | 0.77 | 1.53 | 0.81 |

[1]. $C_u=D_{60}/D_{10}$
[2]. $C_c=D_{30}^2/(D_{10}*D_{60})$

formats and resolutions of the real particles as well as additional procedures undertaken to obtain the desired formats.

The particles in Figure 3.2 are selected for analysis since they represent the general shape characteristics for the materials used in geotechnical engineering applications. The particles *p1, p2, p3*, and *p4* are classified as rounded-high sphericity, rounded-low sphericity, subangular-high sphericity, and angular-high sphericity, respectively based on the roundness scale provided by Powers (1953).

The particle images are captured using Leica DM4000 microscope. For the size of particles considered in this study, a resolution of 1 pixel corresponding to 3.91 μm is used. At higher resolutions than 3.91μm/pixel, the selected particles cover more than the complete image area and boundaries are not visible. The particles in the sample tray are carefully spread out such that they are not touching each other. The focus of the lens is adjusted to obtain a clear image of the particle. Next, the captured images are transferred to the software Leica Qwin for further image processing. The images are then input to a Mathcad 2001 Professional program to obtain the pixel particle outline.

**Table 3.2 –** Initial and sequential formats of the study materials

| Material | Initial Object Format | Resolution / Dimension | Secondary Object Format | Resolution / Dimension | Third Object Format | Resolution / Dimension |
|---|---|---|---|---|---|---|
| Real Particles | Captured Grayscale Image[1] | 391μm/pxl | Array of integers between 0 and 255 | Matrix (rows x columns) varying between (250x250) to (330x330) | [nx2] clockwise direction outline | Four particles average resolution of 223 data points/mm perimeter |
| Real Surfaces | Profilometer Output[2] | Horizontal resolution = 1μm, vertical resolution=32nm, 40 mm length | Surface profile with modified resolution and length | Horizontal resolution = 4μm, vertical resolution = 32nm, 15 mm length, 220 data points/mm | NA | NA |
| Derived Particles | Secondary format real surface profiles | Horizontal resolution = 4μm, vertical resolution = 32nm, 15 mm length, 220 data points/mm | Wrapped surface profile | Three derived particles average resolution of 220 data points/mm perimeter | NA | NA |
| Derived Surfaces | Third object format real particles | Average resolution of 223 data points/mm | Unrolled particle outline | Four derived surfaces with average resolution of 247 data points/ mm perimeter | NA | NA |

[1]The images are captured using Leica DM4000 Digital Microscope.

[2] Taylor Hobson Talysurf Series 2 Profilometer is used to obtain the surface profiles.

NA: Not Applicable.

The details for particle outline extraction from particle images are explained in Section 3.3.1. After obtaining the 2D particle outline in counterclockwise order, desired shape parameter calculations for the particles are executed using the acquired shape outline.

For the study of *real surfaces*, a high-density polyethylene (HDPE), tooled steel and rough concrete surface profiles are adapted from DeJong (2001). The profiles were obtained using a Taylor Hobson Talysurf Series 2 equipped with a 50 mm traverse unit. The tip radius and the vertical range of the sapphire ball for the stylus are 1 μm and 2 mm, respectively. The horizontal and vertical resolutions for the obtained profiles are 0.001mm and 32nm, respectively with the profile length of 40-mm. In order to acquire the same level of resolution in particle and surface topographies, the surface profiles are modified to a horizontal resolution of 0.004mm. The resolution modification from 0.001mm to 0.004mm is achieved by averaging every 4 consecutive data point along the 0.001mm resolution profile and plotting the averaged value as a single data point for the 0.004mm resolution profile. The initial formats and resolutions for the real surfaces are provided in Table 3.2 with the consecutive procedures and resulting formats for any modifications.

The rough finished concrete surface profile used is shown in Figure 3.3 (a). The (HDPE) geomembrane was created using a coextrusion process and the measured profile is shown in Figure 3.3 (b). Figure 3.3 (c) shows a tooled steel surface profile obtained from a new cone penetration test friction sleeve. Apart from the quantitative differences in surface profile relief, the three surfaces represent diverse features. The HDPE geomembrane surface profile is dominated by peaks. On the other hand, the rough finished concrete surface is made up of mostly valleys and flat top peaks. In between the two, tooled steel surface with minor amplitudes has surface features above as well

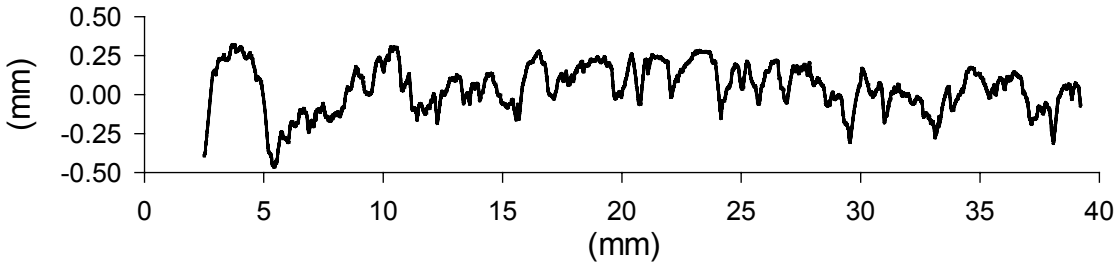


**(a)**

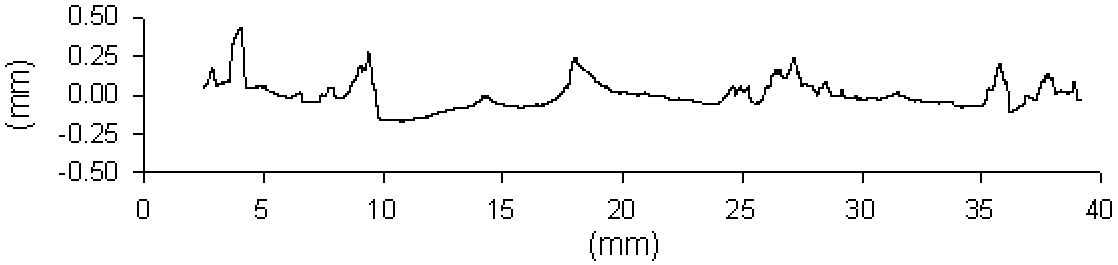


**(b)**

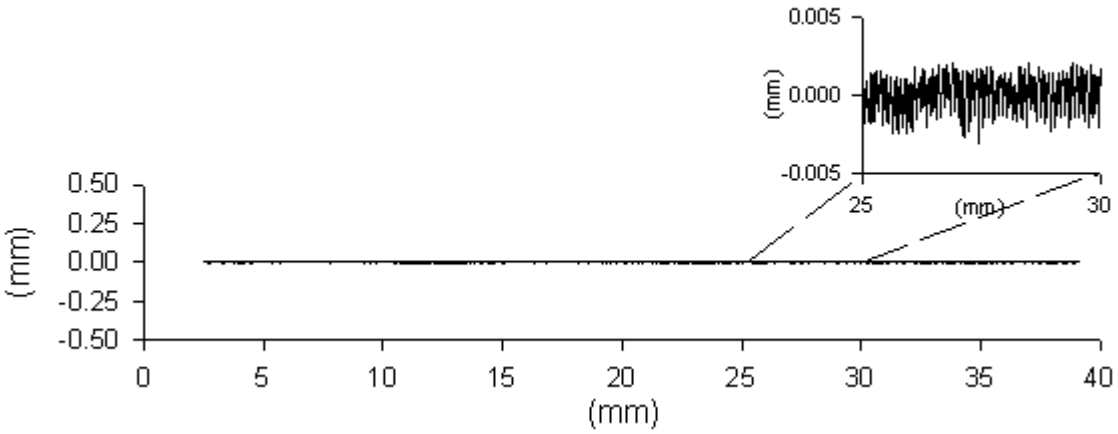


**(c)**

**Figure 3.3 –** Modified surface profiles; **(a)** Rough Finished Concrete, **(b)** HDPE Medium Textured Geomembrane, and **(c)** Tooled Steel (after DeJong, 2001).

as below the mean surface line.

### *3.1.2 Derived Particles*

An important goal in this study is to investigate surfaces as particles by means of particle shape evaluation methods and particles as surfaces utilizing surface roughness methods in an attempt to identify a unified approach to quantifying both components of an interface. This is accomplished by converting real surfaces to derived particles and real particles to derived surfaces. This section describes the derived particle generation procedures, while Section 3.1.3 presents derived surface generation approach.

Derived particles are generated by wrapping real surfaces. In other words, the real surfaces discussed in Section 3.1.1 are wrapped using a set of algorithms in order to reproduce particles on which particle analysis can be performed. The derived particle generation process was also summarized in Table 3.2. A schematic figure showing the process is included in Figure 3.4.

In an attempt to acquire equivalent points/mm resolutions for the real and derived particles, surface profiles are modified to the same points/mm as real particles. As a result, real surfaces wrapped to derived particles have comparable particle outlines to real particles.

Table 3.3 shows the perimeter, number of points, and the points/mm resolution for real particle outlines. The average pts/mm for real particles is 223. On the other hand, original surface profiles are obtained at a resolution of 0.001 mm, corresponding to 1000

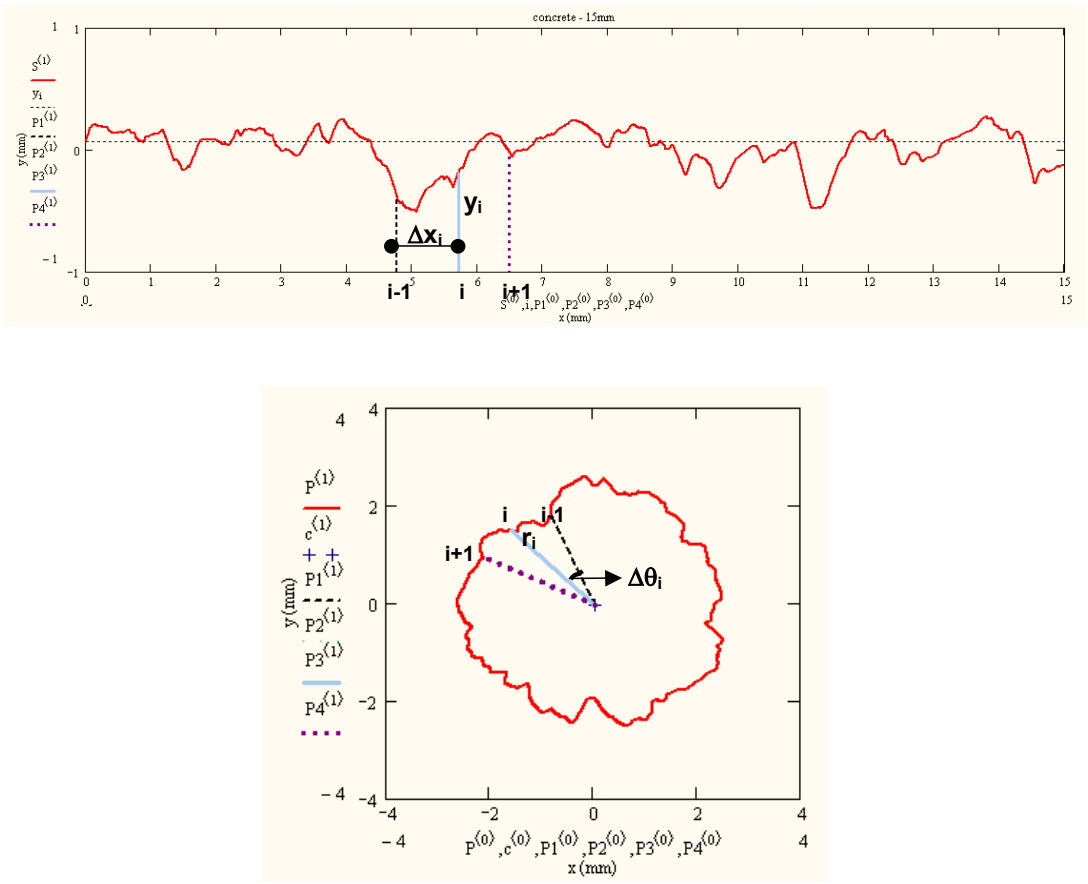


**Figure 3.4 -** Figure showing the derived particle process.

**Table 3.3 –** Resolution properties of the selected real particles.

| Particle | Perimeter (pixels)[1,2] | Perimeter (mm) | Number of data points | Points/mm |
|---|---|---|---|---|
| p1 | 736.1 | 2.88 | 659 | 229.0 |
| p2 | 913.9 | 3.57 | 831 | 232.6 |
| p3 | 736.6 | 2.88 | 663 | 230.2 |
| p4 | 806.1 | 3.15 | 630 | 199.9 |

[1]: 1 pixel = 3.91 μm
[2]: The perimeters are calculated as the summation of distance between the outline points.

pts/mm. Thus, HDPE, rough concrete and steel surface profiles are converted to a resolution of 0.004mm, i.e. 250 pts/mm, by computing the average of every 4-points on the surface profile.

Another adjustment applied to real surface profiles besides resolution change involved surface profile length. As mentioned above, the original real surfaces were obtained with 40 mm horizontal projected length. In order to obtain derived particle outlines, the real surface profiles are wrapped. Wrapping the original 40 mm horizontal length profiles results in derived particle perimeters larger than 40 mm depending on the amplitude characteristics of the individual profile. On the other hand, the real particles have perimeters in the range of 2.88 mm-3.57 mm as shown in Table 3.3. In order to reduce the discrepancy between real and derived particle sizes, a study was conducted to investigate the minimum length of real surface profiles that could be wrapped to obtain derived particles. In reducing the profile length, the criterion used was to ensure that reduced length portion of the surface profile has the same surface characteristics as the original 40 mm long surface profiles. Surface characteristics are measured using Centroid Trace (CT) methods developed by DeJong (2001). In other words, the profile length is reduced as long as its CT surface parameters match the CT surface properties

of the original 40-mm. Profile lengths of 40-mm, 20-mm, 15-mm, 10-mm, 5-mm, and finally 2.5-mm are selected for analysis. In the case of the lower bound of 2.5 mm profile length, the derived particles would have equivalent perimeters as the real particle perimeters (Table 3.3).

The CT for each profile length is generated by rolling a range of diameter circles over the profile and recording circle's centroid locations for each case. The range of circle diameters used depends on the profile length. In the development of the CT method by DeJong (2001), for a 40-mm profile, a diameter range of 0.075mm-20mm was used, corresponding to maximum and minimum profile length to diameter ratio of approximately 533:1 and 2:1, respectively. The minimum circle diameter is controlled by the minimum profile length considered, i.e. 2.5-mm. Based on a profile length to diameter ratio of 500:1, the minimum CT circle diameter was computed as 0.005mm for a 2.5-mm profile length. Similarly, the maximum circle diameter is controlled by the maximum profile length. For 40-mm profile lengths at 0.001mm resolution, the maximum diameter was 20-mm. In the appropriate selection of the maximum circle diameter, forbidden zone edge effects need to be considered. Based on the study by Frost and Saussus (2000), in order to compare the surface properties of different CT profiles (for the range of circle diameters considered) without any bias due to forbidden zone edge effects, all profiles are reduced to the length of the shortest profile. In other words, a certain length (termed as "range") of the CT profile is removed from both ends of the profile. The range for a particular surface profile and its rolling circle is calculated by the rolling circle radius to the surface profile resolution ratio. A 0.001mm resolution, 40-mm long profile has 40,000 data points. On the other hand, a 0.004mm resolution 40-mm long profile has 10,000 data points. For a maximum circle diameter of 20mm, 2,500 data points (for 0.004mm resolution) have to be removed from both profile ends to

consider the forbidden zone edge effects; which results in only 5,000 data points for analysis. Thus, the maximum circle diameter is reduced to 5mm for the real study surface profiles considered (0.004mm resolution, 40 mm length). The maximum 5mm diameter circle is valid for a profile length of 40-mm. For the reduced profile lengths analyzed, the maximum diameter is calculated by matching the profile length to 40 mm ratio with the maximum circle diameter to 5mm diameter ratio (8:1 ratio). Table 3.4 shows the minimum and maximum circle diameters for each profile length.

**Table 3.4 –** The profile lengths and the corresponding circle diameter ranges for the CT analysis.

| Profile Length (mm) | Minimum Circle Diameter (mm) | Maximum Circle Diameter (mm) |
|---|---|---|
| 40 | 0.005 | 5 |
| 20 | 0.005 | 2.5 |
| 15 | 0.005 | 1.875 |
| 10 | 0.005 | 1.25 |
| 5 | 0.005 | 0.625 |
| 2.5 | 0.005 | 0.3125 |

The CT surface parameters plots versus the circle diameter of the selected surface profile lengths are shown in Figure 3.5 for the rough finished concrete profile. The CT surface parameter values for all concrete profile lengths from 20-mm to 2.5-mm are compared with the CT surface parameter values for the original 40-mm long surface profile in terms of the rate of parameter value change and extreme values. The maximum values for the CT surface parameters of concrete profile are provided in Table 3.5 and plotted on Figure 3.6. Although the maximum values and trends for 20-mm and

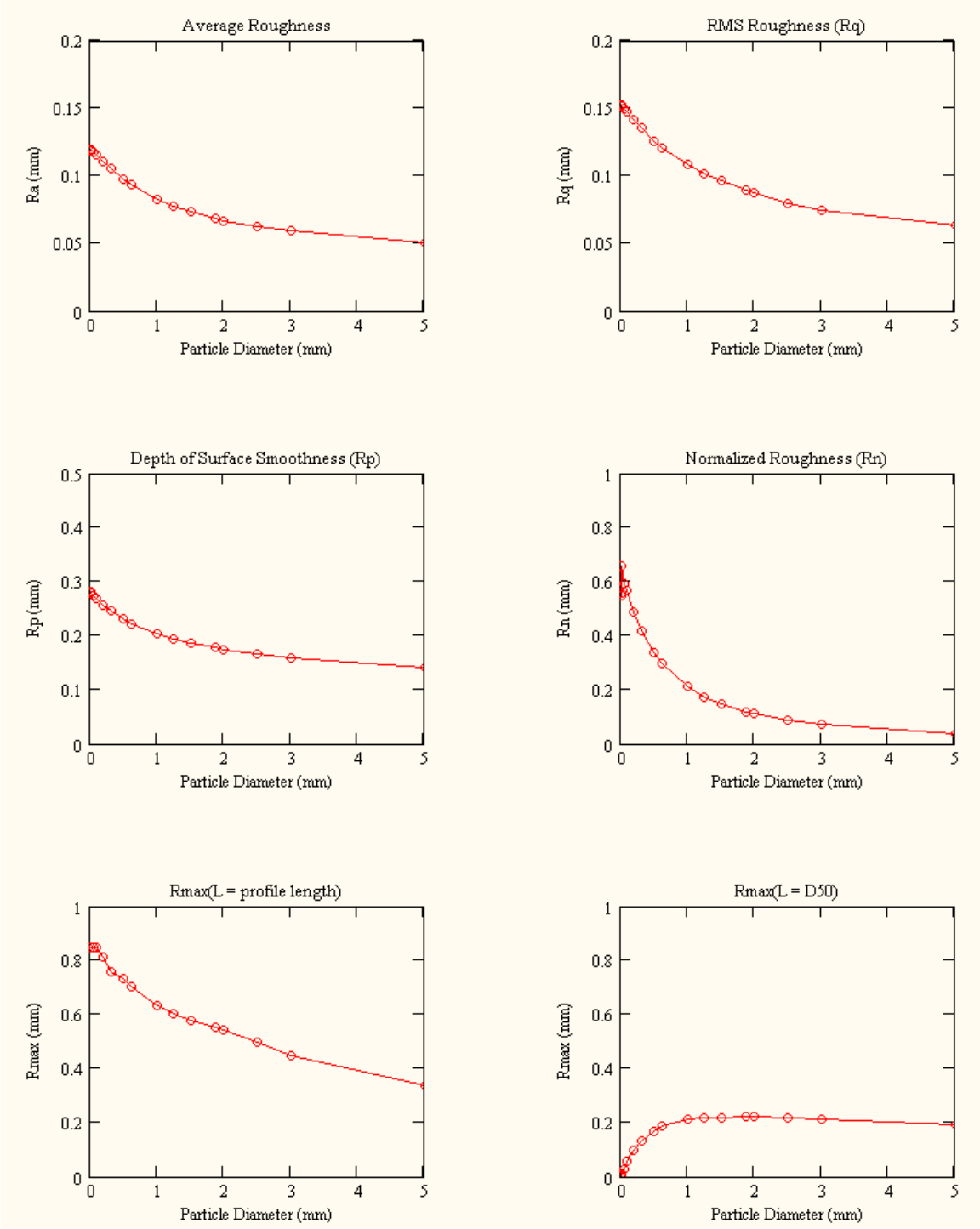


40 mm long – 0.004 mm res – dia = 0.005-5mm.

**Figure 3.5 –** CT surface parameter plots versus the circle diameter for the selected profile lengths.

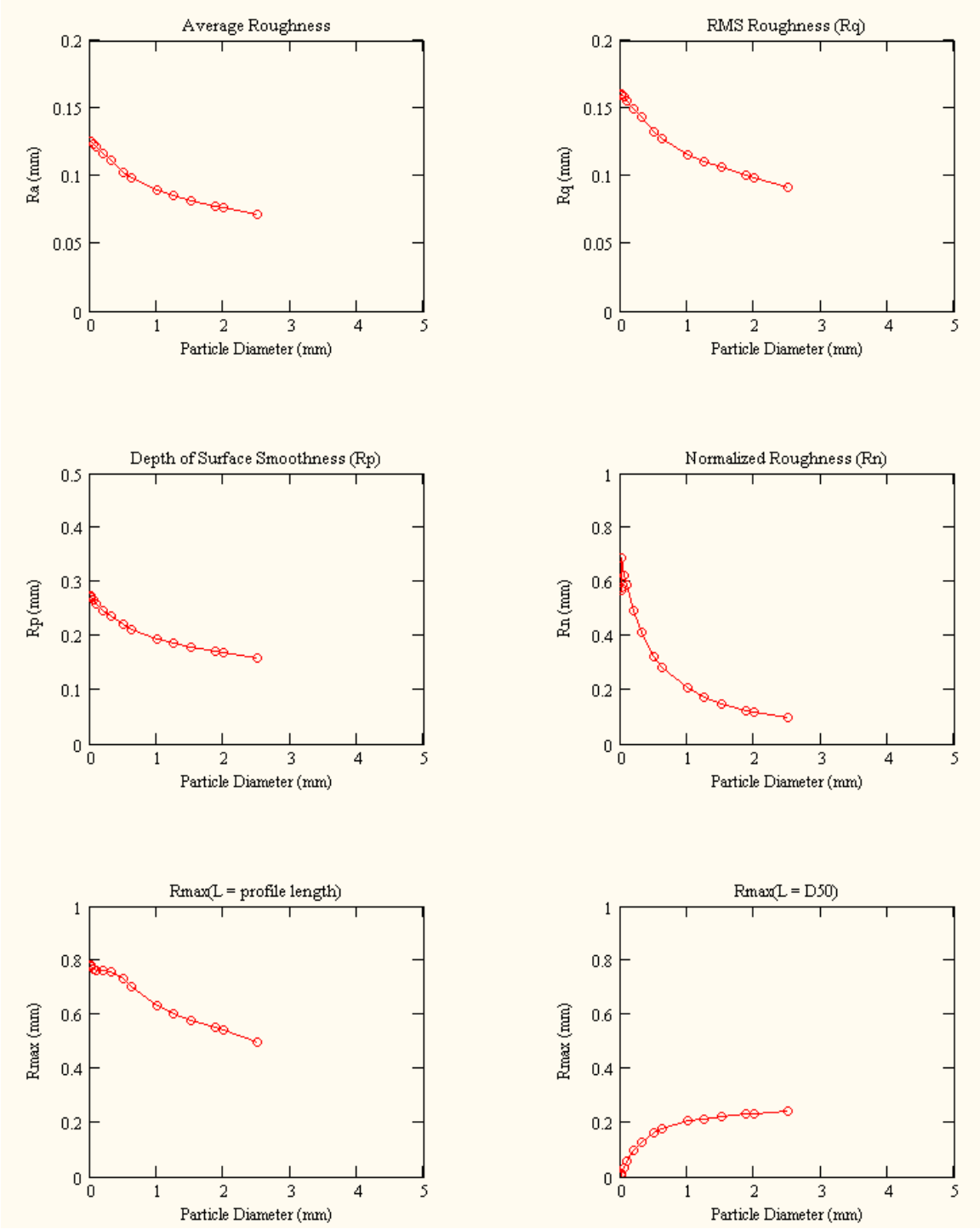


20 mm long-0.004mm res - dia=0.005-2.5mm

**Figure 3.5 (continued).**

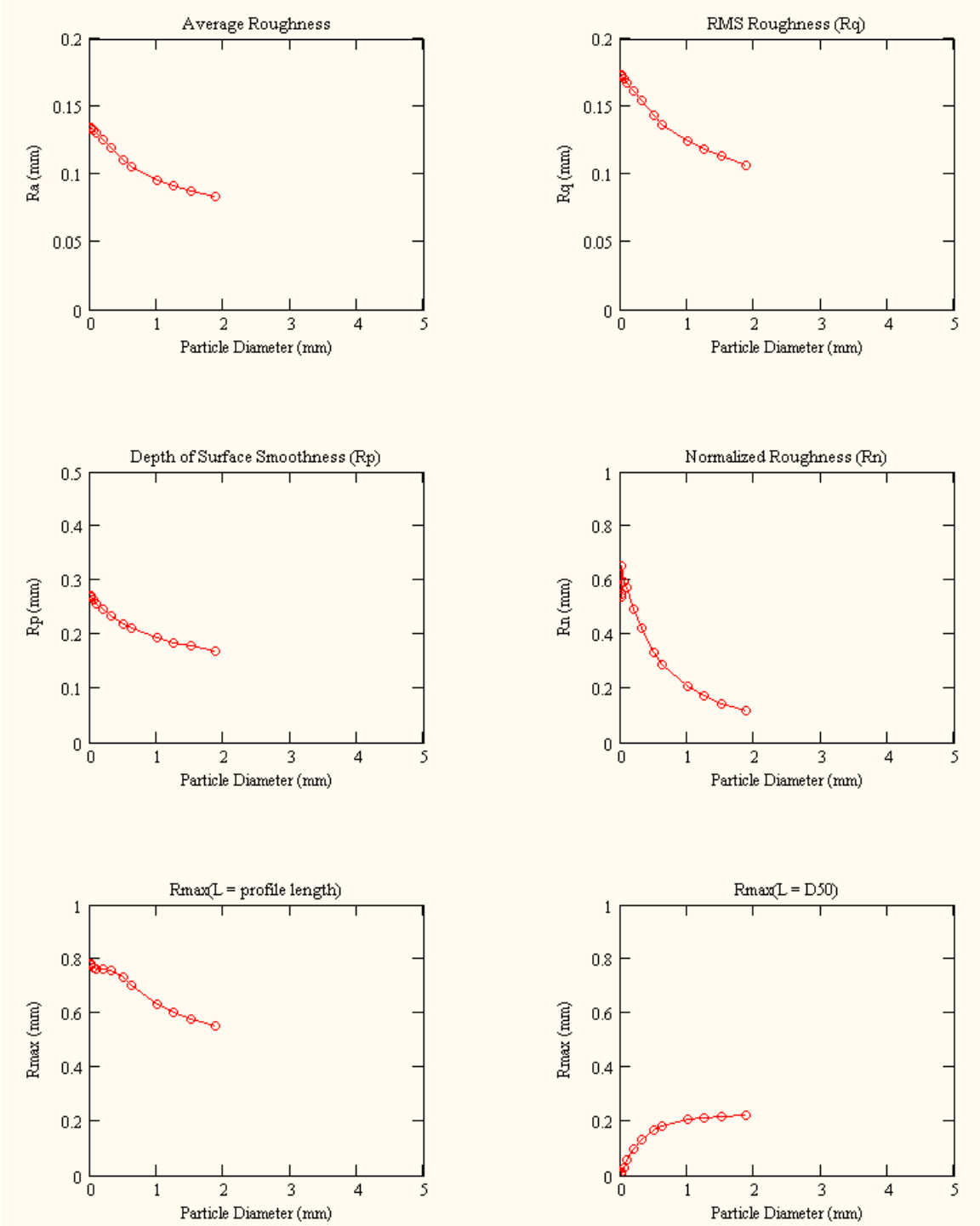


15 mm long-0.004mm res - dia=0.005-1.875mm

**Figure 3.5 (continued).**

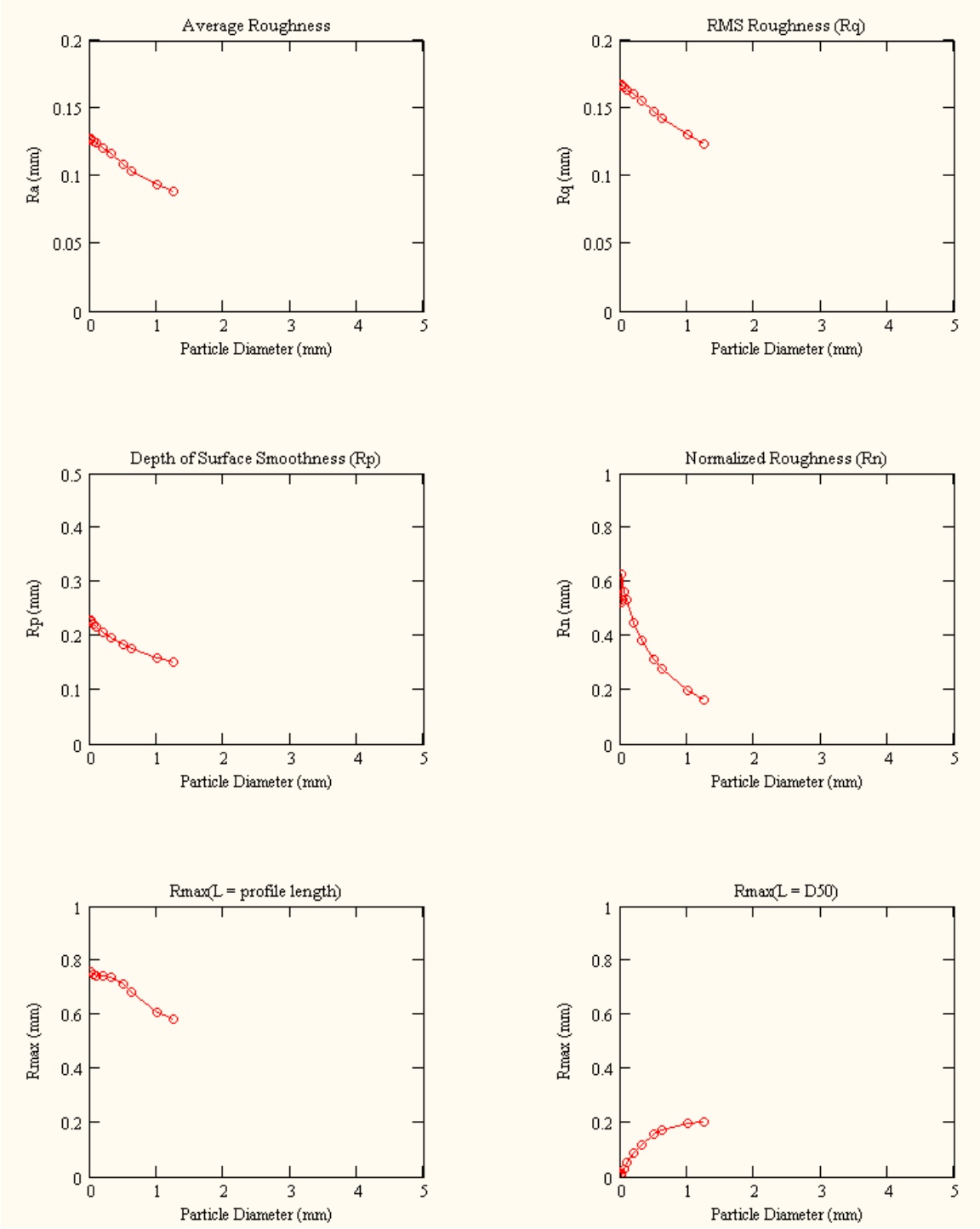


10mm long – 0.004mm res. – dia=0.005-1.25mm.

**Figure 3.5 (continued).**

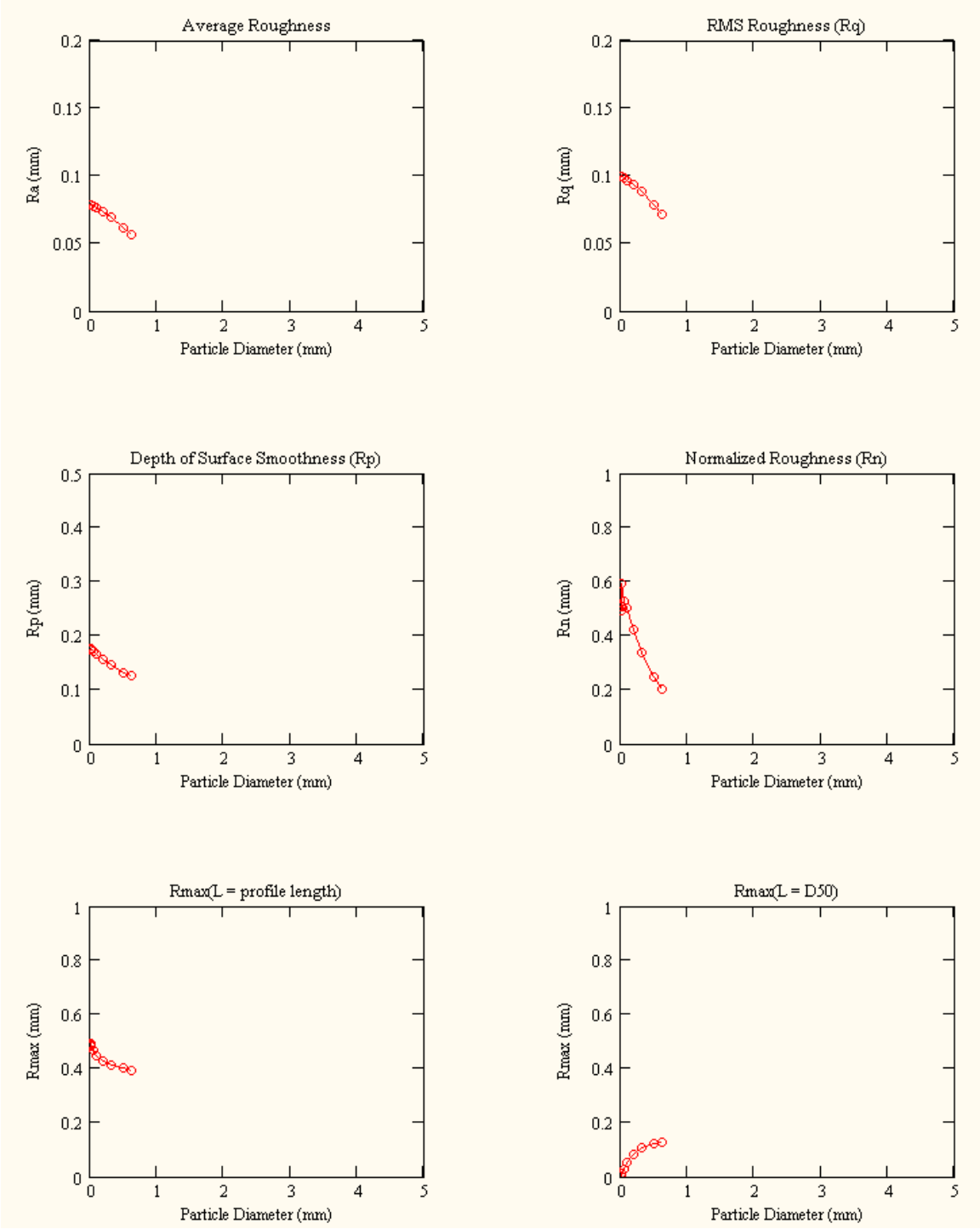


5mm long – 0.004mm res. – dia=0.005-0.625mm.

**Figure 3.5 (continued).**

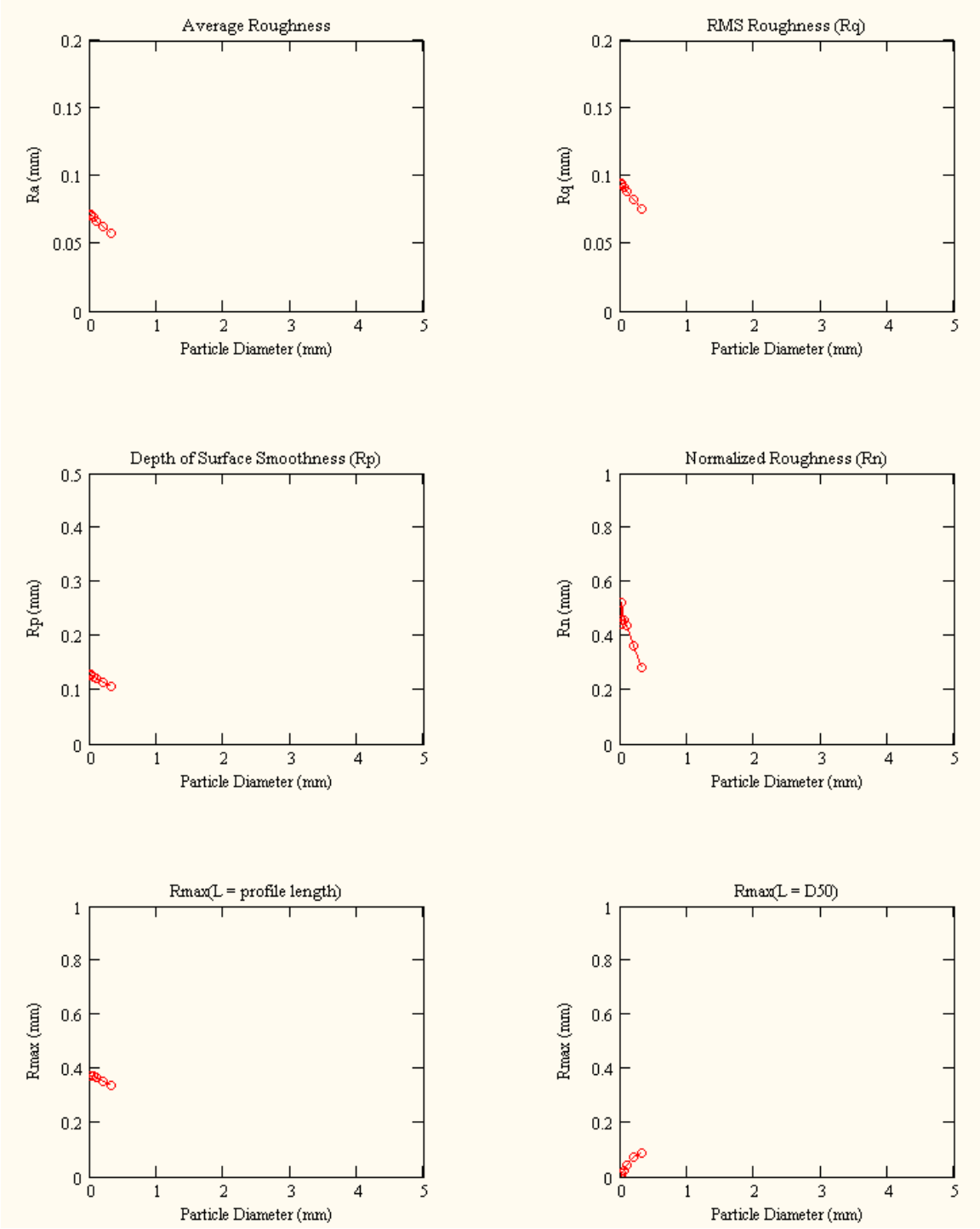


2.5mm long – 0.004mm res. – dia=0.005-0.3125mm.

**Figure 3.5 (continued).**

**Table 3.5 –** The maximum CT surface parameter values for the concrete profile.

| Profile Length | max($R_a$) | max($R_q$) | max($R_p$) | max($R_{max}$) | max ($R_n$) |
|---|---|---|---|---|---|
| mm | mm | mm | mm | mm | - |
| 40 | 0.119 | 0.152 | 0.282 | 0.849 | 0.66 |
| 20 | 0.126 | 0.161 | 0.274 | 0.78 | 0.688 |
| 15 | 0.134 | 0.173 | 0.27 | 0.78 | 0.653 |
| 10 | 0.127 | 0.168 | 0.229 | 0.759 | 0.626 |
| 5 | 0.079 | 0.1 | 0.177 | 0.493 | 0.591 |
| 2.5 | 0.072 | 0.094 | 0.129 | 0.371 | 0.521 |

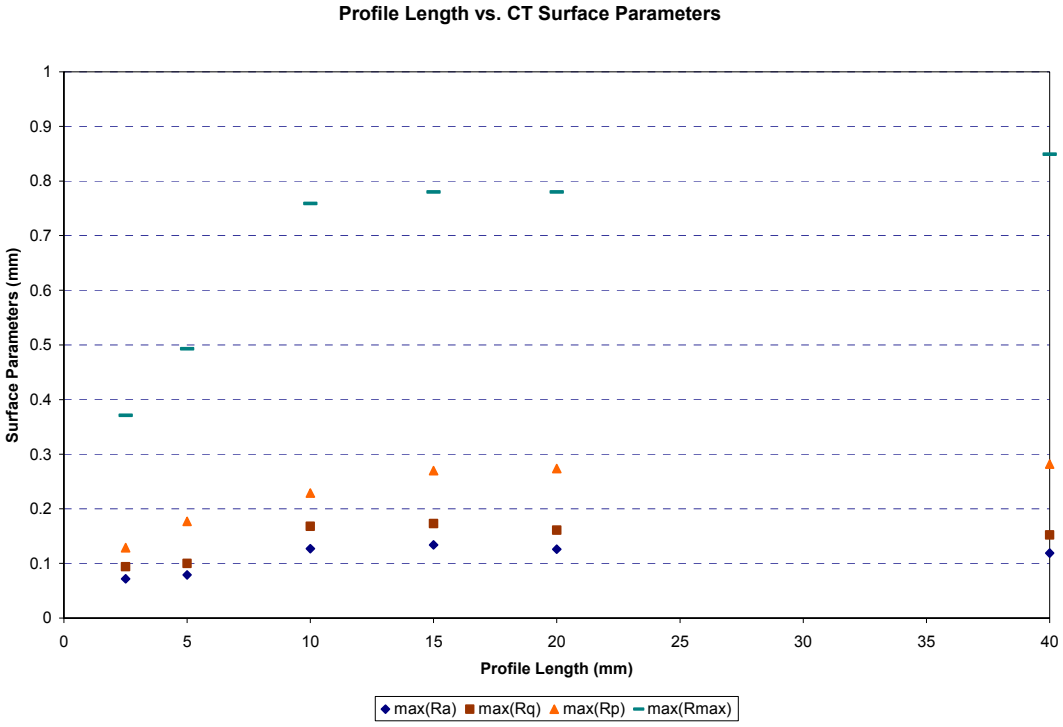


**Figure 3.6 –** The maximum CT surface parameter values for the corresponding profile lengths.

15-mm long profiles match with the original 40-mm long profile, 10-mm long profile CT surface parameter plots deviate from the original 40-mm long concrete profile. For $R_a$ and $R_q$ trends, 10-mm long profile attains larger values than 40-mm long although the rate of change is comparable. On the other hand, $R_p$ and $R_n$ values are less for the 10-mm profile. $R_{max}$ behavior for the two profiles is similar. The correlation between maximum values of all CT surface parameters ($R_a$, $R_q$, $R_p$, $R_n$, $R_{max}$ (L=Profile Length), and $R_{max}$ (L=$D_{50}$)) among the different lengths (40-mm to 2.5-mm) are also investigated and shown in Table 3.6.

**Table 3.6 –** The correlation values for maximum CT surface parameters (concrete).

| | **40** | **20** | **15** | **10** | **5** | **2.5** |
|---|---|---|---|---|---|---|
| **40** | 1.000 | | | | | |
| **20** | 0.995 | 1.000 | | | | |
| **15** | 0.998 | 0.999 | 1.000 | | | |
| **10** | 0.996 | 0.997 | 0.999 | 1.000 | | |
| **5** | 0.937 | 0.968 | 0.955 | 0.952 | 1.000 | |
| **2.5** | 0.884 | 0.927 | 0.910 | 0.907 | 0.991 | 1.000 |

Due to the different trends and maximum values between 40-mm profile length and 10-mm profile length, a minimum profile length of 15-mm is chosen for the remainder of the analysis in this study in order to preserve the surface characteristics of the original 40-mm long surface profile. As shown in Table 3.6, the correlation between the 40-mm profile length and 15-mm profile length CT surface parameters is 0.998. As a result of this analysis, only 15-mm long portion of the surface profiles is utilized to generate

derived particles. For real surface analysis, 15-mm long portion of the 40-mm long profiles are utilized as well.

The next step in derived particle generation is transforming the $(x, y)$ surface profile to an $(\theta, r)$ outline so that the wrapped particle can be acquired by re-converting the polar coordinates to Cartesian coordinates. In this process, although 3,750 data points exist for a 15-mm profile length at 0.004mm resolution, the number of the data points for the total length of the surface profile is modified to 360 data points. This is achieved by increasing the –x value (starting from 0-mm) for 1/360$^{th}$ of the projected profile length at each step for 360 data points. The –y surface elevations at the required –x sampling locations are estimated by interpolating the available data points using second-degree polynomials. In the final step of the number of data points modification, the 15-mm long surface profile at 0.004mm resolution is represented by 360 data points rather than 3,750 data points. The purpose of this modification is to obtain radial coordinates that are 1° apart as $(x, y)$ surface profile is transformed into a $(\theta, r)$ coordinate system.

The rest of the analysis for obtaining a derived particle from a real surface profile is performed with 15-mm long 0.004mm resolution profile represented with 360 data points. In cases where the start (at 0-mm) and end (at 15-mm) points of the reduced profile are not collinear (i.e. do not have the same surface profile height), wrapping a surface to derived particle results in a mismatch between the first and last points of the derived particle causing a gap along the derived particle profile. As mentioned above only 15-mm long portion of the profile is used, thus the start and end data points mostly result in different surface elevations. This is adjusted by rotating the surface profile around the start point. The amount of rotation is determined by the deviation of the line

connecting the start and end points of the surface profile from –x axis. At the end of this stage, the output is 15-mm long surface profile sampled at 360 equal horizontal distance points. Thus, when transformation into radial coordinates is accomplished, the first and last points of the surface profile correspond to $\theta = 0°$ and $\theta = 360°$, respectively.

The $r$ value for each of 360 points (corresponding to 1° apart in radial coordinates from 0° to 360°) is calculated using Eq. 3.1.

$$r_i = (r_{circle\ of\ 15mm}) + ysurface_i - yaverage \quad \textbf{(3.1)}$$

Thus, the difference between the –y surface elevation and the average –y value at point "i" is added to the equivalent radius of a circle with 15-mm perimeter, $15/(2\pi)$.

Upon applying Eq. 3.1 to 360 data points, the data set contains point indices from 0 to 360 with the corresponding $r_i$ values at each index. Considering the indices as $\theta$ values along the circumference of the particle outline, the data set is in $(\theta, r)$ coordinates. To obtain the derived particle, the final step is to re-convert the radial coordinates to Cartesian coordinates using Eq. 3.2.

$$\begin{aligned} x &= r * \cos(\theta) \\ y &= r * \sin(\theta) \end{aligned} \quad \textbf{(3.2)}$$

The derived particles are shown in Figure 3.7, termed as concrete-par, hdpe-par, steel-par corresponding to the wrapped 15-mm section of a rough finished concrete profile, HDPE medium –textured geomembrane profile, and tooled steel profile, respectively.

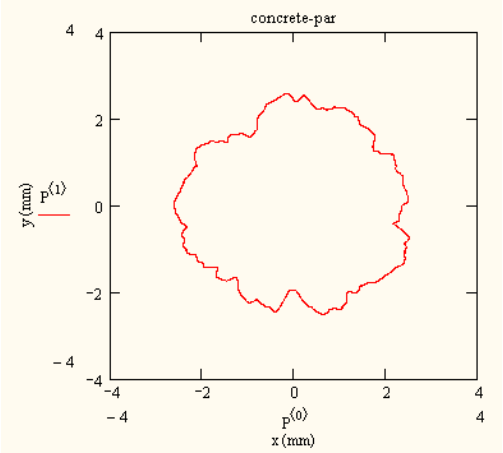


**(a)**

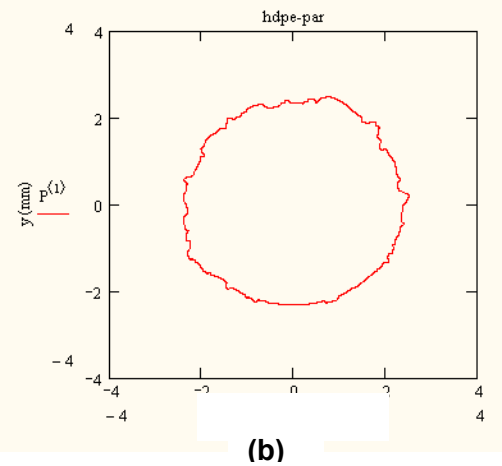


**(b)**

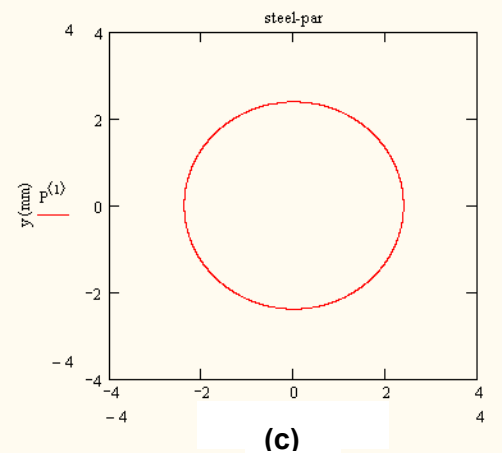


**(c)**

**Figure 3.7 –** Derived particle outlines; **(a)** concrete-par, **(b)** HDPE-par, and **(c)** steel-par.

### *3.1.3 Derived Surfaces*

Derived surfaces are generated by unrolling real particles used. To unroll particle outlines, a different set of algorithms is employed as described below. A relevant concept has been introduced in Appendix B.

Upon reading the particle images in *.bmp format into the corresponding *.prn outline data files, an algorithm $zeroanglecounterclockwise(A)$ is processed which reorders the outline to clockwise from counterclockwise direction, deletes any repeated sequential points, calculates the angle of each data point from the center, and sorts the data in increasing angle. The outline is then input into $ParticleShape(A,N)$ and subsequently to $SampleParticle(A,N)$, where $N$ stands for the number of intervals chosen. If 360 is used as input $N$, the algorithm interpolates the available outline data points in order to sample the particle at 1° intervals. This is followed by $XvsR(A,\deg)$, where for each of the 360 degree intervals around the particle outline (considering a total of 360 intervals as an example), the –x coordinate interval of the surface profile is set at $(particle\ outlline\ \ perimeter/360)$, and the –y coordinate corresponds to the radius measured corresponding to the index. For example, for 360 data point surface profile, a particle outline point at $i=10$ attains an –x surface profile value of $(10*particle\ outline\ \ perimeter/360)$ and a corresponding –y surface value equal to the radius of the particle outline data at $i=10$. Note that the particle outline perimeter is calculated for the total horizontal length of the derived surface profile is calculated from the output of the $SampleParticle(A,N)$ rather than from the original particle outline dataset. In this study, the horizontal profile lengths for the derived surfaces obtained

ranges from 2.7 to 3.3 mm. The derived surfaces generated with this procedure are shown in Figure 3.8.

## 3.2 Validation of Particle Unrolling and Surface Wrapping Algorithms

The particle unrolling and surface wrapping algorithms can be validated by sequentially applying them to a pair of objects (i.e. one particle and its derived surface or one surface and its derived particle) and comparing the initial object with the twice-transformed object. In this section, several acronyms will be used. PART stands for a real particle; whereas DPART stands for a derived particle obtained by wrapping of a real surface.

Similarly, SURF and DSURF stand for a real surface and a derived one via unrolling a real particle outline, respectively. Finally, DDPART and DDSURF stand for a particle obtained by wrapping a DSURF and a surface obtained from unrolling a DPART, respectively. Figure 3.9 (a) and (b) illustrate the process for *part-dsurf-ddpart* and *surf-dpart-ddsurf* conversions, respectively.

In order to investigate further four separate studies are conducted; SURF-DPART conversion with three offset surfaces, PART-DSURF conversion with three proportionate particles, PART-DSURF-DDPART conversion, and SURF-DPART-DDSURF conversion.

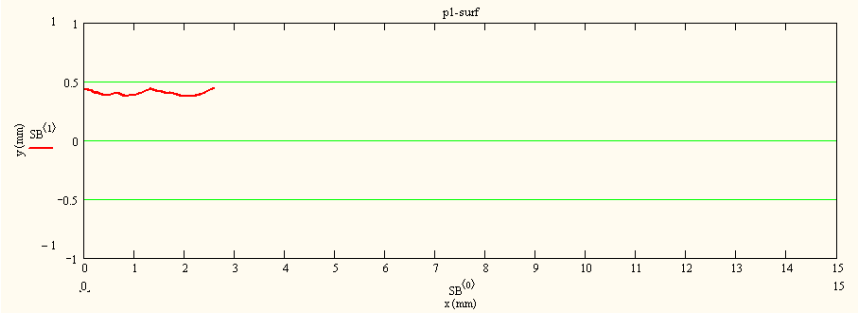


**(a)**

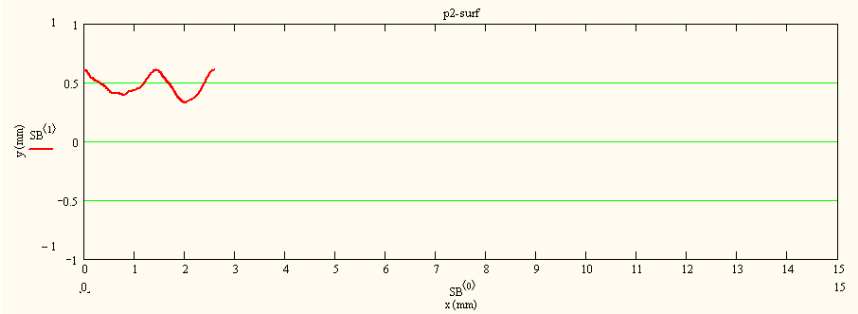


**(b)**

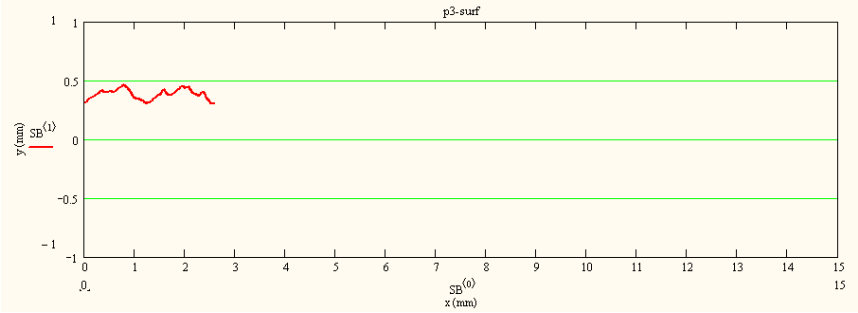


**(c)**

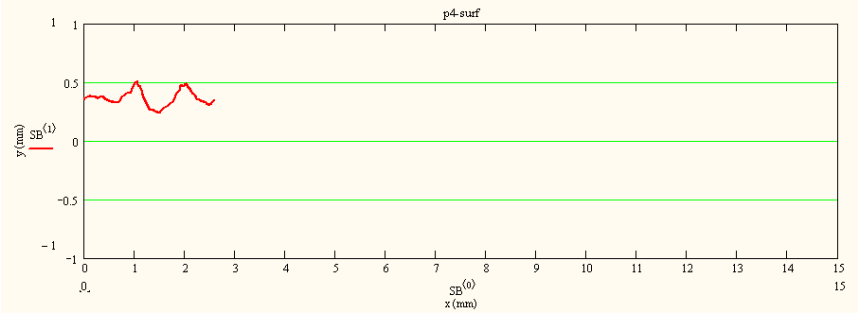


**(d)**

**Figure 3.8 –** Derived surface profiles; **(a)** p1-surf, **(b)** p2-surf, **(c)** p3-surf, and **(d)** p4-surf.

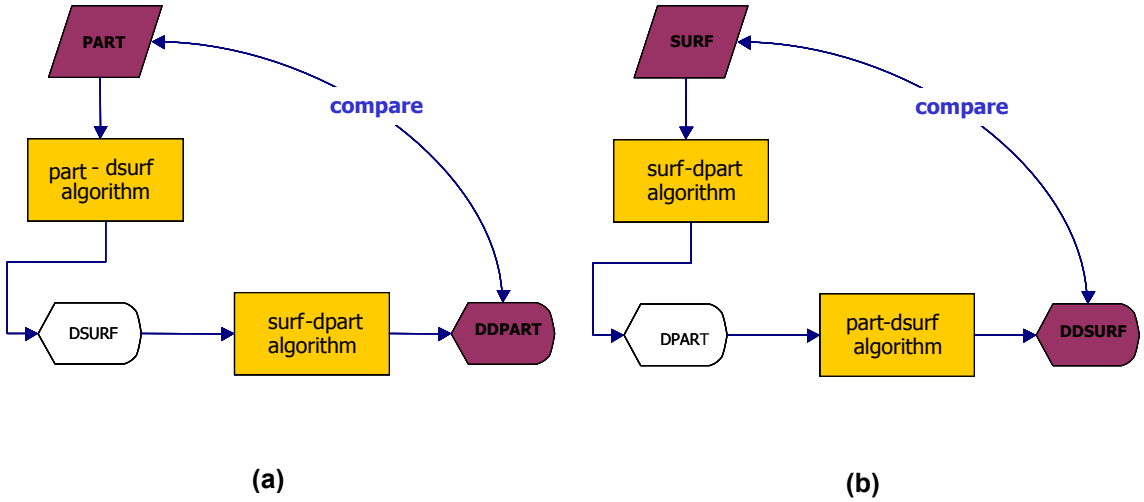


**(a)** **(b)**

**Figure 3.9 –** Schematic drawing of the reversibility of **(a)** PART-DSURF-DDPART conversion, **(b)** SURF-DPART-DDSURF conversion

### *3.2.1 SURF-DPART Conversion with Three Offset Surfaces*

It is important that a given surface profile regardless of its datum plane outputs the same *dpart* when processed through a *surf-dpart algorithm*. The datum plane should not make a difference in either the coordinates or size of the *dpart* when the surface is wrapped. For this purpose, a given surface profile at three different elevations is investigated to ensure the same *dpart* outline. A simple surface that includes two 60° ridges is selected as the input as shown in Figure 3.10.

The surface profiles *S0, S1,* and *S3* are separated from each other by an elevation difference of 0.1 units. These surfaces are then input separately to the *surf-dpart algorithm* as explained in Section 3.1.2 and the result is shown in Figure 3.11, which

clearly shows, the three identical but offset surfaces generate the same particle.

The relevant height and the radius average for the three surfaces and particles are shown in Table 3.7.

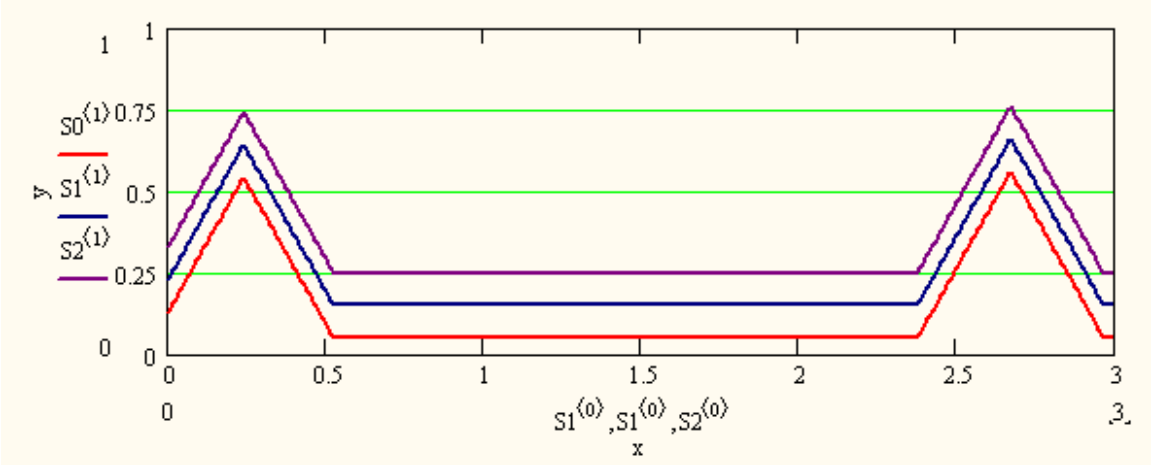


**Figure 3.10 –** Three identical but offset surfaces of two 60° ridge surface.

### *3.2.2 PART-DSURF Conversion with Three Proportionate Particles*

Similar to the analysis in Section 3.1.3, *part-dsurf algorithm* is tested to prove that it would give the same *dsurf* regardless of the input *part's* dimensions, i.e. when three same shape particles with different sizes are input to the algorithm, the output should provide three identical surfaces.

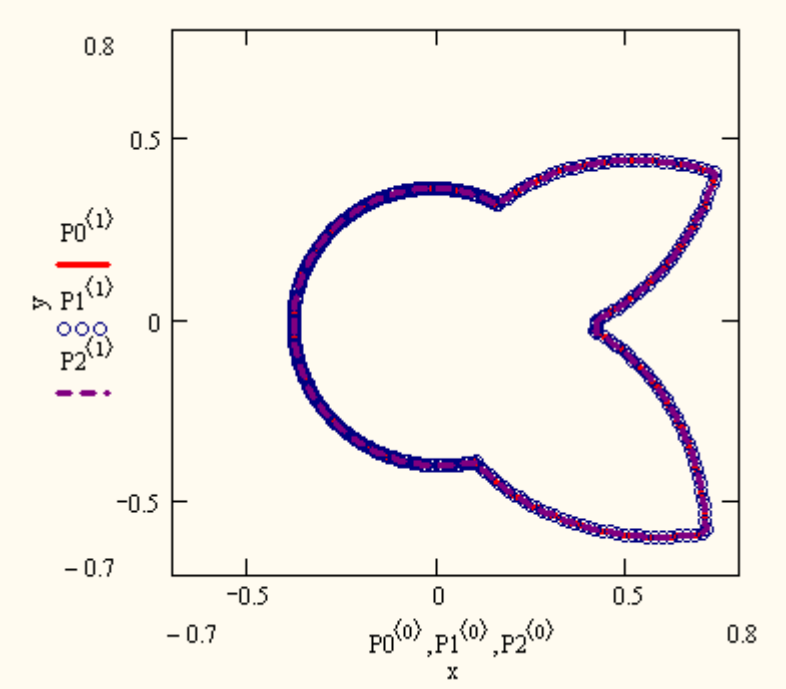


**Figure 3.11 –** The outputs *P0, P1,* and *P2.*

**Table 3.7 –** Height and radius averages for *SO, S1*, and *S2* and *P0, P1*, and *P2*, respectively.

| | | | |
|---|---|---|---|
| **y – yav** | **S0** | **S1** | **S2** |
| | 0.1464 | 0.2464 | 0.3464 |
| **r-rav** | **P0** | **P1** | **P2** |
| | 0.0018 | 0.0018 | 0.0018 |

For this purpose, three particles, *P0, P1,* and *P2* are selected as shown in Figure 3.12.

The three particles are separated from each other by a radius of 0.1 units.

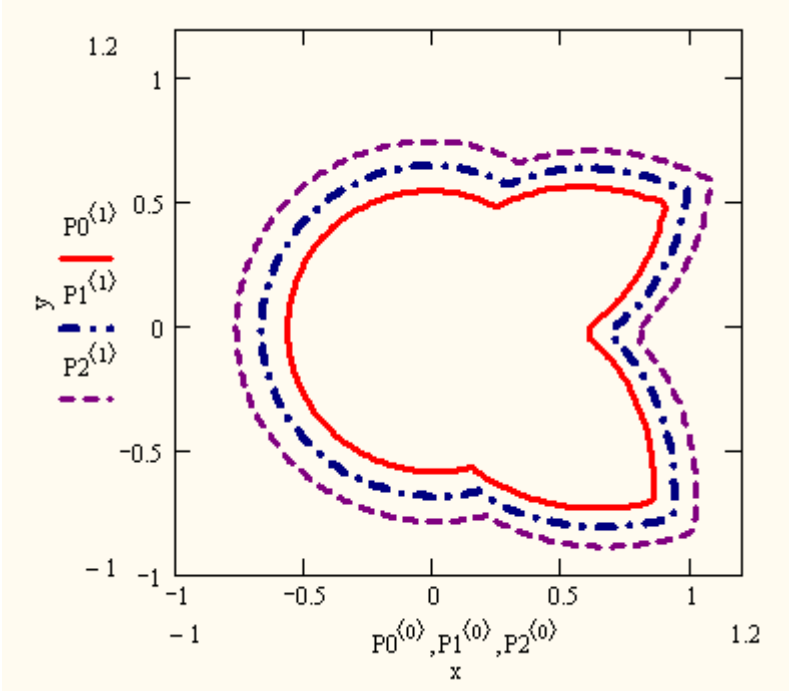


**Figure 3.12 –** Three different size but same shape particles.

The particles shown in Figure 3.12 are separately input to the *part-dsurf algorithm* and the outputs, *SO, S1,* and *S2* corresponding to *part* inputs *P0, P1,* and *P2,* respectively are as shown in Figure 3.13.

In order to demonstrate the superposition ability of the three *dsurfs,* namely *S0, S1,* and *S2*, the radius averages of the three particles were subtracted from their corresponding *dsurf* outputs. That is to say, in Figure 3.13. *S0* is reduced by the average radius of *P0;* and *S1* lowered by the radius average of *P1,* etc. Final observation from Figure 3.13 proves that regardless of the particle size the output of the *part-dsurf algorithm* provides the same surface.

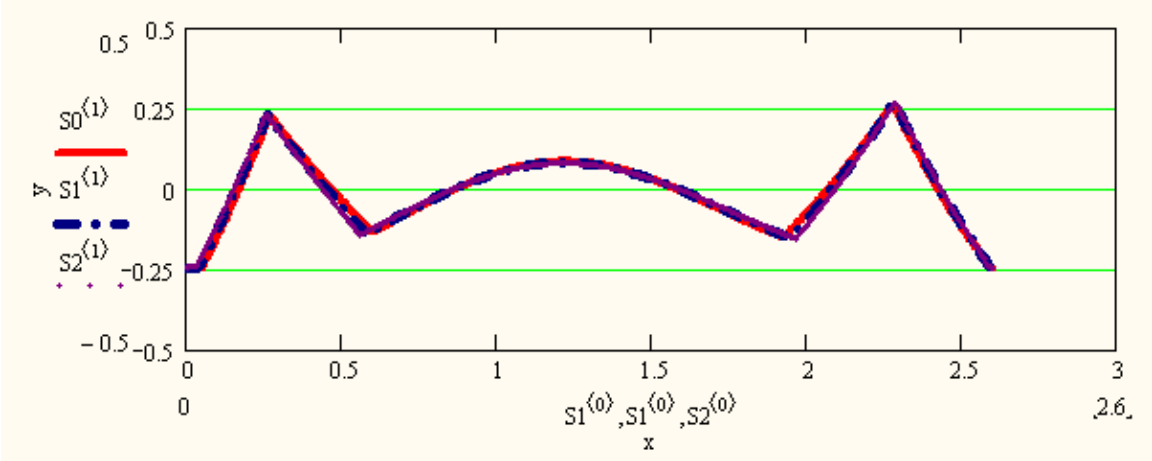


**Figure 3.13 –** The outputs S*0, S1,* and S2.

### *3.2.3 PART-DSURF-DDPART Conversion*

In this section, a real particle *part* is unrolled to obtain *dsurf,* which is subsequently wrapped to yield a *ddpart* as schematically shown in Figure 3.9(a). Four different *part* outlines are investigated. The particle outlines are shown in Figure 3.14. Nomenclature for the further process is as shown in Table 3.8.

**Table 3.8–** Procedure for PART-DSURF-DDPART conversion.

| Process | Particle Unrolling | | Surface Wrapping | | Validation Comparison |
|---|---|---|---|---|---|
| | Input | Output | Input | Output | |
| 1 | PART1 | DSURF1 | DSURF1 | DDPART1 | PART1 – DDPART1 |
| 2 | PART2 | DSURF2 | DSURF2 | DDPART2 | PART2 – DDPART2 |
| 3 | PART3 | DSURF3 | DSURF3 | DDPART3 | PART3 – DDPART3 |
| 4 | PART4 | DSURF4 | DSURF4 | DDPART4 | PART4 - DDPART4 |

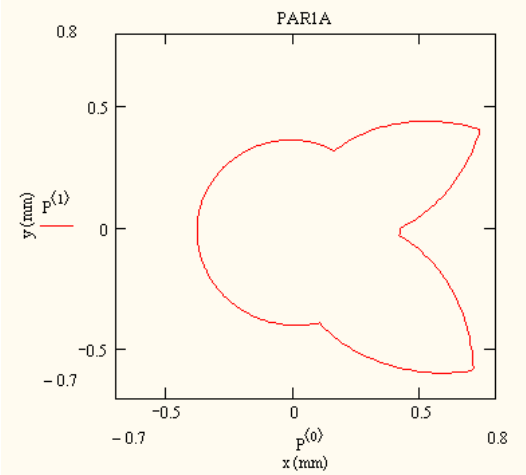


**(PART1)**

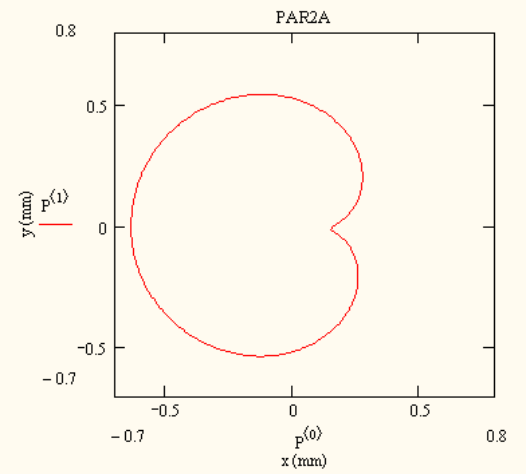


**(PART2)**

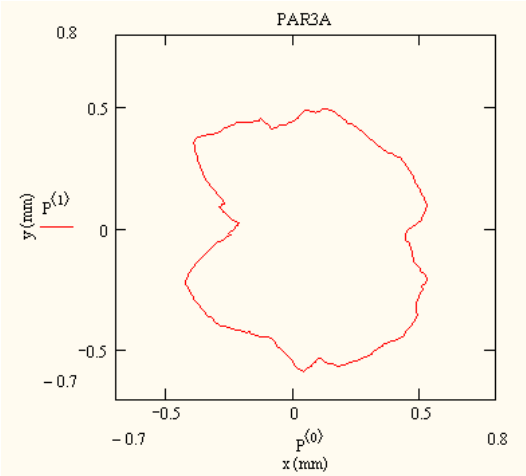


**(PART3)**

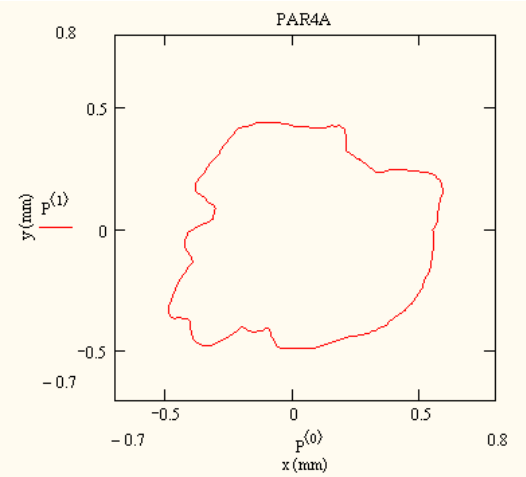


**(PART4)**

**Figure 3.14 –** Four selected PART outlines for validation of PART-DSURF-DDPART conversion.

Figure 3.15 shows the surfaces generated as an output of the particle unrolling. Figure 3.16 and Figure 3.17 demonstrate the output particles for the wrapped surfaces in Figure 3.15 and the validation comparison figures, respectively for the processes 1 to 4 as shown in Table 3.8. Note that in applying the *surf-dpart algorithm* to wrap *dsurf* to *ddpart*, Eq. 3.1 is modified to Eq. 3.3. The reason for modification is the difference in the input, i.e. in Eq. 3.3; the input is a derived surface; whereas in Eq. 3.1 it is a real surface outline.

$$r_i = ysurface_i \tag{3.3}$$

In order to superimpose *part* and the corresponding *ddpart*, for the presentation of Figure 3.17, *part* is repositioned by moving its centroid to the origin. As Figure 3.17 shows PART and DDPART of the four cases match exactly, thereby validating the PART-DSURF-DDPART conversion.

### *3.2.4 SURF-DPART-DDSURF Conversion*

In order to validate the SURF-DPART-DDSURF conversion, four different inputs are investigated. The procedure is shown in Table 3.9. The actual names of the four surfaces used as input for surface wrapping in Table 3.9 are given in Table 3.10.

The surfaces for the validation process are shown in Figure 3.18.

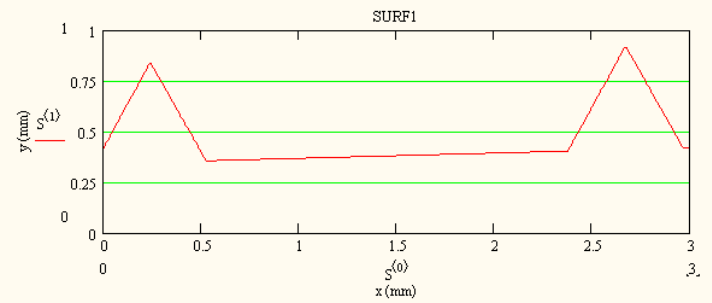


**(DSURF1)**

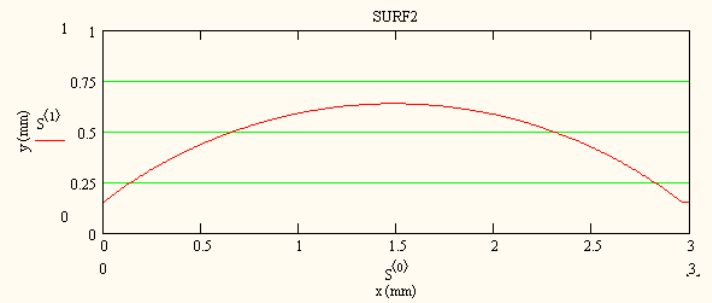


**(DSURF2)**

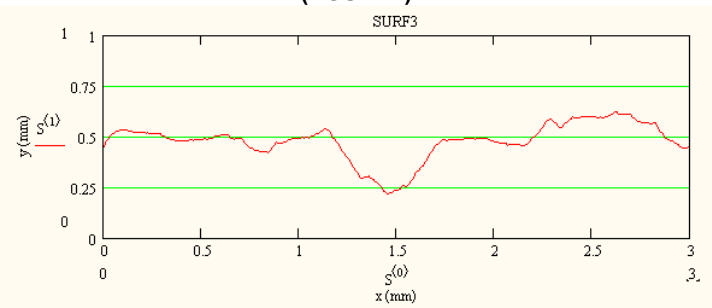


**(DSURF3)**

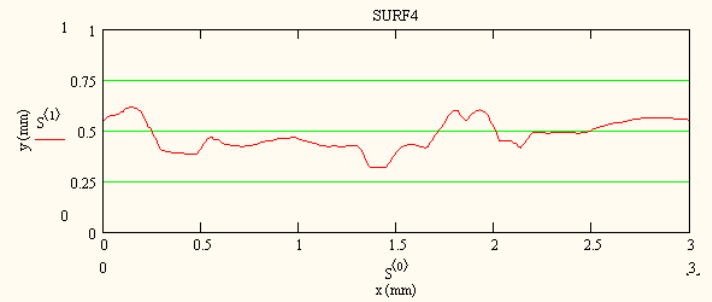


**(DSURF4)**

**Figure 3.15 –** Output of *particle unrolling* for the selected particles during PART-DSURF-DDPART conversion.

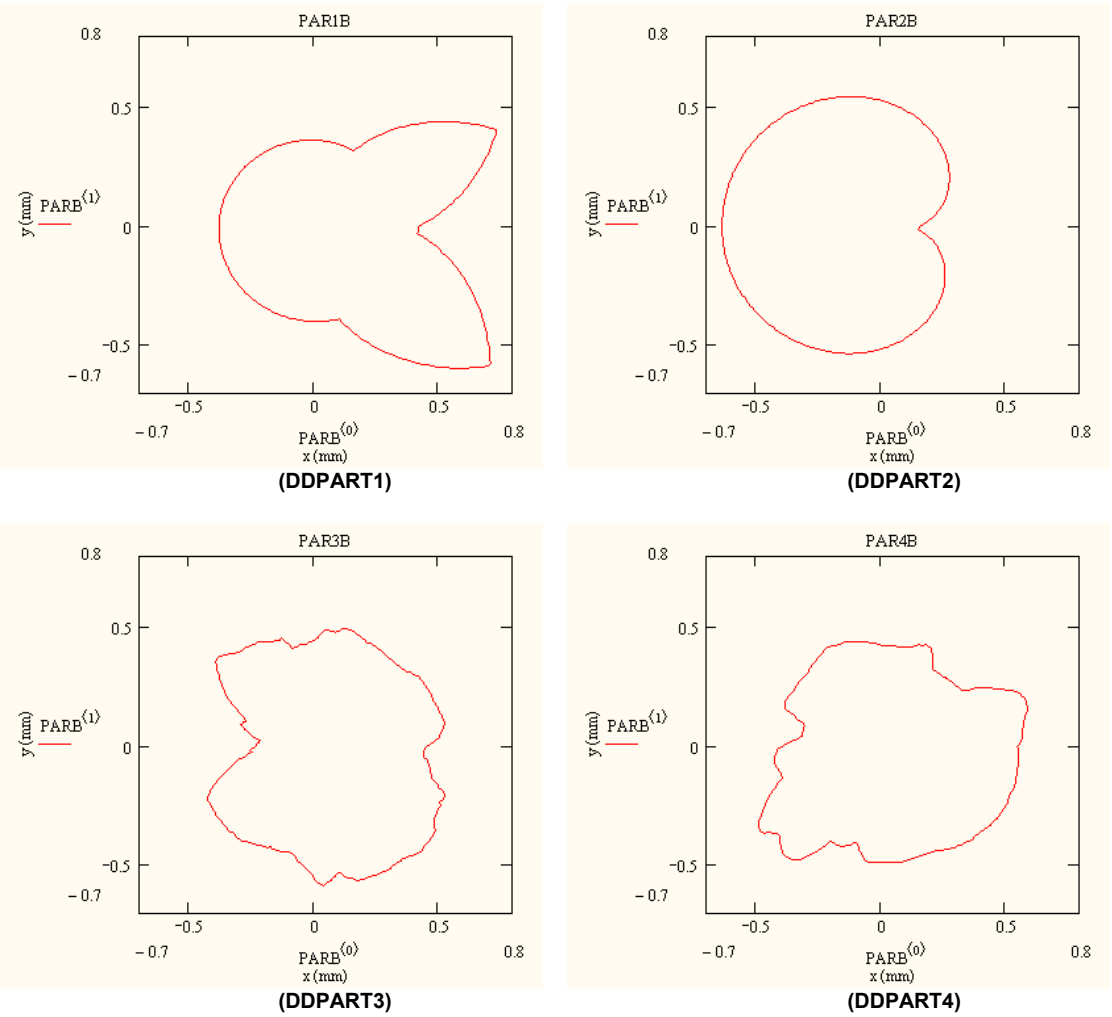


**Figure 3.16 –** Output of *surface wrapping* for the DSURFS of the selected particles during PART-DSURF-DDPART conversion.

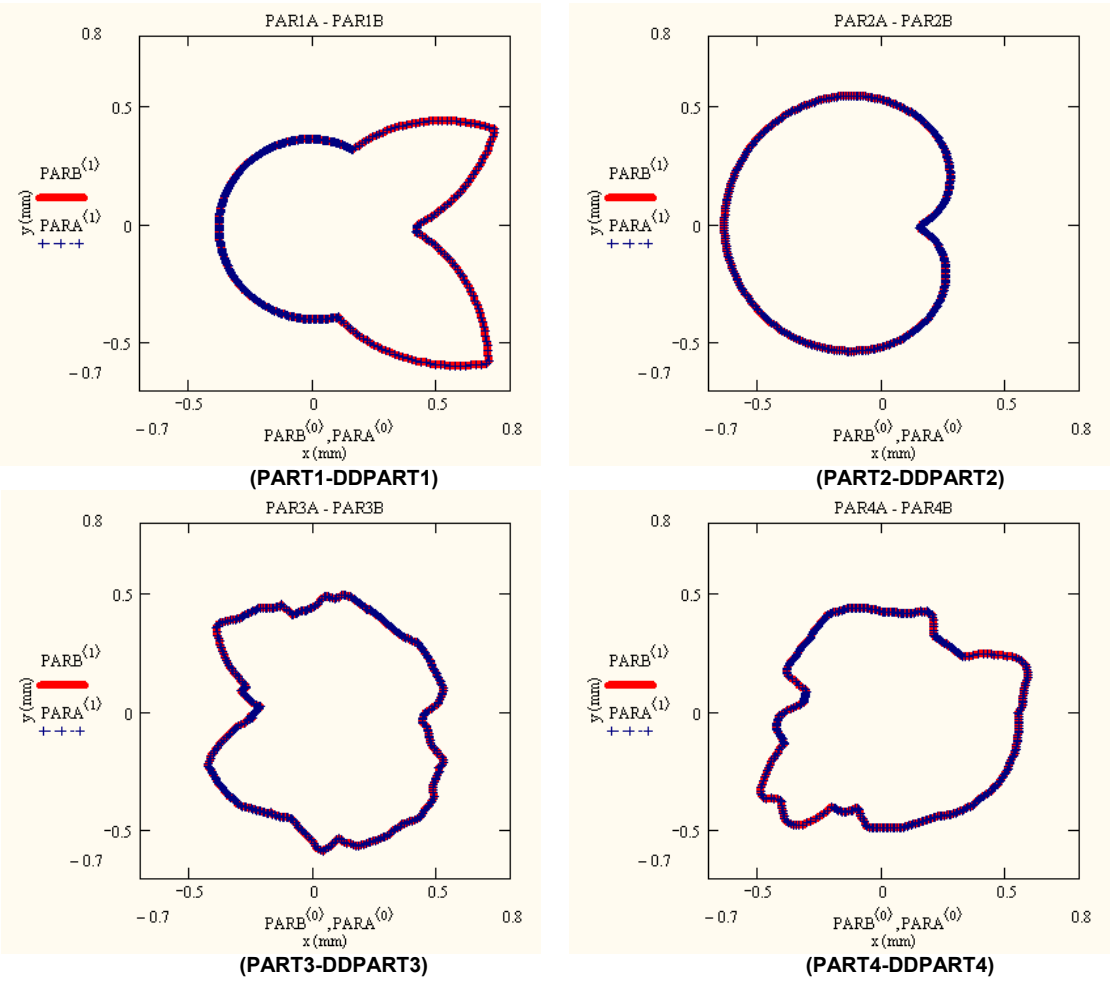


**(PART1-DDPART1)** **(PART2-DDPART2)**

**(PART3-DDPART3)** **(PART4-DDPART4)**

**Figure 3.17 –** Comparison of PART & DDPART for PART-DSURF-DDPART validation.

**Table 3.9–** Procedure for SURF-DPART-DDSURF conversion.

| Process | Surface Wrapping | | Particle Unrolling | | Validation Comparison |
|---|---|---|---|---|---|
| | Input | Output | Input | Output | |
| 1 | SURF1 | DPART1 | DPART1 | DDSURF1 | SURF1 - DDSURF1 |
| 2 | SURF2 | DPART2 | DPART2 | DDSURF2 | SURF2 - DDSURF2 |
| 3 | SURF3 | DPART3 | DPART3 | DDSURF3 | SURF3 - DDSURF3 |
| 4 | SURF4 | DPART4 | DPART4 | DDSURF4 | SURF4 - DDSURF4 |

**Table 3.10–** Surfaces selected for SURF-DPART-DDSURF conversion.

| Abbreviation | Surface Name |
|---|---|
| SURF1 | 60° ridges |
| SURF2 | 2.5 mm arcs |
| SURF3 | 3-mm section of the concrete profile |
| SURF4 | 3-mm section of the HDPE profile |

The output particles, i.e. *dparts,* obtained by processing the four input real surfaces through *surf-dpart algorithm* are shown in Figure 3.19.

The four *dparts* are further input into the *part-dsurf algorithm* to generate the corresponding four *ddsurfs* as shown in Figure 3.20. This process is schematically shown in Figure 3.9 (b).

As explained previously in Section 3.1.2, the *surf-dpart* algorithm requires the rotation of the surface profile prior to wrapping since the elevation of the start and end points of the randomly selected profile are not the same; whereas in *part-dsurf* algorithm no rotations are required. In order to illustrate the superposition property of the conversion, Figure 3.21 shows the input surfaces *(SURF)* shown in Figure 3.18, the rotated surface profiles

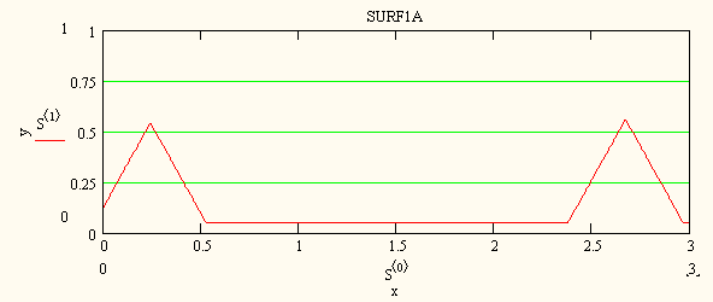


**(SURF1A)**

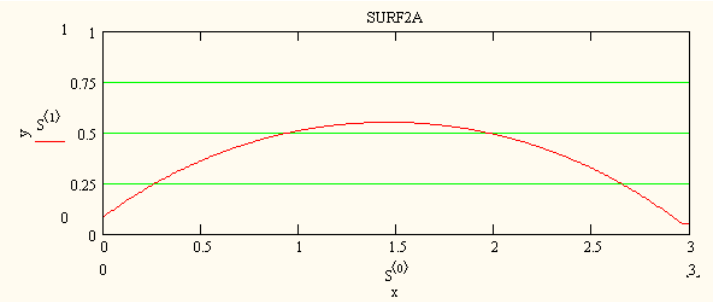


**(SURF2A)**

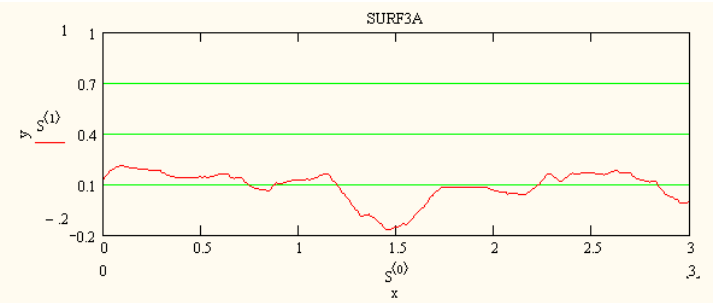


**(SURF3A)**

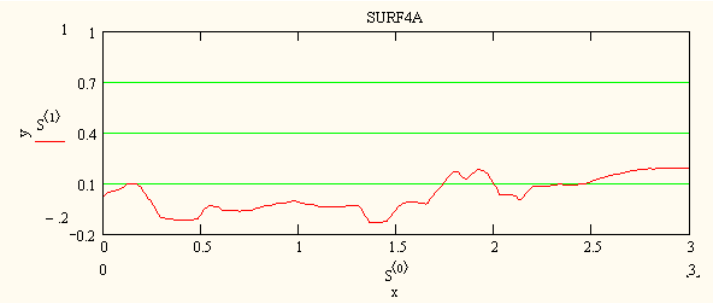


**(SURF4A)**

**Figure 3.18 –** Input surface profiles for SURF-DPART-DDSURF conversion.

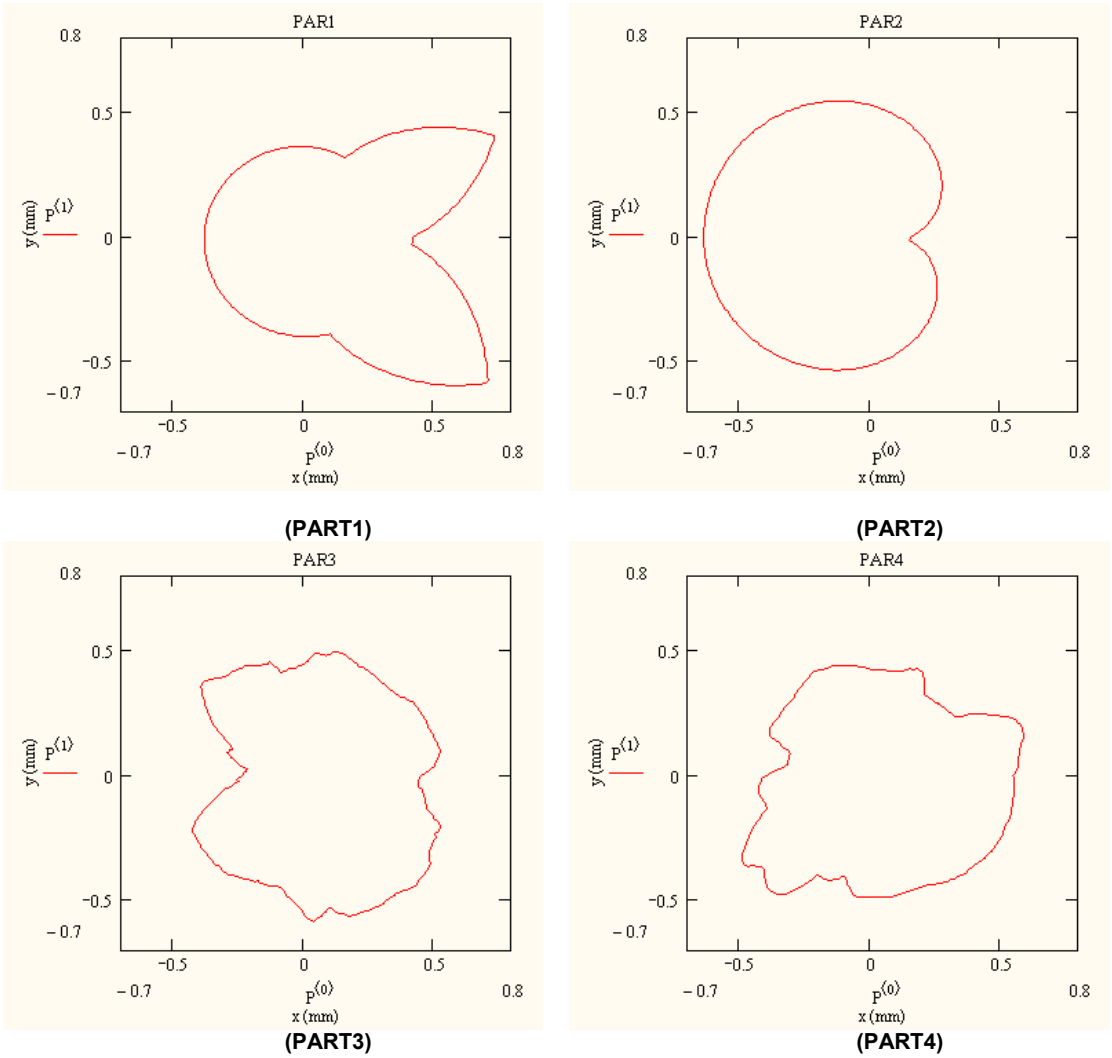


**Figure 3.19 –** Output of *surface wrapping* for the selected surface profiles during SURF-DPART-DDSURF conversion.

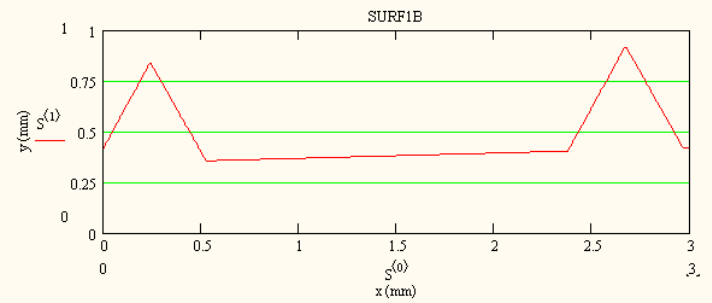


**(SURF1B)**

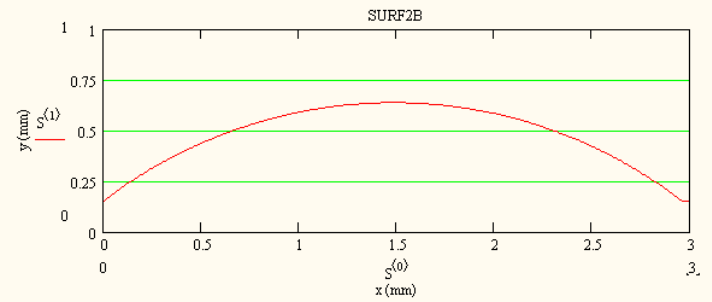


**(SURF2B)**

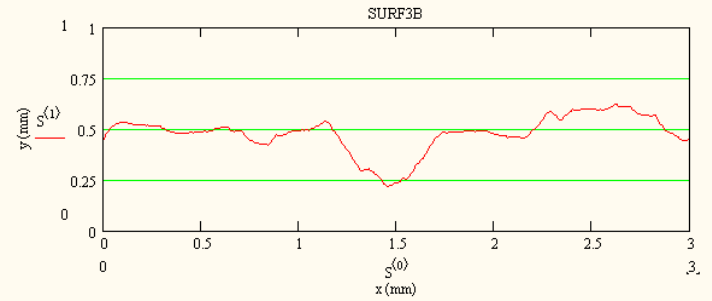


**(SURF3B)**

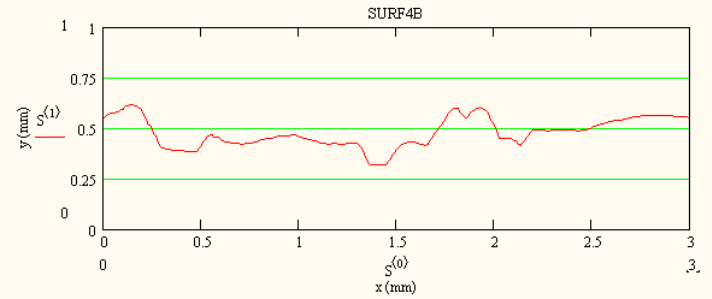


**(SURF4B)**

**Figure 3.20 –** Output of *particle unrolling* for the DPARTS of the selected surface profiles during SURF-DPART-DDSURF conversion.

for the input surfaces (*RSURF*), as well as the generated surface profiles shown in Figure 3.20 as *DDSURF.*

Note that *DDSURF* should be compared to *RSURFA* rather than *SURF*; since, as the particle is unrolled as the final step in *SURF-DPART-DDSURF* conversion, the output profile has already the same start and end –y elevations. As evident from Figure 3.21, *DDSURFB* profiles are elevated compared to the *RSURF* profiles. The elevation difference is not arbitrary for any of the cases and is equal to:

$$elevation \quad difference\,(DDSURF - RSURF) = rdatum - av(RSURF) \tag{3.4}$$

$$rdatum = \frac{3}{2\pi} \tag{3.5}$$

where $rdatum$ stands for the radius of a 3mm-perimeter circle and $av$ stands for the average of *RSURF* –y values. A 3-mm perimeter circle is taken here since the *dsurf* examples shown in Figure 3.20 have 3-mm projected length. In the study materials selected, the real surfaces have 15-mm projected length, in which case a 15mm perimeter circle is used.

As already noted in Section 3.1.2, for *surf-dpart* algorithm, the surface elevation points for real surfaces (taken as 15-mm length, 0.004mm resolution) are processed through the following equation.

$$r_i = (r_{circle\ of\ 15mm}) + ysurfac\ e_i - yaverage \tag{3.6}$$

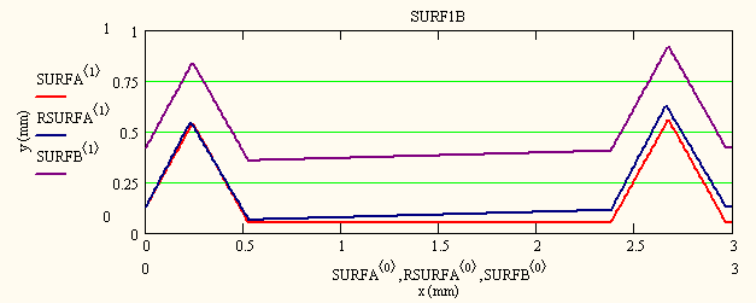


**(DDSURF1)**

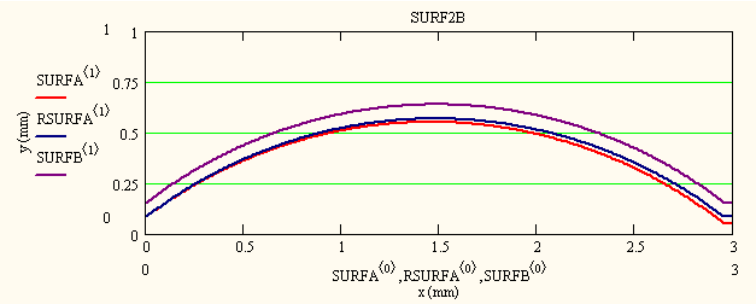


**(DDSURF2)**

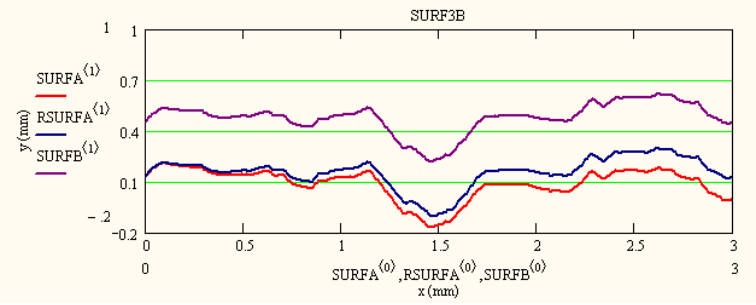


**(DDSURF3)**

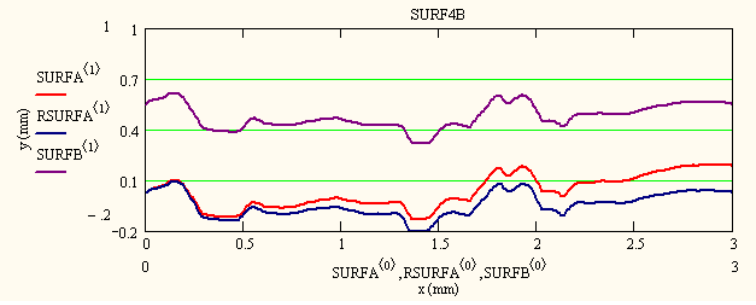


**(DDSURF4)**

**Figure 3.21 –** SURF, RSURF, and DDSURF for the SURF-DPAR-DDSURF conversion.

However, in this exercise for the validation of the algorithms, since 3-mm section profiles are used as the input, this equation is modified to Eq. 3.6:

$$r_i = (r_{circle\ of\ 3mm}) + ysurfac\ e_i - yaverage \quad \textbf{(3.6)}$$

The values corresponding to $av(RSURF)$ and $elevation \quad diffference(DDSURF - RSURF)$ for each study case are tabulated in Table 3.11. Note that in this study $rdatum$ is taken as constant and equal to 0.477.

**Table 3.11 –** Numerical values in relation to the four study cases.

| Surface | Average (RSURF) | Elevation difference |
|---|---|---|
| DDSURF1 | 0.185 | 0.292 |
| DDSURF2 | 0.407 | 0.07 |
| DDSURF3 | 0.156 | 0.322 |
| DDSURF4 | -0.047 | 0.524 |

Thus, in order to reverse the process, the elevation difference value specific for each one of the four cases is subtracted from the *DDSURF* elevation values to obtain *DDSURF2* profiles for comparison as shown in Figure 3.22.

This section clearly demonstrates that *surf-dpart* and *part-dsurf* algorithms can be used to wrap a surface and unroll a particle, respectively. The *dpart* and *dsurf* obtained from this process can further be converted to *ddsurf* (by *part-dsurf algorithm*) and *ddpart* (by *surf-dpart algorithm*), where *ddsurf* and the initial input of *surf* and *ddpart*

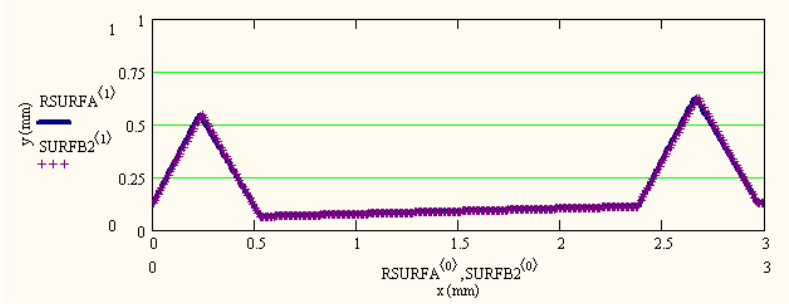


**(RSURF(1)-DDSURF2(1))**

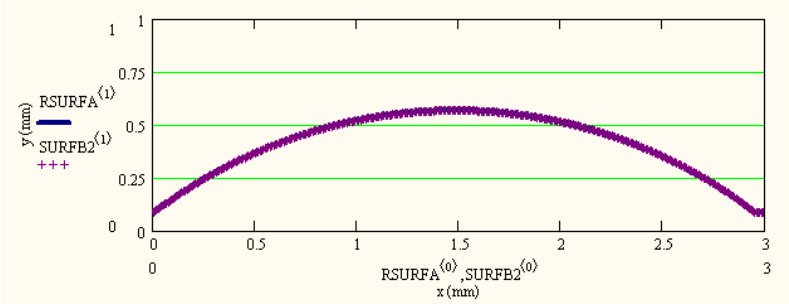


**(RSURF(2)-DDSURF2(2))**

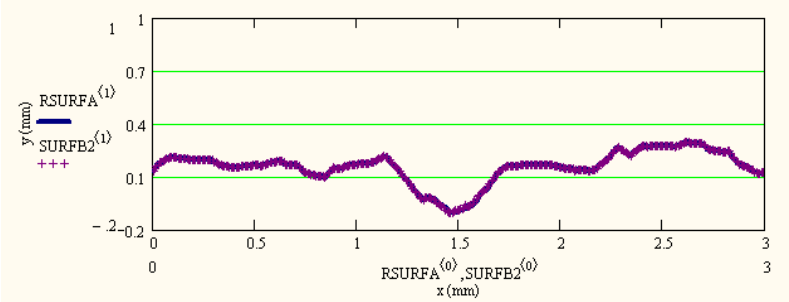


**(RSURF(3)-DDSURF2(3))**

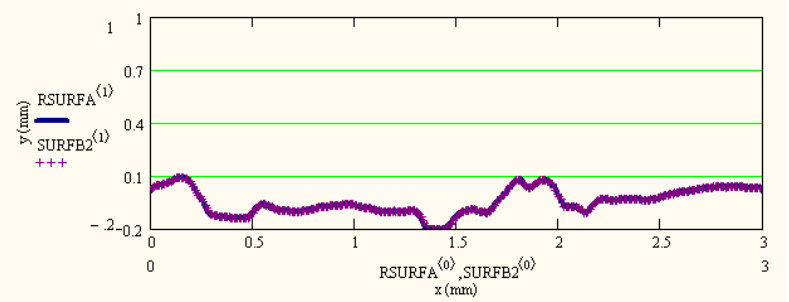


**(RSURF(4)-DDSURF2(4))**

**Figure 3.22–** Comparison of RSURF & DDSUF2 for validation.

and the initial input of *part* match exactly. By being able to apply to a *surf* first *surf-dpart algorithm* to wrap *dpart* and then apply *part-dsurf algorithm* to *dpart* to obtain the unrolled surface, *ddsurf*; where *surf* and *ddsurf* are equivalent, the superposition property of the algorithms is proven.

As the final product of the above algorithms, the real and derived particles and the real and derived surfaces are shown in Figure 3.23 and Figure 3.24, respectively.

## 3.3 Analysis of Particle Shape Characterization Methods

Throughout this section and the following section on surface profiles, the analysis is performed with mathgrams developed by the author. The names and the properties of the mathgrams are provided in Appendix A. Appendix A also provides information regarding the abbreviations used for the mathgram input and outputs. Note that since most of the mathgrams are integrated into each other, the outputs and input abbreviations utilized in Appendix A do not necessarily coincide with the inputs and outputs used within the following sections explaining the calculation methods and mathgrams. This difference is only valid for the input and output abbreviations. The function and name of mathgrams are the same as referred to in the following sections.

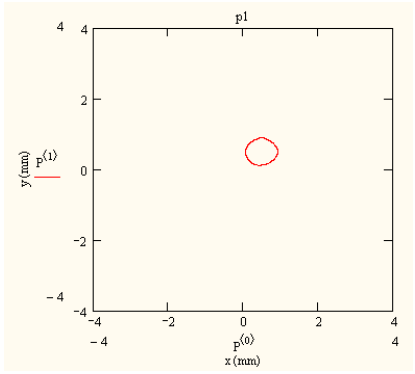


(p1)

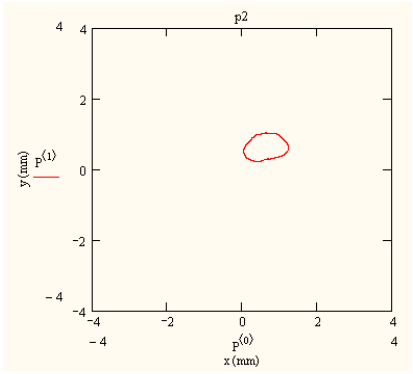


(p2)

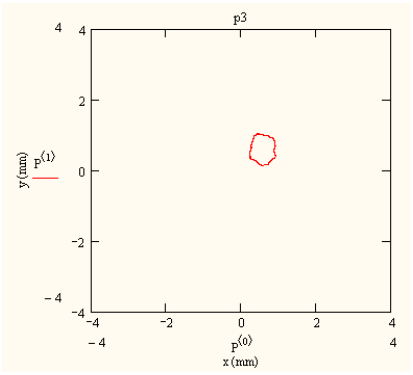


(p3)

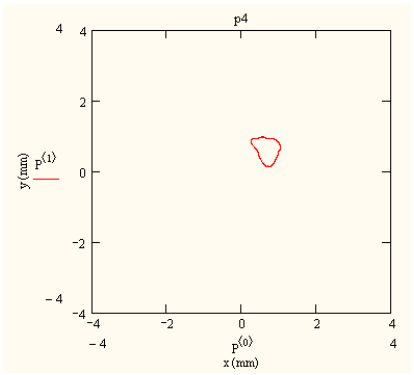


(p4)

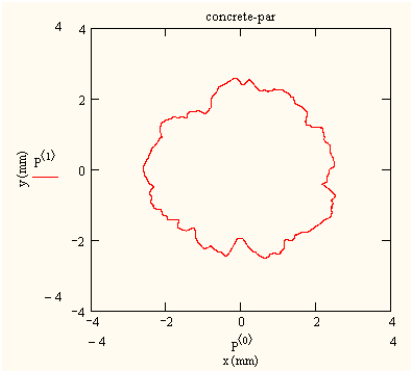


(concrete-par)

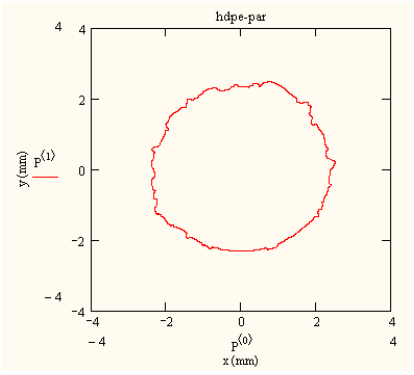


(HDPE-par)

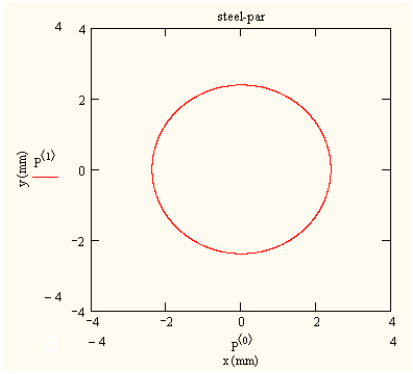


(a)

**Figure 3.23-** Real and derived study particles outlines.

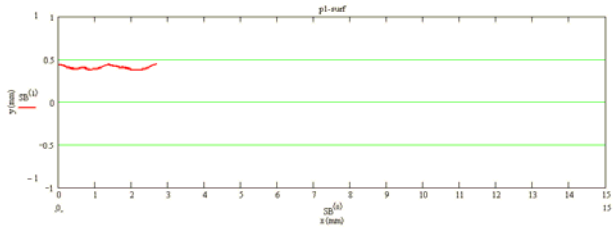

(p1-surf)

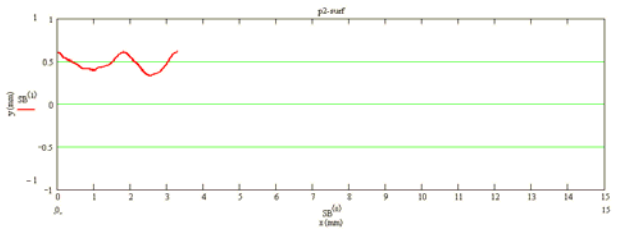

(p2-surf)

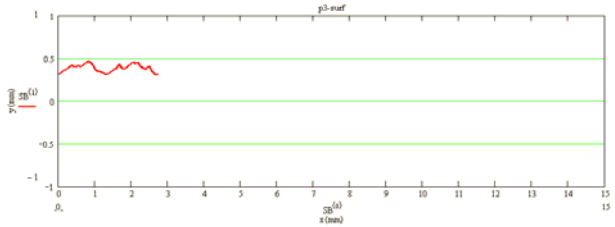

(p3-surf)

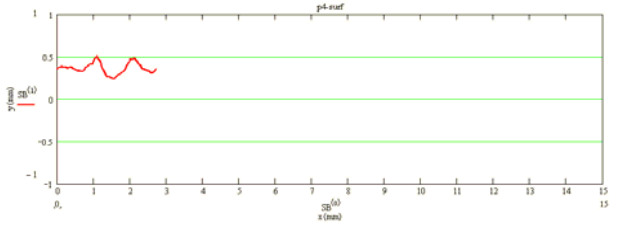

(p4-surf)

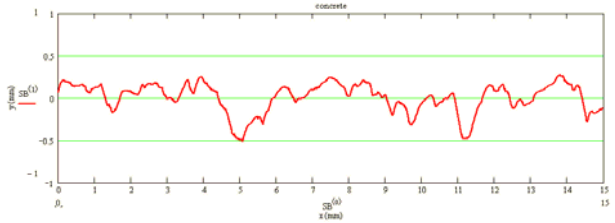

(concrete)

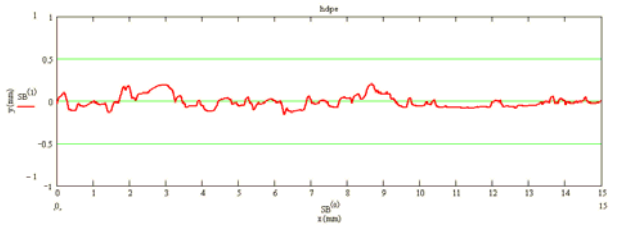

(HDPE)

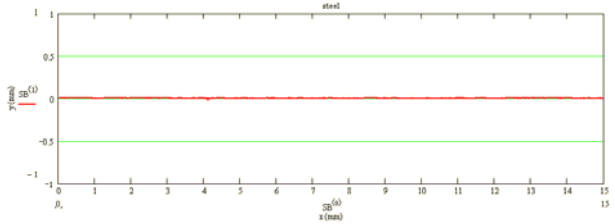

(steel)

**Figure 3.24 –** Real and derived study surface profiles.

### *3.3.1 Image to Particle Outline Procedure - Outline Extraction Algorithm*

In order to perform shape parameter analysis on particles, the images need to be converted to digital data. In doing so, special attention needs to be given to spot concavity along the particle outline. An algorithm able to convert images to digital pixel coordinate data has been developed in this study and the same algorithm is used for all the parameters analyzed. The algorithm explained below is termed as $outline(A, thr)$, where $thr$ stands for the threshold value of pixel distance for concavity analysis.

Mathcad 2001 Professional automatically enables image reading into a matrix corresponding to the grayscale representation of a *.bmp file; such that in the output matrix with a 256-color model, *0* and *255* represent black and white pixels, respectively. Every matrix element corresponds to a single pixel in the image. Any number outside the region *0-255* is represented as modulo 256. It is important to acquire images with high contrast between the particle itself and background so that the particle boundary can be extracted from the background.

The objective is to obtain the boundary in a $(x, y)$ data format. This algorithm extracts the outline in clockwise order. The number of rows and columns in the matrix are denoted as *rows* and *cols,* respectively. In the description below, *i and j* stand for the row and column indices, respectively. In addition, the first and last boundary points extracted in the *ith* scan are denoted as $(xst_i, yst_i)$ and $(xend_i, yend_i)$, respectively. The -*x* coordinate denotes the row index and –*y* coordinate denotes the column index for that specific pixel. The general methodology applied is:

- *First scan (right to left)*
    - Start at *i=0*,
        - For every row, search pixels from *cols* to *j=0*.
        - Stop when 3 consecutive *255* pixel values are encountered in a row. Store the 1st encountered pixel as a boundary pixel.
        - Proceed with the next row
    - Repeat row search until *i=rows*.
- *Second Scan (bottom to top)*
    - Start at the $j = yend_1$
    - For every column, search pixels from $i = xend_1$ to $i = 0$.
    - Stop when 3 consecutive *255* pixel values are encountered in a column. Store the 1st encountered pixel (of the three) as a boundary pixel.
    - Proceed with the next column.
    - Repeat column search until *j=0.*
- *Third scan (left to right)*
    - Start at $i = xend_2$,
        - For every row, search pixels from *j=0* to *cols.*
        - Stop when 3 consecutive *255* pixel values are encountered in a row. Store the 1st encountered pixel as a boundary pixel.
        - Proceed with the next row
    - Repeat row search until *i=0*.
- *Fourth Scan (top to bottom)*
    - Start at the $j = yend_3$
    - For every column, search pixels from $i = xst_1$ to *i=rows*.

- Stop when 3 consecutive *255* pixel values are encountered in a column. Store the 1st encountered pixel (of the three) as a boundary pixel.
- Proceed with the next column.
- Repeat column search until $j = yst_1$.

This search method is similar to the convex hull extraction as schematically shown in Figure 2.14.

However, note that with the above algorithm, reentrant parts of the boundary can be overlooked. The methodology used to manage concavity is explained next.

During the scan process, concavity can be anticipated when the Euclidean distance between the two consecutive pixels is above a threshold value. In that case, an intermediate scan is initiated in clockwise manner shifting to a column search if rows are being scanned or vice versa. There are different concavity situations for each four scans explained above. During a specific scan if point $(x_i, y_i)$ and $(x_{i+1}, y_{i+1})$ are two consecutive boundary pixels identified and if the Euclidean distance between the two pixels is above the threshold value, the following intermediate scans are performed:

- Concavity in First Scan $x_i < x_{i+1}$ :
  - If $y_i > y_{i+1}$, scan starts from $(x_{i+1}, y_i)$. For every column until $j = y_{+!i}$, search is made from to $i = x_{i+1}$ $i = 0$.
  - If $y_i < y_{i+1}$, scan starts from $(x_{i+1}, y_i)$. For every column until $j = y_{i+1}$, search is made from $i = x_{i+1}$ to $i = rows$.
- Concavity in Second Scan $y_i > y_{i+1}$ :

- If $x_i > x_{i+1}$, scan starts from $(x_i, y_{i+1})$. For every row until $i = x_{i+1}$, , search is made from $j = y_{i+1}$ to $j = cols$.
- If $x_i < x_{i+1}$, scan starts from $(x_i, y_i)$. For every row until $i = x_{i+1}$, search is made from $j = y_i$ to $j = 0$.

- Concavity in Third Scan $x_i > x_{i+1}$ :
  - If $y_i > y_{i+1}$, scan starts from $(x_i, y_i)$. For every column until $j = y_{i+1}$, , search is made from $i = x_i$ to $i = 0$.
  - If $y_i < y_{i+1}$, scan starts from $(x_{i+1}, y_i)$. For every column until $j = y_{i+1}$, search is made from $i = x_{i+1}$ to $i = rows$.
- Concavity in Fourth Scan $y_i < y_{i+1}$ :
  - If $x_i > x_{i+1}$, scan starts from $(x_i, y_i)$. For every row until $i = x_{i+1}$, , search is made from $j = y_i$ to $j = cols$.
  - If $x_i < x_{i+1}$, scan starts from $(x_i, y_{i+1})$. For every row until $i = x_{i+1}$, search is made from $j = y_{i+1}$ to $j = 0$.

The quantification of threshold value is determined based on distance properties of the particle images obtained. That is, for particles in this study, the mean and maximum Euclidean distance between two consecutive boundary pixels are determined. The real particles analyzed in this study attains in average 695 boundary pixels. Based on numerical experiments, the Euclidean distance of 10 pixels is selected for concavity threshold. Thus, the intermediate searches are initiated if the distance between two consecutive boundary pixels is above 10 pixels.

When required based on the algorithm generated for the shape parameter, the outline generated was reversed to obtain counterclockwise order. The outlines generated through the abovementioned process are shown in Figure 3.25.

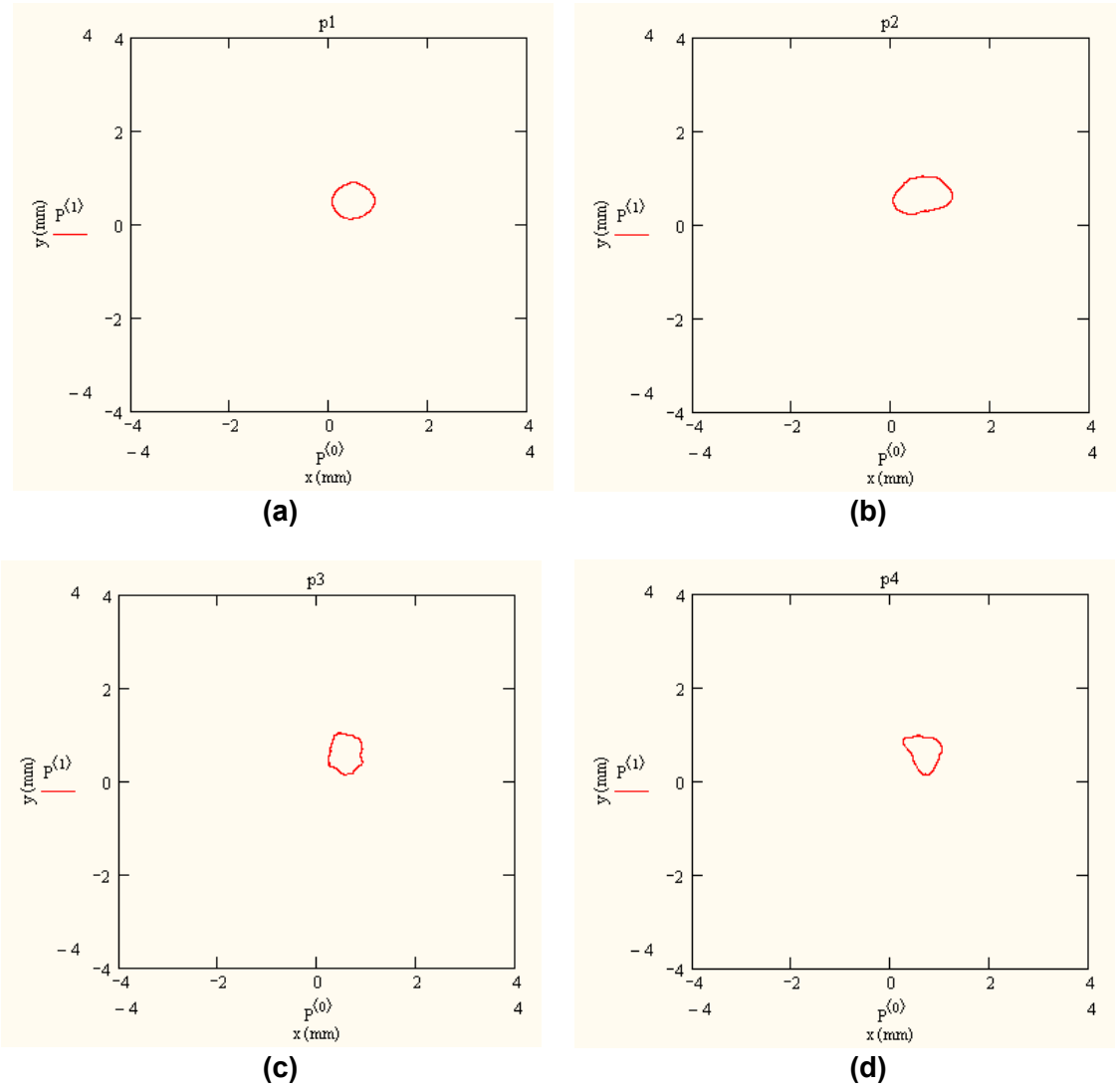


**Figure 3.25 –** Real particle outlines; **(a)** p1, **(b)** p2, **(c)** p3, and **(d)** p4.

### *3.3.2 Selection of Particle Shape Parameters*

Numerous studies have been conducted in particle shape analysis as reviewed in Section 2.3.1 resulting in abundant particle shape parameters. This analysis focuses on only a number of the available particle shape parameters. The selected parameters are based on multiple measurements along the particle outline rather than single measurements that may lead to inaccurate classification of the particle shape such as the aspect ratio. The parameters selected are single-number classifiers, i.e. a single parameter value is obtained rather than shape representation by series. Parameters address different processes. In other words, based on the specific field of study, certain shape characteristics/dimension may be more dominant than others in the development of a parameter. A number of particle shape parameters investigate particle mass behavior rather than individual particles. Some examples include parameters that focus on effects of shape on particles' hydraulic properties (e.g. Dynamic Shape Coefficient), void changes when particle mass is compacted into a standard mold (e.g. Particle Index), on particle rolling motion on an angled surface (e.g. Rollability Shape Factor). In this study, the main objective is to define a unified approach to particles and surfaces involved in interfaces. Thus, parameters that relate broadly to abrasiveness are considered. In addition, the simplicity, objectiveness, and robustness in parameter determination process is taken into account.

The selected particle shape parameters include Sukumaran and Ashmawy Shape and Angularity Factors, Wadell's Roundness, Stachowiak and Hamblin Spike Parameter and Spike Parameter Quadratic, and Boyce and Clark Shape Index. In addition, a new particle shape parameter, Characteristic Radius Ratio (CRR) is defined by utilizing

Voronoi Diagrams. This is inspired by computational geometry "roundness" calculation techniques as further clarified in Section 3.3.7.

### *3.3.3 Sukumaran and Ashmawy Form Factor*

Sukumaran and Ashmawy (2001) defined Form Factor (FF) as a function of Shape and Angularity Factors as explained in Section 2.3.1.2.1. In the following discussion, Shape and Angularity Factors are abbreviated as SF and AF, respectively. The computer programs for SF and AF are written in Mathcad 2001 Professional and the FF is computed from the calculated SF and AF. The modifications from the outlined procedure by Sukumaran and Ashmawy (2001) are explained below.

In their study, Sukumaran and Ashmawy (2001) extract the particle outline from particle images using 9° intervals. However, in this study, the outlines extracted from particle images are not in this format, i.e. with 9° spaced data points. Thus, mathgrams are used to convert the outline to this format. As explained in Section 3.3.1, the outline extraction algorithm is used to obtain the outline in clockwise order. However, for SF and AF analysis, it is perceived appropriate to sort the outline data such that it is counter-clockwise and starts from angle 0. Thus, the outline extraction is followed by another algorithm $zeroanglecounterclockwise(A)$, with a counterclockwise direction output of $[x, y]$ coordinates of the particle $A$. Depending on the chosen angle, the number of intervals, $N$, is determined. In case 9° angle intervals are used, $N$ is input as 40. Subsequently, algorithm $ParticleShape(A, N)$ calculates the centroid of the polygon by area averaging and measures the angle of each outline point in $A$ with respect to the $+x$ axis. For

every sampling radial (e.g. at $9°,18°,27°,\ldots\ldots,360°$), a pair of outline points ( $po\,\mathrm{int}_i$ and $po\,\mathrm{int}_{i+1}$ ) is determined, such that the angle corresponding to the sampling radial line $asample_j$ is between the angle of $po\,\mathrm{int}_i$ and angle of $po\,\mathrm{int}_{i+1}$. Since an outline data point at a certain degree is required, which may not be available from image scanning process, the two points $po\,\mathrm{int}_i$ and $po\,\mathrm{int}_{i+1}$ are joined by a straight line and the $IntPts\,(A,N)$ mathgram finds the intersection of the joined line with the radial sampling line at $asample_j$. The intersection point is located along the straight line between the two endpoints ( $po\,\mathrm{int}_i$ and $po\,\mathrm{int}_{i+1}$ ). The output from $IntPts\,(A,N)$ outline is basically the particle outline sampled at predetermined angle intervals. From here forward, no modifications were engaged for the calculations and the procedure suggested by Sukumaran and Ashmawy (2001) is followed.

The outline is sampled at every $9^\circ$, i.e. $N=40$ as recommended by Sukumaran and Ashmawy (2001). Sukumaran and Ashmawy (Personal Communication, 2004) data points and the corresponding SF and AF numbers calculated by them is obtained and used for algorithm validation. For validation, 10 grains were available and the results are shown in Table 3.12.

Graphs showing the trend for the two sets of data and the regression analysis between the calculated and reported SF values are presented in Figure 3.26 (a) and (b), respectively. Similarly, Figure 3.27 (a) and (b) show the trend and regression analysis between the calculated and reported AF values, respectively.

**Table 3.12 –** Calculated and the reported SF and AF values for 10 grains (Ashmawy, 2004).

| Grain No | SF*(reported) | SF*(calculated) | AF*(reported) | AF*(calculated) |
|---|---|---|---|---|
| 1 | 42.361 | 41.767 | 8.2435 | 7.055 |
| 2 | 27.976 | 27.328 | 10.5174 | 9.392 |
| 3 | 41.246 | 41.61 | 13.0764 | 11.653 |
| 4 | 48.381 | 46.581 | 21.6609 | 20.914 |
| 5 | 27.196 | 26.745 | 12.2670 | 11.576 |
| 6 | 56.752 | 55.536 | 25.3426 | 27.555 |
| 7 | 46.722 | 45.77 | 13.9069 | 13.576 |
| 8 | 41.836 | 41.01 | 19.0912 | 18.178 |
| 9 | 33.712 | 32.01 | 12.9106 | 11.917 |
| 10 | 31.457 | 30.167 | 16.5333 | 15.864 |

* All SF and AF values are in %.

The study by Sukumaran and Ashmawy (2001) also proposed a combined shape parameter referred to as the Form Factor (FF), which is calculated by:

$$Form\ Factor = \sqrt{(Shape\ Factor)^2 + (Angularity\ Factor)^2} \quad \textbf{(3.7)}$$

The FF is not calculated numerically by Sukumaran and Ashmawy (2001) in their study, i.e. only SF and AF are reported. However, to see the correlation between the calculated and reported FF values, the calculated SF and AF by Sukumaran and Ashmawy (2001) is used in Eq. 3.7 to determine the reported FF values for the 10 grains in Table 3.12. Table 3.13 shows the Form Factors calculated from the reported SF and AF values as Form Factor (reported) and the Form Factors that are calculated using the proposed mathgram as Form Factor (calculated).

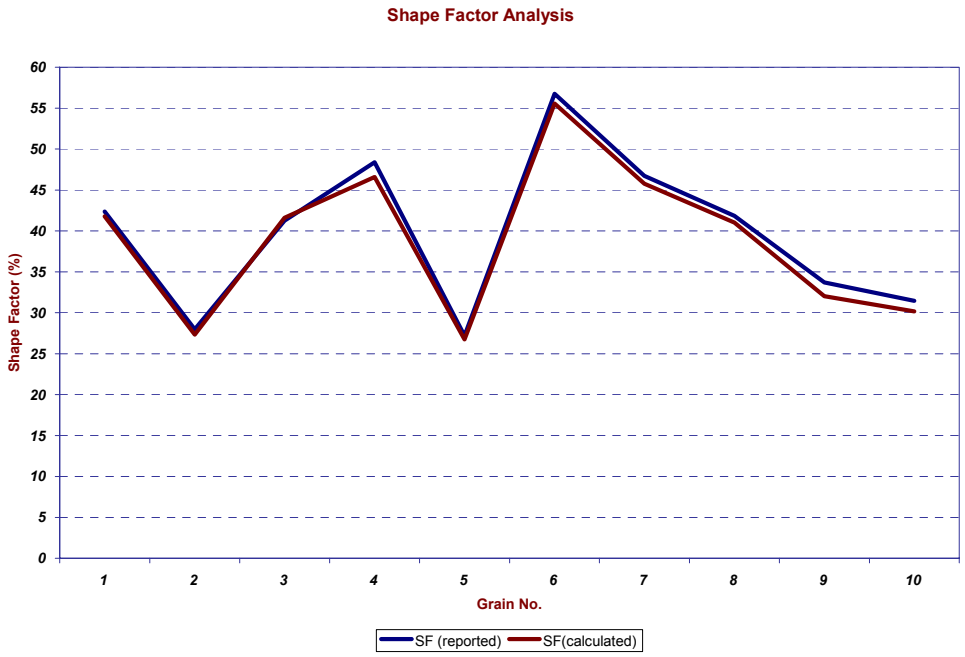


**(a)**

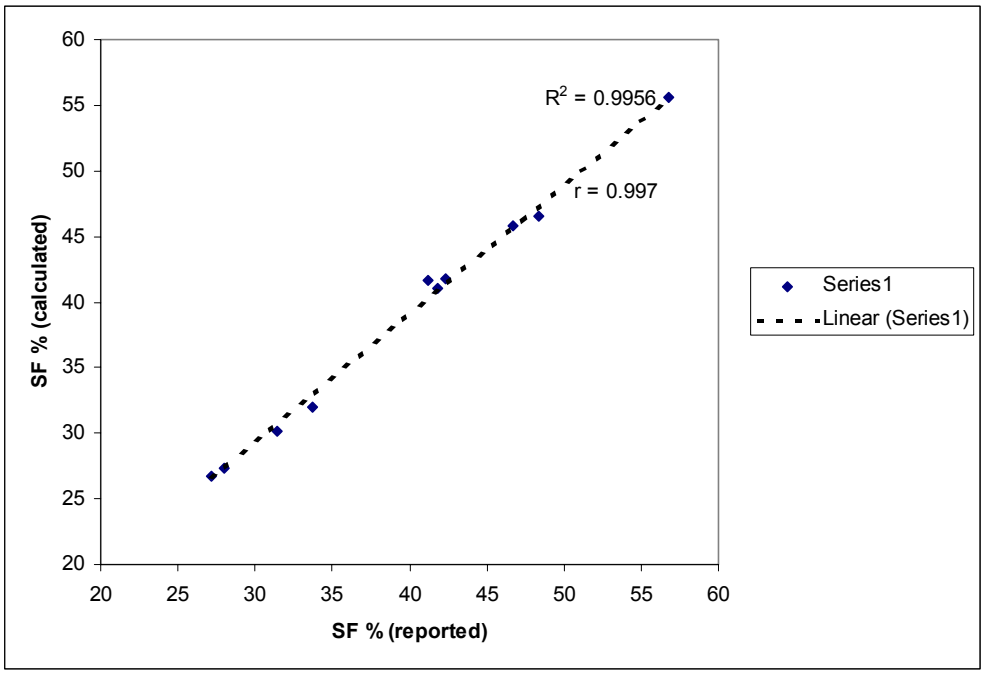


**(b)**

**Figure 3.26 – (a)** Graph showing the trend of SF (calculated) and SF (reported) for the 10 grains used for validation, **(b)** Plot of regression analysis between the calculated and reported SF for the 10 grains used for validation.

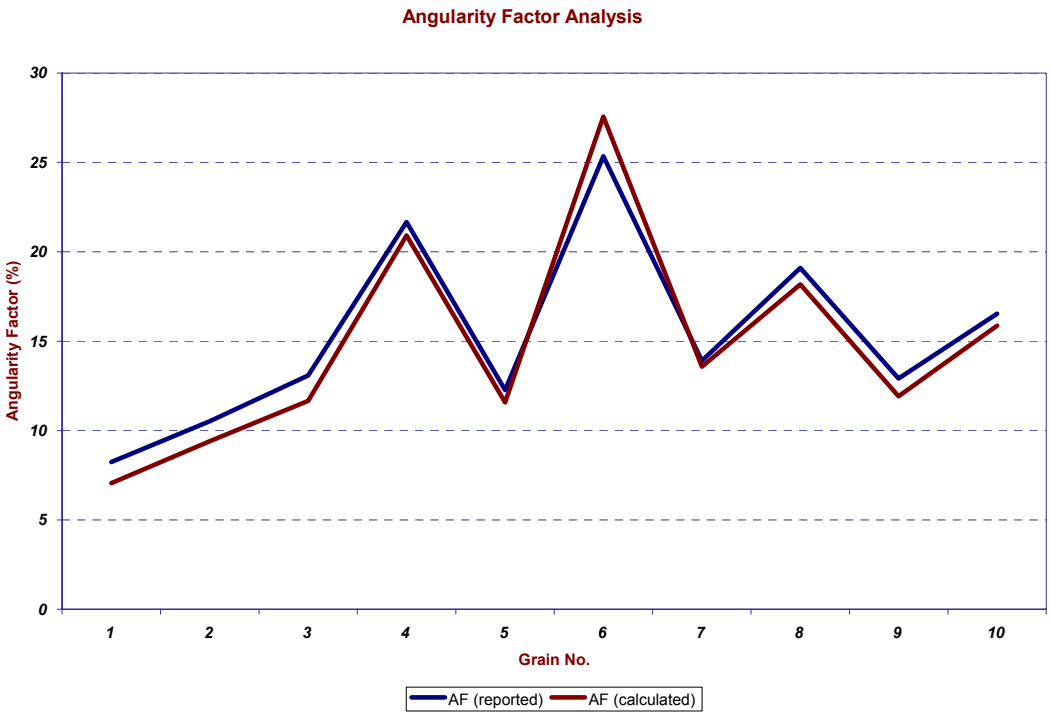


**(a)**

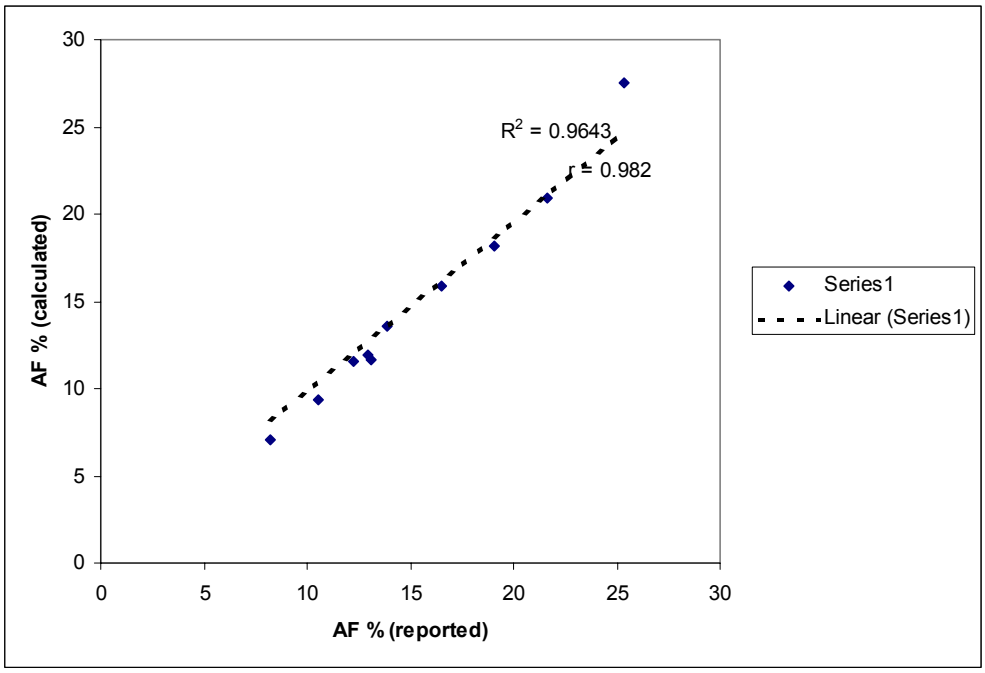


**(b)**

**Figure 3.27 – (a)** Graph showing the trend of AF (calculated) and AF (reported) for the 10 grains used for validation, **(b)** Plot of regression analysis between the calculated and reported AF parameters for the 10 grains used for validation.

**Table 3.13 –** Table of FF values from the reported and calculated SF and AF for 10 grains (Ashmawy, 2004).

| Grain No. | FF* (reported) | FF* (calculated) |
|---|---|---|
| 1 | 43.2 | 42.4 |
| 2 | 29.9 | 28.9 |
| 3 | 43.3 | 43.2 |
| 4 | 53.0 | 51.1 |
| 5 | 29.8 | 29.1 |
| 6 | 62.2 | 62.0 |
| 7 | 48.7 | 47.7 |
| 8 | 46.0 | 44.9 |
| 9 | 36.1 | 34.2 |
| 10 | 35.5 | 34.1 |

* All FF values are in %.

Figure 3.28 (a) and (b) show the trend and regression charts between the reported and calculated FF, respectively. As reported on Figure 3.28 (b), the correlation between the two sets of data is $r = 0.997$, which is considered acceptable. Thus, the same algorithm developed for the validation will be used for the analysis of the study particles.

### *3.3.4 Minimum Zone Circles using Voronoi Diagrams*

#### 3.3.4.1 Particle Shape Characterization by Three Circles Analysis using Characteristic Radius Ratio

A new particle shape parameter is developed using Voronoi Diagrams and the circles associated with the Diagrams, i.e. Maximum Inscribing Circle (MIC) and Minimum Circumscribing Circle (MCC).

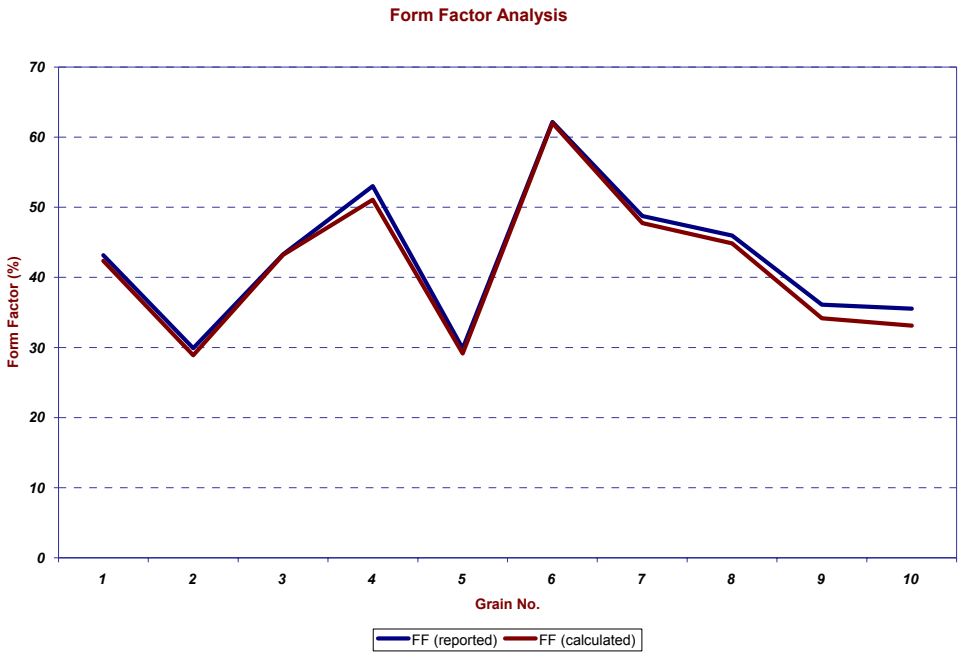


**(a)**

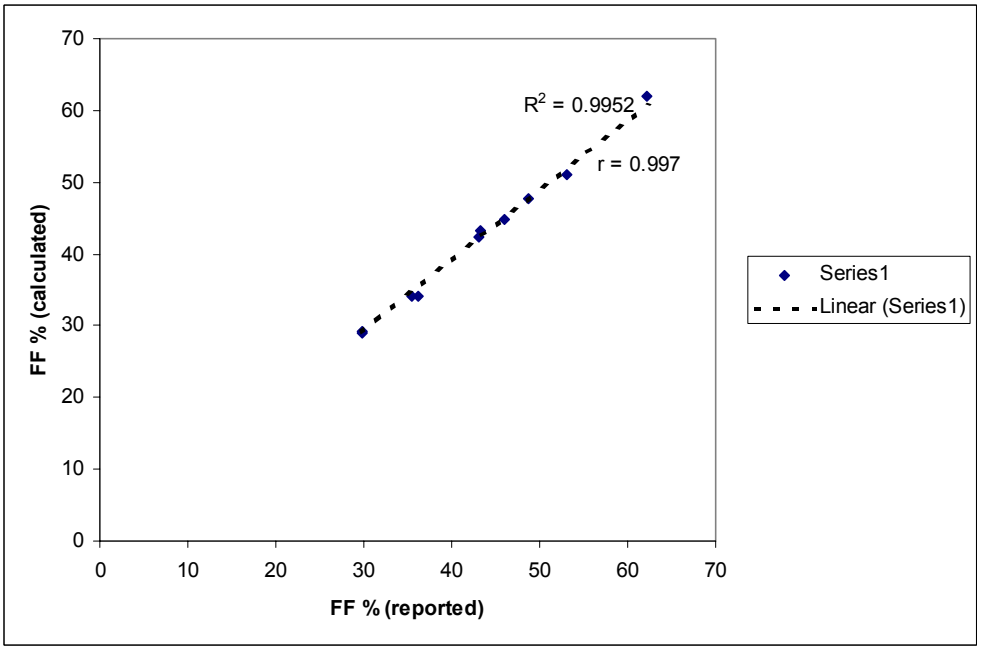


**(b )**

**Figure 3.28 - (a)** Graph showing the trend of FF (calculated) and FF (reported) for the 10 grains used for validation, **(b)** Plot of regression analysis between the calculated and reported FF parameters for the 10 grains used for validation

The computer programs for Voronoi diagram calculation are written in Mathcad 2001 Professional. The modifications to the convex hull calculation and the subsequent Voronoi diagram calculations are summarized below.

If the available input is the gray-scale image of the particle rather than the 2D outline data points, $outline(A, row, col)$ followed by $reverseorder(A)$ is used initially to obtain the 2D outline data points.

With the input as the $(x_i, y_i)$ coordinate points, for the *convex hull determination,* the algorithm proposed by Ye (1995) is used (Section 2.3.1.1.2). The algorithm is performed in two stages. The first task is *polygon extraction,* for which the mathgram $polygonextract(A, E, w)$ is used. The input parameters are:

- $A$ is the matrix containing the $(x_i, y_i)$ particle boundary coordinates in clockwise direction for $i = \{0,1,2,\ldots\ldots,n-1\}$, where $n$ is a positive integer.
- $E$ specifies the distance away from the extremities of the particle outline, that is distance from the leftmost, uppermost, rightmost and bottommost data points of the outline. Each time the scan needs to start/stop from/at the boundary, it looks for the most extreme point located in the previous search. If no priori selected point exists, the margin is stretched $E$ units from the $\max$ or $\min$ extremes of the $x$ and $y$ coordinates. Note that the scan was performed in a clockwise manner; i.e. the first scan is from top to bottom, the second scan is from right to left, the third scan is from bottom to top, and the fourth and last scan is from left to right.
- $w$ designates the number of significant points for the input coordinates. The inputs are at least with $w = 0.01$.

Upon extracting the polygon, the convex hull is determined via $convexhull(A,E,w)$, which calls upon $polygonextract(A,E,w)$ and performs the necessary convexity inspections. The convex hull extraction procedure suggested by Ye (1995) is implemented as described in Section 2.3.1.1.2 utilizing the mathgram $convexhull(A,E,w)$ with the only variation that $P$ is taken as:

$$P_j = -[(x_{j+1} - x_j)(y_{j+2} - y_{j+1}) - (y_{j+1} - y_j)(x_{j+2} - x_{j+1})] \quad \textbf{(3.8)}$$

Note that the polygon is convex iff all the turns are “right turn”. If a turn is not a “right turn”, it is either a “left turn” or the points are “collinear”.

The output of $convexhull(A,E,w)$ is a $[n+1,3]$ matrix, $S$, with $n$ as the number of convexhull points extracted. The convexhull matrix $S$ is:

$$S = \begin{bmatrix} x_0 & y_0 & 0 \\ x_1 & y_1 & 1 \\ \vdots & \vdots & \vdots \\ x_{n-1} & y_{n-1} & n-1 \\ x_0 & y_0 & 0 \end{bmatrix} \quad \textbf{(3.9)}$$

Note that the matrix $S$ contains the $(x_i, y_i)$ convexhull coordinates in the first two columns, and the index number corresponding to these points in the third column. The output of $convexhull(A,E,w)$ is the input for the Voronoi diagram mathgram.

The Voronoi diagram algorithm is written in Mathcad 2001 Professional. The algorithm is in accordance with the technique proposed by Samuel & Shunmugam (2000). The output is a $[5,1]$ matrix denoted as $GQ$:

$$GQ = \begin{bmatrix} MZC\ x_{center} \\ MZC\ y_{center} \\ MCC\ radius \\ MIC\ radius \\ MZ\ radius \end{bmatrix} \quad \textbf{(3.10)}$$

,where $MZC\ x_{center}$ and $MZC\ y_{center}$ are the $(x, y)$ coordinates of the Minimum Zone Circles (MZC) center. The outputs $MCC\ radius$ and $MIC\ radius$ are the Minimum Circumscribing Circle (MCC) and the Maximum Inscribing Circle (MIC) radii, respectively. The $MZ\ radius$ denotes the Minimum Zone radius, which corresponds to the difference between the MCC and MIC radii. In computational geometry, the value $MZ\ radius$ is termed as circularity.

The calculated MCC and MIC radii values are used to develop a new parameter as an extension to the Centroid Trace analysis performed by DeJong (2001).

DeJong (2001) used a circular 2D particle traversing a theoretical surface and developed a Centroid Trace profile for a range of diameter (0.075 mm – 20 mm). The Centroid Trace profile indicated that the particle behaves as a low-pass filter and removes features that are insignificant with respect to its size. Figure 3.29 clearly reveals the importance of relative size between surface features and particles at the interface. As the particle size increases for the same surface features, the size of the valley

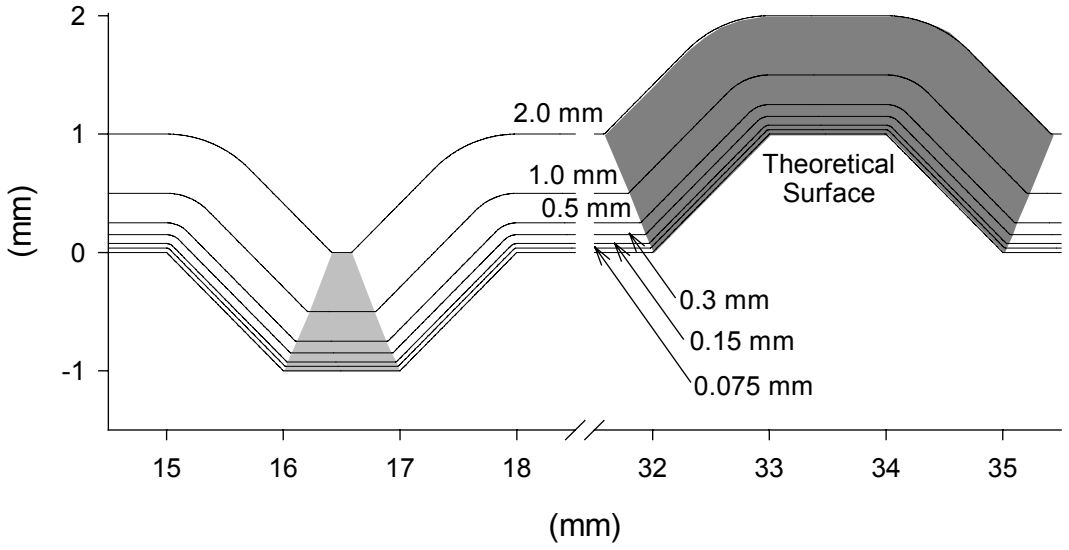


(a)

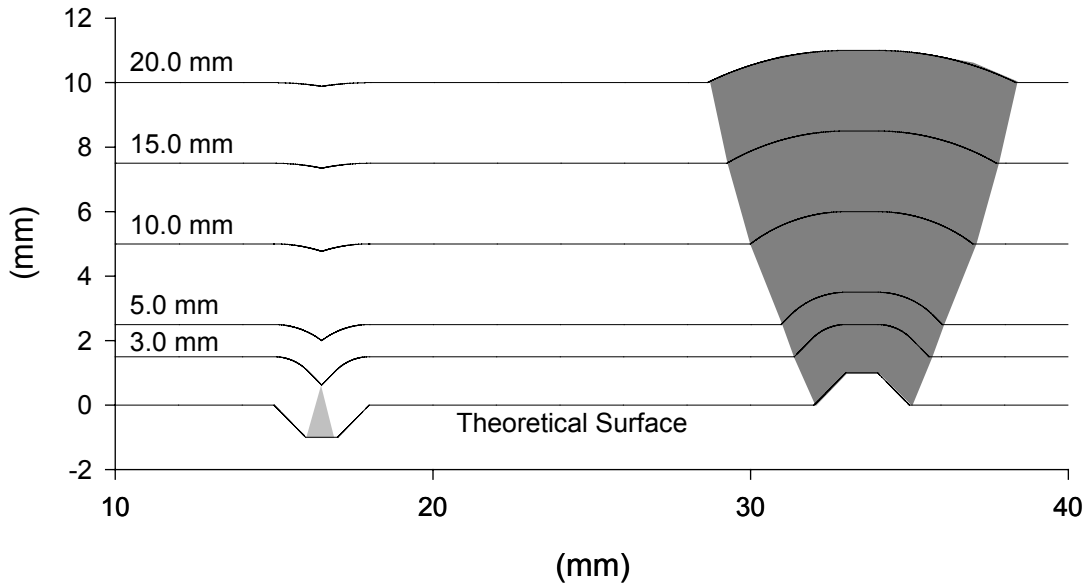


(b)

**Figure 3.29 –** Theoretical profile and Centroid Traces for a range of particles; **(a)** 0.075 – 2.0 mm **(b)** 3.0 – 20.0 mm (after DeJong, 2001).

decreases and the base width of the peak increases with a constant peak height. On the other hand, commonly used filters, e.g. Gaussian and sharp cutoff low pass filters, evaluate an above (peak) or under (valley) surface feature equally although as Figure 3.29 shows the particle experiences a peak and a valley differently. Further analysis showed that the conventional roughness parameters calculated over the range of diameters (0.075 mm – 20 mm), for the same interface system did not capture the relative aspect.

Although DeJong performed the above analysis for a wide range of particle diameter (0.075 mm – 20 mm), for each particle shape the diameter range is different. The interaction with the counterface occurs through the extremities of the outline and different contact points are valid for different combinations of the counterface and particle shape. The specific zone of radius range for any particle shape starts from its Maximum Inscribing Circle (MIC) radius and extends up to its Minimum Circumscribing Circle (MCC) radius. Considering both particle and continuum surfaces are hard enough so that neither of them penetrate into each other and result in shape deformation, for a point closer to the particle centroid than the outline points along the MIC, particle-surface interaction does not take place. Thus, particle-surface interaction is not an issue for circle radius smaller than MIC radius. In other words, for a specific particle-surface interaction case, CT profiles with circle radius within MIC and MCC radius are relevant. A particle shape parameter is developed capturing the particle's macro shape properties using MCC and MIC radii. The Characteristic Radius Ratio (CRR) is defined as:

$$CRR = \frac{r_{mcc} - r_{mic}}{r_{mic}} \quad \textbf{(3.11)}$$

where $r_{mcc}$ and $r_{mic}$ denote the radii of the MCC and MIC, respectively.

Wadell's definition of roundness suggests that a cylinder terminated at each end by a half-sphere has a maximum degree of roundness, i.e. $P = 1$ since the ratio of the radius of curvature of its corners to the radius of the maximum inscribed circle is equal to $1$ (Wadell, 1933). A circle also has maximum roundness. Thus, Wadell's roundness cannot distinguish between the two shapes. However, the two figures have different $CRR$ s. Note that $CRR$ is only relevant to the macro shape. In other words, it cannot distinguish between a smooth elliptical particle and another elliptical particle with a sine wave merged onto the boundary.

Further CRR analysis and specific calculations for the study particles are provided in the corresponding subsection of Chapter 4.

### *3.3.5 Particle Angularity*

#### 3.3.5.1 Meso-Scale Particle Angularity Characterization by Spike Parameter

For the Spike Parameter (SP) calculation, the input is a scanned gray-scale image of the particle in 2D. The outline extraction mathgram $outline(A, thr)$ is executed (see Section 3.3.1). The output is a $[n,2]$ matrix $(x, y)$ pixel boundary coordinates in clockwise direction, where $n$ is the number of data points along the boundary. For the SP calculation, the outline is reversed into counterclockwise direction.

The mathgram $SP(A, r, stpxl, incpxl)$ requires the outline coordinates $A$, ratio for the upper step size limit $r$, initial step size $stpxl$, and step size increment value $incpxl$. Hamblin and Stachowiak (1995) employed an $r$ ratio of 15, initial step size of 40 pixels, and an increment step size of 10 pixels. The input parameters used by Hamblin and Stachowiak (1995) suggest that the initial step size is increased from 40 with increments of 10 pixels until it equals to $1/15$ the number of pixels in the boundary. If the spike angle is calculated to be $\theta \leq 2.9\, rad$, Hamblin and Stachowiak (1995) discarded the spike in an attempt to disregard flat spikes. The same threshold is used in this analysis. Depending on the amount of information available; i.e. quality of the image, different input values can be practiced for $r$, $stpxl$, or $incpxl$. However, in order to validate the algorithm coded by this study, the same input parameters are utilized for the images available in Hamblin and Stachowiak (1995). In their study, Hamblin and Stachowiak (1995) do not specify the number of outline data points or the number of $nsteps$ obtained with the mentioned step size indices. The images used in the original study could not obtained directly from Hamblin and Stachowiak (1995); thus, they were scanned from the study paper. The particle images from Hamblin and Stachowiak (1995) are provided in Figure 3.30.

The comparison of the results reported by Stachowiak (1995) and the output of the mathgram is given in Table 3.14.

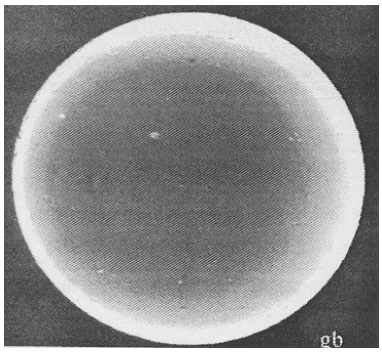


**(a)**

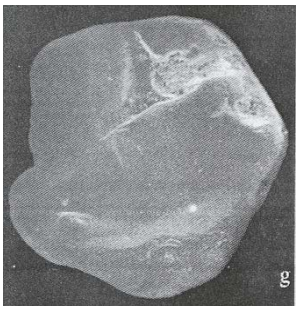


**(b)**

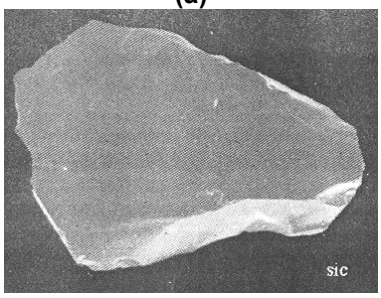


**(c)**

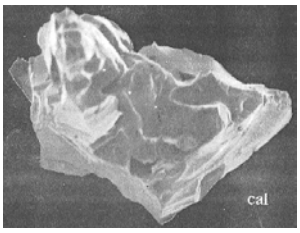


**(d)**

**(e)**

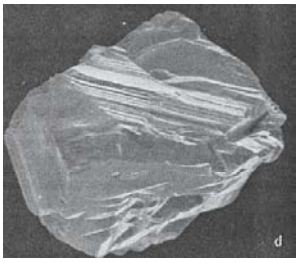


**(f)**

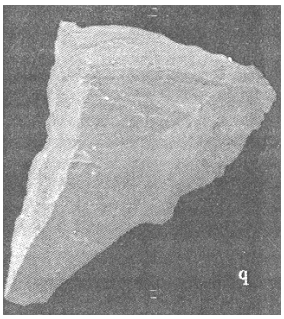


**(g)**

**Figure 3.30 –** Abrasive grit images used for SP & SPQ Analysis (after Hamblin and Stachowiak, 1996); **(a)** glass beads, **(b)** garnet, **(c)** silicon carbide, **(d)** crushed sintered alumina, **(e)** silica sand, **(f)** diamond, **(g)** quartz.

**Table 3.14 –** Table of calculated and reported SP values.

| Abrasive | SP (reported)[1] | SP (calculated)[2] |
|---|---|---|
| a | 0.1369 | 0.191 |
| b | 0.2168 | 0.238 |
| c | 0.2942 | 0.311 |
| d | 0.3591 | 0.391 |
| e | 0.2077 | 0.233 |
| f | 0.2971 | 0.314 |
| g | 0.3239 | 0.35 |

[1] : reported by Hamblin and Stachowiak (1995)
[2] : calculated using the generated algorithm with values of *thr=100* and SP(A,15,40,10).

The trend and regression plots for the two sets of data are as shown in Figure 3.31 (a) and (b), respectively. Clearly, the same trend is observed in both the reported and calculated SP data sets, however, the calculated SP values are consistently higher than the reported SP values.

Two alternative methods are investigated due to lacking data regarding the outline data points or the number of $nsteps$. First alternative method is performed with the scanned images from the photocopied paper, however, rather than using the outline results as the input to SP mathgram, all outlines are modified to number of rows of 360. Note that original particles' outlines average row number is 764. The new outlines are obtained by using $SampleParticle(A,N)$ mathgram, where N is input as 360. The modification of the number of data points is performed to ensure equal $nsteps$ for all images. Original step indices of 15,40,10 are modified to 10,15,1; thus, the step sizes become $15,16,17\ldots\ldots,rows/10$. The upper step size limit of $rows/10$ is equal to $36$ in this case resulting in $21$ $nsteps$. The number of rows of 360 and the modified indices are estimated based on a calibration study. In other words, a perfect "glassbead" image was

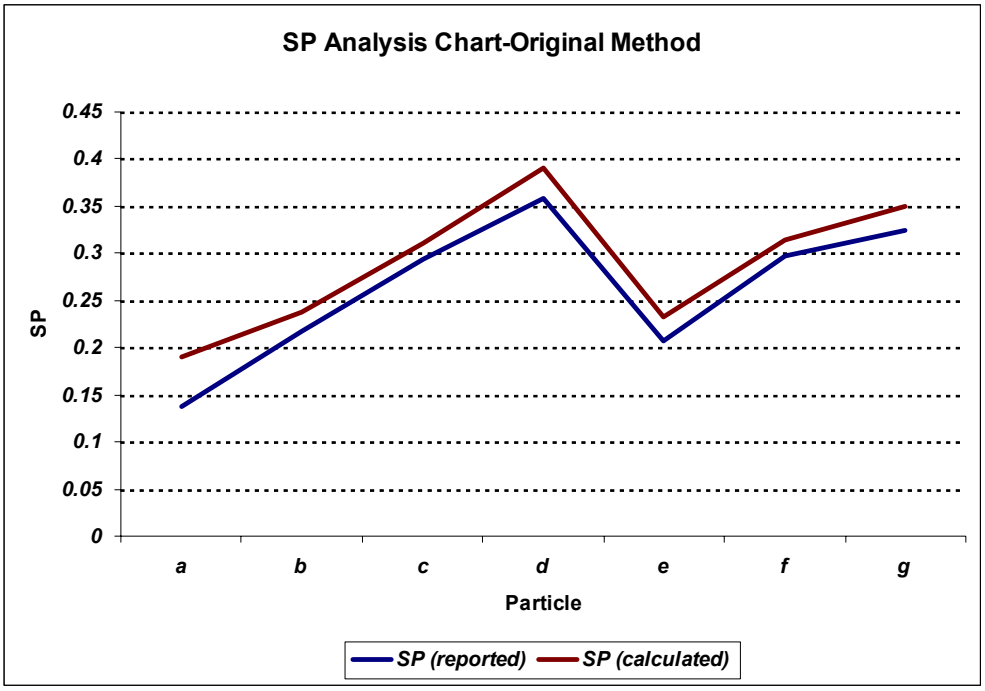


**(a)**

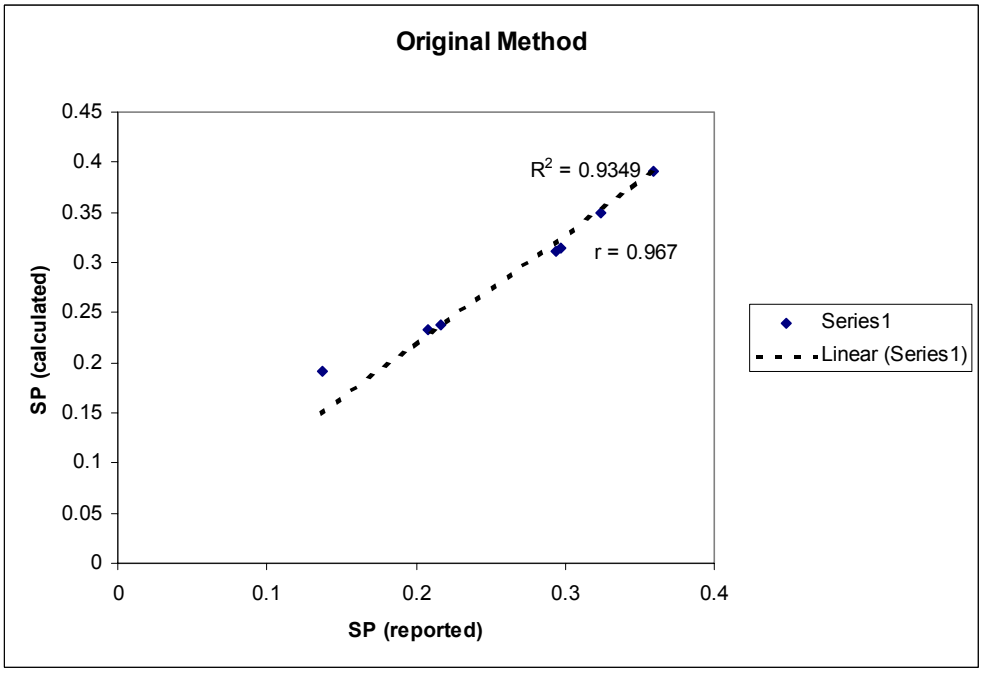


**(b)**

**Figure 3.31 – (a)** Graph showing the trend of SP (calculated) and SP (reported) by Stachowiak (1995), **(b)** Plot of regression analysis between the calculated and reported SP parameters.

input into the mathgram with the modified inputs and 360 data point outline and the reported image “a” SP value could be obtained. Note that image “a” in Figure 3.30 (a) is a “glassbead”. The results of the first method along with the reported SP values are provided in Table 3.15.

**Table 3.15 –** The values of SP reported and SP calculated with the First Alternative Method.

| Particle | SP (reported)[1] | SP (calculated)[2] |
|---|---|---|
| a | 0.1369 | 0.133 |
| b | 0.2168 | 0.222 |
| c | 0.2942 | 0.255 |
| d | 0.3591 | 0.372 |
| e | 0.2077 | 0.206 |
| f | 0.2971 | 0.278 |
| g | 0.3239 | 0.318 |

[1] : reported by Hamblin and Stachowiak (1995)
[2] : calculated using the generated algorithm with values of *thr=100* and SP(A,10,15,1).

The trend and regression plots for the two sets of data are as shown in Figure 3.32 (a) and (b), respectively. In Figure 3.32 (a), same trend is observed in reported and calculated values; however for images “c” and “f” the calculated SP values are lower than the reported.

Note that image distortion is possible while photocopying images from a paper. This is investigated by reading the glassbead particle, particle “a”, into a matrix and observing the matrix measures of the particle. As particle “a” is obtained in matrix form, it is observed that the difference between the lowest and highest matrix rows is 342;

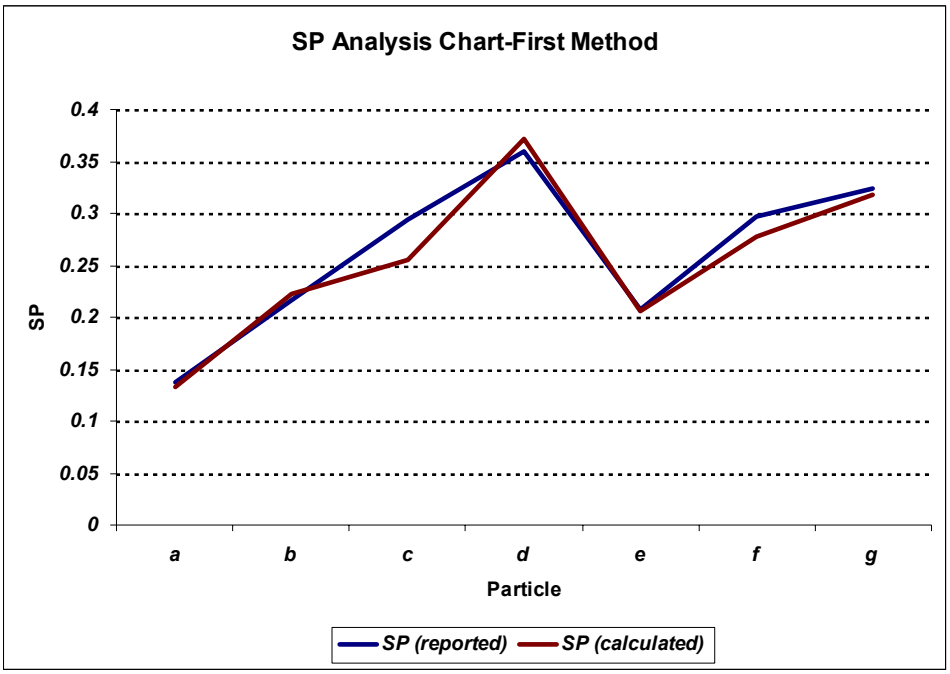


**(a)**

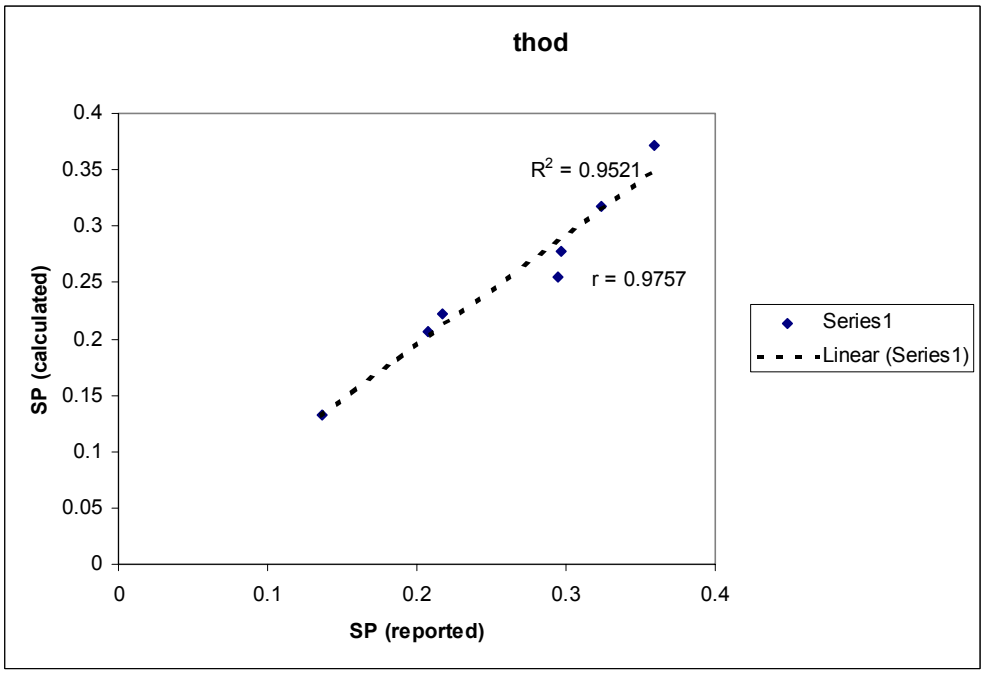


**Figure 3.32 - (a)** Graph showing the trend of SP (calculated – First Method) and SP (reported) by Stachowiak (1995), **(b)** Plot of regression analysis between the calculated and reported SP parameters.

whereas the difference between the extreme right-hand side column and the extreme left-hand side matrix columns is 324. Thus, particle "a" is not symmetrical, which is anticipated in a glassbead particle image. In order to correct the distortion, all images are scaled accordingly with the same ratios for a symmetrical particle "a" and a Second SP Method is performed with the modified images.

The modified images are input into the SP mathgram with the modified input parameters presented in the First Alternative Method. Thus, $SampleParticle(A,N)$ is used with *N* of 360 and the step size indices input as $(10,15,1)$. The results of the Second Alternative Method are presented in Table 3.16.

**Table 3.16 -** The values of SP reported and SP calculated with the Second Alternative Method.

| Particle | SP (reported)[1] | SP (calculated)[2] |
|---|---|---|
| a | 0.1369 | 0.135 |
| b | 0.2168 | 0.237 |
| c | 0.2942 | 0.261 |
| d | 0.3591 | 0.373 |
| e | 0.2077 | 0.21 |
| f | 0.2971 | 0.274 |
| g | 0.3239 | 0.327 |

[1] : reported by Hamblin and Stachowiak (1995).
[2] : calculated using the generated algorithm with values of *thr=100* and SP(A,10,15,1).

The trend and regression plots for the two sets of data are as shown in Figure 3.33 (a) and (b), respectively. In Figure 3.33 (a), although very close values are obtained for images "a", "d", "e", "f", and "g", the reported and calculated values for images "b" and "c"

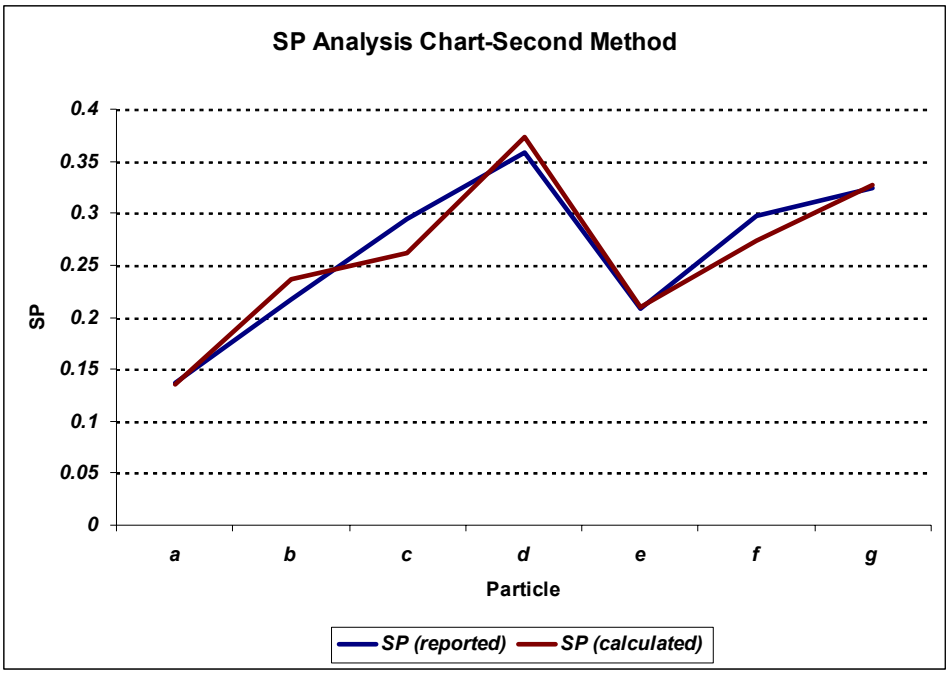


**(a)**

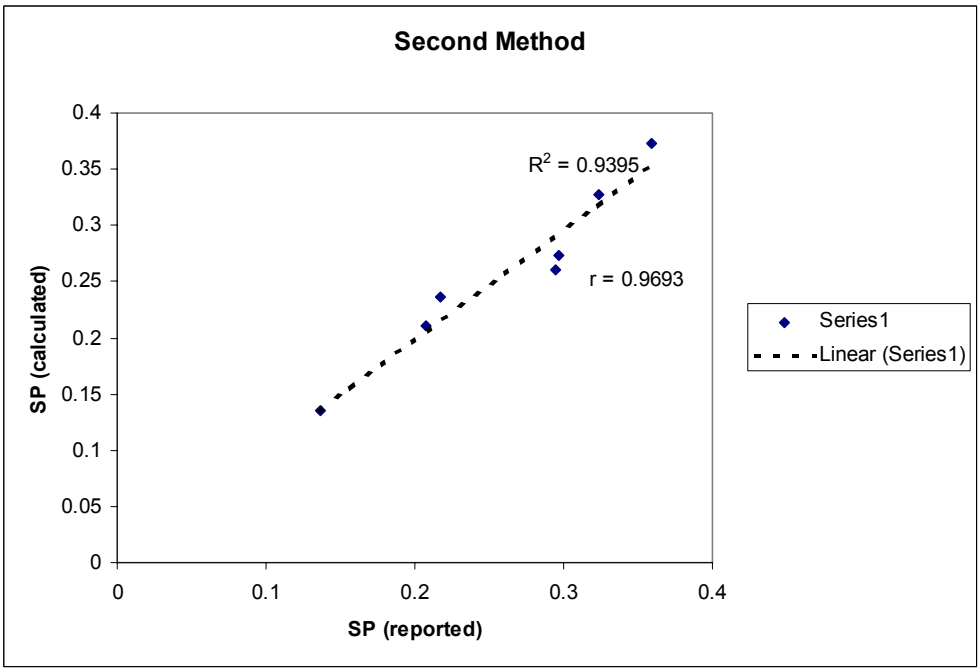


**(b)**

**Figure 3.33 - (a)** Graph showing the trend of SP (calculated – Second Method) and SP (reported) by Stachowiak (1995), **(b)** Plot of regression analysis between the calculated and reported SP parameters.

do not match. This method corrects the image distortion in particle “a”, however, there is no means of knowing the correct distortion coefficients for the other images except to assume that all images have the same distortion coefficient.

Note that in both Figures 3.32(a) and 3.33(a), the calculated and reported messages do not match for images “c, “d”, and “f”; whereas for the other images they are acceptable. All three mismatching particle images have one dimension larger than the other does. Thus, the discrepancy in the SP values could have resulted due to the orientation or elongation of the particle image.

#### 3.3.5.2 Macro-Scale Particle Angularity Characterization by Spike Parameter Quadratic

For SPQ calculation, the input format (e.g. a digital image, an $(x, y)$ data outline) is also optional as explained in the previous section for SP analysis. As in the original method, the LSC radius is determined and spikes are extracted (Section 2.3.1.2.2). The mathgram $spikes(A)$ determines the radius and the corresponding spike index for every point. The spike index is either zero or an integer equal or larger than one. If the distance of the data point to the LS center of the particle is less than the LSC radius, the spike index is set as zero indicating that the data point is inside the LSC. Next, the mathgram $spikes2(A)$ searches within each spike to locate its apex, starting, and end points referred to as $mp$, $sp$, and $ep$, respectively. The output is for any spike index the corresponding three spike point indices and coordinates. Finally, for each spike, $spike4(A)$ rotates the axis, fits the polynomials, and proceeds to obtain the apex angle

as suggested by Hamblin and Stachowiak (1996). The number of data points between $sp - mp$ and between $ep - mp$ segments are compared to find the smallest of the two, which is then set to the number of data points used for both $sp - mp$ and $ep - mp$ segments for that spike. This process is repeated for every spike located. The polynomial fitting is performed starting from $mp$ towards the $sp$ on one end and towards the $ep$ on the other side for the number of data points determined for that spike. Although not mentioned by Hamblin and Stachowiak (1996), in this study, in case the number of data points is less than 3 for any polynomial fitting (e.g. between $sp - mp$ or $ep - mp$ segments), that spike is discarded from the analysis. In case the number of datapoints for any of the segments is equal to 3, $\alpha$ value for that segment is calculated using a straight line as the approximating function (refer to Chapter 2 for explanation of the method terms). For more than 3 points second-degree polynomial regression is performed. The coefficients of the second-degree polynomial are used to estimate $\alpha_1$ and $\alpha_2$. The apex angle, $\theta$ is then computed using the apex angle for the triangle $(sp - mp - ep)$, $\alpha_1$ and $\alpha_2$. If the apex angle for a particular spike is less than $\vartheta \leq 2.9\,rad$, the spike value is taken as zero. For the rest of the acceptable spikes, proposed formula is used to evaluate the SPQ.

Hamblin and Stachowiak (1996) used the particles shown in Figure 3.30 for SPQ calculation as well as for SP. In order to validate the mathgram and the procedure outlined above, the particle images from the study paper were scanned and input into the mathgram. Table 3.17 compares the values obtained using the proposed Mathcad algorithm and the reported values by Hamblin and Stachowiak (1996) for the corresponding particles.

**Table 3.17 –** Table of calculated and reported SPQ values.

| Particle | SPQ (reported) | SPQ (calculated) |
|---|---|---|
| a | 0.0231 | 0.000 |
| c | 0.4247 | 0.3576 |
| d | 0.6008 | 0.6067 |
| e | 0.1919 | 0.1714 |
| f | 0.3958 | 0.2435 |
| g | 0.5336 | 0.5876 |

The trend and regression plots for the two sets of data are as shown in Figure 3.34 (a) and (b), respectively. As reported on the regression graph, the correlation between the two data sets is 0.9496, which is regarded as satisfactory considering the images were not original ones, but rather scanned from the study paper. The additional studies performed for the particle shape parameter SP are not executed for SPQ since SPQ does not require any input parameters except the image outline and the distortion coefficients for the images are ambiguous. Note that similar to SP analysis, for some particle shapes better correlation is observed compared to the particle e.g. “f” where the distortion is the maximum. A reason for the discrepancy could be that the orientation of the particles shown in Figure 3.30 is different from the original orientation Hamblin and Stachowiak (1996) used to obtain the 2D outline. Since particles are 3D in nature, different particle orientations for outline extractions could result in different 2D outlines.

### *3.3.6 Boyce and Clark Shape Index*

As mentioned in Chapter 2, Boyce and Clark (1964) shape parameter, *SI,* analyzes the shape based on its radial distance properties. Since Boyce and Clark (1964)’s primary

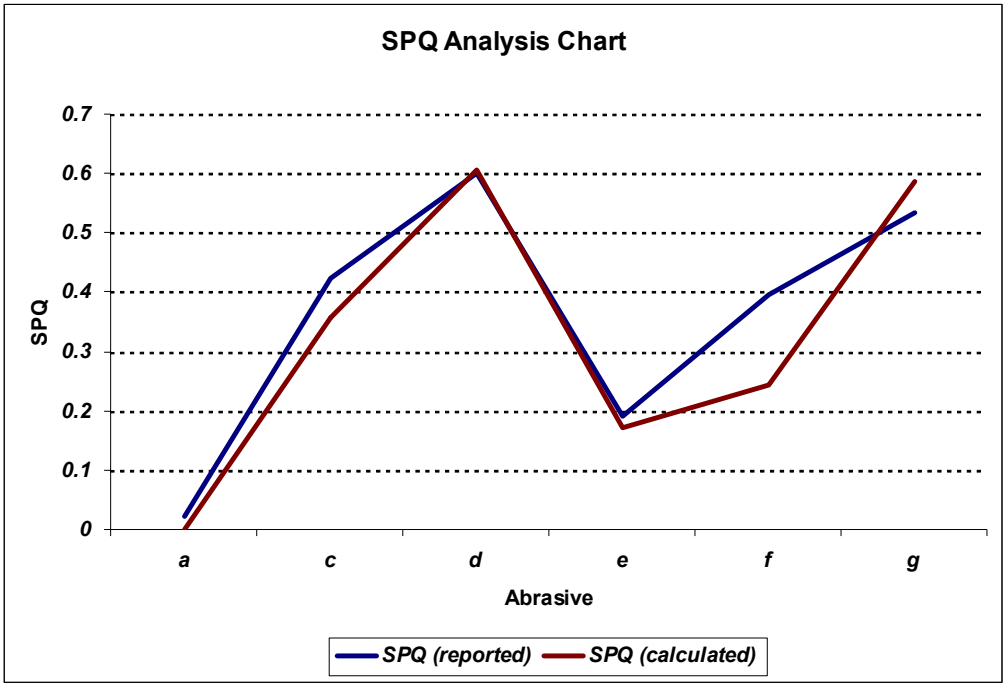


**(a)**

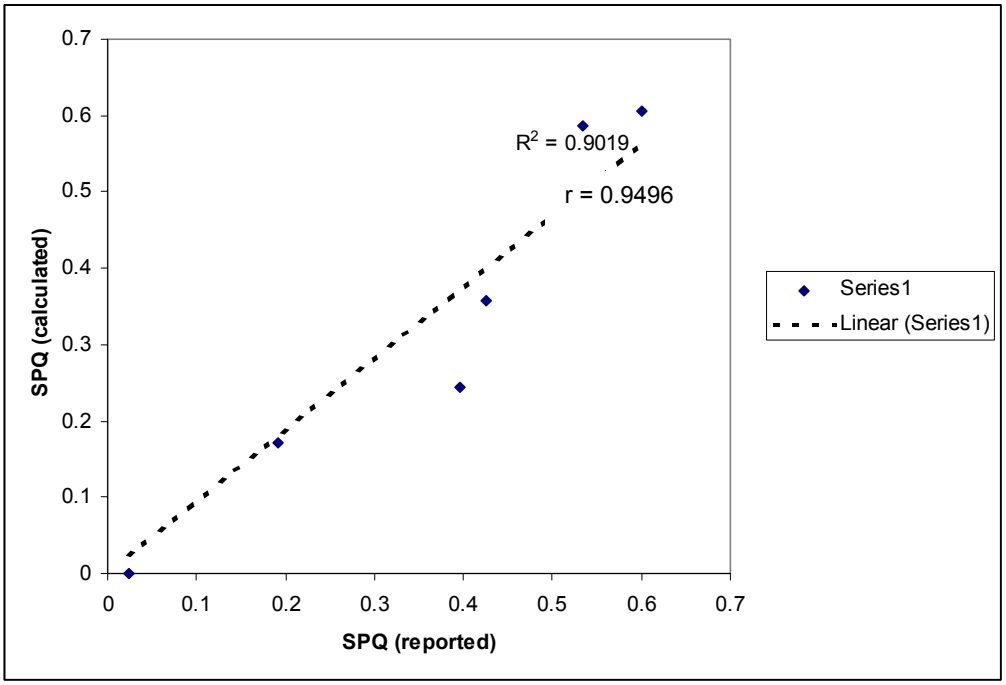


**Figure 3.34 – (a)** Graph showing the trend of SPQ (calculated) and SPQ (reported), **(b)** Plot of regression analysis between the calculated and reported SPQ parameters.

focus was the shape of cities for urban studies, no particle images were available from the original work. However, Boyce and Clark (1964) analyzed geometrical shapes and validation will be performed based on these shapes. Although Boyce and Clark (1964) reported *shape indices* of a 5-star and a cross shape, no information on the specific proportional dimensions of the two is provided; thus, they are omitted in the validation process. The comparison of the results is given in Table 3.18.

**Table 3.18 –** Table of calculated and reported SI values.

| Geometrical Shape | SI* (reported) | SI* (calculated) |
|---|---|---|
| circle | 0 | 0 |
| square | 12 | 11.8 |
| rectangle (2:1 side ratio) | 28 | 27.7 |
| straight line | 175 | 174.6 |

***:** The values are based on 16 radials, thus 22.5° intervals.

The correlation coefficient between the reported and calculated results is 0.999.

### *3.3.7 Wadell's Roundness*

#### 3.3.7.1 Meso-Scale Particle Roundness Characterization by Wadell's Roundness Concept

Prior to analyzing selected study particles for Wadell roundness, previous roundness evaluation studies in the literature were reviewed to obtain a database for Wadell's

roundness calculation studies and to validate the mathgrams. As referenced by Hawkins (1993), an earlier Wadell roundness study of 25 selected particles was performed by Scheiderhöhn (1954). The grain projections of the selected particles and a table of roundness values captured from the original study are provided in Figure 3.35(a) and Figure 3.35(b).

The original study by Scheiderhöhn (1954) is in German; thus, required translation to implement the technique used to evaluate particle roundness. The study included twenty-five particles of approximately the same size. The particle images were projected on a screen through a microscope to obtain a comparable size of 10 cm “middle diameter”. The “middle diameter” is defined as the average of the two lengths; “long diameter” and “short diameter” across the particle, both passing through the center of the Maximum Inscribing Circle (MIC). Upon projection, the longest distance within the outline through the MIC center is measured as the “long diameter” and the “short diameter” is evaluated as the perpendicular distance to the “long diameter”. Projecting each particle to the same “middle diameter” prevented any discrepancy due to particle size.

A hand-drawn scale of concentric circles with radius ranging from 1-150 mm was positioned along the profile outline to select outline sections fitting any of the circles. The separation of circles in the template between 1 and 35 mm radius circles was 2 mm; between 35 and 100 mm, the separation was 5 mm; and between 100 and 150 mm, the separation was 10 mm. If a particle outline section fitted to one of the hand-drawn concentric circles, the corresponding radius was recorded.

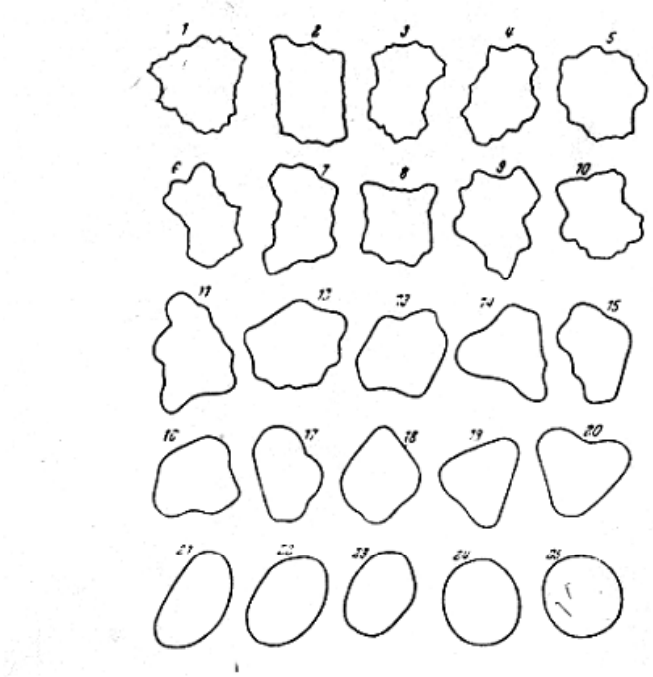

**(a)**

| Grain number | Russel & Taylor Pettijohn classification | Wadell $\left(\frac{\Sigma r}{R}\right)\frac{10^2}{N}$ | Wentworth $\frac{r_1.10^2}{R}$ | Cailleux $\frac{2r_1.10^2}{L}$ | Length / Breadth | Wadell $\frac{d.10^2}{D}$ |
|---|---|---|---|---|---|---|
| 1 | | 0.00 | 0 | 0 | 1.07 | 81 |
| 2 | | 0.02 | 0 | 0 | 1.50 | 74 |
| 3 | Angular | 0.2 | 0 | 0 | 1.43 | 80 |
| 4 | | 0.4 | 0 | 0 | 1.63 | 78 |
| 5 | | 1 | 0 | 0 | 1.04 | 86 |
| 6 | | 15 | 5 | 3 | 1.61 | 73 |
| 7 | | 16 | 2 | 1 | 1.70 | 75 |
| 8 | Subangular | 18 | 4 | 3 | 1.07 | 81 |
| 9 | | 19 | 4 | 3 | 1.41 | 75 |
| 10 | | 20 | 9 | 7 | 1.16 | 81 |
| 11 | | 25 | 10 | 7 | 1.58 | 73 |
| 12 | | 27 | 8 | 6 | 1.29 | 82 |
| 13 | Subrounded | 29 | 16 | 13 | 1.33 | 82 |
| 14 | | 36 | 18 | 15 | 1.15 | 80 |
| 15 | | 37 | 15 | 12 | 1.52 | 77 |
| 16 | | 40 | 19 | 16 | 1.22 | 86 |
| 17 | | 44 | 18 | 14 | 1.58 | 79 |
| 18 | Rounded | 46 | 27 | 22 | 1.30 | 82 |
| 19 | | 51 | 33 | 27 | 1.29 | 80 |
| 20 | | 59 | 42 | 37 | 1.11 | 83 |
| 21 | | 63 | 45 | 32 | 1.92 | 72 |
| 22 | | 68 | 55 | 46 | 1.48 | 83 |
| 23 | Well rounded | 78 | 56 | 43 | 1.45 | 77 |
| 24 | | 89 | 82 | 78 | 1.11 | 95 |
| 25 | | 95 | 90 | 86 | 1.08 | 96 |

**(b)**

**Figure 3.35 - (a)** Grain projections referenced by Hawkins (1993), **(b)** Selected roundness values for grain projections (after Hawkins, 1993).

The study by Scheiderhöhn (1954) did not include all the details required for a thorough analysis. For example, some corners, i.e. segments of the outline fitting the circle template, were ignored and radii of these corners were taken as zero. These corners were defined as “sharp corners” in the study, however a threshold radius value for “sharpness” was not defined. Note that although the radius was taken as zero for “sharp corners”, these corners were included in the total number of corners. Concavity is not directly mentioned in the study, however it is implicit from the statement that only “outward” parts of the outline were taken into account.

The recorded radii were determined a single time by one person; which creates uncertainty concerning user dependency in spotting corners and repeatability of the analyses. No procedure in selecting dominant points was available. Another vague component of the analysis is an error threshold in circle fitting. No threshold value or method was specified for error analysis.

In implementing the above study, no scaling of particle size is necessary since the particle images shown in Figure 3.35(a) are obtained after projecting the particles to similar size rather than with the original particle size.

Dominant points are high-curvature points along the profile as described in Chapter 2. The detailed explanation of the Teh and Chin (1989) dominant point selection and curve estimation methods are provided in Chapter 2. For curve parameter estimation, at least three data points are required; otherwise, the program fits a straight line between the two dominant points. A modification to the existing algorithm is executed, so that in case only two points are selected, the preceding neighboring data point is also included in curve estimation to avoid straight-line approximations. Moreover, since a definition of

"sharp corners" was not provided in the study, three minimum radius threshold values are examined in this study. In the original method, for a 10 cm "middle diameter" projection, it is assumed that the author ignored curvatures with less than 1 mm radius. This assumption is based on the smallest scale in the original circle template, i.e. 1 mm radius circle. This results in a 2 percent of minimum radius to "middle radius" ratio; where "middle radius" is half of the "middle diameter". In addition to 2% minimum radius threshold, 20% and 40% are also investigated.

Two mathgrams were used, *roundnesswadellconcave.mcd* and *fixingroundness.mcd*, abbreviated as *rwc.mcd* and *fxr.mcd*, respectively. In *rwc.mcd*, all the segments between consecutive dominant points are analyzed; whereas in the latter algorithm only segments between pairs are evaluated. Consider that dominant points using Teh and Chin algorithm constitute a set of $\{dom1, dom2, dom3, dom4, \ldots\ldots, dom(n-1), dom(n)\}$. The algorithm *rwc.mcd* evaluates every segment, i.e.

$\boldsymbol{segment\{dom1, dom2\}, segment\{dom2, dom3\}, segment\{dom3, dom4\}, \ldots\ldots .....,}$

$\boldsymbol{segment\{dom(n-1), dom(n)}$ for circle fitting. On the other hand, in *fxr.mcd* analysis, pairs of high-curvature points possibly bounding a corner are spotted by the "user" and for selected point set of $[\{p1, p2\}, \{p3, p4\}, \ldots\ldots, \{p(n-1), p(n)\}]$, Consequently, $segment\{p1, p2\}, segment\{p3, p4\}, \ldots\ldots, segment\{p(n-1), p(n)\}$ are considered for roundness evaluation. Note that in picking points by hand for *fxr.mcd* analysis, the same definition is used as dominant points, i.e. high-curvature points. In the remainder of this study, the dominant points selected by the researcher are referred to as "*handdoms".* In order to perform roundness calculation manually by traveling around the particle outline, a circle template as described in Schneiderhöhn (1954) is also employed in this study.

Upon scanning Figure 3.35(a) from Hawkins (1993), an image analysis program Leica Qwin is used. The images are converted to binary images and the inside of each particle outline is filled. Every particle image is cropped from the original figure of 25 images and the particle images are then extracted with black interiors with a resolution of 340 x 340.

As mentioned above, high curvature points are selected using the Teh and Chin (1989) algorithm and by hand selecting. Prior to performing dominant point selection mathgram with the images in Figure 3.35 (a), the presented examples from Teh and Chin (1989) are investigated with the algorithm. The closed curves experimented in Teh and Chin (1989) are the chromosome-shaped curve, leaf-shaped curve, figure 8-curve and a curve with three different radii semi-circles as shown in Figure 3.36. Although the dominant point selection code used produced exactly matching results for the shapes analyzed in Teh and Chin (1989)[Figure 3.36], for grain projections (Figure 3.35(a)), high discrepancy is observed for the location and number of dominant points by Teh and Chin (1989) algorithm and hand selecting. The presented examples in the original study shown in Figure 3.36 do not resemble the characteristics of the usually encountered grains in geotechnical engineering. Thus, the dominant point selection method proposed by Teh and Chin (1989) may not be appropriate for the wide range of geotechnical particles in practice; but rather perform better for certain images.

Figure 3.37 shows selected particles from Figure 3.35(a), where the data points are shown as empty circles. The Teh and Chin (1989) dominant points are represented by

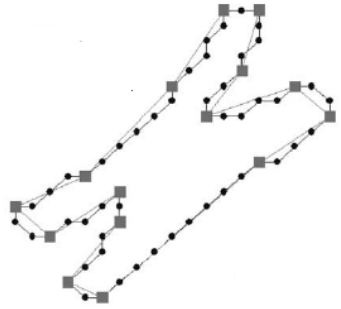

**(a)**

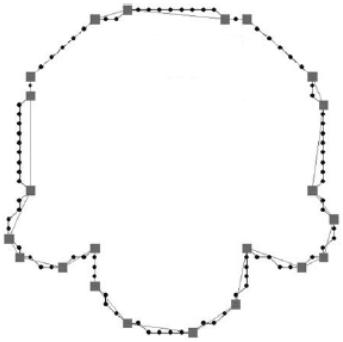

**(b)**

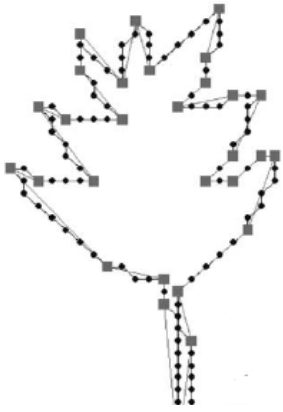

**(c)**

**Figure 3.36 –** Dominant points of the selected shapes by Teh and Chin (1989); **(a)** chromosome shape, **(b)** semicircle curve, and **(c)** leaf curve; —•— original outline points, —■— Teh and Chin (1989) dominant points (after Wu, 2003).

red symbols and the *handdom* points by blue symbols. For the *handdom* study, the selected particles are “w8”,”w19”, and “w24”; where *w8* stands for the 8$^{th}$ particle in the figure numbered from left to right and top to bottom starting with the top left particle. Note that two *handdom* trials are shown for “w8” in an attempt to emphasize the difference in the results when different users define disparate *handdoms* due to the inadequate explanation of the corner selection method by Scheiderhöhn (1954). In the first *w8* trial, every deviation from a straight line was marked as a dominant point; whereas in the second *w8* trial, only the obvious curvatures were selected (please refer to Figures 3.37(a)-(c) and 3.37(d)).

In relation to the grains and *handdoms* in Figure 3.37, Figure 3.38 illustrates the fitted curves between the selected *handdoms* by the roundness algorithms. Note that up to 15 variables can be presented in a Mathcad figure; thus, in cases where more than 15 pairs of *handdoms* are selected, multiple figures of the same particle with fitted circles at different locations are shown. In Figure 3.38, the variable $A$ stands for the extracted data points, *handdom* is the set of the dominant points chosen by the author of this work, and the variable $P$ correspond to the fitted circles between dominant points.

Following *handdom* study, *minimum radius threshold value* is analyzed. In *minimum radius threshold value* investigation; grains *w2*, *w7, w8, w12, w19* and *w24* were input into the roundness algorithm. The results are shown in Table 3.19.

As indicated in Table 3.19, the roundness value is more affected by the minimum radius threshold value as the particle roundness decreases; e.g., the roundness value for particle *w2* varies between 31.5% and 0% for the extreme minimum radius threshold

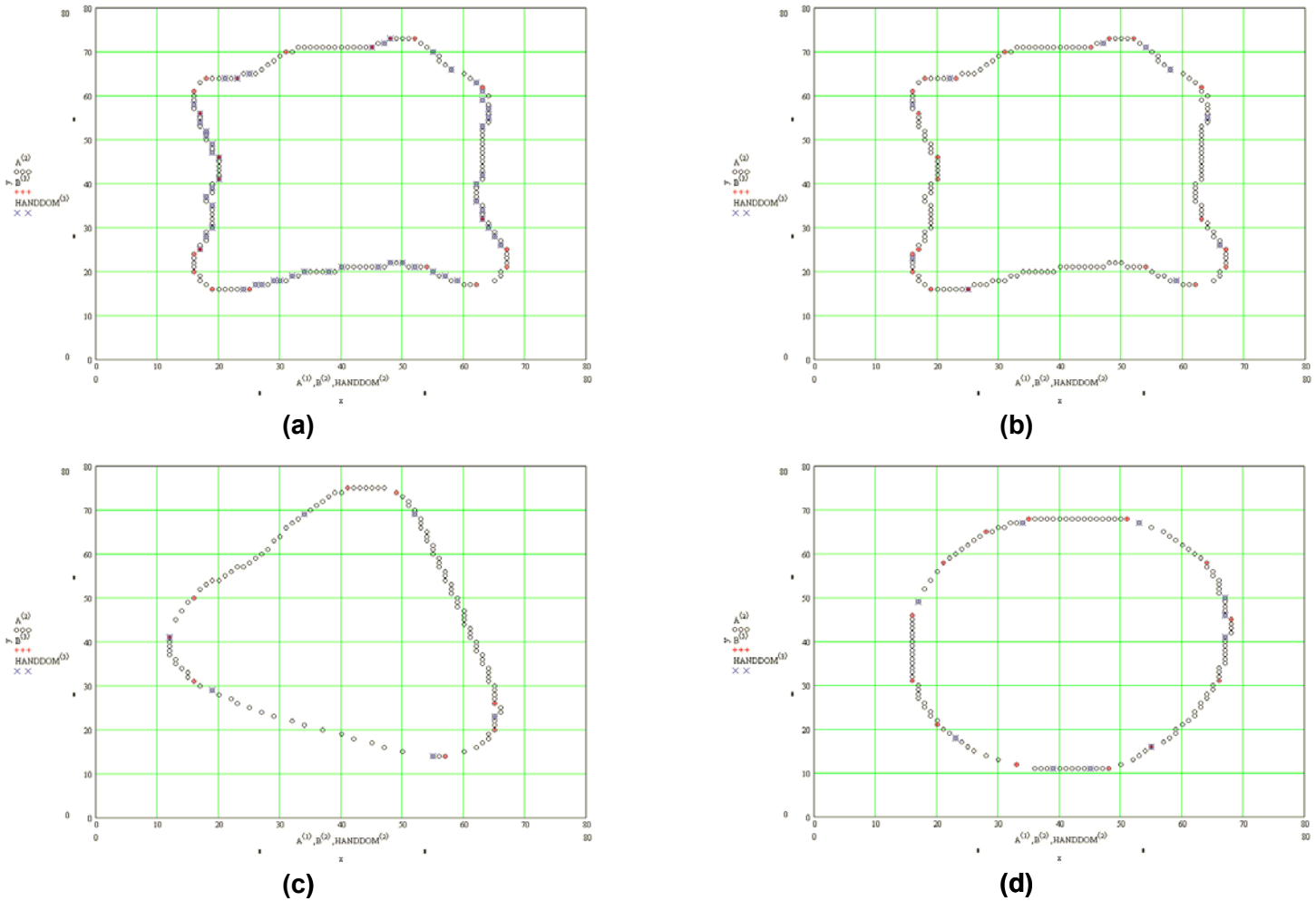


**Figure 3.37 –** Comparison of Teh and Chin (1989) dominant points and *handdoms* for selected grain projections; **(a)** *w8* first trial, **(b)** *w8* second trial, **(c)** *w19,* and **(d)** *w24*

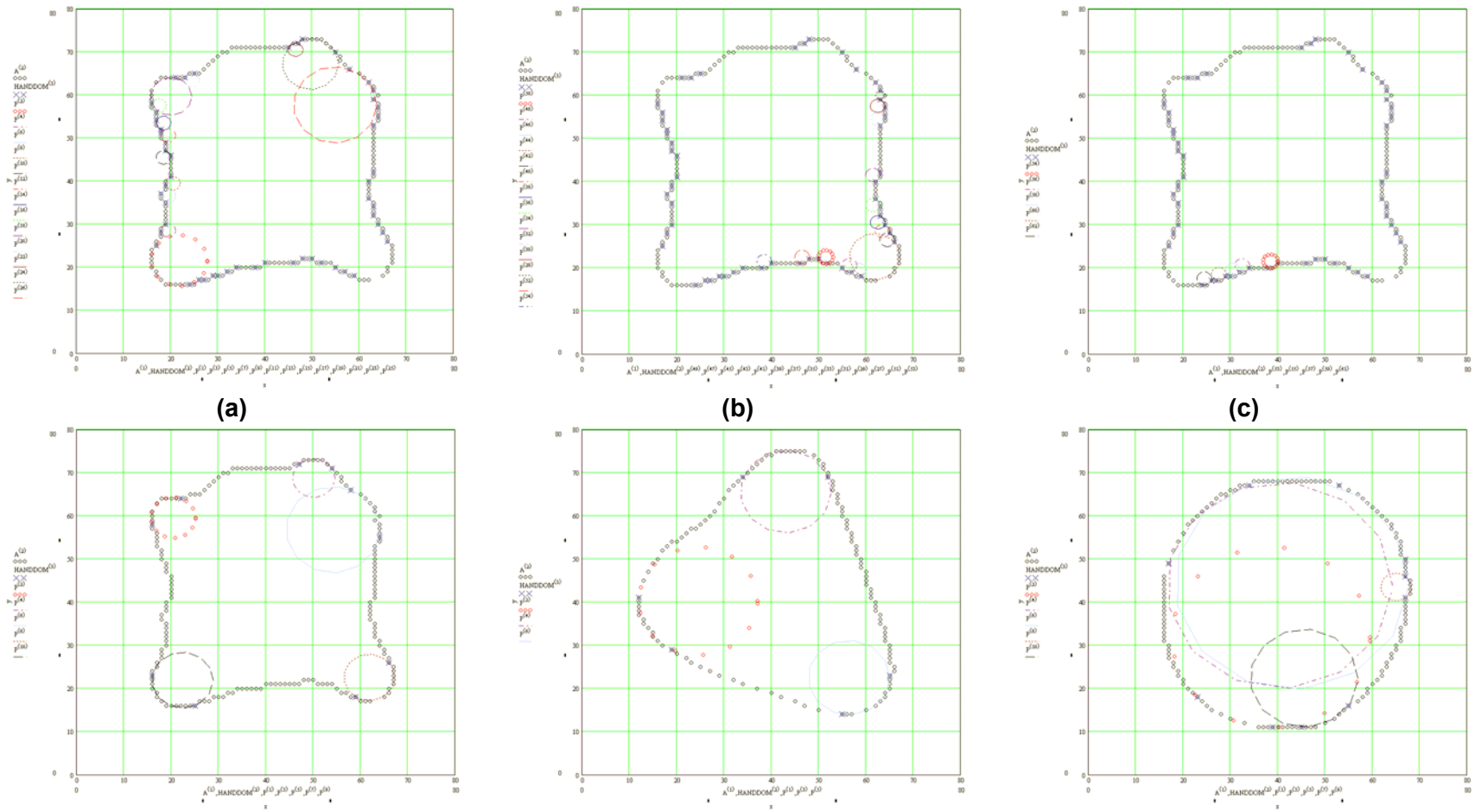

**Figure 3.38–** Sketch of curves executed by the roundness algorithm using *handdoms*; **(a)**, **(b)**, **(c)** *w8* first trial, **(d)** *w8* second trial, **(e)** *w19,* and **(f)** *w24.*

values; whereas for particle *w24*, the roundness values vary between only 68.6% to 59.4%. The calculated roundness values (Col. 4) are closest to the reported values in Col. 2, when the minimum radius threshold is 40%, however, a 40% threshold is not acceptable. Since the results shown in Table 3.19 do not signify a minimum radius threshold value, the 2%, i.e. similar to the smallest scale of 1 mm radius for a 10 cm.

**Table 3.19 –** Computed and reported roundness values for varying minimum radius thresholds.

| particle | R - % (original study) | min.radius.thr | R - % - (this study) |
|---|---|---|---|
| **2** | 0.02 | 2% | 31.5 |
| | | 20% | 18.5 |
| | | 40% | 0 |
| | | | |
| **7** | 16 | 2% | 47.2 |
| | | 20% | 39.0 |
| | | 40% | 0 |
| | | | |
| **8** | 18 | 2% | 44.5 |
| | | 20% | 44.5 |
| | | 40% | 27.0 |
| | | | |
| **12** | 27 | 2% | 51.6 |
| | | 20% | 51.6 |
| | | 40% | 24.1 |
| | | | |
| **19** | 51 | 2% | 55.7 |
| | | 20% | 51.5 |
| | | 40% | 51.5 |
| | | | |
| **24** | 89 | 2% | 68.6 |
| | | 20% | 68.6 |
| | | 40% | 59.4 |

"middle diameter" particle used in the original study, will be used for the remainder of this study.

Figure 3.37 above showed the visual difference between *handdoms* and Teh and Chin (1989) dominant points. A study was conducted as explained below to demonstrate the difference numerically.

First, the entire analysis was performed by hand in accordance with the original study. In addition, the *handdoms* were input into mathgrams; *rwc.mcd* and *fxr.mcd* . The results are reported as *Mathcad (handdom&rwc.mcd)* and *Mathcad (handdom&fxr.mcd)* in Table 3.20. Finally, the dominant points extracted by the Teh and Chin (1989) algorithm were input into *rwc.mcd* to enumerate the *Mathcad (tehandchin&rwc.mcd)* output as shown in Table 3.20.

**Table 3.20 –** Computed Wadell's roundness values of four particles by different methods.

| **Method** | **w2** | **w8 (first trial)** | **w8(second trial)** | **w19** | **w24** |
|---|---|---|---|---|---|
| R - % (original study) | 0.02 | 18 | 18 | 51 | 89 |
| By hand | 9 | 8.8 | 28 | 51 | 63 |
| Mathcad (handdom&rwc.mcd) | 12.5 | 13.5 | 27.2 | 52.2 | 67 |
| Mathcad (handdom&fixr.mcd) | 8.9 | 10.7 | 29.6 | 52.2 | 67 |
| Mathcad (tehandchin&rwc.mcd) | 35 | 28.6 | 28.6 | 50.1 | 55 |

As shown in Table 3.20, even with absolute hand analysis, a different user can affect the result by 218%, i.e. from 8.8% to 28% roundness for *w8 (first trial)* and *w8 (second trial),* respectively. A roundness value for the *first trial* would categorize the particle as *angular-subangular*; whereas the value for the *second trial* corresponds to a *subrounded* particle (Figure 3.35(b)). The difference between the *w8* (*first trial)* and *w8* (*second trial)*

is less pronounced for the Mathcad output roundness results, since as previously shown in Table 3.19, Mathcad algorithms tend to give enormously higher results for less rounded particles and the Mathcad results get closer to the reported values as roundness increases. In other words, for *w8* (*first trial),* Mathcad results are larger than the *handdom* roundness values; whereas for *w8* (*second trial), handdom* and Mathcad roundness values are comparable. Also note the numerical disparity between *Mathcad (handdom&rwc.mcd)* and *Mathcad (tehandchin&rwc.mcd)* results, especially as the particle roundness decreases.

The unreliability of the Teh and Chin (1989) dominant points extracted for real grain projections generates concern regarding the use of the Teh and Chin (1989) dominant point algorithm.

For the final analysis of grain projections in Figure 3.35(a), the *handdom* approach referenced above is applied to more particles. For some particles, more than one set of *handdoms* is reported in Table 3.21, due to uncertainty in the dominant point selection method. Note that upon extracting the high-curvature points by hand, *fxr.mcd* is used rather than *rwc.mcd* , since as noted above, it is assumed that the original roundness is based on curves fitted between pairs of dominant points (refer to the algorithms explanation above).

Although the results in Table 3.21 do not illustrate large differences between different *handdom sets* for a specific particle, nevertheless the reported (Col.2) and the calculated values (Cols. 3&4) do not agree.

**Table 3.21 -** Computed Wadell's roundness values of twelve particles by different methods.

| Particle | R % (original study) | R % ( handdom1) | R % ( handdom2) |
|---|---|---|---|
| **w1** | 0 | 10.9 | 12.7 |
| **w2** | 0.02 | 16.9 | 23.5 |
| **w4** | 0.4 | 20.7 | NA |
| **w5** | 1 | 14.9 | 14.3 |
| **w7** | 16 | 17.6 | NA |
| **w8** | 18 | 29.3 | 24.1 |
| **w9** | 20 | 34.7 | 28.5 |
| **w12** | 27 | 31.2 | NA |
| **w15** | 37 | 54.1 | 51.7 |
| **w18** | 46 | 65.0 | NA |
| **w19** | 51 | 54.7 | NA |
| **w24** | 89 | 92.9 | NA |

**NA :** Not Available

In addition to the images from Schneiderhöhn (1954), 14 other particles with reported Wadell roundness values were analyzed. They are termed as *Wadell2* images in this thesis and abbreviated as "ww(#)hr", where "hr" stands for high resolution. Wadell2 images are captured from Wadell (1932). The original figure captured is as shown in Figure 3.39.

In the study by Wadell (1932), the images are encircled in order to aid the eye in estimating another particle shape parameter, sphericity. Thus, in image analysis, the particles images are eroded and dilated to remove the circumscribing circles. In some cases, binary edit is also applied (refer to Figure 3.40 for the edited images). Similar to the previous analysis, a 300x300 resolution is employed. In Figure 3.39, the top number below the particle image represents the Wadell roundness value as determined by Wadell (1933). Note that the particle numbering system for this analysis is from left to right and top to bottom beginning with the upper left particle.

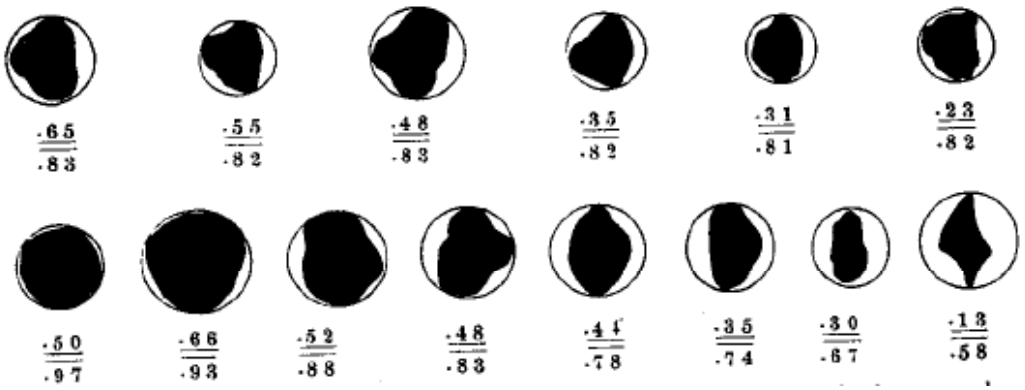


**Figure 3.39 –** Sand grain images termed as *Wadell2* (after Wadell, 1933).

The results from the numerical roundness analysis are provided in Table 3.22. Note that for half of the particles, three sets of *handdoms* are experimented with to emphasize user-dependency of the analysis. The fact that for some particles, the roundness could differ from 0% to 59.09% (for *ww1hr*) in the extreme cases, leads the author to believe that the user-dependency of the method may be the cause of the erroneous results presented thus far.

As the final assessment, the data points are modified to obtain uniform distance particle outlines. A subset of the entire data set is created with approximately the same distance between the points. The distance between the data points is varied as a percentage of the perimeter of the particle outline. The Teh and Chin (1989) dominant point algorithm is also applied followed by the roundness evaluation. Remarkably, for the dominant point extraction method, as the distance between data points increased, the Teh and Chin (1989) dominant points are closer to the selected *handdoms*. Generally, the reverse is expected where more accuracy should be attained with more data points, i.e. less distance between data points. Even with the closest result (at 75% distance of the

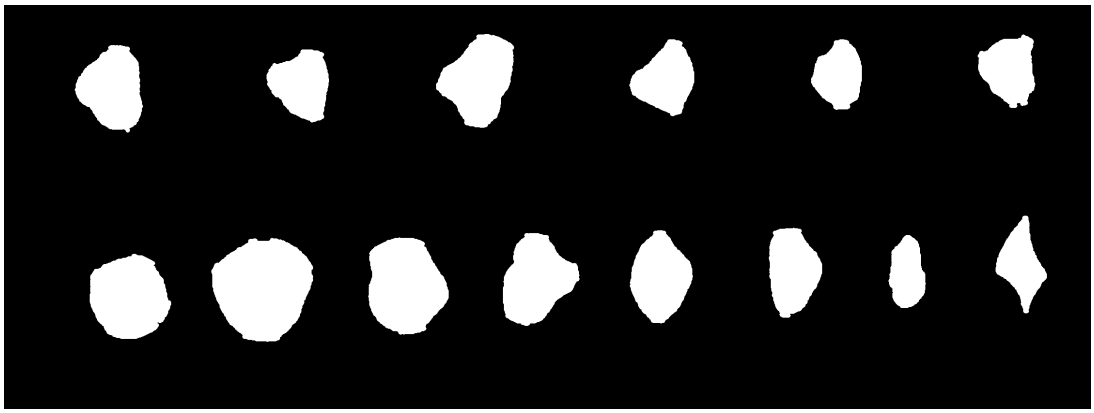

**Figure 3.40 –** Sand grain images grouped under heading *Wadell2* – upon editing (adapted from Wadell, 1933).

**Table 3.22 -** Computed Wadell's roundness values of *Wadell2* using *handdom* approach.

| Particle | R % (original study) | R % (HANDDOM1 & fxr.mcd) | R % (HANDDOM2 & fxr.mcd) | R % (HANDDOM3 & fxr.mcd) |
|---|---|---|---|---|
| **ww1hr** | 65 | 21.523 | 27.847 | 42.939 |
| **ww3hr** | 48 | 30.631 | 41.363 | 38.814 |
| **ww4hr** | 35 | 24.663 | 24.663 | NA |
| **ww5hr** | 31 | 31.302 | 20.673 | NA |
| **ww6hr** | 23 | 24.615 | 23.747 | NA |
| **ww7hr** | 50 | 20.468 | 26.197 | 37.457 |
| **ww8hr** | 66 | 25.627 | 15.837 | NA |
| **ww9hr** | 52 | 81.109 | 38.861 | 70.5 |
| **ww10hr** | 48 | 45.937 | 47.406 | NA |
| **ww11hr** | 44 | 0 | 31.617 | 59.09 |
| **ww12hr** | 35 | 49.12 | 27.019 | NA |
| **ww13hr** | 30 | 51.829 | 46.629 | 45.27 |
| **ww14hr** | 13 | 32.254 | 17.8 | NA |

**NA :** Not Available

perimeter), Teh and Chin (1989) dominant point method does not produce satisfying results as in Table 3.23. Note that some results for a 70% distance are also shown for comparison purposes.

**Table 3.23 -** Computed Wadell's roundness values of *Wadell2* using Teh and Chin (1989) dominant point method.

| Particle | R % (original study) | R % at 75% distance (Tehandchin&rwc.mcd) | R % at 70% distance (Tehandchin&rwc.mcd) |
|---|---|---|---|
| **ww1hr** | 65 | 32.164 | NA |
| **ww3hr** | 48 | 60.772 | 69.331 |
| **ww4hr** | 35 | 39.654 | NA |
| **ww5hr** | 31 | 52.602 | 28.747 |
| **ww6hr** | 50 | 55.178 | 48.078 |
| **ww7hr** | 66 | 0.000 | 60.016 |
| **ww8hr** | 52 | 47.359 | NA |
| **ww9hr** | 48 | 45.361 | NA |
| **ww10hr** | 44 | 22.955 | NA |
| **ww11hr** | 35 | 38.502 | NA |
| **ww12hr** | 30 | 67.183 | 59.047 |
| **ww13hr** | 13 | 40.098 | NA |

**NA :** Not Available

As a result of the above analysis, the Teh and Chin (1989) dominant point extraction method and the Wadell roundness method are not used further in this study. The unreliable results obtained by the Teh and Chin (1989) algorithm for the specific particle outlines considered can be attributed to the algorithm's sensitivity to noise. This drawback of the Teh and Chin algorithm is as also mentioned by Neumann and Teisseron (2002). The Wadell roundness method is determined to be a highly user-dependent method because of its ambiguous corner detection procedure.

## 3.4 Analysis of Surface Roughness Characterization Methods

### *3.4.1 Selection of Surface Roughness Parameters*

As explained in Section 3.1.2, in the process of generating derived particles, the surface profiles are adjusted to 0.004mm resolution and shortened to 15-mm. In order to keep the analysis consistent, for real surface study profiles rather than the original 0.001mm resolution and 40-mm long profiles, 0.004mm resolution and 15-mm long profiles are used. As mentioned in the same section and shown in Figure 3.5, in terms of CT surface parameters the preferred resolution and length (15-mm length at 0.004mm resolution) showed similar trends with the original profiles (40-mm length at 0.001mm resolution). The real surface study profiles are shown in Figure 3.41.

### *3.4.2 Conventional Surface Roughness Parameters*

For the conventional surface roughness parameters, a single Mathcad 2001 Professional algorithm is employed. The parameters calculated include:

- Average Roughness ($R_a$)
- Root Mean Square Roughness ($R_q$)

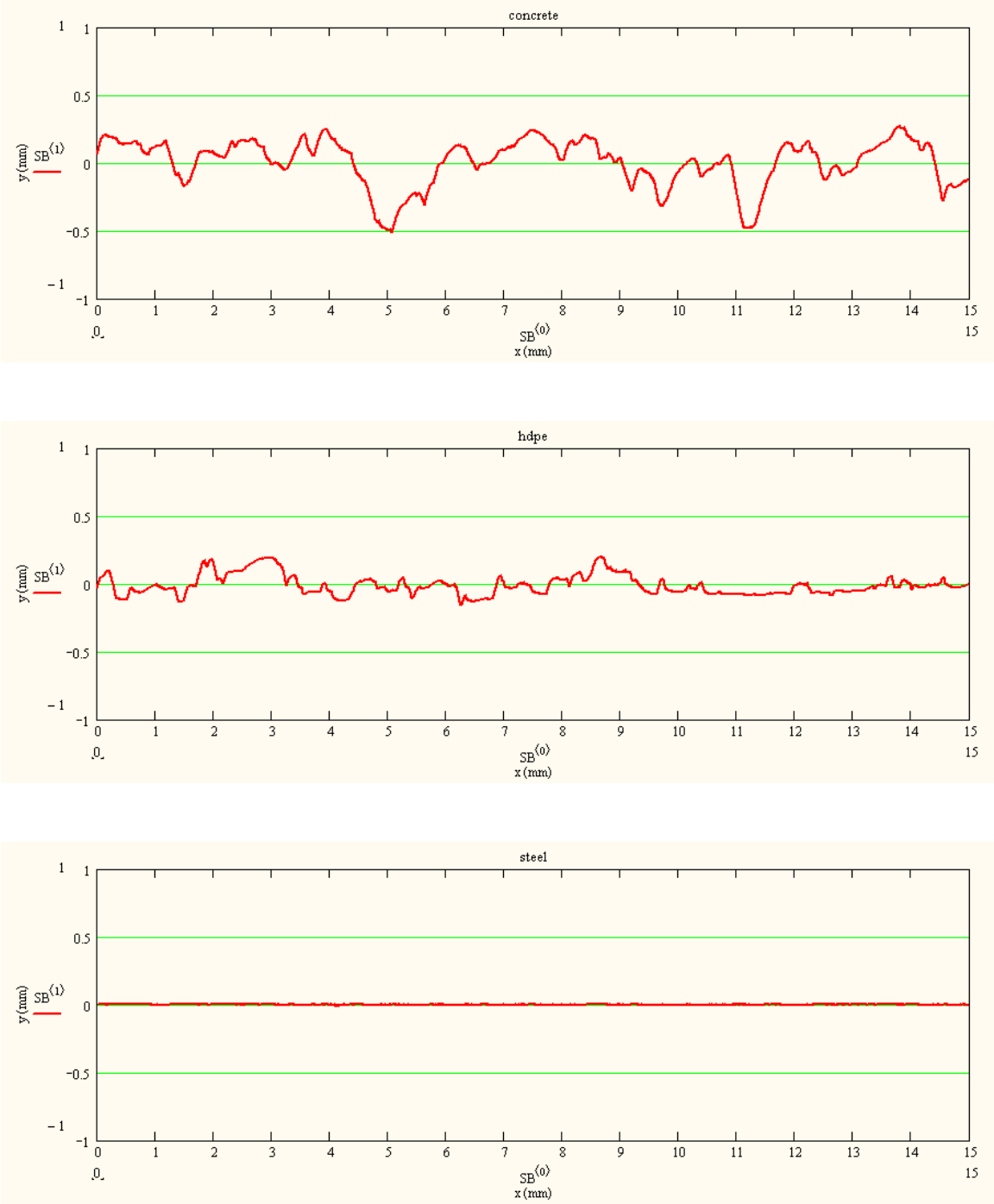


**Figure 3.41 -** Real surface study profiles with 0.004mm resolution and 15-mm length.

- Depth of Surface Smoothness ($R_p$)
- Maximum peak to valley roughness ($R_{max}$)

For validation purposes, the mathgram results are compared to a profilometer output for the same surface roughness parameters. Different surface profiles are used for validation. The validation surface profiles are 50-mm long and obtained with a 0.001mm horizontal spacing. The mathgram output and the surface profilometer automatic results are compared in Table 3.24 and plotted in Figures 3.42 – 3.45 for each surface roughness parameter investigated.

**Table 3.24 –** Table of calculated and reported conventional surface roughness values.

| **Surface Profile Abbreviation** | **$R_a$ (mm)** | | **$R_q$ (mm)** | |
|---|---|---|---|---|
| | **reported** | **calculated** | **reported** | **calculated** |
| Hobas FRP* | 5.93E-03 | 5.92E-03 | 8.17E-03 | 8.17E-03 |
| Packerhead Concrete | 4.45E-02 | 4.40E-02 | 5.85E-02 | 5.90E-02 |
| Steel | 1.99E-02 | 1.90E-02 | 2.49E-02 | 2.40E-02 |
| Vitrified clay | 9.81E-02 | 9.80E-02 | 1.25E-01 | 1.25E-01 |
| **Surface Profile Abbreviation** | **$R_p$ (mm)** | | **$R_{max}$(mm)** | |
| | **reported** | **calculated** | **reported** | **calculated** |
| Hobas FRP* | 5.99E-02 | 5.90E-02 | 8.20E-02 | 8.10E-02 |
| Packerhead Concrete | 2.44E-01 | 2.38E-01 | 4.06E-01 | 4.04E-01 |
| Steel | 7.45E-02 | 7.40E-02 | 1.59E-01 | 1.59E-01 |
| Vitrified clay | 3.83E-01 | 3.82E-01 | 6.09E-01 | 6.07E-01 |

***:**FRP stands for Fiber Reinforced Polymer.

The correlation coefficients for all the conventional roughness values are 0.999.

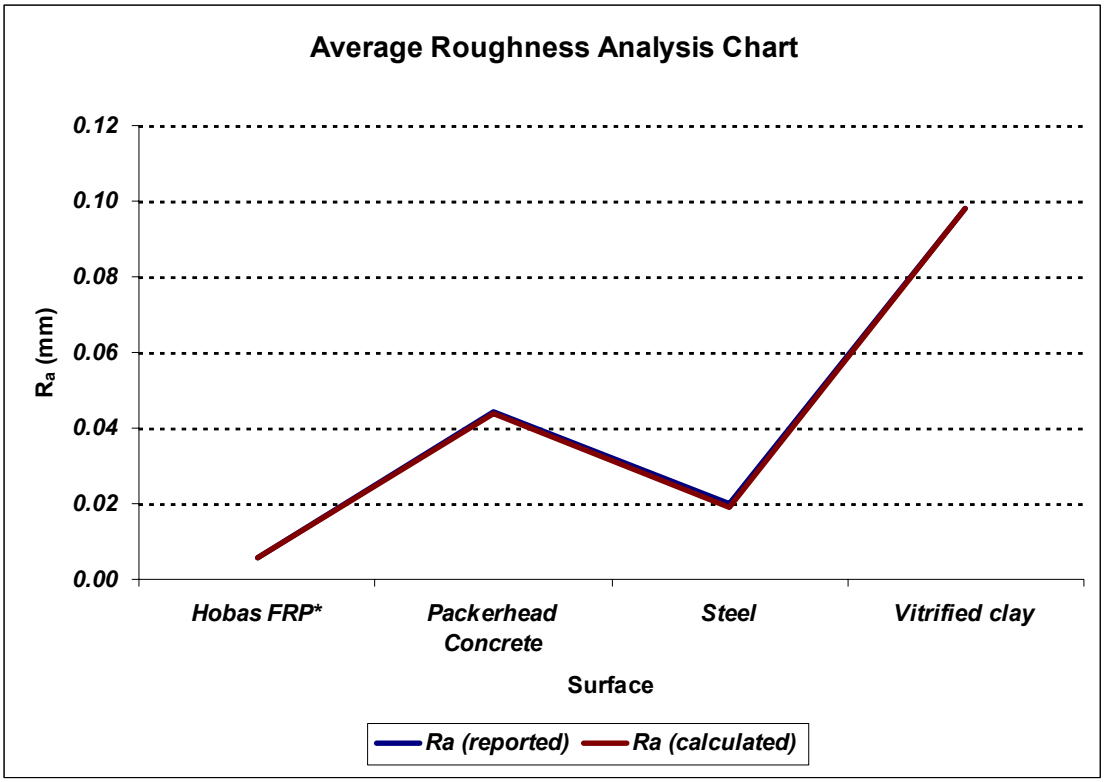


**(a)**

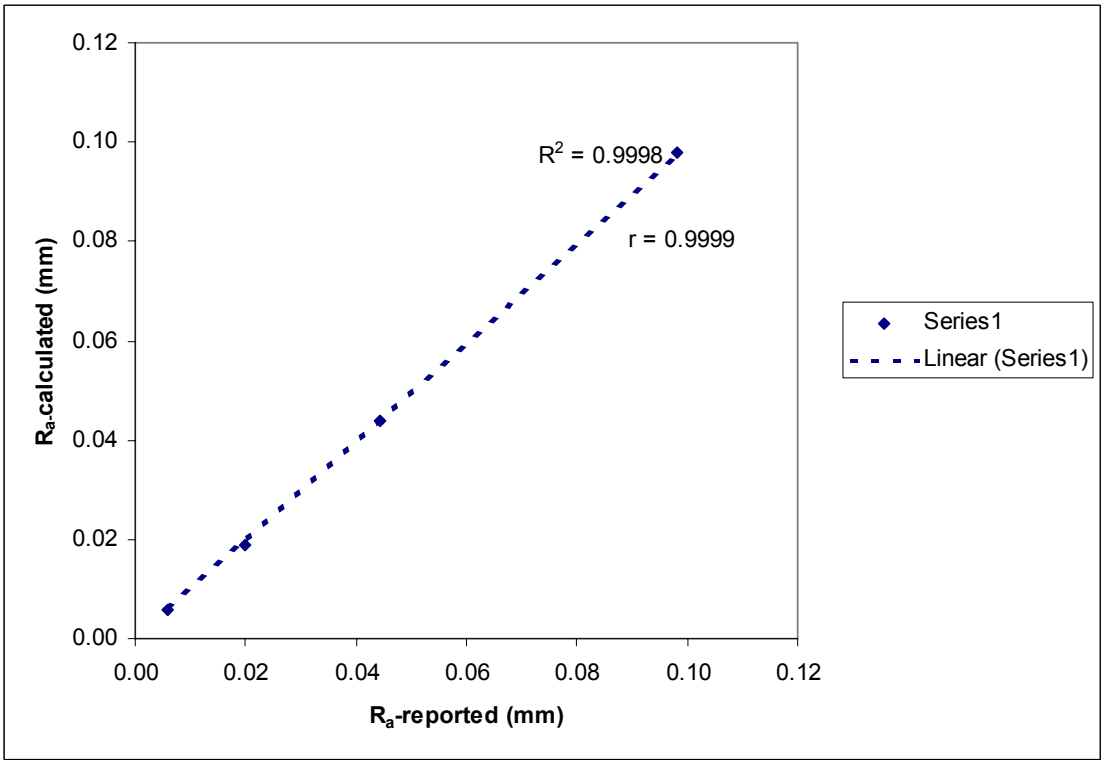


**(b)**

**Figure 3.42 – (a)** Graph showing the trend of $R_a$ (calculated) and $R_a$ (reported), **(b)** Plot of regression analysis between the calculated and reported $R_a$ values.

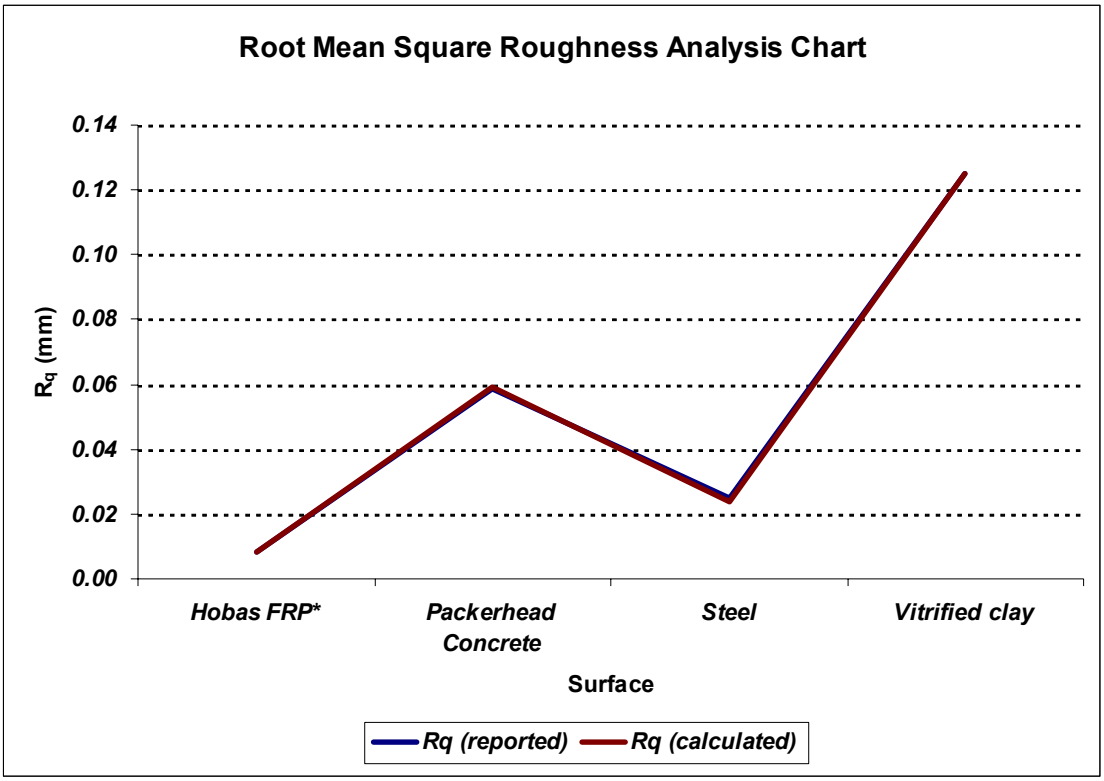


**(a)**

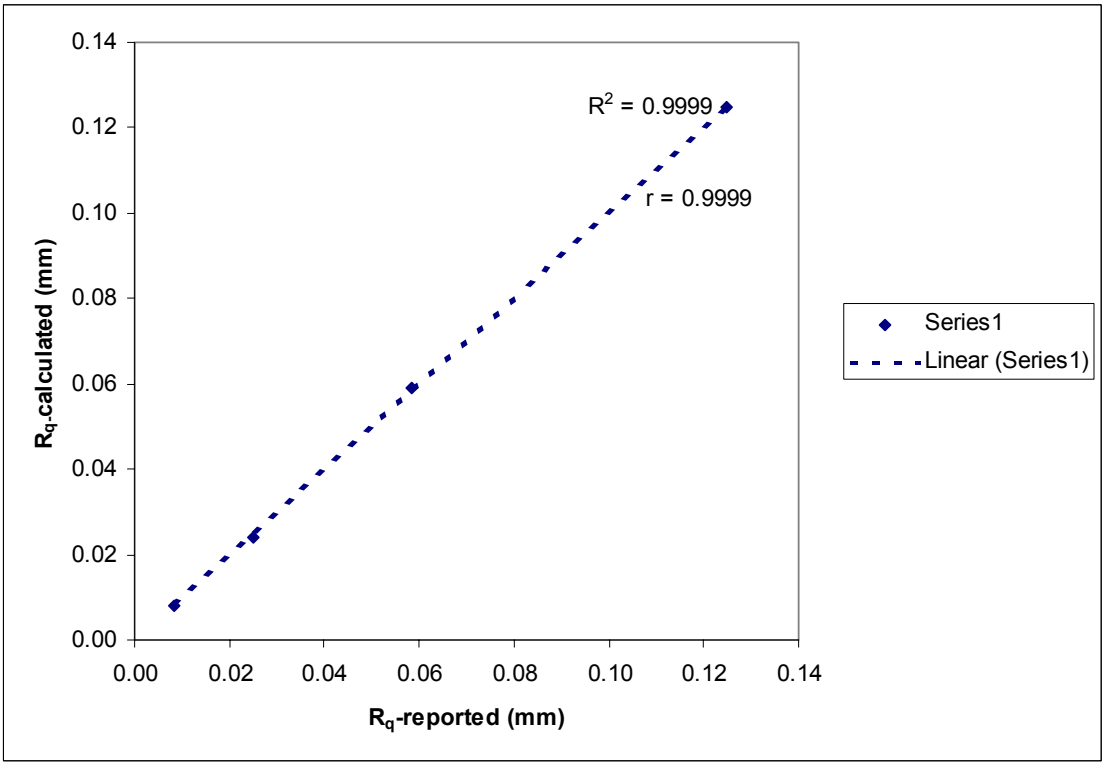


**(b)**

**Figure 3.43 – (a)** Graph showing the trend of $R_q$ (calculated) and $R_q$ (reported), **(b)** Plot of regression analysis between the calculated and reported $R_q$ values.

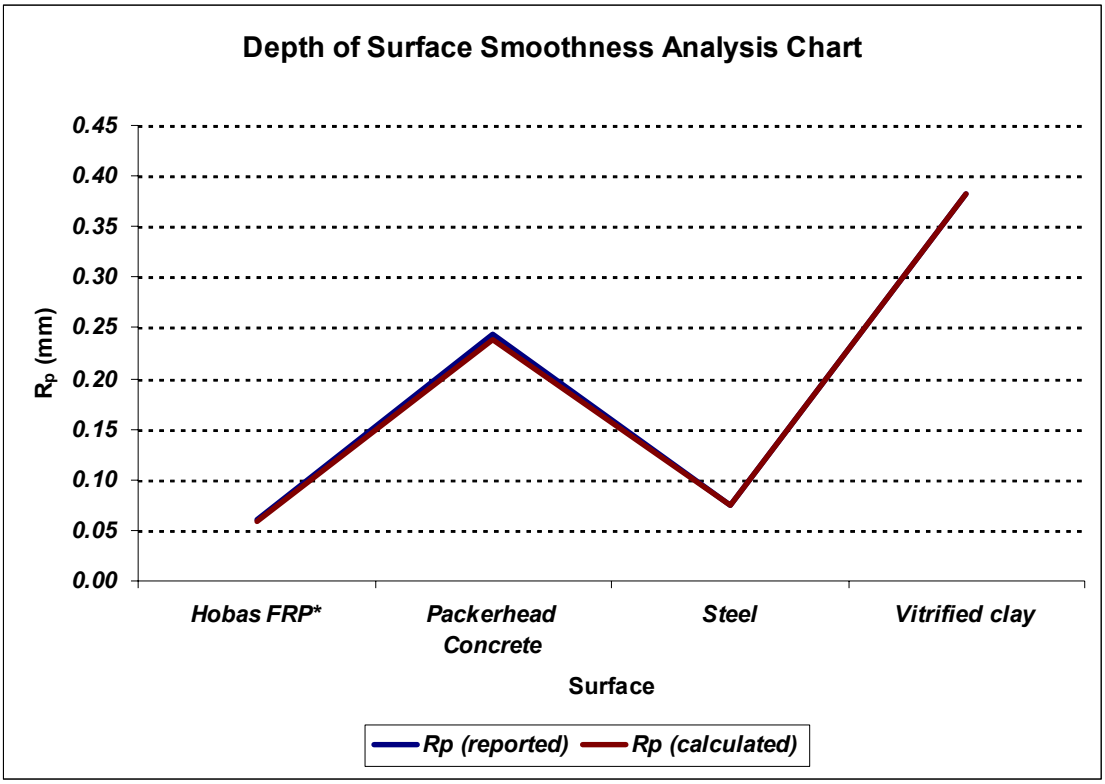


**(a)**

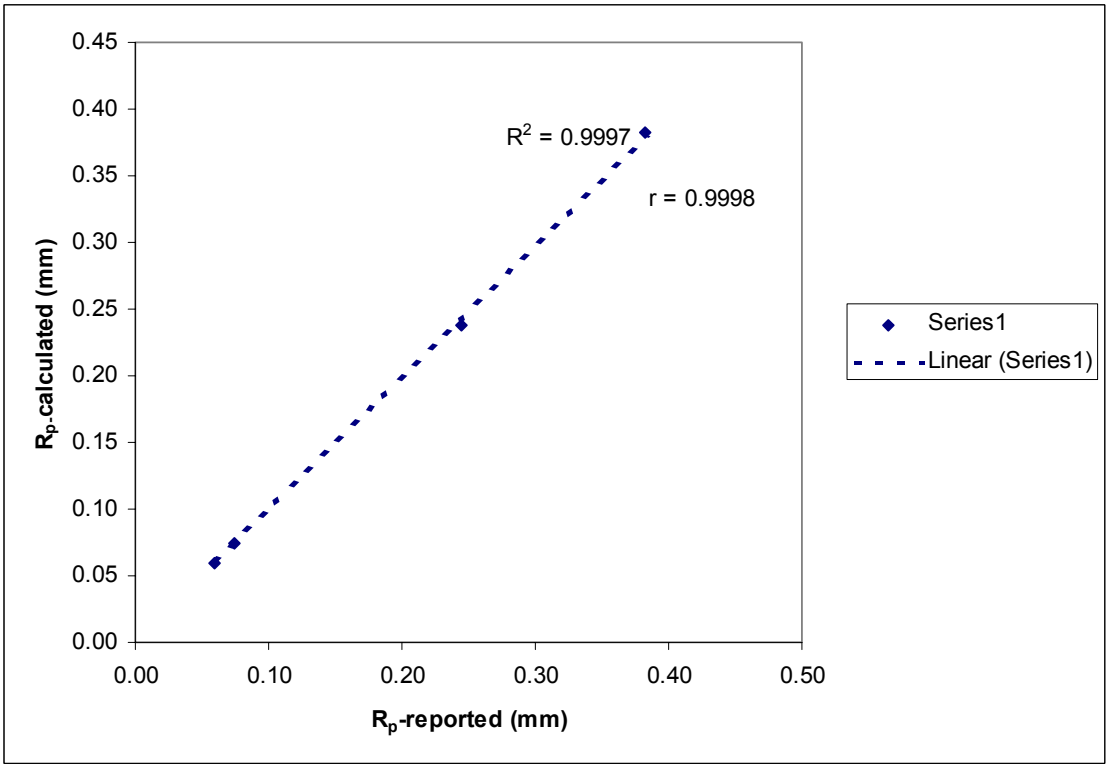


**(b)**

**Figure 3.44 – (a)** Graph showing the trend of $R_p$ (calculated) and $R_p$ (reported), **(b)** Plot of regression analysis between the calculated and reported $R_p$ values.

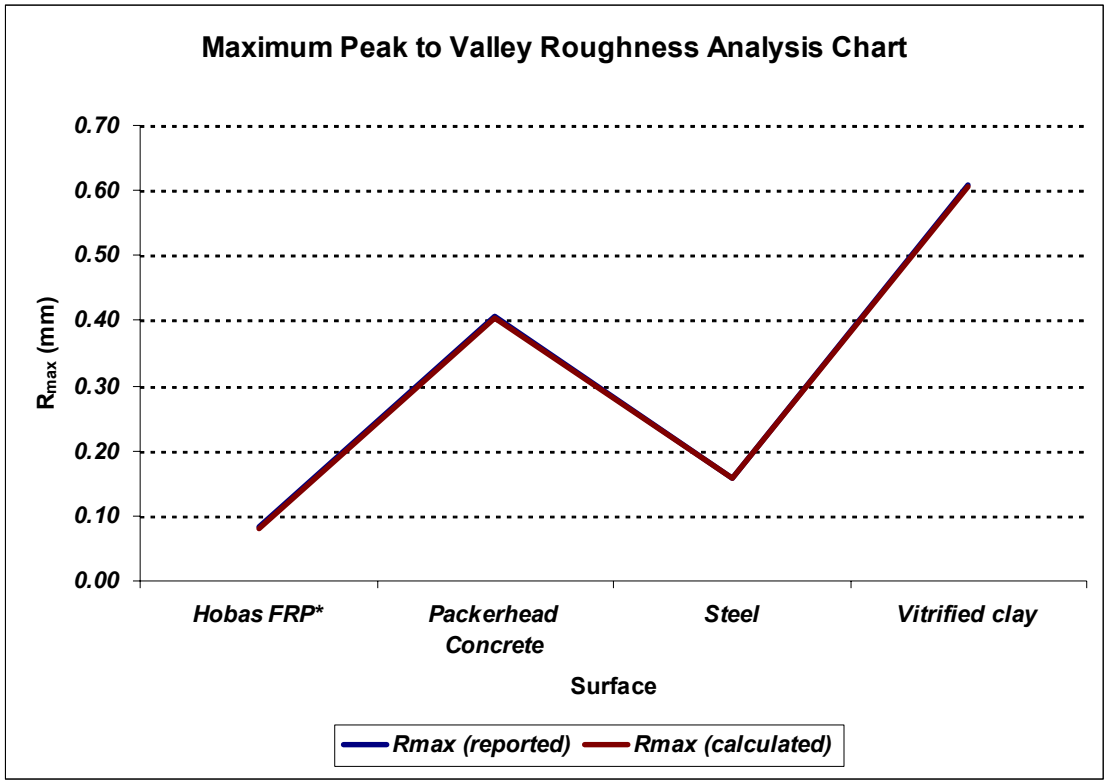


**(a)**

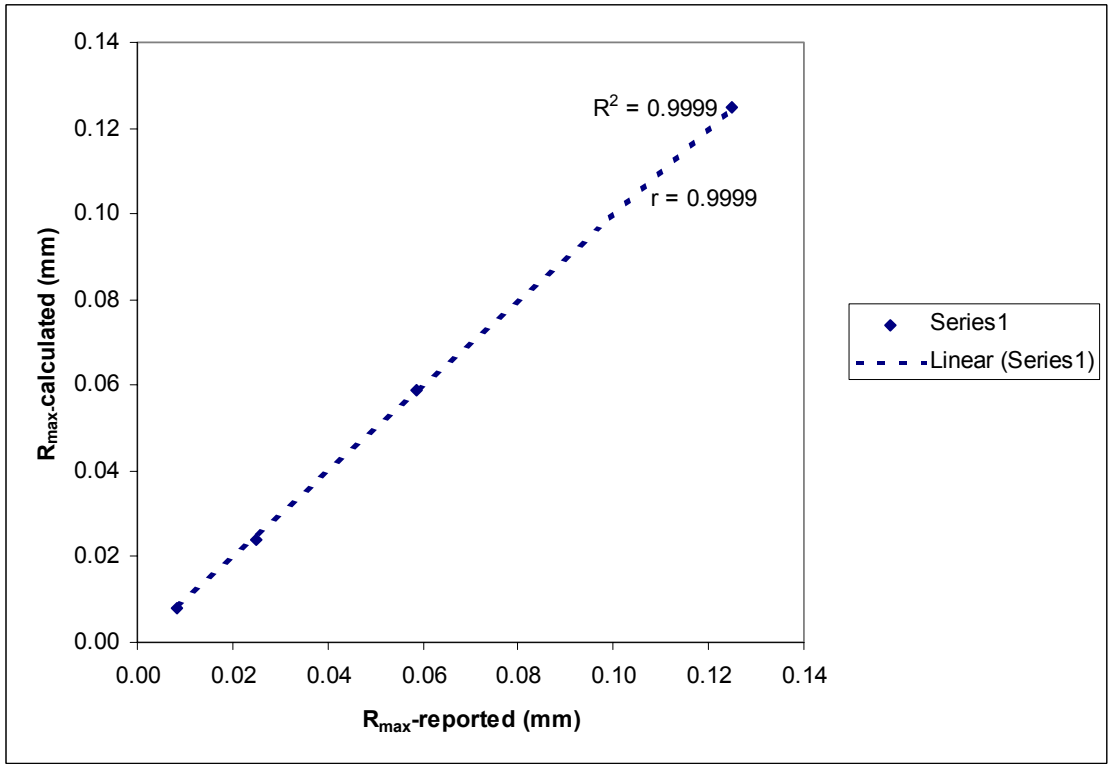


**(b)**

**Figure 3.45 – (a)** Graph showing the trend of $R_{max}$ (calculated) and $R_{max}$ (reported), **(b)** Plot of regression analysis between the calculated and reported $R_{max}$ values.

### *3.4.3 Normalized Roughness Parameter*

For the normalized roughness parameter, a Mathcad 2001 Professional algorithm is used. For a $D_{50} = 0.5mm$, the same profiles analyzed in the previous section assign the following normalized roughness parameters as shown in Table 3.25.

**Table 3.25 –** Table of calculated normalized roughness values for four surface profiles.

| Surface Profile Abbreviation | $R_n$ |
|---|---|
| Hobas FRP | 3.10E-02 |
| Packerhead Concrete | 1.60E-01 |
| Steel | 7.70E-02 |
| Vitrified clay | 2.12E-01 |

### *3.4.4 Spike Parameter Quadratic on Surface Profiles*

The Spike Parameter Quadratic (SPQ) is evaluated in accordance with the algorithm proposed by Stachowiak (1998). In the original method proposed, the above-mean line features are designated as “spikes”. Note that from here forward, the SPQ for surface profiles proposed by Stachowiak (1998) will be referred as SPQ-surf.

The input for the analysis is the $(x_i, z_i)$ coordinates of the extracted surface profile. From this data set, the least squares slope is calculated by:

$$m = \frac{\sum_{i=1}^{n} x_i z_i - n \cdot x_{av} \cdot z_{av}}{\sum_{i=1}^{n} x_i^2 - n \cdot x_{av}^2} \qquad \textbf{(3.12)}$$

where,

$$x_{av} = \frac{\sum_{i=1}^{n} x_i}{n}, \qquad z_{av} = \frac{\sum_{i=1}^{n} z_i}{n}, \qquad \textbf{(3.13)}$$

and $n$ stands for the number of points along the surface profile. The least square slope $m$ is extracted from the –z values by subtracting $x_{av} * m$ from each value and $z_{av,new}$ is computed. For the rest of the calculation, the methodology is explained in Section 2.3.2.1.6.

Unfortunately, as for SP and SPQ for particle outlines, the digital input for the surfaces analyzed in the original study by Stachowiak (1998) were not available. Thus, a digitization program, *Enguage Digitizer*, is utilized to capture the surface profiles used by Stachowiak (1998). Figure 3.46 shows the seven surface profiles used by Stachowiak (1998) upon scanning and digitizing the profiles.

The calculated and reported SPQ-surf values for the surface profiles are provided in Table 3.26.

CAL - **crushed alumina**

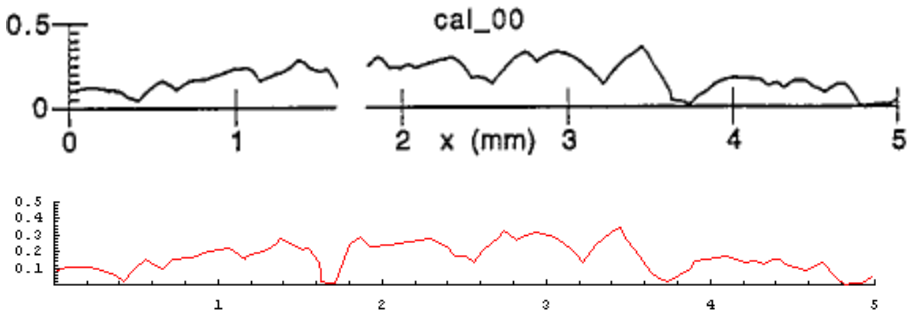


D – **diamond**

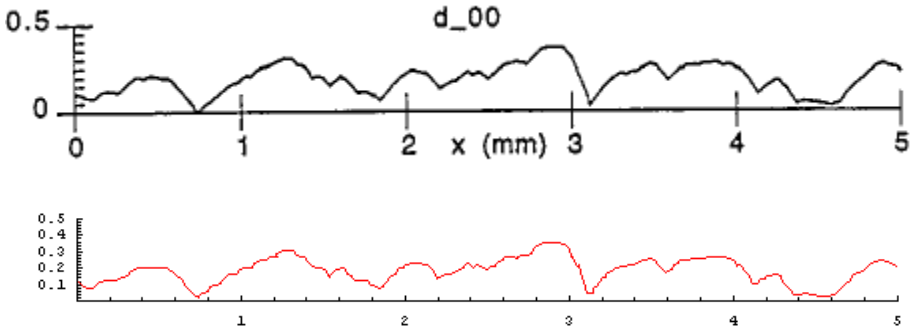


G – **garnet**

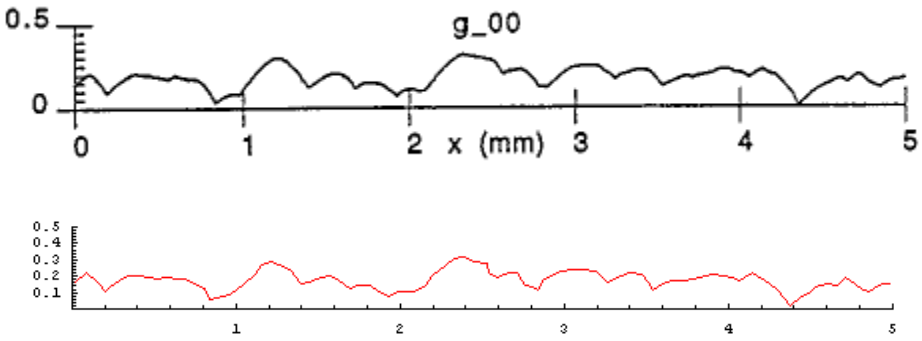


GB - **glassbead**

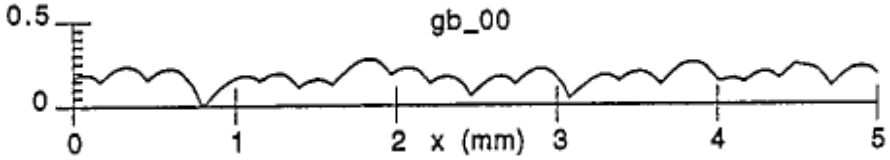


**Figure 3.46 -** Comparison of the original profiles scanned from Stachowiak (1998) shown in black and digitized profiles for processing using *Enguage Digitizer* shown in red (aspect ratio = z/x = 1).

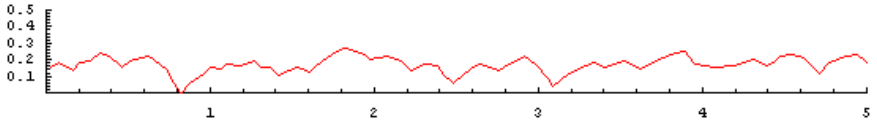


Q – **quartz**

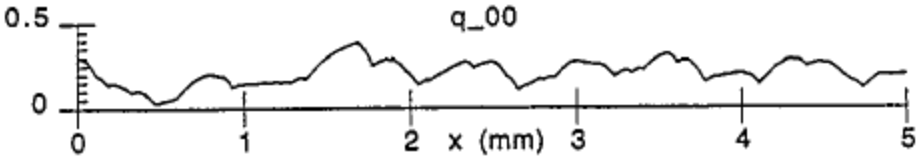


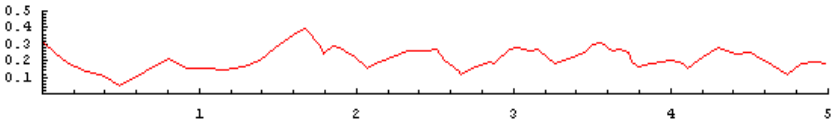


SIC – **silicon carbide**

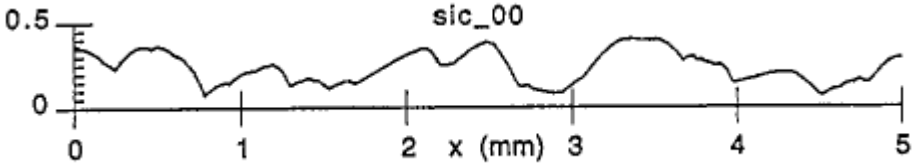


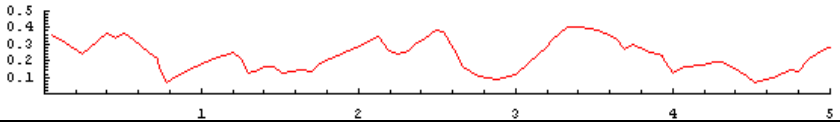


SS – **silica sand**

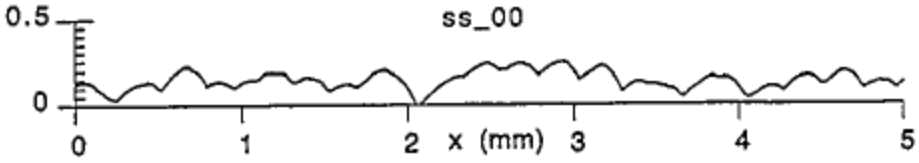


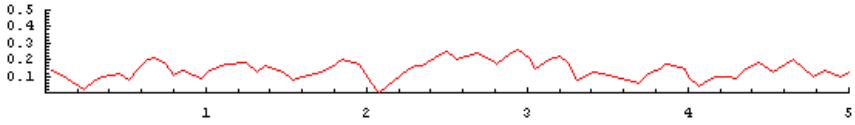


**Figure 3.46 (continued).**

The values shown in Table 3.26 are investigated for correlation and the graph is shown in Figure 3.47. Considering the calculated values are subject to any errors associated with digitization of the surface profiles, a correlation of 0.943 is regarded as appropriate.

**Table 3.26 –** Table of calculated and reported SPQ-surf values for seven abrasive surface profiles.

| Surface Name | SPQ-surf (calculated) | SPQ-surf (reported) |
|---|---|---|
| Cal | 0.4 | 0.38 |
| D | 0.378 | 0.37 |
| G | 0.4 | 0.31 |
| Gb | 0 | 0.111 |
| Q | 0.308 | 0.33 |
| Sic | 0.476 | 0.38 |
| Ss | 0.202 | 0.28 |

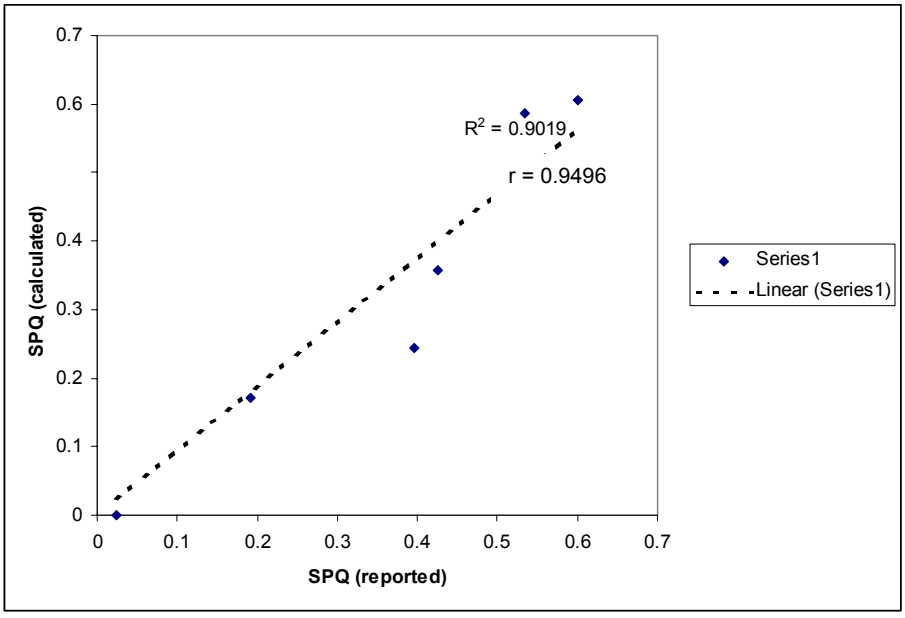


**Figure 3.47 –** Plot of regression analysis between the calculated and reported SPQ-surf parameters.

### *3.4.5 Centroid Trace on Surface Profiles*

The Centroid Trace (CT) method is performed in accordance with the method proposed by DeJong (2001). Typical results are shown in Chapter 4.

## 3.5 Concluding Commentary

This chapter has presented the study materials as well as the analysis methods that are used in consecutive chapters of this work. The selection process and output of the real particles and surfaces were outlined in Section 3.1.1. The study materials contain both the real and derived particles and surfaces. In Section 3.1.2, the detailed process of obtaining derived particles was followed by the explanation of the derived surface generation method in Section 3.1.3. In obtaining the derived versions, the resolution in terms of points/mm and the surface characteristics were taken as the basis for the selection of inputs.

The study materials section was followed by the validation of the *part-dsurf* and *surf-dpart* mathgrams presented through Section 3.2. The mathgrams were proven to result in an output same as the input in two-way conversions, e.g. in *surf-dpart-ddsurf* conversion, the *surf* and *ddsurf* are same profile with an elevation difference that is pre-known.

Subsequently, the study methods for the real and derived particles, namely the Form Factor by Sukumaran and Ashmawy (2001), Minimum Zone Circles using Voronoi

Diagrams, Wadell's Roundness, Particle Angularity by Hamblin and Stachowiak (1995), and Shape Index by Boyce and Clark (1964) were examined. Each method was investigated using the input in the corresponding original work and the algorithms written in Mathcad 2001 Professional. The trends and regression coefficients between the reported and generated particle shape values were presented as justification of the generated algorithm. Only the particle shape method by Wadell's Roundness was extracted from further analysis with the conclusion that the method could not be automated and was user-dependent.

Finally, the study methods for surface roughness analysis were outlined and justified. The study method contained selected conventional roughness parameters, Spike Parameter Quadratic by Stachowiak (1998), and the Centroid Trace Method developed by DeJong (2001).

The justified study method algorithms for the particle and surface roughness measurements are further implemented using the study particles and surfaces in Chapter 4.

# CHAPTER 4

# ANALYSIS RESULTS AND DISCUSSION

## 4.1 Results of Analysis of Particle Shape Parameter Values

### *4.1.1 Sukumaran and Ashmawy Form Factor*

As previously described in Section 3.3.3, Form Factor (FF) is calculated using:

$$(Form \quad Factor)^2 = \sqrt{(Shape \quad Factor)^2 + (Angularity \quad Factor)^2} \tag{4.1}$$

Sukumaran and Ashmawy (2001) used a 9° intervals in their analysis and this study is conducted with the same input corresponding to $N = 40$ intervals around the particle outline. The Shape Factor (SF) and the Angularity Factor (AF) are calculated for the real and derived particles, i.e. *parts* and *dparts* and the results are as shown in Table 4.1.

Figure 4.1(a) shows a plot of the data values for SF versus AF; whereas in Figure 4.1(b) the data points are placed by the corresponding particle outlines.

Using Eq. 4.1 and the SF and AF values calculated in Table 4.1, the Form Factors (FF)

are calculated as shown in Table 4.1.

**Table 4.1 –** SF, AF, and FF values for the study *parts* and *dparts.*

| Particle Name | SF (%) | AF (%) | FF (%) |
|---|---|---|---|
| p1 | 13.5 | 2.0 | 13.6 |
| p2 | 39.5 | 4.8 | 39.8 |
| p3 | 40.1 | 18.0 | 43.9 |
| p4 | 47.7 | 17.7 | 50.9 |
| concrete-par | 41.6 | 58.3 | 71.6 |
| hdpe-par | 18.9 | 11.6 | 22.1 |
| steel-par | 0.0 | 0.0 | 0.0 |

Figure 4.2(a) is a plot of the FF values for the corresponding particles with data points, and (b) shows the particle outlines at the corresponding FF values.

Figure 4.1 shows that AF is affected by the roughness of the particle outline; whereas SF is dependent more on the macro shape of the particle outline. As the AF increases, the shape changes from an almost perfect circle (*steel-par*) to the *HDPE-par*, where *HDPE-par* is superimposed with a much rougher outline. Note that there is not a significant change of AF between *steel-par* (AF=0%) and *p1*(AF=2.0%) and a small increase for *p2* (4.8%). The particles *p3* and *p4* have similar AF values of 18.0% and 17.7%, respectively due to their comparable particle outline roughness, although their general shapes are different. On the other axis, the shape factor (SF) is not affected by the micro-shape, but rather dependent on the macro-shape of the particle. As the SF increases again from *steel-par* (0%) to *p1* (SF=13.5%) and *p2* (SF=39.5%), increase in the aspect ratio is observed, where the *steel-par* is analogous to a circle, particle *p2*

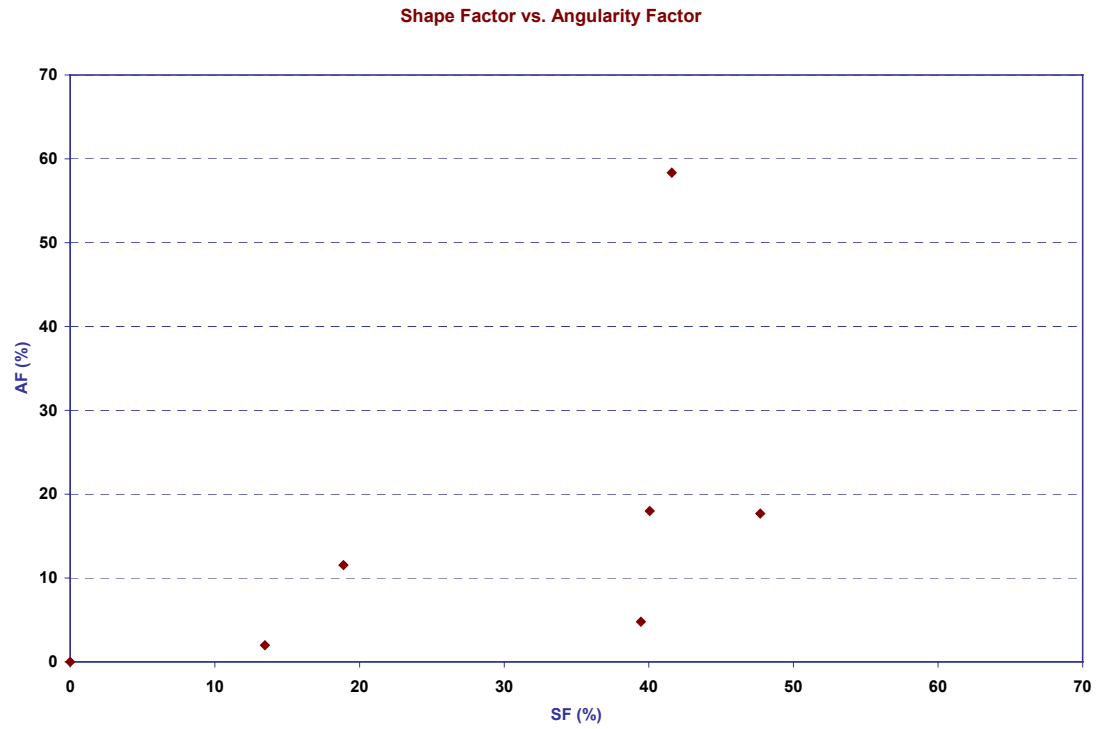


**(a)**

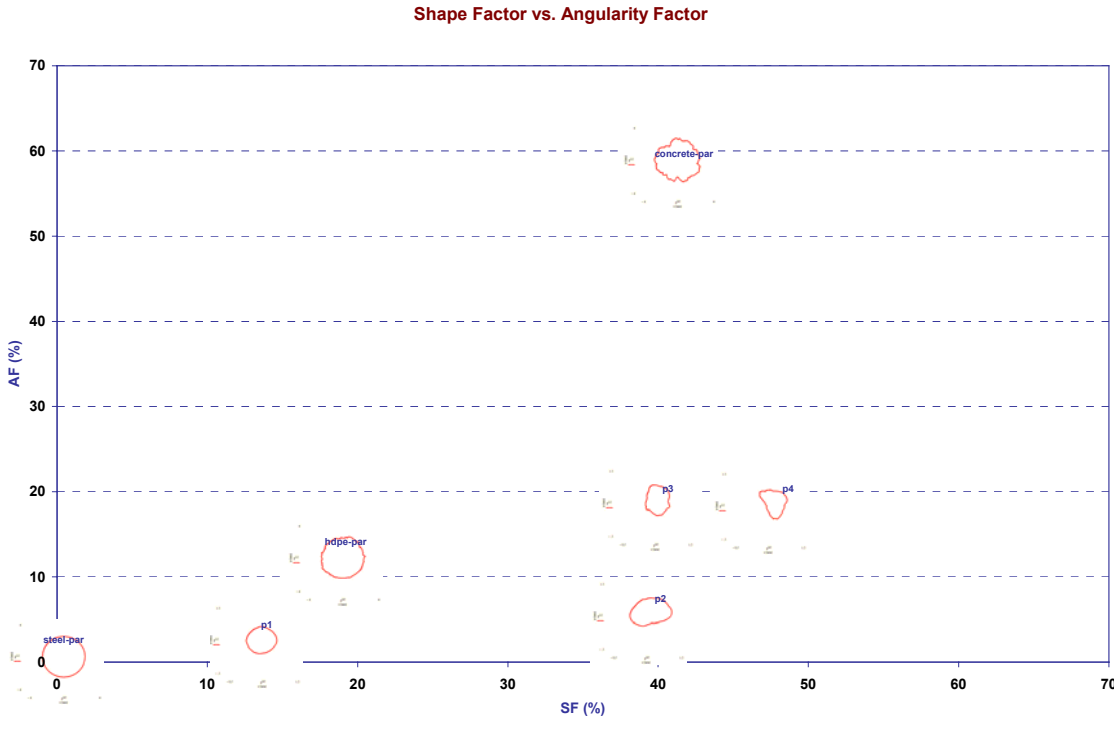


**(b)**

**Figure 4.1–** Plot of SF versus AF for the study particles; **(a)** with data points, **(b)** with particle outlines (the real particle outlines are enlarged for visualization).

resembles a rectangle with the horizontal dimensions almost twice as the vertical dimensions (for the shape shown as *p2*). The particles *p2* and p3 have comparable SF values of 39.5% and 40.1%, respectively due to the similar macro-shape although the micro-shape features are different for two particles. Note that although the size of derived particles, e.g. *concrete-par*, *HDPE-par*, and *steel-par* are not comparable to the size of the real particles (*p1*, *p2*, *p3*, and *p4*), SF and AF are both dimensionless particle shape parameters, where size of the particle does not affect the result.

Figure 4.2 shows the FF for the study particles calculated by inputting SF and AF values in Eq. 4.1. Due to the larger values of SF's compared to AF's, the FF is more correlated to the SF, i.e. the sorting in FF is the same with the sorting by SF except with particles *p4* and *concrete-par.* The reason for the exchange in ordering of these two particles is due to the larger difference in their AF values (58.3% vs. 17.7% for the *concrete-par* and *p4*¸respectively) compared to the minor difference in their SF values (41.6% vs 47.7% for *concrete-par* and *p4,* respectively).

### *4.1.2 Minimum Zone Circles using Voronoi Diagrams*

#### 4.1.2.1 Particle Shape Characterization by Three Circles Analysis using Characteristic Radius Ratio

The process of obtaining the Minimum Zone Circles (MZC), namely the Maximum Inscribing Circle (MIC) and concentric the Minimum Circumscribing Circle (MCC) was explained in Section 3.3.4. A newly developed shape parameter, *CRR,* was introduced as:

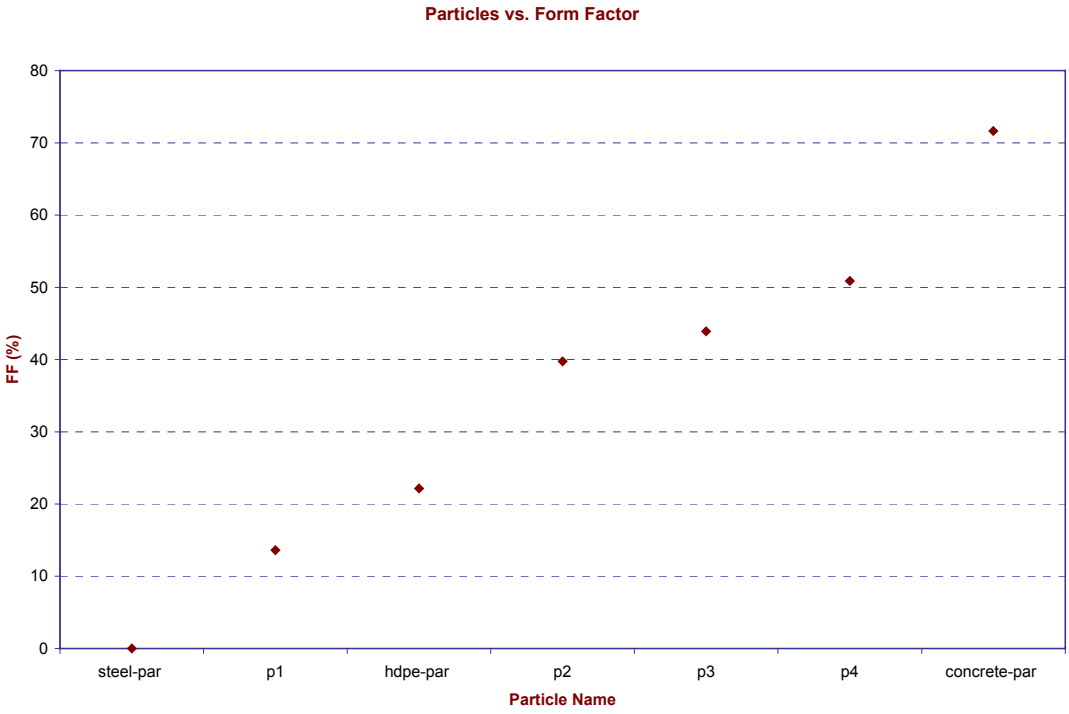


**(a)**

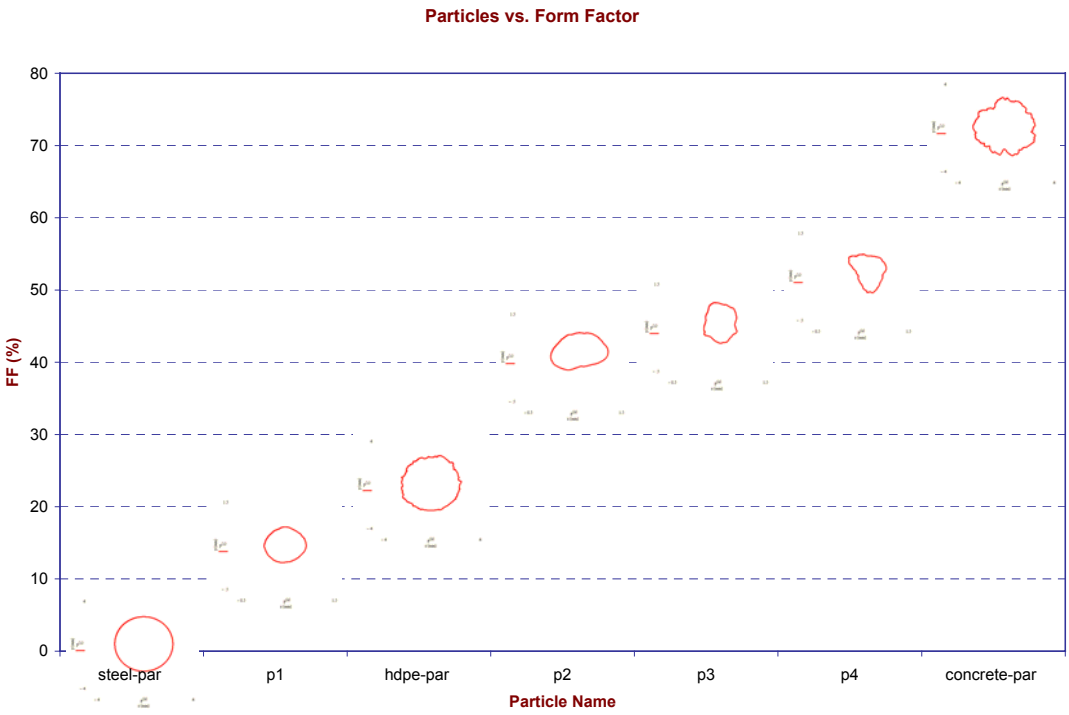


**(b)**

**Figure 4.2–** Plot of FF for the study particles; **(a)** with data points, **(b)** with particle outlines (the real particle outlines are enlarged for visualization).

$$CRR = \frac{r_{mcc} - r_{mic}}{r_{mic}} \quad \textbf{(4.2)}$$

where $r_{mcc}$ and $r_{mic}$ stand for the radius of MCC and MIC, respectively. Although the formulation introduced in CRR may not be unique, its derivation based on Voronoi diagrams for particle shape analysis is new. Figure 4.3 shows the study particles' outlines with the corresponding MIC and MCC circles as well as the centroid of the MZCs. The CRR values for the study particles are shown in Table 4.2. Figure 4.4 shows the CRR values with the data points (a) and with the corresponding study particle outlines (b). By definition, CRR resembles the aspect ratio. It is based on the difference between the radii of two concentric circles, MCC and MIC divided by the radius of MIC. As Figure 4.4 shows as the particle is more decorated with distinct concave or convex segments, the CRR increases due to the decrease in MIC and coincident increase in MCC. Thus, again in the lower end of the CRR value, *steel-par* and *p1* (CRR=17.4%) are observed. Note that also *HDPE-par* is in the lower end between *steel-par* and *p1* and the reason for that is *HDPE-par* has a circular macro-shape and the micro-shape features superimposed on the macro-shape are of small magnitude lowering the difference between the radius values of the MIC and MCC. *Concrete-par* has one dimension slightly longer than the other dimension, with much bigger micro-shape features compared to the *HDPE-par* and thus it has a CRR value larger than *HDPE-par* and *p1.* Study particles *p3, p2,* and *p4* all have larger CRR values due to the elongated macro-shape of the particle. An upside down triangle resembling shape of *p4* has the highest CRR value since a smaller MIC results by the inward segments with a relatively larger MCC determined by the outward segments at the corners.

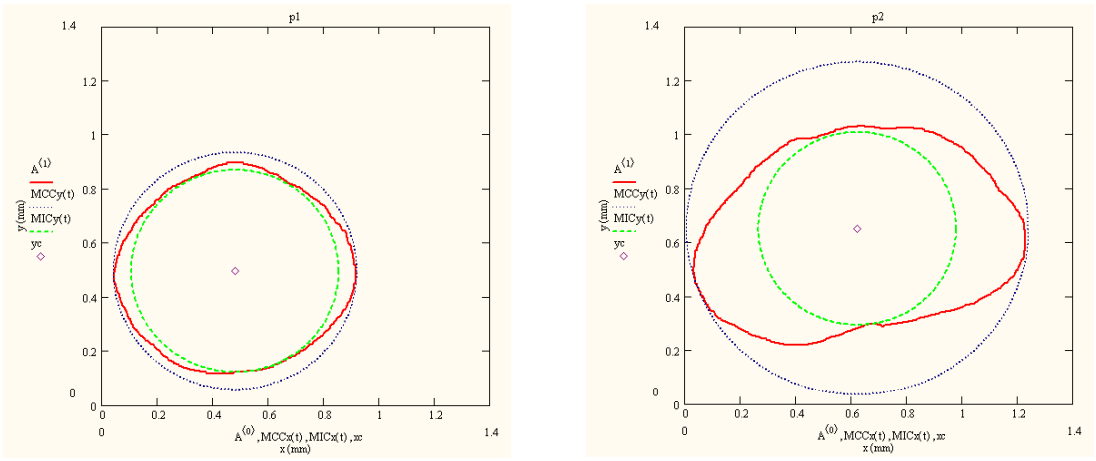


**(p1)** **(p2)**

**(p3)** **(p4)**

**Figure 4.3–** Plot of the particle outlines with MIC and MCC circles and the MZC centroid (the real particle outlines are enlarged for visualization).

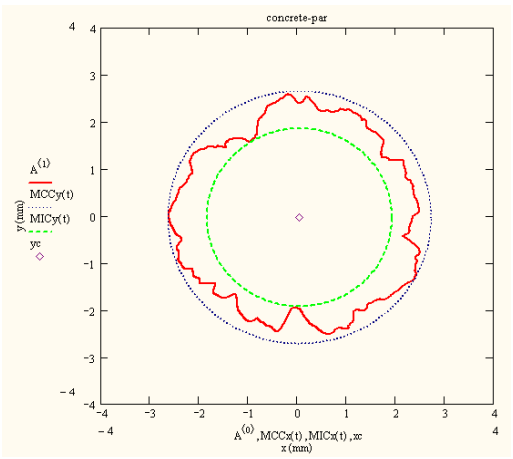


**(concrete-par)**

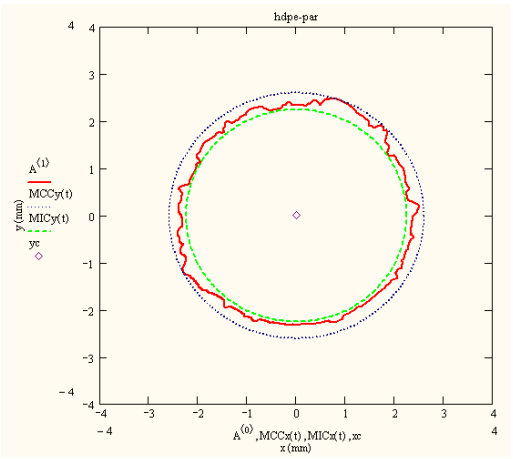


**(HDPE-par)**

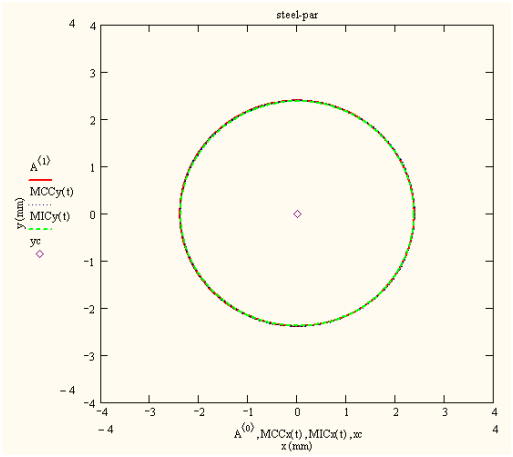


**(steel-par)**

**Figure 4.3 (continued).**

**Table 4.2 –** CRR values for the study *parts* and *dparts.*

| Particle Name | CRR (%) |
|---|---|
| p1 | 17.4 |
| p2 | 72.8 |
| p3 | 61.5 |
| p4 | 81.8 |
| concrete-par | 42.0 |
| hdpe-par | 15.6 |
| steel-par | 0.4 |

### *4.1.3 Particle Angularity*

#### 4.1.3.1 Meso-Scale Particle Angularity Characterization by Spike Parameter

The Spike Parameter (SP) is calculated using the algorithm as explained in Section 3.3.5.1. The input parameters for the study particles are taken in accordance with the study performed in Chapter 3 regarding the input parameters and $nsteps$ (see Section 3.3.5.1). Although the number of average data points for the real particles are 695, real and derived particles are modified to 360 data point outlines and the input parameters $(r, stpxl, incpxl)$ are taken as $(10,15,1)$. The number of step sizes, $nsteps$, is equal to 21 for the mentioned input file and SP parameters. The SP and normalized SP values are shown in Table 4.3. The normalized SP values are calculated using $NSP = (SP - SP_{\min})/(SP_{\max} - SP_{\min})$; where $SP_{min}$ and $SP_{max}$ are equal to 0.113 (*steel-par*) and 0.424 (*concrete-par*), respectively for the study particles.

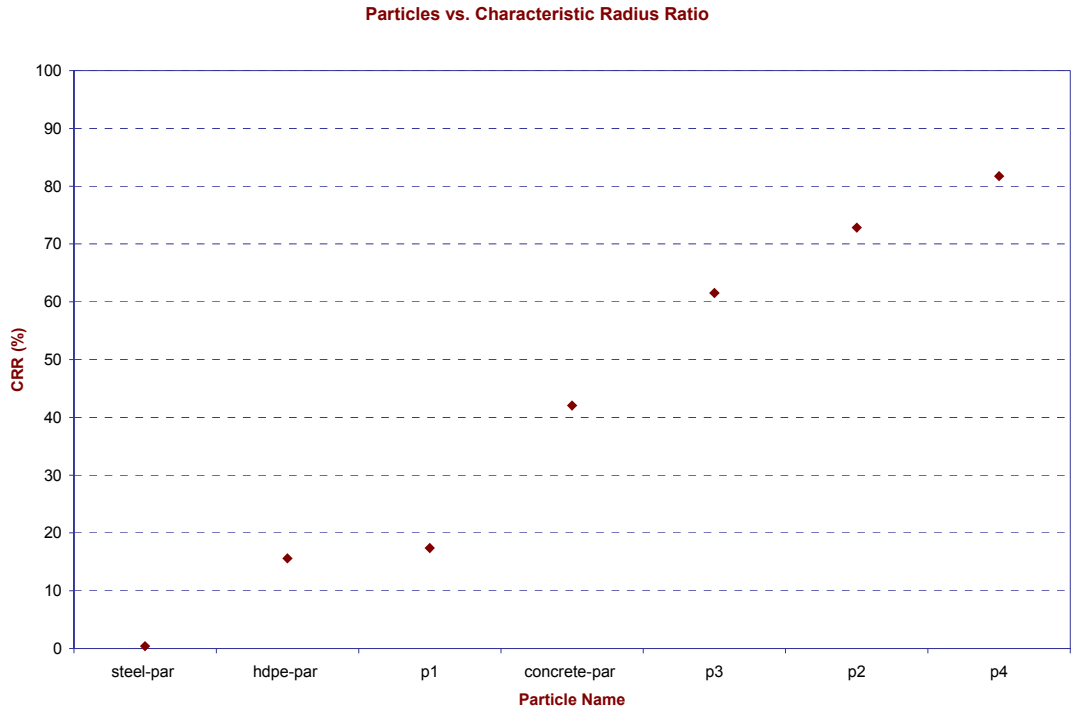


**(a)**

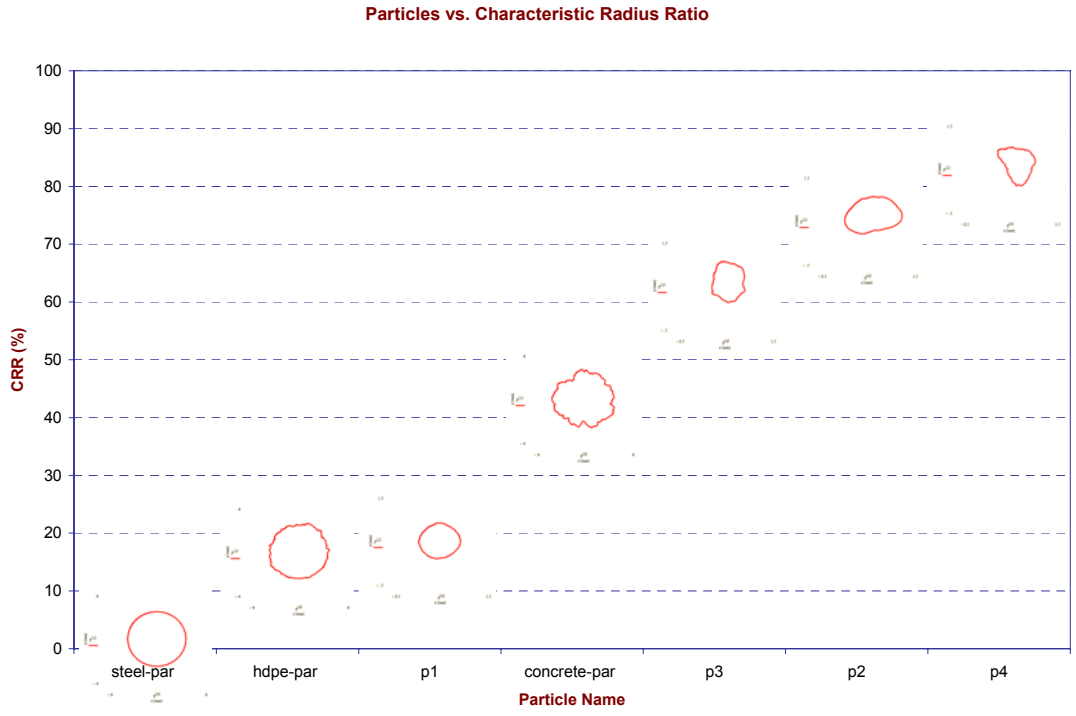


**(b)**

**Figure 4.4–** Plot of CRR for the study particles; **(a)** with data points, **(b)** with particle outlines (the real particle outlines are enlarged for visualization).

**Table 4.3 –** SP values for the study *parts* and *dparts.*

| Particle Name | SP(A,10,15,1) | Normalized SP |
|---|---|---|
| p1 | 0.164 | 0.164 |
| p2 | 0.186 | 0.235 |
| p3 | 0.271 | 0.508 |
| p4 | 0.275 | 0.521 |
| concrete-par | 0.424 | 1.000 |
| hdpe-par | 0.313 | 0.643 |
| steel-par | 0.113 | 0.000 |

In plotting the SP results, NSP values are used rather than SP values since they provide a relative scale among the available study particles. Figure 4.5 shows the NSP values (a) with the data points, and (b) with particle outlines.

The spike parameter (SP) is similar to fractal analysis with the main difference that rather than single line or square segments, etc. a triangle step is used to characterize the particle outline. The parameter is unrelated to the macro shape and solely dependent on the micro-roughness features. As Figure 4.5 shows, the sorting of study particles based on their NSP values results in four particle groups. *Steel-par* is at the lowest end with a NSP value of 0.0. The particles of *p1* and *p2* with NSP of 0.16 and 0.23, respectively; followed by *p3, p4,* and *HDPE-par* (with NSP values of 0.51, 0.52, and 0.64, respectively); and at the other end of the spectrum is the *concrete-par* with a NSP of 1.0. Figure 4.5 clearly shows that the SP is a measure of the micro-shape feature sizes and it is not related to the macro-shape of the particle outline. This is evident especially from the similar SP values attained for *p3, p4,* and *HDPE-par.* Although the three particles have unambiguously different macro-shapes, they are

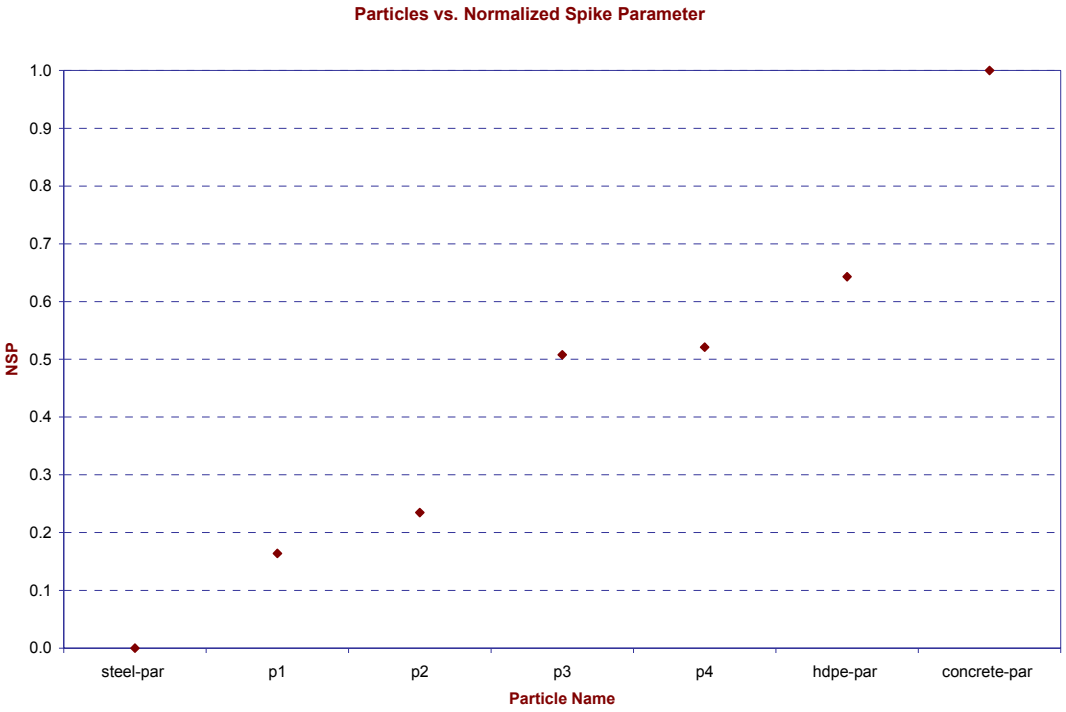


**(a)**

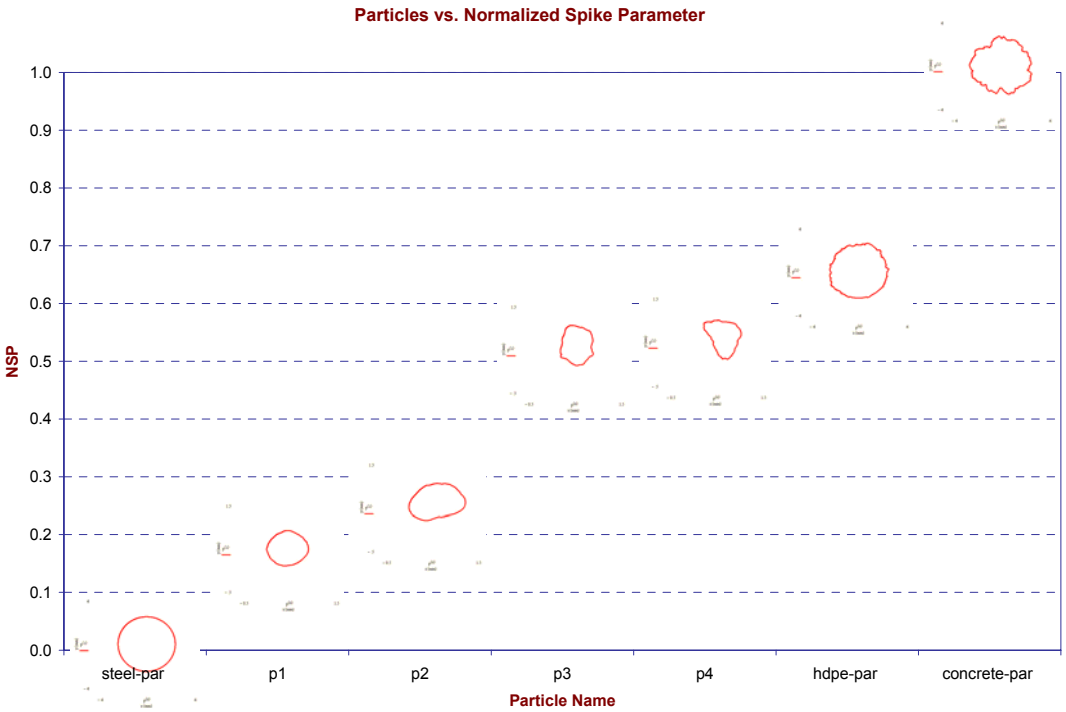


**(b)**

**Figure 4.5–** Plot of NSP for the study particles; **(a)** with data points, **(b)** with particle outlines (the real particle outlines are enlarged for visualization).

decorated with similar size micro-roughness features on the macro-shapes. Additionally, the particles *p1* and *p2* are considerably smooth articles on their surface compared to the (*p3, p4,* and *HDPE-par*) resulting in lower NSP (and SP) values.

#### 4.1.3.2 Macro-Scale Particle Angularity Characterization by Spike Parameter Quadratic

The Spike Parameter Quadratic (SPQ) is calculated using the algorithm as explained in Section 3.3.5.2. The computed values were normalized similar to SP values. Table 4.4 shows the SPQ and NSPQ values for the corresponding study particle.

**Table 4.4 –** SPQ values for the study *parts* and *dparts.*

| Particle Name | SPQ | Normalized SPQ |
|---|---|---|
| p1 | 0.000 | 0.000 |
| p2 | 0.171 | 0.434 |
| p3 | 0.268 | 0.680 |
| p4 | 0.287 | 0.728 |
| concrete-par | 0.382 | 0.970 |
| hdpe-par | 0.394 | 1.000 |
| steel-par | 0.000 | 0.000 |

Figure 4.6 plots the NSPQ values with data points (a) and with particle outlines (b). Figure 4.6 shows that similar to NSP; NSPQ also categorizes the study particles into 4 different types of character behavior. The particles *p1* and *steel-par* have NSPQ values of 0.0. The relatively smooth particle, *p2,* with a rectangular resembling macro-shape

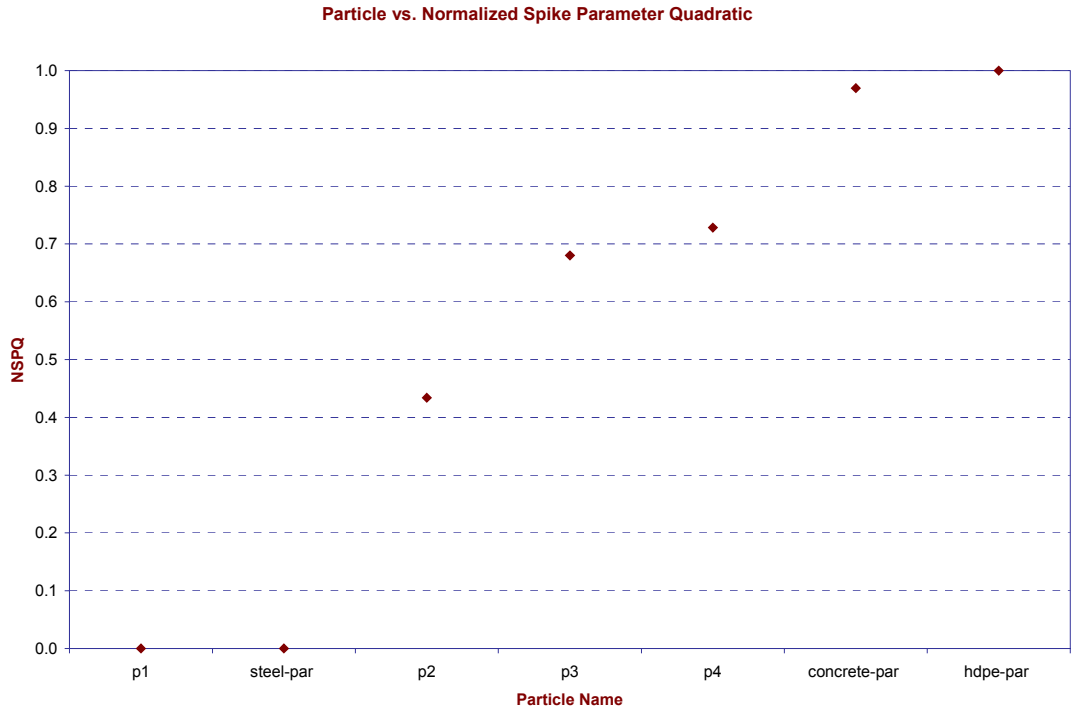


**(a)**

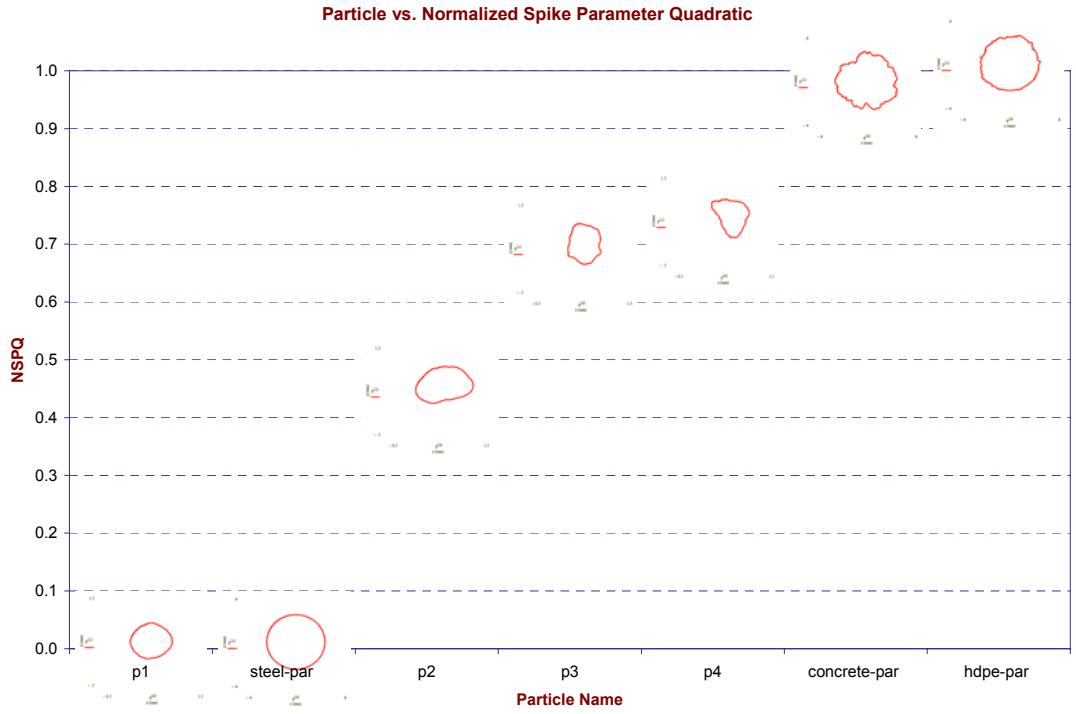


**(b)**

**Figure 4.6–** Plot of NSPQ for the study particles; **(a)** with data points, **(b)** with particle outlines (the real particle outlines are enlarged for visualization).

had two spikes outside the LSC of *p2.* The two spikes have considerably rounder edges compared to the rest of the particles that are up the range. The rounder spikes result in larger spike angles, and consequently lower cosine and subsequently lower SPQ values. The particles (*p3* & *p4*) and (*concrete-par* & *HDPE-par*) have similar SPQ values. Compared to (*concrete-par* & *HDPE-par*), (*p3* & *p4*) particles consist of a larger amount of spikes but with an also larger percentage of round spikes resulting in lower NSPQ than *concrete-par* and *HDPE-par*.

Table 4.5 shows the values of SP and SPQ for the study particles considered. Figure 4.7 is a plot of SP versus SPQ values presented in Table 4.5. The SP and SPQ values are very similar for certain particles, especially p3, p4, and HDPE-par. For the mathgram validation process discussed in Section 3.3.5.1, the particles used in the original study by Hamblin and Stachowiak (1996) were utilized. The SP and SPQ values reported by the authors are presented in Table 4.6 for comparison and corresponding particle images are shown in Figure 3.29.

**Table 4.5 –** SP and SPQ values for the study *parts* and *dparts.*

| Particle Name | SP(A,10,15,1) | SPQ |
|---|---|---|
| p1 | 0.164 | 0.000 |
| p2 | 0.186 | 0.171 |
| p3 | 0.271 | 0.268 |
| p4 | 0.275 | 0.287 |
| concrete-par | 0.424 | 0.382 |
| hdpe-par | 0.313 | 0.394 |
| steel-par | 0.113 | 0.000 |

Regarding values in Table 4.6, SP and SPQ values are similar for especially more circular macro shapes (images a, b, and e); whereas the values diverged for the rectangular or triangular macro shape particles (images c, d, f, and g). SP parameter is

**Table 4.6 –** SP and SPQ values calculated for *Hamblin and Stachowiak (1996) study particles.*

| Particle | SP (reported) | SPQ (reported) |
|---|---|---|
| a | 0.1369 | 0.0231 |
| b | 0.2168 | 0.2515 |
| c | 0.2942 | 0.4247 |
| d | 0.3591 | 0.6008 |
| e | 0.2077 | 0.1919 |
| f | 0.2971 | 0.3958 |
| g | 0.3239 | 0.5336 |

calculated similar to fractal analysis but with triangular steps; whereas SPQ parameter calculation is based on a Least Squares Circle (LSC) of the particle outline. In SPQ, only outline portions outside LSC are considered; whereas SP considers various size spikes throughout the outline. Thus, based on the calculation methods and results presented in Table 4.6, SPQ is more sensitive to macro-shape than SP. However, SPQ is not only macro-shape parameter as discussed below.

The dependence of SPQ to macro shape is also evident in Figure 4.7 (b). SPQ is more sensitive to outline macro-shape than SP is. For example, *steel-par* and *p1* acquire

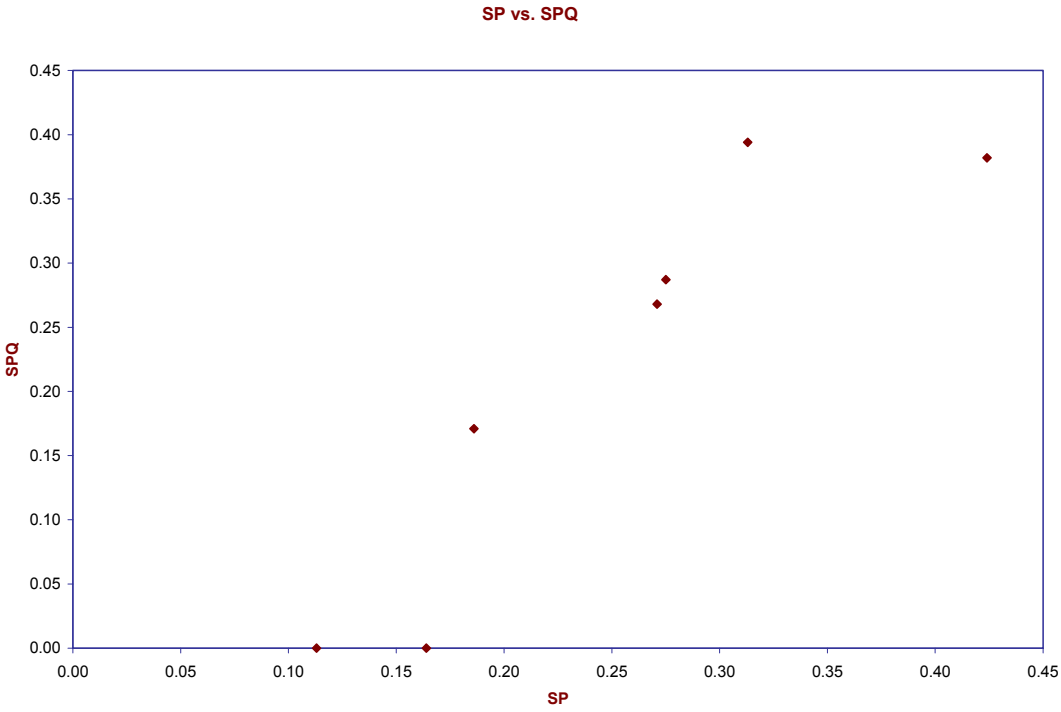


**(a)**

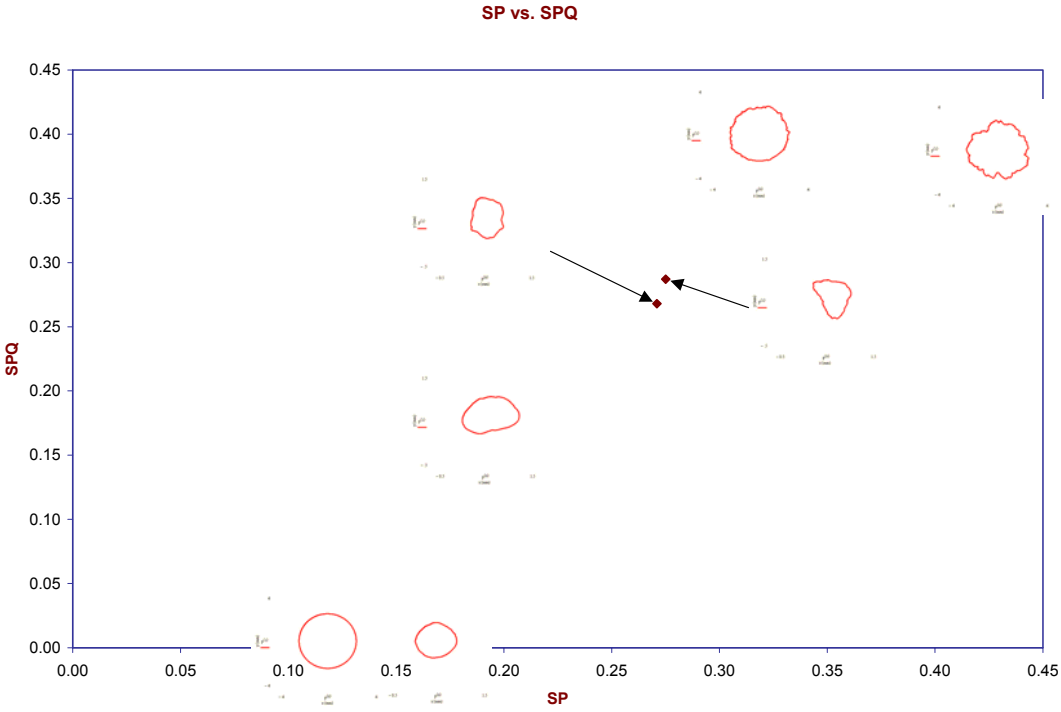


**(b)**

**Figure 4.7–** Plot of SP vs. SPQ for the study particles; **(a)** with data points, **(b)** with particle outlines (the real particle outlines are enlarged for visualization).

same SPQ values and they have circular macro-shape and almost no perturbations along the outline. The particle *p2* is also smooth but deviates from a circular macro shape to a more like rectangular macro shape. Thus, although SP values for *p1* and *p2* attain similar SP values of 0.164 and 0.186, respectively due to their smoothness along the profile, their SPQ values are further apart (SPQ *p1*= 0.000, SPQ *p2* = 0.171). Note that on the upper end of the SPQ spectrum lie *concrete-par* (SPQ = 0.382) and *HPDE-par* (SPQ = 0.394) with similar SPQ but different SP values (SP *concrete-par* = 0.424*,* SP *HDPE-par* =0.313). Considering SPQ groups (*steel-par, p1*) and (*concrete-par, HDPE-par*), both are circular in macro shape but the latter group has considerable amount of perturbation attached along the outline. SPQ groups them based on their macro shape but still the second group with roughness along the profile attains larger SPQ than the former smooth group. SP can differentiate between *steel-par* & *p1;* and between *concrete-par* & *HDPE-par*. As a conclusion, one can state that SP is not related to macro shape but rather on smaller scale roughness along the profile; whereas SPQ tends to signify both the macro and micro shape.

### *4.1.4 Boyce and Clark Shape Index*

Shape index (SI) is calculated as explained in Section 3.3.6. The difference of this particle shape parameter from the other selected is that it is based on radius distribution along the particle profile. The computed SI values are shown in Table 4.7.

Figure 4.8 shows the SI values plotted against the corresponding particle with data points (a), and with the particle outlines (b).

**Table 4.7 –** SI and radial distribution standard deviation values for the study *parts* and *dparts.*

| Particle Name | SI (A,16) | Standard Deviation of the radial distribution |
|---|---|---|
| p1 | 4.0 | 0.3 |
| p2 | 14.8 | 1.1 |
| p3 | 9.4 | 0.7 |
| p4 | 14.3 | 1.1 |
| concrete-par | 5.9 | 0.5 |
| hdpe-par | 2.1 | 0.2 |
| steel-par | 0.0 | 0.0 |

In order to better interpret Figure 4.8, Figure 4.9 is used. Figure 4.9 shows the percentage of radial distribution corresponding to each radial section. This is relevant to the SI measure of a particle, since SI can also be interpreted as how uneven the radial distribution is along the particle outline. As suggested by Boyce and Clark (1964), 16 radials, corresponding to 22.5° intervals is used.

Based on the data used for Figure 4.9, the standard deviations of the radial distributions are calculated and are presented in Table 4.7.

In relation to the statistical properties of the radial distributions shown in Figure 4.9, for all the radial distributions, the average radial percentage is 6.25%, which corresponds to (1 / # or radials) percentage. If the study particles are sorted based on their corresponding SI values and the standard deviation of their radial distributions the sorting is the same. Thus, the shape index (SI) parameter solely characterizes the particle outline based on how similar/different the outline is compared to a perfect circle outline disregarding any micro-roughness features.

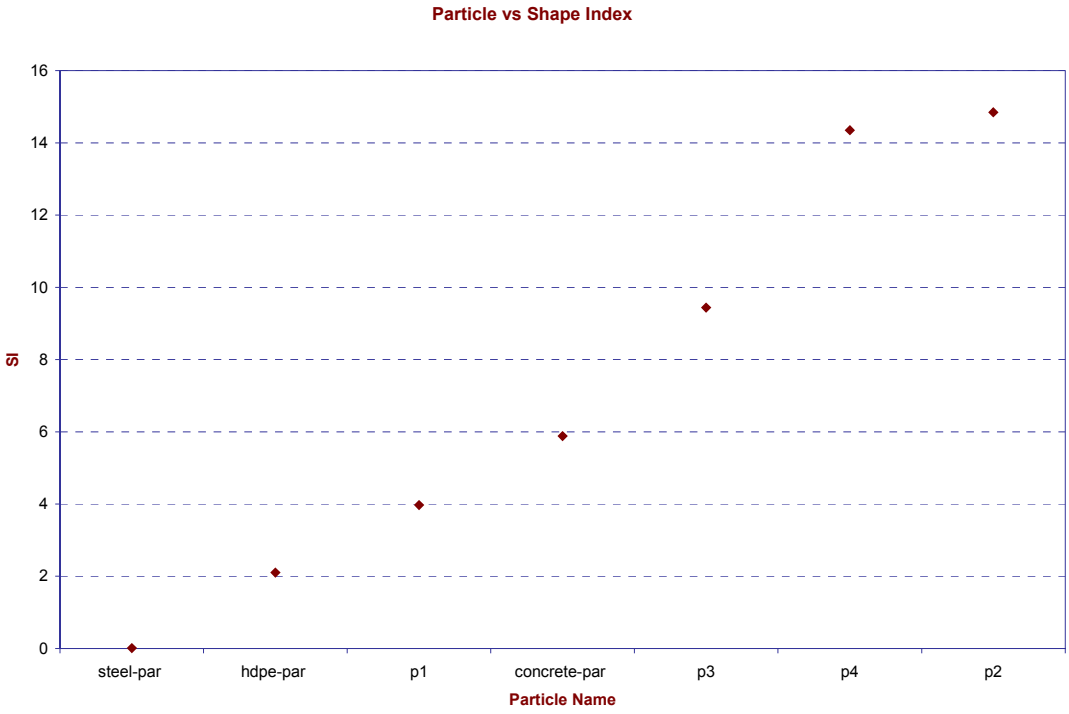


**(a)**

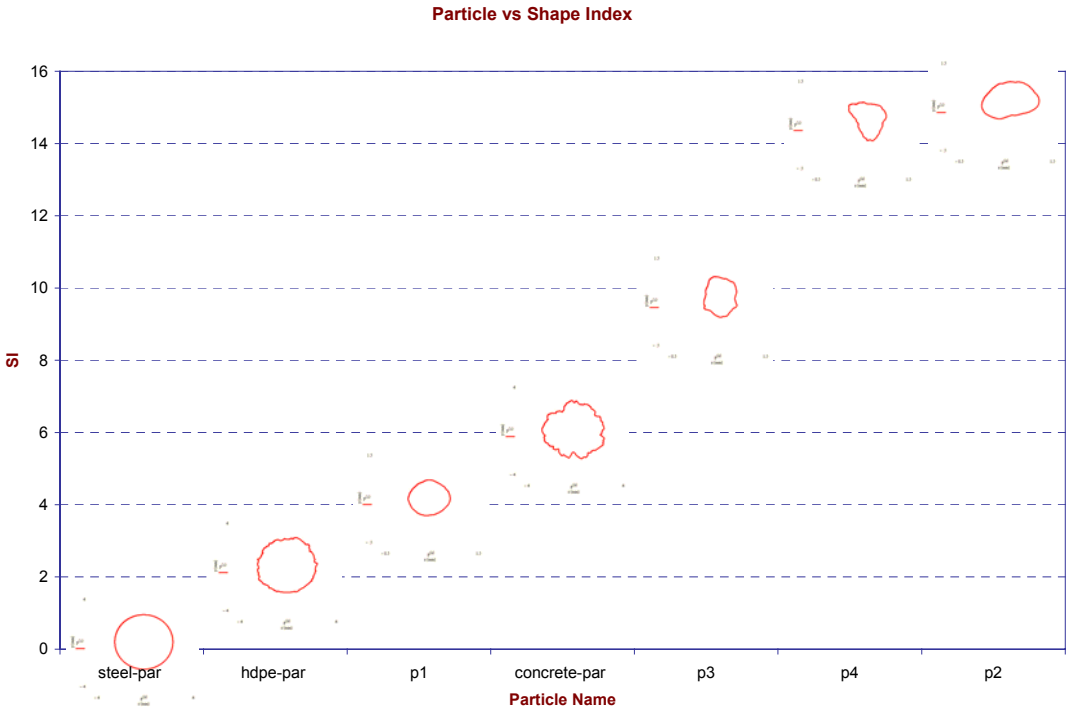


**(b)**

**Figure 4.8–** Plot of SI for the study particles; **(a)** with data points, **(b)** with particle outlines.

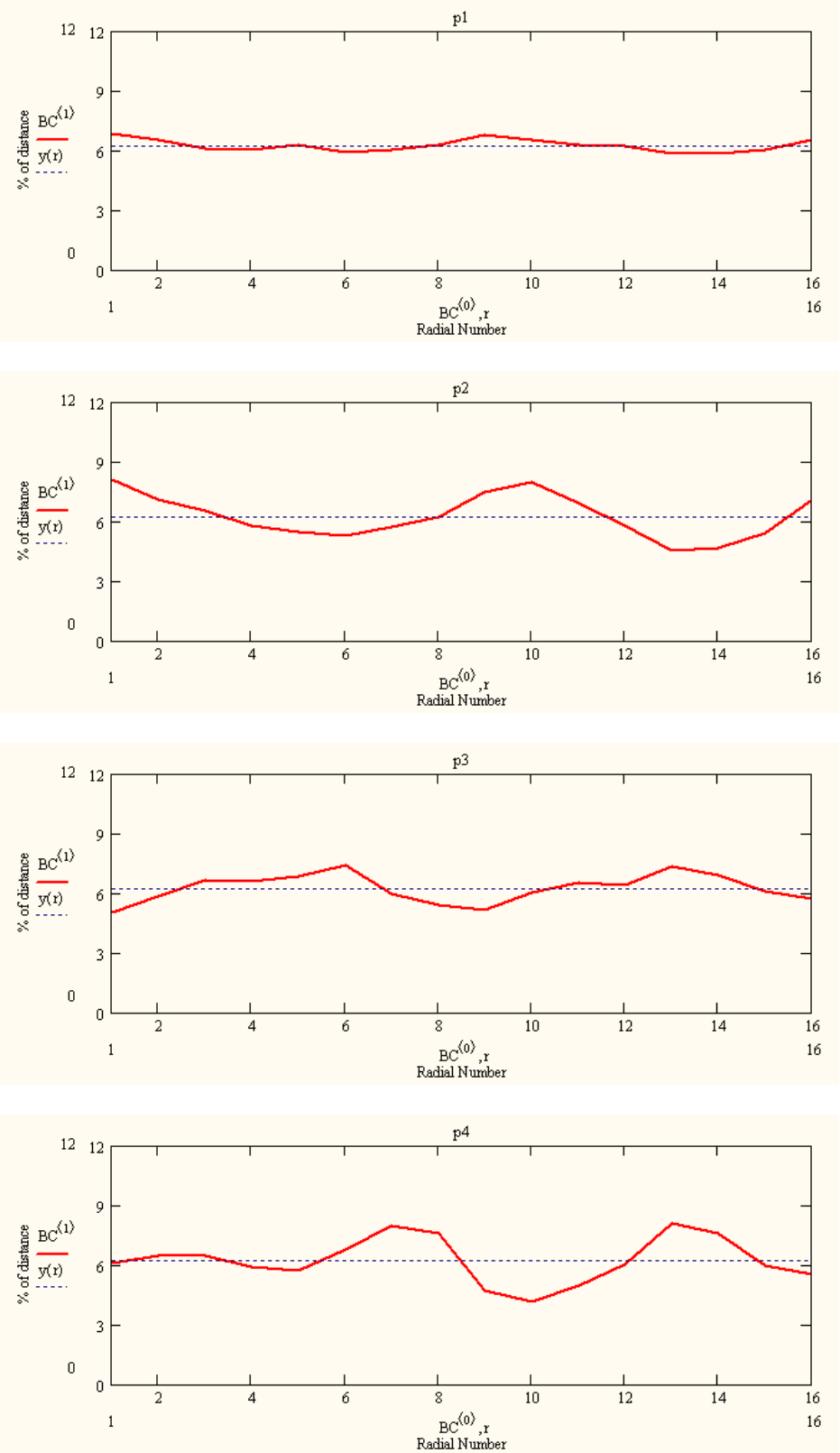


**Figure 4.9–** Plot of radial number vs. % of radial distribution plots for the study materials.

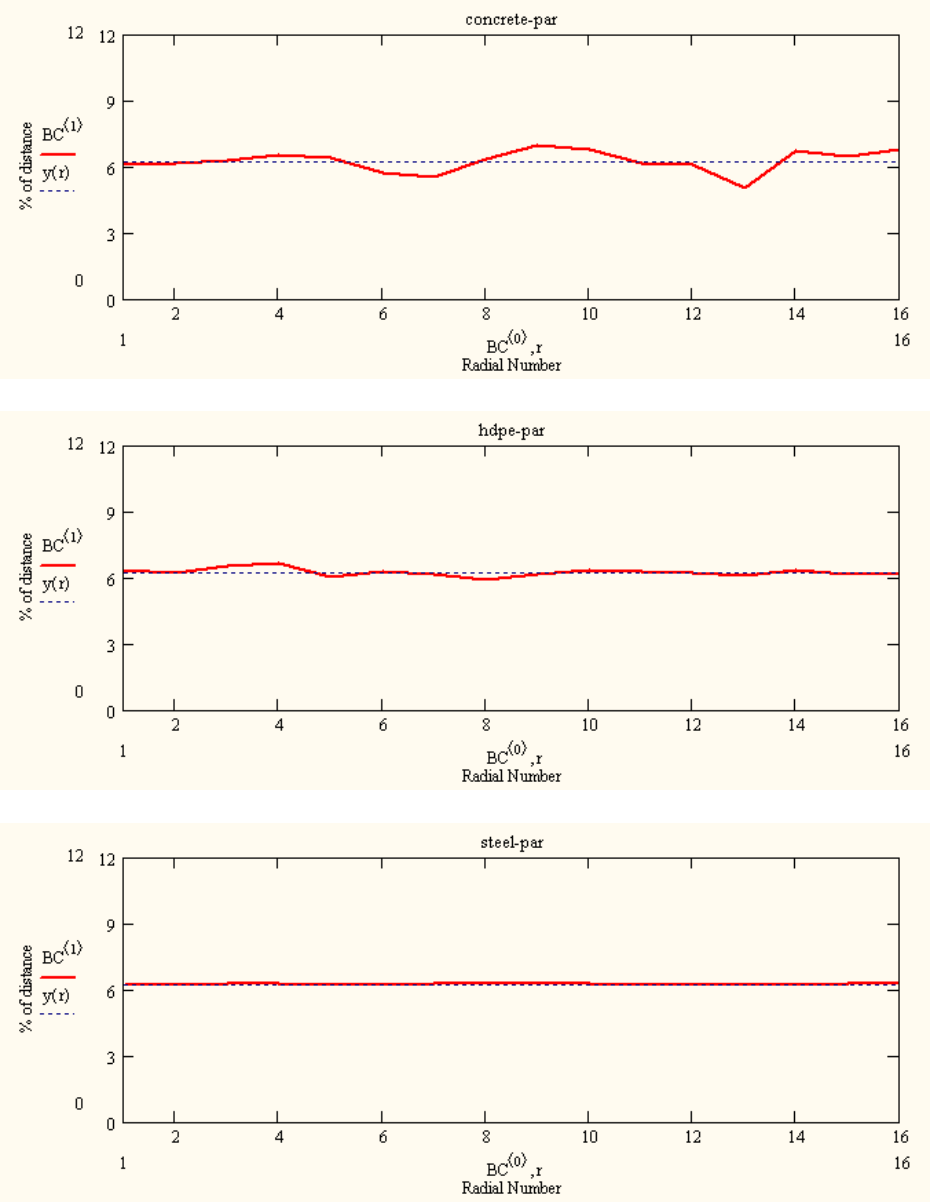


**Figure 4.9 (continued).**

### *4.1.5 Property Differences between Real and Derived Particles*

Figure 3.34 (a) showed 25 particles varying from angular to well-rounded. Each row represents a certain roundness scale. From top to bottom, the rows correspond to angular, subangular, subrounded, rounded, and well-rounded. The selected study particles can be classified based on Figure 3.34 (a) and the classification system shown in Figure 3.34 (b). Both particles *p1* and *p2* are in "well-rounded" class. Particle *p3* resembles particle #12 in the "subrounded" class and *p4* can be placed in the end of the "subangular" or the beginning of "angular" region. Thus, although the range of particles selected for this study do not contain the most angular and the most well-rounded shapes shown in Figure 3.34 (b), they do provide a widespread range from well-rounded to angular particles.

In terms of particle shape parameter values, there is no distinct grouping of real and derived particles.

From visual inspection of Figure 3.22, *dparts* tend to have a more circular macro-shape; whereas *parts* contain circular (*p1),* rectangular (*p2)* as well as a triangular macro-shape (*p4).* Derived particles have circular macro-shape due to the method used to obtain them, i.e. *surf-dpart* algorithm. In *surf-dpart* algorithm, the surfaces are wrapped around a circular shape with a radius equal to $rdatum$ (see Section 3.1.2). This aspect of *dparts* is most evident in the SI values. Shape Index is based on the radial measurements along the outline compared to a circular outline. The ascending order of SI values is (*steel-par, HDPE-par, p1, concrete-par, p3, p4,* and *p2*). The first four

components of the set are circular macro-shapes and all *dparts* are located within this region.

CRR shows the perturbations scale in terms of the difference between radii of MCC and MIC divided by the radius of MIC. Since this parameter is related to macro-shape also, the four lower end particles are all *dparts*¸ and the higher three end particles are *parts.* However, note that CRR also takes into account the magnitude of convex and concave portions along the outline. The radius of MIC is governed by the minimum outline distance from the center; whereas the MCC radius is dependent on the most outward data point on the particle outline. Thus, *concrete-par* value is further apart than *steel-par, HDPE-par,* and *p1* values than it is in terms of SI values.

SF approximates a particle outline by a polygon and compares it to a circular macro-shape. In this case, *concrete-par* is at the higher end since this parameter is more dependent on the meso-scale than CRR and SI. For AF parameter, all *dparts* are dispersed from the lowest (*steel-par* AF = 0.007%) to the highest (*concrete-par* AF = 58.345%)with *HDPE-par* in-between (*HDPE-par* AF = 11.556%). AF is solely dependent on the number and sharpness of the corners and that is why the general circular macro-shape of *dparts* do not result in all *dpart* values grouped within *part* values.

Note that *dparts* have higher convex and deeper concave sections along the profile than *parts.* This can be observed from the SP and SPQ values. SP is derived to quantify particle abrasiveness similar to fractal analysis and SPQ takes into account only the outline points that are outside the least squares circle. For both parameter values, *concrete-par* and *HDPE-par* are at the higher end of the spectrum.

## 4.2 Results of Analysis of Surface Roughness Parameter Values

### *4.2.1 Conventional Roughness Parameters*

As previously mentioned, the selected roughness parameters for surfaces are $R_a$, $R_q$, $R_p$, and $R_{max}$, The calculated values are given in Table 4.8.

As Table 4.8 suggests, different $D_{50}$ values are taken for the derived and real surfaces. For derived surfaces, the average perimeter is 3.2 mm; whereas in real surfaces it is 19.4 mm. Thus, when the diameter values for these parameters are considered, the diameters for derived and real surfaces are 1.01 mm and 6.17 mm, respectively. Rounding the diameter values, finally the $D_{50}$ values for the real and derived surfaces are taken as 6 mm and 1 mm, respectively.

Figure 4.10 to 4.13 are the plots of the surface names vs. the selected conventional roughness parameters.

**Table 4.8 –** Selected conventional surface roughness parameters for study *surfs* and *dsurfs*.

| Surface Name | $D_{50}$ for $R_n$ (mm) | $R_a$ (mm) | $R_q$ (mm) | $R_p$ | $R_{max}$ (mm) |
|---|---|---|---|---|---|
| p1-surf | 1 | 0.0158 | 0.0187 | 0.0373 | 0.0650 |
| p2-surf | 1 | 0.0697 | 0.0811 | 0.1373 | 0.2803 |
| p3-surf | 1 | 0.0354 | 0.0427 | 0.0794 | 0.1638 |
| p4-surf | 1 | 0.0506 | 0.0638 | 0.1442 | 0.2667 |
| concrete | 6 | 0.1348 | 0.1706 | 0.2652 | 0.7803 |
| HDPE | 6 | 0.0564 | 0.0736 | 0.2076 | 0.3497 |
| steel | 6 | 0.0003 | 0.0008 | 0.0024 | 0.0109 |

As Table 4.8 and Figures 4.10, 4.11 and 4.12 suggest, parameters $R_a$, $R_q$, and $R_p$ all sort the surface outlines in the same order since they all depend on the profile height, i.e. vertical dimension. The surface roughness parameter $R_{max}$ is slightly different since it is a difference value of two vertical relief measurements along the profile, maximum and minimum elevations.

### *4.2.2 Normalized Roughness Parameter*

Among the conventional surface roughness parameters, the only parameter that takes into account the horizontal dimension as well as the vertical is the normalized roughness parameter, where the profile is traversed for maximum vertical relief for every horizontal distance of $D_{50}$ and the average is taken. The values for $R_n$ values for the corresponding surfaces are tabulated in Table 4.9. Figure 4.14 shows the surface profile names with their corresponding $R_n$ values.

**Table 4.9 –** Normalized Roughness Parameter values for the study *surfs* and *dsurfs*.

| **Surface Name** | **$R_n$** |
|---|---|
| p1-surf | 0.0559 |
| p2-surf | 0.2215 |
| p3-surf | 0.1368 |
| p4-surf | 0.2299 |
| concrete | 0.1243 |
| HDPE | 0.0544 |
| steel | 0.0013 |

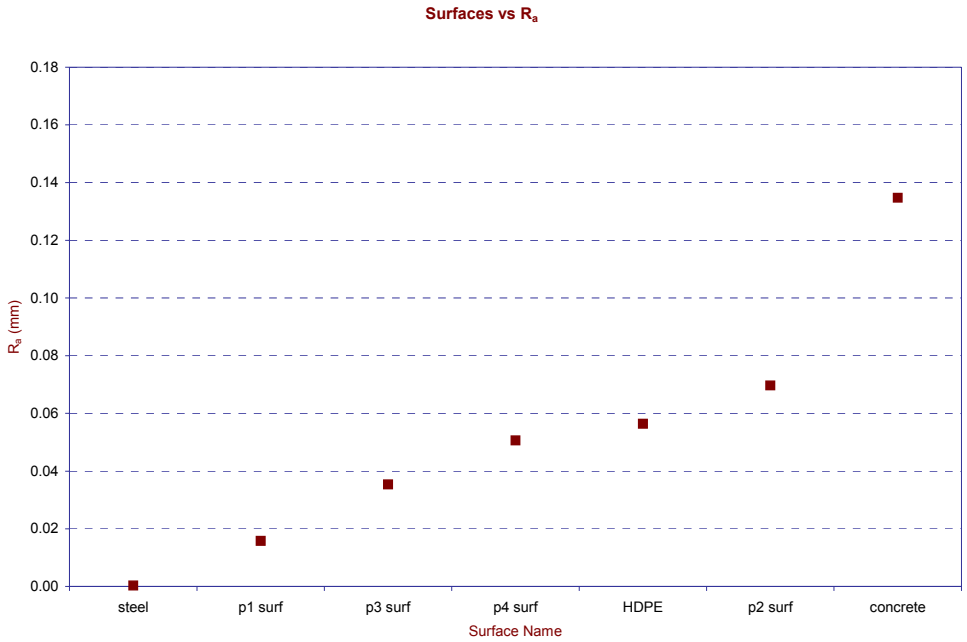


**Figure 4.10–** Plot of surface names vs. average surface roughness parameter ($R_a$).

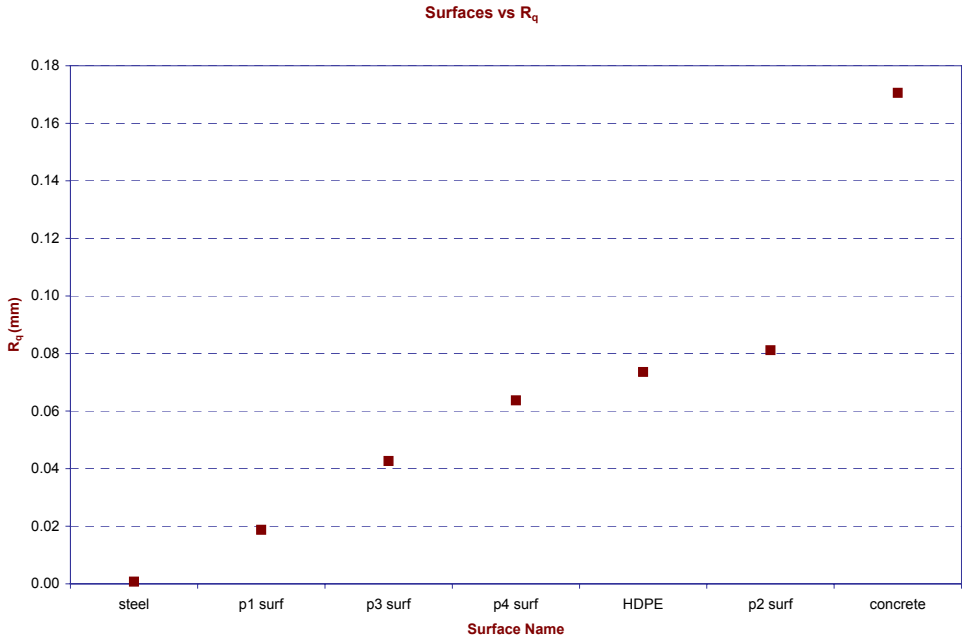


**Figure 4.11–** Plot of surface names vs. root mean square surface roughness parameter ($R_q$).

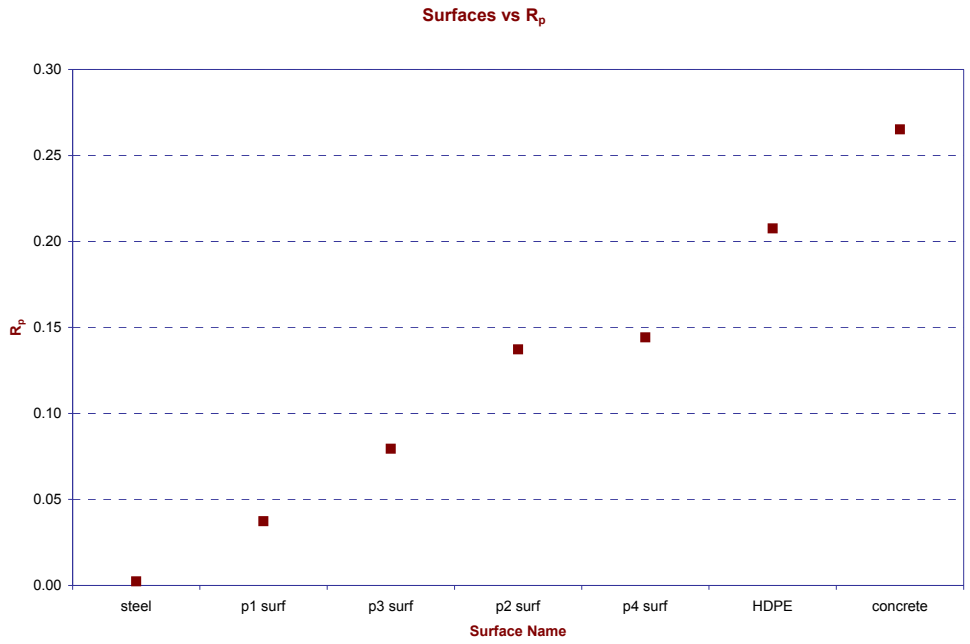


**Figure 4.12–** Plot of surface names vs. depth of surface smoothness ($R_p$).

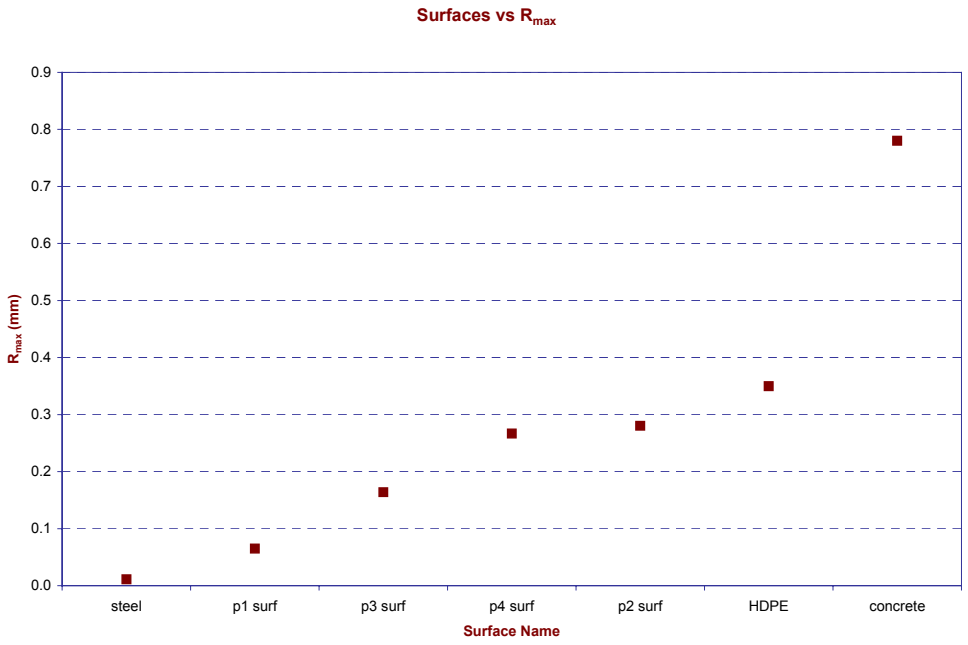


**Figure 4.13–** Plot of surface names vs. maximum peak to valley roughness parameter ($R_{max}$).

The normalized parameter is similar to CRR in particle parameters, which is based on the ratio of the radii difference of MCC and MIC to the radius of MIC. The reason is that the radii difference of MCC and MIC in particles resembles the $R_{max}$ in surface analysis. The normalized surface roughness, $R_n$, calculates $R_{max}$ within each distance of the $D_{50}$ of the particle and then takes the average, which can be viewed as the aspect ratio of surfaces since it finds the ratio of the vertical dimension to the horizontal dimension. $R_n$ sorts the surfaces in the ascending order of *steel*, *HDPE*, *p1-surf*, *concrete*, *p3-surf*, *p2-surf*, and *p4-surf*; whereas CRR particle parameter ordering is *steel-par*, *HDPE-par*, *p1*, *concrete-par*, *p3*, *p2*, and *p4*.

### *4.2.3 Spike Parameter Quadratic on Surface Profiles*

The values for the SPQ-surf are presented in Table 4.10 and the plot of surface names versus SPQ-surf values is shown in Figure 4.15.

**Table 4.10 –** SPQ-surf values for the study *surfs* and *dsurfs*.

| Surface Name | SPQ – surf |
|---|---|
| p1-surf | 0.369 |
| p2-surf | 0.334 |
| p3-surf | 0.437 |
| p4-surf | 0.235 |
| concrete | 0.477 |
| HDPE | 0.532 |
| steel | 0.000 |

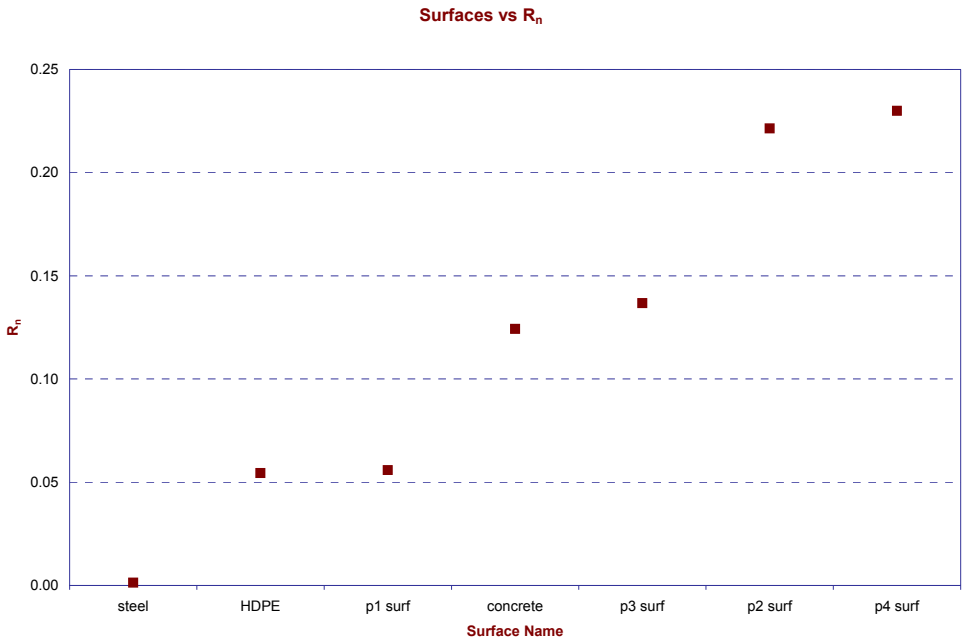


**Figure 4.14–** Plot of surface names vs. normalized roughness parameter ($R_n$).

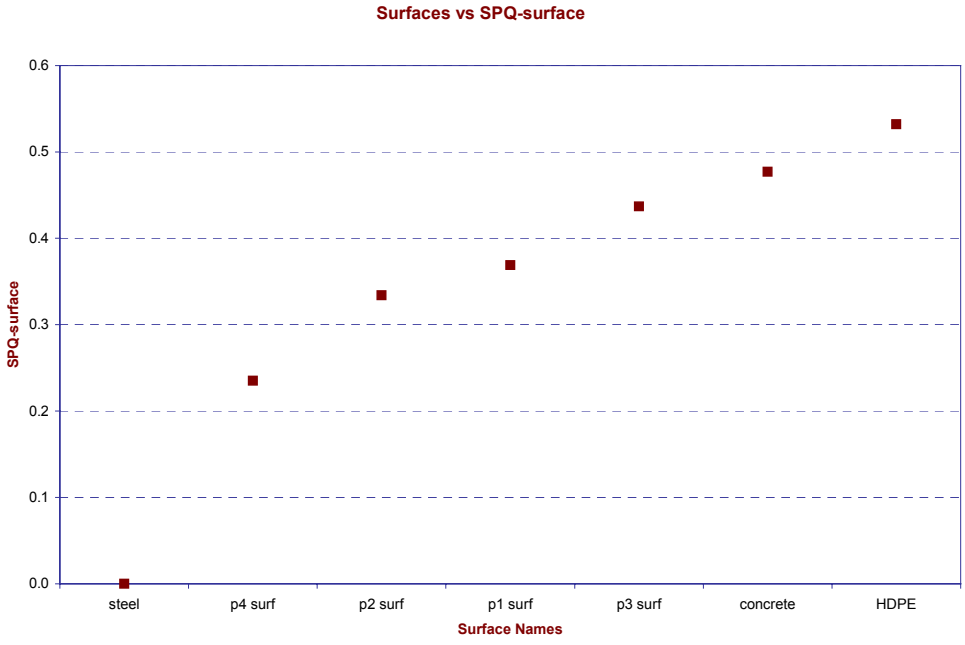


**Figure 4.15–** Plot of surface names vs. SPQ-surf parameter values.

The SPQ-surf, similar to the SPQ for particles is influenced by the number of spikes as well as by the spike angles for each spike. As Table 4.10 suggests, the ordering based on SPQ-surf is not the same as the SPQ for particles although the methods are comparable. That is in SPQ for particles, the ordering is as *p1*, *steel-par*, *p2, p3*, *p4*, *concrete-par*, and *HDPE-par*. However, for SPQ-surf the ascending order is *steel*, *p4-surf*, *p2-surf*, *p1-surf*, *p3-surf*, *concrete*, and *HDPE*. Note that *p1-surf* has moved up the scale compared to the particle *p1*. This is a result of one very sharp spike *in p1-surf* above the average surface height. In the author's opinion, this is a result of the sensitivity of the analysis to small changes in elevation since as one observes the surface profiles, e.g. *p1-surf* and *p4-surf*, it is evident that a particle rolling over *p4-surf* would require more energy than a particle rolling over *p1-surf* which is mostly a smoother profile with only one sharp but small spike. That is, it is believed that *p4-surf* should have SPQ-surf larger than *p1-surf*.

### *4.2.4 Centroid Trace on Surface Profiles*

The Centroid Trace on the real and derived surfaces is performed in accordance with the originally developed method (DeJong, 2001). The selected conventional roughness parameters mentioned in 4.3.1 are also calculated for the surfaces generated by the center of a particular diameter rolling circle of on the surfaces. The plots vs. the various diameter values are shown in Figure 4.16. Note that due to different profile lengths for the real and derived surfaces, different particle ranges with the same minimum diameter value of 0.005mm are used. The profile length for the real surfaces is 15-mm and the average of the profile lengths of the derived surfaces is 3-mm.

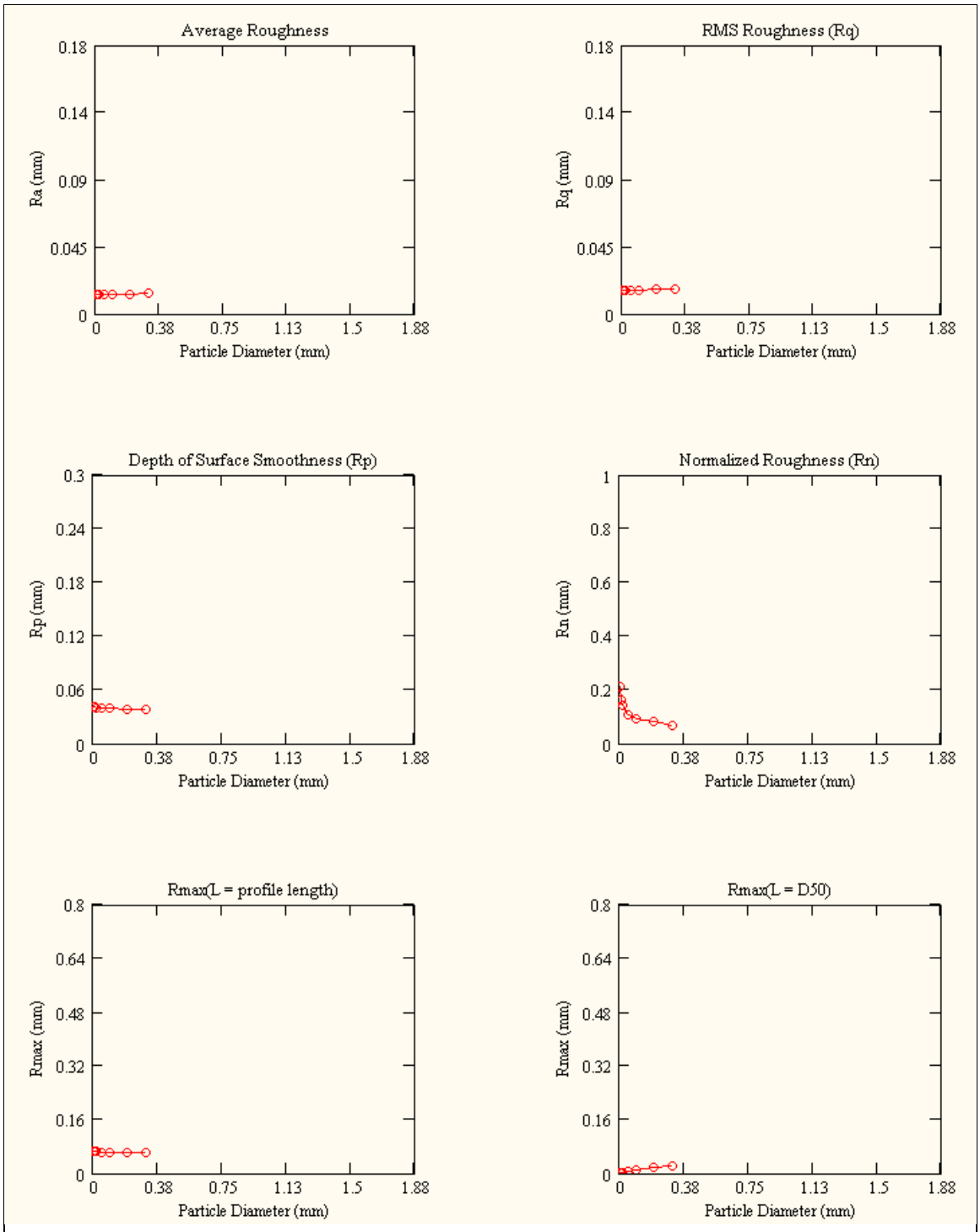


P1-surf CT surface parameters' plots- 3mm length – 0.004mm res – dia=0.005-0.3125 mm.

**Figure 4.16-** CT surface parameters' plots for real and derived surfaces

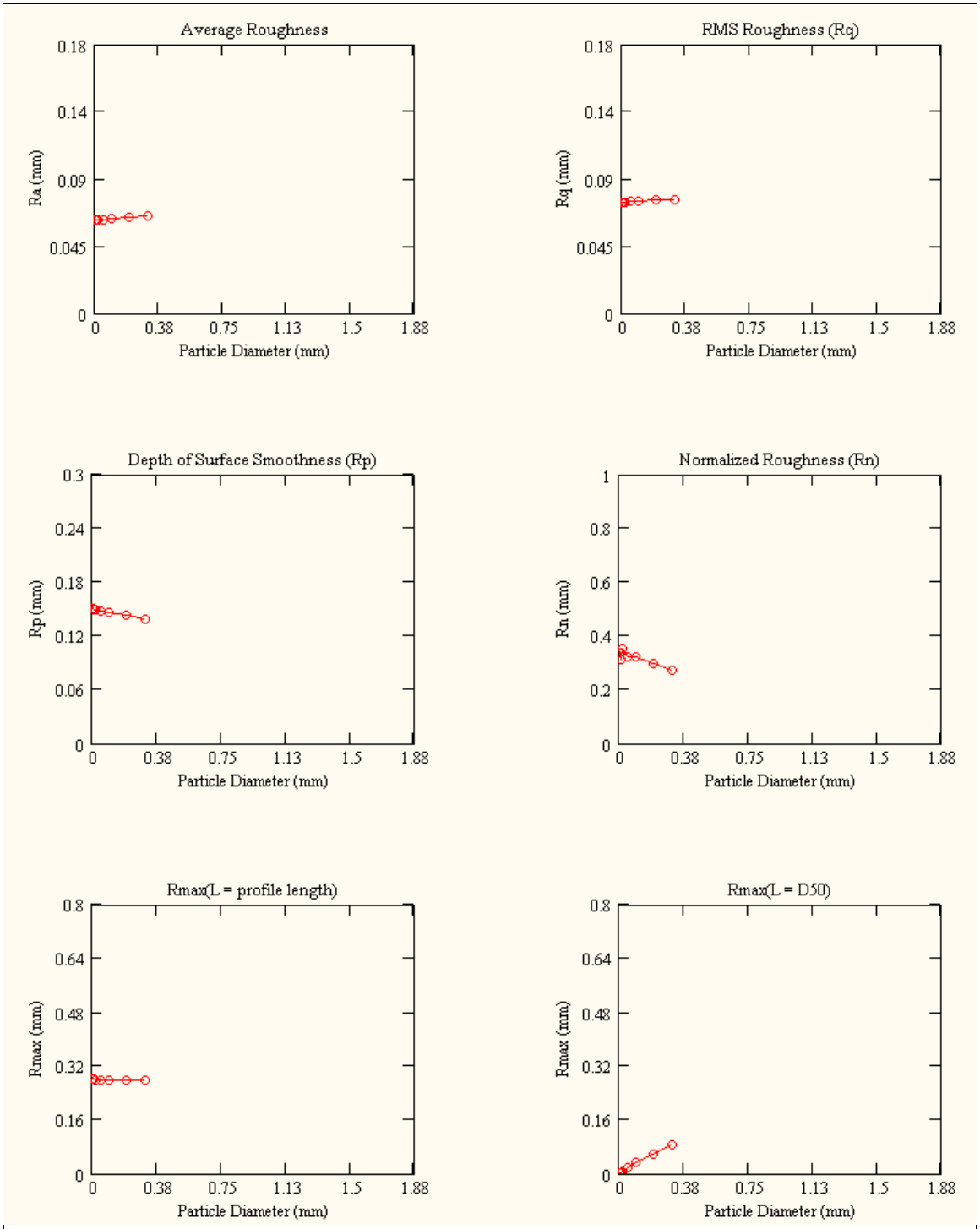


P2-surf CT surface parameters' plots- 3mm length – 0.004mm res – dia=0.005-0.3125 mm.

**Figure 4.16 (continued).**

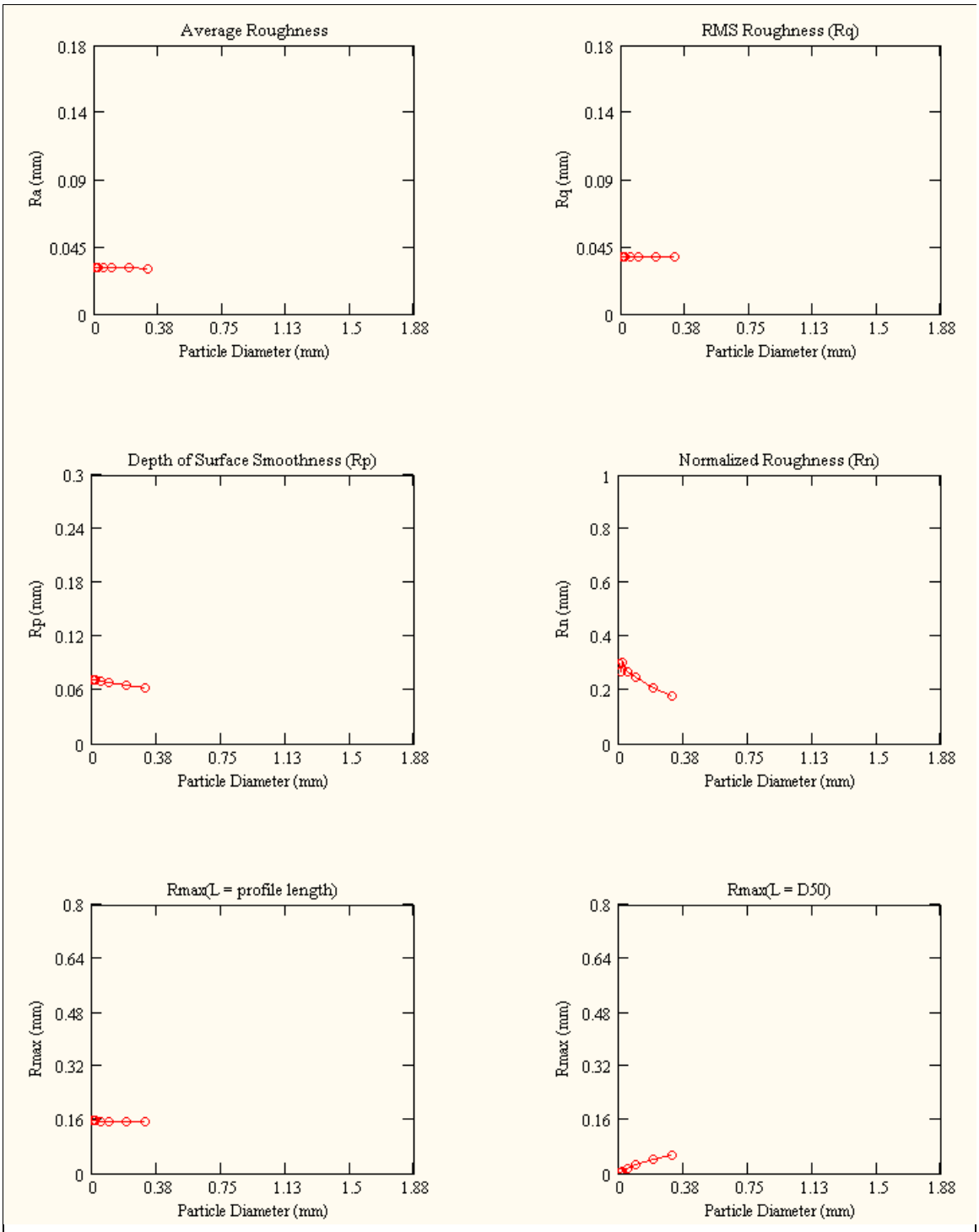


P3-surf CT surface parameters' plots- 3mm length – 0.004mm res – dia=0.005-0.3125 mm.

**Figure 4.16 (continued).**

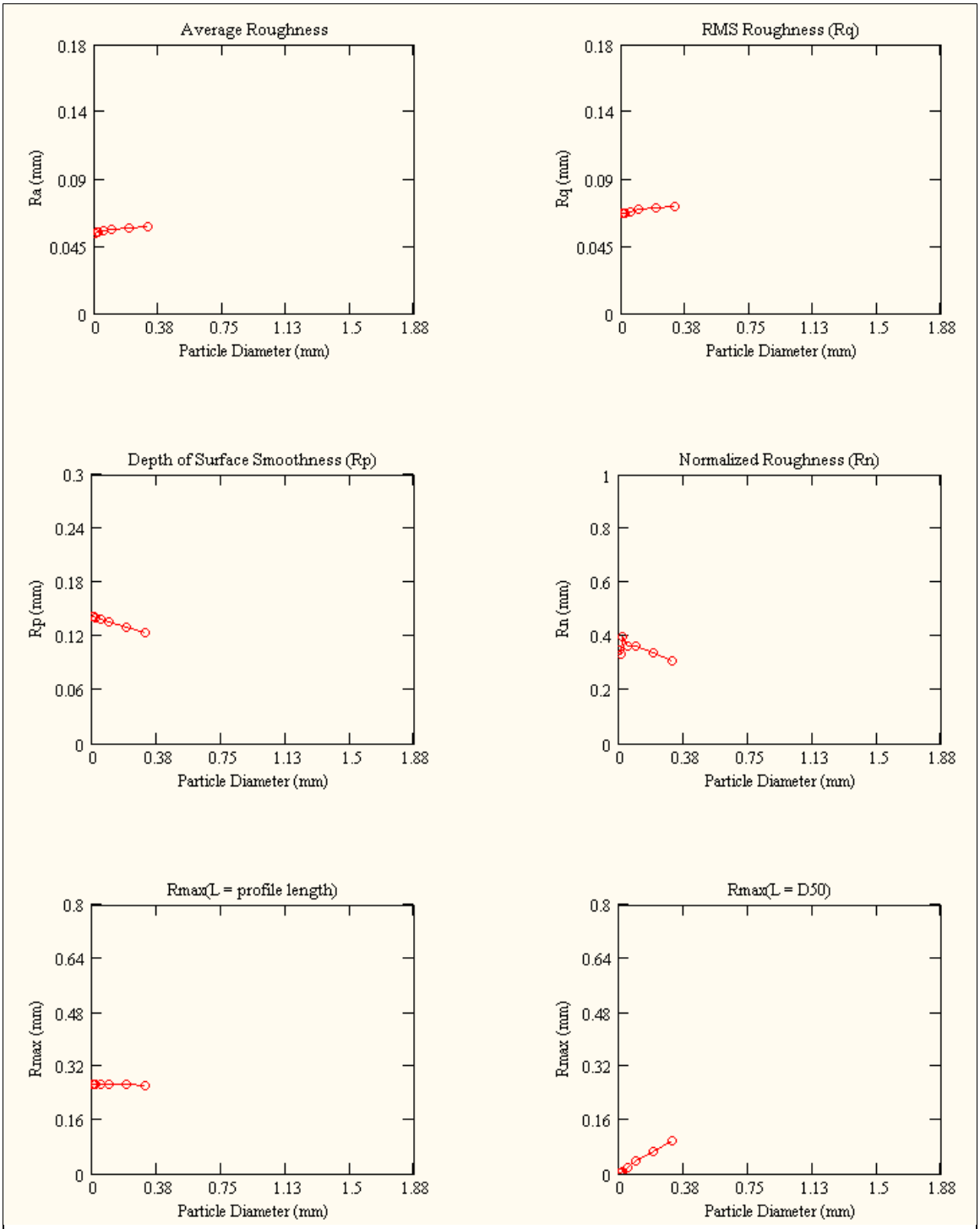


P4-surf CT surface parameters' plots- 3mm length – 0.004mm res – dia=0.005-0.3125 mm.

**Figure 4.16 (continued).**

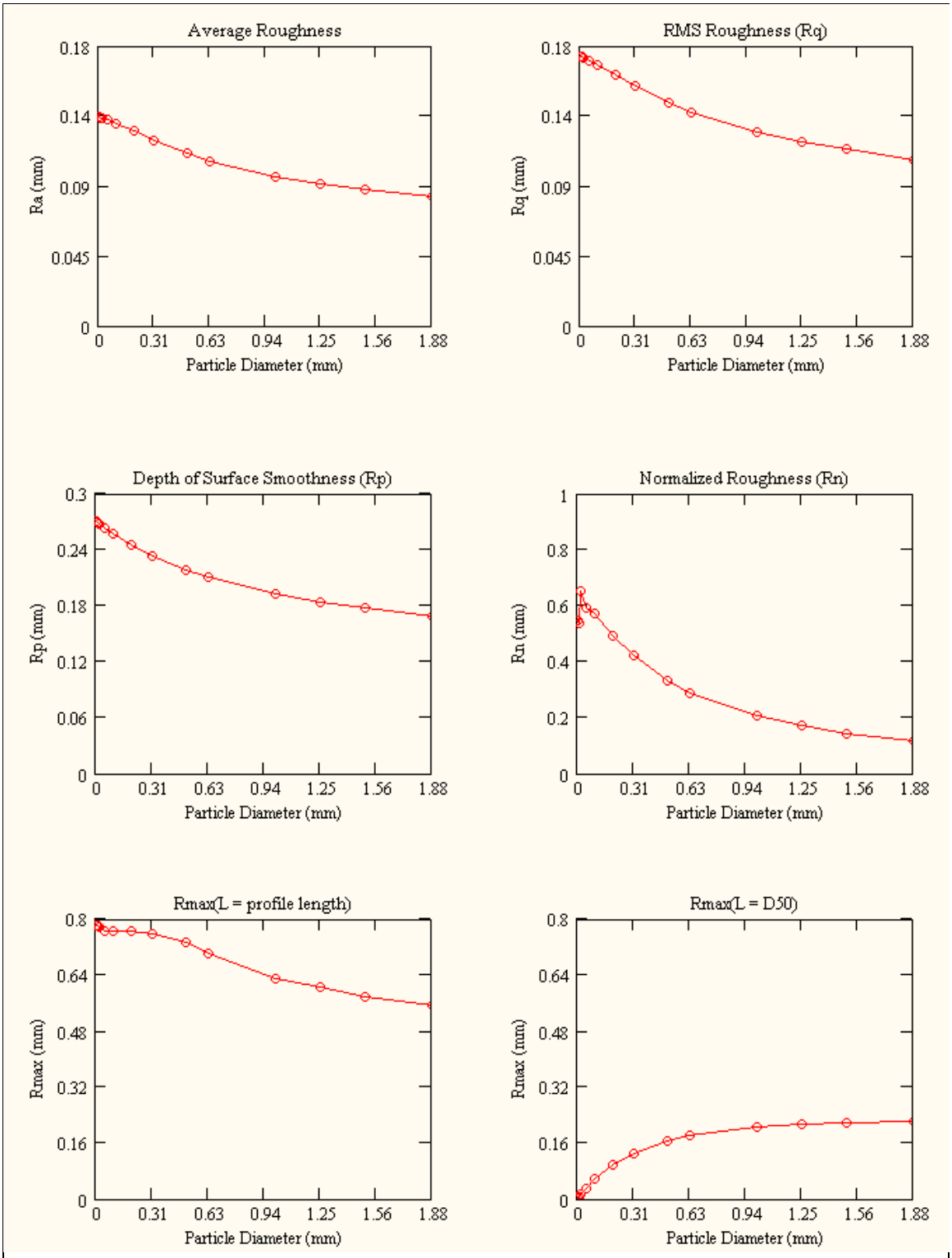


Concrete-S CT surface parameters' plots- 15mm length – 0.004mm res – dia=0.005-1.875 mm.

**Figure 4.16 (continued).**

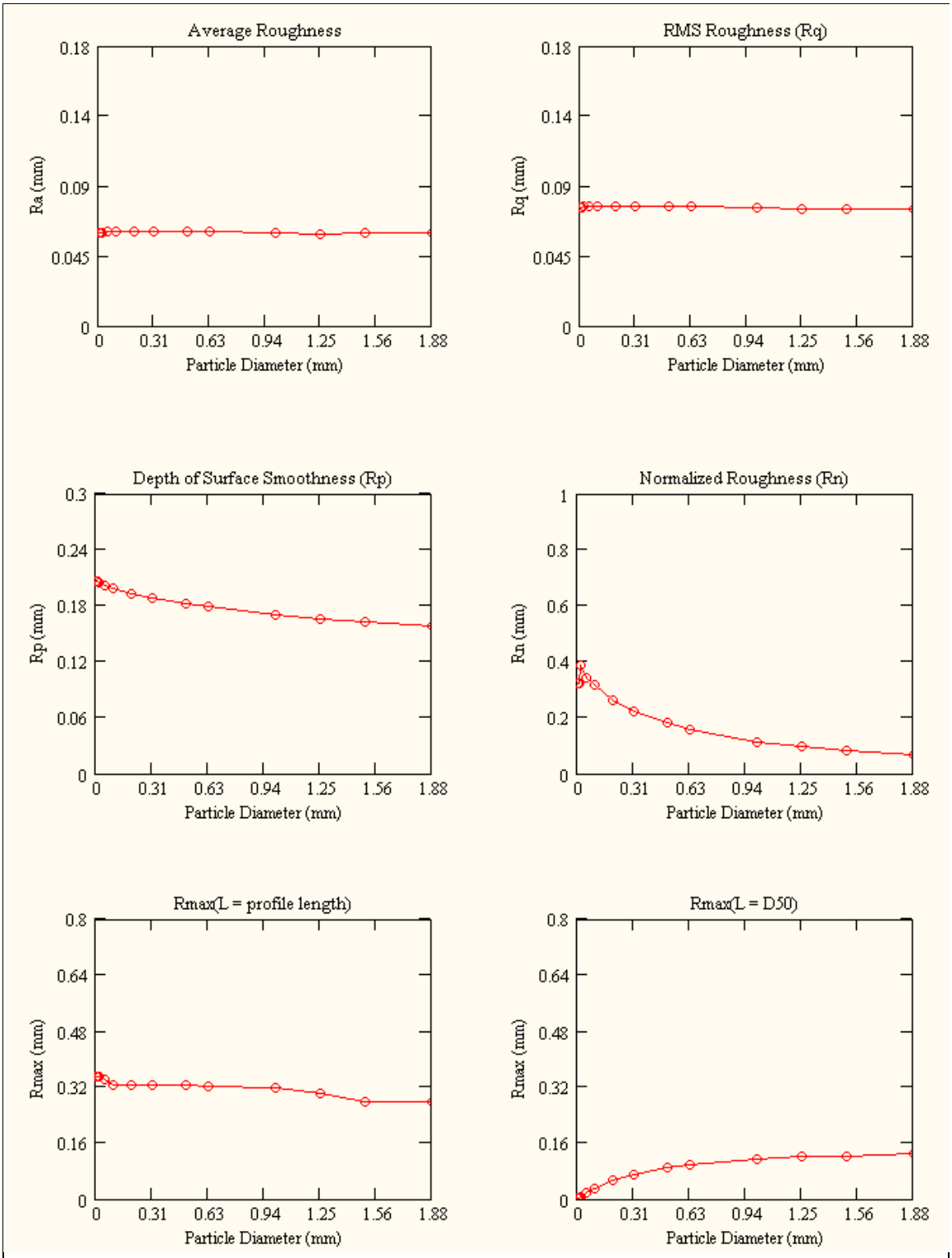


HDPE-S CT surface parameters' plots- 15mm length – 0.004mm res – dia=0.005-1.875 mm.

**Figure 4.16 (continued).**

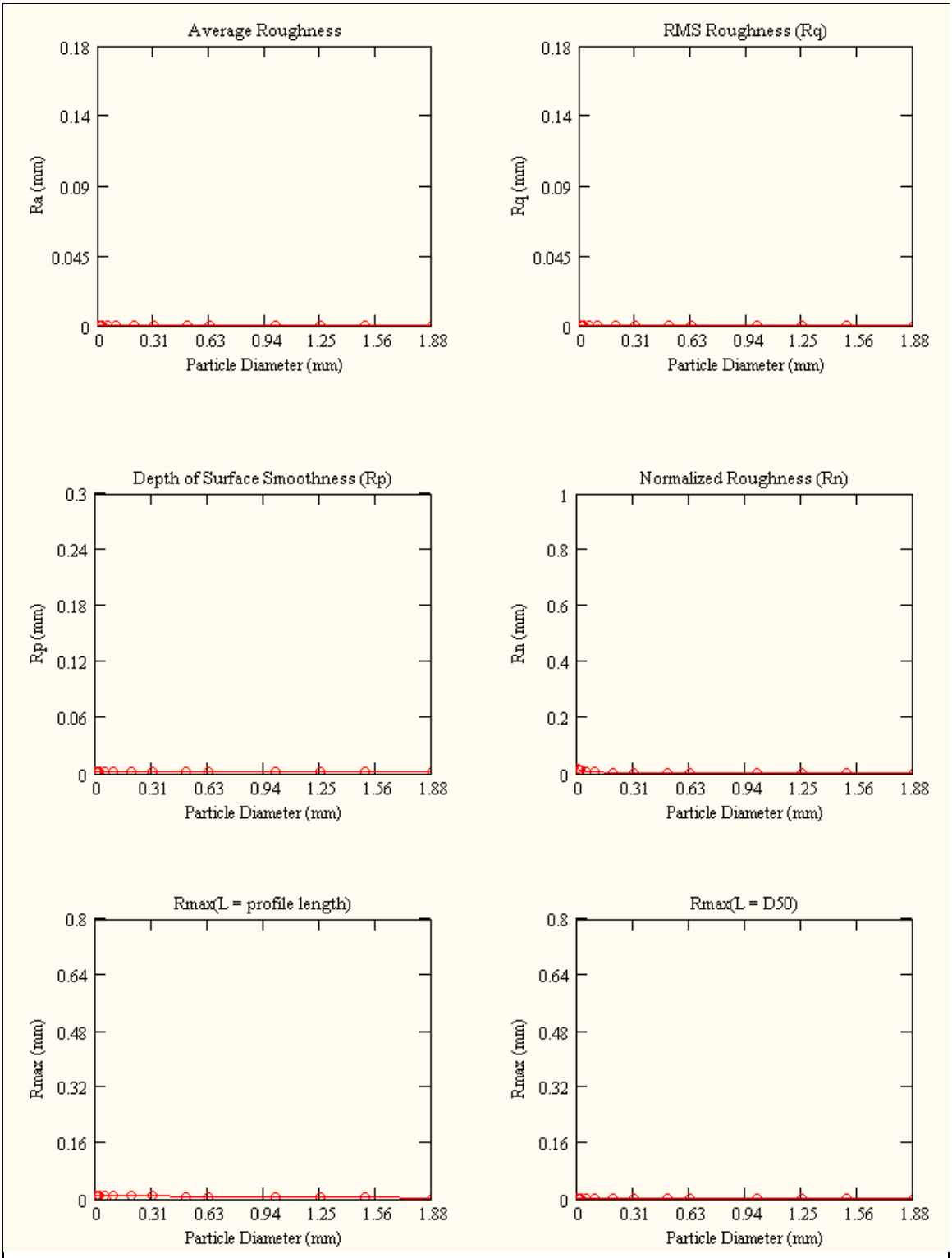


Steel-S CT surface parameters' plots- 15mm length – 0.004mm res – dia=0.005-1.875 mm.

**Figure 4.16 (continued).**

The $R_a$ and $R_q$ for the *p1-surf* decrease by 17.5% and 14.6% for a CT of a 0.005mm circle particle, respectively compared to the original *p1-surf* profile $R_a$ and $R_q$. An increase of 9.96% and 0.03% is observed for the $R_p$ and $R_{max}$ for a CT of a 0.005mm circle particle, respectively compared to the original *p1-surf*. For the diameter range of 0.005mm to 0.313mm, the surface parameter values $R_a$, $R_q$, $R_{max}$, and $R_p$ for the centroid trace along *p1-surf* decrease at most for 1.5%. The insignificant change can be attributed to the mostly smooth texture of the profile, with no predominant valleys or peaks. The parameter $R_n$ increases by over 200% for a particle of 0.005mm since for the original *p1-surf* the $R_n$ is evaluated with a 1mm particle. The $R_n$ decreases about 67.9% over the whole particle diameter range with a substantial decrease beyond particle diameter of 0.02mm.

Compared to *p1-surf*, *p2-surf* CT surface parameters show more change over the same diameter range. Compared to the original *p2-surf*, the CT of a 0.005mm particle show $R_a$ and $R_q$ decrease by 9.62% and 7.56%, respectively. There is minor increase for these parameters (up to 3%) over the considered diameter range. The $R_p$ value for the CT of a 0.005mm is about 9.29% larger than the original *p2-surf* $R_p$ value, but shows a decrease over the diameter range. The same trend but with 53.1% initial increase and 19.2% decrease over the diameter range is marked for $R_n$ parameter. $R_{max}$ parameter change is insignificant over the range considered.

The *p3-surf* has slightly different trends. There is a decrease between the original *p3-surf* and CT of a 0.005mm particle for the parameters $R_a$ (12.4%), $R_q$ (8.6%), $R_p$ (9.4%), and $R_{max}$ (4.1%) and the same parameters show a decrease of 3.2%, 2.6%, 13.9% and 3.2% over the diameter range. For the $R_n$ parameter though, as expected over 100%

increase is observed for the smallest diameter and then around 41% decrease occurs within the diameter range.

The last surface generated from a real particle *p4-surf* has 6.7% and 5.1% increase for the $R_a$ and $R_q$ parameters when the original surface parameters are compared to that of a CT of a 0.005mm particle. Over the diameter range of 0.005mm to 0.3125mm, $R_a$ and $R_q$ parameters exhibit an increase of 7.4% and 5.9%, respectively. $R_p$ increases only slightly at first (1.5%) however more decrease (13.4%) is observed for the range. $R_{max}$ parameter is almost constant. For $R_n$, similar to the above examples initial increase of 51.3% is followed by 10.9% of increase.

The real surface CT parameters possess different characteristics. For the *concrete* surface, the trends for $R_a$, $R_q$, $R_p$, and $R_{max}$ are all decreasing around 37.5%; whereas for $R_n$ there is a substantial initial increase and a 28.9% decrease over the diameter range of 0.005mm to 1.875mm. Note that similar to the surfaces generated from the particles, the original concrete profile $R_n$ value is calculated with a diameter of 6-mm and thus when the smallest diameter of 0.005mm is introduced in the denominator of the $R_n$ parameter the increase is expected.

The *HDPE* profile CT profiles for the diameters considered exhibit almost no change along the diameter range. The parameters $R_p$, $R_{max}$, and $R_n$ exhibit decreasing trends. For $R_p$ and $R_{max}$ the change is 23.3% and 20.3%, respectively and for $R_n$ it is 79%.

The *steel* profile possesses initial surface parameters with different orders of magnitude than the *concrete* and *HDPE* profiles and it is almost a smooth profile. Surface parameters $R_a$, $R_q$, and $R_{max}$ decrease 39.6%, 65.6%, and 64.3%, respectively; whereas

for $R_p$ the decrease is around 7.5%. The $R_n$ parameter exhibit 97% decrease between the smallest diameter and the largest diameter considered.

### *4.2.5 Property Differences between Real and Derived Surfaces*

In selection of real surfaces in this study, the most important criterion was to select commonly used surface profiles in geotechnical engineering while covering the range of surface roughness values encountered. DeJong (2001) investigated the surface roughness of several geomaterials that are usually encountered in geotechnical engineering practice. Some of the geomaterials tested and corresponding $R_a$ values are provided in Table 4.11.

**Table 4.11 –** Average Surface Roughness ($R_a$) values for selected geomaterials (after DeJong, 2001).

| **Material** | **Average Roughness, $R_a$ ($\mu$m)** |
|---|---|
| Concrete block | 115.97 |
| HDPE medium geomembrane | 65.62 |
| Oak (against grain[1]) | 14.47 |
| FRP[2] (against grain[1]) | 12.43 |
| Whitewood (against grain[1]) | 9.49 |
| Whitewood (with grain[1]) | 8.72 |
| FRP (with grain[1]) | 6.57 |
| Oak (with grain[1]) | 4.75 |
| Hardened Steel | 0.336 |
| HDPE smooth geomembrane | 0.103 |
| LPDE[3] smooth geomembrane | 0.101 |

[1]For anisotropic surfaces, average roughness was measured both parallel and perpendicular directions to the grain of the geomaterial, [2]FRP: Fiber Reinforced Polymer, [3]LDPE:Low Density Polyethylene.

As Table 4.11 shows, the value of average roughness can vary by orders of magnitude for a very rough concrete block (115.97 μm) to a very smooth LDPE geomembrane (0.101 μm). Within this scale of variability, the selected three real surfaces in this study are one from the high end (rough finished concrete surface), one from the middle (HDPE medium geomembrane), and the last study surface from the very low end (hardened steel). Thus, one can conclude that the results obtained with the study surfaces are representative of the range of roughness values encountered in the geotechnical engineering practice.

Investigating the differences between *dsurf*s (surfaces generated from the particles) and *surf*s (the real surfaces) visually, one cannot state an obvious difference between them besides the fact that the real surfaces, concrete and HDPE profiles, are decorated with more peaks and valleys. This can be attributed to the original difference between the real particles and surfaces. Due to the processing undertaken in the production of sand particles, the *parts* were subject to wear; whereas the surface profiles, *surfs,* utilized in this study are from the original materials, i.e. they have not been through any process. The worn perturbations in *parts* are transformed into lower peaks and shallower valleys compared to the *surfs.* The smaller change of surface parameters over the diameter range for the *dsurf*s compared to the larger change of surface parameters for the *surf*s does not constitute a difference since for the same diameter range of 0.005mm to 0.3125mm, the *surfs* show comparable amount of change of the surface parameters as the *dsurfs.*

Table 4.8 showed the conventional surface roughness parameter behavior for both data sets. $R_a$ is the average of the deviation of the surface elevations from the mean line;

whereas $R_p$ is the average of the deviation of the surface elevations from the maximum relief along the profile. In Table 4.8, most of the *dsurfs* values are located between steel and HDPE surface profile values, while for both parameters ($R_a$ and $R_p$), concrete is at the upper end. In terms of $R_a$, *p2-surf* attains a larger value than *HDPE*, which is also evident from the surface profile plots in Figure 3.23.

In order to investigate the differences between *dsurfs* and *surfs*, additional surface roughness parameters are calculated. The equations for the additional surface roughness parameters are given in Table 4.12. The values of these parameters corresponding to *surfs* and *dsurfs* are provided in Table 4.13.

**Table 4.12 -** Additional surface roughness parameters' abbreviations and equations.

| Name | Abbreviation | Equation |
|---|---|---|
| Skewness | $R_{sk}$ | $R_{sk} = \frac{1}{N * R_q^3}\left(\sum_{i=1}^{N} Y_i^3\right)$ |
| Kurtosis | $R_{ku}$ | $R_{ku} = \frac{1}{N * R_q^4}\left(\sum_{i=1}^{N} Y_i^4\right)$ |
| Normalized Length | $R_L$ | $R_L = \frac{L_{tot}}{L_{pro}}$ |
| Average Slope | $\Delta_a$ | $\Delta_a = \frac{1}{L}\int_0^L \left\|\frac{dy}{dx}\right\| \cdot dx$ |
| Average Wavelength | $\lambda_a$ | $\lambda_a = \frac{2 * \pi * R_a}{\Delta_a}$ |

**Variables:** ***N*** **= #** of surface profile data points; $\boldsymbol{Y_i}$ **=**height of the profile at point i; $\boldsymbol{R_a}$ **=** average roughness parameter; $\boldsymbol{R_q}$**=** root mean square roughness.

**Table 4.13-** Additional surface roughness parameters values for the study *surfs* and *dsurfs.*

| ***Surfs* and *dsurfs*** | **Surface Name** | **Skewness** | **Kurtosis** | **Normalized Length** | **Average Slope** | **Average Wavelength** |
|---|---|---|---|---|---|---|
| Derived surfaces (*dsurfs)* | p1-surf | 0.446 | -1.004 | 1.062 | 15.681 | 0.353 |
| | p2-surf | 0.147 | -1.086 | 1.095 | 20.255 | 1.187 |
| | p3-surf | -0.194 | -0.891 | 1.11 | 21.174 | 0.574 |
| | p4-surf | 0.198 | -0.433 | 1.148 | 24.074 | 0.711 |
| Real surfaces (*surfs)* | concrete | -1.057 | 0.674 | 1.291 | 34.269 | 1.243 |
| | HDPE | 0.943 | 0.578 | 1.159 | 22.066 | 0.874 |
| | steel | -7.364 | 65.676 | 1.001 | 1.286 | 0.082 |

Skewness is mathematically defined as the third central moment and it signifies the degree of asymmetry of the distribution. Skewness values convey information regarding whether most of the distribution is above or below the mean line and it can be negative or positive. For a surface profile composed mostly of peaks, the skewness is positive, whereas if valleys dominate the surface profile, the skewness is negative. Note that the large negative skewness for steel surface (-7.364) presented in Table 4.13 is not necessarily representative skewness for a steel surface. In other words, since a random 15-mm long portion of the measured steel profile was selected, the randomly chosen section of the steel profile contains mostly valleys. On the other hand, as Figure 3.3 illustrates, 40-mm long steel surface profile consists of almost equal number of peaks and valleys. In terms of the skewness values presented in Table 4.13, for the real and derived surface profiles, *steel* and *p3-surf* surfaces are negatively skewed; whereas the rest is positively skewed. The *dsurfs* are slightly positive. Skewness does not differentiate among the *dsurfs* as well as it does within *surfs*. The absolute value of skewness value is larger for the *surfs* than for *dsurfs.* That is, *surfs* have more surface

perturbations than *dsurfs.* Due to the *part*-surf process, when *parts* are unrolled onto a flat surface the large concave and convex sections of the *part* flatten out.

Kurtosis is mathematically the fourth central moment and a Gaussian distribution has a kurtosis value of 3. If kurtosis is smaller than 3, the distribution has relatively few high peaks and low valleys. If kurtosis larger than 3, the distribution has relatively many high peaks and low valleys. The value of kurtosis for all *dsurfs* is negative; whereas among *surfs,* only *steel* has kurtosis value larger than the Gaussian distribution kurtosis value of 3. Thus, among *dsurfs* and *surfs, dsurfs* have relatively low number of high peaks and deep valleys than *concrete* and *HDPE* surface profiles and *steel* surface attains a high number of high peaks and deep valleys.

Normalized length is a relative measure obtained by the ratio of the surface profile length and the horizontal projected length of the profile. In terms of normalized length, *dsurfs* values are in between *surf* values. As expected, *concrete* and *steel* bound the normalized length values. Although *steel* kurtosis value is larger than *concrete* kurtosis, the normalized length is larger for *concrete.* The reason is that the magnitudes of extremity (peaks and valleys) elevations are larger for the *concrete;* whereas *steel* has not so high peaks and not so deep valleys.

In terms of average slope of the surface profiles, there are no distinct behavior differences between the real and derived surfaces. As anticipated, *steel* surface has the lowest average slope, whereas the largest average slope is observed for the *concrete* profile. The average slope values for the *dsurfs* are in the middle range of *surfs*. *HDPE* profile has 22° slope, whereas *p1-surf*, *p2-surf*, *p3-surf*, and *p4-surf* have 15.6°, 20.2°, 21.1°, and 24.1° average slopes, respectively.

For average wavelength, as expected, the smallest and largest wavelengths correspond to *steel* and *concrete* profiles. Note that the average wavelength for *p2-surf* is comparable to *concrete* average length. The rest of the *dsurfs* profiles attain wavelengths between the *steel* and *HDPE* surface profiles.

## 4.3 Resolution Analysis

### *4.3.1 Particle Shape Parameters*

In this part of the chapter, the resolution of the particle sampling and its effect on the selected particle shape parameters is discussed. For this exercise, one of the particles, *p4,* is randomly chosen.

Although much attention is given to the resolution in surface profiles, particle outline and particle parameter sampling resolution have received comparably less attention. Most particle shape parameter studies do not even mention particle resolution in their study.

Figure 4.17 shows various *p4* outlines with different number of data points, i.e. 10, 20, 45, 90, 180, 360, 750, 1500, and 3750 data points. The particle shape parameters initially analyzed are CRR, SP, and SPQ. Table 4.14 displays particle shape parameter values with varying particle data points. Only these particle shape parameters are analyzed initially, since they require only particle outline as input with no additional parameters. Although SP requires the input parameters needed to calculate $nsteps$, for each outline, the input parameters are modified to acquire the same $nsteps$.

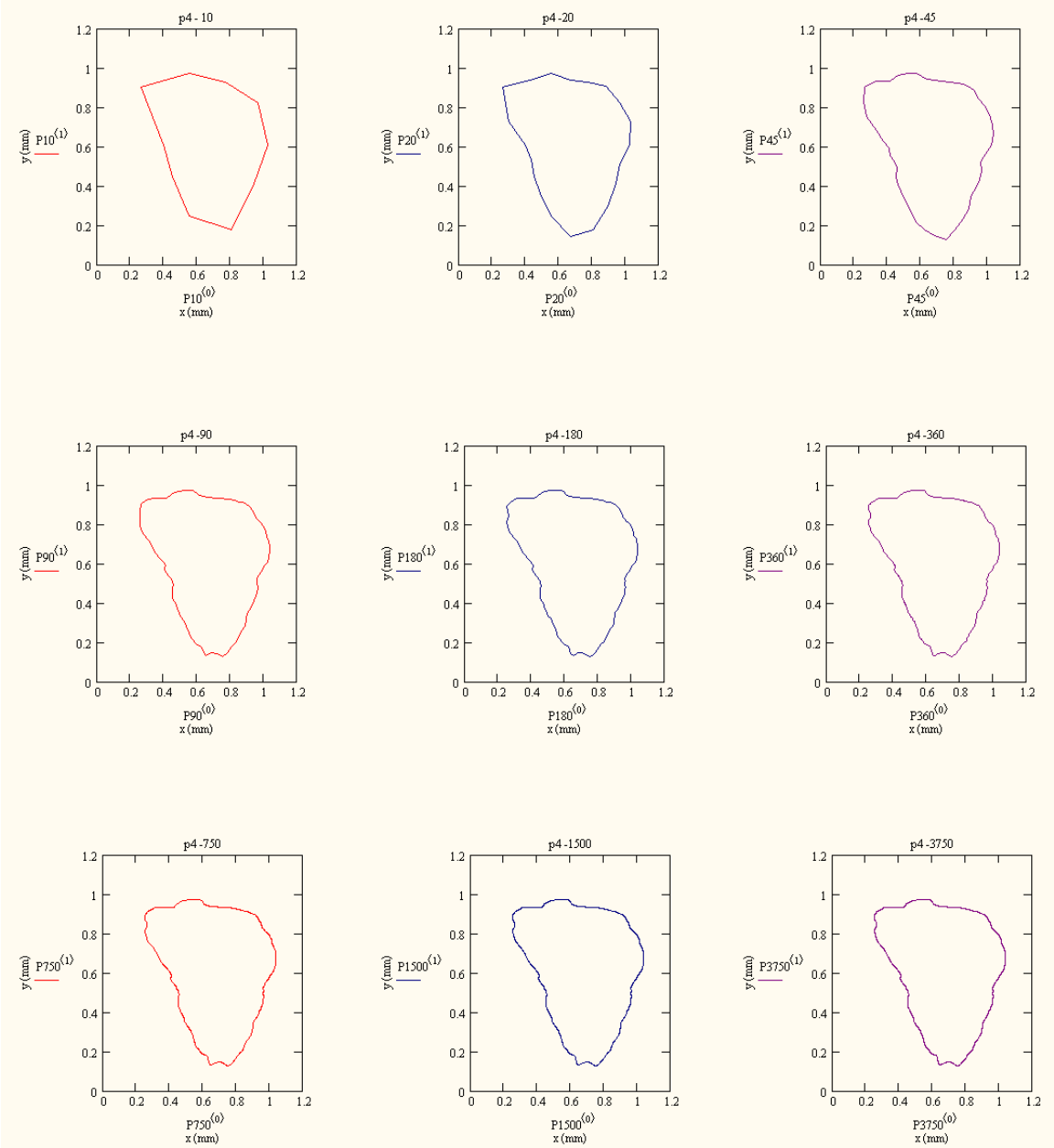


**Figure 4.17 –** Particle *p4* outline at varying number of data points.

**Table 4.14 –** Particle data points and the corresponding CRR, SP, and SPQ particle shape parameters.

| Number of particle data points | Interval Angle (°) | Resolution | CRR (%) | SP | SPQ |
|---|---|---|---|---|---|
| 10 | 36 | 0.2210 | 89.00 | 0.717 | 0.000 |
| 20 | 18 | 0.1194 | 76.74 | 0.540 | 0.000 |
| 45 | 8 | 0.0558 | 83.04 | 0.624 | 0.424 |
| 90 | 4 | 0.0286 | 83.33 | 0.843 | 0.371 |
| 180 | 2 | 0.0145 | 84.23 | 0.573 | 0.287 |
| 360 | 1 | 0.0074 | 85.41 | 0.344 | 0.287 |
| 750 | 0.48 | 0.0036 | 83.16 | 0.270 | 0.299 |
| 1500 | 0.24 | 0.0018 | 82.04 | 0.266 | 0.312 |
| 3750 | 0.096 | 0.0007 | 82.04 | 0.267 | 0.312 |

Note that the resolution corresponding to a particular number of data points is calculated as the ratio of the perimeter to the number of data points. Also, throughout this and following sections, any particle name followed by a number represents the particle outline defined by the following number of data points. In other words, *p2-360* refers to *p2* outline defined by only 360 data points.

In relation to the values displayed in Table 4.14, Figure 4.18 shows the variation of the parameters based on the number of intervals.

As Figure 4.18 shows, the CRR parameter does not change significantly except for 10 and 20 data points, at which values CRR values are erratic due to the sharp corners associated with inadequate particle outline resolution (refer to Figure 4.17). However, beyond 20 data points, CRR is approximately 83%. Note that for the original reported CRR value in Section 4.1.2, the actual data points for *p4* is used. The average

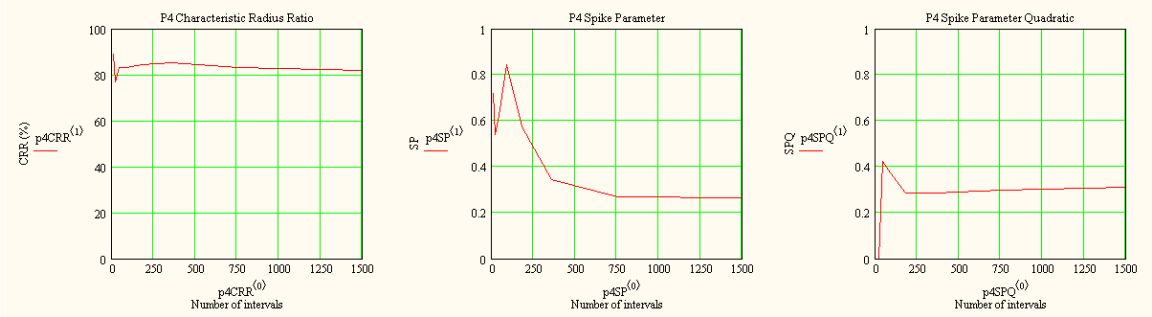


**Figure 4.18 –** Figure showing CRR, SP, and SPQ with the number of data points/intervals.

number of data points for the particle outlines in this study was 696, thus, the answers reported in Section 4.1.2 are from the stable regions shown in Figure 4.18.

For SP parameter, an increasing trend is observed up to 90 data points followed by a decreasing trend. After a relatively sharper decrease at 360 data points from 0.344 to 0.270, the value stabilizes around 0.27. Above 360 data points, there is a minor decrease with the resolution. The increasing pattern for number of data points less than 90 is reasonable since with inadequate number of data points, the particle outline attains sharp points with small spike angles, thereby increasing the SP value. The SP value is stable for number of data points larger than 360.

SPQ parameter has a very similar trend to SP but it requires smaller number of data points/intervals before it stabilizes. At and above 180 data points, SPQ is approximately equal to 0.3.

Both SP and SPQ stabilize beyond a certain threshold value. This is expected since the precision does not affect the results beyond a certain point. The threshold number of data points required to stabilize SP is at a larger value than SPQ. This is because SPQ is a less sensitive parameter, i.e. in SPQ the calculation is based on the parts of the outline outside the least squares circle; whereas for SP more extensive calculation is performed all along the particle profile. If CRR, SP, and SPQ are compared, it is clear that SP is the most sensitive to the number of particle outline data points. SP measures the sharpness and height of each triangle step along the profile and is affected by sharp corners present at low resolution. On the other hand, CRR and SPQ implement approaches more dependent on the general particle outline.

The rest of the particle shape parameters are analyzed with respect to both the number of particle outline data points and the number of sampling intervals for the particle shape parameter. For SF and AF, 40 sampling intervals, every 9°, were used in Section 4.1.1 based on the original study. Sukumaran and Ashmawy (2001) state that 40 intervals represent the cut-off between the angularity (meso-scale shape) and surface roughness (micro-scale shape). However, no basis for this judgment is stated in the original study by Sukumaran and Ashmawy (2001). On the other hand, SI is calculated with16 sampling intervals corresponding to every 6.25°. The change in these parameters with the particle outline data points and parameter sampling interval are presented in the rest of this section.

SF represents the deviation of a particle from a circle outline, whereas AF is based on the number and sharpness of the corners (Sukumaran and Ashmawy, 2001). SF and AF both approximate the particle shape by an equivalent polygon based on the sampling

interval. They are both dimensionless parameters with lower limit of 0% and no theoretical upper limit. The SF is normalized with respect to the SF of a flat particle and AF is normalized with respect to a cross shape particle as the higher end extreme cases for both parameters. Since a cross-shape is considered as the upper AF limit in the original study, in case a higher angularity particle is investigated, the AF value is larger than 100%.

The effect of resolution on SF and AF is investigated using two different particle outlines (*p2* and *p4*) both with 5 different particle outline intervals, i.e. 45, 360,720, 1440, and 2880 particle intervals resulting in particle outlines with 45, 360, 720, 1440, and 2880 data points, respectively. For the SF and AF input sampling interval; 20, 40, 90, 180, 360, 720, 1500, 3,000, 5,000, and 10,000 are utilized. The *p2* and *p4* particle outlines are shown in Figure 4.19 with different number of data points. In addition to the real particle outlines *p2* and *p4*, a derived particle, *concrete-par* is also investigated for the resolution dependence on SF and AF parameters. The *concrete-par* outline is sampled with 180, 250, 360, 720, 2000, and 3750 data points as shown also in Figure 4.19. The input number of sampling intervals for SF and AF parameters are the same with real particles (*p2* and *p4)*.

Table 4.15 displays the values calculated for real particle outlines *p2* and *p4* and Table 4.16 contains the same data for *concrete-par* outline study. Figure 4.20 and 4.21 plot Table 4.15 values for *p2* and *p4,* respectively. Table 4.16 values are plotted in Figure 4.22 as the number of sampling intervals versus the *concrete-par* SF and AF parameter values.

As Figures 4.20-4.22 show, the general trends for all particle outlines *p2*, *p4*, and *concrete-par* are very similar. The SF variation with respect to particle outline samplings is minor. On the other hand, the AF varies with both the particle sampling and number of intervals for AF. For all particle outline samplings, AF has a similar pattern, which magnifies as the particle sampling interval increases. For the variation of AF with the input number of intervals, similar to SF a spike is observed followed by a decreasing trend.

Note that for the values reported in Section 4.1.1, 40 sampling intervals are utilized for SF and AF input with particle outlines represented by 40 data points as suggested in the original study by Sukumaran and Ashmawy (2001).

AF pattern for the real particles has one consistency, i.e. a spike is followed by a decreasing and then a stabilizing trend beyond large number of intervals. The value at which the spike occurs increases with number of data points, i.e. particle outline intervals. For example, for *p2*, a spike for *p2-45* occurs at 90 parameter sampling intervals; whereas for *p2-360, p2-720, p2-1440,* and *p2-2880* the spike is at 360, 720, 1500, and 3000 sampling intervals. It is important to note that the number of AF intervals that spikes occur is in general accordance with the corresponding number of particle outline data points/intervals. The value of particle outline data points change the location of the data points along the profile. Thus, when the particle sampling segments coincide with the AF interval segments, the outline is the most accurate and there are not any errors carried out due to the difference in the number of AF and particle sampling intervals. In case of different AF interval numbers and particle sampling intervals, each AF segment finds the intersection of the AF segment with the outline leading to digitization errors although the difference is not visible to the naked eye.

However, a spike in a trend is not an indicative of stability. As the AF values for different number of outline data points stabilize, the stabilizing value is not the same for any of the number of data points. The stabilized AF value increases with the number of data points defining the outline, which is unacceptable for a particle shape parameter. As general belief suggests, the trends should stabilize with less number of sampling intervals as the number of data points defining the particle outline increases. However, this is not observed in AF behavior shown in Figures 4.20 – 4.22.

For *p2* and *p4* particles, the data suggests that the number of AF intervals should not be larger than the particle sampling. This is based on the observation that comparing *p2-360* and *p2-720*, the AF values are almost identical for up to 360 AF intervals and for *p2-720* and *p2-1440*, AF values are again similar for up to 720 intervals. Comparing *p2-360, p2-720, p2-1440,* and *p2-2880*, all particle samplings have the identical AF values up to 360 intervals. On the other hand, when portion of that data set is analyzed including *p2-720, p2-1440*, and *p2-2880*, AF values are similar for up 720 intervals. The same is valid for *p4*. This may suggest that when AF interval is larger than the particle sampling, the inaccuracy of particle outline estimation by interpolating the available pixels results in superfluous deviation of AF values. The *p2* AF versus number of AF sampling intervals graph for the mentioned data can be observed in Figure 4.23. Note that when the AF interval number is smaller than the particle sampling interval, number of particle outline data points does not have important effect on AF values.

On the other hand, for *concrete-par-180* the spike for AF plot occurs at 180 sampling intervals and for *concrete-par-250, concrete-par-360, concrete-par-720, concrete-par-2000,* and *concrete-par-3750* the largest spikes are at 1500, 720, 1500, 3000, and 3000

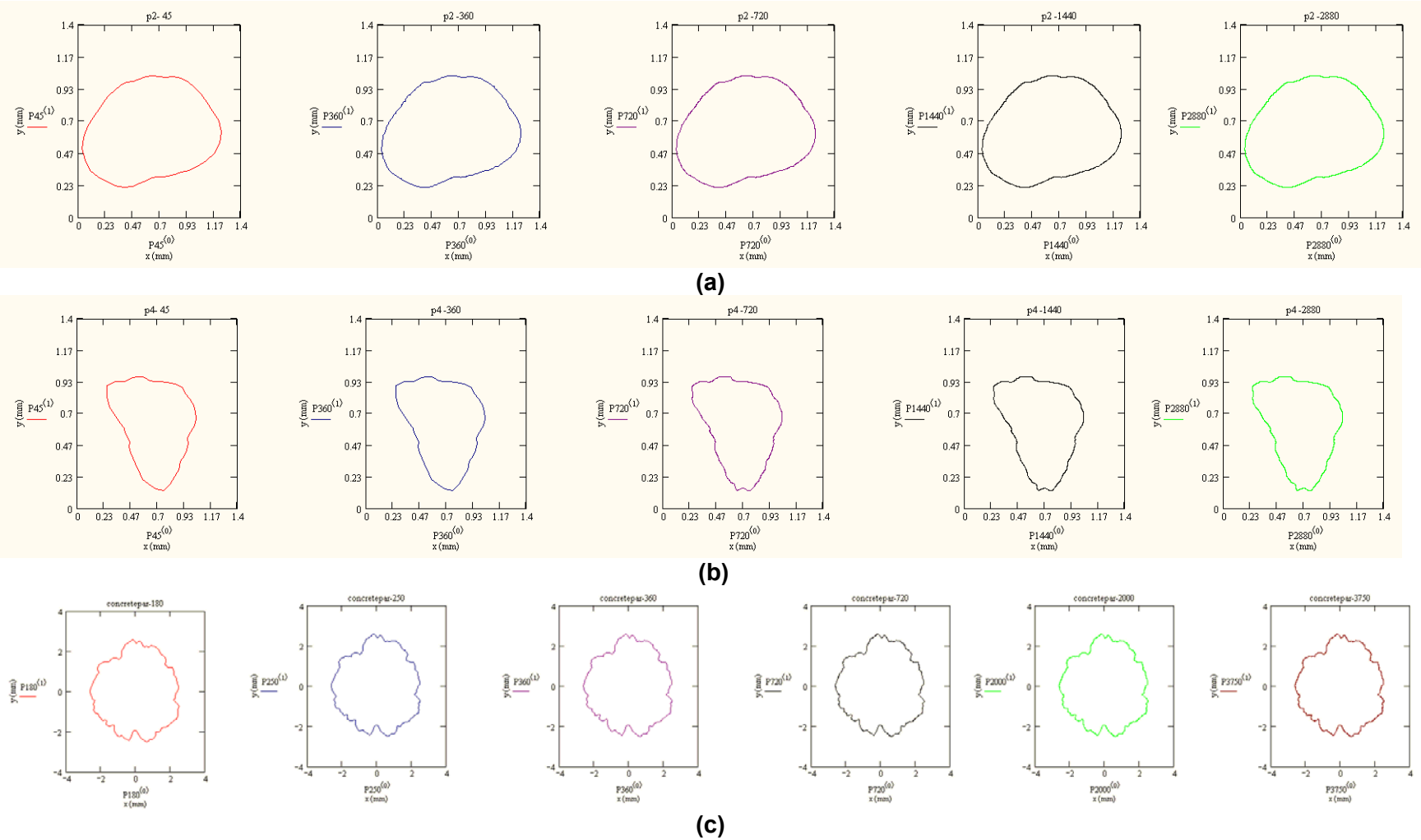


**Figure 4.19 –** *p2*, *p4*, and *concrete-par* sampled at different particle samplings; **(a)** p2, **(b)** p4, and **(c)** concrete-par.

**Table 4.15 –** SF and AF resolution study results for *p4* and *p2* defined by 45, 360, 720, 1440, and 2880 data points.

| | *p2-45* | | | *p4-45* | | |
|---|---|---|---|---|---|---|
| **Sampling interval** | **SF (%)** | **AF (%)** | **FF (%)** | **SF (%)** | **AF (%)** | **FF (%)** |
| 20 | 37.86 | 5.11 | 38.21 | 44.59 | 13.99 | 46.73 |
| 40 | 38.86 | 3.88 | 39.05 | 47.88 | 14.12 | 49.92 |
| 90 | 47.08 | 63.95 | 79.41 | 56.11 | 79.29 | 97.13 |
| 180 | 43.16 | 57.72 | 72.07 | 51.41 | 68.76 | 85.86 |
| 360 | 43.22 | 57.58 | 71.99 | 51.27 | 65.80 | 83.42 |
| 720 | 43.26 | 57.16 | 71.68 | 51.24 | 63.80 | 81.83 |
| 1500 | 43.25 | 56.21 | 70.92 | 51.40 | 67.09 | 84.52 |
| 3000 | 43.26 | 56.13 | 70.87 | 51.41 | 66.47 | 84.03 |
| 5000 | 43.30 | 56.62 | 71.28 | 51.38 | 67.62 | 84.93 |
| 10000 | 43.30 | 57.68 | 72.13 | 51.38 | 66.45 | 84.00 |
| | *p2-360* | | | *p4-360* | | |
| **Sampling interval** | **SF (%)** | **AF (%)** | **FF (%)** | **SF (%)** | **AF (%)** | **FF (%)** |
| 20 | 38.09 | 5.57 | 38.49 | 45.94 | 15.05 | 48.34 |
| 40 | 39.46 | 4.79 | 39.75 | 47.75 | 17.66 | 50.91 |
| 90 | 43.56 | 5.71 | 43.93 | 55.01 | 33.89 | 64.61 |
| 180 | 40.24 | 20.40 | 45.12 | 50.79 | 47.49 | 69.53 |
| 360 | 42.43 | 104.84 | 113.10 | 51.40 | 115.47 | 126.39 |
| 720 | 42.43 | 104.71 | 112.98 | 51.76 | 178.12 | 185.49 |
| 1500 | 42.17 | 73.18 | 84.46 | 51.72 | 137.97 | 147.34 |
| 3000 | 42.29 | 72.80 | 84.20 | 51.82 | 136.86 | 146.34 |
| 5000 | 42.35 | 68.86 | 80.84 | 51.87 | 137.63 | 147.08 |
| 10000 | 42.40 | 69.35 | 81.28 | 51.90 | 136.83 | 146.34 |
| | *p2-720* | | | *p4-720* | | |
| **Sampling interval** | **SF (%)** | **AF (%)** | **FF (%)** | **SF (%)** | **AF (%)** | **FF (%)** |
| 20 | 38.09 | 5.57 | 38.49 | 45.96 | 15.06 | 48.36 |
| 40 | 39.46 | 4.78 | 39.75 | 47.78 | 17.65 | 50.93 |
| 90 | 43.56 | 5.69 | 43.93 | 54.99 | 33.78 | 64.54 |
| 180 | 40.23 | 20.32 | 45.07 | 50.75 | 47.08 | 69.22 |
| 360 | 42.42 | 104.25 | 112.55 | 51.35 | 111.52 | 122.78 |
| 720 | 46.72 | 491.01 | 493.22 | 53.65 | 339.65 | 343.86 |
| 1500 | 45.69 | 387.59 | 390.27 | 53.62 | 305.04 | 309.71 |
| 3000 | 46.44 | 379.25 | 382.08 | 53.97 | 295.46 | 300.35 |
| 5000 | 46.64 | 385.30 | 388.11 | 54.13 | 301.97 | 306.79 |
| 10000 | 46.85 | 374.94 | 377.85 | 54.21 | 304.54 | 309.33 |

**Table 4.15 (continued)**..

| | *p2-1440* | | | *p4-1440* | | |
|---|---|---|---|---|---|---|
| **Sampling interval** | **SF (%)** | **AF (%)** | **FF (%)** | **SF (%)** | **AF (%)** | **FF (%)** |
| 20 | 38.09 | 5.57 | 38.49 | 45.97 | 15.07 | 48.38 |
| 40 | 39.46 | 4.79 | 39.75 | 47.77 | 17.67 | 50.94 |
| 90 | 43.56 | 5.71 | 43.93 | 55.02 | 33.85 | 64.60 |
| 180 | 40.24 | 20.41 | 45.12 | 50.76 | 47.46 | 69.49 |
| 360 | 42.44 | 105.08 | 113.33 | 51.43 | 115.89 | 126.79 |
| 720 | 46.79 | 496.39 | 498.59 | 53.84 | 357.53 | 361.56 |
| 1500 | 47.58 | 889.53 | 890.80 | 54.54 | 409.21 | 412.83 |
| 3000 | 48.61 | 871.44 | 872.80 | 55.14 | 470.26 | 473.48 |
| 5000 | 49.10 | 887.64 | 888.99 | 55.29 | 458.68 | 462.00 |
| 10000 | 49.34 | 869.33 | 870.73 | 55.42 | 457.20 | 460.55 |
| | *p2-2880* | | | *p4-2880* | | |
| **Sampling interval** | **SF (%)** | **AF (%)** | **FF (%)** | **SF (%)** | **AF (%)** | **FF (%)** |
| 20 | 38.09 | 5.57 | 38.49 | 45.97 | 15.07 | 48.37 |
| 40 | 39.46 | 4.79 | 39.75 | 47.77 | 17.67 | 50.93 |
| 90 | 43.56 | 5.71 | 43.93 | 55.02 | 33.84 | 64.59 |
| 180 | 40.24 | 20.44 | 45.13 | 50.77 | 47.69 | 69.66 |
| 360 | 42.44 | 105.24 | 113.48 | 51.47 | 118.75 | 129.43 |
| 720 | 46.80 | 497.49 | 499.69 | 53.97 | 373.54 | 377.42 |
| 1500 | 49.12 | 1090.00 | 1091.11 | 54.91 | 536.77 | 539.57 |
| 3000 | 49.86 | 1134.00 | 1135.10 | 55.46 | 474.83 | 478.06 |
| 5000 | 50.06 | 1095.00 | 1096.14 | 55.58 | 489.26 | 492.40 |
| 10000 | 50.27 | 1057.00 | 1058.19 | 55.66 | 478.52 | 481.75 |

**Table 4.16 -** SF and AF resolution study results for *concrete-par* defined by 180, 250, 360, 720, 2000, and 3750 data points.

| *concrete-par 180* | | | | *concrete-par 720* | | | |
|---|---|---|---|---|---|---|---|
| **Sampling interval** | **SF (%)** | **AF (%)** | **FF (%)** | **Sampling interval** | **SF (%)** | **AF (%)** | **FF (%)** |
| 20 | 31.19 | 19.96 | 37.03 | 20 | 31.07 | 19.83 | 36.86 |
| 40 | 41.36 | 55.43 | 69.16 | 40 | 41.49 | 57.44 | 70.85 |
| 90 | 58.37 | 121.04 | 134.38 | 90 | 58.20 | 118.96 | 132.43 |
| 180 | 57.96 | 187.25 | 196.02 | 180 | 57.76 | 180.15 | 189.18 |
| 360 | 57.97 | 186.17 | 194.98 | 360 | 60.90 | 227.17 | 235.19 |
| 720 | 57.97 | 184.51 | 193.40 | 720 | 61.62 | 219.66 | 228.14 |
| 1500 | 57.61 | 128.18 | 140.53 | 1500 | 62.49 | 311.52 | 317.73 |
| 3000 | 57.833 | 128.934 | 141.31 | 3000 | 62.487 | 309.545 | 315.79 |
| 5000 | 57.918 | 125.85 | 138.54 | 5000 | 62.408 | 221.679 | 230.30 |
| 10000 | 57.967 | 125.529 | 138.27 | 10000 | 62.442 | 214.696 | 223.59 |
| *concrete-par 250* | | | | *concrete-par 2000* | | | |
| **Sampling interval** | **SF (%)** | **AF (%)** | **FF (%)** | **Sampling interval** | **SF (%)** | **AF (%)** | **FF (%)** |
| 20 | 31.516 | 19.891 | 37.27 | 20 | 31.186 | 19.948 | 37.02 |
| 40 | 40.724 | 53.365 | 67.13 | 40 | 41.583 | 58.345 | 71.65 |
| 90 | 58.057 | 112.634 | 126.72 | 90 | 58.376 | 121.082 | 134.42 |
| 180 | 57.106 | 144.643 | 155.51 | 180 | 57.97 | 187.108 | 195.88 |
| 360 | 58.878 | 135.886 | 148.09 | 360 | 61.405 | 249.621 | 257.06 |
| 720 | 59.598 | 186.517 | 195.81 | 720 | 62.171 | 294.583 | 301.07 |
| 1500 | 60.579 | 245.397 | 252.76 | 1500 | 63.188 | 350.852 | 356.50 |
| 3000 | 60.593 | 240.495 | 248.01 | 3000 | 63.813 | 399.049 | 404.12 |
| 5000 | 60.598 | 234.165 | 241.88 | 5000 | 63.908 | 398.798 | 403.89 |
| 10000 | 60.604 | 219.337 | 227.56 | 10000 | 64.05 | 398.64 | 403.75 |
| *concrete-par 360* | | | | *concrete-par 3750* | | | |
| **Sampling interval** | **SF (%)** | **AF (%)** | **FF (%)** | **Sampling interval** | **SF (%)** | **AF (%)** | **FF (%)** |
| 20 | 31.19 | 19.96 | 37.03 | 20 | 31.171 | 19.939 | 37.00 |
| 40 | 41.58 | 58.33 | 71.63 | 40 | 41.589 | 58.278 | 71.60 |
| 90 | 58.40 | 121.32 | 134.64 | 90 | 58.385 | 121.175 | 134.51 |
| 180 | 57.98 | 187.56 | 196.32 | 180 | 58.005 | 187.953 | 196.70 |
| 360 | 61.41 | 252.19 | 259.56 | 360 | 61.415 | 252.209 | 259.58 |
| 720 | 61.89 | 300.56 | 306.86 | 720 | 62.243 | 306.916 | 313.16 |
| 1500 | 61.36 | 215.57 | 224.13 | 1500 | 63.365 | 408.477 | 413.36 |
| 3000 | 61.648 | 229.354 | 237.49 | 3000 | 64.089 | 453.132 | 457.64 |
| 5000 | 61.763 | 226.383 | 234.66 | 5000 | 64.239 | 415.73 | 420.66 |
| 10000 | 61.849 | 227.316 | 235.58 | 10000 | 64.376 | 409.415 | 414.45 |

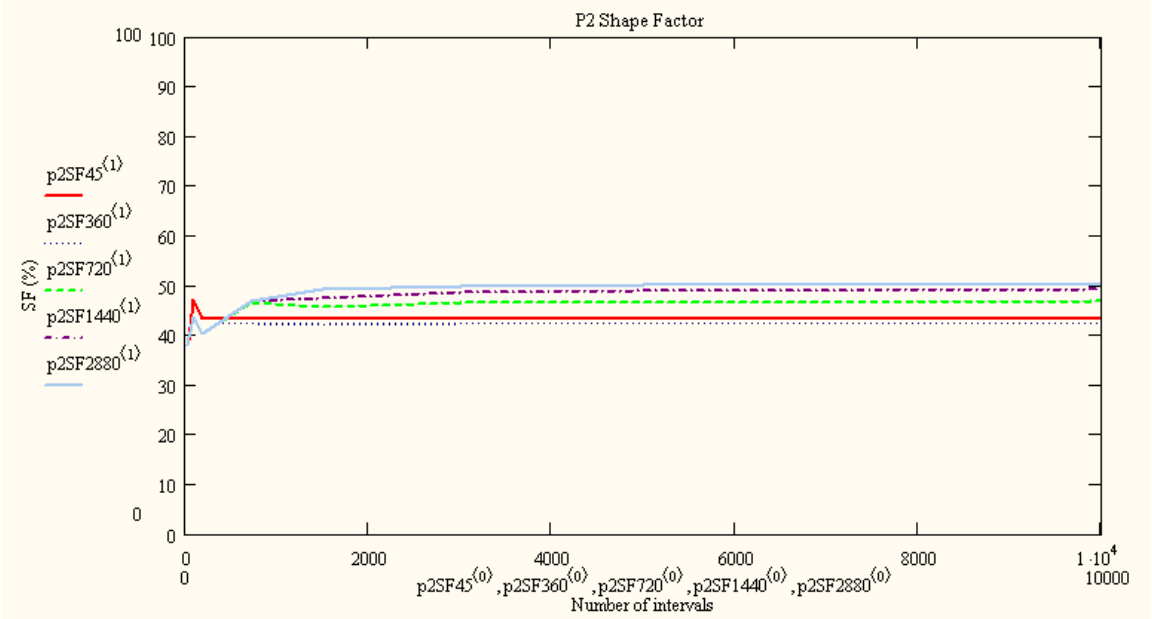


**(a)**

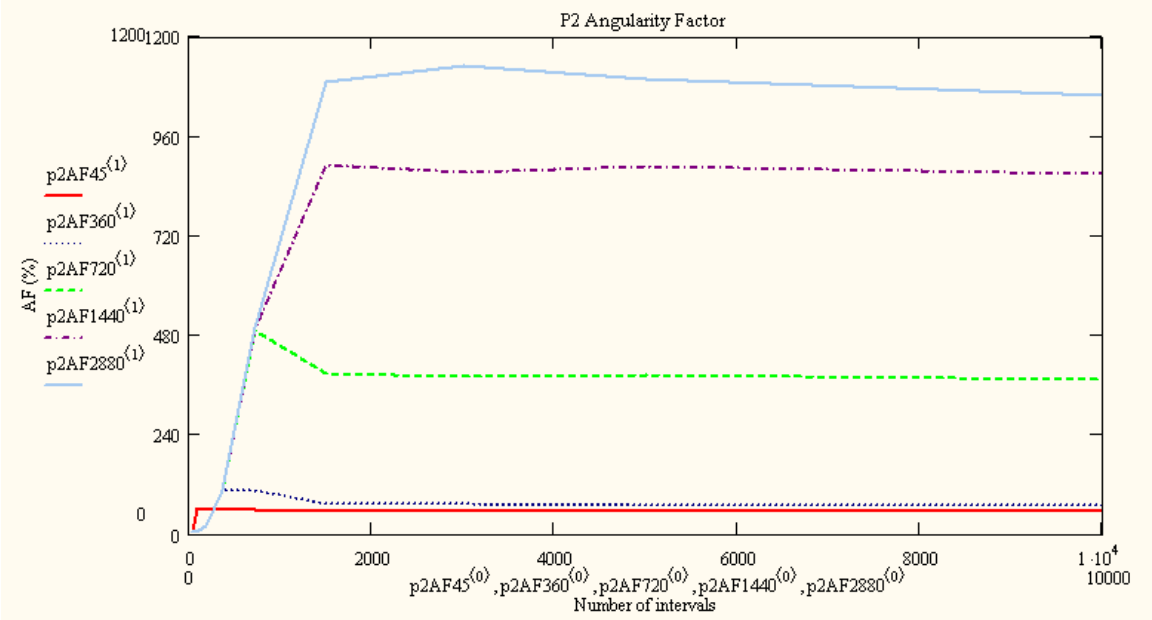


**(b)**

**Figure 4.20 –** *p2* SF and AF variation for different particle outline data points vs. the number of sampling intervals; **(a)** *p2* SF, **(b)** *p2* AF.

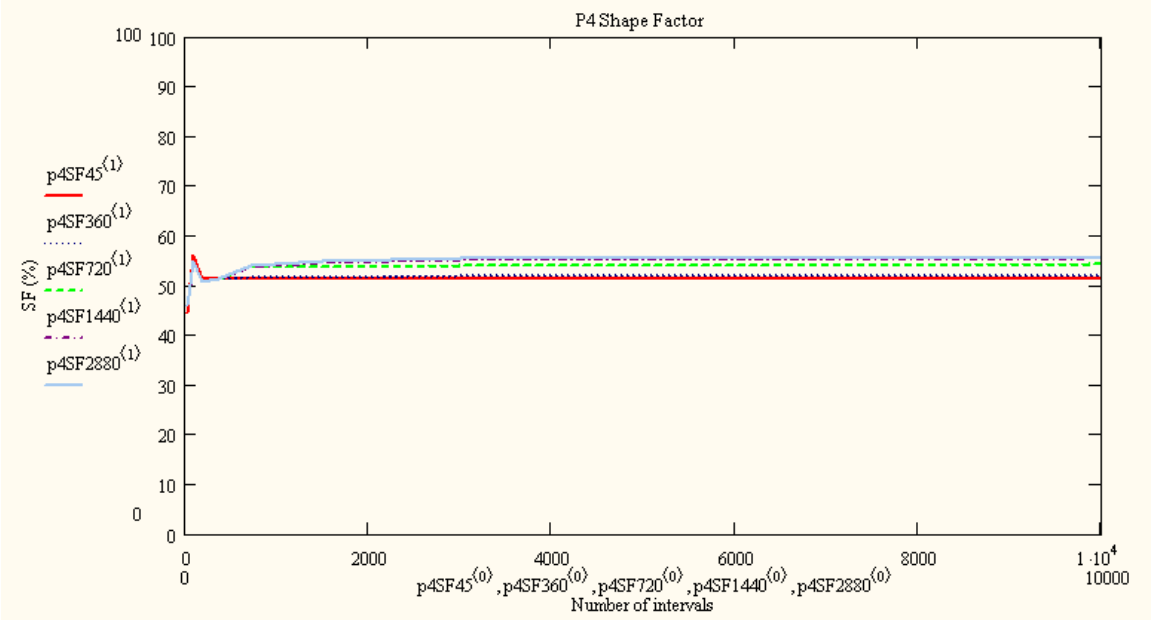


**(a)**

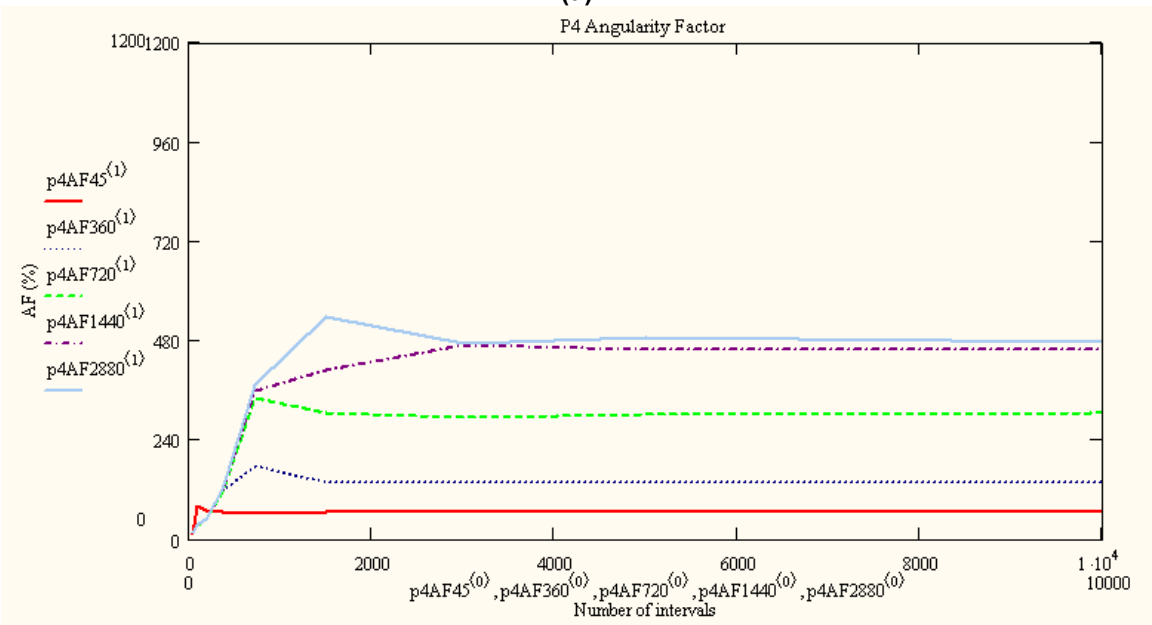


**(b)**

**Figure 4.21 –** *p4* SF and AF variation for different particle outline data points vs. the number of sampling intervals; **(a)** *p4* SF, **(b)** *p4* AF.

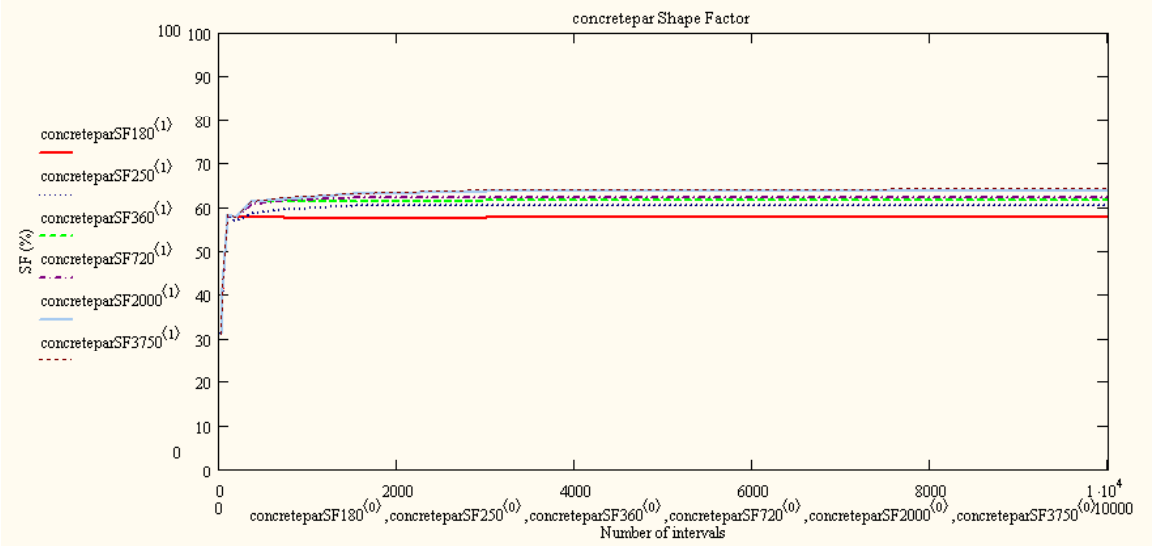


**(a)**

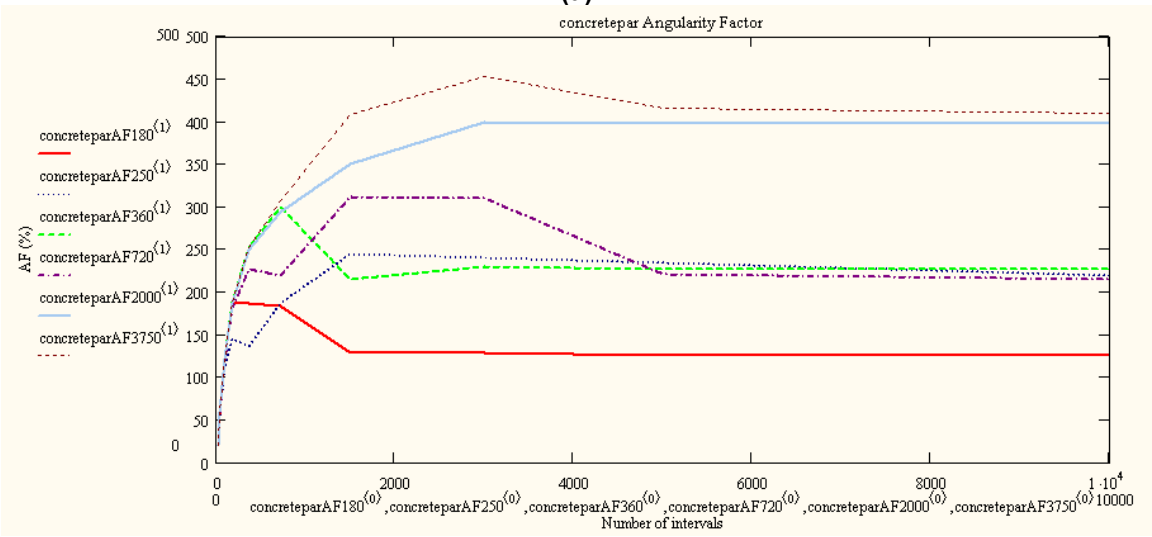


**(b)**

**Figure 4.22 –** *concrete-par* SF and AF variation for different particle outline data points vs. the number of sampling intervals; **(a)** *concrete-par* SF, **(b)** *concrete-par* AF.

sampling intervals. This is similar to the real particles data discussed above but not as evident as the real particle case. As an exception to this general trend, *concrete-par-250* spike is at 1500 number of AF sampling intervals, however, a smaller spike is present at 180 intervals. A different aspect of the *concrete-par* is that there is a strong linear relationship between the number of AF intervals and the AF values up to 90 AF intervals. For the other derived particle SF, AF resolution study (not shown here), this linearity is not observed; thus, it is only the case for concrete-par.

A statistical hypothesis test is performed utilizing Minitab Release 11.12. The null hypothesis is that "Both SF and AF are independent of the particle sampling intervals and number of SF or AF intervals." Balanced Anova results show that the null hypothesis is not plausible based on the results presented above and that they are both highly dependent on the number of particle outline data points and number of parameter sampling intervals.

The number of data points for the particle outline is fixed at a single value and only the effect of sampling interval is investigated by examining the data in Table 4.15 for different sampling intervals. The least amount of AF variation is observed for *p2-45* among other *p2* outline resolutions. For *p2-45,* as the sampling interval increases, AF value also increases up to a value and subsequent decrease is followed by a stabilized AF value of approximately 57 %. Considering the smallest value of AF is for 40 sampling intervals (equal to 3.88), the increase of AF value from 40 sampling intervals to 10,000 sampling intervals is 1385%, which is unacceptable. Even more variation is observed for larger number of outline data points' sets.

Another way of looking at the data in Tables 4.15 and 4.16 is to fix the sampling intervals and vary the number of outline data points. For different data points of *p4* outline, the corresponding AF values with 360 sampling intervals are shown in Table 4.17.

As the values in Table 4.17 suggest, AF values only up to 360 outline data points. In other words, for *p4* outlines represented with larger number of data points than 360, the AF value is stable. This behavior is valid for all sampling intervals. That is, AF values with 720 sampling intervals are stable for particle outlines represented with more than 720 data points. This suggests that provided that the number of particle outline data points is larger than the AF sampling intervals, AF value at that sampling interval is stable. For example, for 20 sampling intervals, AF value is stable for *p4-45, p4-360, p4-720, p4-1440,* and *p4-2880.* On the other hand, AF value is not stable at 2880 sampling intervals for the range of particle outline data points considered.

**Table 4.17 –** Number of *p4* outline data points versus AF values.

| **Number of *p4* outline data points** | **AF* (%)** |
|---|---|
| 45 | 65.80 |
| 360 | 115.47 |
| 720 | 111.52 |
| 1440 | 115.89 |
| 2880 | 118.75 |

*: AF value is obtained with 360 sampling intervals.

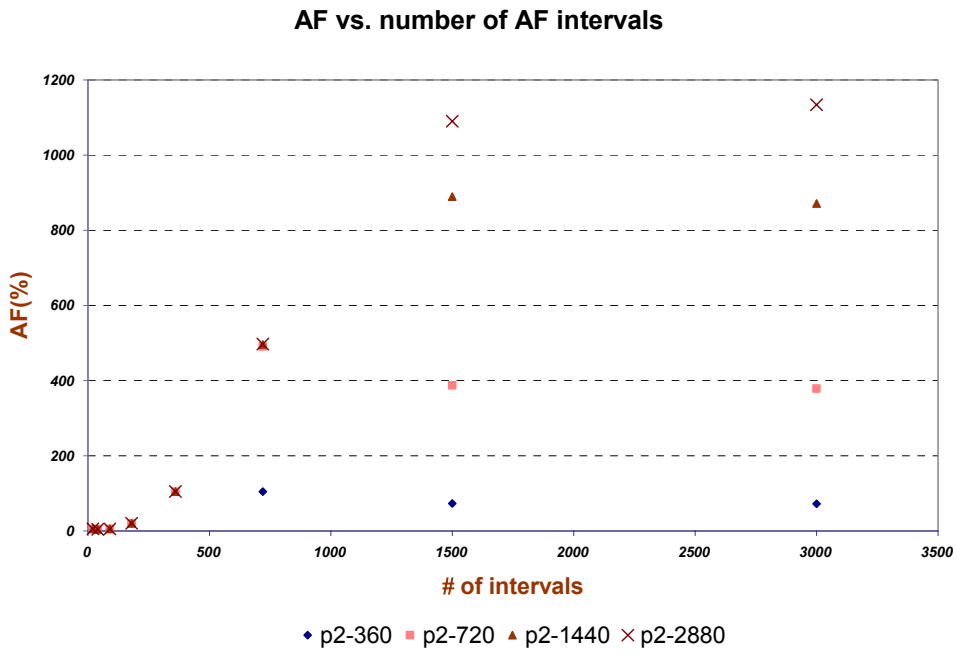


**Figure 4.23 –** AF value versus number of AF sampling intervals for *p2.*

The study conducted to evaluate the effect of resolution on AF resolved that it is highly dependent on both the number of AF sampling intervals and accuracy of the input particle outline; i.e. number of outline data points. Another unusual result is that as the number of outline data points increases, AF variation increases. For example, for *p2-720*, more divergence is observed between 20 to 10,000 AF intervals than for *p2-90*. This result leads to more variation regarding the behavior of AF values. The observed AF behavior is explained by the fact that AF was originally developed for 9° AF intervals and it was not normalized with respect to the number of AF intervals (Personal communication, Ashmawy, 2004). For an elongated particle outline, the AF intervals should be increased but the selection of the appropriate parameters is left to the user.

This study suggests that AF parameter is also user-dependent and hence the results are subjective.

The unexplainable behavior of AF is not apparent for SF. The values for SF are provided in Tables 4.15 and 4.16. The peak variation for SF is marked at 32% at extreme cases, i.e. comparing 20 AF intervals with *p2-45* and 10,000 AF intervals with *p2-2880*. For *p4*, the peak SF variation is 21% at *p4-2880* sampled with 10,000 intervals. The SF values with 360 sampling intervals corresponding to different number of outline data points is given in Table 4.18. The SF value obtained at 360 sampling intervals is stable for 360 and more outline data points. SF decrease at 360 sampling intervals is only 1.8% from 45 to 360 outline data points. Thus, SF is regarded as an acceptable measure of particle shape.

Additional studies were performed to normalize AF with respect to sampling intervals in order to obtain better results. However, as the components of the parameter are investigated, it is apparent that the behavior of AF is highly dependent on the behavior of the sum of angularity terms, Sumangularity, $\sum(\beta_{iparticle} - 180)^2$. The behavior of the

**Table 4.18 -** Number of *p2* outline data points versus SF values.

| Number of particle outline data points | SF* (%) |
|---|---|
| 45 | 43.22 |
| 360 | 42.43 |
| 720 | 42.42 |
| 1440 | 42.44 |
| 2880 | 42.44 |

* : SF value is obtained at 360 sampling intervals.

Sumangularity term with respect to the sampling interval is shown in Figure 4.24 for varying *p4* particle outline data points. The behavior of Sumangularity with sampling interval shown in Figure 4.24 resembles the behavior of AF with sampling interval provided in Figure 4.22. In attempts to stabilize the behavior of AF, the angularity summation was modified by taking the square root of the Sumangularity term, $\sum(\beta_{iparticle} - 180)$ termed as SQRTSumangularity in this study. The behavior of SQRTSumangularity with sampling interval for varying *p4* outline data points is provided in Figure 4.25. As evident from Figure 4.25, the behavior of SQRTSumangularity with sampling interval is more stable than the behavior of Sumangularity with sampling interval shown in Figure 4.24. However, still the stabilizing value is different for every outline data point sets and increases as the outline number of data points increases. The sampling interval at which the plots level out in Figure 4.25 changes with the outline data points. As the number of data points increases, more sampling intervals are required to stabilize AF parameter. Based on this output, the AF parameter is modified to sqrtAF, by taking the square root of every summation term, $sqrtAF = \frac{\sum(\beta_{iparticle} - 180) - \sum(\beta_{icircle} - 180)}{\sqrt{3} * 180 - \sum(\beta_{icircle} - 180)} * 100\%$. The behavior of sqrtAF with sampling interval is shown in Figure 4.26.

Figure 4.26 shows that the behavior of sqrtAF is the same as the behavior of SQRTSumangularity in Figure 4.25. Based on Figure 4.26, the approximate stabilized sqrtAF values for different *p4* outline data points are provided in Table 4.19.

Despite the improvement on the behavior of sqrtAF compared to AF in terms of variability, still 20-fold difference in sqrtAF is present between the 10 data points and

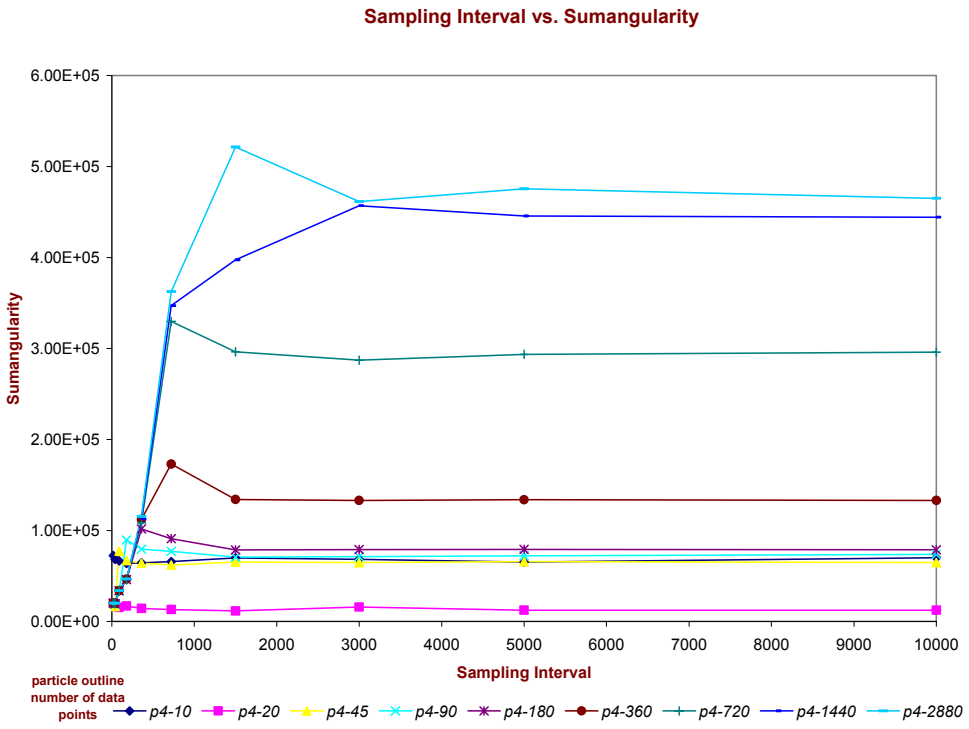


**Figure 4.24 –** Sumangularity versus sampling interval plot for varying *p4* outline data points.

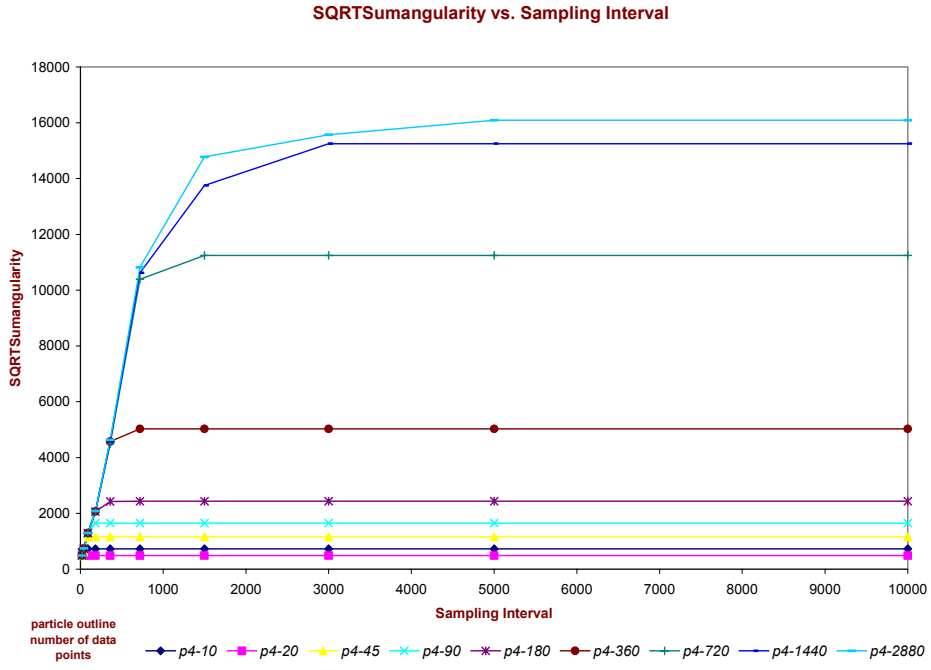


**Figure 4.25 –** SQRTSumangularity versus sampling interval plot for varying *p4* outline data points.

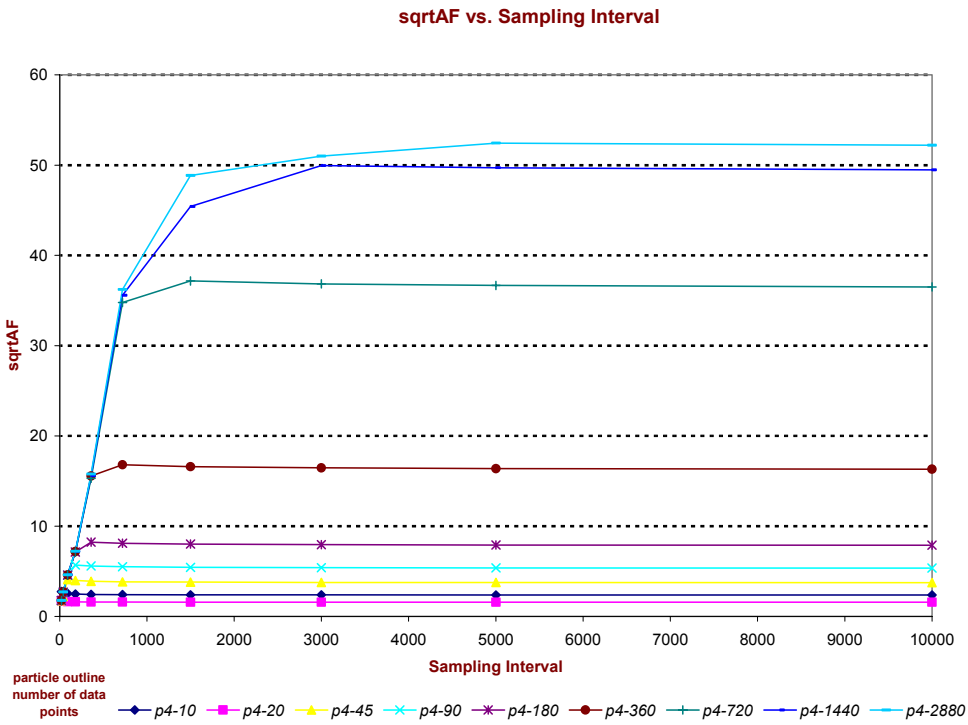


**Figure 4.26 –** sqrtAF versus sampling interval plot for varying *p4* outline data points.

**Table 4.19 –** *p4* outline data points with corresponding sqrtAF stabilized values.

| ***p4* outline number of data points** | **sqrtAF stabilized value** |
|---|---|
| 10 | 2.37 |
| 20 | 1.57 |
| 45 | 3.7 |
| 90 | 5.3 |
| 180 | 7.9 |
| 360 | 16.4 |
| 720 | 36.7 |
| 1440 | 49.7 |
| 2880 | 52.4 |

2880 data points outlines. More studies are required in order to improve AF parameter to obtain a reliable particle shape parameter.

A similar exercise is performed to evaluate the effects of resolution on the Shape Index (SI) particle shape parameter. For SI calculation, the number of sampling intervals is a variable provided as input in the SI mathgram. Table 4.20 displays the output of SI parameter with different number of sampling intervals using the same particle outline. Figure 4.27 plots the results. The results clearly show that at very small number of sampling intervals, the SI attains its highest value. As the sampling intervals increases, the estimated outline by the sampling intervals becomes smoother with less sharp corners. This decreases the outlines deviation from a perfect circular shape. Since SI is a measure of the difference of the outline from the perfect circular outline, SI value decreases with the number of sampling intervals. At eight intervals, it decreases sharply showing an approximately stable trend above16 sampling intervals. This result is in accordance with Boyce and Clark (1964) study suggesting 16 sampling intervals for SI calculation.

**Table 4.20 –** Shape index (SI) resolution study results for *p4*.

| **sampling interval** | 4 | 8 | 15 | 16 | 32 | 75 | 150 | 360 | 750 | 1500 | 3750 |
|---|---|---|---|---|---|---|---|---|---|---|---|
| **SI (p4, #int)** | 15.69 | 15.02 | 13.68 | 14.35 | 14.08 | 13.91 | 13.97 | 13.98 | 13.98 | 13.98 | 13.98 |

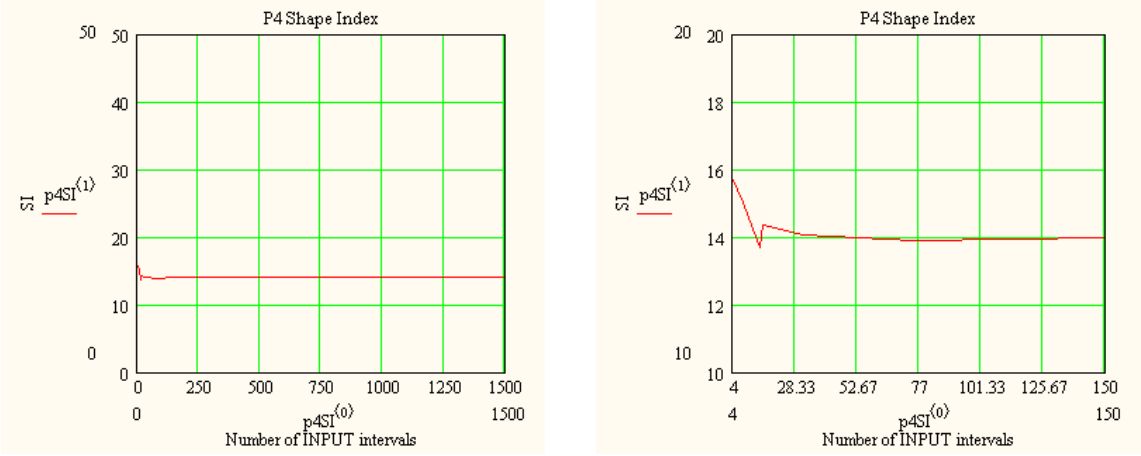


**(a)** **(b)**

**Figure 4.27 –** *p4* Shape Index (SI) variation with the number of sampling intervals; **(a)** Number of sampling intervals from 0 to 1500, **(b)** Magnified section from 0 to 150 numbers of sampling intervals.

### *4.3.2 Surface Roughness Parameters*

Similar to the resolution analysis for particle shape parameters, the sensitivity of the selected surface shape parameters' values to the input surface profile resolution is investigated. The surface roughness parameters selected do not require any input parameters, thus, only the effect of surface profile resolution is examined. For the analysis in Section 4.2, 15-mm long 0.004mm resolution profiles were selected to match the particle outlines in terms of data points/mm resolution. Figure 4.28 displays the *concrete* surface profile at various resolutions. Note that the surfaces are separated by an arbitrary distance from each other for visual purposes to prevent overlapping. The resolution of a 15mm *concrete* profile is varied from 0.002mm, 0.004mm, 0.006mm, 0.01mm, 0.015mm, 0.02mm, 0.05mm, 0.1mm, and 0.5mm. The results of the surface

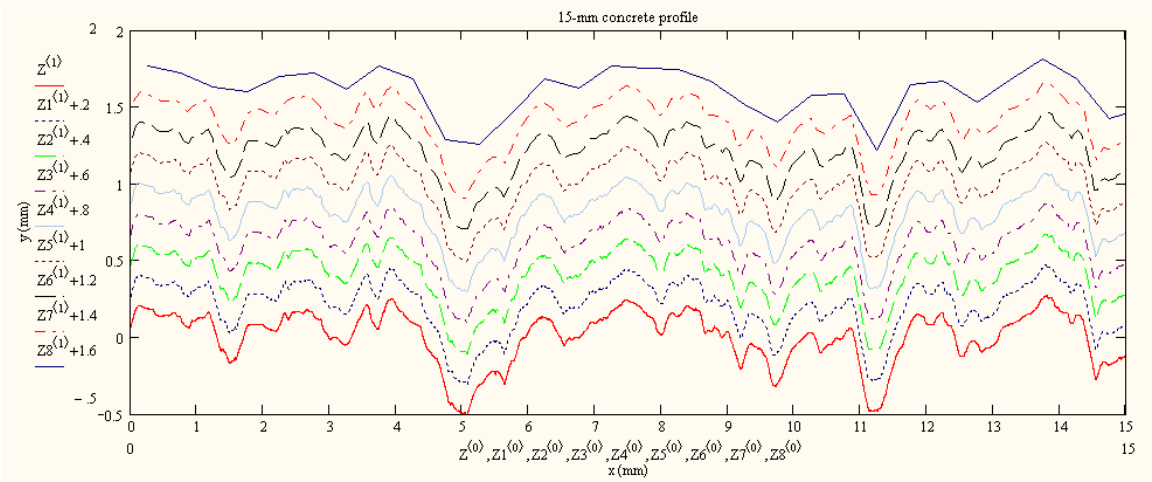


| File Name | Z | Z1 | Z2 | Z3 | Z4 | Z5 | Z6 | Z7 | Z8 |
|---|---|---|---|---|---|---|---|---|---|
| Res (mm) | 0.002 | 0.004 | 0.006 | 0.01 | 0.015 | 0.02 | 0.05 | 0.1 | 0.5 |

**Figure 4.28 –** 15 mm long *concrete* elevated profiles at different resolutions.

shape parameter values for the 15-mm long *concrete* profiles at different resolutions are shown in Table 4.21.

**Table 4.21 –** Surface roughness parameter values for varying resolutions (15-mm long, concrete profile).

| Res(mm) | # data points | $D_{50}$ for $R_n$ (mm) | $R_a$ (mm) | $R_q$ (mm) | $R_p$ (mm) | $R_{max}$ (mm) | $R_n$ | SPQ-surf |
|---|---|---|---|---|---|---|---|---|
| 0.002 | 7501 | 6 | 0.13 | 0.17 | 0.27 | 0.78 | 0.12 | 0.50 |
| 0.004 | 3751 | 6 | 0.13 | 0.17 | 0.27 | 0.78 | 0.12 | 0.48 |
| 0.006 | 2501 | 6 | 0.13 | 0.17 | 0.26 | 0.78 | 0.12 | 0.43 |
| 0.01 | 1501 | 6 | 0.13 | 0.17 | 0.26 | 0.78 | 0.12 | 0.41 |
| 0.015 | 1001 | 6 | 0.13 | 0.17 | 0.26 | 0.78 | 0.12 | 0.39 |
| 0.02 | 751 | 6 | 0.13 | 0.17 | 0.26 | 0.77 | 0.12 | 0.38 |
| 0.05 | 301 | 6 | 0.13 | 0.17 | 0.26 | 0.76 | 0.12 | 0.34 |
| 0.1 | 151 | 6 | 0.13 | 0.17 | 0.25 | 0.75 | 0.12 | 0.26 |
| 0.5 | 31 | 6 | 0.12 | 0.15 | 0.21 | 0.60 | 0.09 | 0.00 |

Among the conventional surface roughness parameters, only, $R_n = \frac{R_{\max}}{D_{50}}$, $R_n$ is normalized with respect to the contacting particle size represented by $D_{50}$. In order to observe the change of $R_n$ with resolution, $D_{50}$ is kept constant at the $D_{50}$ value of 15-mm long 0.004mm resolution concrete profile for all resolutions investigated. The variation of the surface roughness parameters with the surface profile resolution is plotted in Figure 4.29. Although the resolution of the surface profile is varied from 0.002 mm to 0.5 mm, corresponding to 7501 and 31 data points, respectively; the conventional surface roughness parameters $R_a$, $R_q$, $R_p$, $R_{max}$, and $R_n$ do not change significantly. Among the conventional surface roughness parameters, the highest variation is observed in $R_n$ between 0.002mm and 0.5mm resolution surface profiles (28.3%). In theory, $R_{max}$ is expected to vary the most among conventional surface roughness parameters since it is dependent on only two values; whereas $R_n$ is an average of $R_{max}$ values for the length of $D_{50}$ over the length of the surface profile. The results indicate that $R_{max}$ variation is the largest among the surface roughness parameters for all resolutions up to 0.1mm. Another characteristic of the data shown in Table 4.21 is that although the parameter variations between 0.002mm and 0.1mm resolutions for $R_a$, $R_q$, $R_p$, $R_{max}$, and $R_n$ are only 0.4%, 1.1%, 5.3%, 4.0%, and 3.0%, respectively the values increase to 9.9%, 10.2%, 20.8%, 23.5%, and 28.3% between 0.002mm and 0.5mm resolutions. Besides the five fold increase in resolution from 0.1mm to 0.5mm, as Figure 4.28 indicates at 0.5mm resolution all the curves at 0.1mm resolution are replaced with sharp local peaks. However, note that surface profiles are almost never represented with 0.5mm resolution.

On the other hand, the surface roughness parameter SPQ-surf varies considerably with surface profile resolution. The 0.5mm resolution gives an SPQ-surf value of zero, due to the inadequate number of points to represent the spikes with polynomial functions. As

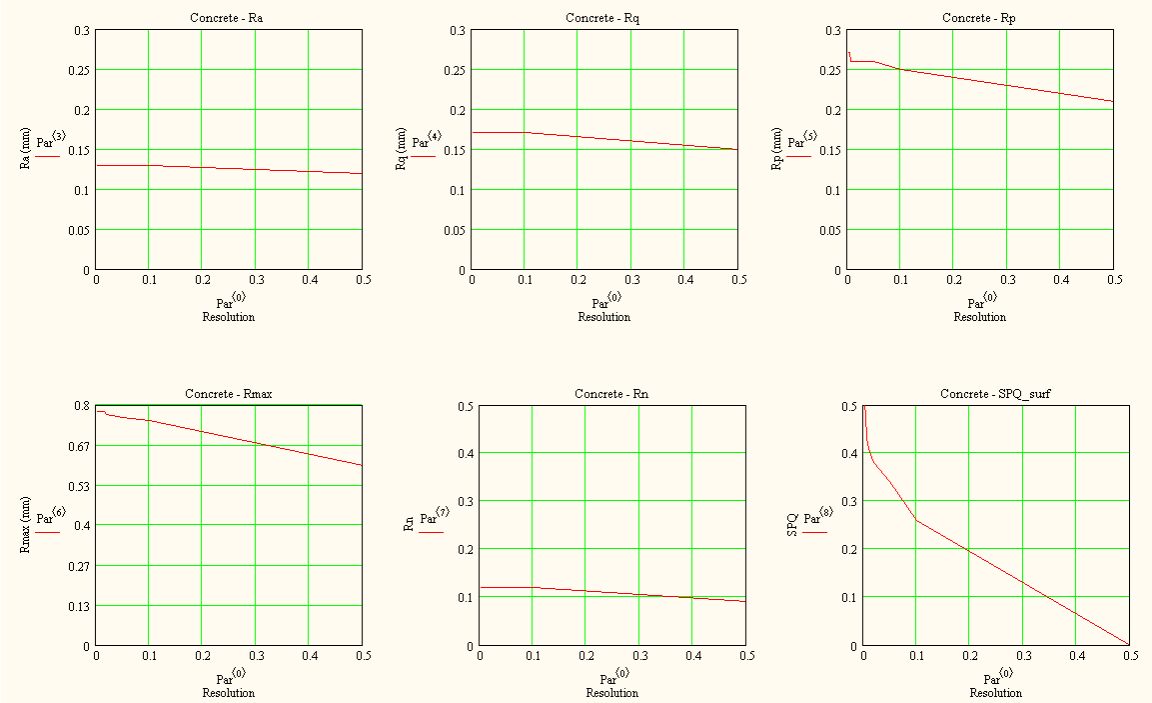


**Figure 4.29 –** Surface roughness parameters versus profile resolution (for 15-mm long concrete profile).

the resolution increases, a smaller number of points are used to define the profile resulting in a smoother estimated profile; which in return increases the spike angles and decreases the SPQ-surf value. Note that although the SPQ-surf decreases from 0.5 to zero, between 0.004mm and 0.01mmresolution, the SPQ-surf varies less from 0.48 to 0.41; thus, at extreme resolution values the SPQ-surf value exhibits the highest rate of decrease with resolution. At the highest resolution, i.e. at 0.002mm resolution, all of the spikes and any present turning points can be located; whereas as the resolution decreases, some of the spikes are not located due to inadequate number of points to define the surface profile. For example, at 0.002mm and 0.004 mm resolutions, all eight spikes are located; whereas at 0.006mm, 0.01mm, and 0.05 mm resolution only 7, 7, and 6 spikes are located, respectively. Note that although 6 of the 8 spikes could be

positioned at 0.05mm resolution, the SPQ-surf value decreases from 0.5 at the highest resolution to 0.34 at 0.05mm resolution. At 0.05mm resolution, the locations of the end and turning points cannot be located accurately and this results in different spike angles and hence diverse SPQ-surf values. At the lowest resolutions of 0.1mm and 0.5mm, only 3 and 0 spikes can be observed, respectively. This study suggests that SPQ-surf is very sensitive to resolution. However, among the commonly used resolution values for surface profiles, the variation of SPQ-surf is not as manifest as at extreme low resolutions.

## 4.4 Concluding Commentary

In this chapter, the developed algorithms for the selected particle shape and surface profile roughness parameters were used with the study materials. The study materials consisted of real and derived, particles and surfaces.

Through Section 4.1, the real and derived study particles were input into the particle parameter algorithms verified in Chapter 3. Among the initially selected particle shape and roughness parameters, only Wadell's Roundness was rejected for further process. The outputs values and plots for the several particle roughness parameters are presented in Section 4.1.

Following Section 4.1, Section 4.2 concentrated on the real and derived surfaces with the surface shape and roughness parameter algorithms. Besides the conventional roughness parameters, Centroid Trace method developed by DeJong (2001) was also investigated for the study surfaces. As the results of the CT analysis showed, the

selected conventional surface parameters show change with the diameters considered, thus, a better representation of the surface characteristics is required that takes into account the relative size of the contacting particle. The possibilities of such parameters will be investigated in Chapter 5.

Section 4.3 is a study of the resolution effect on the particle shape and surface roughness parameters. For particle shape parameters, the influence of the number of data points defining the particle outline and the sampling interval were investigated and the results are reported. For surface roughness parameters, the effect of input surface profile resolution on conventional surface roughness parameters along with SPQ-surf values were examined.

# CHAPTER 5

# DEVELOPMENT OF NEW SURFACE ROUGHNESS AND PARTICLE SHAPE PARAMETERS

The goal of this chapter is to assess the adequacy of surface roughness analysis to capture particle shape and vice versa. This is achieved by modifying surface roughness parameter mathgrams for study particle inputs and particle shape parameter mathgrams for study surface profile inputs.

## 5.1 Development of Equivalent Surface Roughness Parameters based on Particle Shape Analysis

This section is intended to identify an alternative approach of looking at particulate-continuum interfaces. In Chapter 4, the primary interest was to investigate surfaces as derived particles and particles as derived surfaces. Thus, surfaces were analyzed with particle shape parameters and particles with surface roughness parameters.

On the other hand, Chapter 5 introduces new surface roughness measurement techniques derived from particle shape parameters. Thus, appropriate particle shape parameters are modified such that they can be utilized with the surface as the input. If this is achieved, then one can analyze particles and surfaces with a parameter that has

one physical meaning and provide a unified approach to particulate-continuum interfaces.

### *5.1.1 Selected Parameters and Surface Profiles*

As described in Chapter 4, all of the initially selected particle shape parameters were selected for further calculation and analysis except the Wadell's Roundness parameter, which was proven to be too user-dependent. Additionally, Sukumaran and Ashmawy Shape and Angularity Factors are not modified as surface roughness parameters since the algorithms and methodology is explicitly for closed surfaces and thus invalid for surface profiles. Although Stachowiak (1998) developed slightly different SPQ parameters for surface profiles as well as particle outlines, this study investigates the possibility of modifying SPQ for particles into a surface roughness parameter. Thus, the list of selected particle shape parameters is macro-scale particle roundness characterization by Characteristic Radius Ratio (CRR), particle angularity by Spike Parameter and Spike Parameter Quadratic, and Boyce and Clark Shape Index. For this list of particle shape parameters, new mathgrams are generated to capture surface roughness.

Section 4.1 input real and derived particles into particle shape parameters; whereas this section of Chapter 5 utilizes real and derived surfaces as input to modified particle shape parameter mathgrams. The main purpose of this section is to investigate the applicability of particle shape concepts to surface roughness analysis methods in order to generate a coherent analysis frame for particles and surfaces.

Table 5.1 introduces the study surfaces used as an input in this section (shown as "Output"). In addition, Table 5.1 displays the origin and process for the study surface inputs.

**Table 5.1–** Procedure for attaining study surfaces.

| ***Name*** | **Chapter 5 study surfaces** | |
|---|---|---|
| ***Process*** | *Particle Unrolling* | |
| ***Input/Output*** | Input | Output |
| ***Input = Real particles*** | p1 | p1-surf |
| | p2 | p2-surf |
| | p3 | p3-surf |
| | p4 | p4-surf |
| ***Process*** | *No Process* | |
| ***Input/Output*** | Input | Output |
| ***Input = Real Surfaces*** | Concrete surface | |
| | HDPE surface | |
| | Steel surface | |

Thus, *p1-surf*, *p2-surf*, *p3-surf*, *p4-surf*, *concrete surface*, *HDPE surface*, and *steel surface* are used as the study surfaces for this section. Note that no modifications are applied to the real surfaces for Chapter 5, i.e. the surface profiles have 15-mm length and 0.004mm resolution. The surface profiles were shown in Figure 3.23.

### *5.1.2 Surface Roughness Characterization by Characteristic Radius Ratio*

This section focuses on defining CRR for surfaces by a new algorithm in an attempt to

convey the physical interpretation of the CRR to surface shape analysis. The CRR modified for surface inputs is termed as CRR-surf. In Chapter 4, CRR was calculated using Voronoi diagrams and the resulting Minimum Zone Circles for the particle outline inputs. Voronoi diagrams are valid for closed surfaces. The application of Voronoi diagrams on surfaces was analyzed by wrapping surfaces into derived particles and calculating CRR in Chapter 4.

CRR for particles is a relative parameter similar in concept to several used in particle shape analysis, e.g. aspect ratio. However, rather than depending on single measurements of length and breadth (e.g. aspect ratio), CRR utilizes all outline data points to obtain the Voronoi Diagram for the specific outline. Two concentric circles, one containing none of the outline data points with the maximum attainable size, MIC (Maximum Inscribing Circle) and the other encircling all the data points with minimum possible radius, MCC (Minimum Circumscribing Circle) are generated utilizing Voronoi diagrams and computational geometry methods. The common center for MCC and MIC is selected from the candidate centers obtained by the intersection of the farthest and nearest Voronoi Diagrams (see Section 2.4.1.1.2). The common center is the one that gives the minimum radial separation between MCC and MIC when circles for MCC and MIC are drawn from the candidate centers. Subsequently, CRR ratio is calculated as the ratio of the difference of the two circle radii (termed as *roundness* in computational geometry practice) divided by the radius of the MIC and is independent of the particle size.

When the same concept is employed for surfaces, the relevant measures of the Maximum Inscribing Circle (MIC) and Minimum Circumscribing Circle (MCC) correspond to the surface profiles' maximum -y and the minimum -y elevation values, respectively.

Thus, the numerator in CRR-surf is the same as $R_{max}$ in surface profile parameter analysis. The denominator in CRR for particles is the MIC radius corresponding to surface profiles' minimum –y elevation. However, if the minimum –y elevation is used in the denominator for CRR-surf, CRR-surf would convey no information in the horizontal direction. Surface profiles attain different resolutions in –x and –y directions. A relative parameter needs to capture the –y dimensions relative to the –x direction measurements. Thus, as a normalizing term in CRR-surf denominator, $rdatum$, $projected\ \ profile\ \ length/2$, is used. It is assumed that the projected surface profile length is the diameter of an imaginary wrapped particle and half of that value corresponds to the MIC radius in particles. Thus, *CRR-surf* is delineated as:

$$CRR-surf = \frac{y_{\max} - y_{\min}}{rdatum} \quad \textbf{(5.1)}$$

where $rdatum$ is given as:

$$rdatum = \frac{projected\ \ profile\ length}{2} \quad \textbf{(5.2)}$$

*CRR-surf* is calculated for the real and derived surfaces and the results are displayed in Table 5.2. Table 5.3 displays the CRR values calculated for the *parts* and *dparts* in Chapter 4 for comparison with Table 5.2 values.

In relation to the values in Table 5.3, the correlation between CRR & CRR-surf is 0.987. Figure 5.1 (a) shows the regression plot between CRR and CRR-surf values for particles and their corresponding surfaces, respectively. The –x value and –y value of the

**Table 5.2 –** CRR-surf values for the study *surfs* and *dsurfs.*

| Surface Name | CRR - surf |
|---|---|
| p1-surf | 15.16 |
| p2-surf | 53.45 |
| p3-surf | 37.58 |
| p4-surf | 61.66 |
| concrete | 32.68 |
| HDPE | 14.65 |
| steel | 0.46 |

rightmost point in Figure 5.1 (a) designates the CRR for *p1* and CRR-surf for *p1-surf,* respectively. The figure data points are for *p1* & *p1-surf, p2* & *p2-surf*, *p3* & *p3-surf*, *p4* & *p4-surf*, *concrete* & *concrete-par*, *HDPE* & *HDPE-par*, and *steel* & *steel-par* from right to left. Throughout Chapter 5, all regression plots for the particle shape and modified surface roughness parameter have the same ordering. Figure 5.1 (b) is CRR & CRR-surf values versus particle & surface names. In Figure 5.1 (b), the blue triangle data points stand for CRR-surf values for the surface profiles; whereas the red crosses designated CRR value for the particle outlines.

**Table 5.3 –** CRR values for the *parts* and *dparts*.

| Particle Name | CRR |
|---|---|
| p1 | 17.38 |
| p2 | 72.83 |
| p3 | 61.54 |
| p4 | 81.75 |
| concrete-par | 42.05 |
| hdpe-par | 15.61 |
| steel-par | 0.39 |

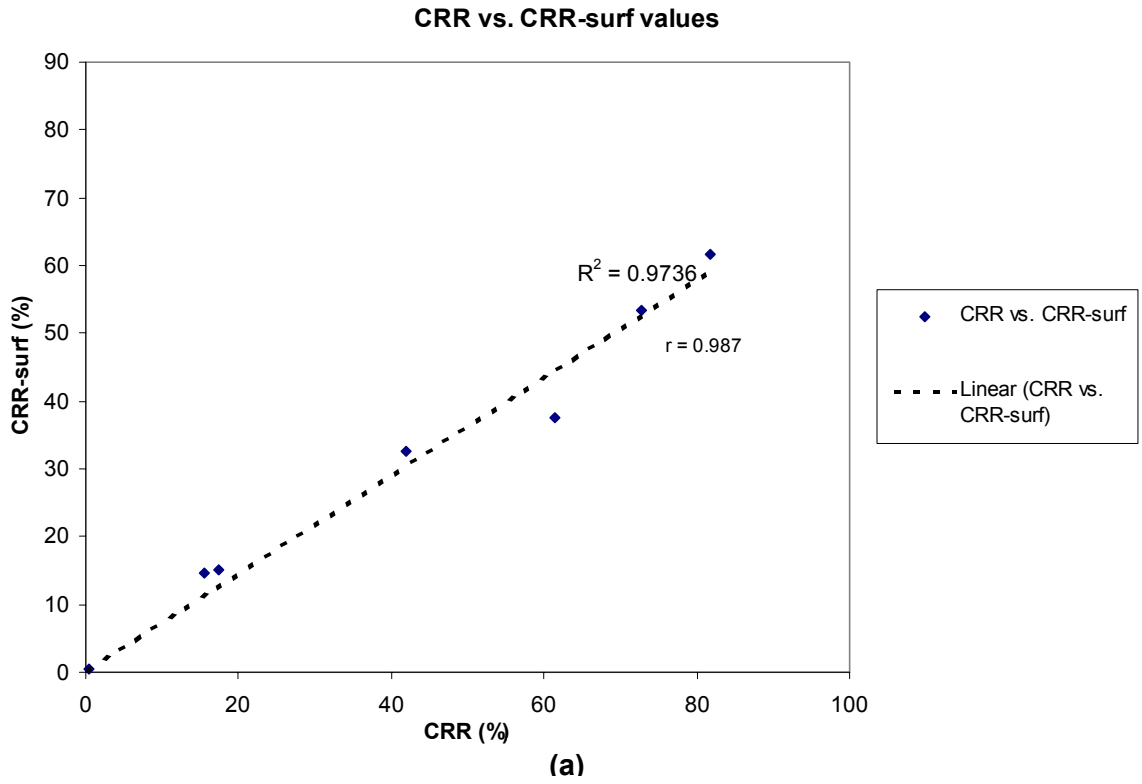


**(a)**

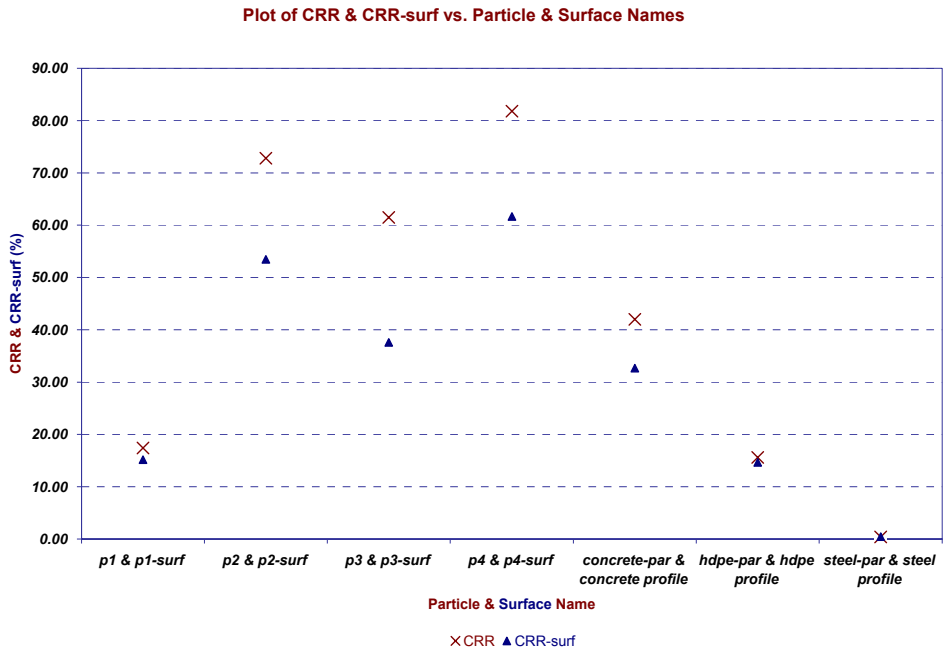


**(b)**

**Figure 5.1 – (a)** Plot of regression for CRR versus CRR -surf values, **(b)** Plot of CRR & CRR-surf versus particle and surface labels.

This study shows that a parameter originally developed for particle shape analysis (CRR) can be modified to assess surface roughness characteristics. CRR value requires surface profiles to be input as derived particles. On the other hand, with CRR-surf mathgram, surface profiles are used without any modification. The ordering of particles based on CRR and the ordering of the corresponding surfaces in relation to CRR-surf are same, which strengthens the argument that CRR and CRR-surf physically convey similar concepts for particles and surfaces, respectively. In observing the surface profiles, it is obvious that steel has the lowest CRR-surf when the CRR-surf is - in simplest terms - the ratio of maximum –y elevation difference to the projected profile length. The ordering of the real surfaces, i.e. steel (CRR-surf = 0.46), HDPE (CRR-surf = 14.65) and the concrete (CRR-surf = 32.68), suggests that for the same profile length (15mm length), the maximum –y elevation deviation along the profile increases from steel, HDPE to concrete; which matches the visual inspection results. The same argument is valid for the relative sorting of the derived surfaces; where *p1-surf, p3-surf, p2-surf,* and *p4-surf* have CRR-surf values of 15.16, 37.58, 53.45, and 61.66, respectively. As the CRR-surf value increases, again for the similar profile lengths of the derived surfaces, the maximum elevation deviation increases. The *HDPE* and *p1-surf* CRR-surf values are comparable and so are the profiles. Note that the ratio of real surface profile lengths to derived surface profile lengths is approximately five. Comparing *p3-surf* and *concrete* profile, *concrete* has a lower CRR-surf value than *p3-surf.* The reason is that for approximately 5 times of the profile length, *concrete* surface profile maximum –y elevation difference is less than 3 times of the *p3-surf* maximum -y elevation difference. Note that for the most inputs, the CRR-surf has lower values than the corresponding particles' CRR values. Considering the numerators in CRR and CRR-surf are the same numerically for the particles and their corresponding surfaces, this difference is a result of the larger $rdatum$ values for all inputs compared to the

corresponding MIC radius values. The construction of MIC in Voronoi diagrams requires that it is concentric with the MCC, thus constraining its size; whereas $rdatum$ is the largest circle that can fit inside the particle based on the lowest data point in the particle/surface outline with no centroid constraints.

This exercise further introduces a new relative surface profile parameter that can compare surface profiles of different lengths with a simple analysis. Note that CRR-surf has a numerator value equal to $R_{max}$ and a denominator that is half of the projected profile length ( $rdatum$ ). In other words, it is a ratio of –z dimensions (mm) to the –x dimensions (mm) and it is dimensionless.

### *5.1.3 Surface Roughness Characterization by Spike Parameter*

The Spike Parameter (SP) was originally developed for particles (Hamblin and Stachowiak, 1995). SP can also be used to analyze surface roughness by using surface profiles as input. No modifications are required to the originally developed mathgram for particle inputs since it is valid for both open and closed surfaces. The results are demonstrated in Table 5.4. The same input values of $r, stpxl$ , and $incpxl$ are used for the study surfaces as suggested the original study.

The correlation between the values represented in Table 5.4 and 4.4 (Spike Parameter values for *parts* and *dparts)* is 0.987. The regression plot for SP versus SP-surf values is provided in Figure 5.2 (a). Figure 5.2 (b) shows the SP & SP-surf values for the

**Table 5.4 –** Spike Parameter values for the *surfs* and *dsurfs.*

| Surface Name | SP-surf (A,15,40,10) |
|---|---|
| p1-surf | 0.222 |
| p2-surf | 0.222 |
| p3-surf | 0.302 |
| p4-surf | 0.320 |
| concrete | 0.421 |
| HDPE | 0.341 |
| steel | 0.152 |

corresponding particle & surface names, where the blue triangles and red crosses correspond to SPQtr-surf for surface profiles and SPQ for the particle outlines, respectively. The ordering of surfaces based on SP-surf is the same with the ordering of the corresponding particles based on SP, with a minor difference between *p3-surf* and *p4-surf*. When SP-surf is used with surface profile inputs, *p3-surf* has lower SP value than *p4-surf.* On the other hand, when SP is used with particles as input, *p4* has lower SP than *p3.* In SP (or SP-surf), the particle outline (or surface profile) is represented by a combination of triangles and abrasiveness is defined in terms of both triangles' sharpness and height. The similarity of the SP and SP-surf values for the particles and surfaces suggests that abrasiveness of a surface and its corresponding wrapped surface (*dpart)* or a particle and its corresponding unrolled particle *(dsurf)* can be expressed using triangular steps along the profile/outline. Thus, a unified approach can be achieved for the components of particulate - continuum interface either by wrapping surface profiles as derived particles and unrolling particle outlines to derived surface profiles or by modifying the particle shape parameter mathgrams for surface profile inputs and vice versa. Chapter 4 focuses on the first approach; whereas Chapter 5 investigates the applicability of the second methodology.

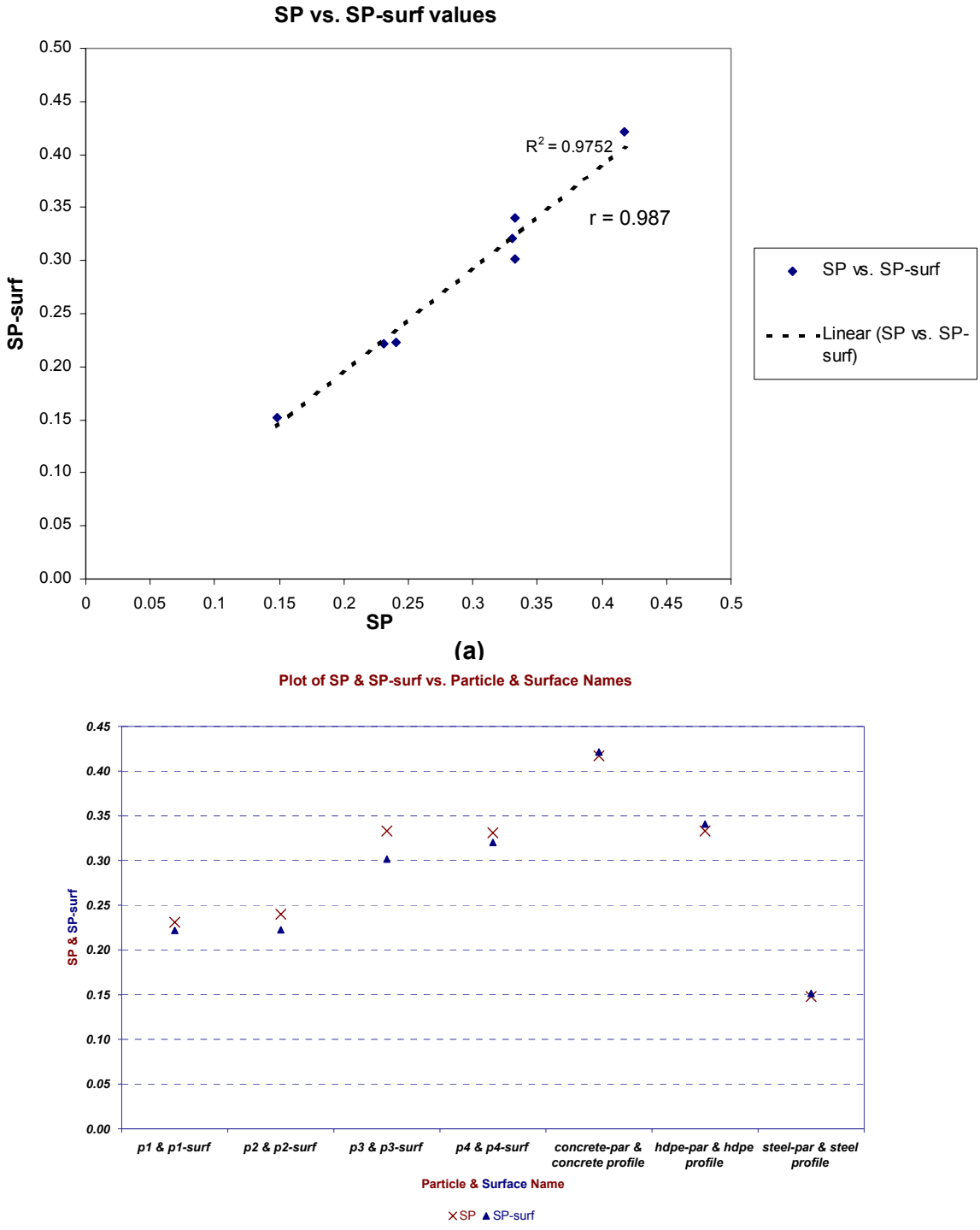


**Figure 5.2 – (a)** Plot of regression for SP versus SP-surf values, **(b)** Plot of SP & SP-surf versus particle and surface labels.

### *5.1.4 Surface Roughness Characterization by Spike Parameter Quadratic*

SPQ parameter for surface profiles developed by Stachowiak (1998) is termed as SPQ-surf in this study. Although particle shape parameter method SPQ and surface shape parameter SPQ-surf are developed as similar methods based on analyzing only the portions of the particle/surface that come into contact with the counterface, the SPQ and SPQ-surf results do not compare as expected. Table 5.5 tabulates both SPQ values (for *parts* and *dparts)* and SPQ-surf values (for *surfs* and *dsurfs*).

Figure 5.3 (a) is a regression plot for SPQ versus SPQ-surf. Figure 5.3 (b) plots SPQ & SPQ-surf values versus particle & surface names. The correlation between SPQ and SPQ-surf values is very poor as shown in Figure 5.3 (a).

**Table 5.5 –** SPQ and SPQ-surf values for *parts* and *surfs*, respectively.

| Particle Name | SPQ | Surface Name | SPQ-surf |
|---|---|---|---|
| p1 | 0.000 | p1-surf | 0.369 |
| p2 | 0.171 | p2-surf | 0.334 |
| p3 | 0.268 | p3-surf | 0.437 |
| p4 | 0.287 | p4-surf | 0.235 |
| concrete-par | 0.382 | Concrete | 0.477 |
| HDPE-par | 0.394 | HDPE | 0.532 |
| steel-par | 0.000 | Steel | 0.000 |

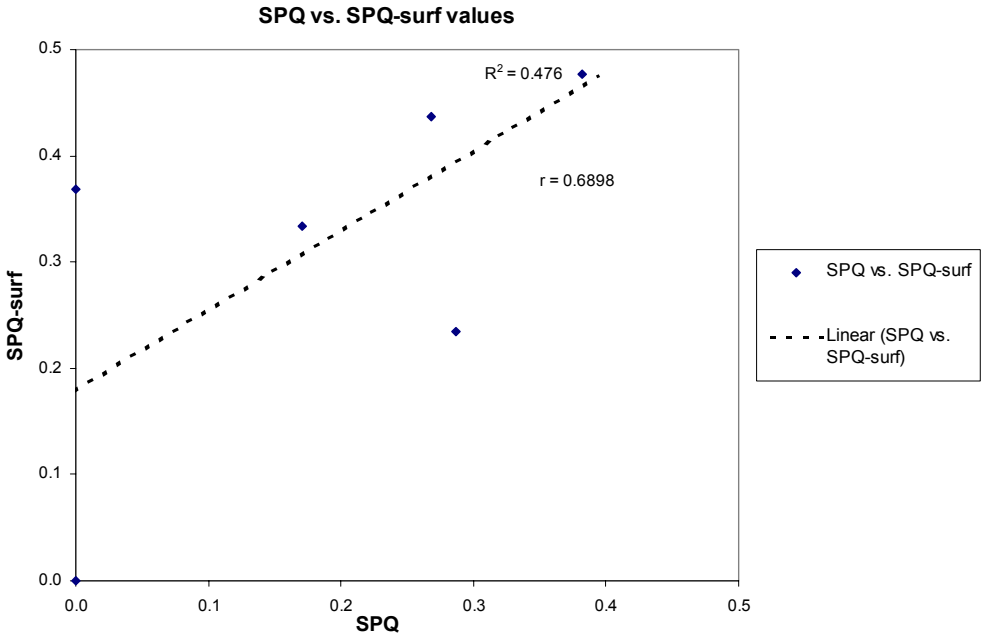


**(a)**

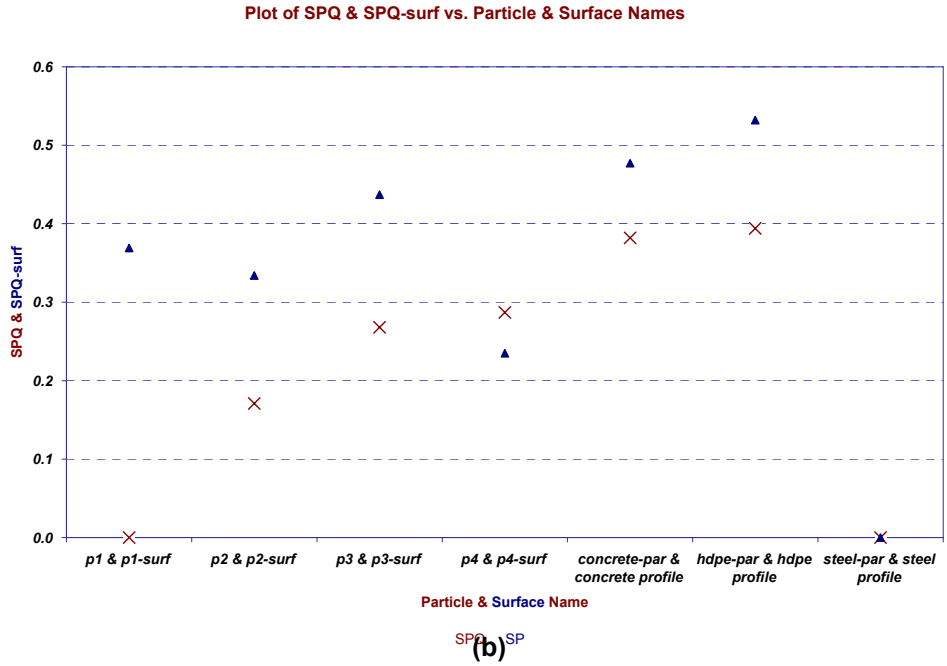


**(b)**

**Figure 5.3 – (a)** Plot of regression for SPQ versus SPQ-surf values, **(b)** Plot of SPQ & SPQ-surf versus particle and surface labels.

For the difference in the results, one argument is that SPQ-surf algorithm is very sensitive to digitization errors. To illustrate this, the following exercise is performed.

A surface profile, *p4-surf* is selected for this exercise. The input surface profile is modified to have 3, 5, and 7 decimal places to observe how sensitive the algorithm is to round-off errors. The numerical SPQ-values obtained for the three sets of data are shown in Table 5.6.

**Table 5.6 –** SPQ-surf values for *p4-surf* with different # of decimal places.

| **# of decimal places** | Three | Five | Seven |
|---|---|---|---|
| **SPQ - surf** | 0.399 | 0.235 | 0.235 |

Note that the actual results for this study are obtained with 8-digits of precision. Still, Table 5.6 shows how sensitive the algorithm is to the number of decimal places, irrespective of the digitization errors that may be carried out during any process. For all the cases in Table 5.6, three spikes are determined; however, for the last spike 3-decimal places *p4-surf* outputs a spike angle of 98.5°; whereas the 5-decimal place and 7-decimal place *p4-surf* have spike angle of 159.8°, which is considerably flatter than the 3-decimal place output. The spike value corresponding to the spike angles of 98.5° and 159.8° are 0.65 and 0.17, respectively. This results in the difference of SPQ-surf values 0.399 and 0.235. The spike angles for the last spike are vastly different due the difference of spikes' located starting points. Figure 5.4 shows for the 3-decimal place

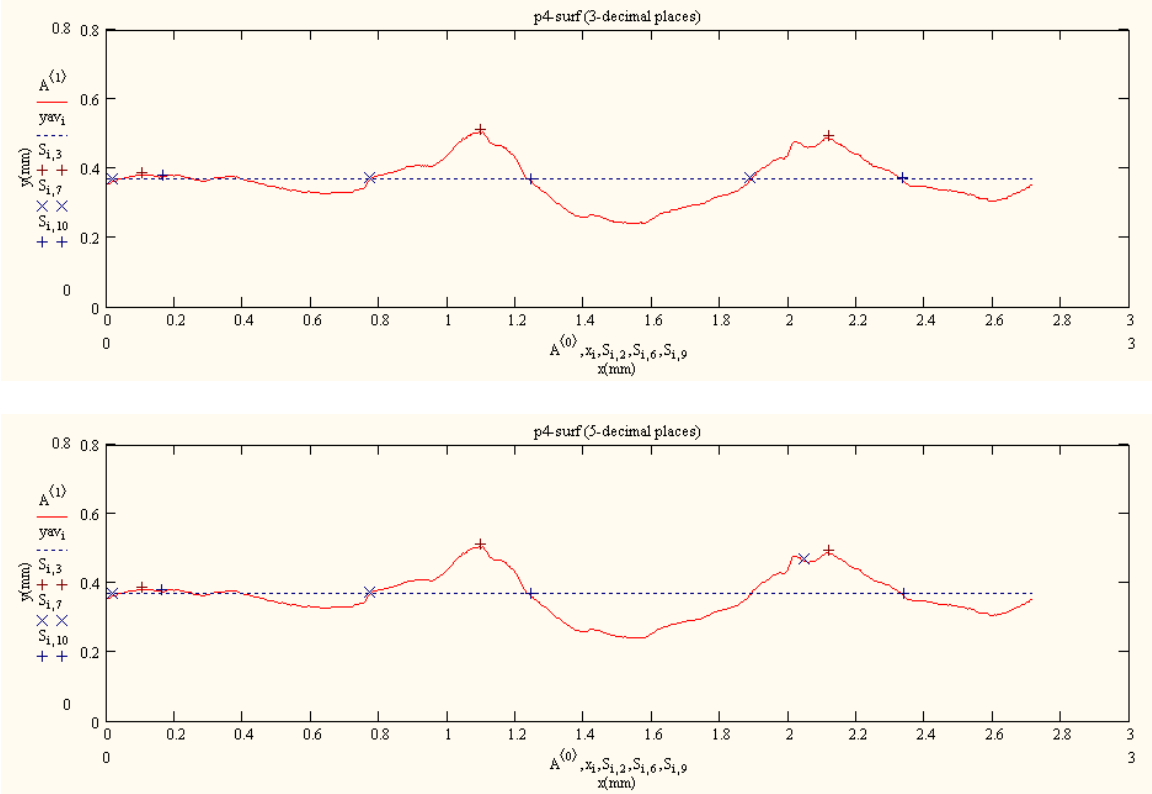


**Figure 5.4 -** The starting, apex, and end points of the spikes located for the 3-decimal places and 5-decimal places p4-surf profile inputs (The "**+**"s denote the apex, and the "**x**"s denote the starting and end points of spikes).

and 5-decimal place the spikes' starting, apex, and end points.

Note that initially the algorithm assigns the same starting points for the two cases, however, while looking for turning points, it locates the new starting point for the 5-decimal place case. Note that the turning point is valid when the vertical relief of the turning pair is greater than 10 percent of the apex height. In reality, when the highest point of the spike is located, i.e. apex point or the middle point, the program searches to the right side as well as the left side of the apex to locate turning points. In the three-decimal place case, the turning point can not be located since the algorithm can not see

the difference in the fifth digit after the decimal point; whereas in the second case it does and locates the new starting point location. The important conclusion of this exercise is that a difference in the fifth digit after the decimal point can cause the SPQ-surf result change between 0.399 and 0.235.

Besides the sensitivity of SPQ-surf to round-off errors, Stachowiak (1998) suggest additional rules during the application of SPQ-surf different from SPQ determination. This is also a source for SPQ and SPQ-surf values divergence. For example, even though a spike may be above the mean line, if its height is less than 25% of the maximum spike height along the profile, it is not considered in the final calculation. In addition, as mentioned in Section 2.4.2.2.6, if a turning point is located to the right (or left) of the spike, then the start point (or end point) is relocated causing the estimated quadratic functions and spike angle values to differ from the original case. To illustrate the effect of additional rules on the difference between SPQ and SPQ-surf values, *p4* SPQ analysis and *p4-surf* SPQ-surf analysis results are compared.

In the final step prior to the implementation of the SPQ equation, a matrix is obtained from the SPQ mathgram, denoting spikes number, start, middle, end points' locations and the calculated spike angles based on the differentiation of the quadratic polynomials. Part of that matrix is shown in Table 5.7. Columns representing data irrelevant to this discussion are not presented.

Regarding Table 5.7 the explanation for the column headings are as follows; *j* = spike number, *($x_m$ & $y_m$)* =–x and –y coordinates for the spike's middle point, *r* = radius of the middle point, ($x_s$ & $y_s$) =–x and –y coordinates for the spike's start point, ($x_e$ & $y_e$) =–x and –y coordinates for the spike's end point, *(Rsq1& Rsq2)* = $R^2$ values for the fitness test of

**Table 5.7 –** The matrix output for *p4* SPQ calculation.

| j | $x_m$ | $y_m$ | r | $x_s$ | $y_s$ | $x_e$ | $y_e$ | Rsq1 | Rsq2 | Spike Angle |
|---|---|---|---|---|---|---|---|---|---|---|
| 1 | 1.04 | 0.7 | 0.382 | 1.04 | 0.684 | 1.028 | 0.727 | 0.8876 | 0.858 | 157.479 |
| 2 | 1.017 | 0.762 | 0.38 | 1.017 | 0.759 | 1.013 | 0.766 | -11 | -11 | 135 |
| 3 | 1.013 | 0.77 | 0.38 | 1.013 | 0.766 | 1.009 | 0.774 | -11 | -11 | 135 |
| 4 | 1.009 | 0.778 | 0.38 | 1.009 | 0.774 | 1.005 | 0.782 | -11 | -11 | 135 |
| 5 | 1.005 | 0.786 | 0.38 | 1.005 | 0.782 | 1.001 | 0.79 | -11 | -11 | 135 |
| 6 | 0.567 | 0.974 | 0.379 | 0.571 | 0.974 | 0.567 | 0.97 | -11 | -11 | 90 |
| 7 | 0.254 | 0.899 | 0.507 | 0.555 | 0.97 | 0.305 | 0.723 | 0.871 | 0.703 | 136.135 |
| 8 | 0.759 | 0.129 | 0.488 | 0.547 | 0.25 | 0.895 | 0.305 | 0.849 | 0.652 | 145.955 |

the two polynomials from start point to middle point and end point to middle point, and *spike angle* = spike angle. The least squares data for the *p4* outline is ($x_c$, $y_c$, r) = (0.699,0.609,0.378).

Based on the data shown in Table 5.7, SPQ mathgram discards spikes #2 to #6, due to the displayed (-11) for *Rsq1* or *Rsq2* indicating inadequate number of data points (<3) for an accurate quadratic polynomial estimation. For *Rsq1* or *Rsq2*, a number other than (–11) designates the $R^2$ value for the estimated quadratic polynomial fit. Thus, only Spikes #1, #7, and #8 are included in the final SPQ equation with the corresponding spike angle values; 157.479°, 136.135°, and 145.955°, respectively.

The *p4* outline, the corresponding *least squares circle*, and the accepted three spikes' start, middle, and end point locations are schematically shown in Figure 5.5.

In order to compare SPQ with SPQ-surf results, the *p4-surf* is also analyzed for SPQ-surf. The matrix obtained prior to the final equation is provided in Table 5.8.

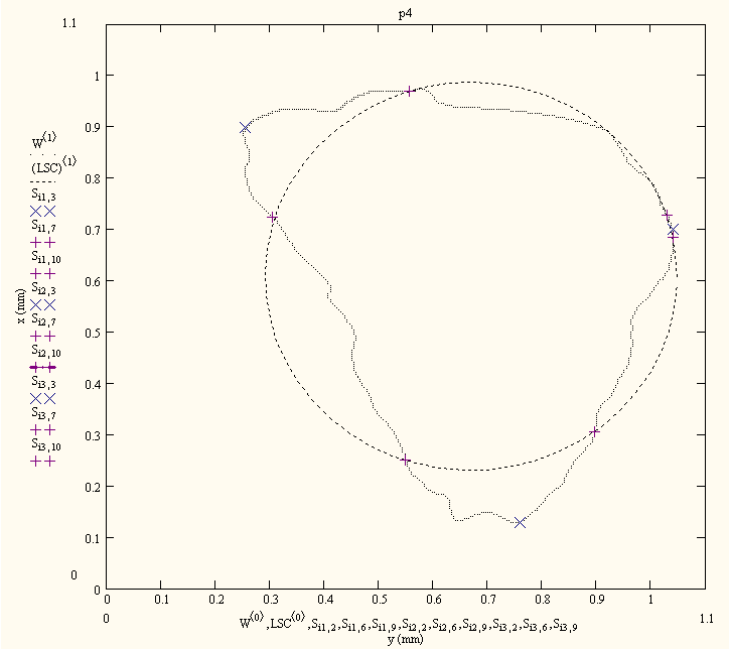


**Figure 5.5 -** *p4* outline with the least squares circle (LSC) and the spike locations (The "**x**" symbols show the spikes' middle points and "**+**" symbols show the start and end points for the spikes).

Different from Table 5.7, Table 5.8 contains the headings, $(i_m,i_s,i_e)$ = indices for the middle, start, and end points, respectively, *rank* = the relative rank of the height with "0" value largest, *(left , right)* = denote if turning points are located to the left or right of the spike middle point, *(Angle)* = spike angle. For the *(left, right)* columns the entries include

**Table 5.8 -** The matrix output for *p4-surf* SPQ-surf calculation.

| j | $i_m$ | $x_m$ | $y_m$ | r | $i_s$ | $x_s$ | $y_s$ | $i_e$ | $x_e$ | $y_e$ | rank | left | right | Rsq1 | Rsq2 | Angle |
|---|---|---|---|---|---|---|---|---|---|---|---|---|---|---|---|---|
| 1 | 27 | 0.1 | 0.39 | 0.39 | 4 | 0.02 | 0.37 | 43 | 0.16 | 0.38 | 2 | no peaks | 43 | 0.777 | 0.889 | 159.77 |
| 2 | 290 | 1.1 | 0.51 | 0.51 | 204 | 0.77 | 0.37 | 329 | 1.24 | 0.37 | 0 | no peaks | no peaks | 0.952 | 0.607 | 138.54 |
| 3 | 561 | 2.12 | 0.5 | 0.5 | 542 | 2.05 | 0.47 | 619 | 2.34 | 0.37 | 1 | 542 | no peaks | 0.71 | 0.792 | 159.76 |

either *"no peak"*, indicating no located turning points or the located *turning points index*, which subsequently replaces the original points for the corresponding start or end points. The average mean line for *p4-surf* is located at y=0.369 mm. Based on the *Rsq1* and *Rsq2* values, none of the spikes is discarded.

The *p4-surf* outline, the *mean average line*, and the spikes' start, middle, and end points are shown in Figure 5.6.

For both p4 SPQ and p4-surf SPQ-surf, 3 spikes are established. The calculation for the implementation of the final equations is tabulated in Table 5.9.

The final values for p4 SPQ and p4-surf SPQ-surf are the same as reported in Table 5.5. Comparing the spike angle values, the biggest difference in the spike angles is between Spike #8 in SPQ and Spike #3 in SPQ-surf. This discrepancy is due to the turning point

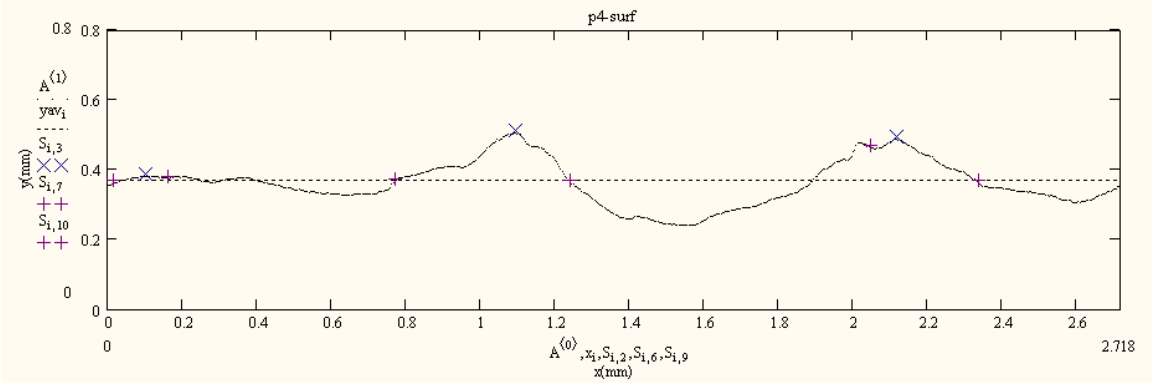


**Figure 5.6 -** *p4-surf* outline with the average mean line and the spike locations (The "**x**" symbols show the spikes' middle points and "**+**"symbols show the start and end points for the spikes).

**Table 5.9 –** Final step for *p4* SPQ and *p4-surf* SPQ-surf computation.

| ***p4* SPQ** | | | ***p4-surf* SPQ-surf** | | |
|---|---|---|---|---|---|
| *Spike No.* | *Spike Angle* | *SPQ* | *Spike No.* | *Spike Angle* | *SPQ* |
| 1 | 157.48 | 0.195 | 1 | 159.77 | 0.176 |
| 7 | 136.14 | 0.374 | 2 | 138.54 | 0.354 |
| 8 | 145.96 | 0.293 | 3 | 159.76 | 0.176 |
| **SPQ** | | *0.287* | **SPQ-surf** | | *0.235* |

rule in SPQ-surf computation. For Spikes #1 in SPQ-surf, a right turning point is located replacing the original end point ($i_e$ = 43) and for Spike #3 in SPQ-surf, a left turning point is located replacing the original start point ($i_s$ = 542). These values are provided in Table 5.8.

Thus, since it is apparent that additional or different rules applied for SPQ-surf by Stachowiak (1998) cause the values of SPQ and SPQ-surf to differ for the corresponding particles and derived surfaces and for the matching derived particles and surfaces, the SPQ for particle shape characterization has been modified to a surface roughness parameter by the author. In other words, rather than using the additional and different rules for SPQ and SPQ-surf as Stachowiak (1998) suggest, this study evaluates the possibility of modifying SPQ to a surface roughness parameter. This surface roughness parameter is designated as SPQtr-surf in the following sections.

Differences between SPQ-surf (Stachowiak, 1998) and SPQtr-surf (this study) are as follows:

1. In SPQ-surf, the least squares slope is removed from the surface profile data elevation points and the average –z elevation is calculated after removing the

slope. However, in SPQtr-surf, this step is omitted and the average –z elevation is calculated based on the initial surface profile data points.

2. After locating the spikes above average –z elevation, SPQ-surf method suggests utilizing 25% of the maximum surface elevation as the allowable surface elevation. That is, a spike is removed from the analysis in SPQ-surf if it has maximum apex point's elevation less than the allowable surface elevation. However, SPQtr-surf mathgram eliminates this step.
3. The mathgram SPQ-surf investigates the presence and location of "turning points" for every spike. If a "turning point" is located, the start or end point of the spike is updated. This step is not included in SPQtr-surf. In other words, start and end points are taken as the points where the spike intersects the average –z elevation at the two ends of the spike.
4. In SPQ calculation, upon locating the start (sp), middle (mp), and end points (ep) for a spike, the particle outline section sp to mp and from mp to ep are transformed to a horizontal and vertical axes. This axes transformation is not suggested in SPQ-surf (Stachowiak, 1998). Similar to SPQ-surf, the mathgram for SPQtr-surf does not include this step since the surface profiles have already horizontal and vertical –x and –y axes.
5. In SPQ-surf, no threshold value for a spike angle is proposed (Stachowiak, 1998). However, since a threshold spike angle value of $2.9\,rad$ was used in SPQ method (Hamblin and Stachowiak, 1995), the same threshold value is utilized in SPQtr-surf. In other words, spike angles larger than $2.9\,rad$ are omitted in the final SPQtr-surf calculation.

The results of SPQtr-surf in addition to SPQ values for the corresponding surfaces and particles are provided in Table 5.10.

**Table 5.10 -** SPQ and SPQtr-surf values for *parts* and *surfs*, respectively.

| Particle Name | SPQ | Surface Name | SPQtr-surf |
|---|---|---|---|
| p1 | 0.000 | p1-surf | 0.000 |
| p2 | 0.171 | p2-surf | 0.000 |
| p3 | 0.268 | p3-surf | 0.292 |
| p4 | 0.287 | p4-surf | 0.197 |
| concrete-par | 0.382 | concrete | 0.383 |
| HDPE-par | 0.394 | HDPE | 0.426 |
| steel-par | 0.000 | steel | 0.000 |

Although there is certainly an improvement in SPQtr-surf values compared to SPQ-surf values presented in Table 5.5 in terms of their correlation with SPQ, there is still noticeable divergence between SPQ and SPQtr-surf. The correlation between the values in Table 5.10 is only 0.9197. A linear trend line between the SPQ and SPQtr-surf datasets is shown in Figure 5.7 (a) with the $R^2$ value. Figure 5.7(b) displays the particle and surface names in the –x axis and the corresponding SPQ and SPQtr-surf values in the –y axis. Note that in Figure 5.7 (b), the blue triangles and red crosses correspond to SPQtr-surf for surface profiles and SPQ for the particle outlines, respectively.

The divergence is explained with SPQ and SPQtr-surf calculation steps for *p4* and *p4-surf*, respectively. In order to be able to compare the particle outline SPQ and derived

surface SPQtr-surf steps, both *p4* and *p4-surf* are input with the same number of data points, 360, so that the locations/indices of the spikes are comparable.

Tables 5.11 and 5.12 display the matrices at the last steps of *p4-360* SPQ and *p4surf-360* SPQtr-surf, respectively.

**Table 5.11 -** The matrix output for *p4-360* SPQ calculation.

| j | $i_m$ | $x_m$ | $y_m$ | r | $i_s$ | $x_s$ | $y_s$ | $i_e$ | $x_e$ | $y_e$ | Rsq1 | Rsq2 | Spike Angle(°) |
|---|---|---|---|---|---|---|---|---|---|---|---|---|---|
| 1 | 14 | 1.039 | 0.701 | 0.381 | 2 | 1.032 | 0.621 | 56 | 0.873 | 0.91 | 0.795 | 0.97 | 159.493 |
| 2 | 145 | 0.254 | 0.899 | 0.506 | 102 | 0.593 | 0.967 | 164 | 0.314 | 0.71 | 0.818 | 0.89 | 132.473 |
| 3 | 280 | 0.753 | 0.129 | 0.487 | 250 | 0.544 | 0.265 | 309 | 0.899 | 0.324 | 0.911 | 0.81 | 143.173 |

Note that Table 5.11 values differ from Table 5.7 values although they represent the same calculation with the same *p4* input. The reason for divergence is that number of outline data points for Table 5.7 and 5.11 inputs are different.

As expected, the same number of spikes is located in Table 5.11 and 5.12. Also, the indices corresponding to each spikes' middle ($i_m$), start ($i_s$) and end ($i_e$) points match for the two datasets since they have the same number of data points and *p4surf* is obtained by unrolling *p4* particle outline utilizing *part-dsurf* mathgram as explained in Chapter 3. However, the spike angles calculated for the same spikes are different for a particle outline and derived surface profile. The spikes angles differ due to the change in data points and their interpolations. Although both datasets are conversions of each other,

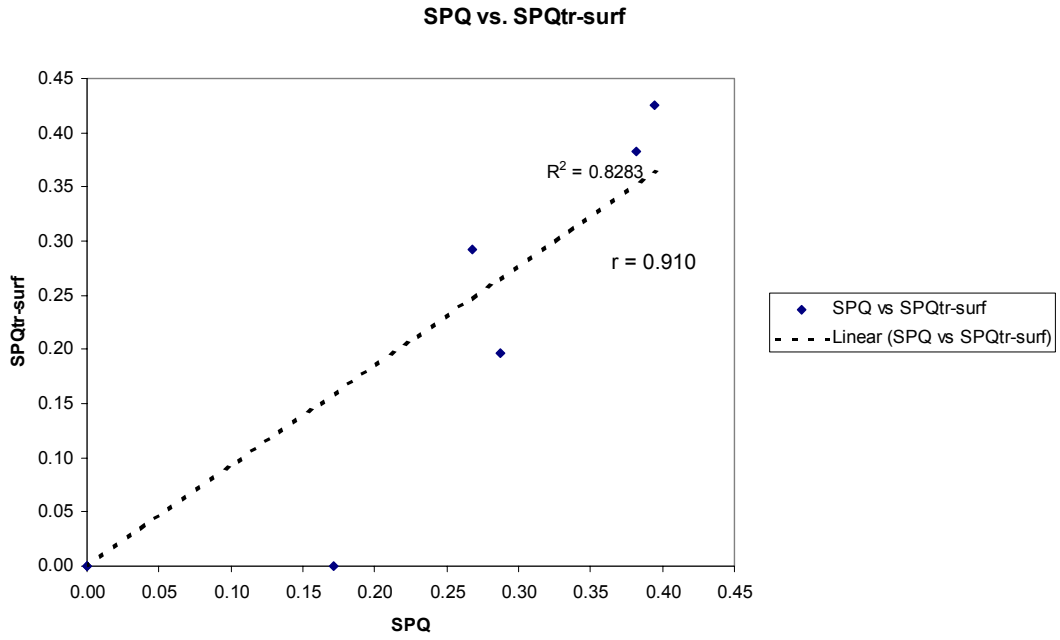


**(a)**

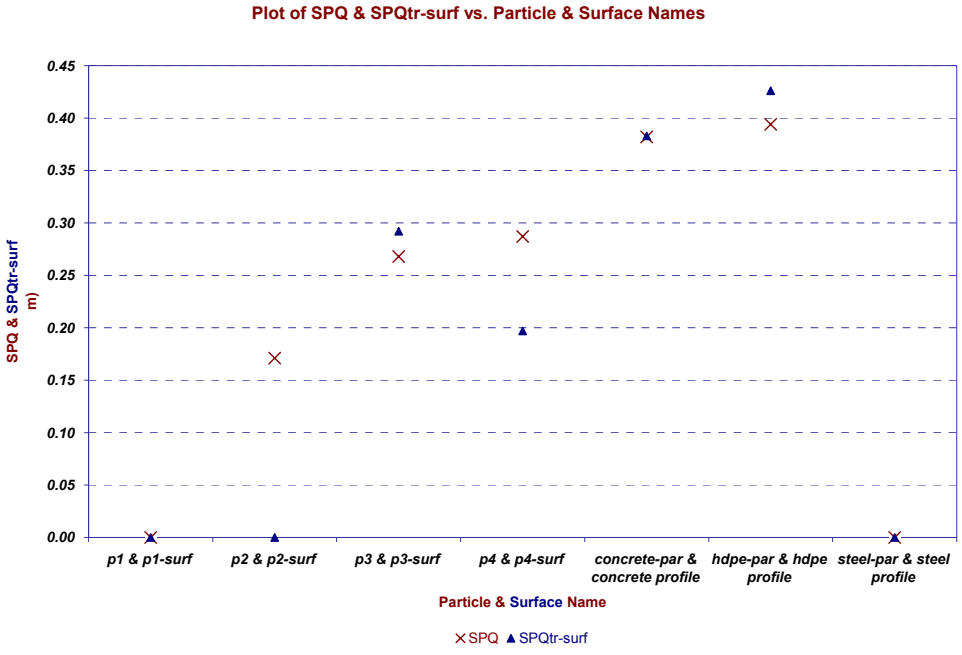


**(b)**

**Figure 5.7 – (a)** Plot of regression analysis between the SPQ for particle outlines and SPQtr-surf for surface profiles, **(b)** Plot of SPQ & SPQtr-surf vs. particle and surface labels.

**Table 5.12 -** The matrix output for *p4surf-360* SPQtr-surf calculation.

| j | $i_m$ | $x_m$ | $y_m$ | r | $i_s$ | $x_s$ | $y_s$ | $i_e$ | $x_e$ | $y_e$ | Rsq1 | Rsq2 | Spike Angle(°) |
|---|---|---|---|---|---|---|---|---|---|---|---|---|---|
| 1 | 14 | 0.106 | 0.382 | 0.382 | 2 | 0.015 | 0.363 | 56 | 0.423 | 0.364 | 0.982 | 0.888 | 177.078 |
| 2 | 145 | 1.095 | 0.506 | 0.506 | 102 | 0.77 | 0.367 | 164 | 1.238 | 0.369 | 0.967 | 0.974 | 171.088 |
| 3 | 280 | 2.114 | 0.487 | 0.487 | 250 | 1.887 | 0.365 | 309 | 2.333 | 0.366 | 0.945 | 0.994 | 157.267 |

the angle of each spike changes as spike data points are converted from a particle to a derived surface. This is a result of the rules applied during particle outline unrolling to a surface profile. *Part-dsurf* algorithm calculates the "radius" values for each data point and uses the same "radius" values as surface profile elevations for *dsurf.* On the other hand, –x values for *dsurf* are increased from $x = 0$ to $x = particle\ perimeter$. The –x increment value depends on the desired number of *dsurf* data points. Thus, the rules applied to –x and –z axes are different and this results in stretching or shrinking of the particular spikes in comparison to the same spikes in particle outline.

### *5.1.5 Surface Roughness Characterization by Shape Index*

The Shape Index (SI) algorithm originally developed for particles in Chapter 4 is modified merely by replacing the radius lengths in particles by the –y elevations in surfaces. Boyce and Clark suggested that the particle outline is sampled with 16 radial test lines. This study uses the same number of radial test lines (Boyce and Clark, 1964).

Different from the SI analysis in Chapter 4, this section utilizes a modified SI mathgram with surface profile as input. Although in SI calculation, 16 particle outline points and 16

sampling intervals were utilized, in SI-surf estimation number of surface profile input data points is not constant. For example, for *dsurfs* (*p1-surf, p2-surf, p3-surf,* and *p4-surf*) 720 and for *surfs* (*concrete, HDPE*, and *steel*) 3750 intervals are utilized. The results are presented in Table 5.13.

Figure 5.8 (a) is a regression plot of SI versus SI-surf values, and Figure 5.8 (b) shows the data points for SI & SI-surf for the corresponding particle & surface names. The values of SI-surf are almost identical with the SI values for the corresponding particles with only insignificant discrepancy (see Section 4.1.4). The correlation between the particle SI and SI-surf values is 0.999 as shown in Figure 5.8 (a).

**Table 5.13 –** Shape Index-surf values for the *surfs* and *dsurfs*.

| Surface Name | SI - surf |
|---|---|
| p1-surf | 4.0 |
| p2-surf | 14.8 |
| p3-surf | 9.2 |
| p4-surf | 14.0 |
| concrete | 5.6 |
| HDPE | 2.4 |
| steel | 0.0 |

The main difference in sampling between particles and surfaces is that in particle outlines sampling is based on equal angle spacing; whereas surfaces are sampled with equal –x distance spacing. In order to determine SI, particle outlines are compared to a perfect circular outline; whereas surface profiles are compared to a straight line.

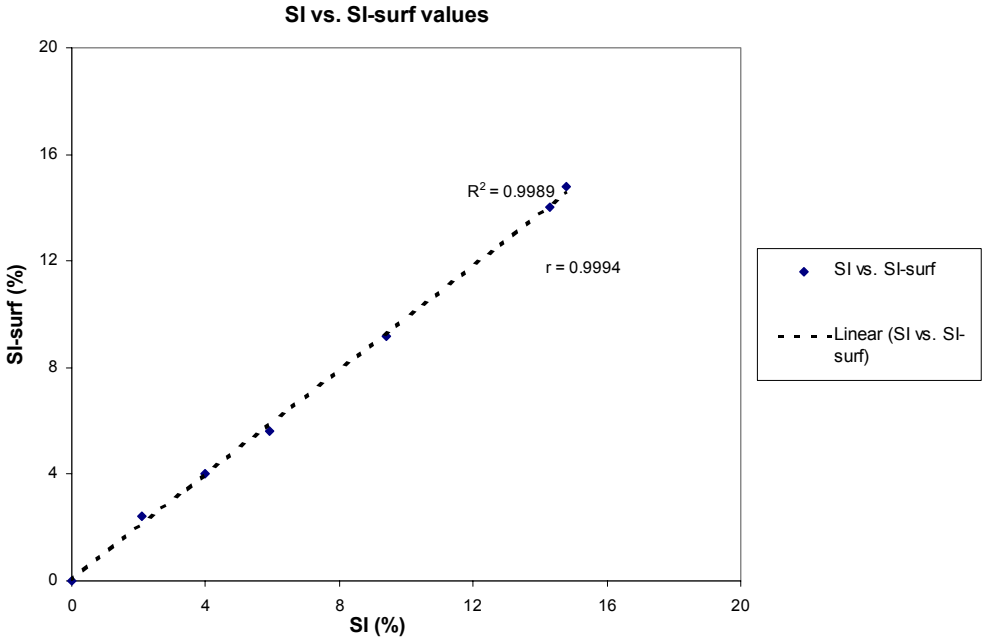


**(a)**

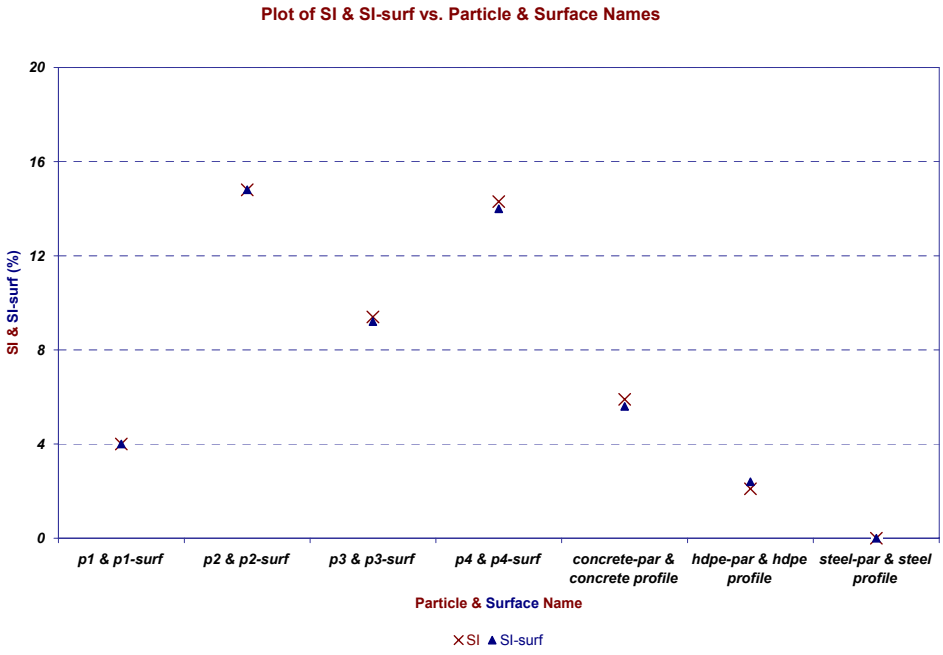


**(b)**

**Figure 5.8 – (a)** Plot of regression analysis between the SI for particle outlines and SI-surf for surface profiles, **(b)** Plot of SI & SI-surf vs. particle and surface labels.

The reason for utilizing different number of intervals in real (3750 intervals) and derived surfaces (720 intervals) compared to 16 intervals for particles is based on a resolution study, for which two surfaces, one derived (*p1-surf*) and one real (*concrete*) are investigated. The results presented in Table 5.14 relate to the sampling interval used for the straight line, i.e. SI-surf parameter. The main conclusion from Table 5.14 is that when surface profiles are input with original number of data points (*surfs* with 3750 data points, *dsurfs* with 720 data points), the sampling interval for the straight line should match the number of data points in the surface profile, i.e. it should be taken as 3750 for *surfs* and 720 for *dsurfs*. As mentioned above, no modifications are performed on real and derived input surface profiles.

Figure 5.9 represents the data outlined in Table 5.14. As evident from the magnified portion of the graphs, *p1-surf* and *concrete* have the lowest SI values at 720 and 3750 intervals, respectively corresponding to exactly the number of data points in *p1-surf* and *concrete* surface profiles.

As mentioned previously, SI parameter compares the particle outline to a circular outline where the particle outline has the same number of data points as the sampling interval used for its associated circle. In other words, the number of intervals for the concrete surface investigated in Table 5.14 applies only to the associated straight line; whereas the input surface (*p1-surf* or *concrete* in Table 5.14) is taken with their original number of data points (*p1-surf* with 720 data points and *concrete* profile with 3750 data points) for each case. In Figure 5.9, the lowest SI-surf value is observed at the number of data points of the input surface profile. Thus, the lowest SI-surf is obtained when the number of surface profile data points match with the sampling interval for the straight line. In other words, SI-surf is the lowest when resolutions for the surface profile and the

**Table 5.14 –** Shape Index-surf values for *p1-surf* and *concrete* profiles for varying number of intervals.

| *p1-surf* | | *Concrete* | |
|---|---|---|---|
| **# of intervals** | **SI-SURF** | **# of intervals** | **SI-SURF** |
| 4 | 17920.0 | 4 | 93670.0 |
| 8 | 8913.0 | 8 | 46790.0 |
| 16 | 4406.0 | 16 | 23340.0 |
| 32 | 2153.0 | 32 | 11620.0 |
| 75 | 861.3 | 75 | 4901.0 |
| 80 | 801.3 | 80 | 4589.0 |
| 150 | 380.7 | 150 | 2401.0 |
| 360 | 100.3 | 360 | 941.9 |
| 720 | 4.0 | 720 | 421.0 |
| 1500 | 51.9 | 1500 | 150.1 |
| 3000 | 76.0 | 3000 | 25.0 |
| 3750 | 80.8 | 3750 | 5.6 |
| 5000 | 85.6 | 5000 | 25.0 |
| 10000 | 92.8 | 10000 | 62.5 |

associated straight line match. The underlying principle for not using the same number of sampling intervals for SI and SI-surf is due to the different resolutions of –x and –y in surface profiles. In particle sampling, the partition is through the centroid by equal angles; whereas in surface sampling the partitioning is inevitably through the –x length by equal –x distance.

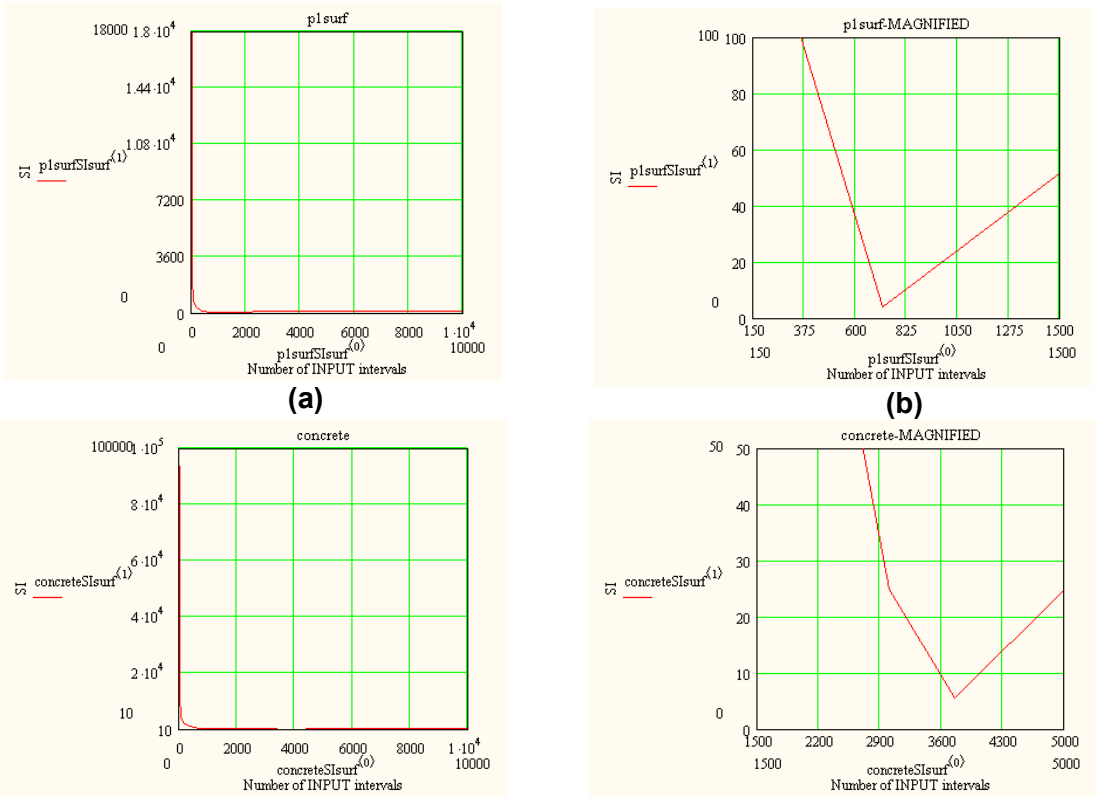


**Figure 5.9 –** Figure showing SI-surf values for selected surface profiles with the number of intervals; **(a)** *p1-*surf, **(b)** *p1-surf* magnified, **(c)** *concrete*, and **(d)** *concrete*-magnified.

## 5.2 Development of Equivalent Particle Shape Parameters based on Surface Roughness Analysis

### *5.2.1 Selected Parameters and Particle Outlines*

The surface shape parameters presented initially in Chapter 2 are the widely-used surface parameters, e.g. average roughness, root mean square roughness, depth of

surface smoothness, maximum peak to valley roughness, normalized roughness parameter in addition to the spike parameter quadratic and centroid trace method. In Chapter 4, real and derived surface profiles were evaluated with the mentioned surface roughness methods. This section involves modification of the surface roughness parameter mathgrams in order to use them with real and derived particle outline inputs. However, not every surface roughness parameter in Chapter 4 is used in this section. The spike parameter quadratic (SPQ) and the centroid trace methods are omitted from this section since both mathgrams are for open surfaces. A centroid trace (CT) method on a particle outline is a prospective topic for a further research. Another reason for omitting SPQ-surf evaluation for wrapped surfaces (*dparts)* or real particles (*parts)* is that an SPQ parameter for particles is already developed in the original study (Section 2.4.1.2.2). In contrast to Section 4.2, where real and derived surfaces were used with the surface shape parameter mathgrams, Section 5.2 investigates the behavior of modified particle shape parameters from surface roughness parameters with wrapped/derived *(dparts)* and real particles *(parts)* inputs.

### *5.2.2 Particle Shape Characterization by Conventional Surface Roughness Parameters*

For the conventional surface roughness parameters, modifications include:

- The resolution of the particle profiles is calculated as a ratio of the perimeter of the particle outline divided by the number of data points of the corresponding outline.

- In surface input mathgrams, the –y elevations of the profiles were used in Chapter 4 for surface roughness parameters. For particle outlines, this value corresponds to the Euclidean distance measured from the centroid of the particle to the outline data points, i.e. the radius.
- For the surface input algorithms utilized in Chapter 4, the diameter of a particle for the determination of the normalized roughness parameter is used as 1.0 mm for the *dsurfs* and 6.0-mm for the *surfs* based on the average perimeter for the *dsurfs* and *surfs,* respectively. For the corresponding wrapped particles generated from the input surfaces in Chapter 4, since the perimeter does not alter for a surface *(surf)* and its corresponding wrapped particle *(dpart)* or for an unrolled surface *(dsurf)* and its corresponding particle *(part)*, same radius values are utilized. Table 5.15 displays the output of the modified mathgrams using real or derived particle outlines as the input.

The results from Chapter 4 where the surface roughness parameter mathgrams were utilized with no modifications and with real and derived surface inputs are provided in Table 5.16 for comparison with the results tabulated in Table 5.15.

The correlation between $R_a$ & $R_a$-part, $R_q$ & $R_q$-part, $R_p$ & $R_p$-part, $R_{max}$ & $R_{max}$-part, and $R_n$ & $R_n$-part are 0.999, 0.999, 0.992, 0.999, and 0.996, respectively where for each parameter pair mentioned the former one is valid for surface profile input and the latter for the particle outline input. Figures 5.10 - 5.14 display new particle shape parameters versus the original surface roughness parameters for the corresponding particle and surface inputs. Note that in the –x axis the first and second labels refer to particle shape and surface roughness parameter values, respectively.

**Table 5.15 –** Output of New Particle Shape Parameters with *part* and *dpart* inputs.

| Particle Name | dia for $R_n$-par | $R_a$ - part | $R_q$ - part | $R_p$ - part | $R_{max}$ - part | $R_n$ - part |
|---|---|---|---|---|---|---|
| *Units* | *mm* | *mm* | *mm* | *mm* | *mm* | - |
| p1 | 1 | 0.016 | 0.019 | 0.037 | 0.065 | 0.055 |
| p2 | 1 | 0.068 | 0.079 | 0.127 | 0.28 | 0.192 |
| p3 | 1 | 0.036 | 0.043 | 0.076 | 0.165 | 0.135 |
| p4 | 1 | 0.052 | 0.065 | 0.128 | 0.267 | 0.216 |
| concrete-par | 6 | 0.128 | 0.167 | 0.295 | 0.788 | 0.12 |
| HDPE-par | 6 | 0.054 | 0.072 | 0.224 | 0.377 | 0.052 |
| steel-par | 6 | 0.0003 | 0.0007 | 0.002 | 0.01 | 0.0013 |

**Table 5.16 –** Output of Conventional Surface Roughness Parameters with *surf* and *dsurf* inputs.

| Surface Name | $D_{50}$ for $R_n$ (mm) | $R_a$ (mm) | $R_q$ (mm) | $R_p$ | $R_{max}$ (mm) | $R_n$ |
|---|---|---|---|---|---|---|
| *Units* | *mm* | *mm* | *mm* | *mm* | *mm* | - |
| p1-surf | 1 | 0.0158 | 0.0187 | 0.0373 | 0.065 | 0.0559 |
| p2-surf | 1 | 0.0697 | 0.0811 | 0.1373 | 0.2803 | 0.2215 |
| p3-surf | 1 | 0.0354 | 0.0427 | 0.0794 | 0.1638 | 0.1368 |
| p4-surf | 1 | 0.0506 | 0.0638 | 0.1442 | 0.2667 | 0.2299 |
| concrete | 6 | 0.1348 | 0.1706 | 0.2652 | 0.7803 | 0.1243 |
| HDPE | 6 | 0.0564 | 0.0736 | 0.2076 | 0.3497 | 0.0544 |
| steel | 6 | 0.0003 | 0.0008 | 0.0024 | 0.0109 | 0.0013 |

## 5.3 Comparison between Particle Shape and Surface Roughness Parameters

The differences between particle shape and surface roughness characterization methods originate from the dissimilarity between a closed particle outline and open surface profile. In addition, the particle outline is self-similar; while the profile is self-affine. Self-similarity implies that the particle outline looks the same at every scale of

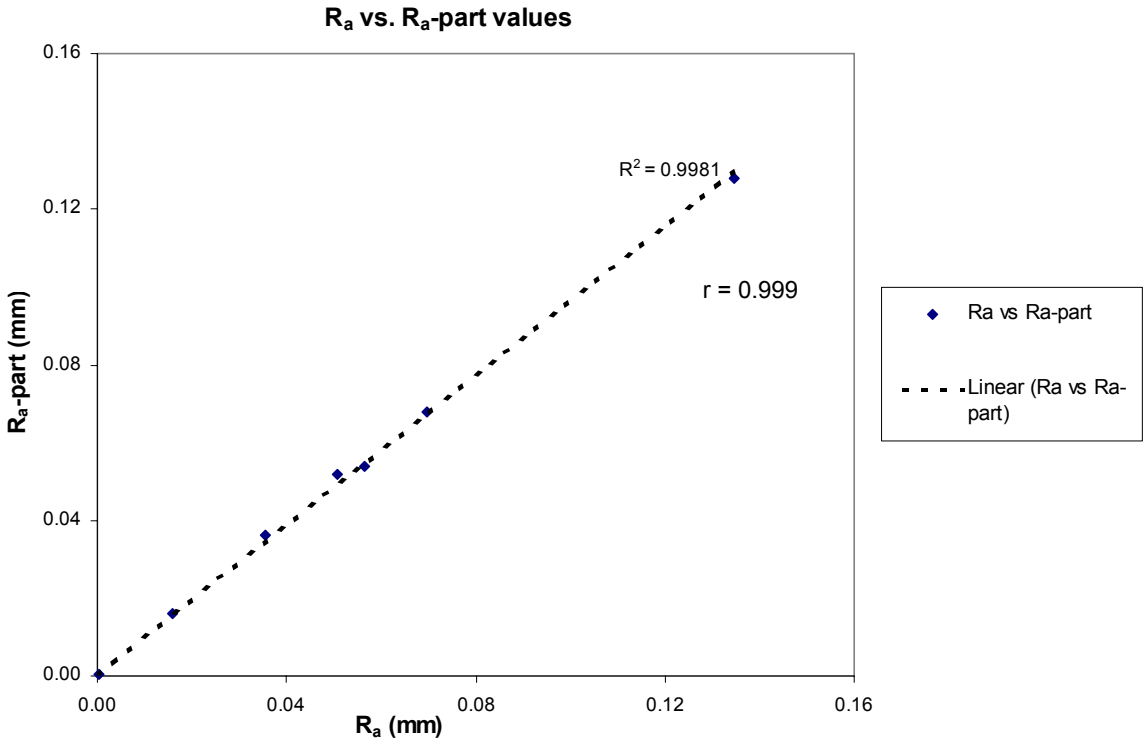


**(a)**

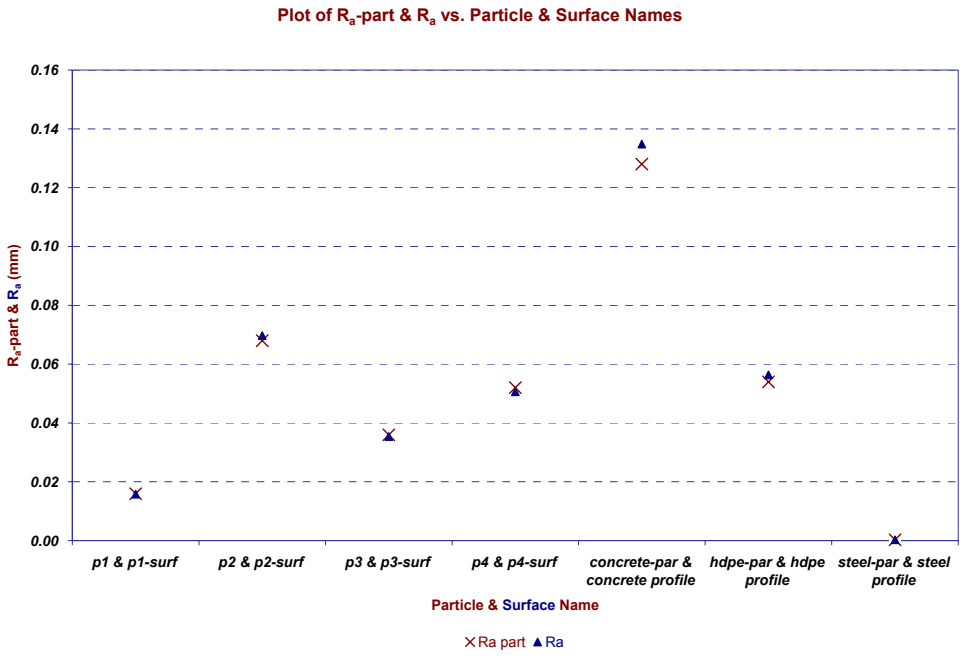


**(b)**

**Figure 5.10 – (a)** Plot of regression analysis between the $R_a$ for surface profiles and $R_a$-part for particle outlines, **(b)** Plot of $R_a$-part & $R_a$ versus particle and surface labels.

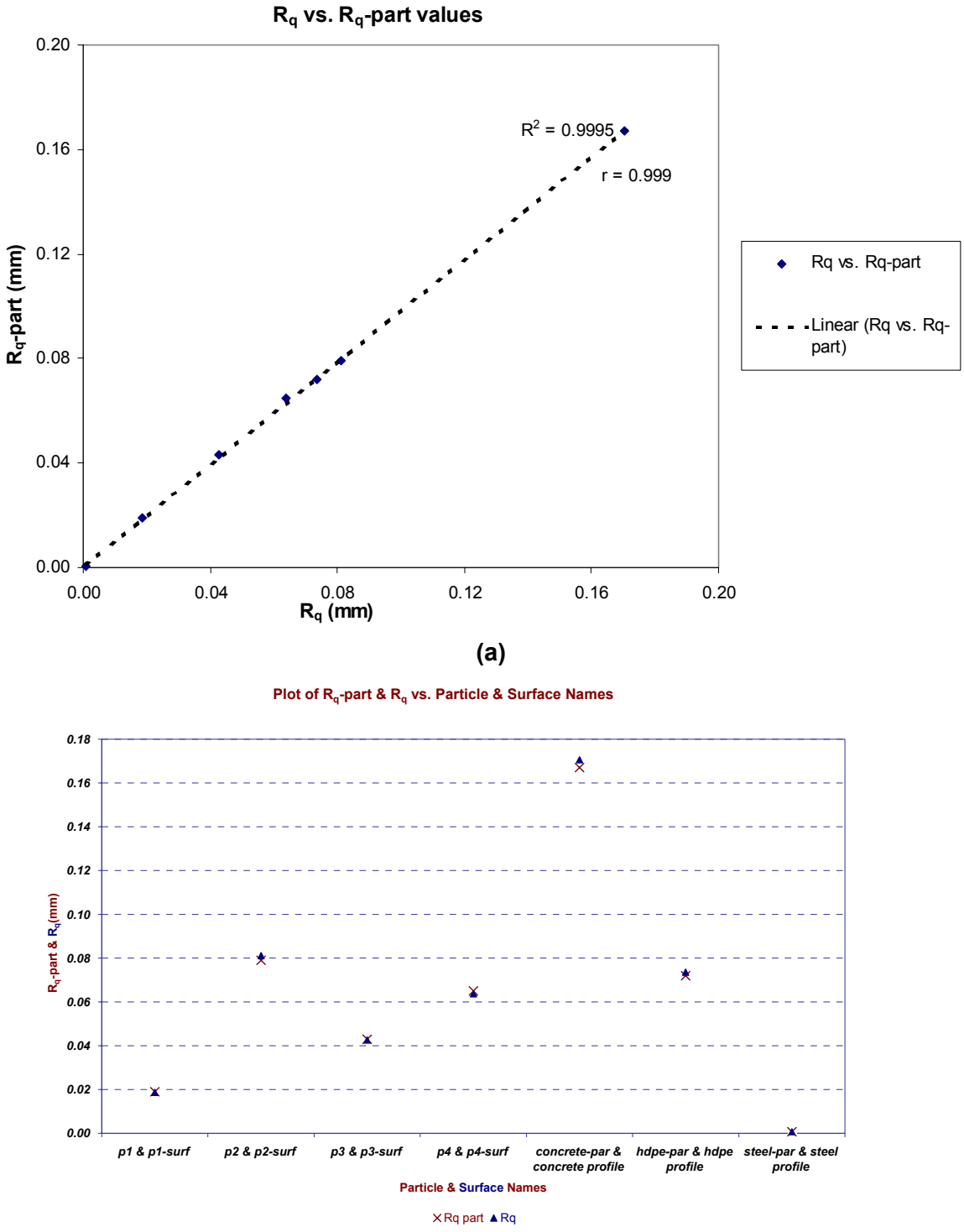


**Figure 5.11 – (a)** Plot of regression analysis between the $R_q$ for surface profiles and $R_q$-part for particle outlines, **(b)** Plot of $R_q$-part & $R_q$ versus particle and surface labels.

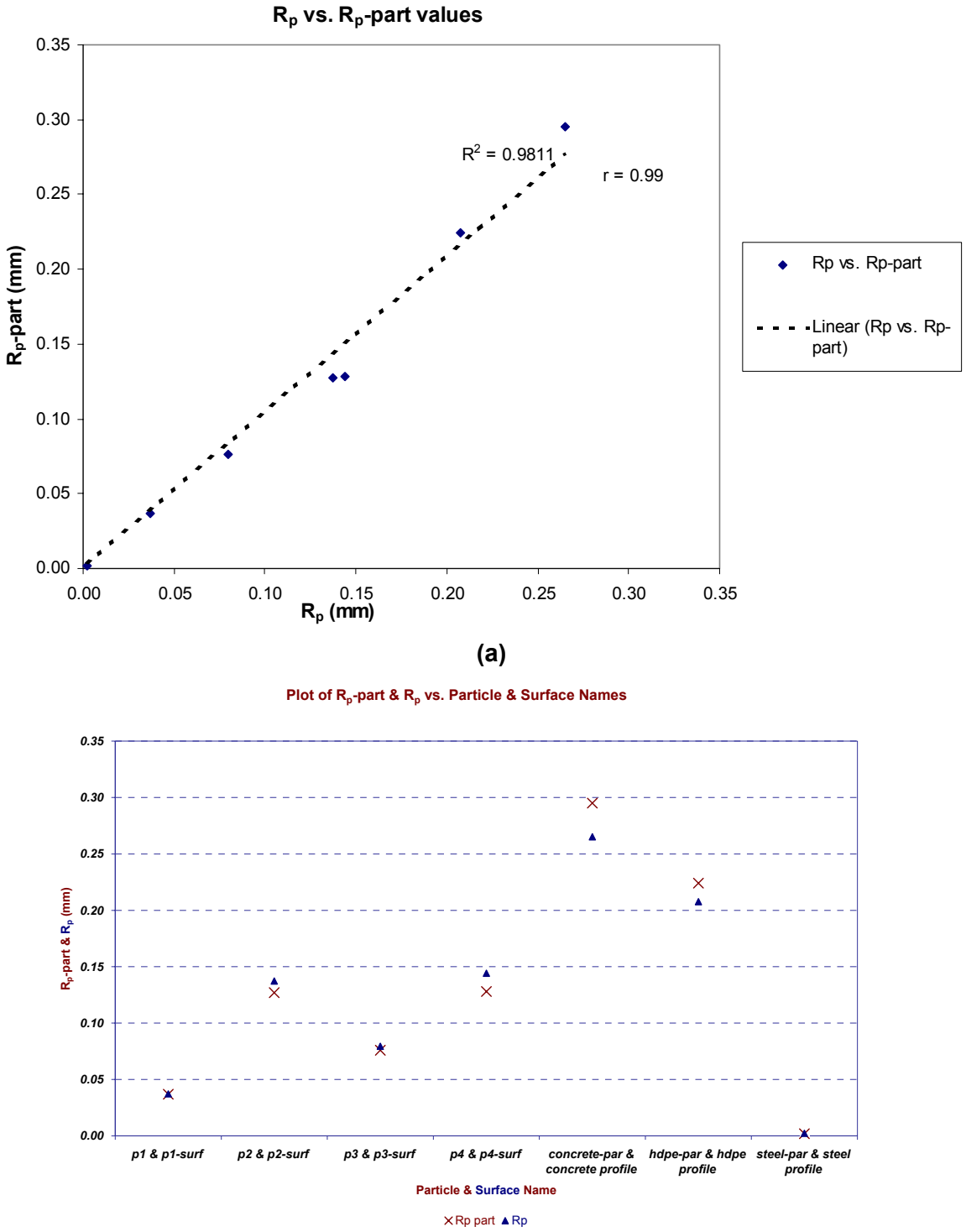


**Figure 5.12 – (a)** Plot of regression analysis between the $R_p$ for surface profiles and $R_p$-part for particle outlines, **(b)** Plot of $R_p$-part & $R_p$ versus particle and surface labels.

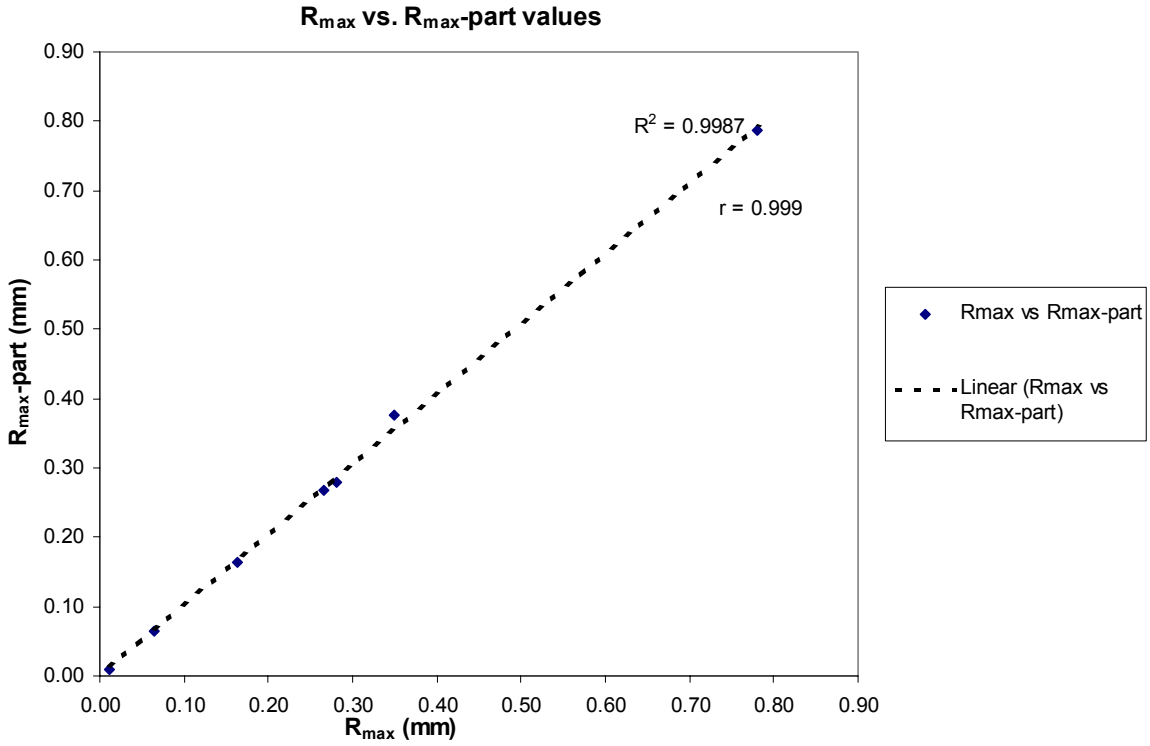


**(a)**

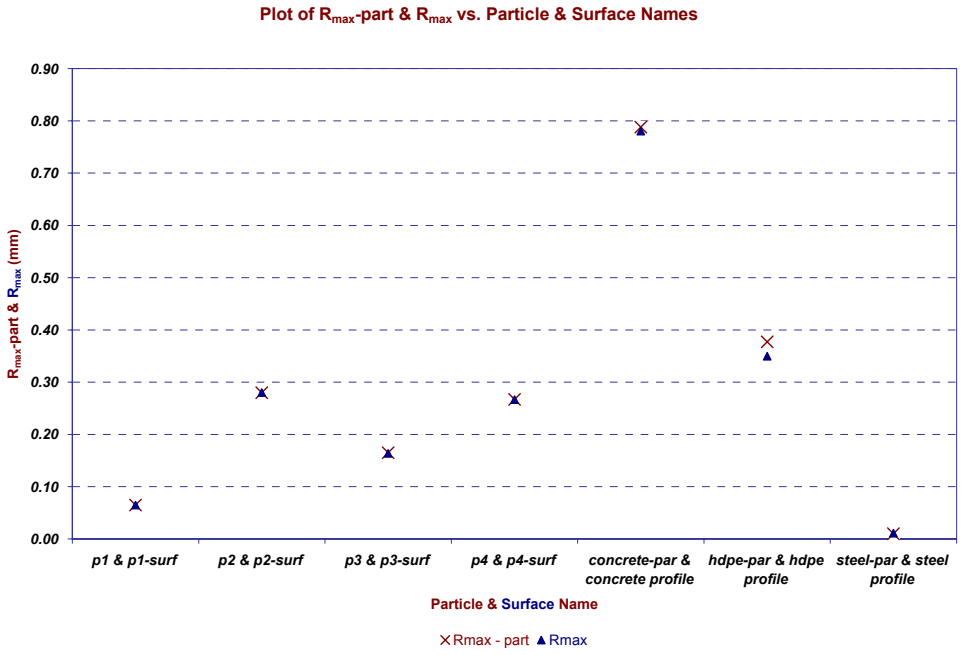


**(b)**

**Figure 5.13 – (a)** Plot of regression analysis between the $R_{max}$ for surface profiles and $R_{max}$-part for particle outlines, **(b)** Plot of $R_{max}$-part & $R_{max}$ versus particle and surface labels.

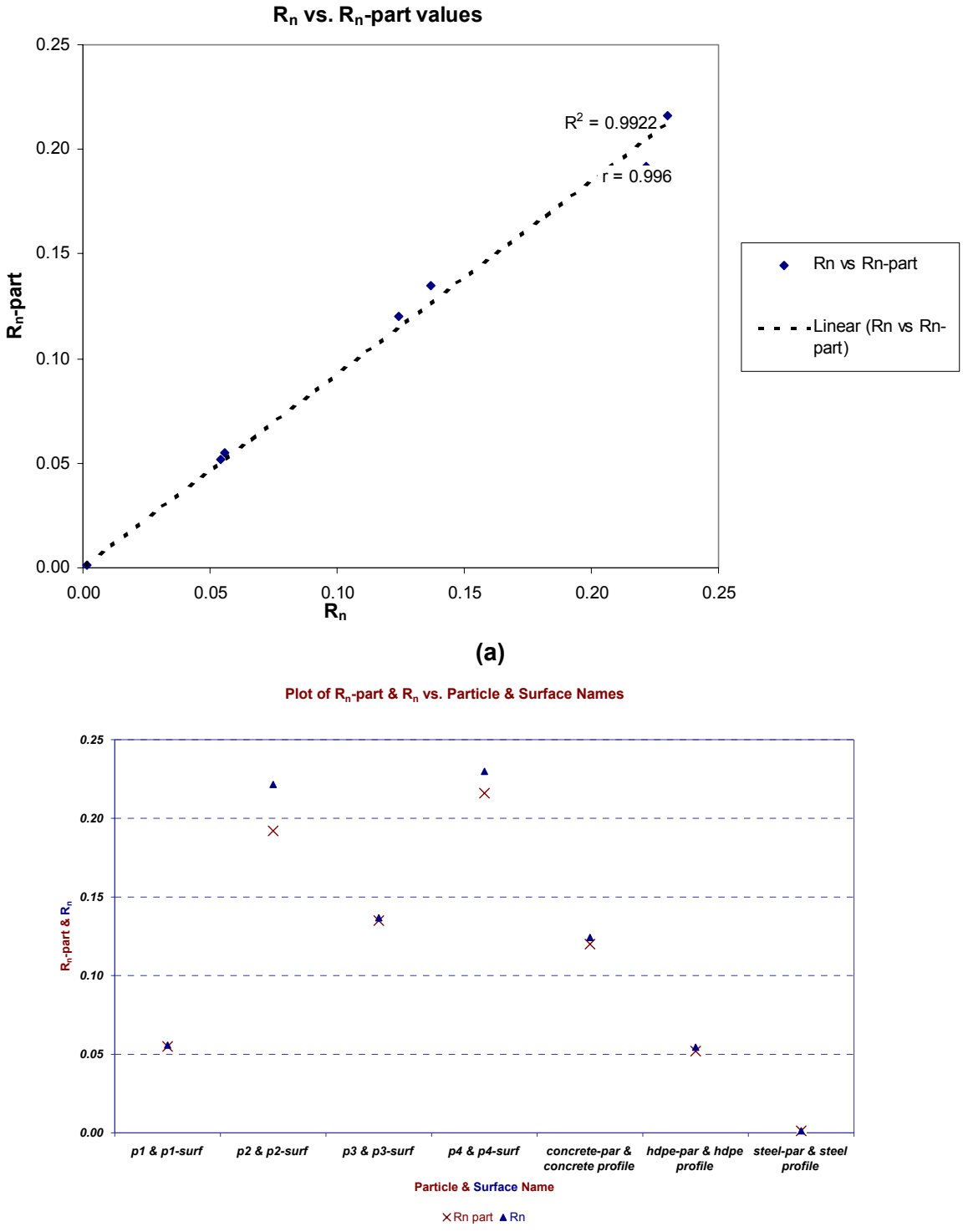


**Figure 5.14 – (a)** Plot of regression analysis between the $R_n$ for surface profiles and $R_n$-part for particle outlines, **(b)** Plot of $R_n$-part & $R_n$ versus particle and surface labels.

size. Self-affine profiles scale by different amounts in vertical (z) and horizontal directions. Another difference between particle outlines and surface profiles is that the units of a surface profile in –x and –z directions may not be the same, e.g. the surface profile may show elevation changes with time (Stachowiak, 1998), whereas both directions have the same dimensions in particle outlines.

Particle shape parameters generally compare the particle outline to a global shape; in many cases, this tends to be a circular outline. Among the particle shape parameters selected in this analysis, SF and AF are derived by representing the particle outline as an equivalent polygon. The SF in particular, compares the equivalent polygon outline to a circular shape. Similarly, in performing the CRR calculation, two concentric circles are used based on the reasoning that the maximum inscribing and minimum circumscribing circles disclose information regarding the abrasiveness of the particle outline. The Spike Parameter represents the particle outline as a combination of triangular steps and does not associate the particle outline to any global shape. The Spike Parameter Quadratic is influenced only by parts of the outline outside its least squares circle based on the idea that the contact with the counterface occurs at the spikes. The Shape Index (SI) particle shape parameter quantifies the difference of radial measurements along the profile from a same number of circular outline radial measurements. Thus, in all selected particle shape parameters except SP, the measurement involves a perfect circular outline.

On the other hand, in surface roughness parameters investigated, only SPQ-surf involves a baseline similar to the concept of a circular outline in particle shape analysis. SPQ-surf takes into account only the surface perturbations that are above the mean elevation line. The rest of the surface roughness parameters analyzed are statistical measurements and do not involve comparison with any idealized profile.

Another difference between particle shape parameters and surface roughness parameters is that except for SPQ-surf, none of the surface shape parameters is based on the understanding of the wear analysis. The surface shape parameters are established with statistical measures; whereas in the derivation of particle shape parameters, the concept of wear and contact of the particle with the counterface is considered.

Studies have also been conducted to investigate the performance of particle and surface shape parameters with resolution change. The results suggest that surface shape parameters do not exhibit any critical variation with the resolution (except for SPQ-surf) since the conventional surface roughness parameters selected result mostly from statistical measures. On the other hand, particle shape parameters involve comparison of the particle outline to a global shape, mostly circular, increasing the variability with resolution.

In an effort to reduce the number of particle shape parameters and discard any redundancies, a cluster analysis is performed with the selected particle shape parameters, namely CRR, SF, AF, SP, SPQ, and SI. In cluster analysis, the order in which clusters are formed and the members of each cluster group designate special pattern within the data set considered. This may be valuable in determining groups of macro-shape, meso-shape, and micro-shape particle shape parameters. It is recognized by the author that the quantity of data is quite small for an accurate statistical analysis; nevertheless, it is believed that cluster analysis can still be utilized as a guide rather than a definite statement. For this exercise, Minitab Release 11.12 – Multivariate Analysis – Cluster Observations is utilized with hierarchic techniques. The primary goal of cluster analysis is to devise a scheme for grouping the objects into classes so that

similar ones are in the same class. For linking the groups, similarity is calculated using centroid method with Euclidean distance measures. All the particle shape parameters are standardized prior to calculating the distance matrix in order to obtain a common scale so that no relatively high valued parameter dominates the lesser-valued parameters. Standardization is accomplished by subtracting the mean value for each parameter and diving the difference with the standard deviation of that data set to attain a data set with mean value of zero and a standard deviation of unity. The final partition criterion in terms of final number of clusters is selected as three clusters in order to acquire the macro-shape, meso-shape, and micro-shape particle parameters in separate clusters. The particle shape parameters with their corresponding values for each real and derived particle are input to the worksheet and the original cluster numbers assigned are provided in Table 5.17. The hierarchical dendrogram is shown in Figure 5.15. Note that the observation numbers are shown along the x-axis of the dendrogram each corresponding to the specified particle shape parameter as tabulated in Table 5.17.

The numerical values calculated within the analysis forming the dendrogram are shown in Table 5.18. Table 5.19 provides the amalgamation steps and the clusters generated in each step.

As Figure 5.15 and Table 5.19, the first shape parameters to cluster is SPQ and SI followed by SP joining to this group in the next step. Both SPQ and SI are based on the difference between the particle outline and a circular shape. In SPQ, this is achieved by considering only the outline sections outside the least squares circle. On the other hand, the equation for SI requires that circular outline radius percentages are subtracted from particle outline radius percentages at the same sampling intervals. The SPQ and SI cluster with a similarity measure of 83.70, and at a larger similarity level

(84.77), SP joins SPQ and SI cluster in the 2nd step. Although the similarity between SP and (SPQ, SI) cluster is 84.77, the similarity level between SP and SPQ is smaller than 83.70 (in Step 1). However, the similarity level increases when the centroid of SPQ is moved to the (SPQ, SI) cluster centroid in the 2nd Step. The similarity between SP and SPQ is already mentioned and shown in Figure 4.7. They are both based on representing the particle outline with triangular shapes. The parameter SP represents the entire outline; whereas SPQ considers only portions of the outline. SP uses several step size triangles. On the other hand, SPQ triangles are formed separately for each spike outside the least squares circle by combining the start point (where the spike first intersects the circle), end point (where it intersects the circle second time), and a middle

**Table 5.17 –** Observation numbers corresponding to the particle shape parameters.

| **Observation Number** | 1 | 2 | 3 | 4 | 5 | 6 | 7 |
|---|---|---|---|---|---|---|---|
| **Particle Shape Parameter** | CRR | SF | AF | FF | SP | SPQ | SI |

**Table 5.18-** The MINITAB output for the particle shape parameters dendrogram.

**Hierarchical Cluster Analysis of Observations**

Standardized Variables, Euclidean Distance, Centroid Linkage

Amalgamation Steps

| Step | Number of clusters | Similarity level | Distance level | Clusters joined | | New cluster | Number of Obs in new cluster |
|---|---|---|---|---|---|---|---|
| 1 | 6 | 83.70 | 1.008 | 6 | 7 | 6 | 2 |
| 2 | 5 | 84.77 | 0.942 | 5 | 6 | 5 | 3 |
| 3 | 4 | 82.15 | 1.104 | 2 | 4 | 2 | 2 |
| 4 | 3 | 66.36 | 2.081 | 3 | 5 | 3 | 4 |
| 5 | 2 | 53.51 | 2.876 | 2 | 3 | 2 | 6 |
| 6 | 1 | 40.75 | 3.666 | 1 | 2 | 1 | 7 |

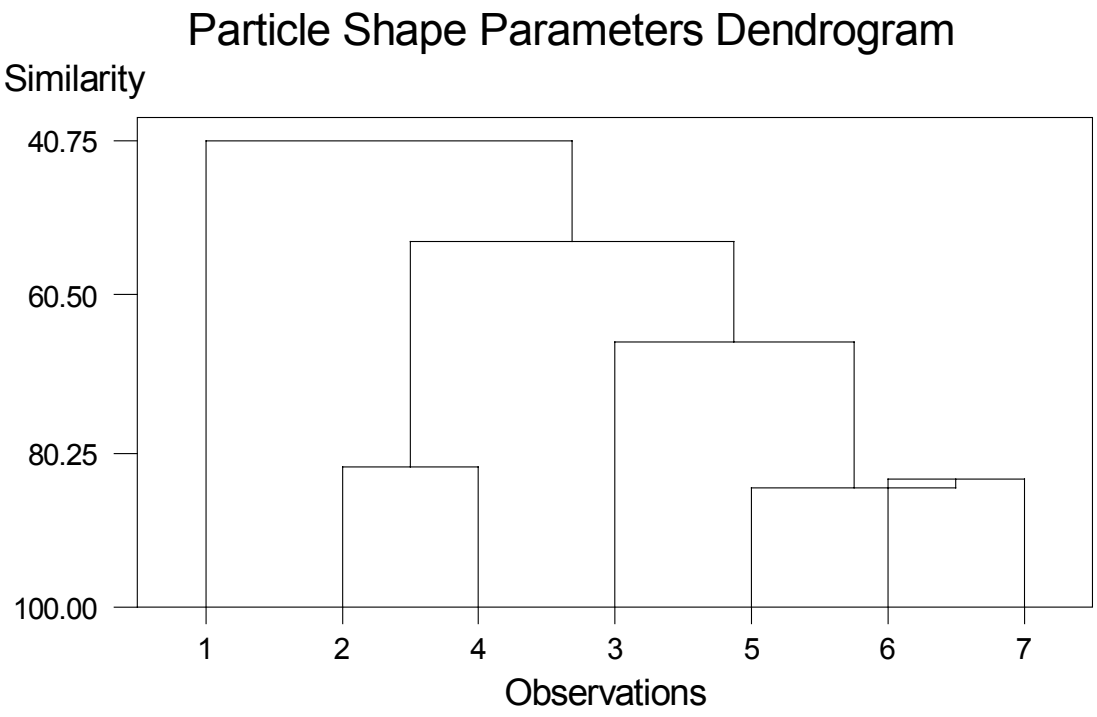


**Figure 5.15-** Particle shape parameters dendrogram using Hierarchical Cluster Observations with Centroid Euclidean distance measures.

**Table 5.19 –** The amalgamation steps and observed cluster groups.

| Step No. | Total Number of Clusters | Observed Clusters |
|---|---|---|
| 1 | 6 | CRR, SF, AF, FF, SP, (SPQ, SI) |
| 2 | 5 | CRR, SF, AF, FF, (SP, SPQ, SI) |
| 3 | 4 | CRR, (SF, FF), AF, (SP, SPQ, SI) |
| 4 | 3 | CRR, (SF, FF), (AF, SP, SPQ, SI) |
| 5 | 2 | CRR, (SF, AF, FF, SP, SPQ, SI) |
| 6 | 1 | (CRR, SI, SPQ, AF, FF, SF, SP) |

point (where maximum local radius occurs within that spike). Thus, while SP may take into account insignificant outline features, SPQ only considers dominant triangles. In Step 3, SF joins with FF in a cluster. This is expected since SF and FF are correlated to a high degree and SF is used for the calculation of FF. Before SF, FF, and AF cluster under a single group, Step 4 shows that AF is linked more to the (SP, SPQ, SI) cluster. However, note that the amalgamation in Step 4 occurs at a similarity level of 66.36 much smaller than the previous step similarity value (82.15). In Step 5, with CRR left as a single member cluster, the other six particle shape parameters merge and finally in Step 6 all the parameters combine. The final partition criteria is three clusters, in which case the analysis ends at Step 4 with three cluster groups. Steps 5 and 6 are shown in order to provide with the reader with complete analysis. Three clusters are selected to visualize the macro-, meso-, and micro- shape parameter groups. Based on Step 4 information, three groups are; macro-shape parameter group as CRR, meso-shape parameter group as (SF, FF), and the micro-shape parameter group as (AF, SP, SPQ, SI). Note that in order to investigate the variability, different linkage methods were also evaluated; however, the final three clusters did not change.

Following cluster analysis, in order to select the most representative of each group, correlation analysis is performed within the micro-shape parameter cluster as shown in Table 5.20.

The correlation analysis in Table 5.20 shows that within the micro-shape group, SP has the highest correlation with all the other cluster members. From the meso-scale shape parameter group (SF, FF), SF is selected since FF is also dependent on AF, member of a micro-shape cluster. Thus, cluster analysis shows that CRR, SF, and SP are sufficient particle shape parameters to capture the macro-, meso-, and micro- shape features of

**Table 5.20 –** Correlation Analysis within micro-shape cluster.

| | *AF* | *SP* | *SPQ* | *SI* |
|---|---|---|---|---|
| **AF** | 1 | | | |
| **SP** | 0.842034 | 1 | | |
| **SPQ** | 0.681751 | 0.904585 | 1 | |
| **SI** | 0.082577 | 0.26643 | 0.24368 | 1 |

the particle outline.

The same analysis is performed on the selected surface shape parameters and provided in this study only as a guide. The observation numbers corresponding to the surface shape parameters are provided in Table 5.21. Centroid Linkage method with Euclidean distances provided the dendrogram shown in Figure 5.16.

The amalgamation steps corresponding to Figure 5.16 are shown in Table 5.22 and Table 5.23 shows the amalgamation steps with the individual surface shape parameters.

Surface shape parameter $R_a$ and $R_q$ are the mean and standard deviations of the elevations along the length of the profile. In Step 1, they merge into a cluster since they are the most related parameters among the whole parameter set. $R_p$ defines the variation of the elevation length from the maximum –y elevation along the profile. It also

**Table 5.21 –** Observation numbers corresponding to the surface shape parameters.

| **Observation Number** | 1 | 2 | 3 | 4 | 5 | 6 |
|---|---|---|---|---|---|---|
| **Particle Shape Parameter** | $R_a$ | $R_q$ | $R_p$ | $R_{max}$ | $R_n$ | SPQ-surf |

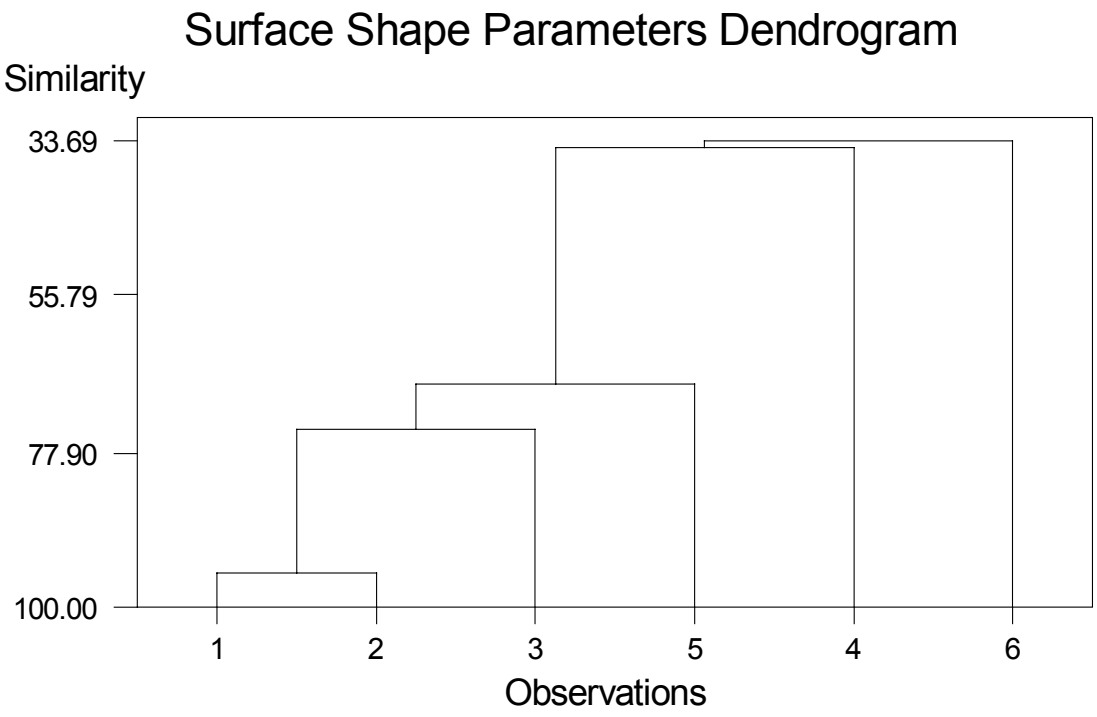


**Figure 5.16-** Surface shape parameters dendrogram using Hierarchical Cluster Observations with Centroid Euclidean distance measures.

**Table 5.22 -** The MINITAB output for the particle shape parameters dendrogram.

**Hierarchical Cluster Analysis of Observations**

Standardized Variables, Euclidean Distance, Centroid Linkage

Amalgamation Steps

| Step | Number of clusters | Similarity level | Distance level | Clusters joined | | New cluster | Number of Obs in new cluster |
|---|---|---|---|---|---|---|---|
| 1 | 5 | 95.10 | 0.275 | 1 | 2 | 1 | 2 |
| 2 | 4 | 74.66 | 1.422 | 1 | 3 | 1 | 3 |
| 3 | 3 | 68.18 | 1.785 | 1 | 5 | 1 | 4 |
| 4 | 2 | 34.60 | 3.669 | 1 | 4 | 1 | 5 |
| 5 | 1 | 33.69 | 3.720 | 1 | 6 | 1 | 6 |

**Table 5.23 –** The amalgamation steps and observed cluster groups.

| Step No. | Total Number of Clusters | Observed Clusters |
|---|---|---|
| 1 | 5 | ($R_a$, $R_q$), $R_p$, $R_{max}$, $R_n$, SPQ-surf |
| 2 | 4 | ($R_a$, $R_q$, $R_p$), $R_{max}$, $R_n$, SPQ-surf |
| 3 | 3 | ($R_a$, $R_q$, $R_p$, $R_n$), $R_{max}$, SPQ-surf |
| 4 | 2 | ($R_a$, $R_q$, $R_p$, $R_n$, $R_{max}$), SPQ-surf |
| 5 | 1 | ($R_a$, $R_q$, $R_p$, $R_n$, $R_{max}$, SPQ-surf) |

contains several measurements taken along the profile. In Step 3, $R_n$ also combines with (Ra, $R_q$, $R_p$) cluster. The similarity levels at which Step 1, 2, and 3 occur are widely spaced at 95.10, 74.66, and 68.18, respectively signifying that the parameters are not linked at a high degree. Step 3 amalgamation results in three clusters, ($R_a$, $R_q$, $R_p$, $R_n$), $R_{max}$, and SPQ-surf. The three clusters are grouped later in Steps 4 and 5 at very low similarity levels; thus, the characteristics of three groups are diverse. The first group statistical parameters are based on several measurements along the profile; whereas, $R_{max}$ is a single measurement along the profile of the maximum and minimum –y elevations. SPQ-surf, on the other hand, is based on a entirely different approach. SPQ examines the abrasivity of the surface profile.

## 5.4 Concluding Commentary on Particle Shape Parameters

This section will be discussing the general aspects of particle shape and particle shape characterization in addition to review of the general characteristics of the selected particle shape parameters in this study.

Although particles are analyzed as individual particles in this study, they never stand alone in nature. They are part of a particle system. Thus, in order to provide a satisfactory analysis, it is important to identify the dimensions of particle system characterization. Scott (2003) has discussed several aspects of particle and particle system characterization. The several dimensions of particle system characterization are shown on Figure 5.17. Seven dimensions were identified; i.e. attribute, complexity, method, technology, scale, application, and composition. The measurable physical properties, such as size, shape, and volume are termed as the *attribute* dimension. The dimensions *method* and *technology* correspond to the means of obtaining the attributes. Although individual particles are considered in this study, particle characterization involves *complexity* dimension as the interest of study shifts from individual particles to particle mass properties. The *scale* refers to the characteristic size of the particle or the particle system. In the broader view, particle characterization also depends on *application,* i.e. the end use of the measurement data and *composition* in terms of the chemical composition and physical state of the complex, e.g. powder, emulsion, slurry. As Scott (2003) discusses, for any specific case, the dimensions *scale*, *complexity*, and

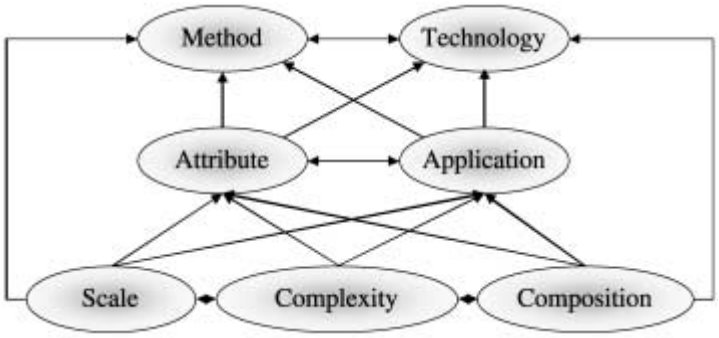


**Figure 5.17 –** Dimensions of particle characterization (after Scott, 2003).

*composition* are given and they directly affect *attribute* and *application*. The properties of the *attribute* and *application* further affect the possibilities for *method* and *technology. Composition* also directly influences the *technology* dimension. Figure 5.17 shows a general view of the complexity of particle characterization. In any particle shape characterization, these dimensions of particle characterization should be recognized. In other words, a thorough particle analysis should consider the scale or scales predominant in a specific application, mechanisms and attributes involved in the existing complexity and also the existing method and technology. However, as this study has shown, the majority of particle shape literature lacks a comprehensive study of these dimensions and results in difficulties when literature studies are reviewed and compared.

In this study, particle images were captured from real particles in order to obtain particle outline data points. The details of the image acquiring are provided in Section 3.1.1. It is important to recognize that the quality of any analysis performed on particle shape analysis starts with proper image acquisition. Particle shape image analysis converts the analog image, seen by the human eye into a digital one for further processing. In the digital image, every pixel corresponds to a surface element of the initial analog image. Upon obtaining the digital image, the next step in image analysis is image segmentation,

where the particle of interest is separated from the background. If the particle contourline is discernible, then a simple step is required to produce a binary image (Pons et al., 1999). However, if the particle outline is not clearly separated from the background, edge enhancement is required. Finally, polishing of the image includes filling in the holes, removing undesired particles within the image frame, and contour smoothing (Pons et al., 1999).

As observed and stated previously in this study, there are discrepancies regarding the particle images about within different particle development methodologies. The image acquisition step is generally not mentioned or briefly described in some studies. However, the quality of any analysis is dependent on the materials used. The particle shape literature contains only a small amount of research conducted on particle image analysis acquisition. An extensive study is provided by Podczeck et al. (1999) discussing several aspects of image analysis in order to suggest a standardized technique. The study was conducted in the field of pharmaceutics. In pharmaceutics, state that pellets are being used in order to control the dosage form before they are either filled into hard gelatine capsules or compacted into tablets. The size and shape of capsules are evaluated using image analysis.

Most of the particle shape parameters examined in this study are based on comparison of the particle outline to a perfect circle outline. It is also important to realize that, in image analysis, even a circle is represented by square/rectangular pixels, which results in an inherent source of error. Podczeck et al. (1999) also discuss the use of table light for illumination since they result in shadow added to the particle outline and thus, suggest the use of dark-field illumination technique, where the light is produced from the top of the image camera (Podczeck and Newton, 1995). The dark-field illumination produces a white image and the shadow produced adds to the background rather than the particle outline.

In image analysis, next source of error is the threshold value selected in order to process a gray-scale image (Podczeck et al., 1999). In order to determine the threshold value effect in image analysis, Podczeck et al. (1999) have varied the threshold value and repeated the tests to determine the particle shape parameters, which were selected as

aspect ratio, projection sphericity, and $e_R$. The definitions for these parameters are provided in Chapter 2; however, they are also shown in Table 5.24.

Based on the tests, aspect ratio and projection sphericity have both found to be insensitive to threshold value change of 1 unit when spherical particles were used. On the other hand, $e_R$ is highly affected by the threshold value even for spherical particles. The dependence of aspect ratio on threshold value became larger as the particle outline moved away from a circular outline.

The magnification effect on the selected particle parameters was investigated using seven different magnification values, varying the pixel size from 20 μm to 100 μm (Podczeck et al., 1999). Podczeck et al. (1999) concluded that a maximum pixel height

**Table 5.24 –** Particle Shape Parameters analyzed by Podczeck et al. (1999).

| Parameter Name | Description | Reference |
|---|---|---|
| Aspect Ratio | $AR = \frac{b}{l}$ | Scheiderhöhn (1954) |
| Circularity | $C = \frac{4\pi \cdot A}{P^2}$ | Cox (1927) |
| Projection sphericity (PS) | $PS = \frac{4 \cdot A}{\pi \cdot d_L^2}$ | Pentland (1927) |
| Shape Factor | $e_R = \frac{2\pi}{P}\frac{r_e}{f} - \sqrt{1-\left(\frac{b}{l}\right)^2}$ <br> $f = 1.008 - 0.231\left(1-\frac{b}{l}\right)$ | Podczeck and Newton (1994, 1995) |

*Parameters used:* $b$: minimum Feret diameter, $l$: maximum Feret diameter, $A$: projected area of the 2D particle outline, $P$: perimeter of the 2D particle outline, $d_L$: longest caliper distance observed around the outline, $r_e$: mean radius from the center of the particle outline, $f$: correction factor.

(corresponding to minimum magnification) of 30 μm is allowed for accurate characterization of a particle of ≈1 mm diameter since at further reduction in pixel size results in erroneous Feret diameter measurements. However, minimum pixel size will depend on both the optical resolution of the imaging system and the digitization procedure used by the imaging analysis software.

In any particle shape study, the purpose of the study guides most of the steps taken. For example, if the purpose is to obtain a particle shape parameter of a certain kind of material, it is important to perform experiments with adequate amount of that material to obtain a representative value. The purpose in this study was to move towards a unified approach to particulate-continuum interfaces, thus as long as the particle outlines selected covered the range of particle outline shapes encountered in the geotechnical study, the number of materials was not a concern. Nevertheless, it is important to recognize the aspects of the goal.

Although number of particles analyzed was not a concern in this study, in order to appreciate the quality of any parameter, the requirements need to be realized. Podczeck et al. (1999) have also discussed the required number of particles in order to obtain a representative particle shape value from a particle mass. One of the most obvious results was that each parameter requires different number of particles that are required for a representative value. In relation to the particle shape parameters provided in Table 5.24, aspect ratio is the least sensitive to particle shape variability, thus it requires the least amount of particles to be used (Podczeck and Newton, 1994). On the other hand, a parameter shape dependent on area or perimeter, e.g. circularity in Table 5.24, is highly dependent on the number of particles to be counted. The $e_R$ is less

dependent on the number of particles to be counted. As far as the number of particles required to be counted was suggested to be a 100 if particle size is as important as the particle shape. A similar study on the number of required particles for a representative particle shape parameter was performed by Pons et al. (1999). The number of particles required for the study performed by Pons et al. (1999) is in accordance with the number reported by Podczeck et al. (1999).

The experiment setup process for the development or analysis of a particle shape parameter has been discussed so far. It is also important to recognize the general problems encountered in particle shape analysis. One of the main concerns with particle shape analysis is that it is impossible to separate size information from particle shape. As mentioned in this study, size is mostly defined as “particle diameter”; however, for non-spherical particle shapes, particle diameter is not unique. In order to overcome this, several size measurements are selected as “equivalent diameter”, where the particle size is related to a spherical particle in terms of a certain measure, e.g. particle volume. In this regard, Matsuyama and Yamamoto (2004) have presented equivalent diameters for several geometrical shapes based on particle volume. Thus, all particles presented in Table 5.25 attain the same volume. As Matsuyama and Yamamoto (2004) discuss, for different shape particles, it is difficult to compare sizes.

The main drawback of the particle shape parameters analyzed in this study was that the parameters utilized insufficient number of outline data points. In relation to the required number of outline sampling intervals, several studies have been performed. The system used by Podczeck and Newton (1994) used 36 length measurements along the outline corresponding to 10° intervals, whereas others have used as little as 8 measurements corresponding to 20° intervals (Lindner and Kleinebudde, 1993). Although as little as

**Table 5.25 –** Various equivalent diameters for several different geometrical shapes (after Matsuyama and Yamamoto, 2004).

| | Cube | Regular tetrahedron | Ellipsoid (aspect ratio = 2) | Sphere |
|---|---|---|---|---|
| Specific length (edge, major, and minor axis) | 81 | 164 | 159<br>79 | 100 |
| Mesh size can be passed | 81 | 142 | 79 | 100 |
| Diameter of a hole can be passed | 114 | 164 | 79 | 100 |
| Diameter equivalent to a projection area | 91 | 122 | 112 | 100 |
| Diameter equivalent to the total surface area | 129 | 122 | 208 | 100 |
| Diameter equivalent in volume to projection ratio | 85 | 67 | 79 | 100 |
| Diameter equivalent to the volume | 100 | 100 | 100 | 100 |

four sampling intervals (corresponding to 90° intervals) are adequate for the "maximum length" determination along the particle outline (Podczeck et al., 1999), the "minimum length" determination depends highly on the number of sampling intervals. Hawkins (1993) argue that at least 10° or less sampling interval angle is required to adequately reproduce the silhouette of a particle. As the number of sampling intervals decrease, the accuracy of the parameters, e.g. circularity, aspect ratio, projection sphericity, also decrease.

In particle shape analysis, there is additional confusion regarding the nomenclature. Some studies refer to roundness while that definition corresponds to angularity for some researchers. Additionally, studies fail to provide sufficient details regarding the image analysis or the sampling interval for the particle outline. For example, even to obtain a simple geometrical measure such as "radius", three possible methods exist. The procedure undertaken is usually not stated in particle shape analysis studies. The length of radius chords could be obtained by (a) calculating the distance of each outline pixel to the centroid, (b) determining the chord lengths that pass through the centroid

and crossing the outline, or (c) callipering, i.e. calculating diameters randomly or regularly around the centroid by rotating the particle outline (Almeida-Prieto et al., 2004). Another misinterpretation in particle shape analysis methods originates from the wide variety of processes in which particle shape becomes important. Most of the methods are only applicable to certain procedures and, thus fail to characterize the particle shape when utilized for diverse applications.

So far in this study, particle shape parameter analysis is explained with additional comments related to the results. The rest of this section attempts to discuss several aspects of the particle shape parameters considered.

CRR is a parameter originally developed in this study utilizing Voronoi diagrams. Although it is dimensionless as desired, it has no upper limit. It increases as the aspect ratio increases, i.e. the largest CRR is obtained for an infinitely long particle. For particles, it is a measure of the macro-shape primarily, however, by taking the difference between the radii of MIC and MCC and dividing by the radius of MIC, it can also distinguish between two particle shapes having the same MIC, but different MCC due to the difference between the valleys and peaks embedded along the outline. CRR coefficient is believed to be more valuable than a similar particle shape parameter; e.g. aspect ratio, in the respect that it is originated from a more fundamental analysis than simply measuring the longest and shortest axes. Aspect ratio relies on single measurements, whereas CRR determination utilizes all data points. Furthermore, the difference of MCC and MIC in the numerator incorporates the scale of perturbations existent along the particle outline in the CRR value, relating to the wear process considered. The CRR value for the real and derived particles considered has a range of 0.4% to 81.8%. For two same length surfaces, one with a larger $R_{max}$ has a larger CRR-

surf value. CRR is smaller for a particle resembling a circle, where the difference between radii of MIC and MCC, i.e. $R_{max}$ is small.

For the Shape Factor (SF) and Angularity Factor (AF) parameters developed by Sukumaran and Ashmawy (2001), SF and AF are related to each other. As the calculation process suggests, both parameters are based on equivalent polygon representation of the outline and both compare the equivalent polygon representation to a circle. It is also evident that SF signifies the deviation of the particle outline from a circular outline; whereas AF is more illustrative of the number and sharpness of the corners. A square term in AF calculation signifies the influence of sharper points. However, as the resolution study on AF concluded, AF is highly user-dependent and results are only valuable at 9° intervals. Values presented in Table 4.1 provide clarification for SF and AF. Comparing different pairs of particle outlines for SF values; *concrete-par* resembles a circular particle outline more than *p4*, thus the SF value for *concrete-par* (41.6%) is lower than the SF value for *p4* (47.7%). On the other hand, *concrete-par* attains considerably sharper and larger number of corners resulting in a larger AF (58.3%) than the *p4* particle outline (17.7%). Similarly, particle outline *p2* is more elongated and smoother compared to the particle outline *HDPE-par*; with the first property resulting in a larger SF (39.5% vs. 18.9%) and lower AF (4.8% vs. 11.6%) for *p2* compared to *HDPE-par*. Comparing two particle outlines, although the number and sharpness of corners is similar for p3 and p4 resulting in very similar values of AF (18% vs. 17.7%), their deviation from a circular particle outline is, i.e. the macro-shape difference manifests itself in larger discrepancy in SF values (40.1% vs. 47.7%). The range of FF values for the real and derived particles considered are 0% to 71.6%, constituting a reasonable range for the range of real and derived particles considered. Although SF and AF are correlated to each other in some aspects, they still capture

different features of the profile. The methodology for SF and AF is solely on the geometry of the particles; however, a more thorough analysis establishing the correlation between the FF factors and the wear coefficients would be more beneficial.

The merit of the Spike Parameter introduced by Hamblin and Stachowiak (1995) is that it is derived to quantify abrasiveness of a particle. In a similar analysis, e.g. the fractal method, the outline is represented by straight lines, boxes, etc. whereas in SP triangle steps are used. The numerical value of the SP is based on the spike value of each triangle calculated as $\cos(\theta/2)\,h$, where the *cosine* term and triangle *height* together defines the abrasiveness of a particular step. That is, even if a triangle's angle is relatively small (sharp point), if it has smaller *height* in relation to the other triangles that can be generated for that specific step, the interaction between counterfaces will not occur at that spike necessarily. Thus, it is the combination of the *sharpness* represented by the *cosine* term and the *size* represented by the *height* term. Another aspect of the SP parameter is that it ignores the valleys throughout the outline and concentrates on the peaks. As the two and three body wear tests performed by Hamblin and Stachowiak (1995) demonstrate, it correlates well with the wear rates as well. The SP value is dimensionless and it varies between 0 (ideally smooth) and 1 (ideally sharp). However, as the original work results by Hamblin and Stachowiak (1995) and this study results show, the SP parameter cannot discriminate well between the particle outlines studied although the range of particle outlines provides a wide range. Comparing SP for particles, the steel-par and concrete-par has SP values of 0.148 and 0.417, respectively; bounding the SP values calculated as the lowest and highest value. However, for a scale of 0 to 1, these two outlines cover only half of the total scale. The same argument is valid for the SP-surf values; where steel and concrete surfaces yield SP values of 0.151 and 0.421, respectively. Similar results are observed in the original study.

Although the particle outlines considered represent a wide range of the particle outline angularity, the SP values reported range from 0.1369 to 0.3591. Nevertheless, based on the two-body abrasive test results performed in the original study, the correlation between the wear rate and SP is not unacceptable, R = 0.981. As for the effect of resolution on SP, as shown in Table 4.14 and Figure 4.18, for higher number of sampling intervals of 360, SP parameter stabilizes. This is acceptable in the sense that SP is a particle shape parameter that is based on "walking" the whole outline and dependent on every data point to estimate the accurate triangle steps. Note that when resolution is low, it results in deceptive triangles and spike values for each step.

It should be noted that although SP method is similar to fractal analysis, SP has one main advantage over fractal methods. In fractal analysis, fractal dimension can vary with the starting point. This has been overcome in SP, by considering every starting point possible for a given stepsize followed by averaging over the different starting points for that specific stepsize and finally averaging the results obtained for varying stepsizes.

An advantage of SPQ over other methods of particle shape calculation methods is that it is derived to signify the abrasion process. In other words, although a shape parameter may give information regarding the shape, it does not necessarily give information regarding which boundary features contact with the counterface. Only portions of the outline outside the least squares circle are of interest. This is analogous to the centroid trace method for surface profile analysis, where above surface features are proved to contribute mostly to a contact case in geotechnical practice.

The particle shape parameter SI is also dimensionless with no real upper limit. Similar to CRR, as the particle outline resembles more of a circular feature, its SI value is

smaller since SI relates the radial distribution of a particle to that of a circle. As mentioned previously, the Shape Index (SI) is developed for use in urban studies. It is intended to correlate the shape of any urban area with characteristics of the urban area; e.g. sales, importance of its central business district. Although clearly the result is more accurate if number of radials is increased, 16 are used in this study to be consistent with the original study. The resolution study for the Shape Index parameter showed that the change in the SI output with the number of intervals larger than 16 does not affect the rank of the particle shape outline.

The reason that only 16 intervals is adequate to stabilize SI, whereas at least 360 are required for SP is due to the method of derivation. In SI, radius length is measured along the profile and for most of the particles encountered in geotechnical practice particles do not have abrupt changes in radius length over small distances. In other words, when fewer points are available for the SI determination it does not affect the results drastically. On the other hand, for parameters similar to SP, where the whole outline is "traveled" and every step influences the output, fewer points are relevant.

## 5.5 Concluding Commentary on the Surface Roughness Parameters

The conventional surface shape parameters do not have a basic mechanism from which they are derived and mostly related solely to vertical amplitude characteristics of the profile. Among the parameters considered, only $R_n$ is a relative normalized measure integrating the size of the contacting particle. The most widely used surface parameter; $R_a$ can attain the same value for two completely different profiles. As they are modified

for particle outlines in Chapter 5, they convey the same concepts and attain same values.

As part of an effort to move towards a unified approach to particulate-continuum characterization, this study has also examined the use of surface roughness parameters transformed into equivalent particle shape parameters. If explored further and developed into regular practice, this can provide a useful tool in particulate-continuum interface characterization. For this purpose, it is important to recognize the advantages and drawbacks of a specific surface roughness analysis method. Surface roughness characterization methods generally incorporate statistical analysis. The main advantage of statistical characterization methods is that they are applicable for several applications. In addition, unlike the most widely used particle shape parameters, surface roughness parameters are mathematically (rather than graphically) defined and easily computed. An advantage of statistical surface roughness measurements is that several well established procedures can be utilized to derive continuous profile height distribution based on the calculated $R_q$, skewness, and kurtosis values (King and Spedding, 1983). King and Spedding (1983) have proposed a system to completely describe the surface profile statistically. In their system, three main groups are identified; height, periodic, and random spatial. The height component of the profile is adequately described with $R_q$, skewness, and kurtosis. Upon separating the random and periodic components of the surface profile, the random and periodic components are described via second order autoregressive function and two component harmonic model. King and Spedding (1983) have validated their system by recreating simulated profiles with the obtained system parameters and comparing the real and simulated profiles. The real and simulated profiles have proven to be closely related.

However, they possess no individual significance to any functional property and none of the surface roughness parameters is an intrinsic property of a real surface. Almost all surface roughness values depend on the scale of measurement. This is due to the "self-similarity" property of real surfaces (Thomas, 1981). For surface roughness parameters, a problem cited by Thomas (1999) is the uncertainty related to the inherent statistical nature of the conventional surface roughness parameters. The variation for the most commonly used surface roughness parameters, $R_a$ and $R_q$, can be even more than 4% (Thomas and Charlton, 1981). For the other surface roughness parameters, coefficients of variation of 15% are not uncommon (Thomas and Charlton, 1981). Thomas and Charlton (1981) have evaluated the coefficient of variation for most of the commonly used surface roughness parameters. Their results clearly showed that $R_a$ and $R_q$ are quite insensitive to range, while extreme-value parameters are quite sensitive. They suggest the use of the lowest range to decrease the variation. A smaller cut-off length results in increased variation. Based on BS1134: 1972 standards, they advice to use a shortest cut-off length of 0.8 mm. The sampling interval did not have a significant effect on $R_a$, $R_q$, skewness, and kurtosis. As the sampling interval decreases, the extreme-value parameter values increase. Sampling interval has an undesirable effect on the texture parameters. The variations of all parameters were significantly larger when measurements were performed in lay direction as opposed to across lay direction. For all cases, $R_a$, $R_q$, and mean slope were the most stable parameters; whereas extreme-value parameters had the least stability.

Another concern related to surface roughness parameters is the "parameter rash" as most termed in 1980s. Several studies have shown, most of the surface profile parameters used are not independent from each other (e.g. Gorlenko, 1981; King and Spedding, 1982). Gorlenko (1981) has shown that $R_a$, $R_q$, and $R_{max}$ can be closely

related. King and Spedding (1982) have developed several relationships between some height measurements and showed that most of the average height surface parameters can be derived using $R_q$, skewness, and kurtosis measurements. The $R_q$ defines the scale of the distribution; whereas skewness and kurtosis define the shape.

In relation to the surface roughness parameters utilized in this study, $R_q$ is more valuable than $R_a$ in the sense that it is more sensitive to outliers. $R_q$ line represents the line that divides the surface profile so that the sum of the squares of the deviations of the profile height above and below is equal to zero.

Although widely utilized, extreme-value surface parameters such as $R_{max}$ are considered inadequate for representing a surface profile due to high variation from sample to sample. One method to reduce that variation is by averaging $R_{max}$ over several consecutive lengths as performed for $R_n$. Nevertheless, $R_{max}$ is still used in surface roughness analysis.

SPQ-surf on the other hand investigates a different aspect of the surface profile. Similar to SPQ for particles, it focuses on the above mean line features and provides more insight. Nonetheless, it still considers the surface profile by itself and does not integrate the particulate medium properties.

As discussed previously, surface roughness of an interface is relative and is dependent on both the particulate and continuum material. The valley and peak features of the surface profile affect the path of the contacting particulate material differently. As shown in Chapter 4 CT study, peak features magnify as the particle size increases; whereas valley features diminish. This is also evident from the increasing CT behavior for $R_{max}$

with particle size. The conventional surface roughness parameters do not signify this aspect. They consider either the vertical or the horizontal characteristics of a 2D surface profile. Most of the surface roughness parameters selected for this study are related to vertical amplitude characteristics of the profile since they are mostly utilized in practice. Among the parameters considered, only $R_n$ is a relative normalized measure integrating the size of the contacting particle.

Previously in Section 4.3, resolution analysis was performed for the particle shape and surface roughness parameters. It was concluded that particle shape parameters varied considerably with resolution; whereas the surface roughness parameters exhibited negligible change. In Chapter 5, the parameters originally developed for surface profile analysis were developed into particle shape parameters by the required transformations and new algorithms. The stability of the surface shape parameters, e.g. $R_a$, $R_q$, $R_p$, $R_{max}$, and $R_n$ with resolution can be observed by investigating the resolution effect on $R_a$-part, $R_q$-part, $R_p$-part, $R_{max}$-part, and $R_n$-part. Note that in the first set of parameters (surface roughness parameters), the resolution of a surface profile input was varied; whereas for the second set of parameters (particle shape parameters), a particle outline resolution is varied as demonstrated below.

For this exercise, a particle outline, *p4*, is selected. In Chapter 4, Figure 4.17 showed the *p4* outline represented with varying number of data points, i.e. 10, 20, 45, 90, 180, 360, 750, 1500, and 3750. The same data is used for $R_a$-part, $R_q$-part, $R_p$-part, $R_{max}$-part, and $R_n$-part change with resolution. The results are provided in Table 5.26.

The stability of the parameters can be observed with small changes in values from an extreme change in number of data points, from 10 to 3750. The maximum variation is

observed for $R_{max}$-part, which is based on only two extreme values of *part* resolution, in the amount of 18% between 10 and 3750 data points.

**Table 5.26 –** Particle outline data points and the corresponding $R_a$-part, $R_q$-part, $R_p$-part, $R_{max}$-part, and $R_n$-part values.

| Number of particle data points | Interval Angle (°) | Resolution[1] | $R_a$ – part[2] | $R_q$ – part[2] | $R_p$ – part[2] | $R_{max}$ – part[2] | $R_n$ – part[3] |
|---|---|---|---|---|---|---|---|
| 10 | 36 | 0.221 | 0.048 | 0.065 | 0.136 | 0.226 | 0.21 |
| 20 | 18 | 0.1194 | 0.048 | 0.062 | 0.144 | 0.259 | 0.22 |
| 45 | 8 | 0.0558 | 0.049 | 0.063 | 0.14 | 0.259 | 0.23 |
| 90 | 4 | 0.0286 | 0.05 | 0.063 | 0.141 | 0.263 | 0.24 |
| 180 | 2 | 0.0145 | 0.05 | 0.064 | 0.143 | 0.265 | 0.24 |
| 360 | 1 | 0.0074 | 0.05 | 0.064 | 0.144 | 0.267 | 0.24 |
| 750 | 0.48 | 0.0036 | 0.051 | 0.064 | 0.144 | 0.267 | 0.24 |
| 1500 | 0.24 | 0.0018 | 0.051 | 0.064 | 0.144 | 0.267 | 0.24 |
| 3750 | 0.096 | 0.0007 | 0.051 | 0.064 | 0.144 | 0.267 | 0.23 |

[1]The resolution is calculated as perimeter to number of data points ratio.
[2]The dimensions are (mm).
[3]The diameter for $R_n$ is taken as 1mm for p4 outline.

## 5.6 Implications of the Study Findings for 3D Characterization Studies

Particles and surfaces are obviously 3D objects. Although, this study has focused on 2D particle and surface properties only, the common goal of the particulate-continuum interface characterization schemes is to move towards a 3D characterization.

This section provides advances and techniques in 3D particle surface and surface topography characterization and quantification techniques along with the contribution of this study to 3D characterization.

In 3D particle surface characterization, two main problems are encountered; obtaining accurate particle surface topography and quantifying the 3D shape properties (Stachowiak and Podsiadlo, 1999). Stachowiak and Podsiadlo (1999) list the available techniques for 3D data acquisition as; atomic force microscopy (AFM), interferometric microscopy (IM), laser scanning confocal microscopy (LSCM), and scanning electron microscopy (SEM) stereoscopy. Although AFM has adequate vertical (~0.1 nm) and horizontal (~0.2 nm) resolutions, it has a limited maximum vertical range (~0.4 μm). Thus, it is unsuitable for most of the particles that has a feature larger than 0.4 μm. on the other hand, LSCM and IM has poor lateral resolutions of 0.4 μm and 0.2 μm, respectively. As Stachowiak and Podsiadlo (1999) signify, this corresponds to 25 surface scans for LSCM and 50 scans for IM, for a particle of 10 μm size. Among these methods, only SEM is appropriate for the range of particle sizes and particle surface topographies considered due to resolution limitations for the remaining techniques. For particles smaller than 10 μm, field emission SEM (FESEM) should be used (Stachowiak and Podsiadlo, 1999). Depending on the magnification and pixel size in the method, the accuracy of the particle surface topography data varies (Stachowiak and Podsiadlo, 1999). In this work, a technique -Partitioned Iterated Function Systems (PIFS)- is used to extract information regarding particle morphology.

Recent methods for quantifying 3D particle surface properties include fractal methods, including ε-blanket, 2D Hurst analysis, variation method, box-counting, Ganti-Bhushan

model (Russ, 1994; Gangepain and Roques-Carmes, 1986; Dubuc et al, 1989; Ganti and Bhushan, 1995). Obviously, conventional 2D measurements on a projected area can also be extended to 3D measurements, e.g. volume in place of area, circumscribing sphere in place of circumscribing circle, etc.

In terms of the CRR parameter introduced in this study, rather than utilizing Minimum Inscribing and Maximum Circumscribing Circles, 3D Voronoi diagrams can be utilized to retrieve circumscribed and inscribed spheres for the particle shape upon which CRR-3D can be calculated in a similar method. If CRR-2D is proven analogous to CRR-3D, another option is evaluating CRR-2D at some cross-sections of a spherical surface and estimating the 3D CRR parameter.

Surface profilometry is the most commonly used 3D surface topography characterization method. Additional methods include laser scanning profilometer, scanning electron microscopy stereoscopy (Stachowiak and Podsiadlo, 2003). The methods used to assess the 3D surface roughness of surface topographies are a function of scale and thus are not unique. They provide measurements of single scale and do not convey the multi-scale nature of the surface topographies (Stachowiak and Podsiadlo, 2001). In addition, it should be realized that anisotropy is an issue in 3D surface roughness measurements since 2D measurements assume isotropic surface profiles.

The surface roughness in 3D has been calculated using 2D roughness parameters and averaging them over several section profiles obtained across the surface topography. Stout et al. (1993) established 14 parameters known as “Birmingham 14” constituting of 4 amplitude, 4 texture, 3 hybrid and 3 “functional” surface roughness parameters. Further details are provided in Stout et al. (1993). Additional methods include 3D

surface roughness parameters, statistical methods, auto-correlation function analysis, and power spectrum methods (Thomas, 1999; Doug et al., 1994, Stout et al., 1993). However, these methods do not address the multi-scale nature of the surface topography. Two approaches for multi-scale characterization are wavelet transformation-based and fractal methods (Russ, 1994; Hasegawa et al., 1996; Ganti and Bhushan, 1995). However, one limitation of these methods is that they are valid for isotropic surfaces and surface topographies generally exhibit anisotropic behavior (Stachowiak and Podsiadlo, 2001). Stachowiak and Podsiadlo (2001) introduce a new method based on PIFS for surface data. This method has been improved in a further study with a advanced additional method based on a combination of fractal and wavelet methods termed as Hybrid Fractal-Wavelet Method valid for multi-scale and non-stationary nature of the surface topographies (Stachowiak and Podsiadlo, 2004).

The measurements obtained from 2D projected areas can be utilized to estimate 3D behavior using stereology methods. Gokhale and Underwood (1990) have introduced an application of stereological techniques that provide assumption-free and unbiased 3D surface roughness estimations based on 2D fracture profile measurements. A brief explanation of the proposed technique is given below.

Fracture surface roughness parameter, $R_S$ is defined as (Gokhale and Underwood, 1990):

$$R_S = \frac{S}{A} \qquad \textbf{(5.3)}$$

where $S$ and $A$ stand for true fracture surface area and apparent projected area on a plane parallel to the mean of the fracture surface, respectively. $R_S$ varies from unity to infinity corresponding to a flat and very rough surface, respectively.

In 2D, $R_s$ is analogous to profile roughness parameter, $R_L$ defined as:

$$R_L = \frac{\lambda_0}{L} \quad \textbf{(5.4)}$$

where $\lambda_0$ is the true length of the fracture profile and $L$ is the apparent projected length on the mean or average topographic direction of the profile (Gokhale and Underwood, 1990). Similar to $R_s$, $R_L$ can have values ranging from unity (a flat surface) to infinity.

Relating $R_L$ and $R_s$ is valuable since it leads to estimation of actual 3D roughness based on easily obtained $R_L$ measurements. Stereological methods have proven to be superior for this application. Stereological methods are assumption-free and do not utilize any approximations (Gokhale and Underwood, 1990).

Gokhale and Underwood (1990) introduced the relation between 3D and 2D roughness as:

$$R_S = \overline{R_L \cdot \psi} \quad \textbf{( 5.5)}$$

where $\psi$ stands for the profile structure factor dependent on the profile orientation distribution function, $f(\alpha)$. The profile orientation distribution function, $f(\alpha)$ can be defined as:

$$\psi = \int_0^{\pi} \sin\theta \int_0^{\pi} \left| \cos(\theta + \frac{\pi}{2} - \alpha) \right| \cdot f(\alpha)\, d\alpha\, d\theta \qquad \textbf{(5.6)}$$

where $\alpha$ denotes the angle between the tangent on the fracture profile and the vertical axis, $f(\alpha)$ is the frequency distribution function of arc element orientations in the fracture profile, and $\theta$ is a dummy variable. Note that $\overline{R_L \cdot \psi}$ is the expected value of the product $R_L \cdot \psi$, not the product of the expected values of $R_L$ and $\psi$ obtained on randomly selected vertical section fracture profiles. In a related study, Gokhale and Drury (1990) investigate further on the required number of vertical section profiles and report that three vertical sectioning planes at 120° are enough to provide a reliable $R_s$ estimation.

With this approach, Dove and Frost (1996) have provided surface roughness measurements for the commonly used parameters utilizing stereological measurements.

In relation to this study, for an approximation of 3D surface roughness parameters, utilization of stereological methods with the selected particle shape and surface roughness measurements can be investigated. In addition, 2D shape and roughness parameters can be extended to 3D with the recognized limitations.

More importantly, in order to better characterize interface mechanisms and develop and understanding of interface roughness, centroid trace method must be extended to 3D. Centroid trace method provides a filtering effect on the surface profile in 2D as well as in 3D depending on the rolling circle or sphere diameter, respectively. Centroid trace method takes into account the relative properties of the particulate and continuum

properties. In terms of surface roughness, it is both sensitive to wavelength and amplitude. The basic idea of CT is that mostly above mean surface features are dominant in interface mechanisms. In other words, the peaks along the profile are a controlling factor in determining the circle's center or the sphere's locus location required to develop the CT. In CT calculation methods, care should be taken to understand the edge effects along the surface profile (DeJong, 2001). In order for a peak along the surface profile to affect the locus of the sphere, the peak has to be located within certain distance of the centroid since a contact is required. This results in sections of certain length at the beginning and end of the profile to be non-influential.

A similar technique in concept, E-system technique has been used to determine the mean line and involves a rolling circle along the profile (Section 2.4.2.3.1). Tholath and Radhakrishnan (1999) have developed 3D application of E-system.

# CHAPTER 6

# SUMMARY, CONCLUSIONS, AND RECOMMENDATIONS

## 6.1 Summary

This thesis has explored specific factors involved in particulate-continuum interfaces. The main objective of the thesis is to move towards a unified approach for characterizing both components (i.e. particle and surface components) of the particulate-continuum interface system. This section summarizes the main tasks achieved in the study.

A total of 64 mathgrams were developed as part of the effort to move towards a unified approach to characterizing particulate-continuum interfaces. In support of the main goal of this study, a number of the mathgrams were specifically developed to permit analyzing particles as surfaces as well as surfaces as particles. In addition, mathgrams for each of the particle shape and surface roughness parameters chosen were also developed. As conveyed in Chapter 5, equivalent surface roughness parameters (based on specific particle shape parameter concepts) as well as equivalent particle shape parameters (based on specific surface roughness parameter concepts) were established and analyzed. Further details on these tasks are given below.

The particles and surfaces selected for analysis in this study represented the range of geomaterials usually encountered in geotechnical practice. As the main contribution of the thesis, the particle outlines (*part*) were unrolled into surface profiles (*dsurf*) based on certain mathematical rules and analyzed with surface roughness parameters. Similarly, surface profiles (*surf*) were wrapped into particle outlines (*dpart*) and investigated by means of particle shape parameters. The two major mathgrams for particle unrolling into surfaces (*part-dsurf algorithm*) and for surface wrapping into particle outlines (*surf-dpart algorithm*) were assessed through several experiments. One was to ensure that the *part-dsurf* algorithm is not dependent on the particle magnification. This was confirmed by the same surface profile output obtained for three different sizes of a simple particle shape input into the *part-dsurf* algorithm. A similar concern for surface profile transformation was the baseline elevation. The *surf-dpart* algorithm was processed with three simple surface profiles at different elevations and the output particle (*dpart*) for all cases had the same size and centroid. Besides the validation of the algorithms individually, the reversibility property was also tested for the two cases of *surf-dpart-ddsurf* and *part-dsurf-ddpart* processes. In other words, to ensure the correctness of the mathgrams, the *surf-dpart* and *part-dsurf* algorithms were subsequently applied to an initial set of surface profiles. It was required and confirmed that the output of *surf-dpart-ddsurf* process produced the same surface profile as the input. Likewise, the *part-dsurf-ddpart* process was investigated to confirm that the *part* input and the *ddpart* outputs were the same particle outlines. Upon validation of the algorithms, modifications were applied to the surface profiles in order to obtain same resolution (number of data points/mm) for both the input surface profiles and particle outlines. The modifications involved investigating the different surface profile lengths through CT analysis.

Based on an extensive literature review, specific particle shape and surface roughness parameters were selected for further analysis. Among the parameters chosen, some were originally developed and utilized manually, whereas others were already executed via algorithms. In order to prevent user-dependency, the manually calculated particle shape parameter (Wadell's Roundness) was also automated. Different approaches such as Voronoi Diagram generation, pattern recognition, urban geography planning, and wear analysis were also introduced as tools in particle shape analysis. Voronoi Diagrams were further used in the development of a new particle shape parameter, CRR. Although particle angularity characterization from wear analysis is not routinely incorporated in geotechnical practice, the relevance of some parameters with the particle-surface interaction was recognized in this study. In particular, SPQ for particle outlines and SPQ-surf for surface profiles were studied (Hamblin and Stachowiak, 1995, 1997). For all the particle shape and surface roughness parameters, mathgrams based on the original study were developed. The mathgrams were validated against the reported results utilizing the authors' original dataset.

The validated mathgrams were implemented using the study particles and surfaces along with the derived particles and surfaces in Chapter 4. The results were discussed to observe any differences between the real and derived components of the dataset since a cluster of derived components could be interpreted as an indication of different behavior caused by the transformation. For both particle shape and surface roughness parameter results, derived components behaved similarly to the real components. Chapter 4 also includes a resolution study for the selected particle shape and surface roughness parameters. For each parameter considered, the specific inputs were varied and the results were investigated. Along with the specific inputs for each parameter,

particle outline or surface profile resolutions were also varied in an effort to signify the importance of proper particle outline or surface profile resolution.

In an effort to move towards a unified approach to particulate-continuum surface profiles, rather than transforming the inputs as derived components (Chapter 3 and 4), another approach was undertaken by introducing transformed parameters in Chapter 5. In other words, equivalent surface roughness parameters were developed based on the concepts of particle shape parameters. Likewise, equivalent particle shape parameters were developed based on the surface roughness parameters. The new parameters were analyzed with the study materials. The results were investigated against their corresponding parameter. For example, an equivalent particle shape parameter ($R_a$-surf) was developed based on the concepts of the surface roughness parameter ($R_a$). The mathematical rules of $R_a$ were modified in order to allow particle shape characterization. Thus, for $R_a$ and $R_a$-surf, the input is a surface profile (real or derived) and a particle outline (real or derived), respectively. The results of $R_a$-part were tested against the results of $R_a$. For instance, $R_a$ value for the *concrete* profile was compared with the $R_a$-part value for the *concrete-par* or $R_a$ value for the *p1-surf* was compared with the $R_a$-part value for the *p1* particle outline.

## 6.2 Conclusions

The conclusions of this thesis are categorized in three sections; particulate-continuum interfaces, particle shape and surface roughness parameter properties, and the techniques for unified particulate-continuum interface analysis proposed in this thesis. The last section of the conclusions contains both the method of transforming the inputs

(derived particles and derived surfaces) for the existing particle shape or surface roughness parameters and the method of transforming the existing parameters (e.g. *SI* for particle shape analysis to *SI-surf* for surface roughness characterization).

### *6.2.1 Particulate-Continuum Interfaces*

The primary purpose of this study is to move towards a unified approach to analyze and characterize particulate-continuum interfaces commonly encountered in geotechnical engineering practice. In order to achieve this, an extensive literature review has been presented. As shown by many previous researchers, particle shape and surface roughness are amongst the most dominant factors affecting the interaction between a particle and a surface. Although their importance is recognized, the particle shape and surface roughness literature still lacks a generally accepted approach to address the particle-surface systems. As presented in this study, abundant approaches are present in both fields with no single recognized parameter for neither particle shape nor surface roughness characterization. The literature review concluded that separate particle shape and surface roughness characterization for a particle-surface system produces two unrelated parameters in terms of their method of derivation, number of outline/profile data points, user-dependency, and robustness. Besides, only a few have concentrated on the importance of the relative properties of the particle and surface.

Some particle shape parameters have been shown to be user-dependent, e.g. the Wadell's Roundness concept. On the other hand, for surface roughness

characterization systems, the user-dependency is mostly minimized through statistical methods. The stability of the surface roughness parameters was confirmed via resolution analysis.

The gap between particle shape and surface roughness parameters in particle-surface system characterization can be satisfied by capturing the relative nature of both components (particle and surface). This can be achieved either by investigating the components in the same format or through the same analytical tools. This study has suggested two perspectives on unified particulate-continuum interface characterization. Conclusions regarding these techniques are provided in Section 6.2.3.

### *6.2.2 Particle Shape and Surface Roughness Parameters*

There are important differences between particle shape and surface roughness characterization methods. The main differences encountered and emphasized in this study are the number of data points utilized and parameter development procedures. Surface profiles attained through profilometer measurement possess an abundant number of data points, typically numbering in the tens of thousands enabling more accurate surface roughness analyses. On the other hand, most particle shape parameters are only based on 5 - 40 outline data points. Obviously, the number of data points utilized for particle outlines are not sufficient. As shown in this study, the particle shape can be greatly distorted with low number of data points. The particle outline can be misrepresented with sharp corners if low number of data points are utilized and quantifying smaller scale measurements, such as roundness along these profiles become inappropriate.

The particle shape parameters selected for this study generally compared the outline to a perfect geometrical shape as the vast majority of the parameters developed do. Although the comparison of a specific shape to an ideal perfect shape, such as a circular outline has physical meaning in most cases considering the nature of the particle-surface interaction, the comparison to a perfect shape resulted in more variation with the combined effect of insufficient number of data points. On the other hand, most of the surface roughness parameters utilized are based on statistical measurements that have established mathematical meanings. The merit of the statistical approaches was observed in the consistency of the conventional surface roughness parameters with surface profile resolution variation.

It was also observed that with some of the particle shape parameters, such as AF, the parameter development relied on a single particle outline resolution. The AF parameter quantified the number and sharpness of the particle corners by representing the particle as an equivalent polygon. The particle polygon was compared to a perfect circle represented by a polygon with the same number of sampling intervals. Since the normalization of the parameter was based on a certain outline resolution, the AF value varied considerably with the number of sampling intervals and particle resolution (see Section 4.3). Intuitively, the estimation errors should be minimized and the parameter values should become more stable as the number of available data points increases. However, the AF parameter behaved unpredictably and result interpretation became problematic as the number of parameter sampling intervals and/or data points representing the outline increased.

A new particle shape parameter, CRR, was developed in this study based on Voronoi diagrams. Although the concept of CRR is not uncommon, the utilization of Voronoi

diagrams for particle shape characterization is introduced in this thesis. The Voronoi diagrams enable the development of the Minimum Zone Circles (Minimum Circumscribing (MCC) and Maximum Inscribing Circles (MIC)). These two concentric circles define the region where particle-surface interaction is relevant. The analysis of CRR with the study materials showed that it is a measure of both macro- and meso-scale.

### *6.2.3 Proposed Techniques for a Unified Particulate-Continuum Interface Analysis*

This study developed and explored real particle (*part*) outline to derived surface (*dsurf*) and real surface profile (*surf*) to derived particle (*dpart*) outline transformation procedures as part of developing a unified system for particle shape and surface roughness analyses for particulate-continuum interfaces in geotechnical engineering. The conversion of *part-dsurf* and *surf-dpart* were both validated to ensure reversibility of the algorithms. Following the transformation process, *dsurfs* derived from real particles (*parts*) were analyzed with *surfs* via surface roughness characterization methods and *parts* were analyzed with *dparts* derived from real surfaces (*surfs*) via particle shape characterization methods. The analyses (*surfs* along with *dsurfs* and *parts* along with *dparts*) did not reflect any abnormal behavior for *dsurfs* or *dparts*. In other words, *dsurfs* behaved similar to *surfs* and *dparts* behaved similar to *parts* utilizing surface roughness and particle shape analyses, respectively. It was suspected that when *parts* are converted to *dsurfs,* surface roughness analysis results could exhibit discrepancy between *surfs* and *dsurfs* values. However, the surface roughness values did not exhibit any clusters for *surfs* and *dsurfs*. Similarly, particle shape analysis results were checked

for dissimilarities for the values of *parts* and *dparts* and none was detected. However, due to the transformation procedures undertaken, there were differences in *part* and *dpart* outlines, as well as between *surf* and *dsurf* profiles. The major difference between *parts* and *dparts* was that *dparts* were more circular in macro-shape due to the procedure applied to transform them from *surfs*, which involves wrapping the *surfs* around a predetermined radius, *rdatum.* In particle unrolling, *dsurfs* resulted in lower peaks and shallower valleys compared to *surfs.* This can be attributed to the origin of the real particle outlines and surface profiles utilized. Due to the processing involved in sand particles, *parts* possessed worn outline perturbations, which transformed into lower peaks and shallower valleys in *dsurfs*; whereas the surface profiles observed were from the original materials that were not involved in any wear process. Nevertheless, the concept of *dsurfs* and *dparts* provides a unified approach to particle-surface interface characterization.

The derived particle and surface approach proposed in this thesis is applicable to all scales, i.e. it is non-dimensional. The main focus of application in this thesis was soil to man-made interface; however, the method may also be applicable to natural processes such as fault gauges, filled fractures, thrust fault occurring in scales of km's.

An alternative unified classification system was introduced in Chapter 5; where new particle shape and surface roughness parameters were derived based on the surface roughness and particle shape characterization methods, respectively. For example, based on the concepts of *SI* (originally a particle shape parameter), a new parameter *SI-surf* was developed for surface roughness analysis. The results showed that the values of *SI* for *parts* and *dparts* correlated well with the values of *SI-surf* for the corresponding

*dsurfs* and *surfs.* The main advantage of this second assessment method is for particle characterization. As verified by the resolution analyses, the existing particle shape parameters are highly dependent on the resolution of the particle outline and/or the sampling interval. With the proposed method, particle characterization can be accomplished using parameters based on more stable statistically based concepts, such as $R_a$*-part,* $R_p$*-part,* $R_n$*-part.* As analyzed, the stability of the surface roughness parameters (e.g. $R_a$, $R_p$, $R_n$) is maintained as they are converted to new parameters for particle shape analysis (e.g. $R_a$*-part,* $R_p$*-part,* $R_n$*-part*). Also, along with its resolution dependence limitations, particle shape parameters convey different concepts to surface roughness characterization.

The study of derived particles and surfaces has important outcomes relevant to particulate-continuum interfaces encountered in geotechnical engineering. Primarily, in any particulate-continuum interface, e.g. Ottawa 20/30 sand and geotextile interface, both components of the interface can be evaluated with the same selected particle shape or surface roughness method. For example, both the Ottawa sand and the geotextile interface can be assessed based on the Shape Factor with geotextile surface converted to a *dpart* or based on $R_q$ (root mean square roughness parameter) with the Ottawa sand outline converted to a *dsurf.* Thus, rather than trying to evaluate the interface roughness based on a single SF parameter for the Ottawa 20/30 sand and a $R_q$ parameter for the geotextile surface, the researcher can use the same assessment technique for both components. The results of the analysis showed no evidence of complications regarding the conversion of *surfs* into *dparts* or the conversion of *parts* into *dsurfs.* Another method introduced in this study was the development of surface parameters based on the same concepts of particle shape parameters and vice versa. To utilize this technique, Ottawa sand can be analyzed using the Shape Index (SI)

particle shape parameter and the geotextile surface can be evaluated using the newly developed SI-surf parameter. Both results are based on the same concept with different inputs and intermediate calculations

This study has shown that for the existing literature on particle shape and surface roughness, the latter discipline offers more stability and less resolution dependence. For the unified particulate-continuum interface characterization methods proposed in this thesis, the preferable choices are surface roughness parameters with *surfs* and *dsurfs* (Chapter 4) or the application of the particle shape parameters developed from surface roughness parameters with *parts* and *dparts* (Chapter 5).

## 6.3 Recommendations

Although this thesis has attempted to cover and analyze existing particle shape and surface roughness literature and to develop a new approach for a unified particle-surface characterization scheme, further study on the presented concept is required to develop it into a widely used practice. Based on the conclusions of this study, recommendations for future studies are provided below.

In the Centroid Trace method, the particle was assumed spherical and the only particle parameter considered was the diameter ($D_{50}$) in 2D. However, since both surface profiles and particles are 3D in nature, their interaction is more complex than simulated by 2D. Thus, CT method needs to be extended to a 3D analysis. In addition, rather than approximating the contacting particle by a perfect spherical shape, the CT method should be improved for real particle outlines. In particulate-continuum interfaces, several

particles are in contact with the surface profile resulting in additional particle mass characteristics and mechanisms to be effective in relative roughness determination. In further improvements of the CT method, these characteristics of the particulate-continuum interfaces should also be incorporated in the CT method and a parameter that quantifies the CT mechanism should be developed

The centroid trace of a particle rolling over any surface profile provides a measure of the interaction between the particle and the surface. This interaction manifests itself as friction at the macro-scale. As mentioned in Chapter 5, part of this study included the development of a perfect surface for any particle outline such that the centroid trace of the particle is a straight line when the particle rolls over its corresponding perfect surface. The system providing a perfectly straight centroid trace can be analyzed as an ideal condition. In other words, similar to a circular particle rolling over a straight line, or a square outlined particle rolling over a catenary, these systems provide a gauge of least resistance. This least resistance case can provide more insight into particle-surface interface characterization.

In relation to particle shape parameters, a joint effort can be arranged to establish a coherent nomenclature in particle shape analysis. There is confusion of nomenclature even for the simplest particle shape parameters; elongation and aspect ratio. Some authors use the two terms as synonyms, whereas others refer to them as different particle shape parameters (Almeida-Prieto, 2003). In most of the particle shape parameter studies, little emphasis is given to image acquisition and details are mostly unspecified. This problem can be overcome by specifying a standard for image acquisition so that the shape characterization can be more reliable. A standard

guideline in image acquisition would also enable and enhance integration of different studies.

The existing shape parameters need to be improved to perform better with resolution. In general, more data points should be used for particle shape analysis to enhance the stability of the parameters. It is preferable to utilize a combination of particle shape parameters to effectively describe the particle shape due to the multi-scale nature of particle shape. No single parameter has been developed to capture all scales of particle shape. In addition, particle shape parameters should be derived based on the process of interest. The three scales of particle shape, i.e. macro-, meso-, and micro-, hold varying degrees of significance in different processes. This aspect of particle shape should not be overlooked when developing parameters for a specific application.
In particle shape analysis, statistical tools should be integrated to better conceive the behavior of the shape parameters. For example, a better analysis can be done by using more than 50 particles and then plotting the cumulative number of particles versus the normalized factors to determine whether the distribution of the parameter resembles a normal distribution. If it does not, then the result may mean that the particle shape parameter is insensitive in detecting the variability of grains. Similarly, with more than 50 particles and already developed particle shape parameters, cluster analysis can be used to group the existing shape parameters and to identify those that represent the macro-, meso-, and micro-scale features. From these shape parameter groups, three parameters that are most correlated with the other group members can be chosen. Although cluster analysis was introduced in this study, it was acknowledged only as a guide. Another statistical tool that is useful in particle shape analysis is principal component analysis, which can be used to reduce the number of variables with minimal loss of information. As a result of the principal component analysis, new parameters as

a linear combination of several different scale shape parameters can be derived. In the author's opinion, it is also important that a shape parameter is based on several measures rather than single extreme measures along the surface profile. In other words, rather than relying on a small number of measurements of the outline (e.g. for the aspect ratio, only length and width are considered), parameters that take into account more data points should be favored.

Since most of the available surface roughness characterization parameters are defined statistically, they do not convey a physical meaning. A study investigating the correlations between the existing surface roughness parameters and applications can be beneficial in order to observe which statistical parameter conveys the most information regarding a specific process. Another problem with surface roughness parameter is the abundance of parameters used, as in particle shape analysis. Additionally, most of the surface roughness parameters can be derived from the other surface roughness parameters, which makes them impractical and dependent.

The most important recommendation of this study is to further study the application of derived particles and derived surfaces with a more exhaustive study material set to further investigate the benefits of derived particles and surfaces in the understanding of interfaces. The proposed derived particle and surface technique provides a unified approach to both particle shape and surface roughness in particulate-continuum surfaces. This system can be enhanced by observing the behavior of several particles and surfaces with other particle shape and surface roughness parameters. For a much larger number of study materials and methods, statistical tools can be used to acquire meaningful results.

Although this study proposes a new method for evaluating the performance of particulate-continuum surfaces, it does not support the results with any laboratory experiments. In the author's view, laboratory tests are required for verification before accepting any idea as a standard application. However, note that in any laboratory test, factors other than particle shape and surface roughness cannot be eliminated. Thus, care should be taken to isolate the effect of particle shape and surface roughness by controlling the other factors and setting them to ideal constant values. A large number of laboratory tests would be required to isolate the effect of particle shape and surface roughness. Laboratory experiments can be performed to measure the interface friction between any particulate-continuum system. As stated in this study, any particulate-continuum system can be analyzed with the particle component as *part* and the contacting surface component as *dpart* using a particle shape parameter or with the particle component as *dsurf* and the contacting surface component as *surf* using a surface roughness parameter. In the first case (system analyzed as *part* and *dpart)*, the ratio of the appropriate particle shape parameter for the *part* and *dpart* can be investigated for its correlation with the interface friction. It is important to recognize the importance of different feature scales in both components of the particulate-continuum system. In other words, in order for a thorough study, more than a single parameter may be correlated with the interface friction. Another study that requires laboratory testing is the quantification of wear in a particulate-continuum surface. Upon contact and friction between the particle and surface in a particulate-continuum surface, both components show different degrees of wear. The difference between an accepted parameter ratio before and after friction can be an indication of the amount of wear that occurs during friction in particulate-continuum interfaces. The correlation of this ratio difference to the wear amount, in terms of mass, can also be investigated.

# APPENDIX A

# TABLE OF MATHGRAMS

**Table A.1 –** Table of the mathgrams and abbreviations utilized in the study.

| PROCESS | Mathgram Name | Function | Size (kb) | Mathgrams called | Input | Output | Enhancement over Previous Implementation |
|---|---|---|---|---|---|---|---|
| Grayscale Image to matrix conversion | one | Convert *.bmp into a matrix. | 48 | -- | A, thr | M | |
| Matrix to outline conversion | outline | Gives the outline in clockwise direction. | 48 | one | A,thr, dist | P | Concavity considered |
| Outline enhancement | zeroangle counterclockwise | Reverses the outline into counterclockwise direction, sorts in increasing angle order starting from 0°. | 48 | outline | P | P1 | Increasing angle |
| Particle shape analysis | centroid | Locates particle centroid from a [nx2] outline matrix based on area based method. | 48 | -- | P1 | cent =(xc,yc) | - |
| Particle shape analysis | Leastcircle | Provides the ($x_c$,$y_c$,r) based on averaging and minimizing the distance between the centroid and data points. | 48 | -- | P1 | (xc,yc,r) | - |
| Particle shape analysis | perimeter | Calculates the sum of distance between the data points. | 48 | -- | P1 | per | - |
| Outline enhancement | ParticleShape | Based on the number of sampling intervals required and the angle of each data point, it locates every sampling interval between the correct pair of data points. | 48 | -- | P1, N, cent | P2 | - |
| Outline enhancement | SampleParticle | Finds the intersection of each sampling point with the outline assuming a linear connection between data points if no data point is located at that specific sampling angle. | 48 | ParticleShape | P1 | P3 | - |

**Table A.1 (continued)**.

| | | | | | | | |
|---|---|---|---|---|---|---|---|
| Derived Surface Calculation | XvsR | Divides the particle perimeter into N intervals to obtain the distance interval on the derived surface profile –x axis. The radius of each point is taken as elevation and displayed in the –y axis. | 221 | SampleParticle | P1 | Sder | - |
| Derived Particle calculation | modres | Modifies the resolution of the surface profile (from 0.001mm to 0.004mm) by averaging subsequent 4 surface profile data points and plotting as a single data point. | 199 | -- | S | S1 | - |
| Derived Particle calculation | bringtozero | Takes 15mm long portion of the 0.004 mm resolution surface profile starting from point with index ibeg and shifts the 15 mm long profile to 0 mm. | 199 | -- | S1,res, ibeg | S2 | - |
| Derived Particle calculation | wrap | Divides the horizontal axis to the number of intervals (*int*) input and determines between which data points is every vertical sampling test line. | 199 | bringtozero | S1,res,ibeg, int | S3 | - |
| Derived Particle calculation | SampleSurface | Finds the intersection of each sampling point with the surface profile assuming data points are connected linearly if no data point is located at that specific sampling angle. | 199 | wrap | S1,res,ibeg, int | S4 | - |
| Derived Particle calculation | rotate | Rotates the surface profile, S4, around the starting point so that the start and end data points of the surface profile form a line parallel to the –x axis. | 199 | SampleParticle | S1,res,ibeg, int | Srot | - |

**Table A.1 (continued)**.

| | | | | | | | |
|---|---|---|---|---|---|---|---|
| Derived Particle calculation | particle | Wraps Srot to obtain the derived particle. Details are provided in the Derived Particle Section. | 199 | rotate | S1,res,ibeg, int | Pder | - |
| Voronoi Diagram Extraction | polygonextract | Starting at the right top end of the image, the mathgram locates the extreme outline points at the right, bottom, top and left parts of the outline. | 328 | -- | P1,E,w | | - |
| Voronoi Diagram Extraction | convexhull | Outputs the convexhull based on the polygonextract mathgram output. | 328 | polygonextract | P1,E,w | CH | - |
| Voronoi Diagram Extraction | line | Outputs m and b for the line equation y = mx +b between two points. | 328 | -- | A1 | (m,b) | - |
| Voronoi Diagram Extraction | edge | Outputs m and b for the lines connecting the edges of the convexhull | 328 | line | CH | L | - |
| Voronoi Diagram Extraction | intpoints | Outputs the intersection point coordinates of two lines. | 328 | -- | L2 | (xint,yint) | - |
| Voronoi Diagram Extraction | equidist | Outputs the (m,b) coefficients for the equidistant (ED) lines for every outline edge in Voronoi Diagram Extraction. | 328 | line | CH | LEQ | - |
| Voronoi Diagram Extraction | FEpoint | Calculates the intersection point where the equidistant line intersects the polygon other than its originating location on one of the edges. | 328 | intpoint | CH | FE | - |
| Voronoi Diagram Extraction | centers | Outputs the intersection points between the ED lines, which are candidates for the NEAR and FAR centers of the Voronoi Diagram. | 328 | equidist, intpoint | CH | C | - |

**Table A.1 (continued)**.

| | | | | | | | |
|---|---|---|---|---|---|---|---|
| Voronoi Diagram Extraction | nearandfarcenters | With c=0, the output is NEAR centers based on the convexhull, with c=9, the output is the FAR centers. | 328 | equidist, edge, centers | CH, c | NC or FC | - |
| Voronoi Diagram Extraction | FARcenters | Outputs the FAR center coordinates while updating the convexhull at each iteration by dropping common vertices until three or less vertices are left. | 328 | line,intpoint | CH | TFC | - |
| Voronoi Diagram Extraction | farthestVORONOI | Outputs the farthest Voronoi Diagram. The results are C1Afar1 with X=1 and C1Afar2 with X=2. | 328 | -- | P1,E,w,X, CH,FE,TFC | C1Afar1 or C2Afar2 | - |
| Voronoi Diagram Extraction | inHULL | Outputs the transformed inner hull, where vertices are updated. | 328 | -- | P1, E, w | AIn | - |
| Voronoi Diagram Extraction | convexINHULL | Outputs the inner convexhull, i.e. the boundary of the largest empty subset of given points. | 328 | -- | AIn, E, w | SIn | - |
| Voronoi Diagram Extraction | nearHULL | Combines the steps of inHULL and convexINHULL and locates the points of the convex inner hull that correspond to the initial dataset to determine the nearHULL. | 328 | inHULL, convexINHULL | P1, AIn, SIn | NearS | - |
| Voronoi Diagram Extraction | NEARcenters | Outputs the NEAR centers based on the nearHULL output. | 328 | line,intpoint | P1, E, w, NearS | TNC | - |
| Voronoi Diagram Extraction | nearestVORONOI | Outputs the nearest Voronoi Diagram. | 328 | NEARcenters, | P1,E,w, NearS | C1Anear | - |

**Table A.1 (continued)**.

| | | | | | | | |
|---|---|---|---|---|---|---|---|
| Voronoi Diagram Extraction | finitio | The Farthest and Nearest Voronoi Diagrams are superimposed and the candidate MZC centers are located. For every center, MCC and MIC are formed. The center that gives the minimum radial separation between the MCC and MIC is the MZC center. | 328 | -- | P1,E,w,C 1Anear,C 1Afar1 | C1Afin | - |
| Dominant Point Selection | chaincode | Outputs the Freeman chain code. | 113 | one, outline | P | f | - |
| Dominant Point Selection | tehandchin | Outputs the dominant points extracted using Teh and Chin (1989) algorithm. | 113 | -- | x,y,f | TC | - |
| Wadell's Roundness | roundnessnothr | Calculates the arc parameters for pairs of dominant points. | 123 | -- | P, TC, MIC r, MCC r | I | - |
| Wadell's Roundness | concavitytest | Performs a concavity test to determine if the calculated arc centers are inside or outside the convexhull of the particle outline. | 123 | roundnessnothr | P, TC, CH, MIC r, MCC R | CT | - |
| Wadell's Roundness | fixingroundness | Sections of the CT matrix showing "inside" centers are extracted and Wadell's roundness is calculated for the estimated arc parameters. Only segments between pairs of consecutive dominant points are analyzed. Details are provided in Section 3.3.7.1. | 123 | concavitytest | P1, TC, MIC r, MCC r, minthr | R1 | Arc segments with radius smaller than *minthr* input are included in the number of arcs but not the summation of radii. Arc segments with radius larger than MIC radius are not included in the analysis. |
| Wadell's Roundness | roundnesswadell_ concave | All segments between consecutive dominant points are analyzed. Details are provided in Section 3.3.7.1. | 123 | concavitytest | P1, TC, MIC r, MCC r, minthr | R2 | - |

**Table A.1 (continued)**.

| | | | | | | | |
|---|---|---|---|---|---|---|---|
| Sukumaran and Ashmawy Shape Factor and Angularity Factor (SF, AF) | DevCircle | Calculates the chord deflections (chdef) for a perfect circular shape sampled with SF and AF intervals, SAFint. | 156 | -- | SAFint | *chdef* | - |
| Sukumaran and Ashmawy SF and AF | SFandAF | Calculates the SF and AF in %. | 156 | ParticleShape, SampleParticle, DevCircle | P1,N, SAFint | (SF,AF) | - |
| Spike Parameter (SP) | SP | Outputs the SP value based on the method proposed by Hamblin and Stachowiak (1995). | 119 | outline, one, zeroanglecounter clockwise, ParticleShape, SampleParticle | A, r, stpxl, incpxl | SP value | - |
| Spike Parameter Quadratic (SPQ) | spikes(A) | SPQ, spikes(A) measures the radius for each point and index for the spike output, a value of 0 at column 3 means it is inside the least squares circle. | 254 | one, outline,zeroangle counterclockwise , leastsquares,cen troid | P1 | SPQ1 | Goodness of fit test |
| Spike Parameter Quadratic (SPQ) | spikes2(A) | Calculates the location (index,start,middle,end point pixels) for the number of spikes observed in spikes(A). | 254 | spikes | P1 | SPQ2 | - |
| Spike Parameter Quadratic (SPQ) | spikes4(A) | For every spike, the mathgram transforms the coordinates and fits quadratic functions to calculate the apex spike angle. The spike angles are averaged to calculate the final SPQ value. | 254 | spikes, spikes2 | P1 | SPQ | If the number of data points between start and middle point or the middle and en point is smaller than 3 it discards the spike since regression cannot be performed. |
| Boyce and Clark Shape Index (SI) | BC | Calculates the SI in %. | 120 | one, outline, zeroanglecounter clockwise, SampleParticle, centroid | P1, Sint | SI | - |

**Table A.1 (continued)**.

| | | | | | | | |
|---|---|---|---|---|---|---|---|
| Surface Profile Enhancement | changeres | Calculates the resolution of the surface profile and changes it to the desired resolution and length. | 73 | -- | S, res, length | S2 | - |
| Conventional Surface Roughness Parameter Calculation | Parameters | Outputs the conventional surface roughness parameters. | 73 | -- | S2, diapar, res | PAR | - |
| Centroid Trace (CT) Profile Calculation | EffProf | Calculates the Centroid Trace (CT) of the particle rolling over the surface. | 20 | -- | S2, dia, Range, Bugger, Inc | EffP | - |
| Centroid Trace Profile Calculation | Effcombi | Calculates CT over one surface profile with a range of diameters. | 76 | EffProf | S2, Buffer, Inc, res, dia, DiaNum | E | - |
| Centroid Trace Profile Calculation | Effcombiorder | Adjusts all the surface profile lengths for the different parameters to the same length. | 76 | -- | S2, E, Buffer, res, dia, DiaNum | Enew | - |
| Surface Roughness Parameter Calculation for CT profile | Parameterscombi | Calculates the conventional surface roughness parameters for the range of circular particle diameters considered. | 76 | Parameters | Enew, res, dia, DiaNum | Pcombi | - |
| Surface Roughness Parameter Calculation for CT profile | Rn | Calculates the Normalized Roughness Parameter for the CT profiles of the range of diameters. | 76 | -- | Enew, Pcombi, res, DiaNum | NR | - |
| Surface Roughness Parameter Calculation for CT profile | Parametersfinal | Combines the results of Pcombi and NR. | 76 | -- | NR, Pcombi | Pfinal | - |

**Table A.1 (continued)**.

| | | | | | | | |
|---|---|---|---|---|---|---|---|
| Spike Parameter Quadratic (SPQ) for surface profiles | spikessurf | Outputs the original and updated surface profile data points and the corresponding spike number. | 75 | -- | S2 | SPQsurf 1 | - |
| SPQ for surface profiles | spikes2surf | Outputs the spikes start, middle, and point indices and (x,z) data points. | 75 | spikessurf | S2 | SPQsurf 2 | - |
| SPQ for surface profiles | spikes3surf | Updates SPQsurf2 by removing the spikes below the threshold allowable –z value. | 75 | spikessurf, spikes2surf | S2 | SPQsurf 3 | - |
| SPQ for surface profiles | spikes33surf | Locates turning points if present for every spike and updates SPQsurf3 with turning point index points. | 75 | spikessurf, spikes3surf | S2 | SPQsurf 4 | - |
| SPQ for surface profiles | spikes4surf | Fits quadratic polynomial functions to each spike segments. | 75 | spikessurf, spikes33surf | S2 | SPQsurf | - |
| Chapter 5 Surface Roughness Parameters | CRRsurf | Outputs surface roughness parameter CRRsurf based on the concept of the particle shape parameter CRR.. | 59 | -- | S2 | CRRsurf | - |
| Chapter 5 Surface Roughness Parameters | SPsurf | Outputs surface roughness parameter SPsurf based on the concept of the particle shape parameter SP. | 96 | -- | S2, r, stpxl, incpxl | SPsurf | - |
| Chapter 5 Surface Roughness Parameters | SIsurf | Outputs surface roughness parameter SIsurf based on the concept of the particle shape parameter SI. | 113 | -- | S2, rows | SIsurf | - |
| Chapter 5 Particle Shape Parameters | Surf parameters for parts | Outputs diapar for Rn-part, Ra-part, Rq-part, Rmax-part, and Rn-part. | 111 | -- | P1, diapar-part | PAR-part | - |

**Table A.1 (continued)**.

| INPUT AND OUTPUT ABBREVIATIONS USED | |
|---|---|
| A | The grayscale particle image captured in *.bmp format. |
| Thr | Threshold value between 0 and 255 required to capture the outline from the grayscale image, taken as 255. |
| M | Array of integers ranging between 0 and 255 obtained upon reading the grayscale image. |
| P | The particle outline matrix in *.prn format, clockwise direction. |
| N | Number of rows in outline matrix. |
| R | Radius of a circle with the same perimeter as the particle outline. |
| Dist | The threshold distance value for concavity analysis. |
| P1 | Angle sorted outline in counterclockwise direction starting from 0°. |
| cent | $(x_c,y_c)$, i.e. the –x and –y coordinates of the particle centroid. |
| Per | Particle perimeter. |
| N | Number of data points required for the particle outline. |
| P2 | (nx7) matrix, where the columns are ($x_i$, $y_i$, $x_{i+1}$, $y_{i+1}$, $asample_j$, $apoint_i$, $apoint_{i+1}$). The test line at the angle of $asample_j$ is located between point *i* and point *i+1* located at $apoint_i$ and $apoint_{i+1}$ degrees, respectively. |
| P3 | (nx8) matrix, where the columns are ($x_{int}$, $y_{int}$, $asample_j$, $r_i$, $x_i$, $y_i$, $x_{i+1}$, $y_{i+1}$ ). The sampling line at $asample_j$ intersects the outline at point *int* with ($x_{int}$, $y_{int}$) coordinates and $r_i$, stands for the distance of point *int* to the particle centroid. |
| Sder | The derived surface profile in (Nx2) matrix format. |
| S | The profilometer output in 0.001mm resolution and 40-mm length. |
| S1 | Modified surface profile with 0.004mm resolution and 40-mm length. |
| res | Resolution of the surface profile. |
| ibeg | The surface profile data point index from where 15-mm length portion is taken. |
| S2 | Modified surface profile with 0.004mm resolution and 15-mm length. |
| S3 | (nx7) matrix with the columns showing ($i,i+1,x_i,z_i,x_{i+1},y_{i+1},xS_j$). The surface profile points with indices of *i* and *i+1* are located at each ends of the sampling interval located at the –x location of $xS_i$. |
| S4 | The surface profile obtained with the intersection points of the sampling intervals. |
| Srot | Rotated S4 surface profile such that start and end data points are collinear. |
| Pder | Derived particle outline. |
| SAFint | Sampling intervals for Sukumaran and Ashmawy (2001) and Ashmawy (2001) and Ashmawy Shape and Angularity Factor Calculation. |
| E | The pixel margin away from the extreme points located on the outline for polygonextract mathgram. |
| w | The number of significant points for the outline points. |
| CH | [n+1,3] matrix, where n is the number of convexhull points extracted and the first and last rows are the same. The first and second column represent [x,y] coordinates of the located convexhull points and the 3rd column displays the index of the number. |
| m,b | The slope and constant for the line equation y = mx+b. |
| A1 | (2x2) matrix for the [x,y] coordinates of two points. |
| L | (nx2) matrix, where n is the number of lines formed between the convexhull points. The first and second columns correspond to m and b for the equations. |
| L2 | (2x2) matrix. The first row is the $(m_1,b_1)$ values for the first line. The second row is the $(m_2,b_2)$ values for the second line. |

**Table A.1 (continued)**.

| | |
|---|---|
| LEQ | (nx2) matrix, where n is the number of convexhull points. The first and second columns correspond to m and b coefficients of the equidistant lines. |
| FE | (nx3) matrix, where n is the number of convexhull points. The first and second columns represent –x and –y locations of the intersection points. The third column is the index for the edge from where the equidistant line originates. |
| C | (nx2) matrix, where n is the number of candidate centers obtained by the intersection of Equidistant lines. The first and second column represent the (x,y) coordinates of the intersection points. |
| NC | The (x,y) coordinates of the NEAR centers for the Voronoi Diagram. |
| FC | The (x,y) coordinates of the FAR centers for the Voronoi Diagram. |
| TFC | (nx5) matrix, where n is the number of FAR centers. The 1st and 2nd columns are (x,y) locations of the FAR centers. The 3rd and 4th columns designate the vertex indices that form the edge for which the FAR center is valid. The 5th column is the iteration number the center is located. Note that when the FAR centers are located, several iterations are performed since the edges that are common to two of the centers are dropped and the convexhull is updated until the point where 3 or less vertices remain forming the convexhull. |
| C1Afar1 | The Farthest Voronoi Diagram points. |
| C1Afar2 | (x,y,min radius, MCC radius) of the center that gives the minimum radius if the vertices are used as centers. |
| AIn | Transformed outline to form the inner hull. |
| Sin | Convex inner hull based on AIn. |
| NearS | (n+1,3) matrix, where n is the number of near hull vertices. The data points of the original dataset corresponding to the vertices of the Convex Inner Hull are taken as vertices of the inner hull and the (x,y) coordinates are located in the first 2 columns. The third column is the near hull vertex index. Note that the first and last points of the NearS matrix are the same. |
| TNC | (nx5) matrix, where n is the number of NEAR centers. The 1st and 2nd columns are (x,y) locations of the NEAR centers. The 3rd and 4th columns designate the vertex indices that form the edge for which the NEAR center is valid. The 5th column is the iteration number the center is located. |
| C1Anear | Nearest Voronoi Diagram points. |
| C1Afin | (5x1) matrix. The row values correspond to the MZC $x_c$, MZC $y_c$, MCC radius, MIC radius, MZC radius from the row =1 to row = 5. MZC, MCC, and MIC stand for Minimum Zone Circles, Minimum Circumscribing Circle, and Maximum Inscribing Circle. |
| f | (nx3) matrix, where n is the number of data points. The 1st and 2nd columns correspond to the (x,y) coordinates of the data points and the 3rd column is the calculated Freeman chain code. |
| TC | (nx3) matrix, where n is the number of dominant points extracted by the Teh and Chin (1989) method. The 1st column is the index of the number in the original data set. The 2nd and 3rd columns are the (x,y) coordinate of the dominant point. |
| I | (nx8) matrix, where n is the number of dominant points. The 1st and 2nd columns indicate the indices of the pair of consecutive dominant points between which arc is fitted. The 3rd, 4th, and 5th columns correspond to the $x_c$, $y_c$, and radius values for the estimated arc, respectively. The 6th column is the total curve error. The 7th column is the maximum segment error divided by the corresponding radius, and finally the 8th column is an index representing whether an arc could be fitted or not possible. |
| CT | (nx11) matrix, where n is the number of dominant point pairs between which arc segments could be fitted. The first 7 columns of CT correspond to the first 7 columns of the "I" matrix for the estimated arc-fitted pairs. The 8th and 9th columns are the (x,y) coordinates of the intersection points. The 10th column designate whether the arc center is inside or outside the convexhull, i.e. checks concavity. |
| minthr | Minimum radius value that is to be considered in the Wadell's Roundness calculation. |

**Table A.1 (continued)**.

| | |
|---|---|
| R1 | Wadell's Roundness value calculated using *fixingroundness* mathgram. |
| R2 | Wadell's Roundness value calculated using *roundnesswadellconcave* mathgram. |
| SAFint | The number of intervals for Sukumaran and Ashmawy (2001) Shape and Angularity Factor. |
| chdef | (nx1) vector, where n corresponds to SAFint. The values are the calculated chord deflections for a perfect circular image. |
| SF | Sukumaran and Ashmawy (2001) Shape Factor (%). |
| AF | Sukumaran and Ashmawy (2001) Angularity Factor (%). |
| r | The number of outline points is divided by this constant to determine the maximum stepsize for SP calculation. |
| stpxl | The smallest pixel stepsize that is increased until it is equal or larger than (# rows / r). |
| incpxl | The size of the increment pixel, which is added to stpxl at each iteration to reach the maximum stepsize (# rows / r). |
| SP | Hamblin and Stachowiak (1995) Spike Parameter. |
| SPQ1 | (nx4) matrix, where n is the number of outline data points. The $1^{st}$ and $2^{nd}$ columns are the (x,y) coordinates of the outline data points, the $3^{rd}$ column designates the radius from the least squares center to the outline data point, and the $4^{th}$ column is the spike index. The spike index is 0 if the data point is inside the least squares circle, and non-zero if outside the least squares circle. |
| SPQ2 | (nx11) matrix, where n is the number of spikes observed. The $1^{st}$ column specifies the index of the spike. The $2^{nd}$ , $3^{rd}$ , and $4^{th}$ columns correspond to the index, -x coordinate, and –y coordinate of the spike's middle (apex) point, respectively. The $5^{th}$ column is the radius for the apex, the $6^{th}$, $7^{th}$, and $8^{th}$ columns correspond to the index, -x coordinate, and –y coordinate of the spike's start point, respectively. The $9^{th}$, $10^{th}$, and $11^{th}$ columns are the spike's end point's index, -x coordinate, and –y coordinate, respectively. |
| Sint | The number of intervals for the calculation of Boyce and Clark Shape Index (SI). |
| SI | Shape Index value (%). |
| diapar | The diameter of the particle for normalized surface roughness parameter ($R_n$) calculation. |
| res | Resolution of the surface profile. |
| PAR | (6x1) vector. The $1^{st}$ row is the "diapar". The remaining rows correspond to the following conventional surface roughness parameters; $R_a$, $R_q$, $R_p$, $R_{max}$, and $R_n$. |
| dia | The diameter of the desired circular particle diameter rolling over the surface profile. |
| Range | The section of the surface profile omitted to prevent edge effects based on the circle radius. |
| Buffer | Additional section of the surface profile removed to prevent edge effects. |
| Inc | A dummy value to initiate the CT calculation mathgram. |
| DiaNum | The number of range of diameters to calculate CT profile. |
| EffP | The CT profile for a single particle rolling over the surface profile. It is a (nx2) matrix, where n is the number of surface profile data points after Range and Buffer sections are removed from the 15-mm surface profiles. The $1^{st}$ and $2^{nd}$ columns correspond to –x and –z values for the CT profile. |
| E | CT profiles for a range of particle diameters considered. It is a (nxc) matrix, where n corresponds to the number of surface profile data points for the longest CT surface profile (for the smallest diameter). The number of columns is twice the DiaNum. The $1^{st}$ and $2^{nd}$ columns represent the CT –x and –z surface profile data points for the smallest diameter, the $3^{rd}$ and $4^{th}$ columns represent the CT –x and –z surface profile data points for the second smallest diameter, and etc. |
| Enew | Adjusted CT profiles to the shortest length in E matrix. It is a (nxc) matrix, where n corresponds to the number of surface profile data point for the shortest profile length in "E", and c is twice the DiaNum. |

**Table A.1 (continued)**.

| | |
|---|---|
| Pcombi | (5xDiaNum) matrix. The 1st column is the surface roughness parameters calculated for the first smallest diameter and 2nd column is the second smallest diameter, and so on. The 1st row represents the diameter of the rolling circular particle, the 2nd, 3rd, 4th, and 5th rows are the $R_a$, $R_q$, $R_p$, and $R_{max}$ surface roughness parameter calculated for the CT profile |
| NR | (1xDiaNum) matrix. The 1st column is the surface roughness parameters calculated for the first smallest diameter and 2nd column is the second smallest diameter, and so on. The single row values correspond to the $R_n$ surface roughness values for the CT profile. |
| Pfinal | (6xDiaNum) matrix. It is the same as Pcombi except the added last row representing the $R_n$ surface roughness parameter for the CT profile. |
| SPQsurf1 | (nx4) matrix., where n is the number of surface profile data points. The 1st and 2nd columns represent the original surface profile –x and –z surface profile data points, respectively. The 3rd column is the updated the –z surface profile data points after removing the slope, and the 4th column is the spike index. The 4th column has 0 if the 3rd column –z values is below the average surface elevation of the updated profile. |
| SPQsurf2 | (nx11) matrix, where n corresponds to the number of spikes located on the surface profile. The 1st column is the spike's index. The 1st, 2nd, and 3rd columns represent the index, -x, and –z surface profile values for the middle point, the 4th column is the elevation value for the middle point. The 5th, 6th, and 7th columns correspond to the index, -x and –z surface values for the start point. The 8th, 9th, and 10th columns display the index, -x, and –z surface values for the end point. |
| SPQsurf3 | (nx11) matrix, where n corresponds to the number of updated spikes above the allowable –z elevation. The columns represent the same values as SPQsurf2. |
| SPQsurf4 | (nx16) matrix, where n is the same as SPQsurf3. The columns represent the same values as SPQsurf3, however, if turning points are located for a particular spike, the corresponding start and end points are assigned updated values. |
| SPQsurf | The SPQ-surf value. |
| CRRsurf | Surface roughness parameter based on the concept of the particle shape parameter CRR. |
| SPsurf | Surface roughness parameter based on the concept of the Hamblin and Stachowiak Spike Parameter. |
| rows | The number of data points for the surface profile. |
| SIsurf | Surface roughness parameter based on the concept of the Boyce and Clark Shape Index. |
| diapar-part | Diameter of a circular particle for the calculation of $R_n$-part. |
| PAR-part | (6x1) vector. The 1st row is the "diapar-part". The remaining rows correspond to the following conventional surface roughness parameters modified to calculate the particle shape; $R_a$-part, $R_q$-part, $R_p$-part, $R_{max}$-part, and $R_n$-part. |

# APPENDIX B

# THE SQUARE WHEEL

In their interesting work, Hall and Wagon (1992) revisited the problem of square wheel. The primary goal of the study was to investigate the relationship between the geometrical shapes of the wheels and the surfaces they roll.

As mentioned previously, Centroid Trace (CT) method provides the user with the centroid path of a 2D circular particle rolling over any surface. A straight centroid trace can be obtained for several conditions. The simplest case is a perfect circle rolling over a flat surface. Another interesting example is a square wheel rolling over a catenary profile. As the first case, second case provides a smooth ride, i.e. with a straight centroid trace along the length of the catenary. Inspired by this concept, Hall and Wagon (1992) further explored several particle shapes (termed as wheels in Hall and Wagon, 1992) and their corresponding perfect surfaces (termed as roads in Hall and Wagon, 1992).

The mathematical details for this study are provided in Hall and Wagon (1992). The main assumption in this model is that enough friction between the road and the wheel (i.e. particle and surface in this study) exists so that no slipping occurs. Thus, the motion of the wheel is pure rolling.

Hall and Wagon (1992) have also provided closed form solutions for several types of wheel – road combinations; including road solutions for polygonal, off-centered elliptical, and centered elliptical wheels; and wheel solutions for tilted sawtooth, elliptical, and cycloidal roads.

The mathematical background provided by Hall and Wagon (1992), personal discussions with Stan Wagon, and programming language Mathematica 4.1 were used

to obtain a wheel-road, i.e. particle-surface, algorithm for this study. The square wheel concept is presented in this study as a tool that could be made use of via laboratory experiments. Any wheel-road combination provided in this study clearly provides the smoothest rolling over any surface with a straight-line centroid trace.

The perfect roads for *parts* and *dparts* analyzed in this study are provided in Figures B.1 – B.7. Note that the roads are shown for one full rotation of the particle and for each particle-surface combination, 5 locations, every 72°, are provided.

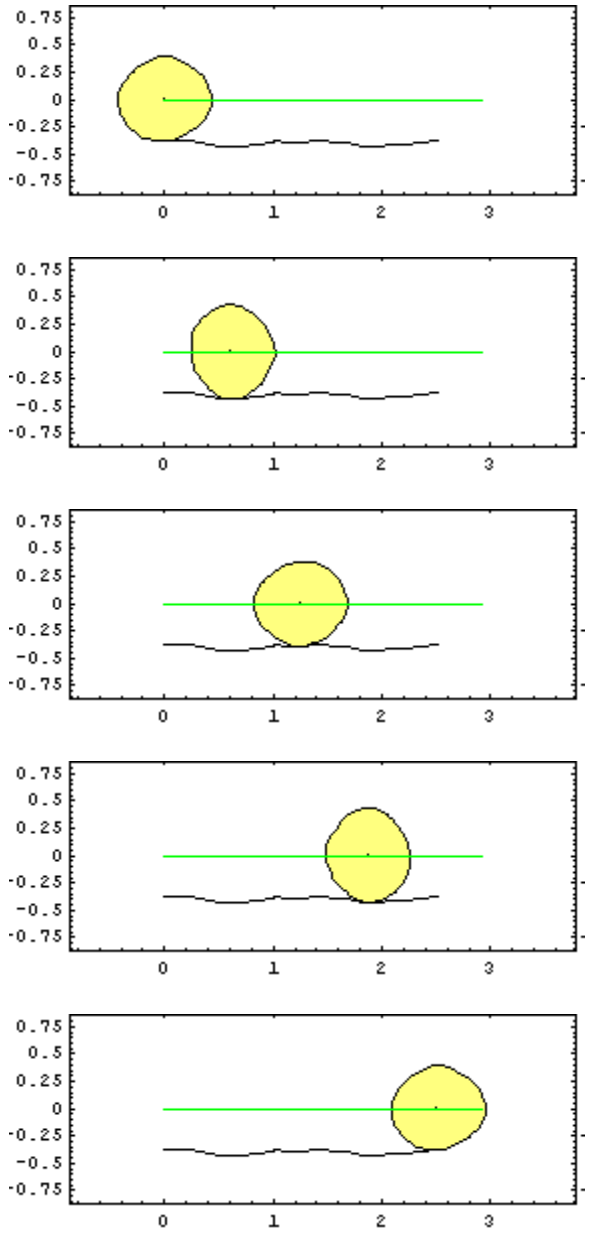


**Figure B.1 -** Particle *p1* rolling over its perfect road with a straight line centroid trace.

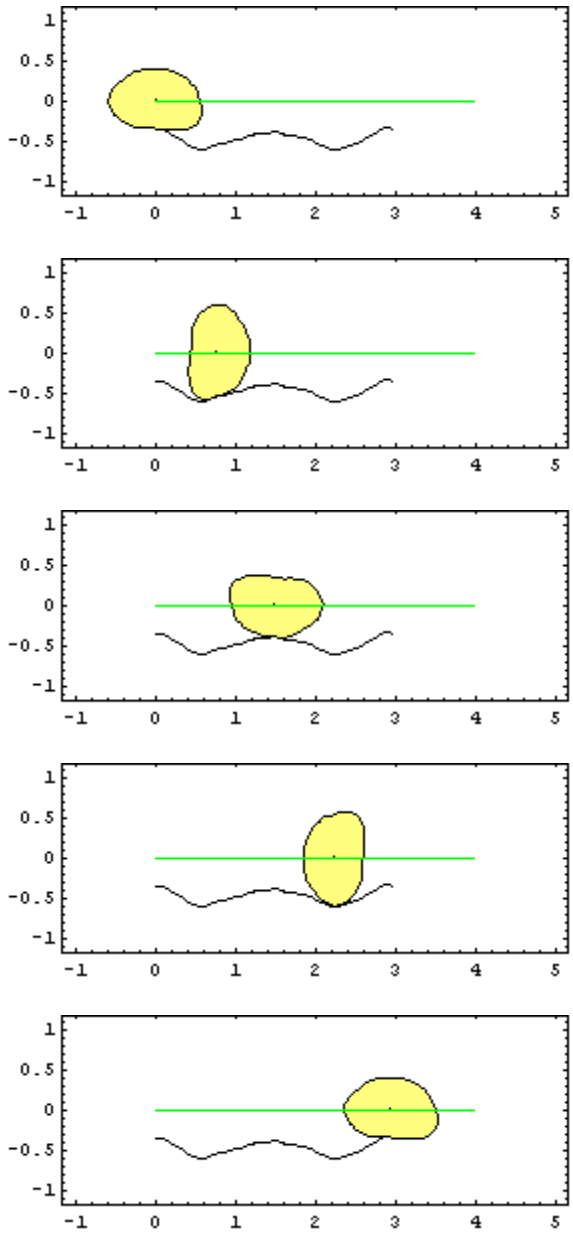


**Figure B.2 -** Particle *p2* rolling over its perfect road with a straight line centroid trace.

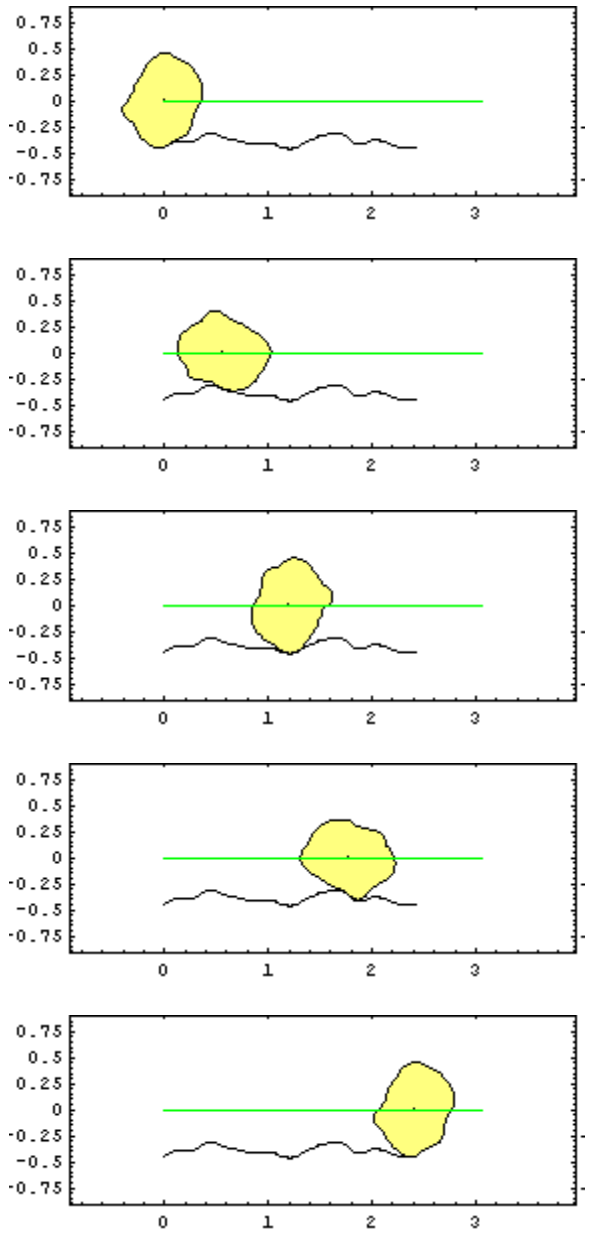


**Figure B.3 -** Particle *p3* rolling over its perfect road with a straight line centroid trace.

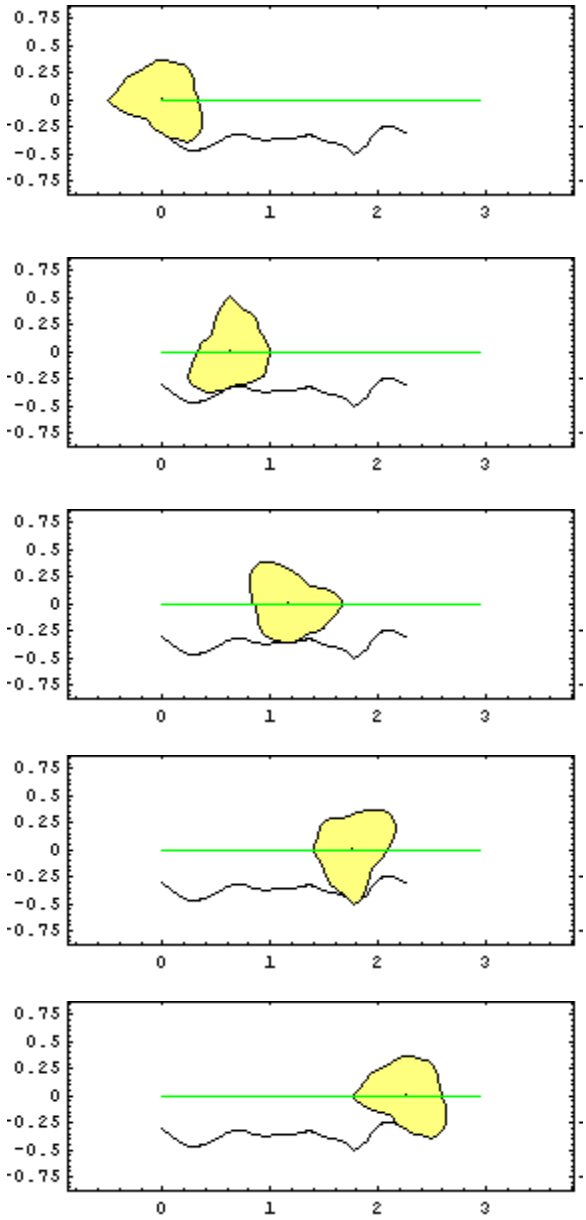


**Figure B.4 -** Particle *p4* rolling over its perfect road with a straight line centroid trace.

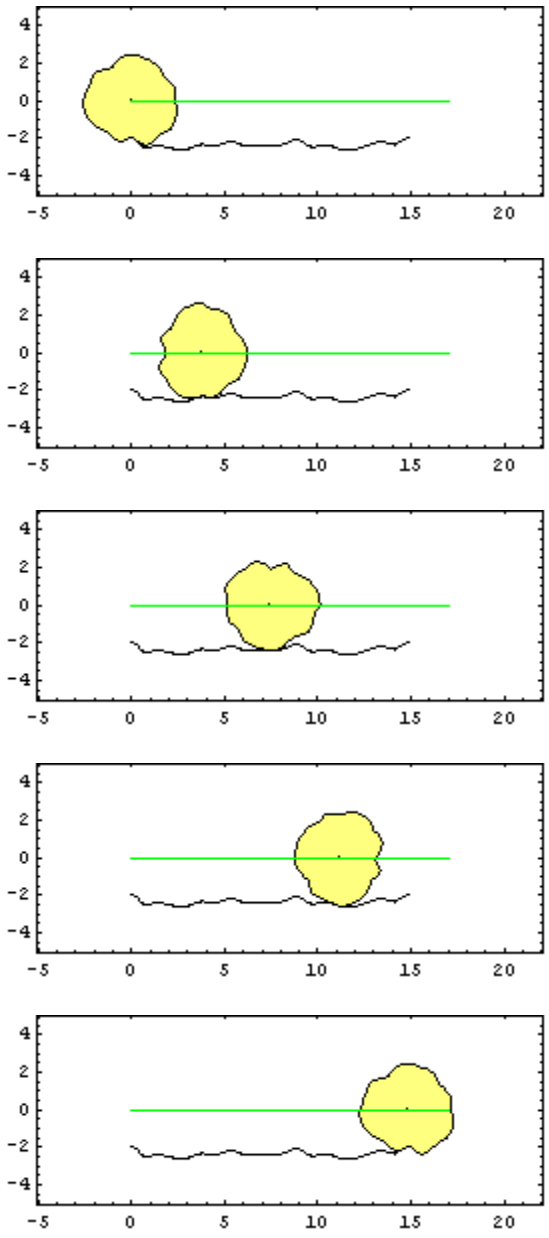


**Figure B.5 -** Particle *concrete-par* rolling over its perfect road with a straight line centroid trace.

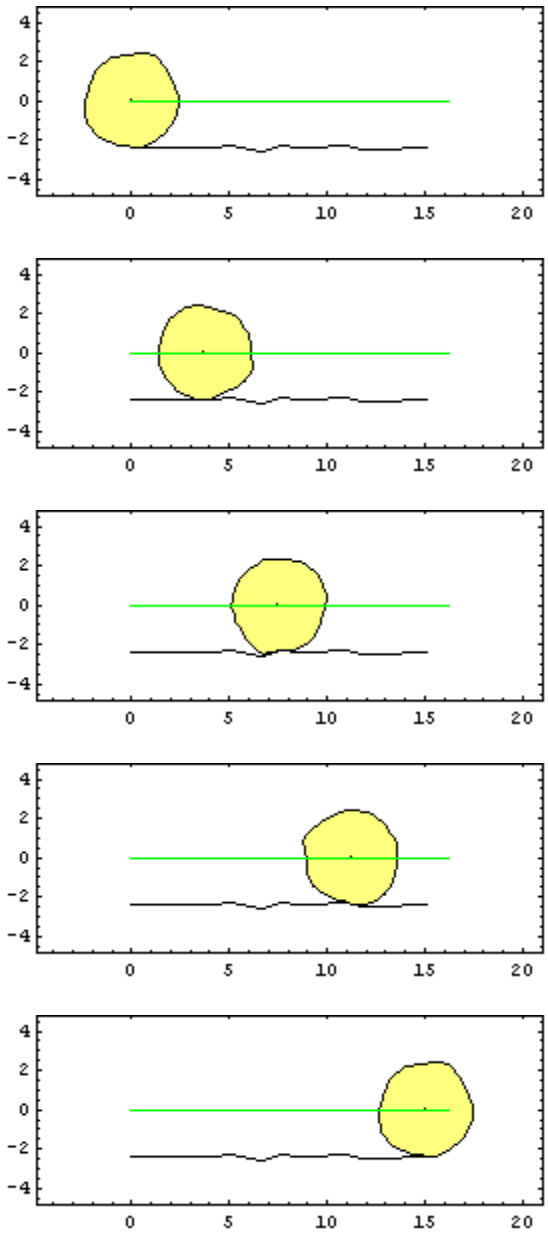


**Figure B.6 -** Particle *HDPE-par* rolling over its perfect road with a straight line centroid trace.

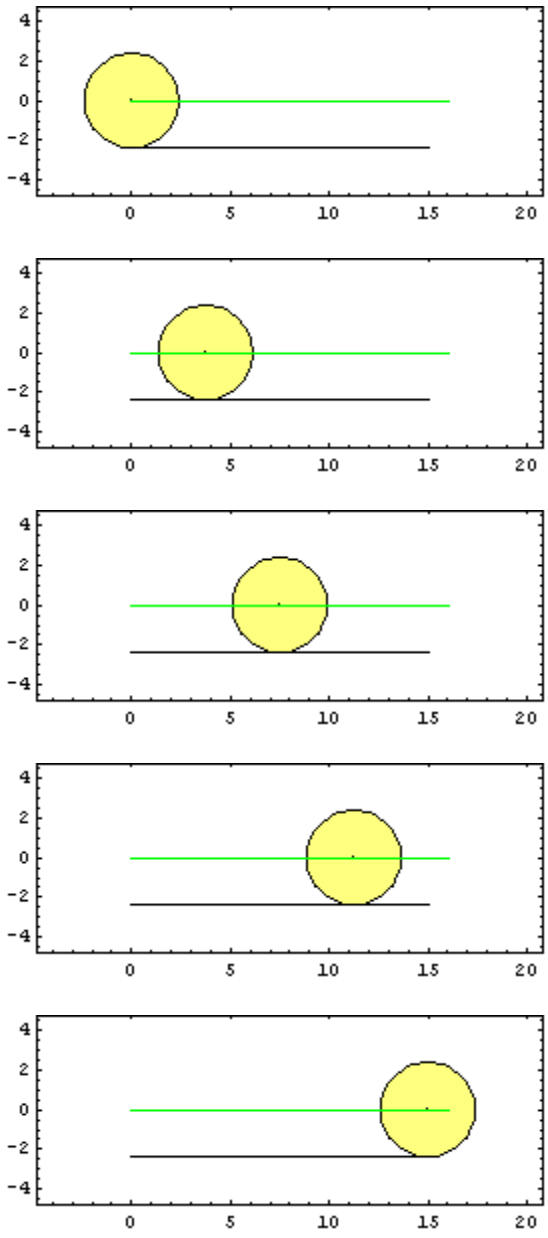


**Figure B.7 -** Particle *steel-par* rolling over its perfect road with a straight line centroid trace.

# REFERENCES


Adamson, A. W. (1982) Physical Chemistry of Surfaces, Wiley, New York.

Allen, T. (1997) Particle Size Measurement – Powder Sampling and Particle Size Measurement, Vol. 1, Fifth Edition, Chapman & Hall, 525 pp.

Almeida-Prieto, S., Blanco-Mendez, J., and Otero-Espinar F. (2004) "Image Analysis of the Shape of Granulated Powder Grains", *Journal of Pharmaceutical Sciences,* Vol. 93, No.3, pp. 621-634.

Angus, H.T. (1979) "The Significance of Hardness", *Wear*, Vol. 54, Issue 1, pp. 33-78.

Ansari, N. and Huang, K. (1991) "Non-parametric Dominant Point Detection", *Pattern Recognition*, Vol. 24, pp. 849-862.

ANSI/ASME Y 14.5M. Dimensioning and Tolerancing, New York: American National Standards Institute; The American Society of Mechanical Engineers, 1982.

Antoine, R. and Courard, L. (1996) "Perforation Strength of Geosynthetics and Sphericity of Coarse Grains: A New Approach", *Geotextiles and Geomembranes*, Vol. 14, pp. 585–600.

Ashmawy, A. K. (2004), Personal Communication.

ASME. (1995) Surface Texture (Surface Roughness, Waviness, and Lay) B46.1, New York NY, 112 pp.

ASTM D 2488-90 (1996) Standard Practice for Description and Identification of Soils (Visual-Manual Procedure). ASTM*,* Vol. 04.08, *Soil and Rock.*

Athanasopoulos, G. A. (1993) "Effect of Particle Size on the Mechanical Behavior of Sand-Geotextile Composites", *Geotextiles and Geomembranes,* Vol. 12, pp. 255 – 273.

Attneave, F. (1954) "Some Information Aspects of Visual Perception", *Psychol. Rev*., Vol. 61, pp. 183-193.

Aurenhammer, Franz and Klein, Rolf (2000) *Voroni Diagrams* in Handbook of Computational Geometry, Sack, J.R. and Urrutia, J. (Eds.), Elsevier Science.

Avitzur, B. and Nakamura, Y. (1986) “Analytical Determination of Friction Resistance As a Function of Normal Load and Geometry of Surface Irregularities”, *Wear*, Vol. 107, pp. 367-383.

Avitzur, B., Eto, M., and Kay E. (1991) “Rolling vs. Sliding Friction”, *PED-Vol. 54/TRIB-Vol.2, Tribological Aspects in Manufacturing, ASME*, pp. 165-175.

Axen, N., Jacobson, S., and Hogmark, S. (1994) “Influence of Hardness of the Counterbody in Three-body Abrasive wear – an overlooked hardness effect”, *Tribology International*, Vol. 27, No. 4, pp. 233-243.

Barrett, P. J. (1980) “The Shape of Rock Particles, A Critical Review”, *Sedimentology,* Vol. 27, pp. 291-303.

Bauer, G. E. & Mowafy, Y. M. (1990) “The Effect of Grid Geometry and Aggregate Size on the Stress Transfer Mechanism”, *Proc. 4th International Conference on Geotextiles, Geomembranes, and Related Products* (Vol. 2), ed. G. D. Hoedt. Balkema, The Hauge, The Netherlands, p. 801.

Beddow, J. K. (1980). Particulate Science and Technology, Chemical Publishing Co., Inc, New York, N.Y., 725 pp.

Beddow, J. K., Hua, L., Vetter, A. F. and Carmichael, G. (1984) “Principles and Applications of Morphological Analysis in Particulate Technology”, *Powder Technology, Papers presented at the International Symposium on Powder Technology, Kyoto, Japan, Sept. 28-Oct. 1, 1981,* K. Iinoya, J. K. Beddow and G. Jimbo (Eds.), Hemisphere Publishing Corporation, McGraw-Hill International Book Company, 823 p.

Beddow, J. K., Nasta, M. D. and Philip, G. C. (1980) “Characteristics of Particle Signatures”, *Testing and Characterization of Powders and Fine Particles*, J. K. Beddow and T. P. Meloy (Eds.), Heyden, 195 p.

Bernier, T. and Landry, J.-A. (2003) “ A New Method for Representing and Matching Shapes of Natural Objects”, *Pattern Recognition*, Vol. 36, pp. 1711-1723.

Bhushan, B. (1999) Principles and Applications of Tribology, John Wiley & Sons, Inc., 1020 pp.

Bodziony, J. and Kraj, W. (1983) “On Certain Geometric Characteristics of A Single Convex Grain” *Advances In the Mechanics And The Flow Of Granular Materials,* Vol. 1, 1st Edition, Trans Tech Publications, Gulf Publishing Company.

Boulanger, J. (1992) “The “Motifs” Method: An Interesting Complement to ISO Parameters for Some Functional Problems”, *International Journal of Machine Tools & Manufacture*, Vol. 32, No. 1 / 2, pp. 203 – 209.

Bowden, F. P. and Tabor, D. (1950). The Friction and Lubrication of Solids, Part I, Clarendon Press, Oxford, UK.

Bowden, F. P. and Tabor, D. (1964). The Friction and Lubrication of Solids, Part II, Clarendon Press, Oxford University Press, Oxford, UK.

Bowen, P. (2002) "Particle Size Distribution Measurement from Millimeters to Nanometers and from Rods to Platelets", *Journal of Dispersion Science and Technology,* Vol. 23, No. 5, pp. 631-662.

Briggs, L. I., McCulloch, D. S. and Moser, F. (1962) "The Hydraulic Shape of Sand Particles", *Journal of Sedimentary Petrology,* Vol. 32, No. 4, pp. 646-656.

Briscoe, B. J. (1992) "Friction of Organic Polymers", *Fundamentals of Friction: Macroscopic and Microscopic Processes,* I. L. Singler and H. M. Pollock (Eds.), Kluwer, Dordrecht, The Netherlands, pp. 167-182.

Brumund, W. F. and Leonards, G. A. (1973) "Experimental Study of Static and Dynamic Friction between Sand and Typical Construction Materials", *Journal of Testing and Evaluation, JTEVA,* Vol. 1, No. 2, pp. 162 – 165.

Chetwynd, D.G. (1985) "Applications of Linear Programming to Engineering Metrology", Vol. 199, pp. 93-100.

Chetwynd, D.G., and Phillipson, P.H. (1980) "An Investigation of Reference Criteria Used in Roundness Measurement", *J. Phys. E. Sci. Instrum*, Vol. 13, pp. 530-538.

Church, T. (1968) "Problems Associated with the Use of the Ratio of Martin's Diameter to Feret's Diameter as A Profile Shape Factor", *Powder Technology,* Vol. 2, pp. 27-31.

Clark, H.McI. and Hartwich, R.B. (2001) "A Re-Examination of The 'Particle Size Effect' in Slurry Erosion", *Wear*, Vol. 248, pp. 147–161.

Clark, M. W. (1981) "Quantitative Shape Analysis: A Review", *Mathematical Geology,* Vol. 13, No. 4, pp. 303-320.

Cox, E.P., (1927) "A Method of Assigning Numerical and Percentage Values to the Degree of Roundness", *J. Paleontol. 1,* pp. 179-183.

Croften, M. W. (1885), *Encyclopedia Britannica*, 9,19,768.

Czarnecka, E. and Gillott, J. E. (1980) "Roughness of Limestone and Quartzite Pebbles by the Modified Fourier Method", *Journal of Sedimentary Petrology,* Vol. 50, pp. 857-868.

Danish, P.B. and Shunmugam, M.S. (1991) "An Algorithm for Form Error Evaluation Using the Theory of Discrete and Linear Chebyshev Approximations", *Comp. Meth. Appl. Mech. Eng.* Vol**.** 92**,** pp. 309–324.

Davies, R. (1975) "A Simple Feature-Space Representation of Particle Shape", *Powder Technology,* Vol. 12, pp. 111-124.

DeJong, J. T. (2001) “Investigation of Particulate-Continuum Interface Mechanisms and Their Assessment through a Multi-Friction Sleeve Penetrometer Attachment”, Ph.D. Thesis, School of Civil and Environmental Engineering, Georgia Institute of Technology, Atlanta, Georgia, USA, 353 pp.

DeJong, J. T., Frost, J. D., and Sacs, M. (2000) “Relating Quantitative Measures of Surface Roughness and Hardness to Geomaterial Interface Strength”, *GeoEng2000,* Australia, CD-ROM.

DeJong, J. T., Frost, J.D., and Saussus, D. R. (2002) “Measurement of Relative Surface Roughness at Particulate-Continuum Interfaces”, *ASTM Journal of Testing and Evaluation,* Vol. 30, No.1, pp. 8-19.

Diepenbroek, M., Bartholomä, A. and Ibbeken, H. (1992) “How Round Is Round? A New Approach to the Topic “Roundness by Fourier Grain Shape Analysis”, *Sedimentology,* Vol. 39, pp. 411-422.

Dietzsch, M., Papenfuß, K., Hartmann, T. (1998) “The MOTIF – Method (ISO 12085) – a Suitable Description for Functional, Manufactural and Metrological Requirements” *International Journal of Machine Tools & Manufacture*, Vol. 38, No. 5 – 6, pp. 625 – 632.

DIN 4762. Surface Roughness – Terms and Definitions, Deutsches Institut fur Normung, Berlin, 1989.

Dobkins, J. E., Jr. & Folk, R. L. (1970) “Shape Development on Tahiti-nui”, *Journal of Sedimentary Petrology”,* Vol. 40, pp. 1167-1203.

Dong, W.P., Sullivan, K. J. (1994) “Comprehensive Study of Parameters for Characterization Three-Dimensional Topography.IV. Parameters for Characterizing Spatial and Hybrid Properties”, *Wear*, Vol. 178, pp. 45-60.

Dong, W. P., Sullivan, P. J., Stout, K. J. (1994) “Comprehensive Study of Parameters for Characterizing Three-Dimensional Topography. III. Parameters for Characterizing Amplitude and Some Functional Properties”, *Wear,* Vol. 178, pp. 29-43.

Dove, J. E. and Frost, J. D. (1996) “A Method for Measuring Geomembrane Surface Roughness”, *Geosynthetics International,* Vol. 3, No. 3, pp. 369-392.

Dove, J. E. and Frost, J. D. (1999) “Peak Friction Behavior of Smooth Geomembrane–Particle Interfaces”, *ASCE Journal of Geotechnical and Geoenvironmental Engineering,* Vol. 125, No. 7, pp. 544-555.

Dove, J. E. and Harpring, J. C. (1999) “Geometric and Spatial Parameters For Analysis of Geomembrane/Soil Interface Behavior”, *Proc. Geosynthetics ’99,* Boston, MA, pp. 575-588.

Dove, J. E., Frost, J. D. and Dove, P.M. (1996) “Geomembrane Microtopography By Atomic Force Microscopy”, *Geosynthetics International,* Vol. 3, No. 2, pp. 227-245.

Dove, J. E., Frost, J.D., Han, J. and Bachus, R.C. (1997) “The Influence of Geomembrane Surface Roughness on Interface Strength”, *Proc. Geosynthetics ’97,* Vol. 2, pp. 863-876.

Dubuc, B., Zucker, S. W., Tricot, C., Quiniou, J. F. and Wehbi, D. (1989) “Evaluating the Fractal Dimension of Surfaces”, *Proceedings of the Royal Society London Series A*, Vol. 425, pp. 113–127.

Ebara, H., Fukuyama, N., Nakano, H., and Nakanishi, Y. (1992) “A Practical Algorithm for Computing the Roundness”, *IEICE Transactions on Information & Systems*, Vol. E75-D, No. 3, pp. 253-257.

Ehrlich, R. and Weinberg, B. (1970) “An Exact Method for Characterization of Grain Shape”, *Journal of Sedimentary Petrology,* Vol. 40, No. 1, pp. 205-212.

Estrin, Y., Arndt, S., Heilmaier, M. and Brechet, Y. (1999) “Deformation Behavior of Particle Strengthened Alloys: A Voronoi Mesh Approach”, *Acta mater*, Vol. 47, No. 2, pp. 595-606.

Fahl, C. F. (1982) “Motif Combination – A New Approach to Surface Profile Analysis” *Wear*, Vol. 83, pp. 165-179.

Finnie, I. (1960) “Erosion of Surfaces by Solid Particles”, *Wear,* Vol. 3, pp. 87-103.

Free, E. E. (1911) “The Movement of Soil Material By Wind”, *Bull. Div. Soils, U. S. Dep. Agric.,* Vol. 68.

Freeman, H. and Davis, L.S. (1977) “A Corner-Finding Algorithm for Chain-Coded Curves”, *IEEE Transactions on Computers*, Vol. C-26, pp. 297-303.

Frost, J. D. and Han, J. (1999) “Behavior of Interfaces between Fiber-Reinforced Polymers and Sands”, *Journal of Geotechnical and Geoenvironmental Engineering,* Vol. 125, No. 8, pp. 633-640.

Frost, J. D., Lee, S.W., and Cargill, P. E. (1999) “The Evolution of Sand Structure Adjacent to Geomembranes”, *Proc. Geosynthetics ’99 Conference,* Vol. 1, pp. 559-573.

Furuuchi, M. and Gotoh, K. (1992) “Shape Separation of Particles”, *Powder Technology*, Vol. 73, pp. 1-9.

Gangepain, J. J. and Roques-Carmes, C. (1986) “Fractal Approach to Two-Dimensional and Three-Dimensional Surface Roughness”, *Wear,* Vol. 109, pp. 119-126.

Ganti, S. and Bhushan, B. (1995) “Generalized Fractal Analysis and Its Application to Engineering Surfaces”, *Wear,* Vol. 180, pp. 17-34.

Gåhlin, R. and Jacobson, S. (1999) “The Particle Size Effect in Abrasion Studied by Controlled Abrasive Surfaces”, *Wear*, Vol. 224, pp. 118–125.

Gibson, J.J. (1950). The Perception of the Visual World. Houghton.

Gokhale, A. M. and Drury, W. J. (1990) “A General Method for Estimation of Fracture Surface Roughness: Part II. Theoretical Aspects”, *Metallurgical Transactions A,* Vol. 21A, pp. 1193-1199.

Gokhale, A. M. and Underwood, E. E. (1990) “A General Method for Estimation of Fracture Surface Roughness: Part I. Practical Considerations”, *Metallurgical Transactions a,* Vol. 21A, pp. 1201–1207.

Gokhale, A. M., and Underwood, E. E. (1990) “A General Method for Estimation of Fracture Surface Roughness: Part II. Theoretical Aspects.”, *Metallurgical Transactions A,* 21A, pp. 1193-1199.

Gore, G.J. and Gates, J.D. (1997) “Effect of Hardness On Three Very Different Forms of Wear”, *Wear*, Vol. 203-204, pp. 544-563.

Gorlenko, O.A. (1981) “Assessment of Surface Roughness Parameters and Their Independence”, *Precision Engineering,* Vol. 3, No. 2, pp. 105-108.

Gupta, L. and Srinath, M. D. (1987) “Contour Sequence Moments for the Classification of Closed Planar Shapes”, *Pattern Recognition,* Vol. 20, No. 3, pp. 267-272.

Hamblin, M. G. and Stachowiak, G. W. (1993) “Comparison of Boundary Fractal Dimension from Projected and Sectioned Particle Images. Part I—Technique Evaluation”, *Journal of Computer Assisted Microscopy*, Vol. 5, No. 4, pp. 291–300.

Hamblin, M. G. and Stachowiak, G. W. (1995) “A Multi-scale Measure of Particle Abrasivity”, *Wear,* Vol. 185, pp. 225-233.

Hamblin, M. G. and Stachowiak, G. W. (1995) “A Multi-scale Measure of Particle Abrasivity, and Its Relation to Two-body Abrasive Wear”, *Wear,* Vol. 190, pp. 190-196.

Hamblin, M. G. and Stachowiak, G. W. (1995) “Application of the Richardson Technique to the Analysis of Surface Profiles and Particle Boundaries”, *Tribology Letters*, Vol. 1, pp. 95–108.

Hamblin, M. G. and Stachowiak, G. W. (1996) “Description of Abrasive Particle Shape and Its Relation to Two-Body Abrasive Wear”, *Tribology Transactions,* Vol. 39, pp. 803-810.

Hamblin, M. G. and Stachowiak, G. W. (1997) “Description of Surface Abrasivity and Its Relation to Two-Body Abrasive Wear”, *Wear*, Vol. 206, pp. 69-75.

Hamblin, M.G. and Stachowiak, G. W. (1993) “Comparison of Boundary Fractal Dimension from Projected and Sectioned Particle Images. Part I – *Technique Evaluation*”, *Journal of Computer Assisted Microscopy,* Vol. 5, No. 4, pp. 291-300.

Hamrock, R. J. (1994). Fundamentals of Fluid Film Lubrication, McGraw-Hill Inc., New York, NY, 690 pp.

Hasegawa, M., Liu, J., Okuda, K., Nunobiki, M. (1996) “Calculation of the Fractal Dimensions of Machined Surface Profiles”, *Wear,* Vol. 192, pp. 40-45.

Hawkins, A. E. (1993). The Shape of Powder-Particle Outlines, Research Studies Press Ltd., John Wiley & Sons Inc, 150 pp.

Hebb, D.O. (1949). The Organization of Behavior, Wiley, New York.

Hentschel, M.L. and Page, N.W. (2003) “Selection of Descriptors for Particle Shape Characterization”, *Particle and Particle Systems Characterization,* Vol. 20, pp. 25-38.

Heywood, H. (1947) “Symposium on Particle Size Analysis, *Institute of Chemical Engineers*” Suppl. 25, 14, 55.

Hoffman, D. D. and Richards, W. A. (1984) “Parts of Recognition”, *Cognition*, Vol. 18, pp. 65-96.

Hokkirigawa, K. and Kato, K. (1988) “The Effect of Hardness On The Transition Of The Abrasive Wear Mechanisms Of Steels”, *Wear*, Vol. 123, pp. 241-251.

Horng, J. –H and Li, J.T. (2001) “A Dynamic Programming Approach for Fitting Digital Planar Curves with Line Segments and Circular Arcs”, *Pattern Recognition Letters*, Vol. 22, pp. 183-197.

Horng, J. –H and Li, J.T. (2002) “An Automatic and Efficient Dynamic Programming Algorithm for Polygon Approximation of Digital Curves”, *Pattern Recognition Letters,* Vol. 23, No. 1-3, pp. 171-182.

Hryciw, R. D. and Irsyam (1993), M. “Behavior of Sand Particles Around Rigid Ribbed Inclusions During Shear”, *Soils and Foundations,* Vol. 33, No. 3, pp. 1–13.

Huang, J. (1999) “An Exact Solution for the Roundness Evaluation Problems”, *Precision Engineering*, Vol. 23, pp. 2-8.

Huang,S.C. and Sun, Y.N. (1999) “Polygonal Approximation using Generic Algorithms”, *Pattern Recognition*, Vol. 32, pp. 1409-1420.

Hyslip, J. P. and Vallejo, L. E. (1997) “Fractal Analysis of the Roughness and Size Distribution of Granular Materials”, *Engineering Geology,* Vol. 48, pp. 231-244.

Illenberger, W. K. (1991) “Pebble Shape (And Size)”, *Journal of Sedimentary Petrology,* Vol. 61, No. 5, pp. 756-767.

Inesta, J.M., Buendia, M., and Sarti, M.A. (1998) “Reliable Polygonal Approximation of Imaged Real Objects Through Dominant Point Detection”, *Pattern Recognition*, Vol. 31, No. 6, pp. 685-697.

Ishai, I. And Tons, E. (1977) “Concept and Test Method for a Unified Characteriztaion of the Geometric Irregularity of Aggregate Particles”, *Journal of Testing and Evaluation,* JTEVA, Vol. 5, No. 1, pp. 3-15.

Ishigaki, H. & Kawaguchi, I. (1981) “A Conversion Method From the E System to the M System in Measuring Surface Roughness”, *Wear*, Vol. 70, pp. 295 –301.

ISO 4287. Surface roughness - Terminology - Part I: Surface and Its Parameters, ISO, Geneva, 1984.

ISO/R 1101-1983. Technical drawings – Geometrical Tolerancing- Guidelines, ISO, Geneva, 12-01.

Janoo, V. C. (1998) “Quantification of Shape, Angularity, and Surface Texture of Base Course Materials”, *U.S. Army Cold Regions Research and Engineering Laboratory*, Special Report 98-1, 28 pp.

Johnson, K. L. (1985). Contact Mechanics, Clarendon Press, Oxford, UK.

Jones, D.R.V. and Dixon, N. (1998) “Shear Strength Properties of Geomembrane/Geotextile Interfaces”, *Geotextiles and Geomembranes*, Vol. 16, pp. 45-71.

Juran, I., Knockenmus, G., Acar, Y. B. & Arman, A. (1988) “ Pull-out Response of Geotextiles and Geogrids (synthesis of available experimental data)” *Geotechnical Special Publication* (No. 18), R. D. Holtz (Ed.). ASCE, New York, USA, pp. 92 – 111.

Kaiser, M.J. and Morin, T.L. (1994) “Centers, Out-of-Roundness Measures, and Mathematical Programming*”, Computers Ind. Engng*, Vol. 26, No. 1, pp. 35-54.

Kaye, B. H. (1978) “Specification of the Ruggedness and/or Texture of a Fine Profile by its Fractal Dimension”, *Powder Technology,* Vol. 21, pp. 1-16.

Kaye, B. H. (1989). A Random Walk Through Fractal Dimensions, VCH, Verlagsgesellschaft, Weinheim, Germany, 1989.

Kaye, B.H., Clark, G.G., and Liu, Y. (1992) “Characterizing The Structure of Abrasive Fine Particles”, *Particle and Particle System Characterization*, Vol. 9, pp. 1-8.

Khruschov, M. M. (1957) “Resistance of Metals to Wear by Abrasion-As Related to Hardness”, *Proc. Conf. On Lubrication and Wear*, Institution of Mechanical Engineers, London, pp. 655.

Khruschov, M. M. (1974) “Principles of Abrasive Wear”, *Wear*, Vol. 28, pp. 69-88.

King, T. G. and Spedding, T. A. (1982) “On the Relationship between Surface Profile Height Parameters”, *Wear,* Vol. 83, pp. 91-108.

King, T. G. and Spedding, T. A. (1983) “Towards a Rational Surface Profile Characterization System”, *Precision Engineering,* Vol. 5, No. 4, pp. 153-160.

Kramer, I.R. and Demer, L.J. (1961) “The Effect of Surface Removal on the Plastic Behavior of Aluminum Single Crystals”, *Metallurgical Society of AIME - Transactions*, Vol. 221, pp. 780 – 786.

Krause, H. and Tackenberg, W. (1980) “The Influence Of Hardness Difference On The Frictional and Wear Behavior of Steel/copper Alloy Pairs in Plane Sliding Friction Under Mixed Friction Conditions, *Wear*, Vol. 64, pp. 291-302.

Krumbein, W. C. (1941) “Measurement and Geological Significance of Shape and Roundness of Sedimentary Particles”, *Journal of Sedimentary Petrology,* Vol. 11, No. 2, pp. 64-72.

Krumbein, W. C. and Pettijohn, F. J. (1902). Manual of Sedimentary Petrography, Kirtley F. Mather (Eds.), Appleton-Century Crofts, Inc., New York, 549 p.

Lai, K. and Wang, J. (1988) “A Computational Geometry Approach to Geometric Tolerancing”, *6th North American Manufacturing Research Conf.*, pp. 376-379.

Le, V. and Lee, D.T. (1991) “Out-of-roundness Problem Revisited”, *IEEE Transactions on Pattern Analysis & Machine Intelligence*, Vol. 13, pp. 217-223.

Leavers,V.F. (2000) “An Active Angularity Factor for The Characterization of Abrasive Particles”, *Wear*, Vol. 239, pp. 102-110.

Lee, G. Y., Dharan, C.K.H., and Ritchie, R.O. (2002) “A Physically-Based Abrasive Wear Model for Composite Materials”, *Wear*, Vol. 252, pp. 322-331.

Lee, S.W. (1998) “Influence of Surface Topography on Interface Strength and Counterface Soil Structure.” Ph.D. Thesis, School of Civil and Environmental Engineering, Georgia Institute of Technology, Atlanta, Georgia, USA, 336 pp.

Lees, G. (1964) “A New Method for Determining Angularity of Particles”, *Sedimentology,* Vol. 3, pp. 2-21.

Leyton, M. (1989) “Inferring Casual History From Shape”, *Cognitive Science*, Vol. 13, pp. 357-387.

Lindner, H., Kleinebudde, P. (1993) “Anwendung der Automatischen Bildanalyse zur Characterisierung von Pellets”, *Pharm. Ind,* Vol. 55, pp. 694-701.

Ling, F. F. (1989) “The Possible Role of Fractal Geometry in Tribology”, *Tribology Transactions,* Vol. 32, No. 4, pp. 497–505.

Loncaric, S. (1998) “A Survey of Shape Analysis Techniques”, *Pattern Recognition*, Vol. 31, pp. 983-1001.

Luerkens, D. W., Beddow, J. K. and Vetter, A. F. (1982) “Morphological Fourier Descritors”, *Powder Technology,* Vol. 31, pp. 209-215.

Majumdar, A. and Bhushan, B. (1990) “Role of Fractal Geometry in Roughness Characterization and Contact Mechanics of Surfaces”, *Transactions ASME Journal of Tribology*, Vol. 112, pp. 205–216.

Majumdar, A. and Bhushan, B. (1990) “Role of Fractal Geometry in Roughness Characterization and Contact Mechanics of Surfaces”, *Journal of Tribology,* Vol. 112, pp. 205-216.

Majumdar, A. and Tien, C. L. (1990) “Fractal Characterization and Simulation of Rough Surfaces”, *Wear*, Vol. 136, pp. 313–327.

Markwick, A. H. D. (1937) “The Shape of Crushed Stone and Gravel and Its Measurement”, *Chem. Ind.,* Vol. 56, pp. 206-213.

Masad, E., Olcott, D., White, T. and Tashman, L. (2001) “Correlation of Imaging Shape Indices of Fine Aggregate with Asphalt Mixture Performance”, *Transportation Research Board, 80th Annual Meeting, January 7-11, 2001, Washington, D. C., Paper No. 01-2132.*

Matsuyama, T. and Yamamoto, H. (2004) “Particle Shape and Laser Diffraction: A Discussion of the Particle Shape Problem”, *Journal of Dispersion Science and Technology,* Vol. 25, No. 4, pp. 409-416.

McCarthy, C. J. (1976) “Recent Advances in the characterization of particulates using automatic evaluation of shape descriptors”, *Microstructural Science,* Vol. 4, pp. 339-346.

Medalia, A. I. (1970) “Dynamic Shape Factors of Particles”, *Powder Technology,* Vol. 4, pp. 117-138.

Meloy, T. P. (1977) “A Hypothesis for Morphological Characterization of Particle Shape and Physiochemical Properties”, *Powder Technology,* Vol. 16, pp. 233-253.

Misra, A. and Finnie, I. (1981) “On The Size Effect in Abrasive and Erosive Wear”, *Wear*, Vol. 65, pp. 359-373.

Mora, C.F. and Kwan, A.K.H. (2000) “Sphericity, Shape Factor, and Convexity Measurement of Coarse Aggregate for Concrete Using Digital Image Processing”, *Cement and Concrete Research*, Vol. 30, pp. 351-358.

Mummery, L. Surface texture analysis: the handbook, Hommelwerke, Muhlhausen, 1990.

Murthy, T.R.S., and Abdin, S.Z., (1980) “Minimum Zone Evaluation of Surface”, *Int. J. Machine Tool Design & Research*, Vol. 20, No. 2, pp. 123-126.

Murthy, T.S.R. (1986) “A Comparison of Different Algorithms for Circularity Evaluation”, *Precision Engineering*, Vol. 8, pp. 19-23.

Neumann, R. and Teisseron, G. (2002) “Extraction of Dominant Points by Estimation of the Contour Fluctuations”, *Pattern Recognition,* Vol. 35, pp. 1447-1462.

Nouguier-Lehon, C., Cambou, B., and Vincens, E. (2003) “Influence of Particle Shape and Angularity on the Behavior of Granular Materials: A Numerical Analysis”, *International Journal for Numerical and Analytical Methods in Geomechanics,* Vol. 27, pp. 1207-1226.

Novaski, O. and Barczak, A.L.C. (1997) “Utilization of Voronoi diagrams for Circularity Algorithms”, *Precision Engineering*, Vol. 20, No. 3, pp.188-195.

O’Rourke, T. D., Druschel, S. J. and Netravali, A. N. (1990) “Shear Strength Characteristics of Sand-Polymer Interfaces”, *ASCE Journal of Geotechnical and Geoenvironmental Engineering,* Vol. 116, No. 3, pp. 451 – 469.

Orford, J. D. and Whalley, W. B. (1983) “The Use of The Fractal Dimension to Quantify The Morphology of Irregular-Shaped Particles”, *Sedimentology,* Vol. 30, pp. 655-668.

Oxford English Dictionary, Oxford, 1961.

Paikowsky, G., Player, C. M. and Connors, P. J. (1995) “A Dual Interface Apparatus for Testing Unrestricted Friction of Soil Along Solid Surfaces”, *Geotechnical Testing Journal,* GTJODJ, Vol. 18, No. 2, pp. 168-193.

Palasamudram, S.L. and Bahadur, S. (1997) “Particle Characterization for Angularity and the Effects of Particle Size and Angularity on Erosion In A Fluidized Bed Environment”, *Wear*, Vol. 203-204, pp. 455-463.

Pavlidis, T. (1978) “A Review of Algorithms for Shape Analysis”, *Computer Graphics Image Process*, Vol. 7, pp. 243-258.

Pei, S. C. and Horng, J. H. (1995) “Fitting Digital Curve Using Circular Arcs” *Pattern Recognition,* Vol. 28, No. 1, pp. 107-116.

Pei, S.C. and Horng, J.H. (1996) “Optimum Approximation of Digital Planar Curves Using Circular Arcs”, *Pattern Recognition*, Vol. 29, No. 3,pp. 383-388.

Pellegrin, D. V. De and Stachowiak, G.W. (2002) “Assessing the Role of Particle Shape and Scale In Abrasion Using “Sharpness Analysis”, Part I. Technique Development”, *Wear*, Vol. 253, pp. 1016-1025.

Pellegrin, D. V. De. and Stachowiak, G.W. (2001) “A New Technique for Measuring Particle Angularity Using Cone Fit Analysis”, *Wear*, Vol. 247, pp. 109-119.

Pentland, A. (1927) “A Method of Measuring the Angularity of Sands”, *Proceedings and Transactions of the Royal Society of Canada,* Vol. 21.

Pintaude, G., Tschiptschin, A.P., Tanaka, D.K. and Sinatora, A. (2001) “The Particle Size Effect on Abrasive Wear of High-Chromium White Cast Iron Mill Balls”, *Wear*, Vol. 250, pp. 66-70.

Podczeck, F. (1997) “A Shape Factor to Assess the Shape of Particles Using Image Analysis”, *Powder Technology,* Vol. 93, pp. 47-53.

Podczeck, F. and Newton, J. M. (1995) “The Evaluation of a Three-Dimensional Shape Factor for the Quantitative Assessment of the Sphericity and Surface Roughness of Pellets”, *International Journal of Pharmacology,* Vol. 124, pp. 253-259.

Podczeck F., Rahman S.H., and Newton J.M. (1999) “Evaluation of a Standardized Procedure to Assess the Shape of Pellets using Image Analysis”, *International Journal of Pharmacology,* Vol. 19, pp. 123-138.

Pons, M.N., Vivier, H., Belaroui, K., Bernard-Michel, B., Cordier, F., Oulhana, D., and Dodds, J.A. (1999) “Particle Morphology: from Visualisation to Measurement”, *Powder Technology,* Vol. 103, pp. 44-57.

Poon, C.Y. and Bhushan, B. (1995) “Comparison of Surface Roughness Measurements By Stylus Profiler, AFM and Non-Contact Optical Profiler”, *Wear*, Vol. 190, pp. 76-88.

Potyondy, J. G. (1961) “Skin Friction between Various Soils and Construction Materials”, *Geotechnique,* Vol. 11, pp. 339 – 353.

Powers, M. C. (1953) “A New Roundness Scale for Sedimentary Particles”, *Journal of Sedimentary Petrology,* Vol. 23, pp. 117-119.

Preparata, F.P. and Shamos M.I. (1985). Computational Geometry An Introduction, Springer-Verlag, 390 pp.

Radhakrishnan, V. (1970) “Effect of Stylus Radius on the Roughness Values Measured with Tracing Stylus Instruments”, *Wear*, Vol. 16, pp. 325 – 335.

Radhakrishnan, V. (1980) “Surface Profile Analysis by Changing the Stylus Radius” *Indian Journal of Technology*, Vol. 18, pp.173 –178.

Rice, S.L., Nowotny, H., and Wayne S.F. (1985) “Specimen-Counterface Bulk Hardness Effects in Impact Wear of 17-4 Ph Steel Pairs”, *Wear*, Vol. 103, pp. 175-185.

Richards,W. and Hoffman, D.(1985) “Codon Constraints on Closed 2-D Shapes”, *Computer Vision Graphics Image Process*, Vol. 31, pp. 265-281.

Richardson, R.C.D. (1968) “The Wear of Metals by Relatively Soft Abrasives”, *Wear*, Vol. 11, pp. 245.

Rigney, D. A. (1994) “The Roles of Hardness In The Sliding Behavior of Materials”, *Wear*, Vol. 175, pp. 63-69.

Riley, N. A. (1941) “Projection Sphericity”, *Journal of Sedimentary Petrology,* Vol. 11, pp. 94-97.

Rosenfeld, A. and Wezska, J.S. (1975) “An Improved Method of Angle Detection on Digital Curves”, *IEEE Transactions on Computers*., Vol. C-24, pp. 940-941.

Rosin, P.L. (1997) “Techniques for Assessing Polygonal Approximation of Curves”, *IEEE Transactions on Pattern Analysis and Machine Intelligence*, Vol. 19, pp. 1393-1394.

Roy, U. and Zhang, X. (1992) “Establishment of A Pair of Concentric Circles with the Minimum Radial Separation for Assessing Roundness Error”, *Computer Aided Design*, Vol. 24, No. 3, pp. 161-168.

Roy, U.R. and Zhang, X., (1994) “Development and Application of Voronoi Diagrams in the Assessment of Roundness Error in an Industrial Environment” *Computers & Industrial Engineering*, Vol. 26, pp. 11–26.

Russ, J. C. (1992) “Characterizing and Modelling Fractal Surfaces”, *Journal of Computer Assisted Microscopy*, Vol. 4, pp. 73–126.

Russ, J. C. (1994). Fractal Surfaces, Plenum Press, New York.

Salotti, M. (2001) “An Efficient Algorithm for the Optimal Polygonal Approximation of Digital Curves”, *Pattern Recognition Letters*, Vol. 22, pp. 215-221.

Salotti, M. (2002) “Optimal Polygonal Approximation of Digitized Curves Using The Sum of Square Deviations Criterion”, *Pattern Recognition*, Vol. 35, pp. 435-443.

Samuel, G.L., and Shunmugam, M.S. (2000) “Evaluation of Circularity from Coordinate and Form Data Using Computational Geometric Techniques”, *Precision Engineering*, Vol. 21, pp. 251-263.

Sander, M. (1991). A Practical guide to the assessment of surface texture, Feinpruf Perthen, Gottingen, 1991.

Sarkar, B., Singh, L.K. and Sarkar, D. (2003) “Approximation of Digital Curves With Line Segments and Circular Arcs Using Genetic Algorithms”, *Pattern Recognition Letters*, Vol. 24, No. 15, pp. 2585-2595.

Sarkar, D. (1993) “A Simple Algorithm for Detection of Significant Vertices for Polygonal Approximation of Chain-Coded Curves”, *Pattern Recognition Letters*, Vol. 14, pp. 959-964.

Schneiderhöhn, P. (1954) “Eine vergleichende Studie über Methoden zur quantitativen Bestimmung von Abrundung und Form an Sandkörnern”, *Heidelb. Beitr. Miner. Petrogr.,* Vol. 4, pp. 172-191.

Schneiderhöhn, P. (1954) “Eine vergleichende Studie über Methoden zur quantitativen Bestimmung von Abrundung und From an Sandkörnern”, *Heidelberger Beiträge zur Mineralogie und Petrographie*, Vol. 4, pp. 172-191.

Schwarcz, H. P. and Shane, K. C. (1969) “Measurement of Particle Shape by Fourier Analysis”, *Sedimentology,* Vol. 13, pp. 213-231.

Scott, P. J. (1992) “The Mathematics of Motif Combination and Their Use for Functional Simulation”, *International Journal of Machine Tools & Manufacture,* Vol. 32, No. 1/2, pp. 69-73.

Scott, D. M. (2003) “Characterizing Particle Characterization”, *Particle and Particle System Characterization,* Vol. 20, pp. 305-310.

Shunmugam, M. S. & Radhakrishnan, V. (1976) “An Analysis of the Reference Lines of the Surface Profile and Its True Replica”, *Wear*, Vol. 40, pp. 155-163.

Shunmugam, M. S. & Radhakrishnan, V. (1976) “Comparison of Different Methods for Computing the Two-Dimensional Envelope for Surface Finish Measurements”, *Computer Aided Design*, Vol. 8, No. 2, pp. 89–93.

Shunmugam, M. S. (1987) “Comparison of Motif Combination with Mean Line and Envelope Systems Used for Surface Profile Analysis”, *Wear*, Vol. 117, pp. 335-345.

Shunmugam, M.S. (1987) “New Approach for Evaluating Form Errors of Engineering Surfaces”, *Computer Aided Design*, Vol. 19, pp. 368-374.

Sneed, E. D. & Folk, R. L. (1958) “Pebbles in The Lower Colorado River, Texas, A Study In Particle Morphogenesis”, *Journal of Geology,* Vol. 66, pp. 114-150.

Sorby, H. C. (1880) “On the Structure and Origin of Non-Calcareous Stratified Rocks”, *Q. J. Geol. Soc. Lond*., Vol. 36, pp. 46-92.

Stachowiak, G. W. (1998) “Numerical Characterization of Wear Particles Morphology and Angularity of Particles and Surfaces”, *Tribology International,* Vol. 31, No 1-3, pp. 139-157.

Stachowiak, G. W. (2000) “Particle Angularity and Its Relationship to Abrasive and Erosive Wear”, *Wear,* Vol. 241, pp. 214-219.

Stachowiak, G. W. and Hamblin, M. G. (1995) “Application of Fractals - The Description of Shape of The Particles Found In Tribological Systems”, *Mechanical Engineering Transactions, Journal of the Institute of Engineers Australia,* ME 20, No. 2, pp. 127-136.

Stachowiak, G. W. and Podsiadlo, P. (1999) “Surface Characterization of Wear Particles”, *Wear,* Vol. 225-229, pp. 1171-1185.

Stachowiak, G. W. and Podsiadlo, P. (2001) “Characterization and Classification of Wear Particles and Surfaces”, *Wear,* Vol. 249, pp. 194-200.

Stachowiak, G. W. and Podsiadlo, P. (2004) “Classification of Tribological Surfaces”, *Tribology International XX,* Vol. 37, No. 2, pp. 211-217.

Stockham, J. D. (1977) “What Is Particle Size: The Relationship Among Statistical Diameters”, *Particle Size Analysis,* J. D. Stockham and E. G. Fochtman (Eds.), Ann Arbor Science Publishers Inc., 140 pp.

Stout, K. J., Sullivan, P. J., Dong, W.P., Mainsah, E., Lou, N., Mathia, T., Zahouani, H.(1993) “The Development of Methods for the Characterization Roughness in

Three Dimensions", Commission of the European Communities, Directorate General XII, Science, Research and Development, Report EUR 15178 EN.

Sukumaran, B. & Ashmawy, A. K. (2001) "Quantitative Characterization of the Geometry of Discrete Particles", *Géotechnique,* Vol. 51, No. 7, pp. 619-627.

Swanson, P. A. (1984) "The Measurement of Abrasive Particle Shape and Its Effect on Wear", *ASLE Transactions,* Vol. 28, No. 2, pp. 225-230.

Swanson, P.A. and Vetter, A.F. (1984) "The Measurement of Abrasive Particle Shape and Its Effect on Wear", *ASLE Transactions*, Vol. 28, No.2, pp. 225-230.

Teh, C. and Chin, R.T. (1989) "On the Detection of Dominant Points on Digital Curves", *IEEE Transactions on Pattern Analysis and Machine Intelligence*, Vol. 11, No. 8, pp. 859-872.

Tholath, J. and Radhakrishnan, V. (1999) "Three-Dimensional Filtering of Engineering Surfaces Using Envelope System", *Precision Engineering,* Vol. 23, pp. 221-228.

Thomas, T. R. (1981) "Characterization of Surface Roughness", *Precision Engineering*, Vol. 3, No. 2, pp. 97-104.

Thomas, T. R. (1998) "Trends in Surface Roughness", *International Journal of Machine Tools & Manufacture,* Vol. 38, No. 5-6, pp. 405-411.

Thomas, T. R. (1999). Rough Surfaces, Second Edition, Imperial College Press, 278 pp.

Thomas, T. R. and Charlton, G. (1981) "Variation of Roughness Parameters on Some Typical Manufactured Surfaces", *Precision Engineering,* Vol. 3, No. 2, pp. 91-96.

Thomas, T.R., editor (1982). Rough Surfaces, Longman, New York, 260 pp.

Torrance, A. A. (1981) "A New Approach To The Mechanics of Abrasion", *Wear*, Vol. 67, pp. 233.

Torrance, A.A. (1981) "An Explanation of Hardness Differential Needed for Abrasion", *Wear*, Vol. 68, pp. 263-266.

Uesugi, M. & Kishida, H. (1986b) "Frictional Resistance at Yield between Dry Sand and Mild Steel." *Soils and Foundations,* Vol. 26, No. 4, pp. 139-149.

Uesugi, M. and Kishida, H. (1986a), "Influential Factors of Friction between Steel and Dry Sands", *Soils and Foundations,* Vol. 26, No. 2, pp. 33- 46.

Uesugi, M. and Kishida, H. (1986b), "Frictional Resistance at Yield between Dry Sand and Mild Steel", *Soils and Foundations,* Vol. 26, No. 4, pp. 139 - 149.

Uesugi, M., Kishida, H. and Tsubakihara, Y. (1988) “Behavior of Sand Particles in Sand-Steel Friction”, *Soils and Foundations,* Vol. 28, No. 1, 107 – 118.

Uesugi, M., Kishida, H. and Uchikawa, Y. (1990) “Friction Between Dry Sand and Concrete Under Monotonic and Repeated Loading”, *Soils and Foundations,* Vol. 30, No. 1, pp. 115-128.

Vaid, Y.P. and Rinne, N. (1995) “Geomembrane Coefficients of Interface Friction”, *Geosynthetics International,* Vol. 2, No. 1, pp. 309–325.

Vallejo, L. E. (1995) “Fractal Analysis of Granular Materials”, *Géotechnique,* Vol. 45, No. 1, pp. 159-163.

Vallejo, L.E. and Zhou, Y. (1995) “Fractal Approach to Measuring Roughness of Geomembranes”, *Journal of Geotechnical Engineering,* Vol. 121, No. 5, pp. 442-446.

Vandenberg, S. and Osborne, C. F. (1992) “Digital Image Processing Techniques, Fractal Dimensionality and Scale-Space Applied to Surface Roughness”, *Wear*, Vol. 159, pp. 17–30.

Verspui, M.A., Velden, P. van der, and Slikkerveer, P.J. (1996) “Angularity Determination of Abrasive Powders”, *Wear*, Vol. 199, pp. 122-126.

von Weingraber, H. (1972) “Suitability of the Envelope Line as a Reference Standard For Measuring Roughness”, *Microtechnic,* Vol. XI. No. 1.

Wadell, H. (1932) “Volume, Shape, and Roundness of Rock Particles”, *Journal of Geology*, Vol. 40, pp. 443-451.

Wadell, H. (1933) “Sphericity and Roundness of Rock Particles”, *Journal of Geology*, Vol. 41, pp. 310-331.

Wadell, H. (1934) “Shape Determinations of Large Sedimental Rock Fragments”, *Pan-Am. Geol.,* Vol. 61, pp. 187-220.

Wadell, H. (1935) “Volume, Shape and Roundness of Quartz Particles”, *Journal of Geology,* Vol. 43, pp. 250-279.

Wang, L.B., Lai, J.S., and Frost, J.D. (1997) “Fourier Morphological Descriptors of Aggregate Profiles”, *Proceedings of Engineering Foundation Conference on “Imaging Technologies: Techniques and Applications in Civil Engineering”,* Davos, ASCE, pp. 76 – 87.

Wentworth, C. K. (1919) “A Laboratory and Field Study of Cobble Abrasion”, *Journal of Geology,* Vol. 40, 507-521.

Wentworth, C. K. (1933) “The Shapes of Rock Particles: A Discussion”, *Journal of Geology,* Vol. 41, pp. 306-309.

Wertheimer, M. (1923) *Laws of Organization in Perceptual Forms* in A Source Book of Gestalt Psychology, W.D. Ellis (Eds.), Harcourt Brace, Jovanovic.

Whitehouse, D. J. (1982) “The Parameter Rash - Is There a Cure?”, *Wear,* Vol. 83, pp. 75-78.

Williams, J.A. (1996). Engineering Tribology, Oxford Science Publications, New York, 488 pp.

Winkelmolen, A. M. (1982) “Critical Remarks on Grain Parameters, with Special Emphasis on Shape”, *Sedimentology,* Vol. 29, pp. 255-265.

Winkelmolen, A. W. (1971) “Rollability, A Functional Shape Property of Sand Grains”, *Journal of Sedimentary Petrology,* Vol. 41, No. 3, pp. 703-714.

Wu, W. and Wang, M.J. (1993) “Detecting the Dominant Points by the Curvature-Based Polygonal Approximation”, *Engin. Graphical Models and Image Processing*, Vol. 55, No. 2, pp. 79-88.

Wu, Wen-Yen (2003) “Dominant Point Detection Using Adaptive Bending Value”, *Image and Vision Computing,* Vol. 21, pp. 517-525.

Xie Y. and Bhushan, B. (1996) “Effects of Particle Size Polishing Pad and Contact Pressure in Free Abrasive Polishing”, *Wear*, Vol. 200, pp. 281–295.

Ye, Qin-Zhong (1995) “A Fast Algorithm for Convex Hull Extraction in 2D Images”, *Pattern Recognition Letters,* Vol. 16, pp. 531-537.

Yeralan, S. and Ventura, J.A. (1988) “Computerized Roundness Inspection”, *Int. J. Prod. Res*., Vol. 26, No. 12, pp. 1921-1935.

Yeralan, S. and Ventura, J.A. (1989) “The Minimax Center Estimation Problem for Automated Roundness Inspection”, *European Journal of Operational Research,* Vol. 41, pp. 64-72.

Yin, P.Y. (1998) “A New Method for Polygonal Approximation Using Genetic Algorithms”, *Pattern Recognition Letters*, Vol. 19, pp. 1017-1026.

Yoshimi, Y. and Kishida, T. (1981) “Friction between Sand and Metal Surfaces”, *Proc. 10th International Conference on Soil Mechanics and Foundation Engineering,* Stockholm, Sweden, Vol. 1, pp. 831 – 834.

Yudhbir and Abedinzadeh, R. (1991) “Quantification of Particle Shape and Angularity Using the Image Analyzer”, *Geotechnical Testing Journal*, GTJODJ, Vol. 14, No. 3, pp. 296-308.